2019

DESIGN AND SYNTHESIS OF MOLECULAR PROBES FOR MEDICAL AND ENVIRONMETAL APPLICATIONS

Payagala Udawattage Ashvin Iresh Fernando
University of Rhode Island, ashvin89@live.com

DESIGN AND SYNTHESIS OF MOLECULAR PROBES FOR MEDICAL AND ENVIRONMETAL APPLICATIONS

BY

PAYAGALA UDAWATTAGE ASHVIN IRESH FERNANDO

A DISSERTATION SUBMITTED IN PARTIAL FULFILLMENT OF THE

REQUIREMENTS FOR THE DEGREE OF

DOCTOR OF PHILOSOPHY

IN

CHEMISTRY

UNIVERSITY OF RHODE ISLAND

2019

DOCTOR OF PHILOSOPHY DISSERTATION

OF

PAYAGALA UDAWATTAGE ASHVIN IRESH FERNANDO

APPROVED:

Dissertation Committee:

Major Professor Brenton DeBoef

Mindy Levine

Al Bach

Nasser H. Zawia
DEAN OF THE GRADUATE SCHOOL

UNIVERSITY OF RHODE ISLAND

2019

ABSTRACT

The main aim of this dissertation was to design and synthesize molecular probes with ease to be used in medical and environmental applications. The first chapter focuses on a novel pseudo-rotaxane probe that can be used in ^{129}Xe imaging, which was synthesized using commercially available cyclodextrin moieties with a one-step reaction. This is probe can be synthesized in high yields and results in an acceptable level of hyperCEST depletion percentage. The second chapter showcases pillararenes as a potential candidate for ^{129}Xe imaging. In addition, this chapter discusses the aid of a computational programs to design the supramolecular scaffold before the synthesis. The third chapter is an extension of the first chapter, which focuses on designing rotaxanes probes, which are interlocked molecular structures. Furthermore, these novel cyclodextrin based rotaxanes were able to capture a positively charged guest which gives an access point to use these as a potential drug delivery agent. Chapter 4 describes on a novel supramolecular scaffold that is synthesized using a co-pillararene. This fluorescent co-pillararene is capable of switching from a self-inclusion form to an open form via temperature, solvent and external guests, which makes this pillararene an excellent molecular switch. Chapters 5 and 6 elaborate the use of water-soluble pillararene structures in toxicant removal via host-guest inclusion phenomena and self-aggregation with the use of commercially existing double-stranded DNA. Chapter 7 deviates from the supramolecular regime and discusses the development of novel antibiotic drug molecules and their novel functionalization to increase their potency.

ACKNOWLEDGMENTS

Firstly, I would like to express my sincere gratitude to my advisor Prof. Brenton DeBoef for the continuous support of my Ph.D. study and related research, for his patience, motivation, and immense knowledge. His guidance helped me in all the time of research and writing of this thesis. I could not have imagined having a better advisor and mentor for my Ph.D. study. Also, he gave me the full freedom to pursue research leads and helped me to be an independent researcher. This opened me up to multiple research collaborations and exposed me into the massive world of chemistry. I also must mention that one of the most exciting things I have done is brainstorming ideas, and most of these ideas came out by brainstorming in Brenton's office. So, I am very much grateful for that, due to that made me who I am today which is an Organic Chemist who would always think out of the box. Also, I must thank my supervisor for allowing me to participate in multiple conferences such as ACS meetings, XeMAT and Gordon Conferences. Participating in these conferences helped me a lot to think in ways I never thought of thinking about organic chemistry.

Besides my advisor, I would like to thank the rest of my thesis committee: Prof. Mindy Levine, Prof. Al Bach, Prof. Yana Reshetnyak and Prof. Jie Shen for their insightful comments and encouragement, but also for the hard questions which incented me to widen my research from various perspectives.

My sincere thanks also go to Prof. Jason Dwyer, Prof. Mindy Levine, Prof. Jie Shen, Prof. Steve Gregory Prof. Matthew Kiesewetter and Prof. Dugan Hayes who provided me an opportunity to work with them in multiple research collaborations and gave access to their laboratories and research facilities. Without their precious support, it would not be possible to conduct these diverse research projects.

I would like to acknowledge especially, Prof. ville-veikko telkkito inviting me to the University of Oulu, Finland to work with his research group for two weeks in Xenon MRI based research work. It was an absolute delight to work with him and his highly qualified research team.

Furthermore, I would like to thank Scott Karas for being a fantastic team member and working long nights in the lab with me and making it fun to work. I also want to extend my gratitude to Brianna Peloquin, John Christy, Samantha Donahue, Paul Cesana, Adrianna Mendieta, Cassie Chartier, Marina Carro and Max Zavell. These Undergraduate students helped me in numerous ways from running multiple reactions to analyzing data. Without their dedicated work ethic, I would not have been able to perform all these projects. Furthermore, I want to extend my thank you notes for Prof. William Euler and Prof. Sze Yang in helping me understand complex chemistry topics.

I also want to thank my fellow lab mates Anita Oppong, David Robinson, Lauren Seveney, Kassie Piccard and Carson Hasselbrink for engaging in stimulating discussions, for all the fun we have had in the last five years and all the encouragement. Also, I thank my friends in the following institution for guiding me and enlightening me with thoughtful discussions about life and science, Zach Brown, Robert Chevalier, Shyamal Kishore, Inush Kalana, Rukshika Hwawasam, Sauradip Chaudhuri, Dana Discenza, Nuwan Bandara and Buddini Karawadeniya.

Last but not least, I would like to thank my parents, my brother and grandmother for supporting me spiritually throughout writing this thesis and my life in general. This is very much true for my wife Brianna Peloquin who was there with me and made me push for greatness even when the path was rough and tough. So, thank you all for making this Ph.D. an exciting one and a one to remember forever.

"*Set a limit of no limit, Found a way from no way*" – Henry Lee

PREFACE

The dissertation of my research has been presented in a manuscript format according to the guidelines of the graduate school of the University of Rhode Island. The complete dissertation is divided into seven manuscripts. The first manuscript (Chapter 1) was published in *ACS Omega* in 2018 with authors Ashvin Fernando, Francis Hane, Braedan R. J. Prete, Brianna Peloquin, Scott Karas, Sauradip Chaudhuri, Simrun Chahal, Yurii Shepelytskyi, Alanna Wade, Tao Li, Brenton DeBoef, and Mitchell S. Albert. The second manuscript (Chapter 2) will be submitted to *Nature Scientific reports* in 2019 with authors Ashvin Fernando, Yurii Shepelytskyi, Francis Hane, Paul Cesana, Adriana Mendieta, Alanna Wade, Mitchell S. Albert, and Brenton DeBoef. The third manuscript (Chapter 3) will be submitted to *ACS organic letters* in 2019 with authors Ashvin Fernando, John Christy, Brianna Peloquin, Paul Cesana, Samantha Donahue and Brenton DeBoef. The fourth manuscript (Chapter 4) will be submitted to *Chemical Communications* in 2019 with authors Ashvin Fernando, Paul Cesana, Adriana Mendieta, Cassandra, Al Bach, and Brenton DeBoef. The fifth manuscript (Chapter 5) will be submitted to *Supramolecular chemistry* in 2019 with authors Ashvin Fernando, Teresa Mako, Adelaide Levenson, Paul Cesana, Adriana Mendieta, Mindy Levine, and Brenton DeBoef. The sixth manuscript (Chapter 6) will be submitted to *ACS Biomacromolecules* in 2019 with authors Ashvin Fernando, Paul Cesana, Adriana Mendieta, Jason R Dwyer, and Brenton DeBoef. The seventh manuscript (Chapter 7) will be submitted a *journal of antibiotics* 2019 with authors Samantha A. Donahue, Ashvin Fernando, Gerwald Jogl, Paul Cesana, Breton DeBoef, and Steven T. Gregory.

TABLE OF CONTENTS

ABSTRACT ii
ACKNOWLEDGMENTS iii
PREFACE v
TABLE OF CONTENTS vi
LIST OF TABLES viii
LIST OF SCHEMES ix
LIST OF FIGURES x
1 CHAPTER 1 1
1.1 REFERENCES 14
1.2 Supporting Information 18
2 CHAPTER 2 87
2.1 References 99
2.2 Supporting Information 103
3 CHAPTER 3 127
3.1 References 142
3.2 Supporting Information 144
4 CHAPTER 4 218
4.1 References 233
4.2 Supporting Information 235
5 CHAPTER 5 290
5.1 References 308
5.2 Supporting Information 308
6 CHAPTER 6 406
6.1 References 421
6.2 Supporting Information 424

7 CHAPTER 7 431
7.1 References *445*
7.2 Supporting Information *446*

LIST OF TABLES

Table 1-1: Characterization and HyperCEST Data for Pseudorotaxanes 8

Table 1-2: Calculated binding energies for pseudorotaxanes 69

Table 1-3: Computed distances between guest and host for 2⊂CB6 70

Table 1-4: Computed distances between guest and host for 1⊂CB6 71

Table 1-5: Computed distances between guest and host for 2⊂CB7 72

Table 1-6: Computed distances between guest and host for 1⊂CB7 73

Table 1-7: Computed distances between guest and host for 2⊂CB8 74

Table 1-8: Computed distances between guest and host for 1⊂CB8 75

Table 1-9: Computed distances between guest and host for 2⊂α-CD 76

Table 1-10: Computed distances between guest and host for 1⊂α-CD 77

Table 1-11: Computed distances between guest and host for 1⊂α-CD 78

Table 1-12: Computed distances between guest and host for 1⊂β-CD 79

Table 1-13: Computed distances between guest and host for 2⊂γ-CD 80

Table 1-14: Computed distances between guest and host for 1⊂γ-CD 81

Table 3-1: Stabilization energies and docking scores of complexes 136

Table 4-2: The data represents the yields that were obtained with the change of the brominated monomer equivalents and the type of Lewis acid 243

Table 4-1: Various click reaction conditions that were used during the screening process of identifying the correct reaction conditions for the ThT-based CoP5A synthesis 258

Table 5-1: Association constants obtained from fluorescence titrations 302

Table 7-1: Inhibition zones chart, all the above distances are measured from the end of the disk 443

LIST OF SCHEMES

Scheme 2-1: Synthesis and computed structures of neutral and decacationic pillararenes 92

Scheme 3-1: Reaction scheme for the complete synthesis of γ-CD rotaxane 1:1 and γ-CD rotaxane 1:2 130

Scheme 3-2: Reaction scheme for the complete synthesis of ThT-rotaxane 1:1 and ThT-rotaxane 1:2 135

Scheme 4-1: The complete synthetic scheme of synthesis of dual-ThT appended Co-P5A 236

Scheme 6-1: Schematic representation of the self-assembled dsDNA-dmWSP5A composite material for encapsulation of PFOA 410

LIST OF FIGURES

Figure 1.1:Proposed binding of Xe via formation of a ternary complex and detection via HyperCEST 4

Figure 1.2: Structures of hosts and guests used in this study 6

Figure 1.3: Free Induction Decay (FID) spectra of 10 mM aqueous solution of 1⊂γ-CD following off-resonance (+255 ppm, left) and on-resonance (+128 ppm, center) HyperCEST pulses. HyperCEST depletion z-spectrum of a 10 mM aqueous solution of 1⊂γ-CD (right). Each data point indicates the HyperCEST depletion when the molecule is irradiated with a pulse at a given chemical shift off-set. 10

Figure 1.4: ^{1}H NMR spectra indicating the formation of the ter-nary complex (25 oC, [γ-CD] = [1] = 100 mM.) A/ ^{1}H NMR spectrum of γ-cyclodextrin. B/ ^{1}H NMR spectrum after addition of 1 equiv of 1. C/ ^{1}H NMR spectrum after addition of 1.5 atm xenon 11

Figure 1.5: ^{1}H NMR of Guest 1 20

Figure 1.6: ^{13}C NMR of Guest 1 21

Figure 1.7: ^{1}H NMR of Guest 2 23

Figure 1.8: ^{13}C NMR of Guest 2 24

Figure 1.9: ^{1}H NMR of 2⊂CB6 26

Figure 1.10: ^{1}H NMR (magnified) of 2⊂CB6 in the region of the guest protons 27

Figure 1.11: ^{1}H NMR of 1⊂CB6 28

Figure 1.12: ^{1}H NMR (magnified) of 1⊂CB6 in the region of guest protons 29

Figure 1.13: ^{1}H NMR of 2⊂CB7 30

Figure 1.14: ^{1}H NMR (magnified) of 2⊂CB7 in the region of guest protons 31

Figure 1.15: ^{1}H NMR of 1⊂CB7 32

Figure 1.16: ^{1}H NMR (magnified) of 1⊂CB7 in the region of guest protons 33

Figure 1.17: ^{1}H NMR of 2⊂CB8 34

Figure 1.18: ^{1}H NMR (magnified) of 2⊂CB8 in the region of guest protons..... 35

Figure 1.19: ^{1}H NMR of 1⊂CB8 36

Figure 1.20: ^{1}H NMR (magnified) of 1CB8 in the region of guest protons..... 37

Figure 1.21: ^{1}H NMR of 2⊂α-CD..... 39

Figure 1.22: ^{1}H NMR (magnified) of 2⊂α-CD in the region of guest protons..... 40

Figure 1.23: ^{1}H NMR of 1⊂α-CD..... 41

Figure 1.24: ^{1}H NMR of 2⊂β-CD..... 42

Figure 1.25: ^{1}H NMR of 1⊂β-CD..... 43

Figure 1.26: ^{1}H NMR (magnified) of 1 β-CD in the region of guest protons..... 44

Figure 1.27: ^{1}H NMR of 2⊂γ-CD..... 45

Figure 1.28: ^{1}H NMR (magnified) of 2⊂γ-CD in the region of guest protons 46

Figure 1.29: ^{1}H NMR (magnified) of 2⊂γ-CD in the region of H-3 proton of γ-CD 47

Figure 1.30: ^{1}H NMR of 1⊂γ-CD..... 48

Figure 1.31: ^{1}H NMR (magnified) of 1⊂γ-CD in the region of guest protons 49

Figure 1.32: ^{1}H NMR (magnified) of 1⊂γ-CD in the region of H-3 proton of γ-CD 50

Figure 1.33: 1H-NMR stacked plot of γ-cyclodextrin and varying guest (1) 52

Figure 1.34: 1:1 Binding curve for the association of 1 with γ-CD. 53

Figure 1.35: 1:1 Binding curve for the association of 1 with γ-CD. 53

Figure 1.36: 1:1 Binding curve for the association of 2 with γ-CD. 54

Figure 1.37: 1:1 Binding curve for the association of 2 with γ-CD. 54

Figure 1.38: Mass spectrum of α-CD..... 56

Figure 1.39: Mass spectrum of β-CD..... 57

Figure 1.40: Mass spectrum of γ-CD 58

Figure 1.41: 1⊂γ-CD (ESI+, 5 uL/min, FS, 20 uM/20 uM) – m/z 1707.6307 59

Figure 1.42: 3⊂γ-CD (ESI+, 5 uL/min, FS, 20 uM/20 uM) – m/z 1679.5996 60

Figure 1.43: 1⊂α-CD (ESI+, 5 uL/min, FS, 20 uM/20 uM) – m/z 1707.6307..... 61

Figure 1.44: 3⊂α-CD (ESI+, 5 uL/min, FS, 20 uM/20 uM) – m/z 638.2887 62

Figure 1.45: 1⊂β-CD (ESI+, 5 uL/min, FS, 20 uM/20 uM) – m/z 733.3298 63

Figure 1.46: ITC of 1 with γ-CD in water 65

Figure 1.47: ITC of 1 with γ-CD in bovine plasma 66

Figure 1.48: Analysis of ITC binding data for 1 with γ-CD in water 67

Figure 1.49: Analysis of ITC binding data for 1 with γ-CD in bovine plasma 68

Figure 1.50: HyperCEST pulse sequence 83

Figure 1.51: Apparatus for obtain HP Xe spectra 84

Figure 1.52: Custom-made coil and sample chamber 84

Figure 2.1: Comparison of Xe-binding hosts 90

Figure 2.2: L to R: molecular dynamics simulations of Xe and 3 using 1830 water molecules; computed hydrophobic surface of **3** is shown in red; Xe binds ot the hydrophobic surface of **3** .. 93

Figure 2.3: Stacked ^{1}H-NMR of **2** in $CDCl_3$ (top) and **3 in** DMSO-d_6 (bottom). Product peaks are highlighted 94

Figure 2.4: Left image; Fluorescence quenching phenomena when Xe (aq) added into a solution of WSP5A (aq) in phosphate buffer.(Gaussian curve smoothing using Origin lab software), right image; occupancy curve with respect to the concentration of $Xe_{(aq)}$ used 95

Figure 2.5: Left, HyperCEST depletion spectra for Xe binding in water-soluble pillar[5]arene. Right, energy minimized molecular model of Xe-bound P[5]A with the use of molecular dynamics. 97

Figure 3.1: ^{1}H NMR of 1 106

Figure 3.2: ^{13}C NMR of **1** 107

Figure 3.3: ^{1}H NMR of **2** 109

Figure 3.4: ^{13}C NMR of **2** 110

Figure 3.5: ^{1}H-NMR of **3** 112

Figure 3.6: ^{13}C-NMR of **3** 113

Figure 3.7: Mass spectrum of 3 for $[M - 3Br]^{3+}$ Calculated $C_{95}H_{121}O_{10}N_{20}Br_7$ 754.1270 114

Figure 3.8: Mass spectrum of 3 for $[M - 5Br]^{5+}$ Calculated $C_{95}H_{121}O_{10}N_{20}Br_5$ 420.1090 114

Figure 3.9: Mass spectrum of 3 for $[M - 6Br]^{6+}$ Calculated $C_{95}H_{121}O_{10}N_{20}Br_4$ 336.9378 115

Figure 3.10: Mass spectrum of 3 for $[M - 7Br]^{7+}$ Calculated $C_{95}H_{121}O_{10}N_{20}Br_3$ 277.2442 115

Figure 3.11: The above figures represent the experimental setup for obtaining the saturated Xe solution in DI water 116

Figure 3.12: Fluorescence quenching phenomena when Xe was added in to a solution of P5A in phosphate buffer (before curve smoothening was applied) 118

Figure 3.13: Fluorescence quenching phenomena when Xe was added in to a solution of P5A in phosphate buffer (Gaussian curve smoothing using Origin lab software) 119

Figure 3.14: Occupancy curve for WSPA 122

Figure 3.1: ^{1}H-NMR of 3 (400 MHz, DMSO-d_6) 131

Figure 3.2: ROESY NMR of 3 (400 MHz, DMSO-d_6). The arrows point towards the regions of H3 and H5 protons NOE correlation with C-D protons of the guest molecule. Mixing time = 500 ms 134

Figure 3.3: Images of 3 (to the left) and 10 (to the right) after docking using MOE software, the surfaces represent the hydrophobic surface of the cyclodextrin and the ligand placement inside the hydrophobic centroid 137

Figure 3.4: from top to bottom, energy minimized molecular models of γ-CD rotaxane 1:1, γ-CD rotaxane 2:1 and γ-CD rotaxane 1:2 138

Figure 3.5: Stacked image of methylimidazolium guest, 1:1 γ-CD rotaxane and complexation of the host and the guest in 1:1 ratio 139

Figure 3.6: The expanded in images of the imidazole ^{1}H NMR peaks displaying the shielding effect of these peaks in the presence of the 1:1 rotaxane system showing that the cavity itself is exhibiting the hydrophilic effects 140

Figure 3.7: ^{1}H NMR of Thioflavin analog 146

Figure 3.8: Mass spectrum of Thioflavin analog 147

Figure 3.9: ^{1}H NMR of Thioflavin analog based linker 149

Figure 3.10: ^{13}C NMR of Thioflavin analog based linker 150

Figure 3.11: Mass spectrum of Thioflavin analog based linker 151

Figure 3.12: ^{1}H NMR of **9** 153

Figure 3.13: ^{13}C NMR of **9** 154

Figure 3.14: Mass spectrum of **9** 155

Figure 3.15 : ^{1}H NMR of **2** 157

Figure 3.16: ^{13}C NMR of **2** 158

Figure 3.17: Mass spectrum of **2** 159

Figure 3.18: ^{1}H NMR of imine **1** 161

Figure 3.19: Mass spectrum of imine **1** 162

Figure 3.20: ^{1}H NMR of **1** 164

Figure 3.21: ^{13}C NMR of **1** 165

Figure 3.22: Mass spectrum of **1** 166

Figure 3.23: ^{1}H NMR of reaction with **1** and **2** [without γ-CD] 168

Figure 3.24: ^{13}C NMR of reaction with **1** and **2** [without γ-CD] 169

Figure 3.25: Mass spectrum of reaction with **1** and **2** [without γ-CD] 170

Figure 3.26: ^{1}H NMR of **3** 172

Figure 3.27: ^{1}H NMR of **4** 173

Figure 3.28: ^{13}C NMR of **3** 174

Figure 3.29: ROESY NMR of **3**, with a mixing time 500 ms 175

Figure 3.30: Complete mass spectrum of **3** 176

Figure 3.31: mass spectrum of 3 at the range of 1006 – 1016 m/z 177

Figure 3.32: mass spectrum of 3 at the range of 2017 – 2028 m/z 178

Figure 3.33: Complete mass spectrum of **4** 179

Figure 3.34: mass spectrum 4 at the range of 1655-1668 m/z 180

Figure 3.35: Complete mass spectrum of 5 180

Figure 3.36: mass spectrum of 5 at the range of 2620 - 2880 m/z 181

Figure 3.37: mass spectrum of 5 at the range of 2680 - 2780 m/z 182

Figure 3.38: ^{1}H NMR for **6** 184

Figure 3.39: ^{13}C NMR for **6** 185

Figure 3.40: COSY spectrum for **6** 186

Figure 3.41: ROESY spectrum for **6**, with a mixing time of 500 ms 187

Figure 3.42: ^{1}H NMR of **8** 188

Figure 3.43: ^{13}C NMR of **8** 189

Figure 3.44: The COSY spectrum of **8** 190

Figure 3.45: ROESY spectrum of 8, with a mixing time of 500 ms 191

Figure 3.46: ^{1}H NMR of **7** 192

Figure 3.47: ^{13}C NMR of **7** 193

Figure 3.48: COSY of **7** 194

Figure 3.49: ROESY of **7**, with a mixing time of 500 ms 195

Figure 3.50: Complete mass spectrum of **6** 196

Figure 3.51: mass spectrum of 6 at the range of 800 – 1800 m/z 196

Figure 3.52: mass spectrum of **6** at the range of 925 – 939 m/z 197

Figure 3.53: mass spectrum of **6** at the range of 1846 - 1874 m/z 197

Figure 3.54: Complete mass spectrum of 7 198

Figure 3.55: mass spectrum of 7 at the range of 1500 - 3000 m/z 198

Figure 3.56: mass spectrum of **7** at the range of 1475 - 1540 m/z 199

Figure 3.57: mass spectrum of **7** at the range of 2950 - 3030 m/z 199

Figure 3.58: Complete mass spectrum of **8** 200

Figure 3.59: mass spectrum of **8** at the range of 2150 - 2850 m/z 200

Figure 3.60: mass spectrum of **8** at the range of 2535 - 2615 m/z 201

Figure 3.61: ^{1}H NMR of **10** 203

Figure 3.62: ^{13}C NMR of **10** 204

Figure 3.63: ROESY spectrum of **10** 205

Figure 3.64: mass spectrum of **10** 206

Figure 3.65: mass spectrum of **10** 206

Figure 3.66: NMR titration with 1 and γ-CD 208

Figure 3.67: Binding curve for **1** and γ-CD 209

Figure 3.68: Computational modeling for **4** and one γ-CD molecule 211

Figure 3.69: Computational modeling for **3** 212

Figure 3.70: Computational modeling for **10** 213

Figure 3.71: Computational modeling for **1** and **2** γ-CD molecules 214

Figure 3.72: Computational modeling for **4** 215

Figure 3.73: Computational modeling for **11** (ThT based γ-CD rotaxane 2:1) 216

Figure 4.1: Optimized synthesis of functionalized co-pillararenes. (Molecular modeling images with propargyl group highlighted.) 221

Figure 4.2: Cartoon representation of the self-inclusion behavior with the change of conditions 222

Figure 4.3: L to R, ThT Co-P5A in a simulated environment surrounded with CHCl3 molecules (Self-inclusion form), ThT Co-P5A in a simulated environment surrounded with DMSO molecules (Free-form) 224

Figure 4.4: Top, ThT based CoP5A in CDCl3 and bottom, ThT based CoP5A in DMSO-d_6 225

Figure 4.5: Temperature study of ^{1}H-NMR of ThT-CoP5A in $CDCl_3$ 226

Figure 4.6: ROESY spectrum of ThT Co-P5A in $CDCl_3$ 228

Figure 4.7: Fluorescence emission spectra of ThT self-assembled CoP5A, with the addition of DMSO. The excitation wavelength used was 304 nm 229

Figure 4.8: Stacked ^{1}H NMR of the non-water soluble and water-soluble ThT CoP5A 230

Figure 4.9: Titration of Adiponitrile in to ThT-CoP5A in CDCl3 at 298K, the boxes show zoomed images of the area, except red box indicates the binding of adiponitrile in the cavity of the ThT Co-P5ATitration of Adiponitrile in to ThT-CoP5A in $CDCl_3$ at 298K, the boxes show zoomed images of the area, except red box indicates the binding of adiponitrile in the cavity of the ThT Co-P5A 231

Figure 4.10: ^{1}H NMR of Brominated monomer 238

Figure 4.11: ^{13}C-NMR of Brominated monomer 239

Figure 4.12: ^{1}H-NMR of proapargylated monomer 241

Figure 4.13: Top: the flash chromatogram of the 1:10 equivalents in hexane/dichloromethane solvent system. Peaks correspond to products that were recovered. Bottom: flash chromatogram of the 1:5 equivalents in hexane/dichloromethane solvent system 244

Figure 4.14: ^{1}H-NMR of Co-pillar[5]arene 245

Figure 4.15: ^{13}C-NMR of Co-pillar[5]arene 246

Figure 4.16: Mass spectrum of Co-pillar[5]arene 247

Figure 4.17: ^{1}H NMR of Thioflavin 249

Figure 4.18: Mass spectrum of Thioflavin 250

Figure 4.19: ^{1}H NMR of Thioflavin-6-Br linker 252

Figure 4.20: ^{13}C NMR of Thioflavin-6-Br linker 253

Figure 4.21: ^{1}H NMR of Thioflavin-6-azide linker 255

Figure 4.22: Mass spectrum of Thioflavin-6-azide linker 256

Figure 4.23: ^{1}H-NMR of ThT-CoP5A in $CDCl_3$ 259

Figure 4.24: ^{1}H-NMR of ThT-CoP5A in DMSO-d_6 260

Figure 4.25: ^{13}C-NMR of ThT-CoP5A in DMSO-d_6 261

Figure 4.26: ROESY spectra of ThT-CoP5A in $CDCl_3$ 262

Figure 4.27: Zoomed image of ROESY spectra of ThT-CoP5A in $CDCl_3$ 263

Figure 4.28: TOCSY spectra of ThT-CoP5A in $CDCl_3$ 264

Figure 4.29: Zoomed image of TOCSY spectra of ThT-CoP5A in $CDCl_3$ 265

Figure 4.30: HMBC spectra of ThT-CoP5A in DMSO-d_6 266

Figure 4.31: TOCSY spectra of ThT-CoP5A in $CDCl_3$ 267

Figure 4.32: Mass spectra of ThT-CoP5A in methanol 268

Figure 4.33: ^{1}H-NMR of water-soluble ThT-CoP5A in DMSO-d_6 270

Figure 4.34: COSY spectrum of water soluble ThT-CoP5A in DMSO-d_6 271

Figure 4.35: ROESY spectrum of water soluble ThT-CoP5A in DMSO-d_6 272

Figure 4.36: ^{13}C NMR spectrum of water soluble ThT-CoP5A in DMSO-d_6 273

Figure 4.37: Absorbance curve for ThT-CoP5A in chloroform 274

Figure 4.38: SEM images, as indicated from the arrows each one represents the increase of the level of magnification and decrease of the particle size ranging from 100 µm to 200 nm. The yellow boxes indicate the area that was zoomed in. The sample was loaded on to a platform and then it was gold spluttered. This gold spluttered surface was used to observe the surface in its dried form under vacuum. 275

Figure 4.39: SEM image of ThT-CoP5A at 100 µm level 276

Figure 4.40: SEM image of ThT-CoP5A at 20 µm level 277

Figure 4.41: SEM image of ThT-CoP5A at 10 µm level 278

Figure 4.42: SEM image of ThT-CoP5A at 2 µm level 279

Figure 4.43: SEM image of ThT-CoP5A at 1 µm level 280

Figure 4.44: SEM image of ThT-CoP5A at 1 µm level 281

Figure 4.45: SEM image of ThT-CoP5A at 1 µm level 282

Figure 4.46: SEM image of ThT-CoP5A at 1 µm level 283

Figure 4.47: SEM image of ThT-CoP5A at 1 µm level 284

Figure 4.48: Titration of ThT-6-azide to a solution of CoP5A in $CDCl_3$ solvent 285

Figure 4.49: Titration of ThT-6azide to a solution of CoP5A in $CDCl_3$ 286

Figure 4.50: Computational model after molecular dynamics in $CHCl_3$ solvent system. 287

Figure 4.51: Zoomed image of the Computational model after molecular dynamics in $CHCl_3$ solvent system. 288

Figure 4.52: Computational model after molecular dynamics in DMSO solvent system 289

Figure 4.53: Computational model after molecular dynamics in DMSO solvent system. (Space filling model) 289

Figure 5.1: Illustration of the synthesis of pillar[5]arene 3 via cyclization of monomer 1 in the presence of dichloroethane solvent, followed by nucleophilic substitution of the terminal bromine moieties on compound 2.Three-dimensional structures underneath the reaction scheme show energy-minimized molecular conformations. 295

Figure 5.2: Array of toxicants and small molecules that were used in the binding study with supramolecular host 3, with calculated stabilization energies of the toxicants upon binding in host 3 (obtained via Spartan 16) shown.The values given represents the stabilization energy for the final complex formation between the toxicant and **3.** The equation used is $\Delta\Delta H \text{ stabilation energy} = \Delta H\ \mathbf{3} + \text{guest} - \Delta H\mathbf{3} - \Delta H(\text{guest})$. Top - Cartoon image represents the binding phenomena taking place between **3** and the toxicants. 297

Figure 5.3: Computed images of analytes docked in macrocycle 3. (A) Naproxen; (B) PFOA; (C) Cyclophosphamide; and (D) 1,10-Phenanthroline 299

Figure 5.4: ^1H NMR spectra of: (A) macrocycle 3; and (B) macrocycle 3 and naproxen 10 in a 1:1 molar ratio. The concentrations of the guest and host were 10 mM each 300

Figure 5.5: Fluorine NMR spectra of: (A) Perfluorooctanoic acid (PFOA); and (B) complex between PFOA and supramolecular host 3 300

Figure 5.6: Sample fluorescence titrations of analytes with cationic host 3 used to determine binding constants: (A) with simazine guest; and (B) with phenanthrene guest. The black line represents the calculated values and the red line represents the experimentally determined values 303

Figure 5.7: Job's plot analysis of binding of cationic host 3 with: (A) anthracene and (B) phenanthrene small molecule guests 303

Figure 5.8: Linear discriminant analysis of analyte-induced responses upon binding in cationic host 3 305

Figure 5.9: (A) Schematic illustration of removal of toxicant-bound pillararene with cationic exchange resin; (B) Quantitative assessment of the amount of 3 that was removed by different cation resin types.The black line represents Dowex Marathon resin, the red line represents Dowex 50WX2 resin, and the blue line represents Amberlite IRN150 resin. (C) Quantitative assessment of the amount of naproxen removed after treatment of **3** with resin and (D) Quantitative assessment of the amount of phenanthrene removed after treatment of **3** with resin 306

Figure 5.10: ^{1}H NMR of brominated monomer 316

Figure 5.11: ^{13}C NMR of 1 317

Figure 5.12: ^{1}H NMR of Brominated pillar[5]arene **2** 319

Figure 5.13: ^{13}C NMR of Brominated pillar[5]arene **2** 320

Figure 5.14: ^{1}H-NMR of **3** 322

Figure 5.15: ^{13}C-NMR of **3** 323

Figure 5.16: $[M - 3Br]^{3+}$ Calculated $C_{95}H_{121}O_{10}N_{20}Br_7$ 754.1270 324

Figure 5.17: $[M - 5Br]^{5+}$ Calculated $C_{95}H_{121}O_{10}N_{20}Br_5$ 420.1090 324

Figure 5.18: $[M - 6Br]^{6+}$ Calculated $C_{95}H_{121}O_{10}N_{20}Br_4$ 336.9378 325

Figure 5.19: $[M - 7Br]^{7+}$ Calculated $C_{95}H_{121}O_{10}N_{20}Br_3$ 277.2442 325

Figure 5.20: ^{1}H spectrum of proapargylated monomer 327

Figure 5.21: Flash chromatogram for the purification of Proapargylated P5A, Product was separated at 23 – 35 CV. First peak corresponds to the unreacted proapargylated monomer 329

Figure 5.22: ^{1}H NMR of proapargylated P5A 330

Figure 5.23: Mass spectrum of proapargylated P5A 331

Figure 6.1: Synthesis of dmWSP5A (left), cartoon representation of the dmWSP5A (right) 409

Figure 6.2: Stochiometric assay of dsDNA with dmWSP5A. From R to L decreasing WSP5A concentration while the dsDNA concentration was held constant 411

Figure 6.3: Zoomed image of self-assembled composite material in aqueous media (gelatinous) 412

Figure 6.4: L to R, Stable self-assembled composite material in ultra-pure water after six months, Composite material after drying under vacuum and crushed dried composite material 413

Figure 6.5: IR analysis of the starting materials and the dried composite material 414

Figure 6.6: Thermogravimetric analysis (TGA) of dsDNA, dmWSP5A and dried composite .. 415

Figure 6.7: L to R, Protein patch map, the blue is positively charged dmWSP5A, and red regions are for negatively charged phosphate backbone, Ligand interaction diagram of dmWSP5A to dsDNA 416

Figure 6.8: 19F NMR of PFOA capture through the self-assembled composite material 417

Figure 6.9: L to R, hydrophobic pocket present in dmWSP5A, Docked PFOA inside the dmWSP5A 418

Figure 6.10: ^{19}F NMR titration of WSP5A and dsDNA into the PFOA solution, number of scans = 15,000 419

Figure 6.11: PFOA bound inside the cavity of the dmWSP5A after multiple iterations using molecular dynamics with *AMBER 19* force field..... 427

Figure 6.12: Protein patches representation of the dsDNA and WSP5A..... 428

Figure 6.13: Electrostatic potential map representation of dsDNA and WSP5A 429

Figure 6.14: H-bonding interactions between the WSP5A and dsDNA 430

Figure 7.1: Topmost, Complete structure of Thermus thermophilus 70S ribosome in its native form, (Bottom left) Active pocket inside the ribosome docked with CAM, (Bottom right) Distances from CAM towards surrounding amino acids present inside the pocket 436

Figure 7.2: Topmost, Complete structure of Chloramphenicol acetyltransferase. (Bottom left) Active pocket inside the CAT enzyme docked with CAM (A more open pocket compared to the ribosome pocket), (Bottom right) Distances from CAM towards surrounding amino acids 437

Figure 7.3: Synthetic scheme and substrate scope for the synthesis of derivatives of CAM using isothiocyanates 438

Figure 7.4: Ligand interaction diagrams for CAM, CAM base and CAM derivative compared with ribosome pocket binding (Left side images) and CAM acetyltransferase binding (right side images) 439

Figure 7.5: Flow chart diagram representation of the procedure implemented for the growth inhibition zone study in growth media described in methods 440

Figure 7.6: Representation of a disk assay and the control disk, the dark area is an indication of no growth zone of the bacteria or knows as an inhibition zone 441

Figure 7.7: Left: B. subtilis 168 (Cam-sensitive); Right: B. subtilis with pC194 (Cam-resistant). All new derivatives inhibit Cam-resistant strain 442

Figure 7.8: In vitro protein synthesis obtained via raw fluorescence units vs. time, excitation at 470 nm and emission is monitored at 520 nm 444

Figure 7.9: Chloramphenicol reference ^{1}H NMR before the hydrolysis 448

Figure 7.10: 1H NMR of CAM base (Hydrolysis of CAM 449

Figure 7.11: ^{13}C NMR of CAM base 450

Figure 7.12: Stacked ^{1}H NMR of CAM and CAM base 451

Figure 7.13: Mass spectrum of CAM base 452

Figure 7.14: ^{1}H NMR of 1-((1R,2R)-1,3-dihydroxy-1-(4-nitrophenyl)propan-2-yl)-3-(4nitrophenyl)thiourea 454

Figure 7.15: ^{13}C NMR of 1-((1R,2R)-1,3-dihydroxy-1-(4-nitrophenyl)propan-2-yl)-3-(4nitrophenyl)thiourea 455

Figure 7.16: Mass spectrum of 1-((1R,2R)-1,3-dihydroxy-1-(4-nitrophenyl)propan-2-yl)-3-(4nitrophenyl)thiourea 456

Figure 7.17: ^{1}H NMR of 1-(4-chlorophenyl)-3-((1R,2R)-1,3-dihydroxy-1-(4-nitrophenyl)propan-2-yl)thiourea..... 458

Figure 7.18: ^{13}C NMR of 1-(4-chlorophenyl)-3-((1R,2R)-1,3-dihydroxy-1-(4-nitrophenyl)propan-2-yl)thiourea..... 459

Figure 7.19: Mass spectrum of 1-(4-chlorophenyl)-3-((1R,2R)-1,3-dihydroxy-1-(4-nitrophenyl)propan-2-yl)thiourea 460

Figure 7.20: ^{1}H NMR of 1-(4-acetylphenyl)-3-((1R,2R)-1,3-dihydroxy-1-(4-nitrophenyl)propan-2-yl)thiourea..... 462

Figure 7.21: ^{13}C NMR of 1-(4-acetylphenyl)-3-((1R,2R)-1,3-dihydroxy-1-(4-nitrophenyl)propan-2-yl)thiourea..... 463

Figure 7.22: Mass spectrum of 1-(4-acetylphenyl)-3-((1R,2R)-1,3-dihydroxy-1-(4-nitrophenyl)propan-2-yl)thiourea 464

Figure 7.23: ^{1}H NMR of 1-(3,5-bis(trifluoromethyl)phenyl)-3-((1R,2R)-1,3-dihydroxy-1-(4-nitrophenyl)propan-2-yl)thiourea 466

Figure 7.24: ^{13}C NMR of 1-(3,5-bis(trifluoromethyl)phenyl)-3-((1R,2R)-1,3-dihydroxy-1-(4-nitrophenyl)propan-2-yl)thiourea 467

Figure 7.25: Mass spectrum of 1-(3,5-bis(trifluoromethyl)phenyl)-3-((1R,2R)-1,3-dihydroxy-1-(4-nitrophenyl)propan-2-yl)thiourea 468

Figure 7.26: ^{1}H NMR of 1-(2-chloro-4-nitrophenyl)-3-((1R,2R)-1,3-dihydroxy-1-(4-nitrophenyl)propan-2-yl)thiourea 470

Figure 7.27: ^{13}C of 1-(2-chloro-4-nitrophenyl)-3-((1R,2R)-1,3-dihydroxy-1-(4-nitrophenyl)propan-2-yl)thiourea 471

Figure 7.28: ^{1}H NMR of 1-(3,5-dichlorophenyl)-3-((1R,2R)-1,3-dihydroxy-1-(4-nitrophenyl)propan-2-yl)thiourea 473

Figure 7.29: ^{13}C NMR of 1-(3,5-dichlorophenyl)-3-((1R,2R)-1,3-dihydroxy-1-(4-nitrophenyl)propan-2-yl)thiourea 474

Figure 7.30: Mass spectrum of 1-(3,5-dichlorophenyl)-3-((1R,2R)-1,3-dihydroxy-1-(4-nitrophenyl)propan-2-yl)thiourea 475

Figure 7.31: ^{1}H NMR of 1-((1R,2R)-1,3-dihydroxy-1-(4-nitrophenyl)propan-2-yl)-3-(4-methoxyphenyl)thiourea 477

Figure 7.32: ^{13}C NMR of 1-((1R,2R)-1,3-dihydroxy-1-(4-nitrophenyl)propan-2-yl)-3-(4-methoxyphenyl)thiourea 478

Figure 7.33: Mass spectrum of 1-((1R,2R)-1,3-dihydroxy-1-(4-nitrophenyl)propan-2-yl)-3-(4-methoxyphenyl)thiourea 479

Figure 7.34: ^{1}H NMR of 1-((1R,2R)-1,3-dihydroxy-1-(4-nitrophenyl)propan-2-yl)-3-(3,5-dimethylphenyl)thiourea 481

Figure 7.35: ^{13}CNMR of 1-((1R,2R)-1,3-dihydroxy-1-(4-nitrophenyl)propan-2-yl)-3-(3,5-dimethylphenyl)thiourea 482

Figure 7.36: Mass spectrum for 1-((1R,2R)-1,3-dihydroxy-1-(4-nitrophenyl)propan-2-yl)-3-(3,5-dimethylphenyl)thiourea 483

Figure 7.37: Disk assay for CAM base without any functionalization using Thermus thermophilus HB27 484

Figure 7.38: Binding of 1-(3,5-bis(trifluoromethyl)phenyl)-3-((1R,2R)-1,3-dihydroxy-1-(4-nitrophenyl)propan-2-yl)thiourea to the ribosome pocket, with the generated surface for the receptor 486

Figure 7.39: Van der Waals interactions of 1-(3,5-bis(trifluoromethyl)phenyl)-3-((1R,2R)-1,3-dihydroxy-1-(4-nitrophenyl)propan-2-yl)thiourea with the ribosome amino acids 487

Figure 7.40: Ligand interaction diagram of 1-(3,5-bis(trifluoromethyl)phenyl)-3-((1R,2R)-1,3-dihydroxy-1-(4-nitrophenyl)propan-2-yl)thiourea to the ribosome 487

Figure 7.41: Binding of 1-(3,5-bis(trifluoromethyl)phenyl)-3-((1R,2R)-1,3-dihydroxy-1-(4-nitrophenyl)propan-2-yl)thiourea to the CAM acetyl transferase pocket, with the generated surface for the receptor 488

Figure 7.42: Van der Waals interactions of of 1-(3,5-bis(trifluoromethyl)phenyl)-3-((1R,2R)-1,3-dihydroxy-1-(4-nitrophenyl)propan-2-yl)thiourea with the CAM acetyl transferase amino acids 489

Figure 7.43: Ligand interaction diagram of 1-(3,5-bis(trifluoromethyl)phenyl)-3-((1R,2R)-1,3-dihydroxy-1-(4-nitrophenyl)propan-2-yl)thiourea for the CAM acetyl transferase enzyme 489

Figure 7.44: Binding of 1-((1R,2R)-1,3-dihydroxy-1-(4-nitrophenyl)propan-2-yl)-3-(4nitrophenyl)thiourea to the ribosome pocket, with the generated surface for the receptor 490

Figure 7.45: Van der Waals interactions of 1-((1R,2R)-1,3-dihydroxy-1-(4-nitrophenyl)propan-2-yl)-3-(4nitrophenyl)thiourea with the CAM acetyl transferase amino acids 491

Figure 7.46: Ligand interaction diagram of 1-((1R,2R)-1,3-dihydroxy-1-(4-nitrophenyl)propan-2-yl)-3-(4nitrophenyl)thiourea for the CAM acetyl transferase enzyme 491

Figure 7.47: Binding of 1-((1R,2R)-1,3-dihydroxy-1-(4-nitrophenyl)propan-2-yl)-3-(4nitrophenyl)thiourea to the CAM acetyl transferase pocket, with the generated surface for the receptor 492

Figure 7.48: Van der Waals interactions of 1-((1R,2R)-1,3-dihydroxy-1-(4-nitrophenyl)propan-2-yl)-3-(4nitrophenyl)thiourea with the CAM acetyl transferase amino acids 493

Figure 7.49: Ligand interaction diagram of 1-((1R,2R)-1,3-dihydroxy-1-(4-nitrophenyl)propan-2-yl)-3-(4nitrophenyl)thiourea for the CAM acetyl transferase enzyme 493

Figure 7.50: Binding of 1-(4-chlorophenyl)-3-((1R,2R)-1,3-dihydroxy-1-(4-nitrophenyl)propan-2-yl)thiourea to the ribosome pocket, with the generated surface for the receptor 494

Figure 7.51: Van der Waals interactions of 1-(4-chlorophenyl)-3-((1R,2R)-1,3-dihydroxy-1-(4-nitrophenyl)propan-2-yl)thiourea with the ribosome amino acids..... 495

Figure 7.52: Ligand interaction diagram of 1-(4-chlorophenyl)-3-((1R,2R)-1,3-dihydroxy-1-(4-nitrophenyl)propan-2-yl)thiourea to the ribosome..... 495

Figure 7.53: Binding of of 1-(4-chlorophenyl)-3-((1R,2R)-1,3-dihydroxy-1-(4-nitrophenyl)propan-2-yl)thiourea to the CAM acetyl transferase pocket, with the generated surface for the receptor..... 496

Figure 7.54: Van der Waals interactions of 1-(4-chlorophenyl)-3-((1R,2R)-1,3-dihydroxy-1-(4-nitrophenyl)propan-2-yl)thiourea with the CAM acetyl transferase amino acids..... 497

Figure 7.55: Ligand interaction diagram of 1-(4-chlorophenyl)-3-((1R,2R)-1,3-dihydroxy-1-(4-nitrophenyl)propan-2-yl)thiourea for the CAM acetyl transferase enzyme..... 497

Figure 7.56: Binding of 1-((1R,2R)-1,3-dihydroxy-1-(4-nitrophenyl)propan-2-yl)-3-(4-methoxyphenyl)thiourea to the ribosome pocket, with the generated surface for the receptor ... 498

Figure 7.57: Van der Waals interactions of 1-((1R,2R)-1,3-dihydroxy-1-(4-nitrophenyl)propan-2-yl)-3-(4-methoxyphenyl)thiourea with the ribosome amino acids..... 499

Figure 7.58: Ligand interaction diagram of 1-((1R,2R)-1,3-dihydroxy-1-(4-nitrophenyl)propan-2-yl)-3-(4-methoxyphenyl)thiourea to the ribosome..... 499

Figure 7.59: Binding of 1-((1R,2R)-1,3-dihydroxy-1-(4-nitrophenyl)propan-2-yl)-3-(4-methoxyphenyl)thiourea to the CAM acetyl transferase pocket, with the generated surface for the receptor 500

Figure 7.60: Van der Waals interactions of 1-((1R,2R)-1,3-dihydroxy-1-(4-nitrophenyl)propan-2-yl)-3-(4-methoxyphenyl)thiourea with the CAM acetyl transferase amino acids..... 501

Figure 7.61: Ligand interaction diagram of 1-((1R,2R)-1,3-dihydroxy-1-(4-nitrophenyl)propan-2-yl)-3-(4-methoxyphenyl)thiourea for the CAM acetyl transferase enzyme..... 501

Figure 7.62: Binding of 1-((1R,2R)-1,3-dihydroxy-1-(4-nitrophenyl)propan-2-yl)-3-(3,5-dimethylphenyl)thiourea to the ribosome pocket, with the generated surface for the receptor ... 502

Figure 7.63: Van der Waals interactions of 1-((1R,2R)-1,3-dihydroxy-1-(4-nitrophenyl)propan-2-yl)-3-(3,5-dimethylphenyl)thiourea with the ribosome amino acids 503

Figure 7.64: Ligand interaction diagram of 1-((1R,2R)-1,3-dihydroxy-1-(4-nitrophenyl)propan-2-yl)-3-(3,5-dimethylphenyl)thiourea to the ribosome 503

Figure 7.65: Binding of 1-((1R,2R)-1,3-dihydroxy-1-(4-nitrophenyl)propan-2-yl)-3-(3,5-dimethylphenyl)thiourea to the CAM acetyl transferase pocket, with the generated surface for the receptor 504

Figure 7.66: Van der Waals interactions of 1-((1R,2R)-1,3-dihydroxy-1-(4-nitrophenyl)propan-2-yl)-3-(3,5-dimethylphenyl)thiourea with the CAM acetyl transferase amino acids 505

Figure 7.67: Ligand interaction diagram of 1-((1R,2R)-1,3-dihydroxy-1-(4-nitrophenyl)propan-2-yl)-3-(3,5-dimethylphenyl)thiourea for the CAM acetyl transferase enzyme..... 505

Figure 7.68: Binding of 1-(2,5-dihydrofuran-2-yl)-3-((1R,2R)-1,3-dihydroxy-1-(4-nitrophenyl)propan-2-yl)thiourea to the ribosome pocket, with the generated surface for the receptor 506

Figure 7.69: Van der Waals interactions of 1-(2,5-dihydrofuran-2-yl)-3-((1R,2R)-1,3-dihydroxy-1-(4-nitrophenyl)propan-2-yl)thiourea with the ribosome amino acids..... 507

Figure 7.70: Ligand interaction diagram of 1-(2,5-dihydrofuran-2-yl)-3-((1R,2R)-1,3-dihydroxy-1-(4-nitrophenyl)propan-2-yl)thiourea to the ribosome..... 507

Figure 7.71: Binding of 1-(2,5-dihydrofuran-2-yl)-3-((1R,2R)-1,3-dihydroxy-1-(4-nitrophenyl)propan-2-yl)thiourea to the CAM acetyl transferase pocket, with the generated surface for the receptor..... 508

Figure 7.72: Van der Waals interactions of 1-(2,5-dihydrofuran-2-yl)-3-((1R,2R)-1,3-dihydroxy-1-(4-nitrophenyl)propan-2-yl)thiourea with the CAM acetyl transferase amino acids..... 509

Figure 7.73: Ligand interaction diagram of 1-(2,5-dihydrofuran-2-yl)-3-((1R,2R)-1,3-dihydroxy-1-(4-nitrophenyl)propan-2-yl)thiourea for the CAM acetyl transferase enzyme..... 509

Figure 7.74: Binding of 1-(3,5-dichlorophenyl)-3-((1R,2R)-1,3-dihydroxy-1-(4-nitrophenyl)propan-2-yl)thiourea to the ribosome pocket, with the generated surface for the receptor 510

Figure 7.75: Van der Waals interactions of 1-(3,5-dichlorophenyl)-3-((1R,2R)-1,3-dihydroxy-1-(4-nitrophenyl)propan-2-yl)thiourea with the ribosome amino acids 511

Figure 7.76: Ligand interaction diagram of 1-(3,5-dichlorophenyl)-3-((1R,2R)-1,3-dihydroxy-1-(4-nitrophenyl)propan-2-yl)thiourea to the ribosome 511

Figure 7.77: Binding of 1-(3,5-dichlorophenyl)-3-((1R,2R)-1,3-dihydroxy-1-(4-nitrophenyl)propan-2-yl)thiourea to the CAM acetyl transferase pocket, with the generated surface for the receptor 512

Figure 7.78: Van der Waals interactions of 1-(3,5-dichlorophenyl)-3-((1R,2R)-1,3-dihydroxy-1-(4-nitrophenyl)propan-2-yl)thiourea with the CAM acetyl transferase amino acids 513

Figure 7.79: Ligand interaction diagram of 1-(3,5-dichlorophenyl)-3-((1R,2R)-1,3-dihydroxy-1-(4-nitrophenyl)propan-2-yl)thiourea for the CAM acetyl transferase enzyme 513

Figure 7.80: Binding of 1-(4-acetylphenyl)-3-((1R,2R)-1,3-dihydroxy-1-(4-nitrophenyl)propan-2-yl)thiourea to the ribosome pocket, with the generated surface for the receptor 514

Figure 7.81: Van der Waals interactions of 1-(4-acetylphenyl)-3-((1R,2R)-1,3-dihydroxy-1-(4-nitrophenyl)propan-2-yl)thiourea with the ribosome amino acids 515

Figure 7.82: Van der Waals interactions of 1-(4-acetylphenyl)-3-((1R,2R)-1,3-dihydroxy-1-(4-nitrophenyl)propan-2-yl)thiourea with the ribosome amino acids 515

Figure 7.83: Binding of 1-(4-acetylphenyl)-3-((1R,2R)-1,3-dihydroxy-1-(4-nitrophenyl)propan-2-yl)thiourea to the CAM acetyl transferase pocket, with the generated surface for the receptor .. 516

Figure 7.84: Binding of 1-(4-acetylphenyl)-3-((1R,2R)-1,3-dihydroxy-1-(4-nitrophenyl)propan-2-yl)thiourea to the CAM acetyl transferase pocket, with the generated surface for the receptor .. 517

Figure 7.85: Ligand interaction diagram of 1-(4-acetylphenyl)-3-((1R,2R)-1,3-dihydroxy-1-(4-nitrophenyl)propan-2-yl)thiourea for the CAM acetyl transferase enzyme 517

Figure 7.86: Binding of 1-(2-chloro-4-nitrophenyl)-3-((1R,2R)-1,3-dihydroxy-1-(4-nitrophenyl)propan-2-yl)thiourea to the ribosome pocket, with the generated surface for the receptor 518

Figure 7.87: Ligand interaction diagram of 1-(2-chloro-4-nitrophenyl)-3-((1R,2R)-1,3-dihydroxy-1-(4-nitrophenyl)propan-2-yl)thiourea to the ribosome 519

Figure 7.88: Binding of 1-(2-chloro-4-nitrophenyl)-3-((1R,2R)-1,3-dihydroxy-1-(4-nitrophenyl)propan-2-yl)thiourea to the CAM acetyl transferase pocket, with the generated surface for the receptor 520

Figure 7.89: Ligand interaction diagram of 1-(2-chloro-4-nitrophenyl)-3-((1R,2R)-1,3-dihydroxy-1-(4-nitrophenyl)propan-2-yl)thiourea for the CAM acetyl transferase enzyme 521

1 CHAPTER 1

Published in *ACS Omega*, **2018**, *3* (1), pp 677–681

Cyclodextrin-Based Pseudorotaxanes: Easily Conjugatable Scaffolds for Synthesizing Hyperpolarized Xenon-129 Magnetic Resonance Imaging Agents

Francis T. Hane,*,†,‡,∥ Ashvin Fernando,§,∥ Braedan R. J. Prete,† Brianna Peloquin,§ Scott Karas,§ Sauradip Chaudhuri,§ Simrun Chahal,† Yurii Shepelytskyi,† Alanna Wade,† Tao Li,† Brenton DeBoef,*,§ and Mitchell S. Albert†,‡

†Department of Chemistry, Lakehead University, 955 Oliver Road, Thunder Bay, Ontario P7B 5E1, Canada ‡Thunder Bay Regional Research Institute, 980 Oliver Road, Thunder Bay, Ontario P7B 5E1, Canada §Department of Chemistry, University of Rhode Island, 140 Flagg Road, Kingston, Rhode Island 02881, United States

ABSTRACT

Hyperpolarized (HP) xenon-129 (Xe) mag- netic resonance (MR) imaging has the potential to detect biological analytes with high sensitivity and high resolution when coupled with xenon-encapsulating molecular probes. Despite the development of numerous HP Xe probes, one of the challenges that has hampered the translation of these agents from in vitro demonstration to in vivo testing is the difficulty in synthesizing the Xe-encapsulating cage molecule. In this study, we demonstrate that a pseudorotaxane, based on a γ-cyclodextrin macrocycle, is easily synthesized in one step and is detectable using HyperCEST-enhanced 129Xe MR spectroscopy.

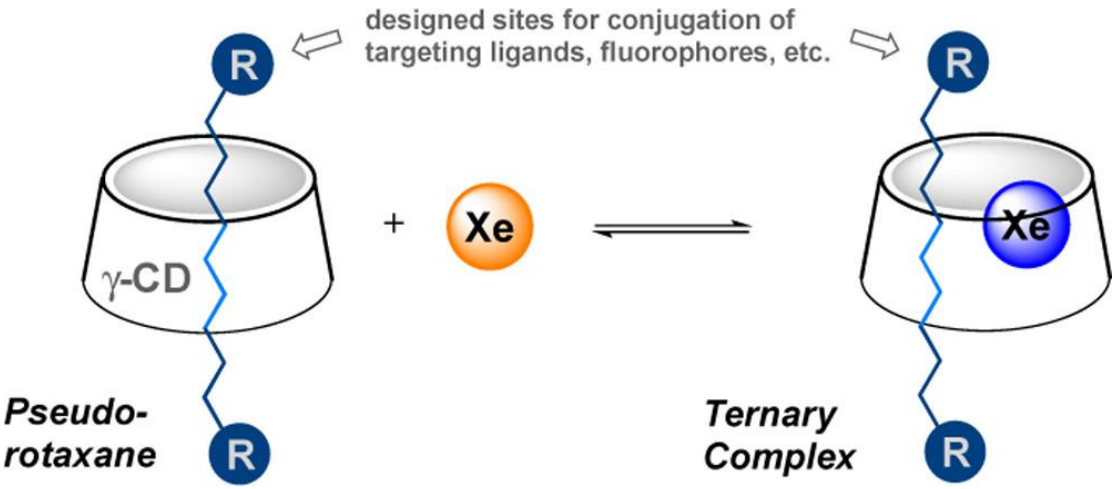

Introduction

Hyperpolarized (HP) xenon-129 magnetic resonance imaging (MRI) has the potential to become a molecular imaging platform for safely producing highly resolved three-dimensional images of biochemical phenomena through the use of xenon- capturing molecular probes. Currently, the most prevalent molecular imaging techniques, positron emission tomography and single-photon emission computed tomography, involve the administration of radiolabeled chemical probes. Other methods for enhancing MR sensitivity, such as parahydrogen-induced polarization, signal amplification by reversible exchange, and dissolution dynamic nuclear polarization, and dynamic 1H imaging techniques, such as paramagnetic chemical exchange saturation transfer, involve the difficult synthesis of molecular probes using parahydrogen, specific isotopes, or toxic metal ions before the imaging experiment is performed[1-3]. Contrastingly, molecular probes based on the pseudorotaxanes described herein are simple to synthesize and the inclusion of the nonradioactive, nontoxic 129Xe isotope occurs spontaneously in situ. Xe gas can be inhaled, and its biodistribution can be imaged using an MRI instrument with a broadband coil.[4–6] HP Xe atoms cannot, by themselves, be tuned to target particular regions in the body, but targeted HP Xe biosensors that are capable of binding both biochemical receptors and xenon atoms in vivo have been postulated as a new molecular imaging platform.[7–9]

Employing hyperpolarized nuclei and a saturation transfer pulse sequence, known as HyperCEST, provides up to a billion times sensitivity enhancement compared to that of thermally polarized nuclei, allowing for picomolar concentrations of the Xe-encapsulating probe to be detected.[10-11] We recently disclosed the first in vivo images of an HP Xe probe in a live animal using the millimolar quantities of the nontargeted Xe cage, cucurbit[6]uril (CB6).[12] This work demonstrated that molecular probes can be imaged in vivo via HyperCEST, but despite this work and numerous other prototypes,[8,13–25] targeted HP Xe MRI biosensors have yet to be used for in vivo imaging in a whole animal. The development of these potential biosensors has not been slowed by a lack of interest in

the techniques or by barriers in MRI technology. In our opinion, the problem is more fundamental: the supramolecular hosts that encapsulate xenon are difficult to synthesize and functionalize, so sufficient quantities of the targeted probes for in vivo imaging are simply not available. Herein, we describe the development of a new class of water- soluble HP Xe biosensors that use a pseudorotaxane to encapsulate HP Xe and can be imaged using a HyperCEST pulse sequence. The modular nature of the probes and their facile synthesis should allow for the rapid development of targeted molecular probes for HP Xe MRI (Figure 1)

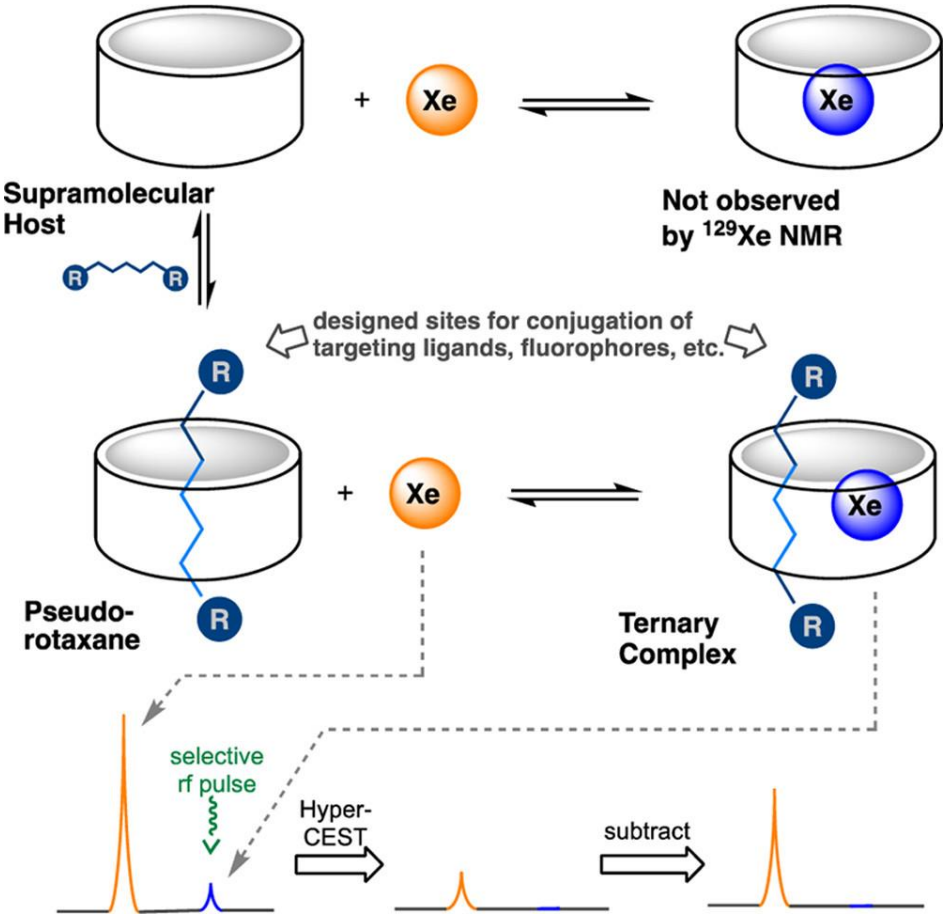

Figure 1.1:Proposed binding of Xe via formation of a ternary complex and detection via HyperCEST

Until recently, the hollow, ball-shaped molecular cages, known as cryptophanes, appeared to be privileged structures in the field of HP Xe imaging.[26–28] Cucurbit[6]uril (CB6) and cucurbit[7]uril

(CB7) have also been reported as HP Xe probes,[11,29-30] but the larger cucurbit[8]uril (CB8) does not show any affinity for Xe. α, β, and γ-cyclodextrins (CDs), which are truncated cone-shaped macrocycles composed of six, seven, or eight D-glycopyranoside units, are some of the most commonly used hosts in supramolecular chemistry,[31] and they would be ideal components of 129Xe probes because they are nontoxic and water soluble (Figure 2).

Unfortunately, either α, β, and γ-CD fail to bind Xe in aqueous media or the reversible binding has too fast of an exchange rate to form a distinct peak that is observable by129Xe NMR at room temperature.[32,33] We hypothesized that macrocycles that were too large to bind Xe on their own, such as CB8, β-CD, and γ-CD, could be threaded with long alkyl chains to create pseudorotaxane complexes that were capable of forming a ternary complex with Xe (Figure 1).[34] Rotaxanes are well-known supramolecular species composed of a molecular axle that is threaded through a tube-shaped host, creating a noncovalently bound structure. To serve as a Xe cage, the inner diameter of the rotaxane macrocycle must be large enough to fit both the molecular axle and a Xe atom in its hydrophobic core. However, a macrocycle that is too large would not be detectable using HyperCEST because the Xe would exchange in and out of the host at a rate that is too high to support HyperCEST detection. Prior to this work, the only precedent for the formation of this kind of ternary complex with Xe was reported by Cohen, who showed that a pillararene could simultaneously bind hexane and Xe.[35] To test the above mentioned hypothesis, we designed a series of new pseudorotaxanes based on cucurbiturils and cyclodextrins to determine their potential as xenon hosts.

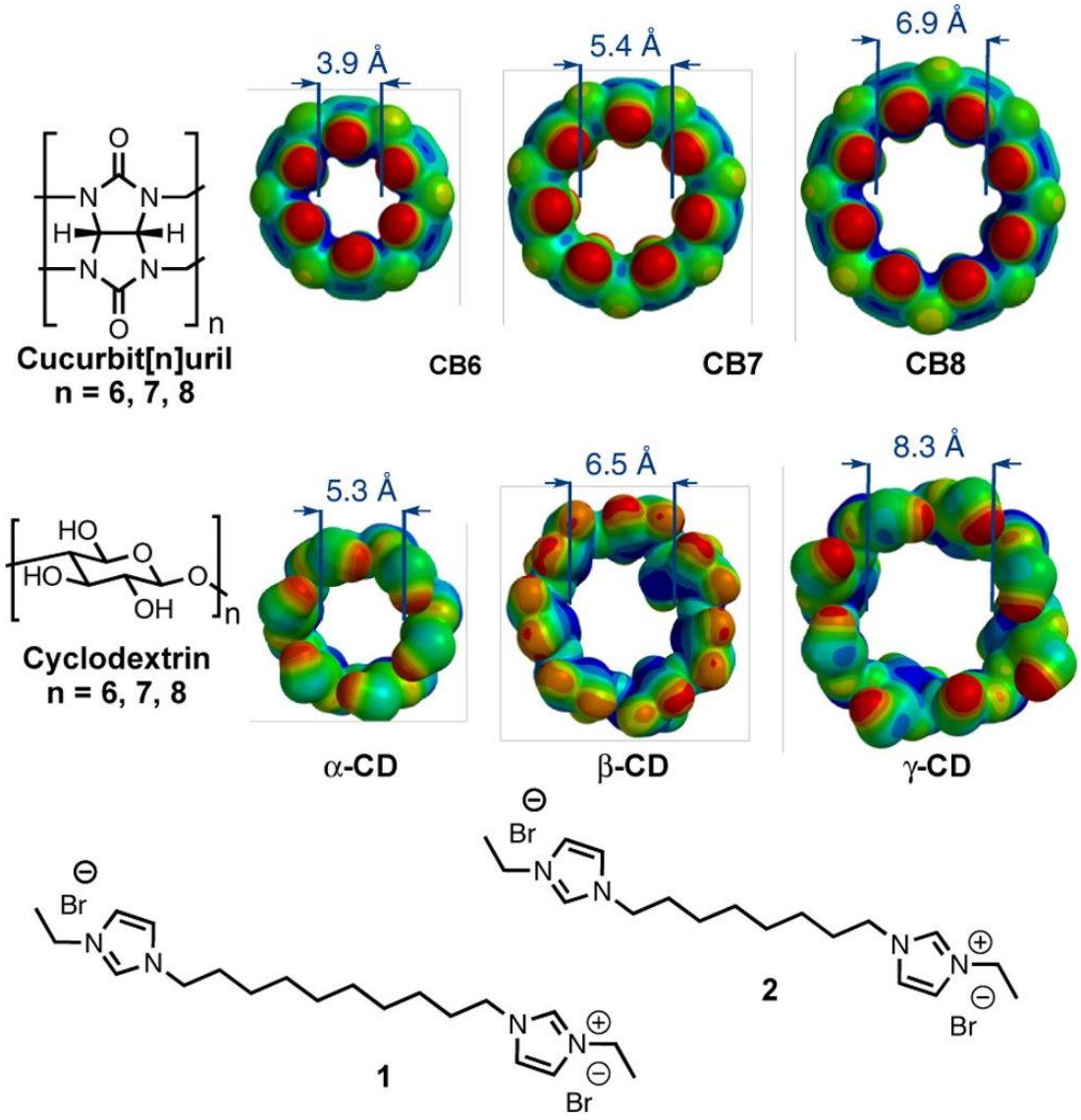

Figure 1.2: Structures of hosts and guests used in this study

RESULTS AND DISCUSSION

Three cucurbiturils (CB6, CB7, and CB8) and three cyclo- dextrins (α, β, and γ-CD) were chosen as the host molecules. These six macrocycles were threaded with 8- and 10-carbon molecular threads that contained terminal ethylimidazolium groups, which served to enhance the water solubility of the hydrophobic alkanes and enabled facile detection by mass spectrometry (1 and 2).[36] In all of the cases studied, the rapid formation of threaded complexes was observed by mass spectrometry and 1H NMR, though most cases showed rapid host−guest exchange on the NMR time scale. Analysis by 129Xe NMR identified the promising scaffolds

that combined the desired attributes of facile synthesis with MR detectability via HyperCEST. For the HP Xe studies, we used a custom-built fritted phantom inside a custom dual-tuned 1H/129Xe radiofrequency (RF) coil to acquire all free induction decay (FID) spectra. The aqueous solutions of the pseudor- otaxanes were placed inside the fritted phantom, and HP Xe was introduced below the fritted phantom, creating micro- bubbles that percolated vertically through the sample. A series of saturation prepulses at a variety of chemical shift offsets were loaded into user interface software of the GE Achieva 3T MR scanner. Spectra with different saturation prepulses were acquired approximately every 6 s.

As expected, irradiation at +128 ppm (relative to the peak corresponding to xenon gas) produced a 67% depletion for a sample of unthreaded CB6, thus confirming that our experimental method was reliable (Table 1, entry 1). However, it should be noted that contrary to previous reports, we did not observe a HyperCEST signal for CB7 (entry 4).[37] None of the studies with cucurbituril-derived pseudorotaxanes produced any HyperCEST attenuation (entries 2−3, 5−6, and 8−9), likely indicating that there is not sufficient space to bind xenon in the cavity of the supramolecular complex. Gratifyingly, we found that cycodextrin-based pseudorotax- anes reversibly encapsulated Xe and could be detected by 129Xe magnetic resonance spectroscopy. HyperCEST depletions of

43 and 52% were observed for the γ-CD containing C8 and C10 diethylimidazolium bars (2 ⊂ γ-CD and 1 ⊂ γ-CD, respectively, entries 17 and 18).

Entry	Pseudo-rotaxane	Cavity Volume (Å^3)[a]	HyperCEST (%)[c]	δ (ppm)[b]
1	CB6	164	67%	+128
2	+ **2**	52	0%	-
3	+ **1**	41	0%	-
4	CB7	279	0%	-
5	+ **2**	82	0%	-
6	+ **1**	79	0%	-
7	CB8	479	0%	-
8	+ **2**	138	0%	-
9	+ **1**	125	0%	-
10	α-CD	174	0%	-
11	+ **2**	52.1	0%	-
12	+ **1**	48.1	0%	-
13	β-CD	262	0%	-
14	+ **2**	85.1	0%	-
15	+ **1**	74.2	0%	-
16	γ-CD	427	0%	-
17	+ **2**	170.1	43%	+128
18	+ **1**	176.2	52%	+128

[a]Volume of xenon binding pocket based on computed host and pseudorotaxane structures. See the Supporting Information for details.

[b]Depletion of the peak corresponding to unbound Xe. Samples were dissolved in water (2 mL, 10 mM), and one-dimensional 129Xe spectra were recorded. HyperCEST spectra were subsequently acquired using a series of off-resonance pulses varying by 5 ppm

Table 1-1: Characterization and HyperCEST Data for Pseudorotaxanes

Like CB6, the maximum HyperCEST depletion for the γ-CD pseudorotaxanes occurred when the samples were irradiated at a frequency of +128 ppm, relative to the Xe gas-phase signal.

HyperCEST depletion spectra for 1 ⊂ γ-CD are shown in Figure 3. Importantly, the magnitude of the HyperCEST depletion for 1 ⊂ γ-CD was comparable to that of CB6, a xenon cage that we have recently shown to be amenable.

to in vivo HP Xe MRI.12 1H NMR also confirms the formation of the ternary pseudorotaxane−xenon complex [(Xe·1) ⊂ γ-CD, Figure 4]. Formation of the pseudorotaxane with γ-CD and 1 can be monitored by an upfield shift in the triplet corresponding to the proton attached to the C3 position in the cyclodextrin. This proton is positioned on the interior of the macrocycle, so it is shielded when the pseudorotaxane forms. Subsequent binding of xenon further shifts the C3−H peak upfield, indicating that the xenon also binds to the interior of the macrocyclic host. No shifts of the protons corresponding to the ethylimidazolium groups of the host pseudorotaxane are observed. Whereas these spectra might not, by themselves, be definitive evidence for the formation of the proposed ternary complex, when considered in the context of the HyperCEST data shown in Figure 3, the data are consistent with the formation of a ternary complex. Importantly, the control experiments in entries 10, 13, and 16 of Table 1 show that xenon does not form a binary complex with cyclodextrins that can be detected by HyperCEST.

The formation of the pseudorotaxanes was observed by mass spectrometry. Additionally, NMR and isothermal calorimetry (ITC) binding studies were used to characterize the most promising pseudorotaxanes.[38] The association constant, Ka, for 1 ⊂ γ-CD was determined by NMR in pure water to be 2.94×10^3 M^{-1} at 300 K, and the Ka for 2 ⊂ γ-CD was determined to be 4.10×10^3 M^{-1} at 300 K. ITC was also used to corroborate the Ka for 1 ⊂ γ-CD in pure water, 1.00×10^4 M^{-1} at 300 K. Importantly, ITC in fetal bovine serum also showed formation of the pseudorotaxane complex, though the binding affinity was two orders of magnitude lower, 1.01×10^2 M^{-1} at 300 K. This indicates that the pseudorotaxanes form in complex, biological media, so they could find application as hyperpolarized xenon biosensors.

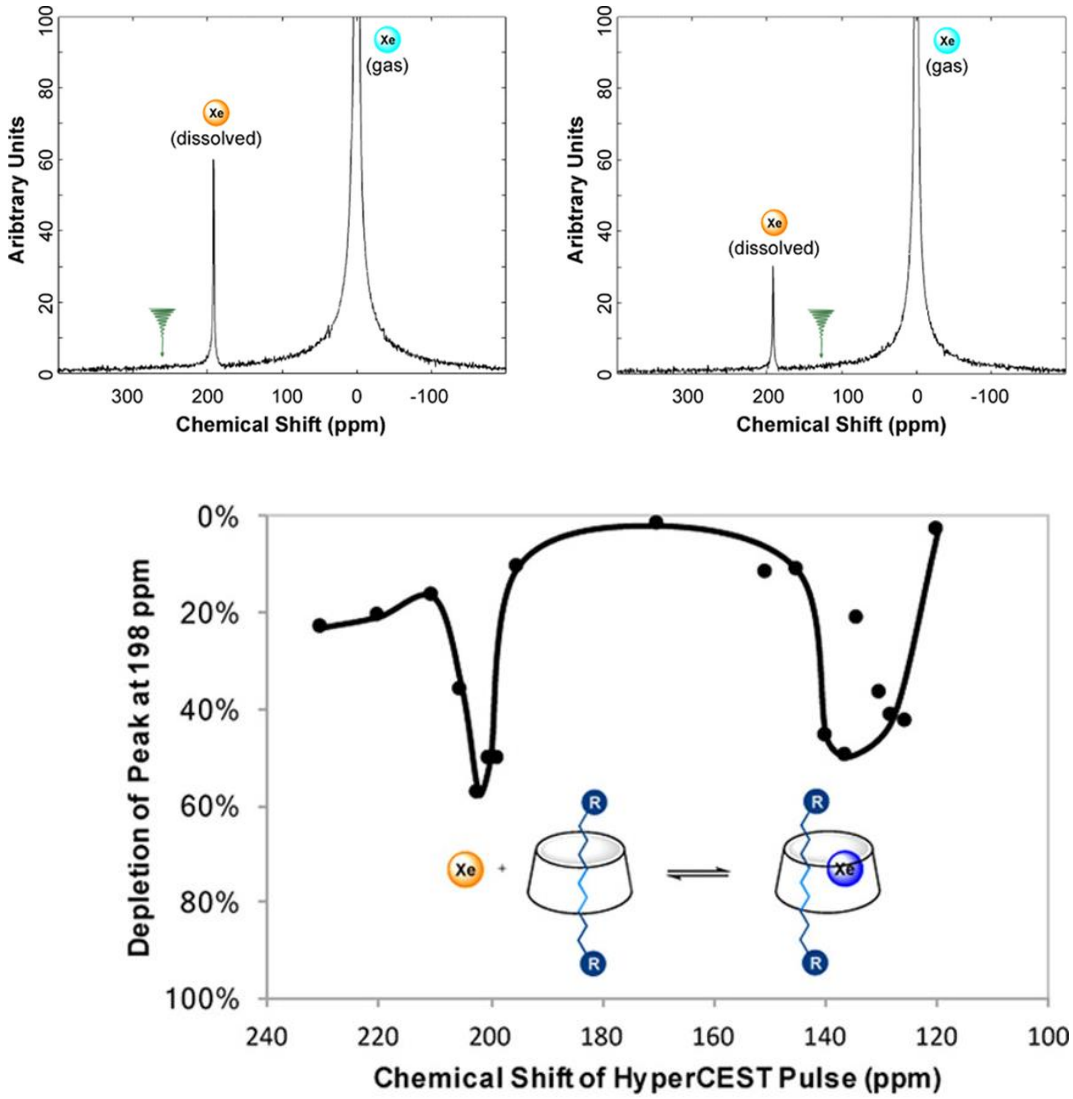

Figure 1.3: Free Induction Decay (FID) spectra of 10 mM aqueous solution of 1⊂γ-CD following off-resonance (+255 ppm, left) and on-resonance (+128 ppm, center) HyperCEST pulses. HyperCEST depletion z-spectrum of a 10 mM aqueous solution of 1⊂γ-CD (right). Each data point indicates the HyperCEST depletion when the molecule is irradiated with a pulse at a given chemical shift off-set.

The data shown herein indicate that two parameters can be used to predict the ability of a pseudorotaxane to form a ternary complex with xenon. First, the pseudorotaxane must form a 1:1 host−guest complex. Our data does not probe a wide range of host−guest association constants, but it appears that an affinity on the order of 103 is sufficient.

Second, the pseudorotaxane must contain an internal hydrophobic cavity with a volume of approximately 164−176 Å3 (Table 1, entries 1, 17, and 18). These parameters explain why all the pseudorotaxanes with hosts besides γ-CD failed to bind Xe; they simply did not have a large enough internal cavity. α-Cyclodextrin also has a cavity that is of sufficient size to bind Xe (174 Å3, entry 10), and this binding has been previously reported;[32] however, the chemical shift of the bound complex is 3 ppm away from the peak corresponding to dissolved xenon, too close to be observed, as our HyperCEST pulse is ~10 ppm wide.

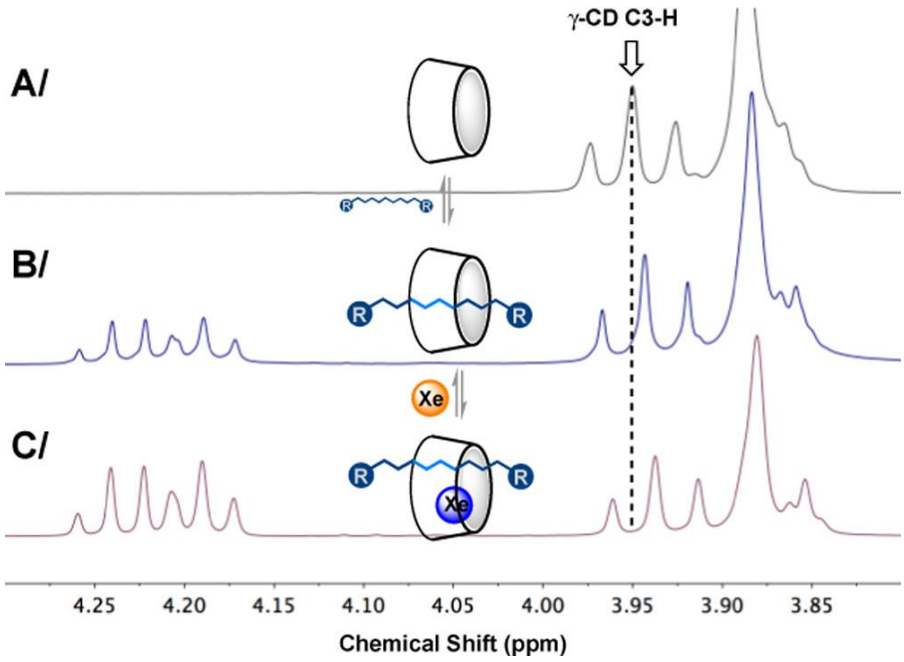

Figure 1.4: ^{1}H NMR spectra indicating the formation of the ter-nary complex (25 oC, [γ-CD] = [1] = 100 mM.) A/ ^{1}H NMR spectrum of γ-cyclodextrin. B/ ^{1}H NMR spectrum after addition of 1 equiv of 1. C/ ^{1}H NMR spectrum after addition of 1.5 atm xenon

It should be noted that the pseudorotaxanes that we are describing herein are markedly distinct from the rotaxane-based HP Xe probes that have been recently described by Dmochowski, Pines, and Francis.19,39 In those cases, a threaded CB6 structure was synthesized that could not bind Xe, but when the thread was severed, either by action of an enzyme or by a change in pH, the CB6 was released, and a signal was observed. These probes represent a creative approach for synthesizing "turn on" HP Xe sensors; contrastingly, the rotaxanes that we describe herein are a new scaffold that is capable of producing an HP Xe signal via formation of a ternary binding motif The data shown in Table 1 and Figure 3 were obtained using a Phillips Achieva 3T clinical whole-body MR scanner, which provides significant advantages over conventional NMR spectrometers, namely, the ability of performing whole-body imaging experiments. These advantages come with some trade-offs, specifically the ability of acquiring HyperCEST depletion spectra with a Lorenzian fit line, such as in the data processed for cryptophane and cucurbituril agents, as demonstrated by others using high-field, high-resolution NMR spectrome- ters.[11,39–42] However, the use of a clinical scanner bodes well for eventual clinical translation of our techniques to in vivo experiments, which we recently demonstrated using a non- targeted 129Xe contrast agent.[12]

In conclusion, we have discovered a novel method for synthesizing potential HP Xe probes using pseudorotaxane structures of γ-CD. These supramolecular complexes form a novel ternary structure in the presence of HP Xe, which can be detected via 129Xe MR spectroscopy. Current efforts in our laboratories are dedicated to synthesizing rotaxane-based probes that will not dissociate and in the application of these new probes for targeted molecular imaging.

NMR HyperCEST Detection. Natural abundant 129Xe gas

was polarized to 26−30% using a Xemed polarizer (Xemed, Durham, NH). Next, 1.0 mL of sample was drawn into a glass frit cell using a syringe. The cell was then inserted into a custom RF coil tuned to the Larmor frequency of 129Xe (35.33 MHz) at 3T, where HP 129Xe gas was introduced to the vessel from the Tedlar bag in the pressure chamber, which was pressurized at 35 kPa above

atmosphere. The solution was mixed with HP 129Xe gas as it passed through the fine fritted disc and produced several microbubbles, which continuously dissolved into solution and exited the vessel through the outflow tube. The concentration of 129Xe at any point during the experiment was between 1 and 10 mM. A Philips Achieva 3T clinical scanner was used to collect all NMR spectra. The RF pulse length was determined with the use of ref B1, a parameter of Philips MR scanners. The pulse length and flip angle were used to calculate the amplitude of the RF pulse and field strength. In this study, the B1 field strength was determined by the scanner to be 15.9 μT. In the acquisition of NMR spectra, a pulsed saturation pre-pulse train consisting of 96−20 ms 3-lobe sinc pulses with 0 ms pulse intervals was applied at various chemical shift offsets.

Free induction decay (FID) spectra were acquired at various chemical shift frequency offsets, approximately 5 ppm apart. Each FID spectra was acquired approximately 6 s apart. Off- resonance FID spectra were obtained quarterly in this series and acquired with a saturation pre-pulse at +271 ppm off- resonance from the gas-phase peak. A HyperCEST depletion spectrum was collected for each sample (see the Supporting Information) by measuring HyperCEST depletion at various frequency offsets from the Xe gas-phase peak. A minimum of three spectra were obtained at each of the various chemical shifts, and a plot of the mean signal depletion as a function of the frequency of the chemical shift offset (z-spectrum) was produced. The mean signal-to-noise ratio (SNR) obtained from all control spectra for individual samples was used in the measurement of signal depletion. The SNR for each spectrum was calculated using MATLAB (MathWorks, Natick, MA). To measure signal depletion, the mean HyperCEST saturation spectrum SNR was subtracted from the mean control spectrum SNR. This difference was then divided by the mean control spectrum SNR to produce the signal depletion by the HyperCEST effect.

1.1 REFERENCES

(1) Massoud, T. F.; Gambhir, S. S. Genes Dev. 2003, 17, 545.

(2) Kurhanewicz, J.; Vigneron, D. B.; Brindle, K.; Chekmenev, E. Y.; Comment, A.; Cunningham, C. H.; DeBerardinis, R. J.; Green, G. G.; Leach, M. O.; Rajan, S. S.; Fizi, R. R.; Ross, B. D.; Warren, W. S.; Mallory, C. R. Neoplasia 2011, 13, 81.

(3) Nikolaou, P.; Goodson, B. M.; Chekmenev, E. Y. Chem. Eur. J. 2015, 21, 3156.

(4) Albert, M. S.; Cates, G. D.; Driehuys, B.; Happer, W.; Saam, B.; Springer, C. S.; Wishnia, A. Nature 1994, 370, 199.

(5) Oros, A.-M.; Shah, N. J. Phys Med Biol 2004, 49, R105.

(6) Fox, M. S.; Couch, M. J.; Albert, M. S. Magnetic Resonance Imaging of the Brain Using Hyperpolarized 129Xe. In Hyperpolarized Xenon-129 Magnetic Resonance; Concepts, Production, Techniques and Applications; Royal Society of Chemistry: Cambridge, 2015; pp 407–425.

(7) Spence, M. M.; Rubin, S. M.; Dimitrov, I. E.; Ruiz, E. J.; Wemmer, D. E.; Pines, A.; Yao, S. Q.; Tian, F.; Schultz, P. G. Proc. Natl. Acad. Sci. 2001, 98, 10654

(8) Schröder, L. Phys Med 2013, 29, 3.

(9) Schröder, L. Xenon Biosensor HyperCEST MRI. In Hyperpolarized and inert gas MRI: From technology to application in research and medicine; Albert, M. S., Hane, F. T., Eds.; Academic Press: London, 2016; pp 263–278.

(10) Schröder, L.; Lowery, T. J.; Hilty, C.; Wemmer, D. E.; Pines, A. Science 2006, 314, 446–449.

(11) Bai, Y.; Hill, P. A.; Dmochowski, I. J. Anal. Chem. 2012, 84, 9935–9941.

(12) Hane, F. T.; Li, T.; Smylie, P.; Pellizzari, R. M.; Plata, J. A.; DeBoef, B.; Albert, M. S. Sci. Rep. 2017, 7, 41027.

(13) Wang, Y.; Dmochowski, I. J. Acc. Chem. Res. 2016, 49, 2179.

(14) Stevens, T. K.; Palaniappan, K. K.; Ramirez, R. M.; Francis, M. B.; Wemmer, D. E.; Pines, A. Magn. Reson. Med. 2013, 69, 1245.

(15) Mynar, J. L.; Lowery, T. J.; Wemmer, D. E.; Pines, A.; Fréchet, J. M. J. J. Am. Chem. Soc. 2006, 128, 6334.

(16) Stevens, T. K.; Ramirez, R. M.; Pines, A. J. Am. Chem. Soc. 2013, 135, 9576.

(17) Shapiro, M. G.; Ramirez, R. M.; Sperling, L. J.; Sun, G.; Sun, J.; Pines, A.; Schaffer, D. V.; Bajaj, V. S. Nat. Chem. 2014, 6, 629.

(18) Bai, Y.; Wang, Y.; Goulian, M.; Driks, A.; Dmochowski, I. J. Chem. Sci. 2014, 5, 3197.

(19) Wang, Y.; Roose, B. W.; Philbin, J. P.; Doman, J. L.; Dmochowski, I. J. Angew. Chem. Int. Ed. 2015, 128, 1765.

(20) Riggle, B. A.; Wang, Y.; Dmochowski, I. J. J. Am. Chem. Soc. 2015, 137, 5542.

(21) Seward, G. K.; Bai, Y.; Khan, N. S.; Dmochowski, I. J. Chem. Sci. 2011, 2, 1103.

(22) Rose, H. M.; Witte, C.; Rossella, F.; Klippel, S.; Freund, C.; Schröder, L. Proc. Natl. Acad. Sci. 2014, 111, 11697.

(23) Kotera, N.; Dubost, E.; Milanole, G.; Doris, E.; Gravel, E.; Arhel, N.; Brotin, T.; Dutasta, J. P.; Cochrane, J.; Mari, E.; et al. Chem. Commun. 2015, 51, 11482.

(24) Tassali, N.; Kotera, N.; Boutin, C.; Léonce, E.; Boulard, Y.; Rousseau, B.; Dubost, E.; Taran, F.; Brotin, T.; Dutasta, J.-P.; et al. Anal. Chem. 2014, 86, 1783.

(25) Khan, N. S.; Riggle, B. A.; Seward, G.; Bai, Y.; Dmochowski, I. J. Bioconjugate Chem. 2015, 26, 101.

(26) Huber, G.; Beguin, L.; Desvaux, H.; Brotin, T.; Fogarty, H. A.; Dutasta, J.-P.; Berthault, P. J. Phys. Chem. A 2008, 112, 11363–11372.

(27) Fogarty, H.; Berthault, P.; Brotin, T.; Huber, G.; Desvaux, H.; Dutasta, J. P. J. Am. Chem. Soc. 2007, 129, 10332.

(28) Bartik, K.; Luhmer, M.; Dutasta, J. P.; Collet, A.; Reisse, J. J. Am. Chem. Soc. 1998, 120, 784.

(29) El Haouaj, M.; Luhmer, M.; Ko, Y. H.; Kim, K.; Bartik, K. J. Chem. Soc. Perkin Trans. 2 2001, 2, 804.

(30) Schnurr, M.; Sloniec Myszk, J.; Döpfert, J.; Schröder, L.; Hennig, A. Angew. Chem. Int. Ed. 2015, 54, 13444.

(31) Sharma, N.; Baldi, A. Drug Delivery 2016, 23, 729.

(32) Bartik, K.; Luhmer, M.; Heyes, S. J.; Ottinger, R.; Reisse, J. J. Magn. Reson. B 1995, 109, 164.

(33) Song, Y.-Q.; Goodson, B. M.; Taylor, R. E.; Laws, D. D.; Navon, G.; Pines, A. Angew. Chem. Int. Ed. 1997, 36, 2368.

(34) Xue, M.; Yang, Y.; Chi, X.; Yan, X.; Huang, F. Chem. Rev. 2015, 115, 7398.

(35) Adiri, T.; Marciano, D.; Cohen, Y. Chem. Commun. 2013, 49, 7082.

(36) McCune, J. A.; Rosta, E.; Scherman, O. A. Org. Biomol. Chem. 2017, 15, 998.

(37) Schnurr, M.; Sloniec Myszk, J.; Döpfert, J.; Schröder, L.; Hennig, A. Angew. Chem. Int. Ed. 2015, 54, 13444–13447.

(38) Thordarson, P. Chem. Soc. Rev. 2011, 40, 1305.

(39) Finbloom, J. A.; Slack, C. C.; Bruns, C. J.; Jeong, K.; Wemmer, D. E.; Pines, A.; Francis, M. B. Chem. Commun. 2016, 52, 3119.

(39) Schnurr, M.; Sydow, K.; Rose, H. M.; Dathe, M.; Schröder, L. Adv. Healthc. Mater. 2015, 4, 40.

(40) Klippel, S.; Döpfert, J.; Jayapaul, J.; Kunth, M.; Rossella, F.; Schnurr, M.; Witte, C.; Freund, C.; Schröder, L. Angew. Chemie Int. Ed. 2014, 53, 493.

(41) Kunth, M.; Witte, C.; Hennig, A.; Schröder, L. Chem. Sci. 2015, 6, 6069.

(42) Kunth, M.; Witte, C.; Schröder, L. NMR Biomed. 2015, 28, 601.

1.2 SUPPORTING INFORMATION

Cyclodextrin-based Pseudorotaxanes: Easily Conjugatable Scaffolds for Synthesizing Hyperpolarized Xenon-129 Magnetic Resonance Imaging Agents

Experimental Section

Reagents

Substrates, including 1-ethylimidazole, 1,8-dibromooctane, 1,10-dibromodecane, 1,5-dibromopentane, cucurbit[6]uril, cucurbit[7]uril, cucurbit[8]uril, α-cyclodextrin, β-cyclodextrin and γ-cyclodextrin were purchased from Sigma-Aldrich, Fisher Scientific, and TCI chemicals. All reagents were stored under an inert atmosphere before use. Unless otherwise noted, all reactions were performed under N_2.

Instrumentation

NMR spectra were obtained using a Bruker Avance 300 MHz and 400 MHz spectrometers. Low resolution mass spectrometry was performed using a Shimadzu LRMS-2020. High resolution mass spectrometry was performed using a Thermo Scientific LTQ Orbitrap XL™ instrument. Isothermal calorimetry was performed using TA Instruments TAM III™ instrument.

Synthesis of guest molecules

Synthesis of C_{10} diethylimidazolium guest, 1

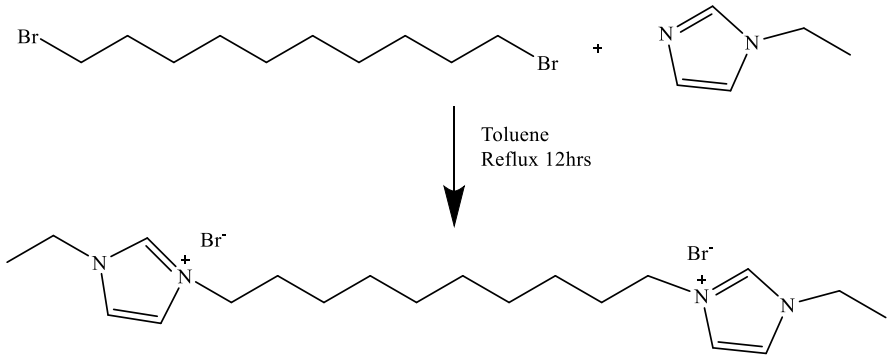

1-Ethylimidazole (1.942 mL, 20 mmol) and 1,10-dibromodecane (1.792 mL, 8 mmol) were dissolved in toluene (15 mL) and refluxed for 12 hours. Once complete, the toluene was decanted, and the crude product was washed with diethyl ether (3 x 20 mL) and dried under vacuum until a white solid product formed (2.20 g, 56% yield). Spectral data matched the reported values.[1]

^{1}H NMR (400 MHz, DMSO-d_6) δ 9.34 (s, *J* = 1.7 Hz, 2H), 7.85 (dd, *J* = 5.8, 1.9 Hz, 4H), 4.20 (dq, *J* = 14.3, 7.3 Hz, 8H), 1.79 (p, *J* = 7.3 Hz, 4H), 1.43 (t, *J* = 7.3 Hz, 6H), 1.25 (s, 12H).

^{13}C NMR (101 MHz, DMSO-d_6) δ 136.1, 122.8, 122.6, 49.2, 44.6, 29.8, 29.2, 28.8, 25.9, 15.5.

HRMS ESI (m/z): [M+] calculated for $C_{20}H_{36}N_4^{2+}$ 166.1467, observed 166.1455.

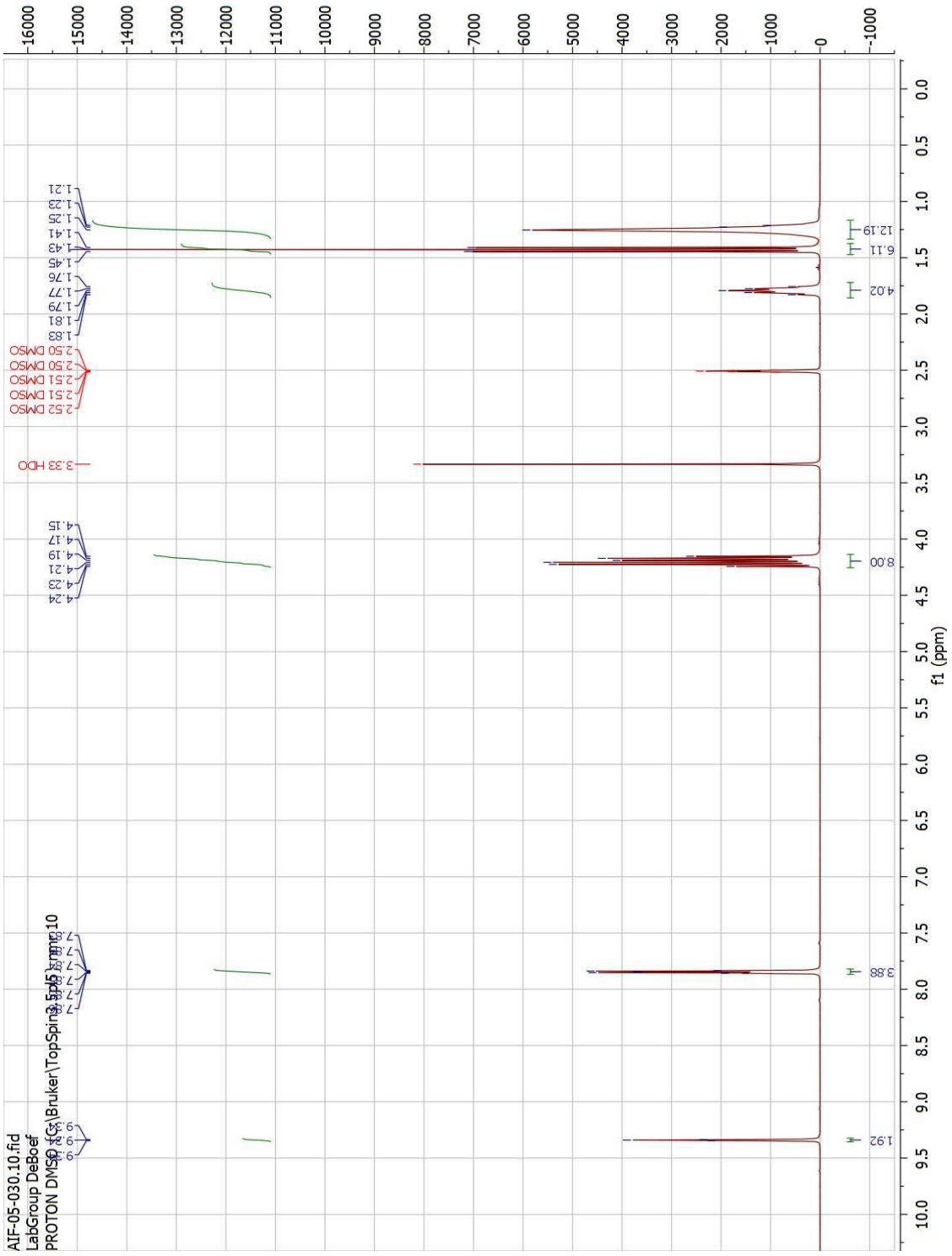

Figure 1.5: ^{1}H NMR of Guest 1

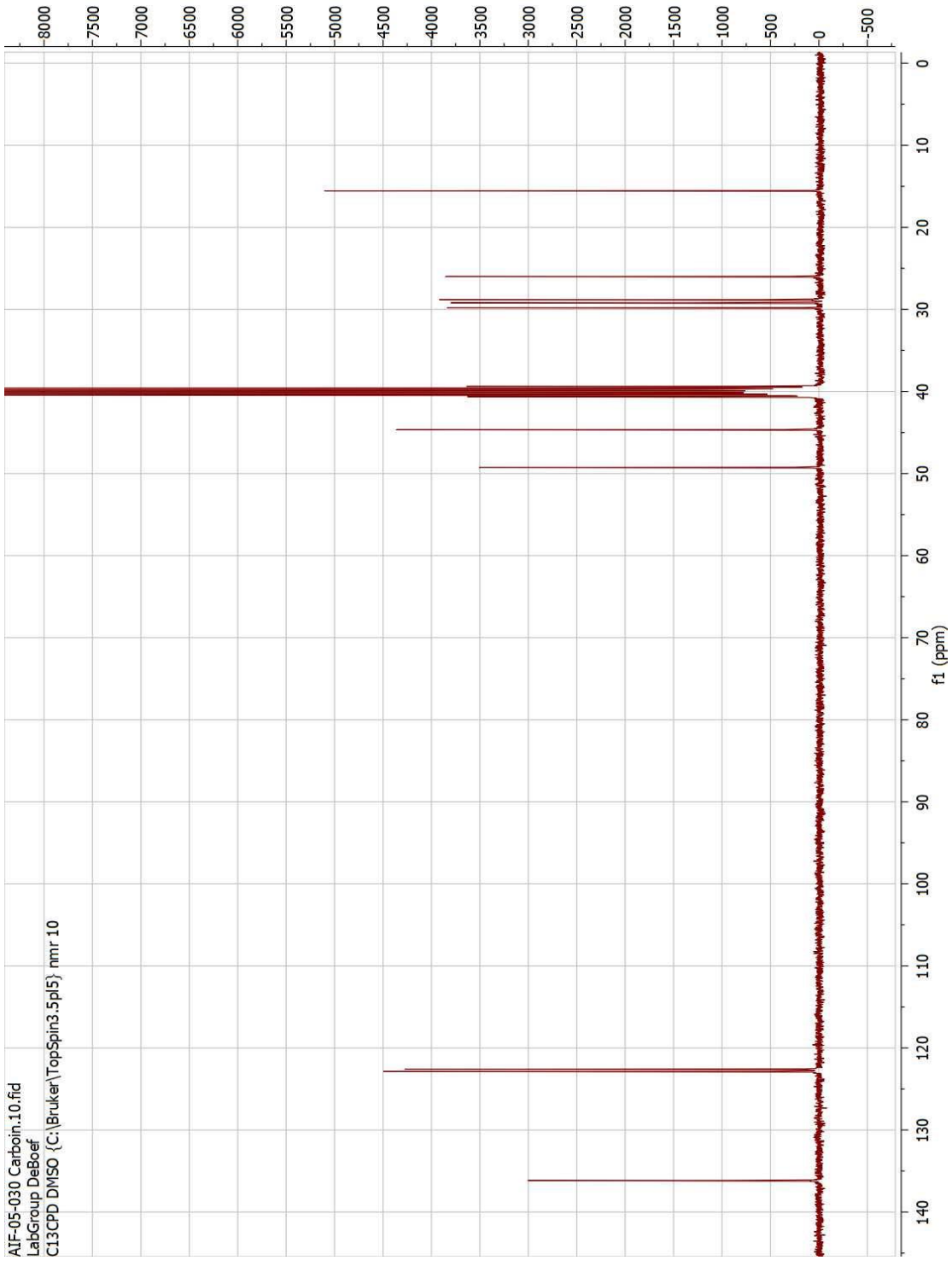

Figure 1.6: ^{13}C NMR of Guest 1

Synthesis of C_8 diethylimidazolium guest, 2

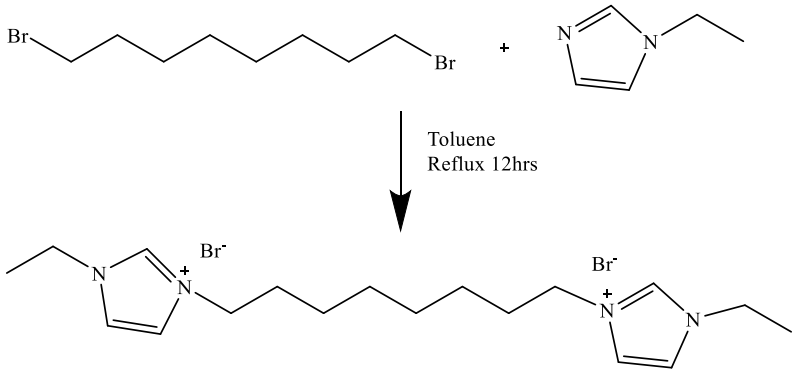

1-Ethylimidazole (1.06 mL, 11 mmol) and 1,8-dibromooctane (808.7 µL, 4.4 mmol) were dissolved in toluene (15 mL) and refluxed for 12 hrs. Once complete, the toluene was decanted, and the crude product was washed with diethyl ether (3 x 20 mL) and dried under vacuum until a white solid product formed (0.51 g, 38% yield). Spectral data matched the reported values.[1]

^{1}H NMR (400 MHz, DMSO-d_6) δ 9.40 (s, 2H), 7.86 (d, *J* = 1.7 Hz, 4H), 4.11 (m, 8H), 1.79 (p, *J* = 7.2 Hz, 4H), 1.42 (t, *J* = 7.3 Hz, 6H), 1.12 (m, 8H).

^{13}C NMR (101 MHz, DMSO-d_6) δ 136.2, 122.8, 122.6, 49.2, 49.6, 29.7, 28.6, 25.8, 15.6.

HRMS ESI (m/z): [M+] calculated for $C_{18}H_{32}N_4^{2+}$ 152.1308, observed 152.1298.

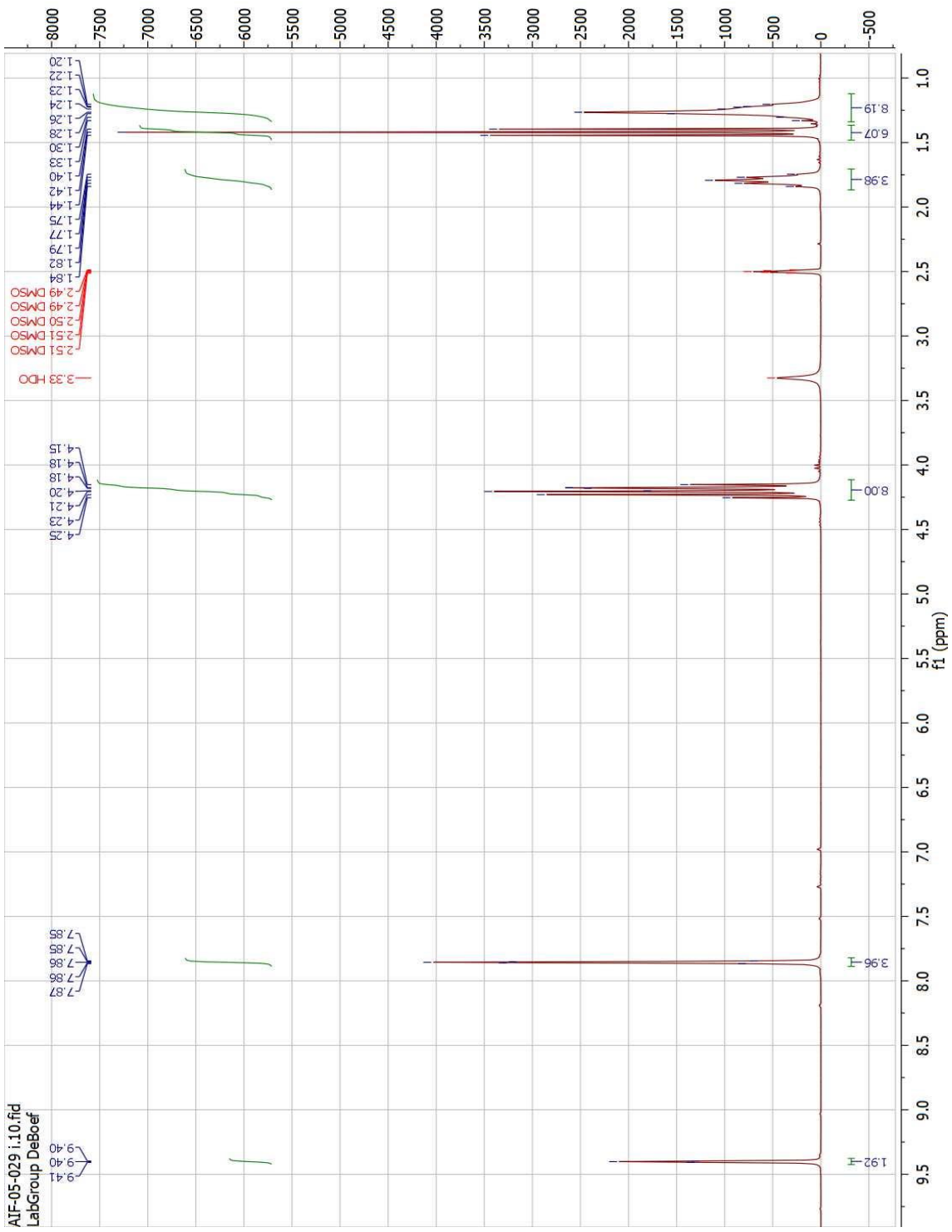

Figure 1.7: ^{1}H NMR of Guest 2

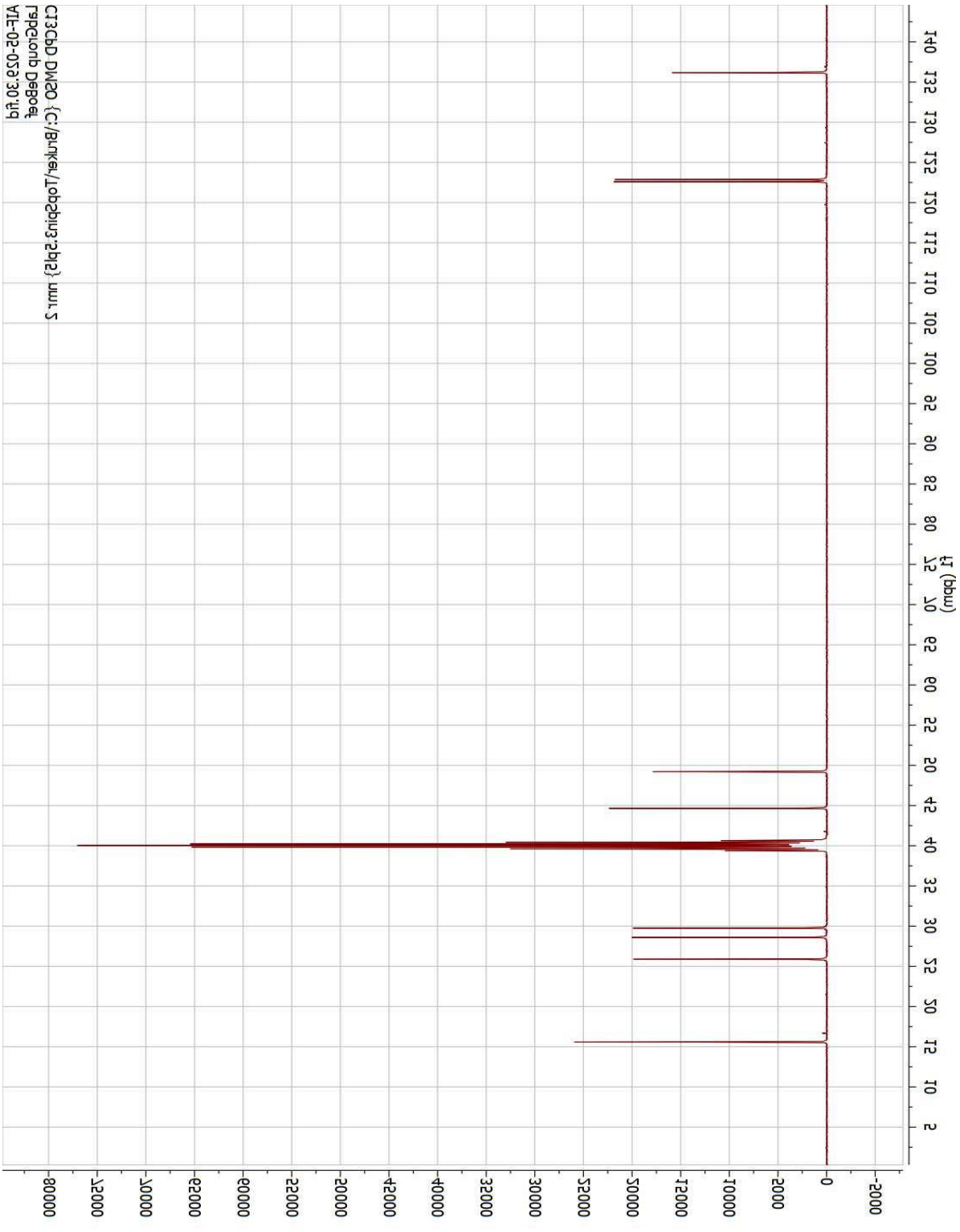

Figure 1.8: ^{13}C NMR of Guest 2

Synthesis of pseudorotaxanes using cucurbit[n]urils and bars

10 mM stock solutions of cucurbit[n]uril (n= 6, 7, 8) and the guests were prepared using D_2O as the solvent. Using the above stock solutions, 0.25 mL of the host and 0.25 mL of the guest were mixed inside a GC vial. The threading of the guest into the host was achieved by heating the solution inside the GC vial to 85 ^oC for 3 min. This solution was then cooled to room temperature and transferred to an NMR tube. While the initial CB solutions were cloudy, the final pseudorotaxane solutions were clear and homogeneous. ^1H NMR spectra were then acquired at 300 K. ^1H NMR was performed to see the movement of the alkyl protons in the guest and the movement of the guests after the inclusion complexes were formed.

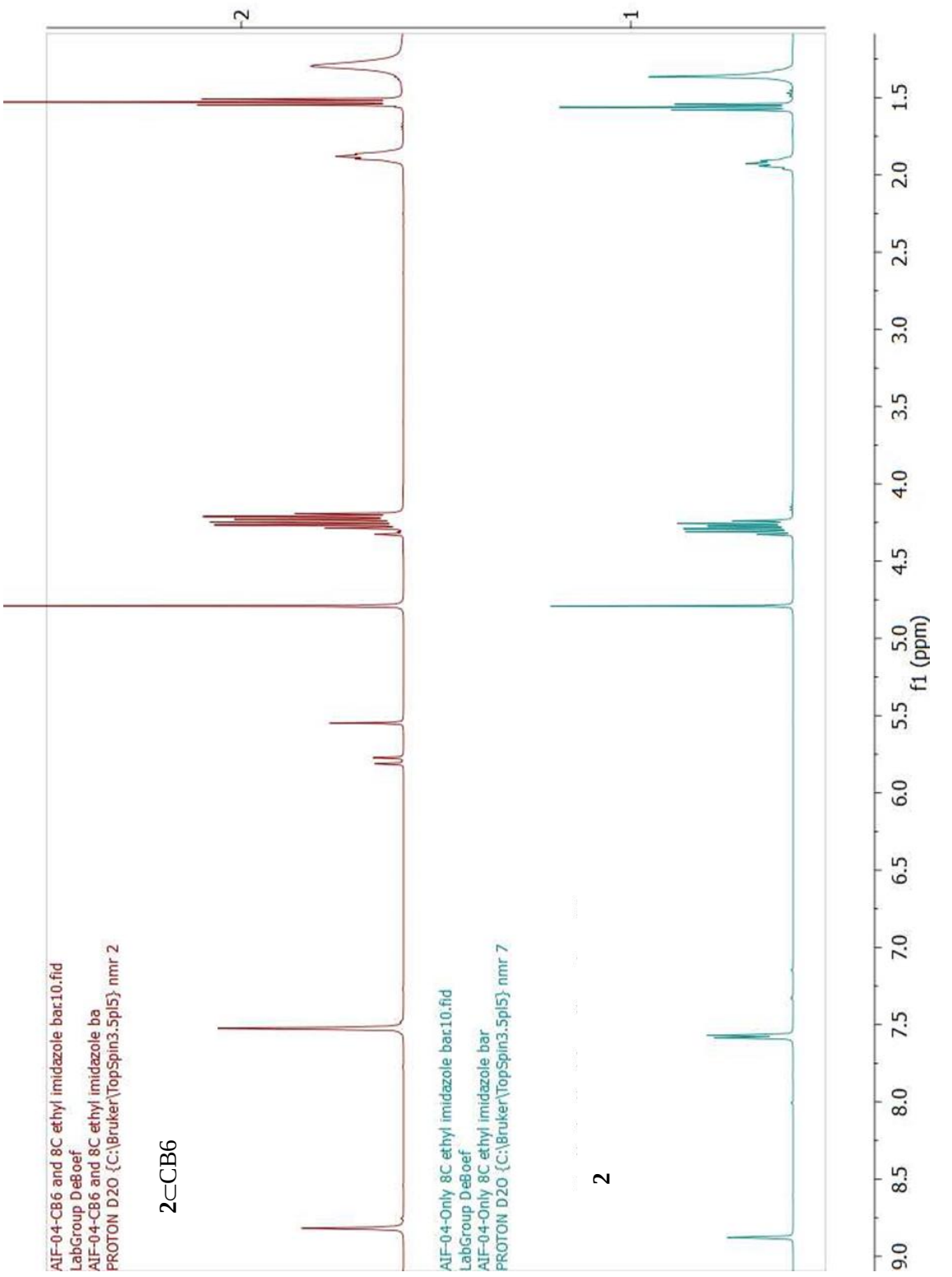

Figure 1.9: ^{1}H NMR of 2⊂CB6

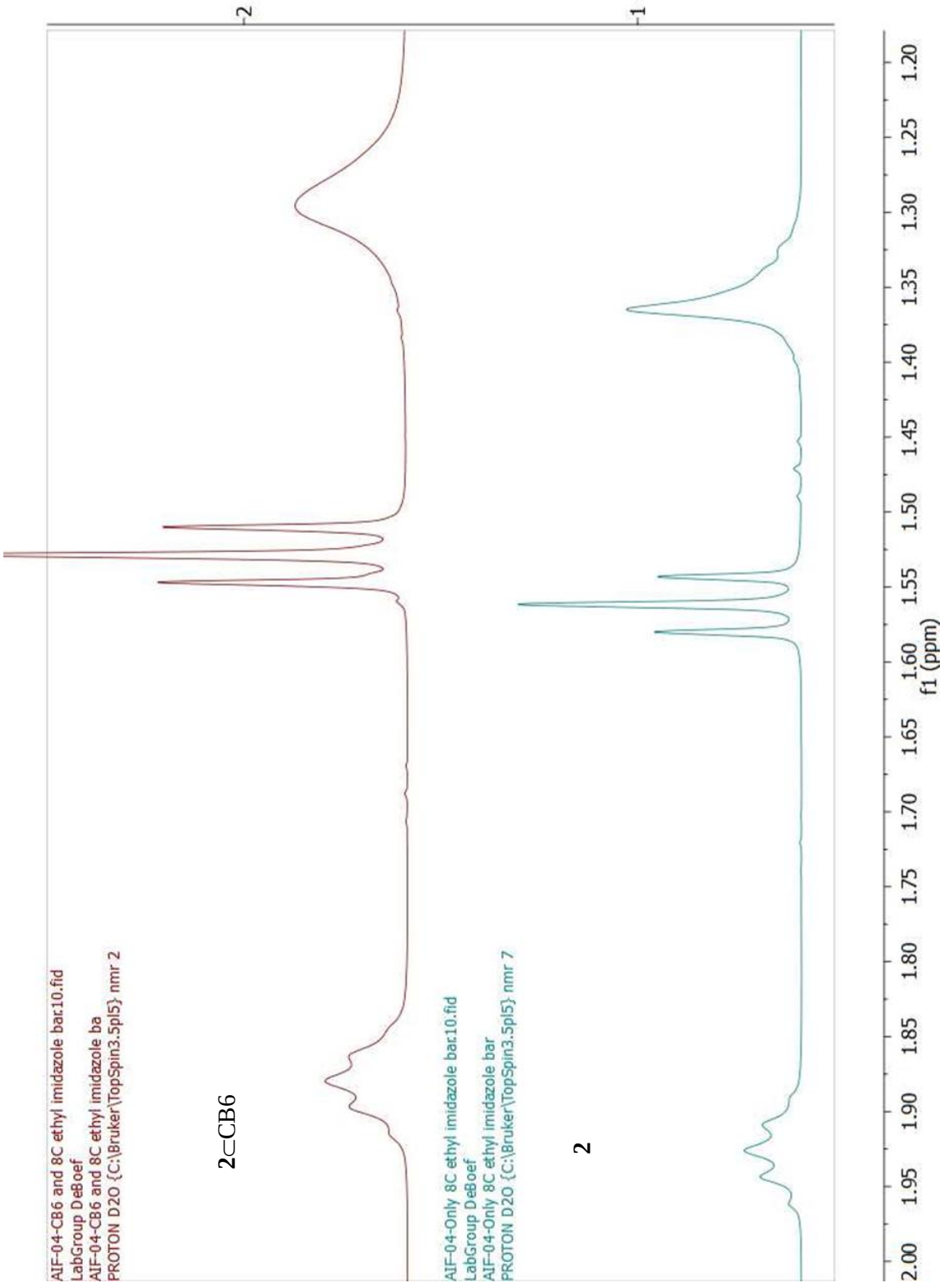

Figure 1.10: ^{1}H NMR (magnified) of 2⊂CB6 in the region of the guest protons

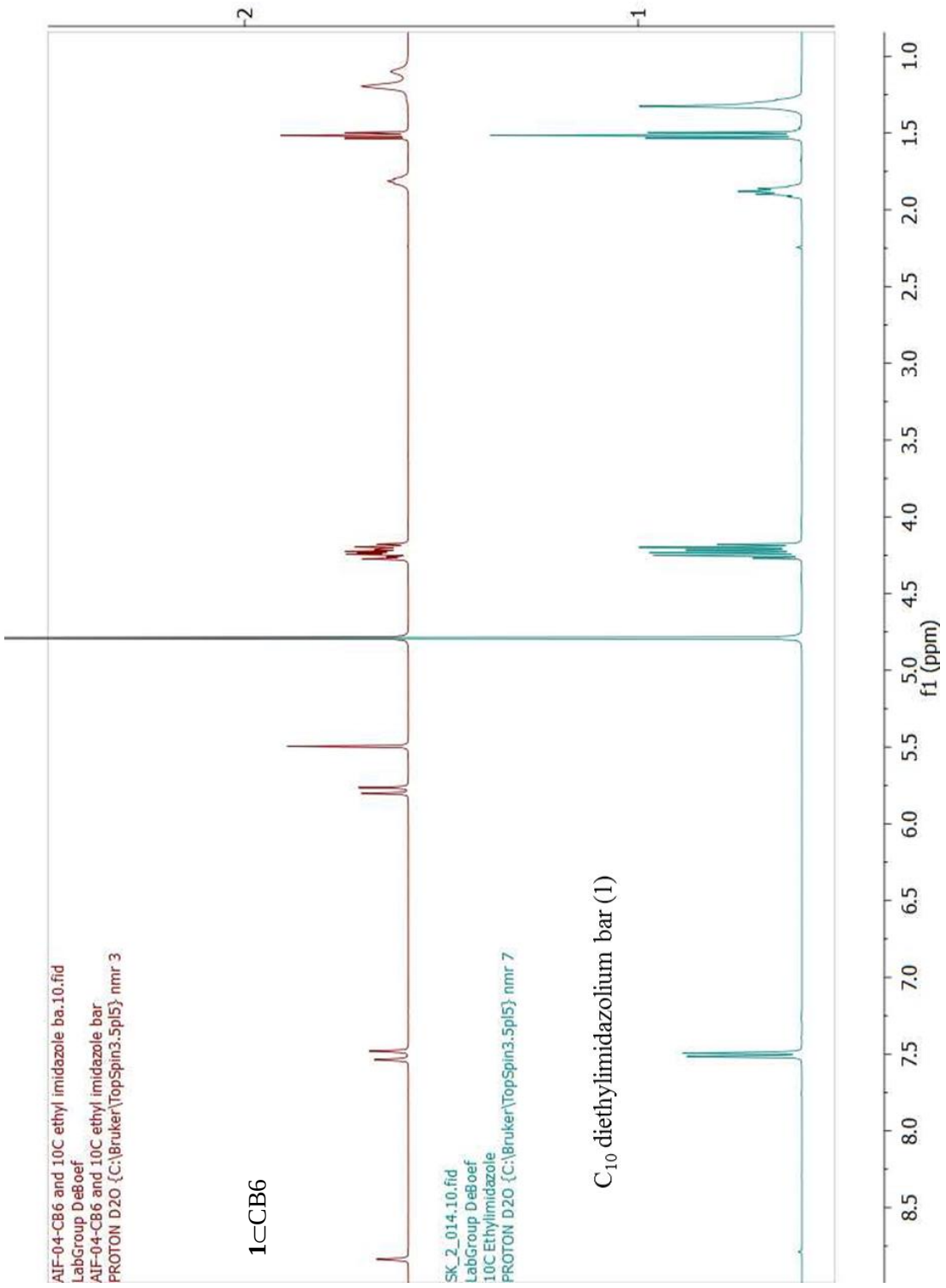

Figure 1.11: ^{1}H NMR of 1⊂CB6

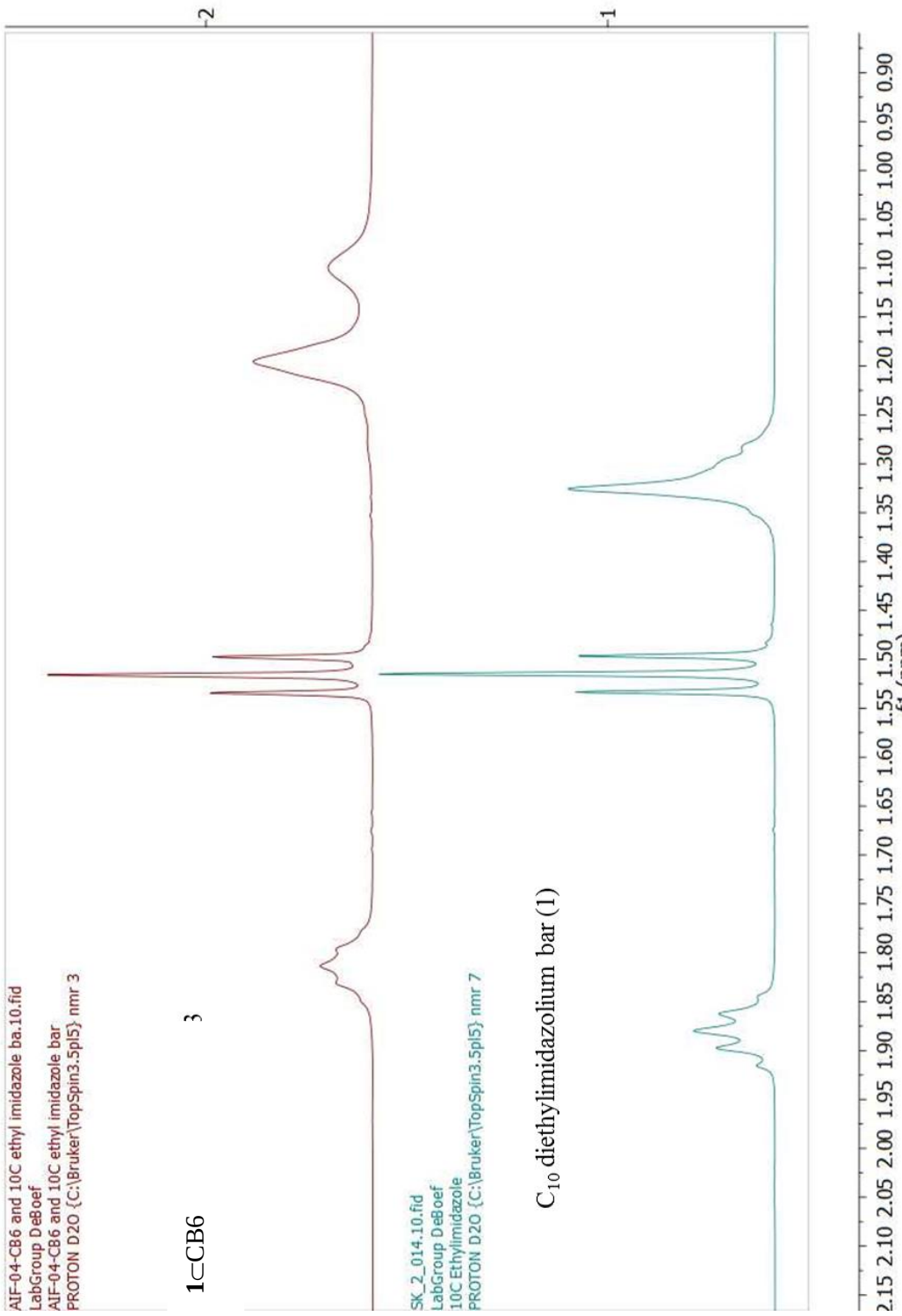

Figure 1.12: ^{1}H NMR (magnified) of 1⊂CB6 in the region of guest protons

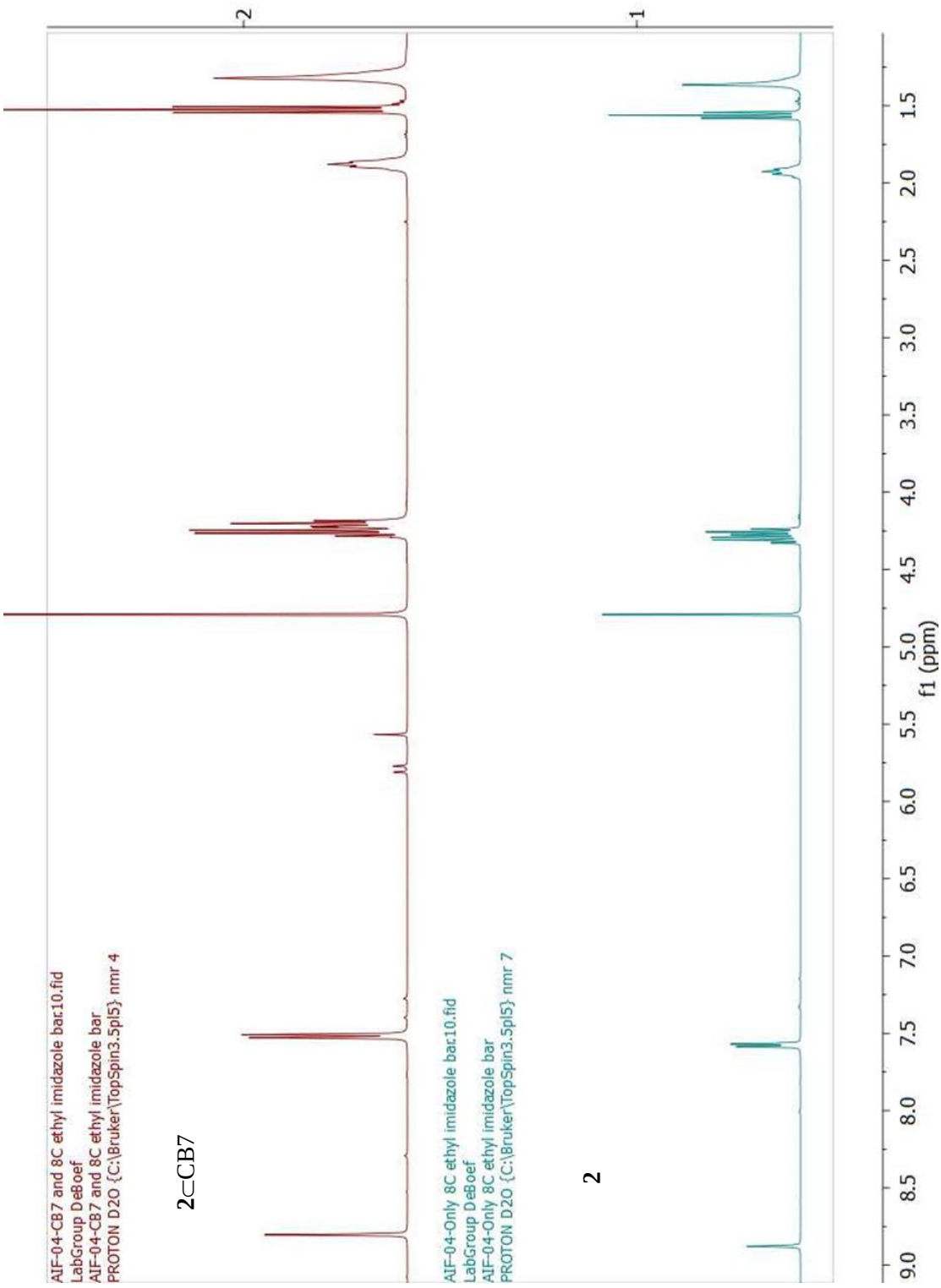

Figure 1.13: ^{1}H NMR of 2⊂CB7

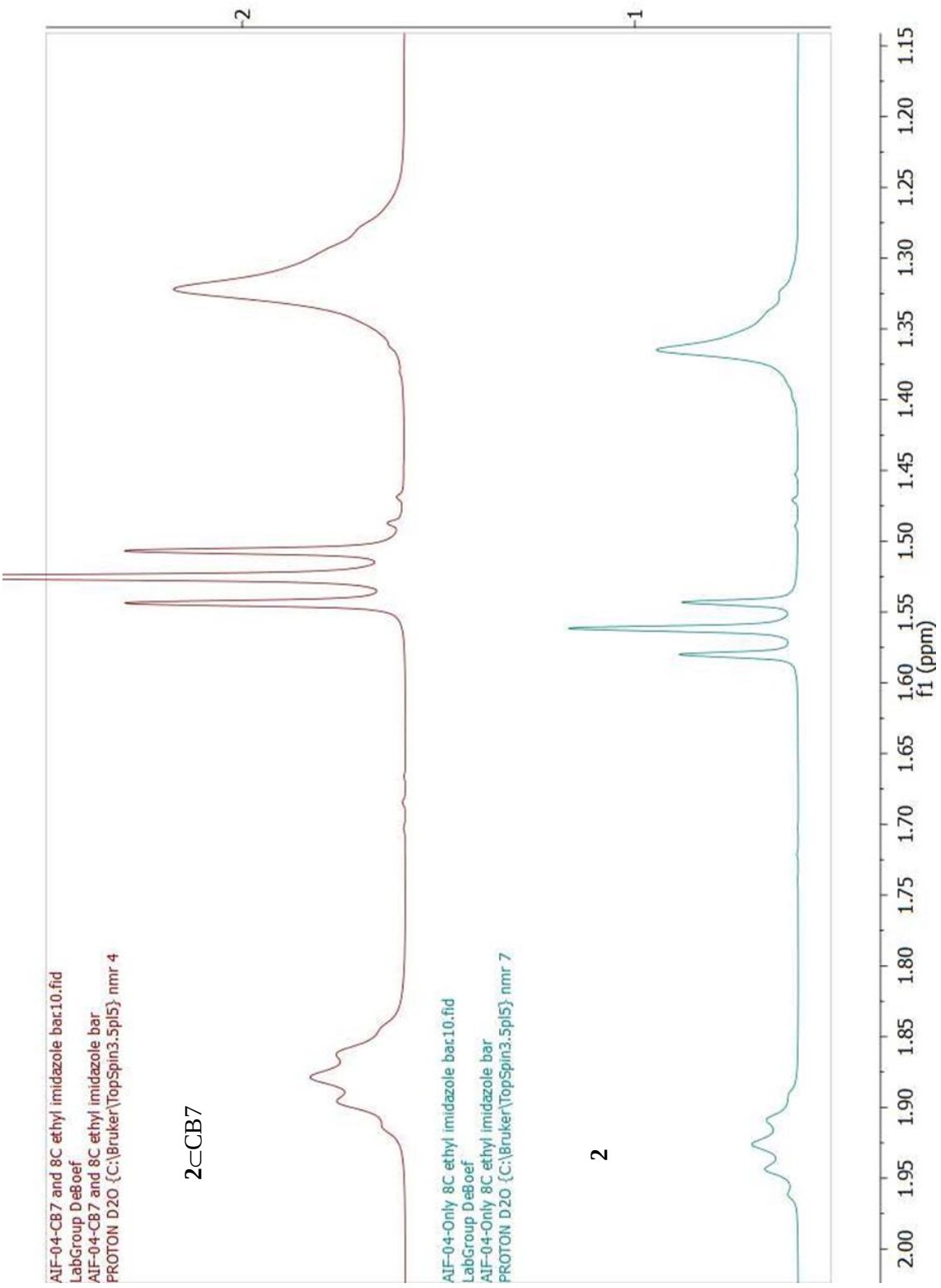

Figure 1.14: ^{1}H NMR (magnified) of 2⊂CB7 in the region of guest protons

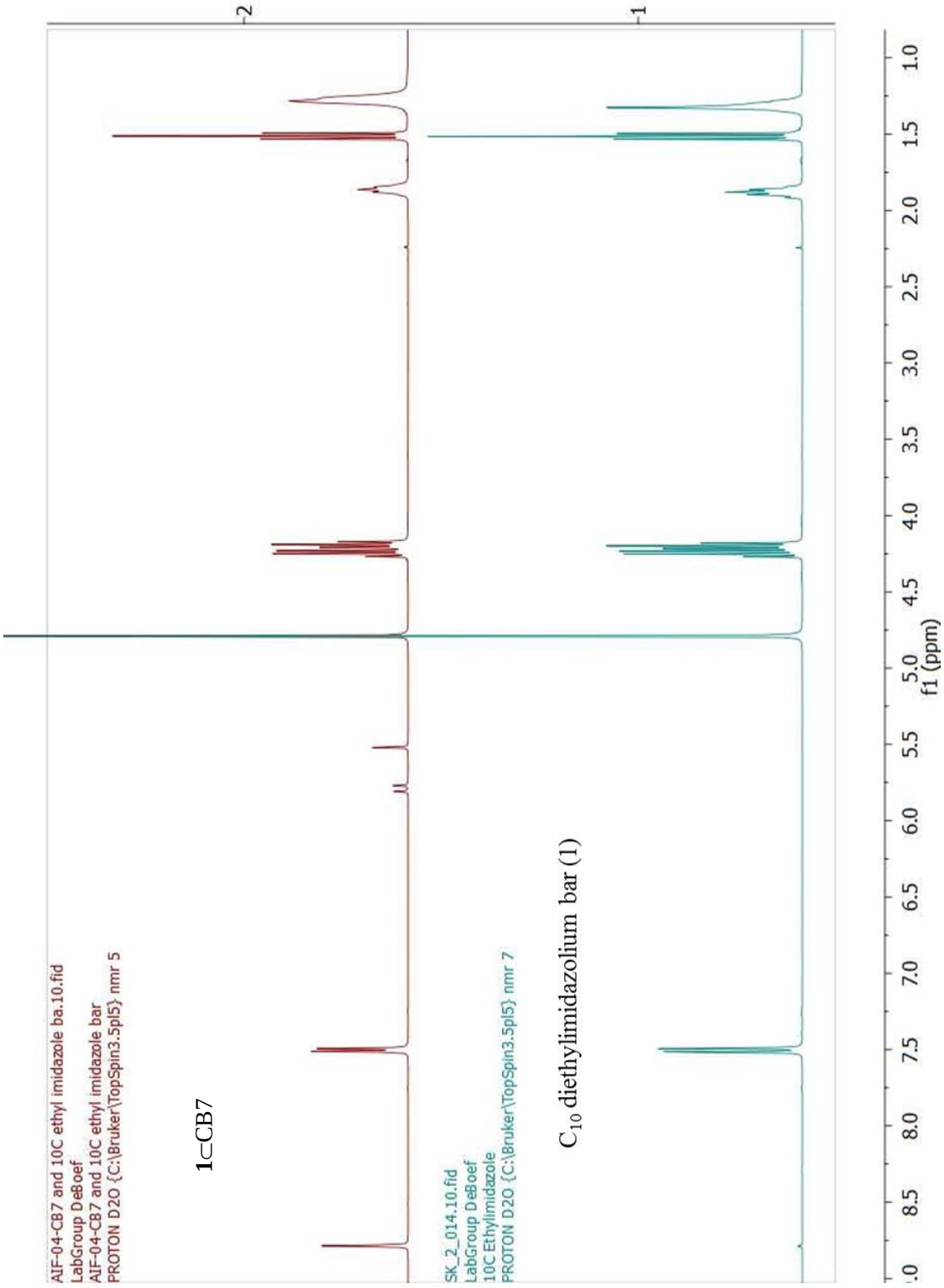

Figure 1.15: ^{1}H NMR of 1⊂CB7

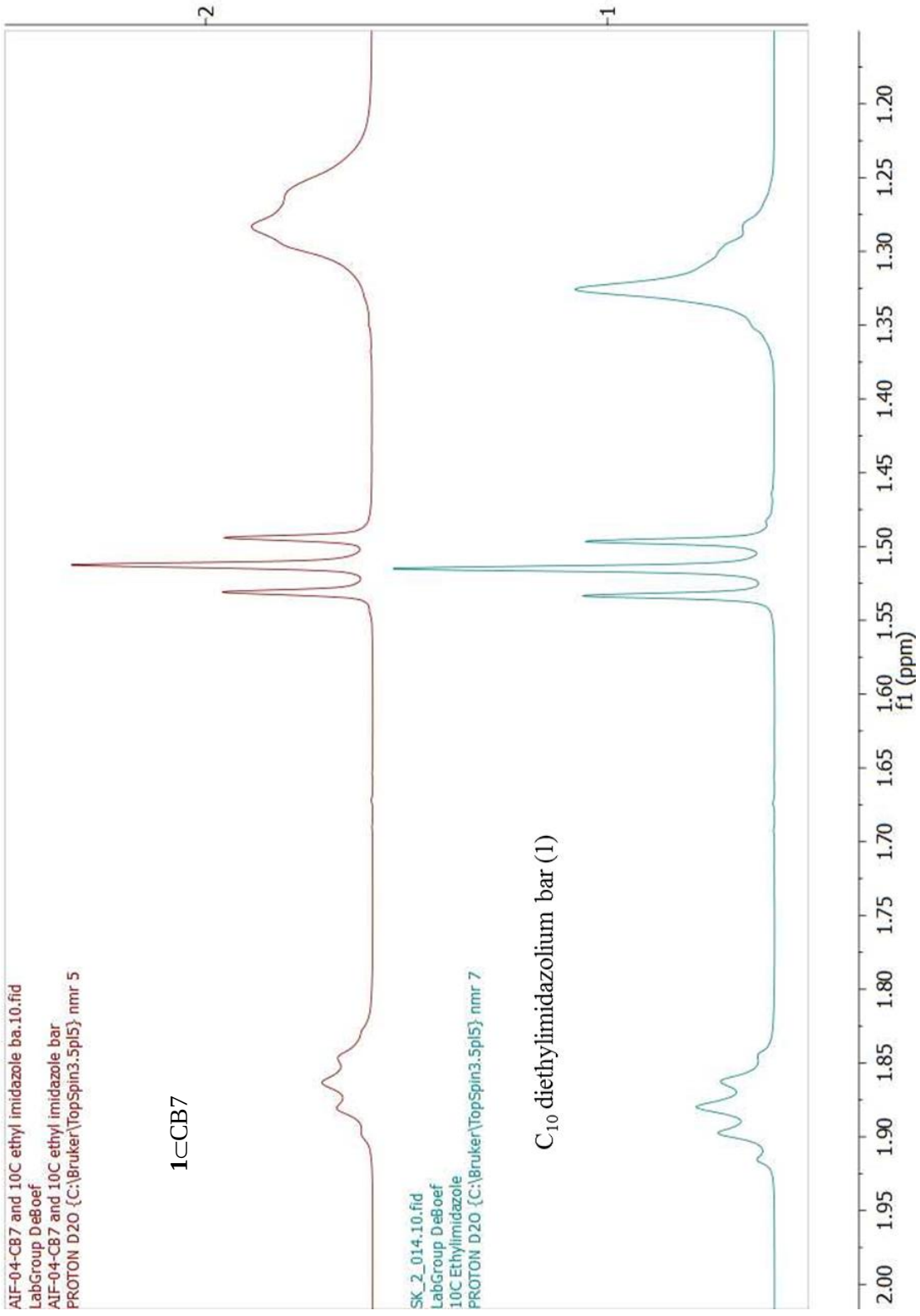

Figure 1.16: ^{1}H NMR (magnified) of 1⊂CB7 in the region of guest protons

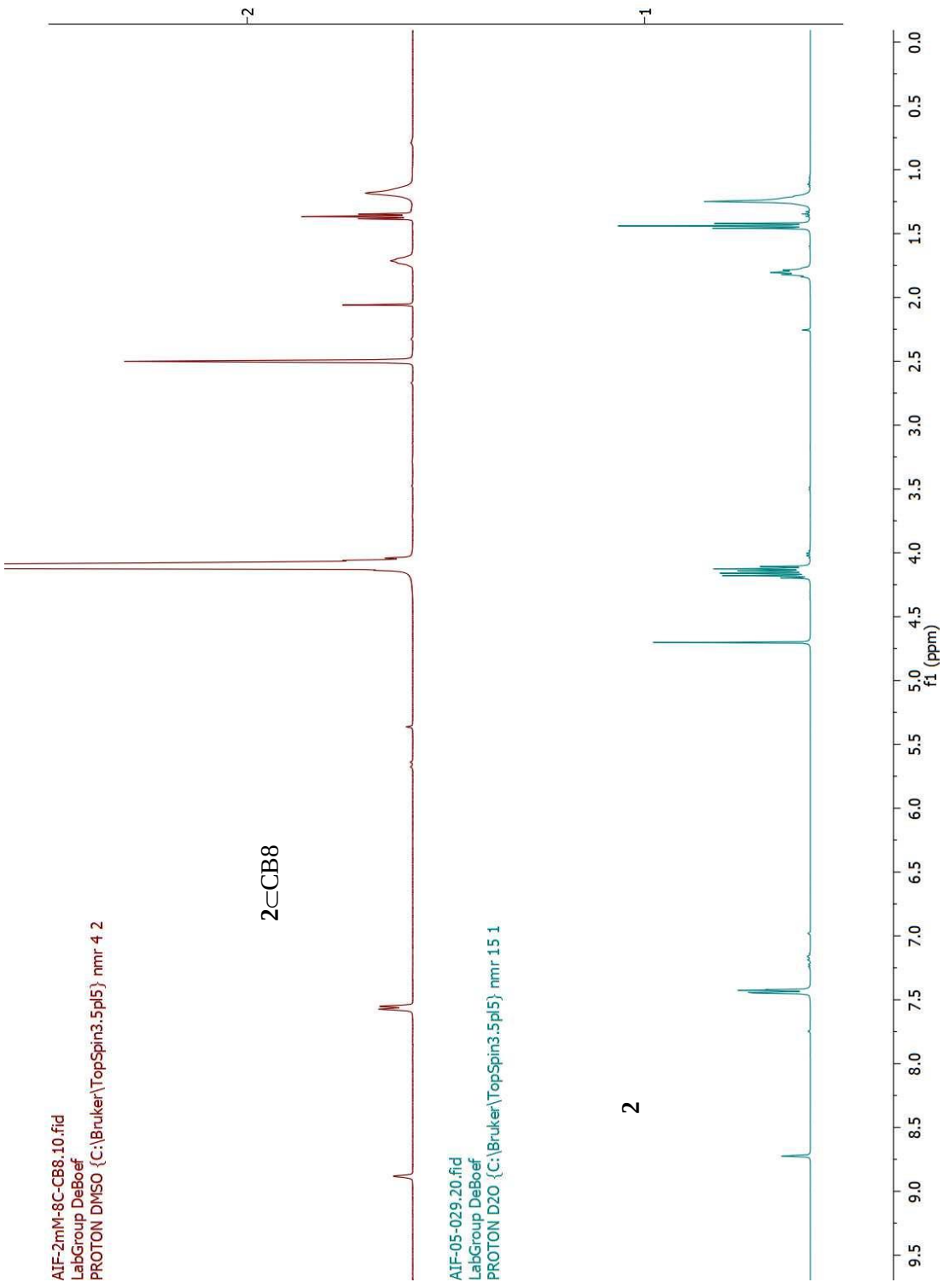

Figure 1.17: ^{1}H NMR of 2⊂CB8

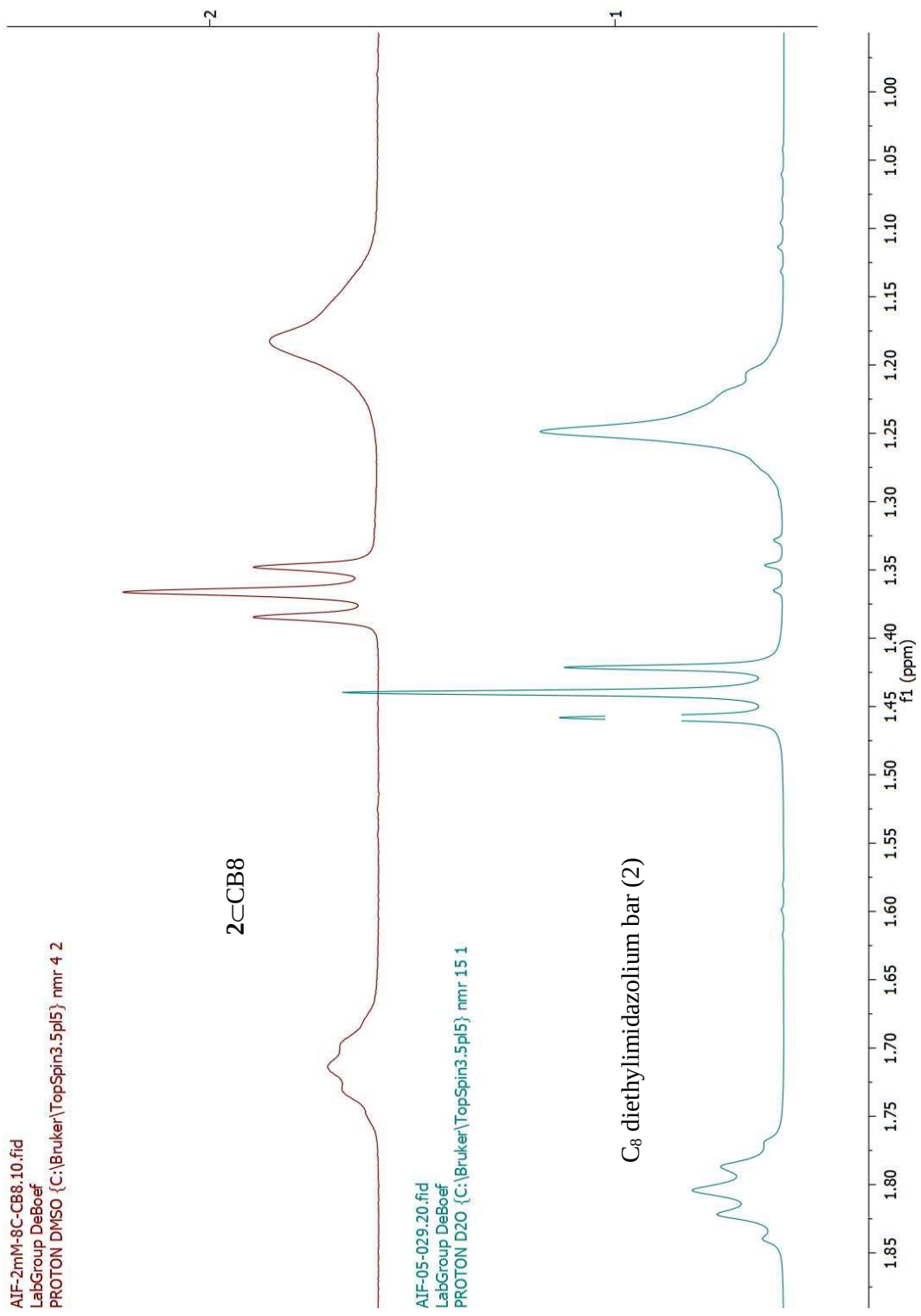

Figure 1.18: ^{1}H NMR (magnified) of 2⊂CB8 in the region of guest protons

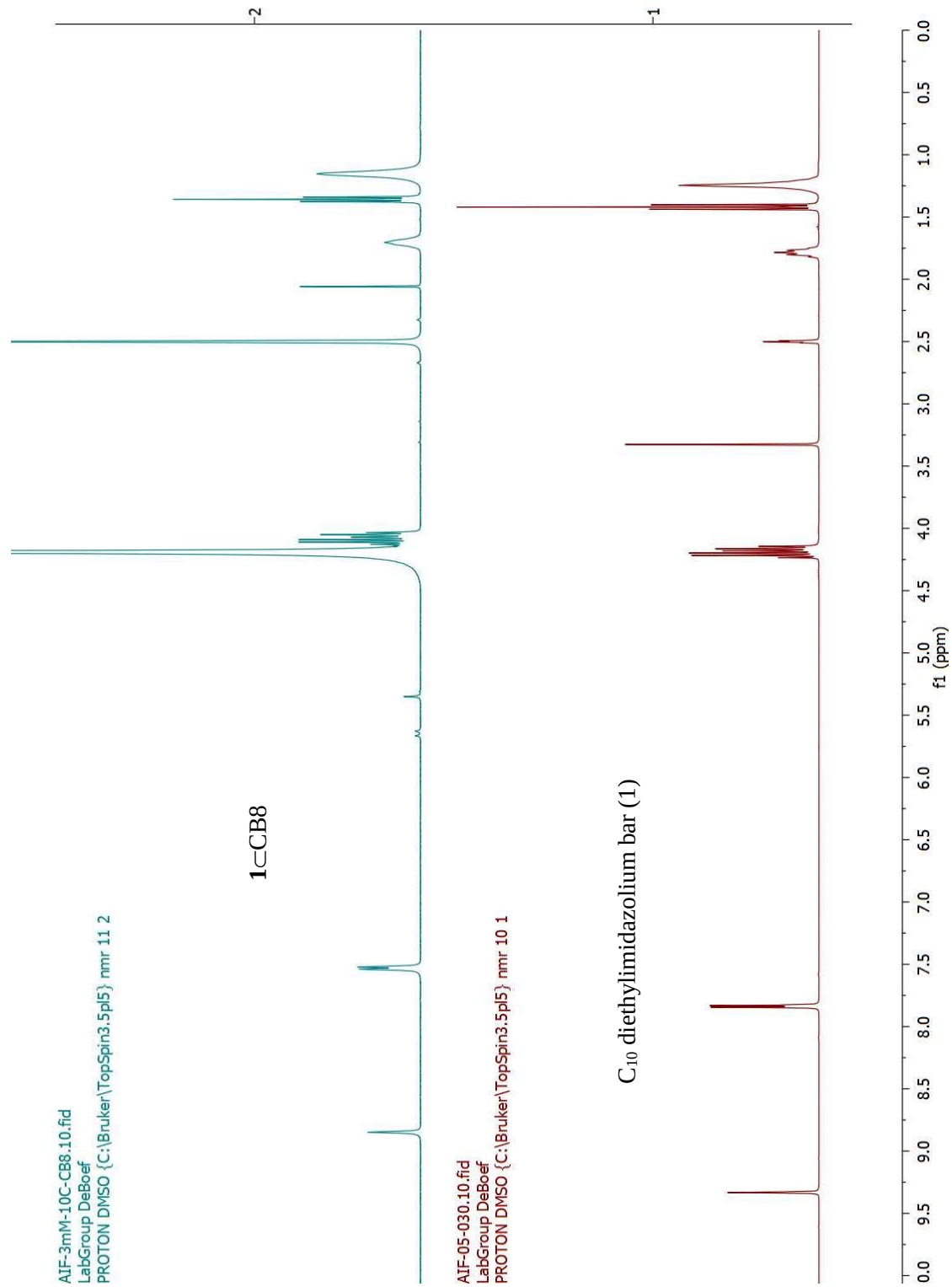

Figure 1.19: ^{1}H NMR of 1⊂CB8

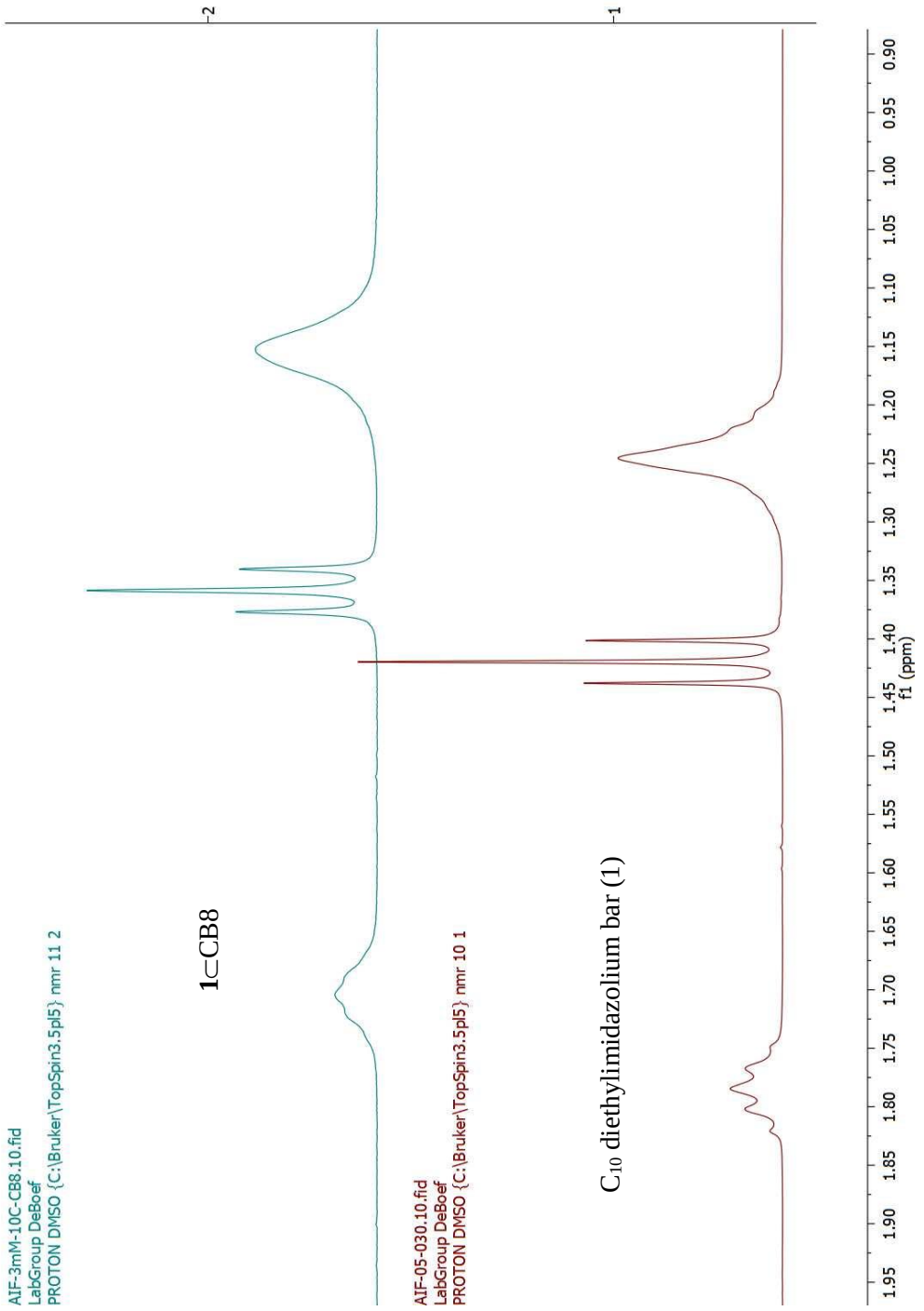

Figure 1.20: ^{1}H NMR (magnified) of 1CB8 in the region of guest protons

Synthesis of Pseudorotaxanes using α, β, and γ-CDs

10 mM stock solutions of cyclodextrins (α, β, γ) and the guests were prepared using D_2O as the solvent. Using the above stock solutions, 0.25 mL of the host and 0.25 mL of the guest were mixed inside a GC vial. The threading of the guest in to the host was achieved by heating the solution inside the GC vial to 40 ^oC for 3 min. This solution was then cooled to room temperature and transferred to a NMR tube. The final solutions containing the pseudorotaxanes were clear and homogeneous. All ^1H NMR spectra were acquired at 300 K. ^1H NMR was performed to see the movement of the alkyl protons in the guest and the movement of the cyclodextrins' H-3 proton and H-5 protons, which are present inside the cavity of the CDs.

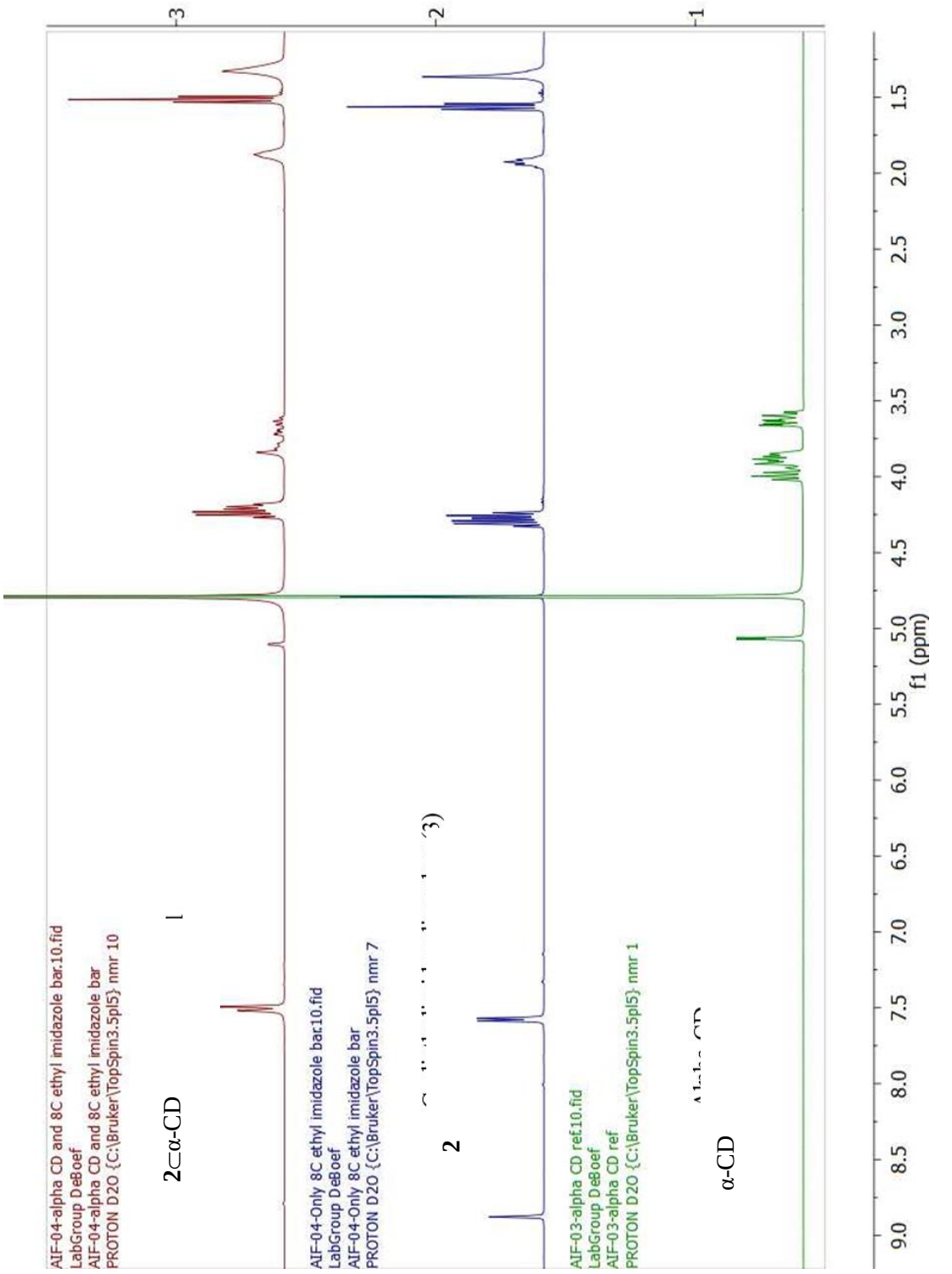

Figure 1.21: ^{1}H NMR of 2⊂α-CD

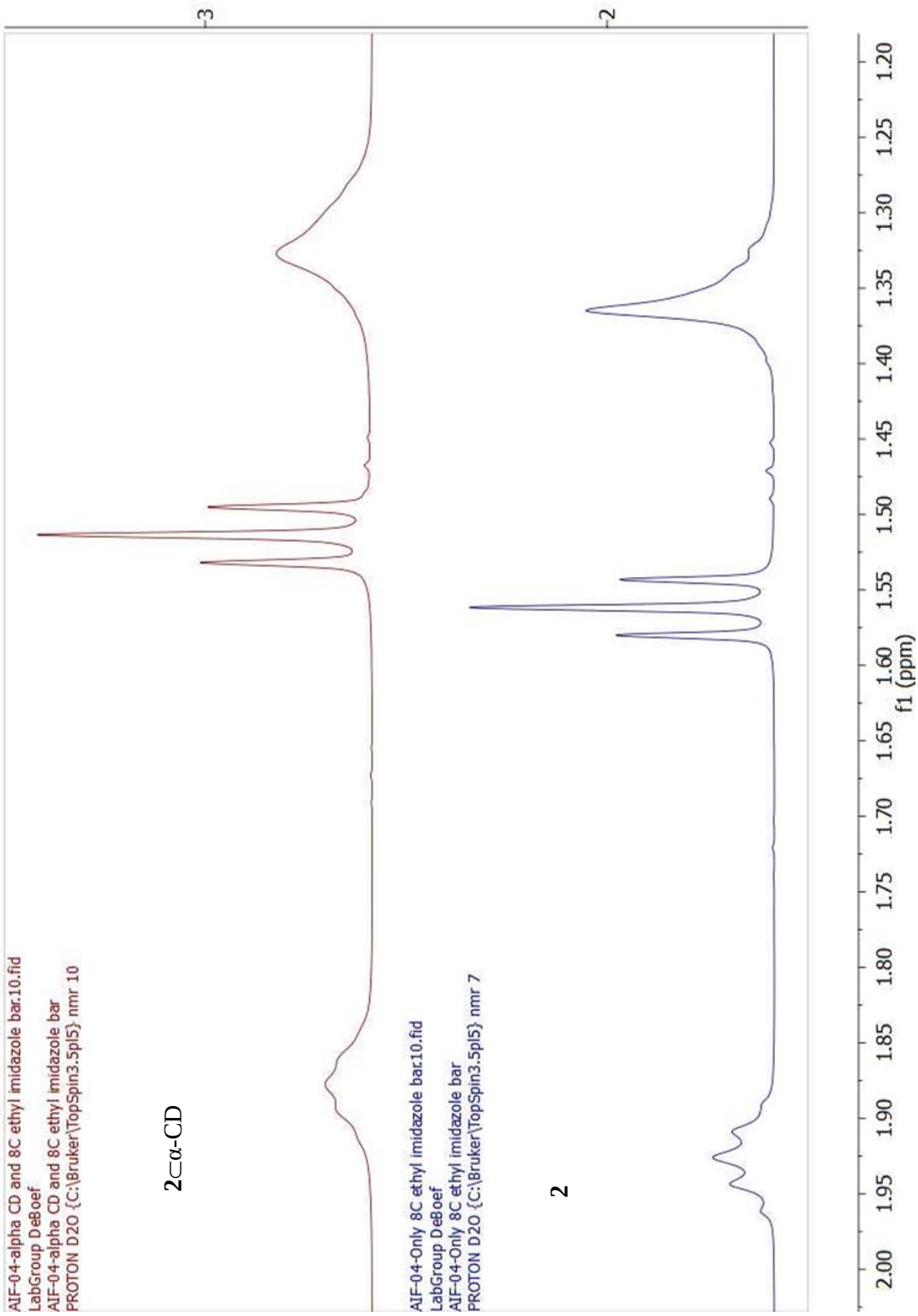

Figure 1.22: ^{1}H NMR (magnified) of 2⊂α-CD in the region of guest protons

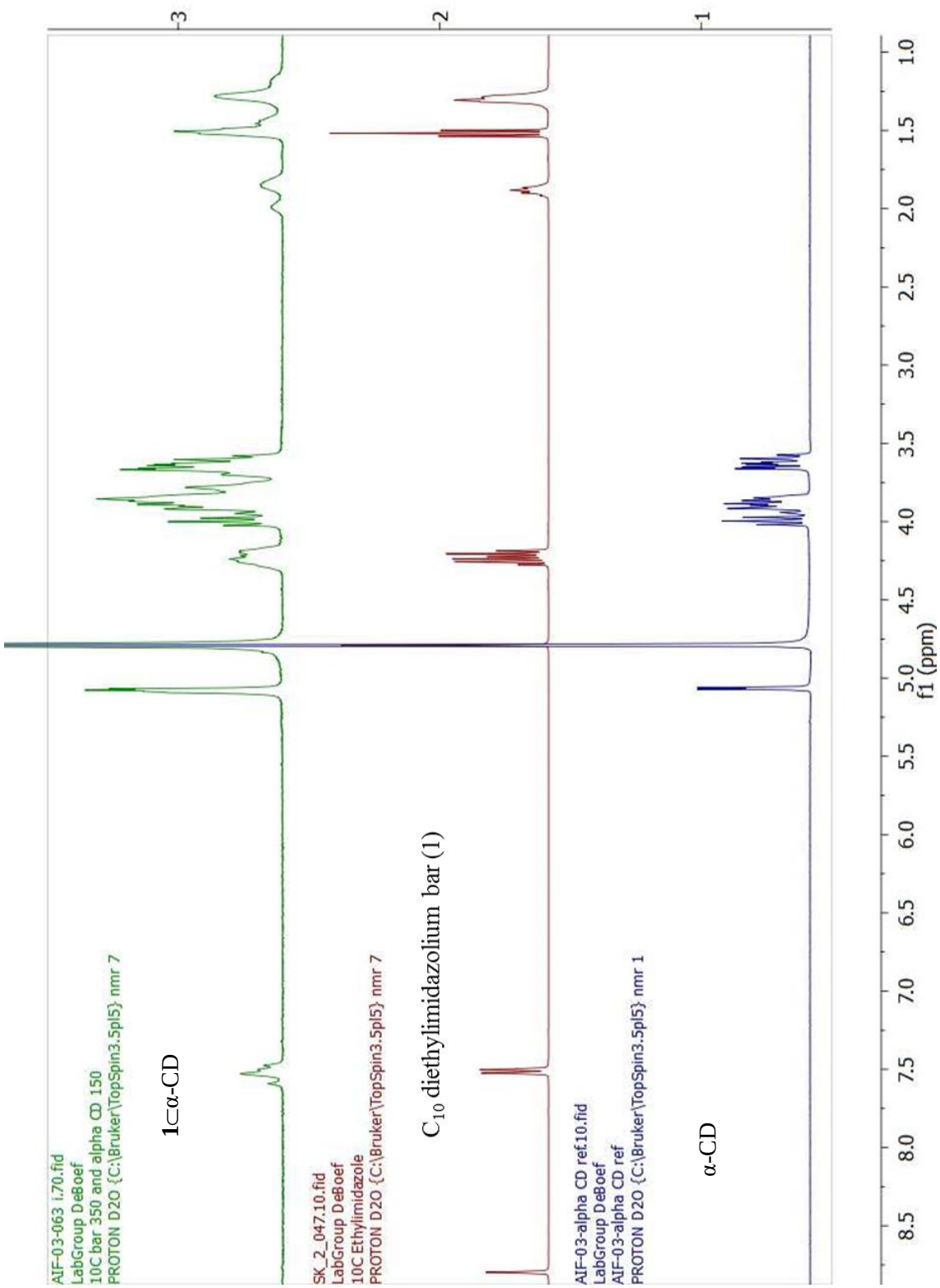

Figure 1.23: ^{1}H NMR of 1⊂α-CD

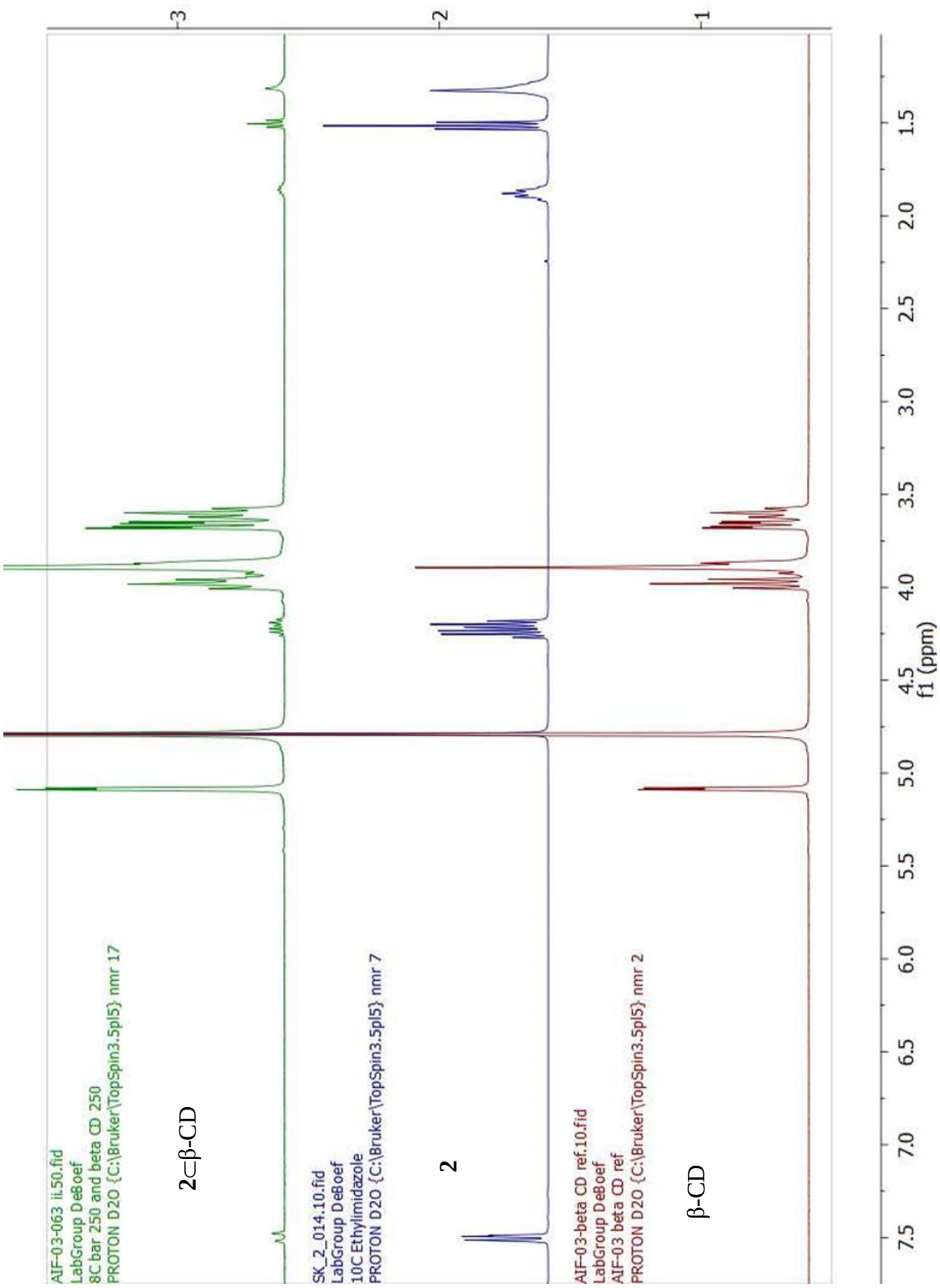

Figure 1.24: ^{1}H NMR of 2⊂β-CD

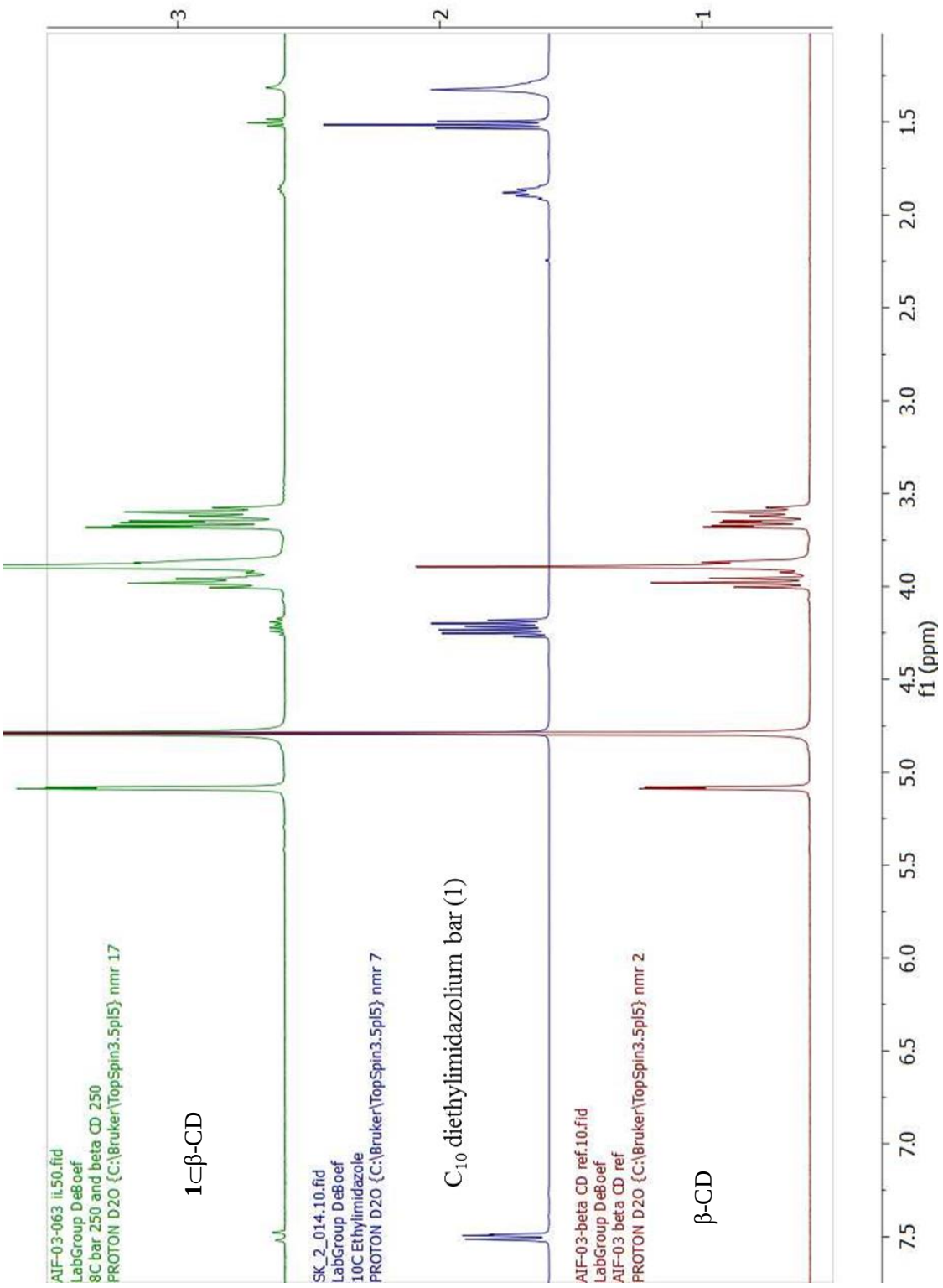

Figure 1.25: ^{1}H NMR of 1⊂β-CD

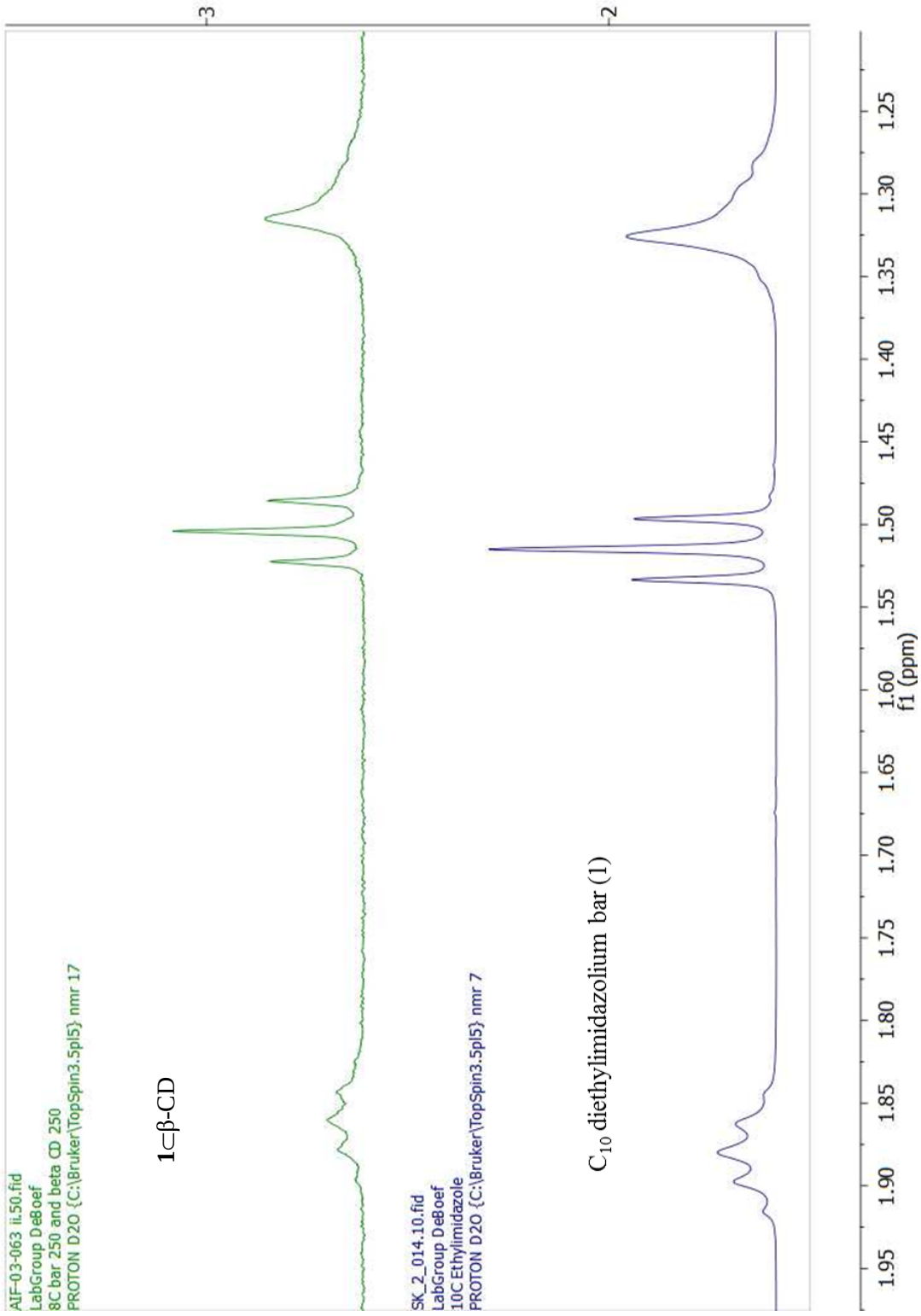

Figure 1.26: ^{1}H NMR (magnified) of 1□β-CD in the region of guest protons

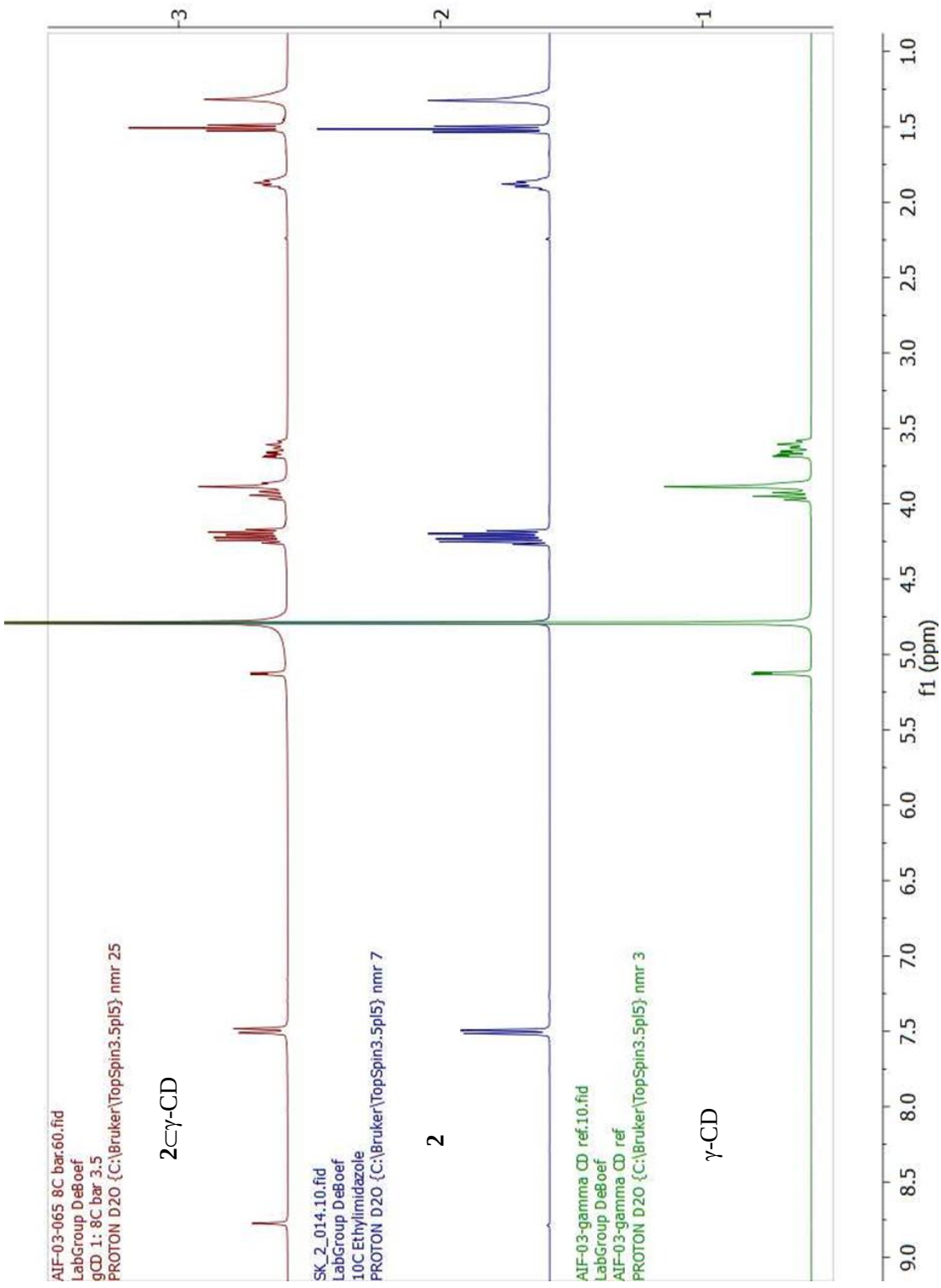

Figure 1.27: ^{1}H NMR of 2⊂γ-CD

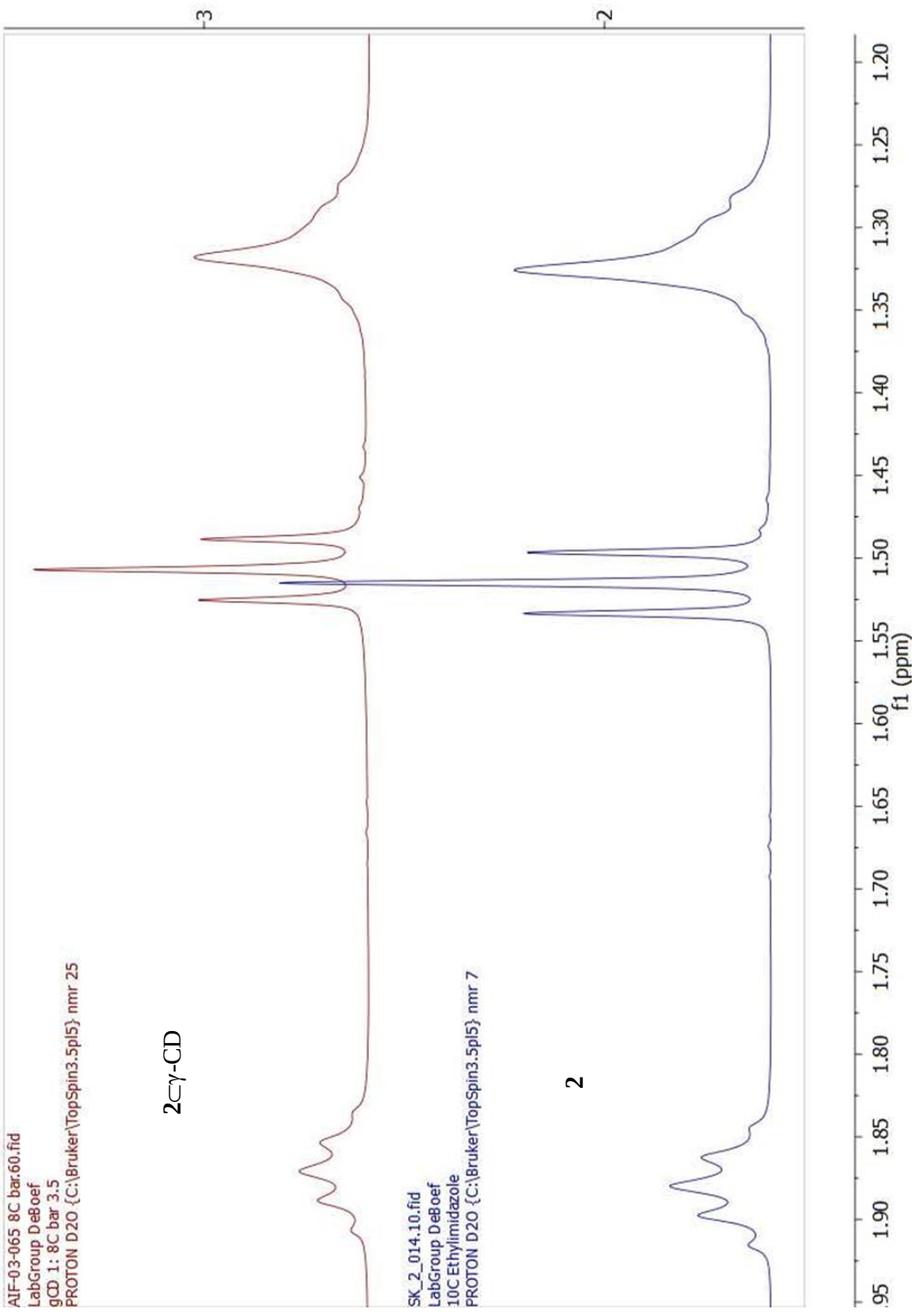

Figure 1.28: ^{1}H NMR (magnified) of 2⊂γ-CD in the region of guest protons

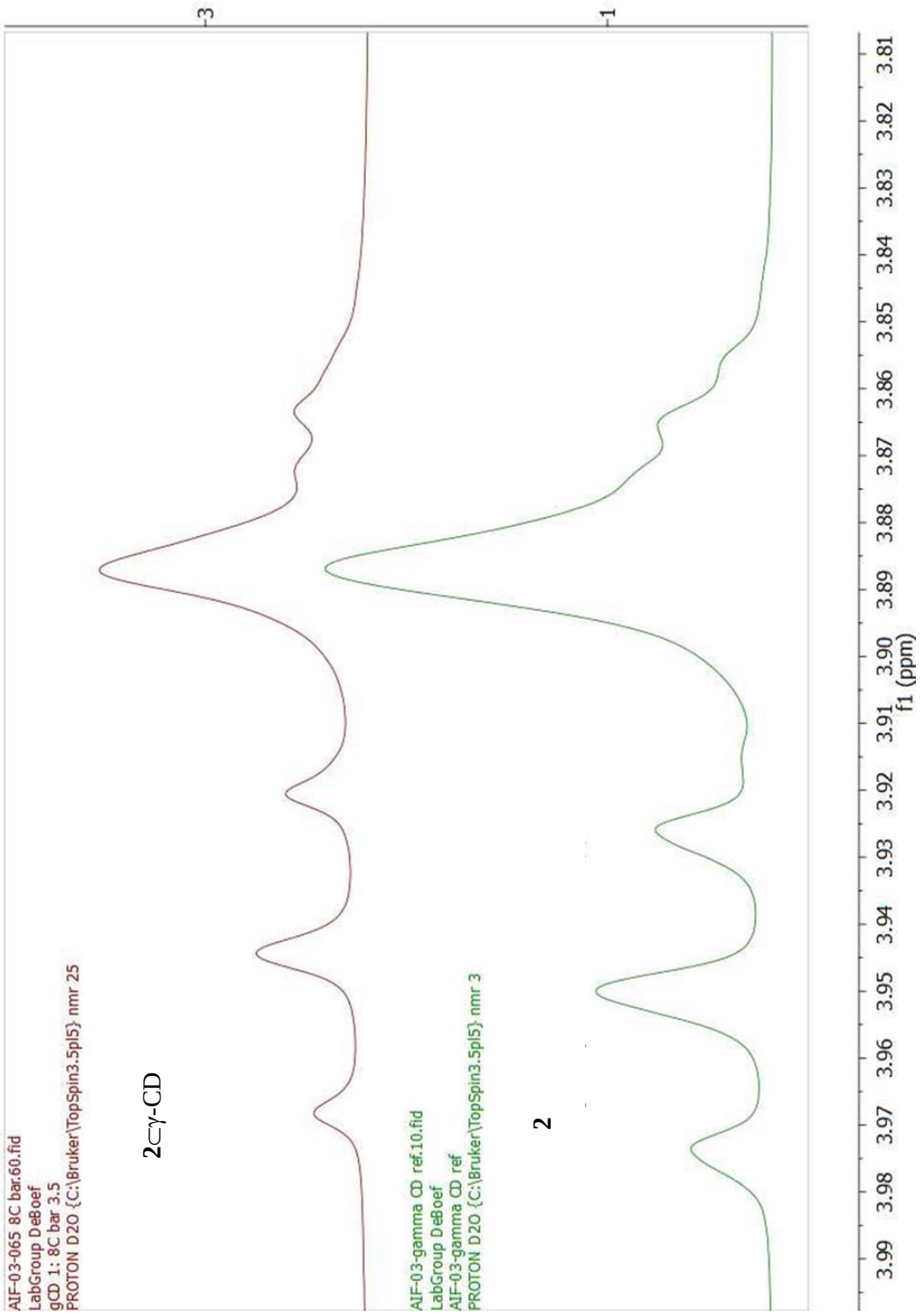

Figure 1.29: ^{1}H NMR (magnified) of 2⊂γ-CD in the region of H-3 proton of γ-CD

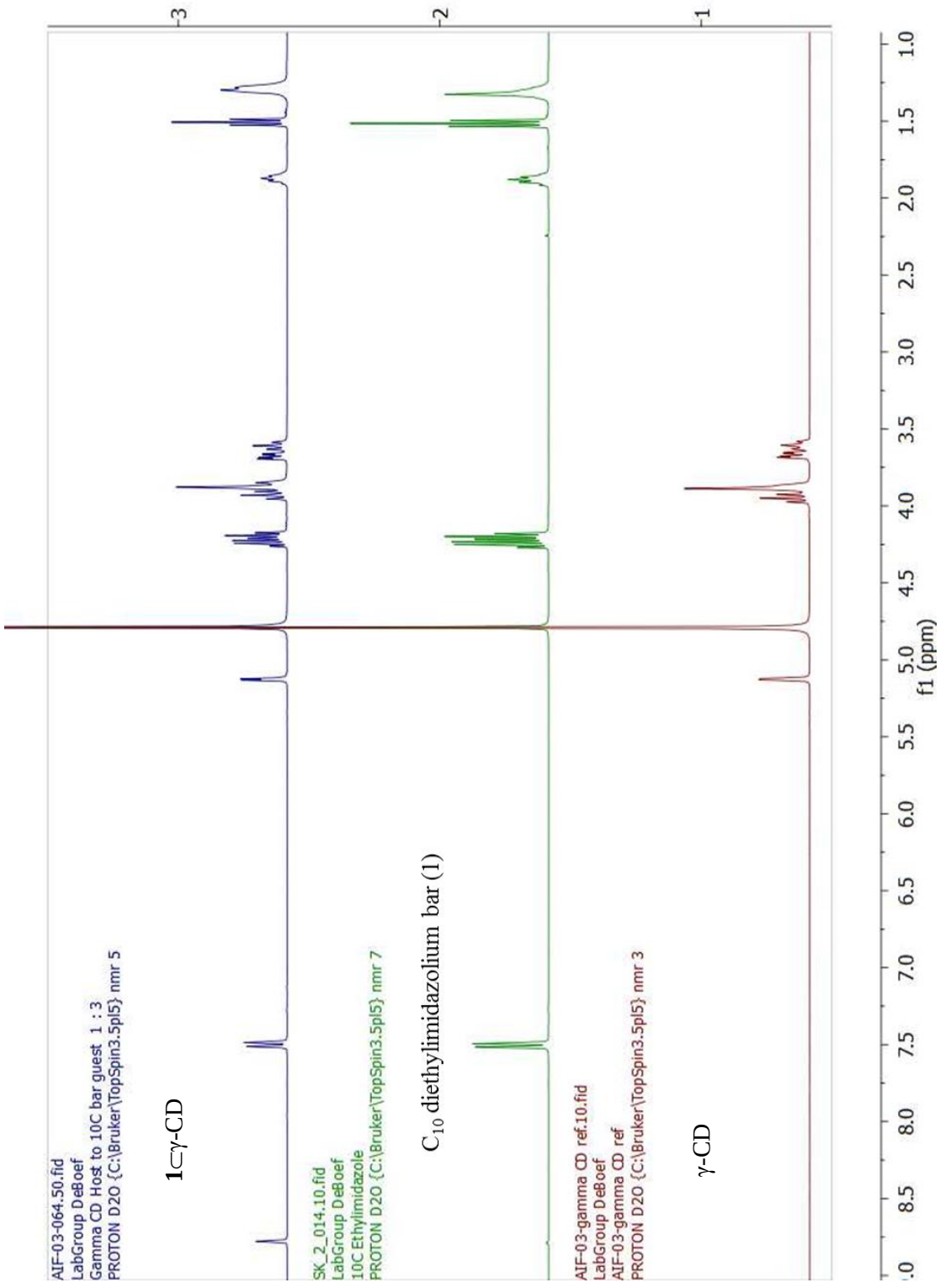

Figure 1.30: ^{1}H NMR of 1⊂γ-CD

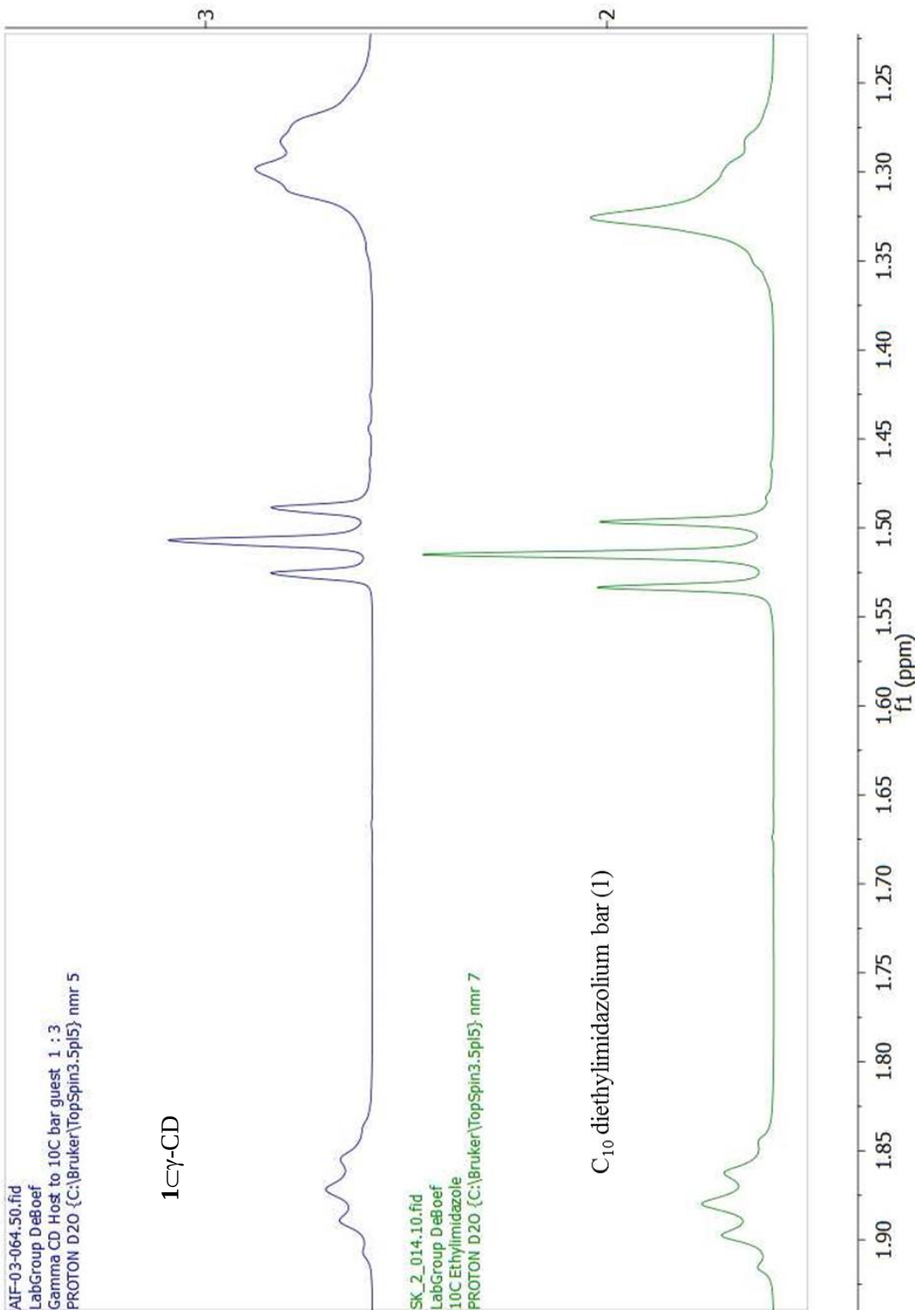

Figure 1.31: ^{1}H NMR (magnified) of 1⊂γ-CD in the region of guest protons

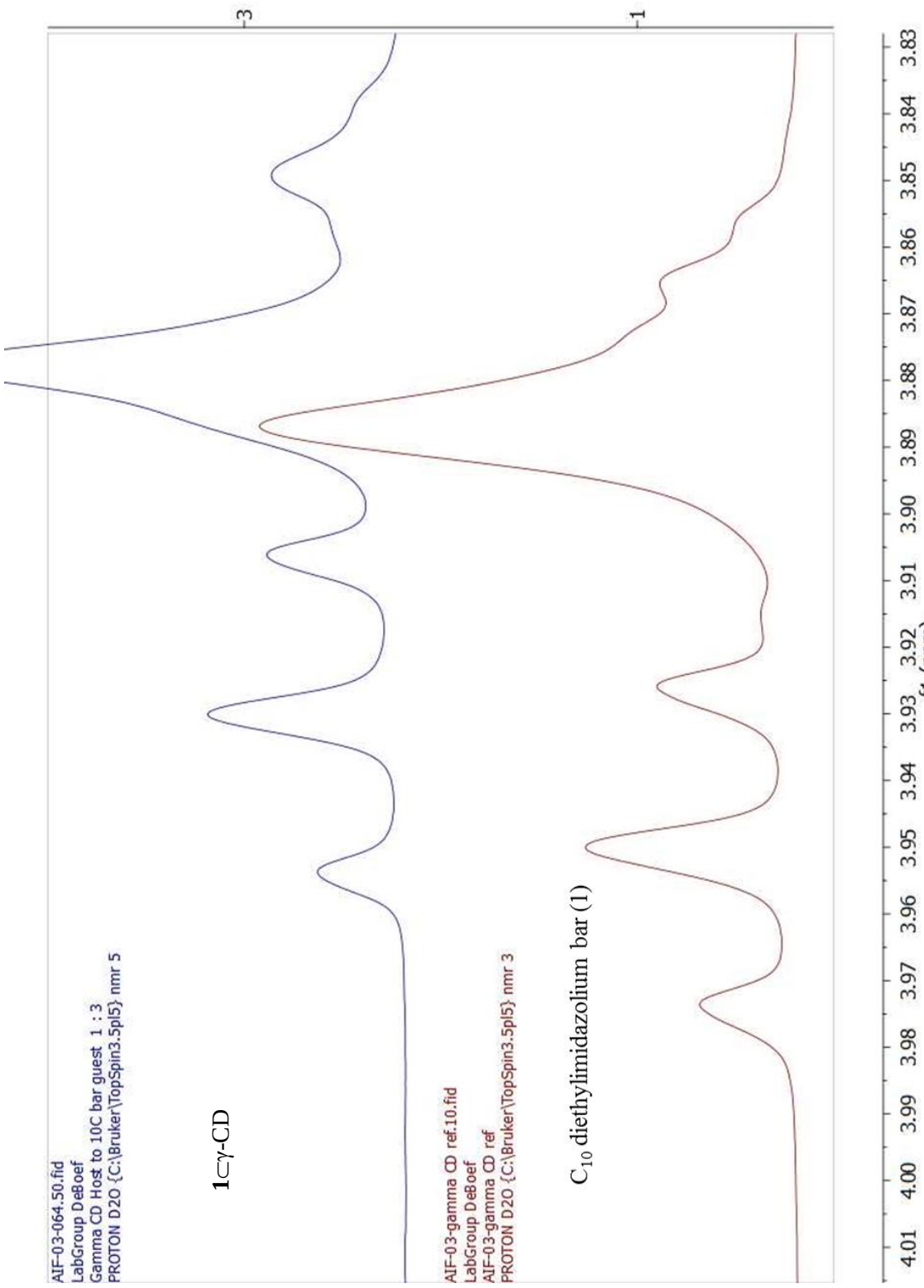

Figure 1.32: ^{1}H NMR (magnified) of 1⊂γ-CD in the region of H-3 proton of γ-CD

Determination of association constants for host cyclodextrins and guests

The NMR titration experiments were conducted per the following procedures.[2] The host CD concentrations were kept constant while the guest concentration was increased periodically. Stock solutions of 2 mM host (cyclodextrin) and 200 mM guest were prepared. A series of NMR samples were prepared in 5 mm NMR tubes. The series ranged from 0.111 mM to 200 mM. All samples were then heated for 3 min at 40 ^{o}C to facilitate the threading of the guest in to the host. All samples were cooled to room temperature before the ^{1}H NMR experiments. All ^{1}H NMR were performed at 300 K. The H-3 proton of the host CD was monitored. Data was processed using an Excel spreadsheet using the equation shown below. The plots are shown below. The data were also evaluated using the "OpenDataFit" website, which is an online free fitting program found at supramolecular.org.[2] The two different analysis methods provided similar results.

The following equation was used to calculate the association constant:

$$\Delta\delta = \left(\frac{\Delta\delta_{max}}{2[H_0]}\right) + \{[H_0] + [G_0] + \frac{1}{K} - ((\left([H_0] + [G_0] + \frac{1}{K}\right)^2 - 4[H_0]\Big[G_0]\Big)^{\frac{1}{2}}\}$$

where $\Delta\delta$ = change in chemical shift after the addition of the guest, $[H_0]$ = initial host concentration, $[G_0]$ = initial concentration, and K = association constant. $\Delta\delta$ was plotted as a function of the guest concentration.

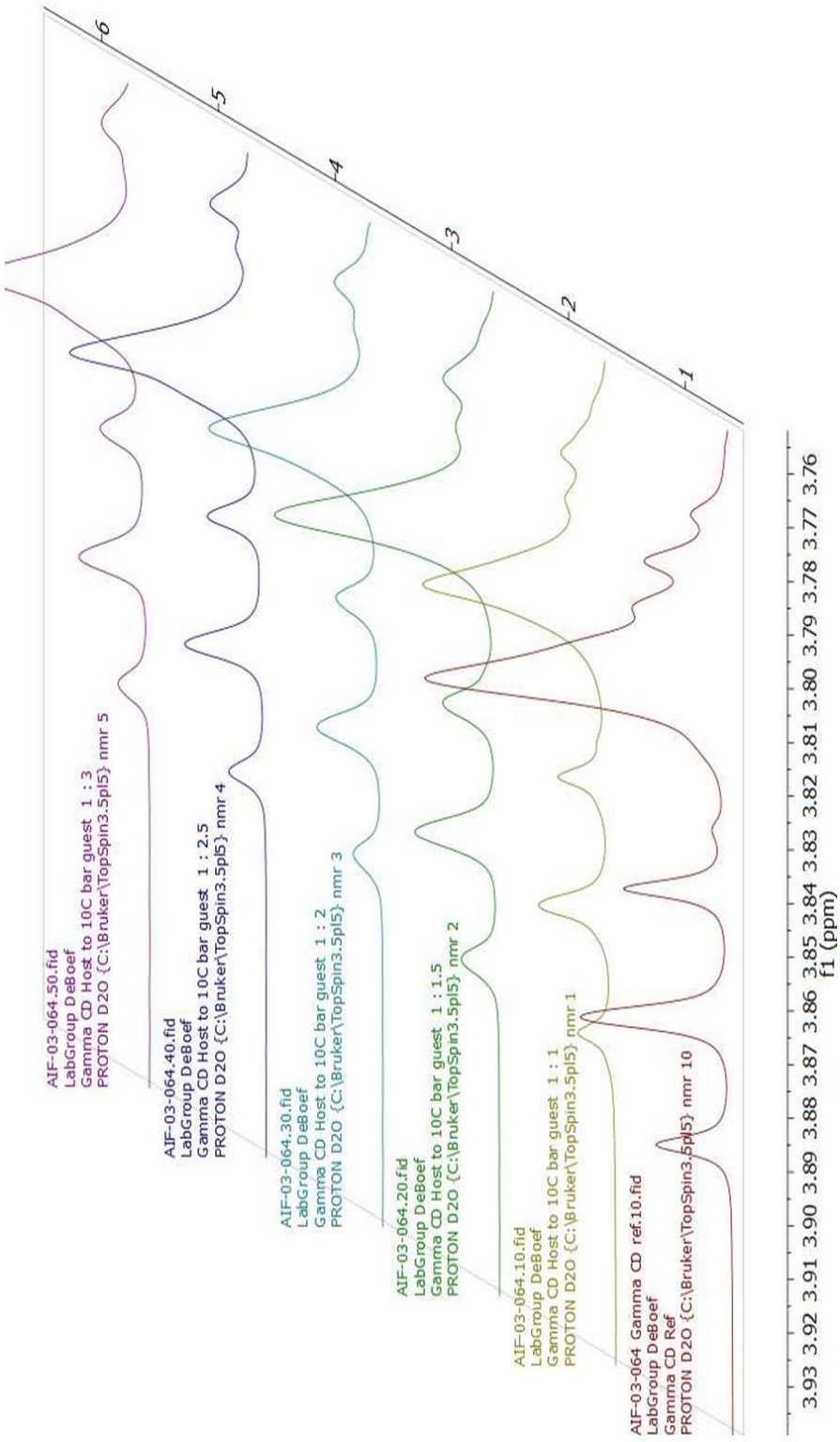

Figure 1.33: 1H-NMR stacked plot of γ-cyclodextrin and varying guest (1)

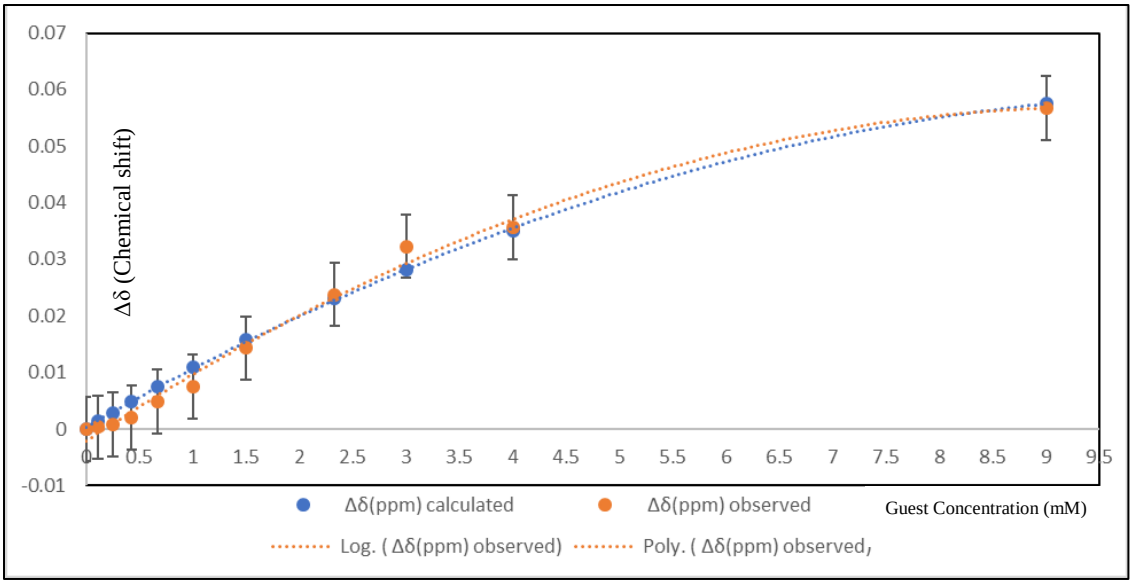

Figure 1.34: 1:1 Binding curve for the association of 1 with γ-CD.

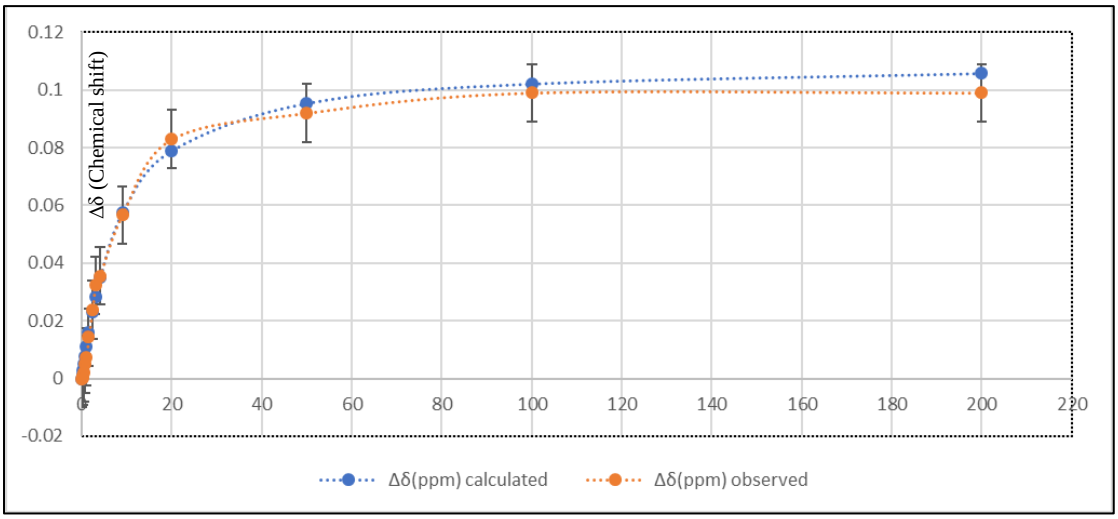

Figure 1.35: 1:1 Binding curve for the association of 1 with γ-CD.

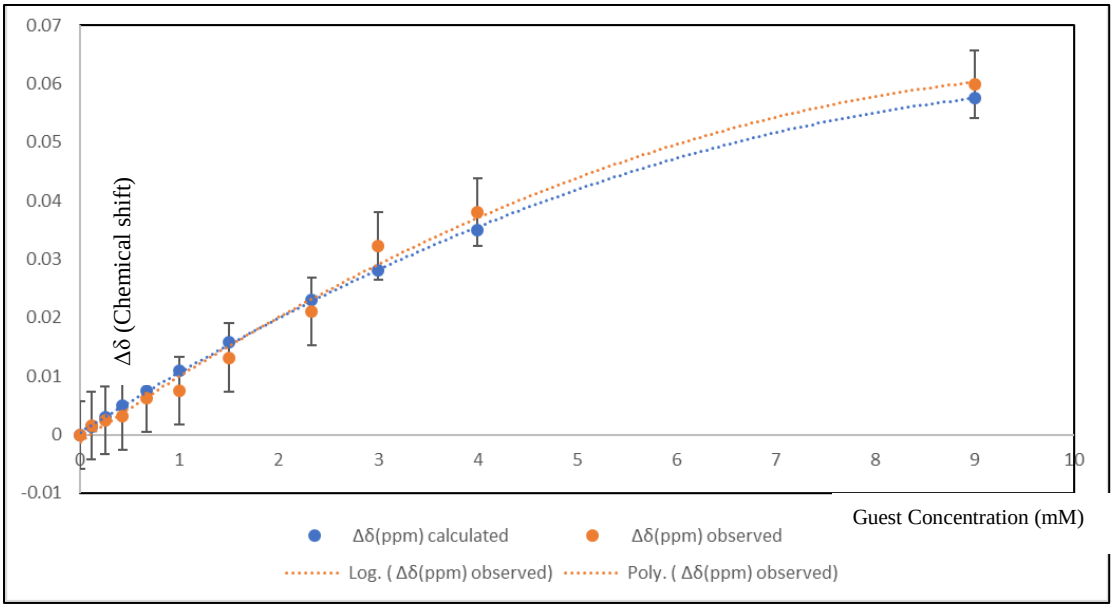

Figure 1.36: 1:1 Binding curve for the association of 2 with γ-CD.

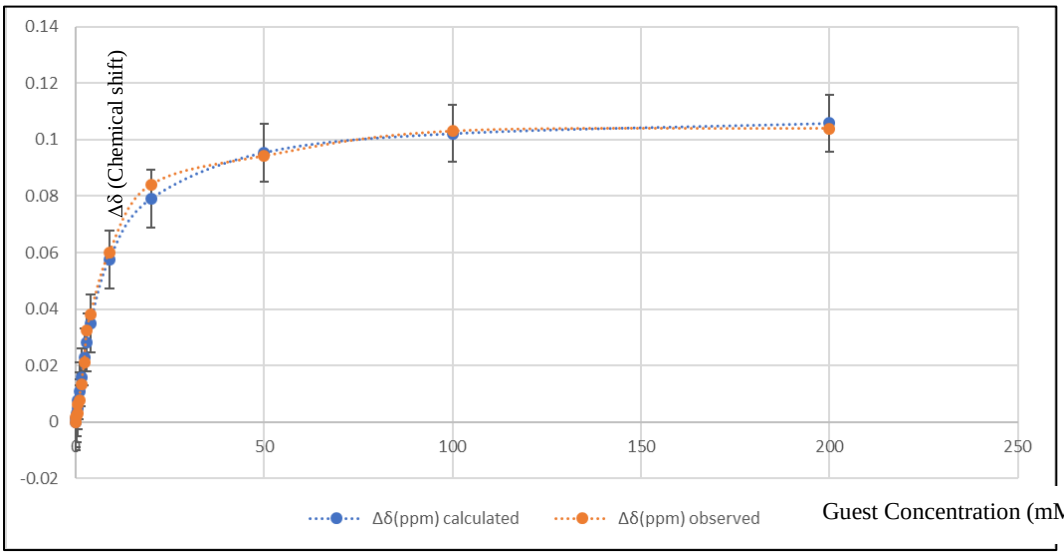

Figure 1.37: 1:1 Binding curve for the association of 2 with γ-CD.

Mass spectroscopic studies

All compounds were prepared in the deionized water at a concentration of 200 μM for both guest and host molecules separately and as a mixture. Then they were diluted to 20 μM (each) in a solution of methanol/water (50/50) to produce the standards for mass spectrometric analysis. The final solutions were infused into a Thermo Scientific LTQ Orbitrap XL™ (Waltham, MA, USA) mass spectrometer at a rate of 10 μL/min using electrospray ionization source in a positive mode. The rest of the ionization and ion optics parameters were as follows: sheath gas 15, auxiliary gas 3, spray voltage 5 kV, capillary temperature 275 °C, capillary voltage 47 V, tube lens 225 V, multipole 00 offset -5.5 V, lens 0 -6.0 V, multipole 0 offset -5.75 V, lens 1 -10.0 V, gate lens -46.0 V, multiple 1 offset -19.5 V, multipole RF amplitude 400.0 V, front lens -6.75 V. The mass spectra were collected using full scan mode with resolution of 30000 in the range between 100 and 2000 amu. The spectra were averaged over at least 50 micro scans with 10.0 ms maximum injection time and 2.0×10^5 ions for AGC target settings.

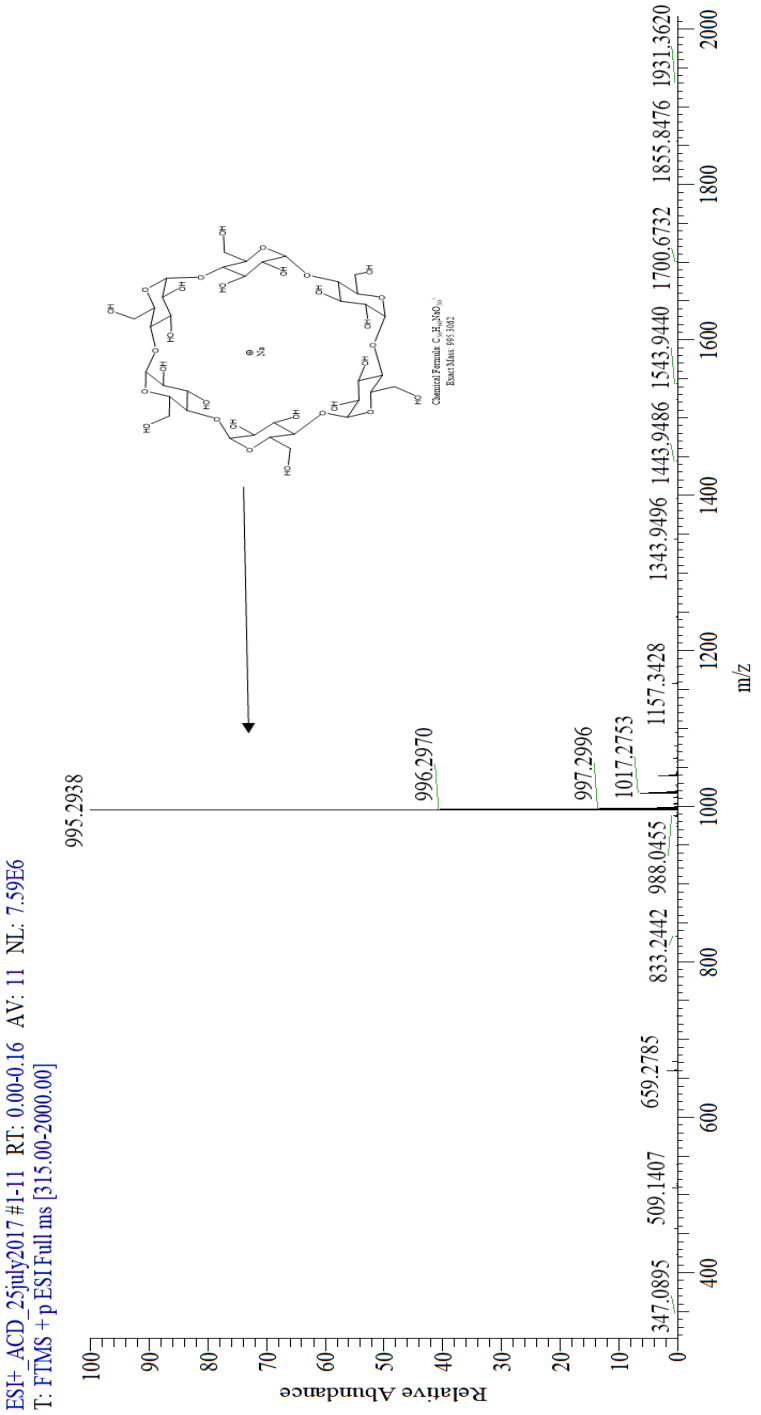

Figure 1.38: Mass spectrum of α-CD

.

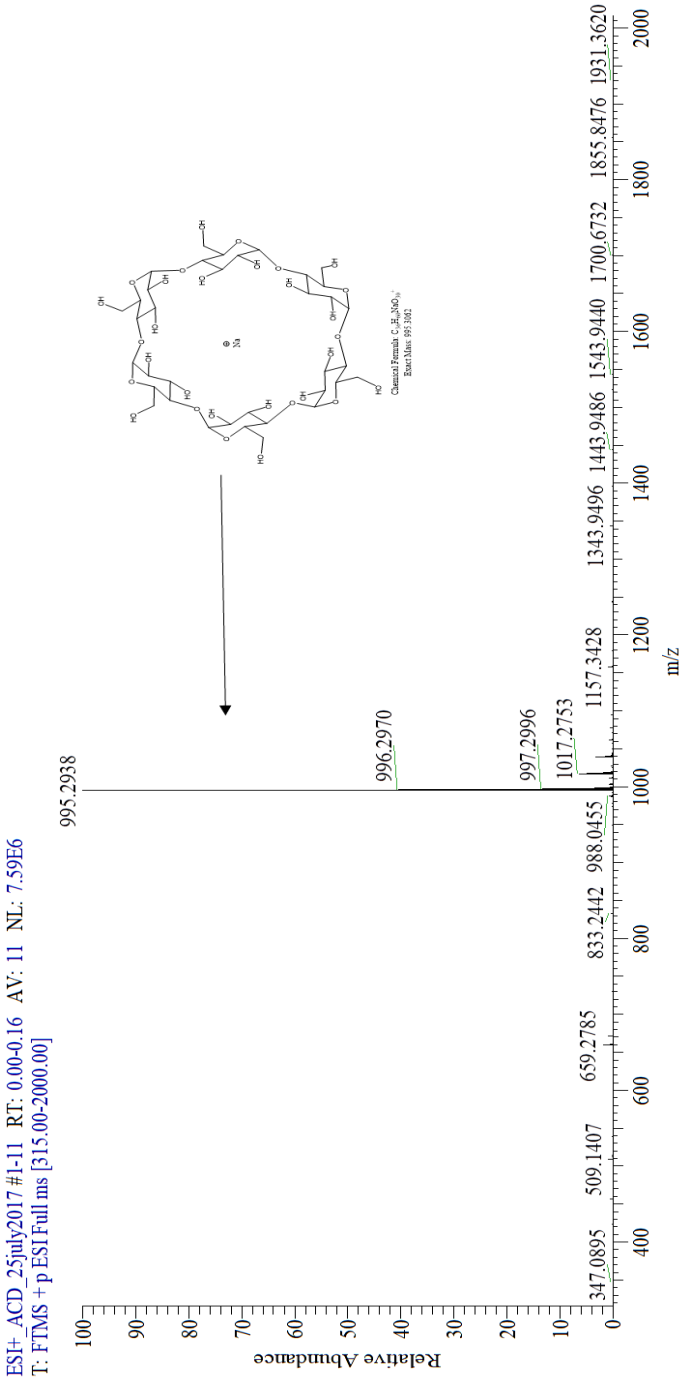

Figure 1.39: Mass spectrum of β-CD

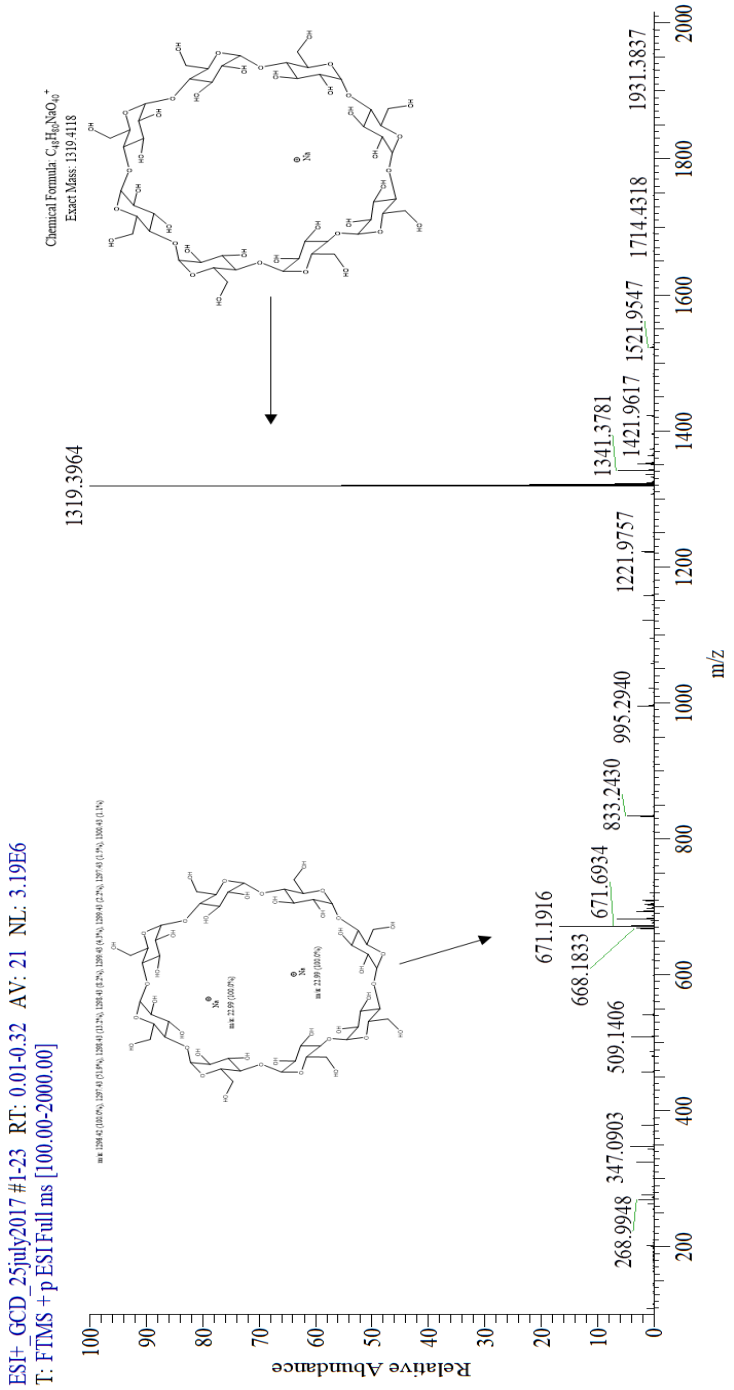

Figure 1.40: Mass spectrum of γ-CD

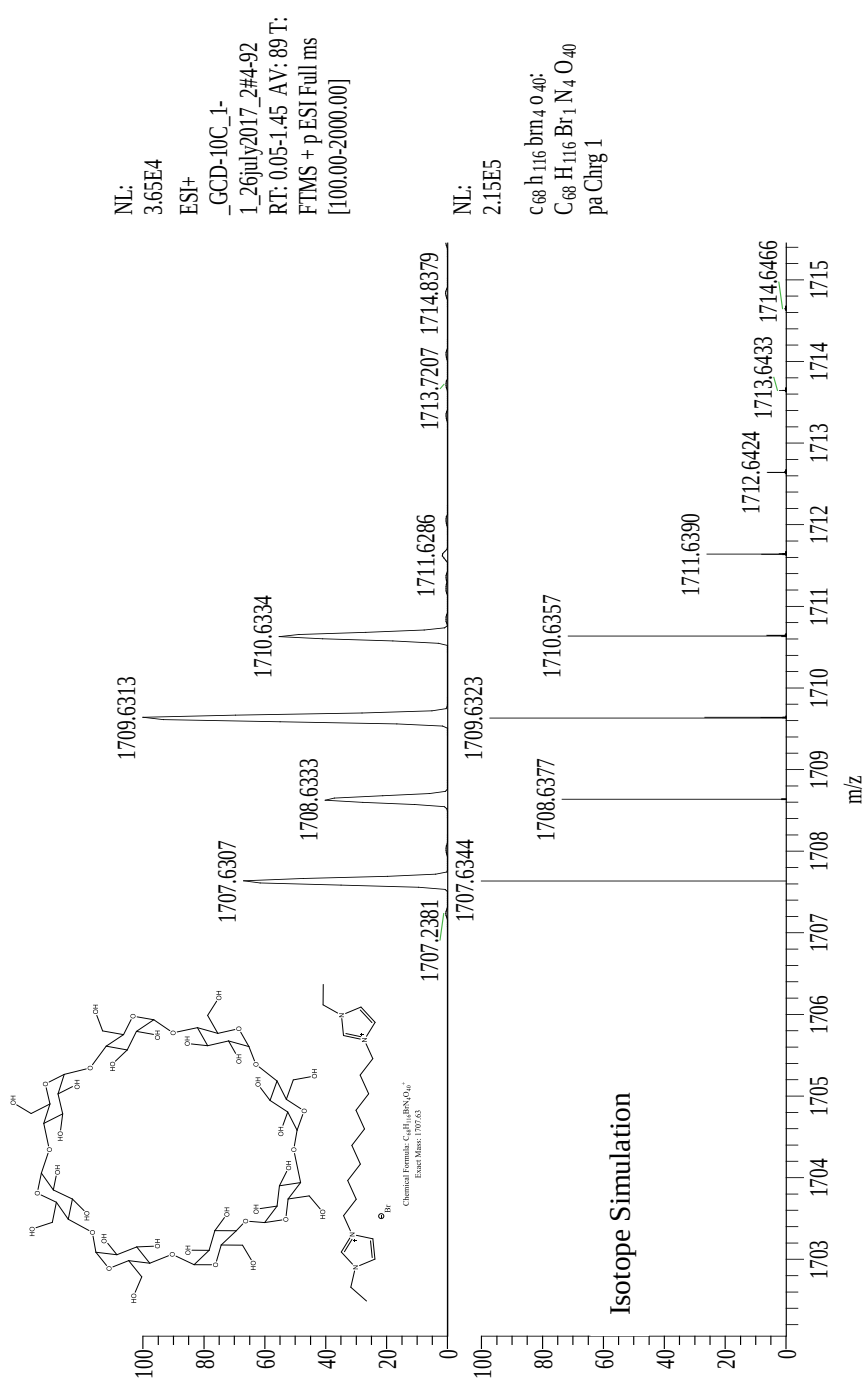

Figure 1.41: 1⊂γ-CD (ESI+, 5 uL/min, FS, 20 uM/20 uM) – m/z 1707.6307

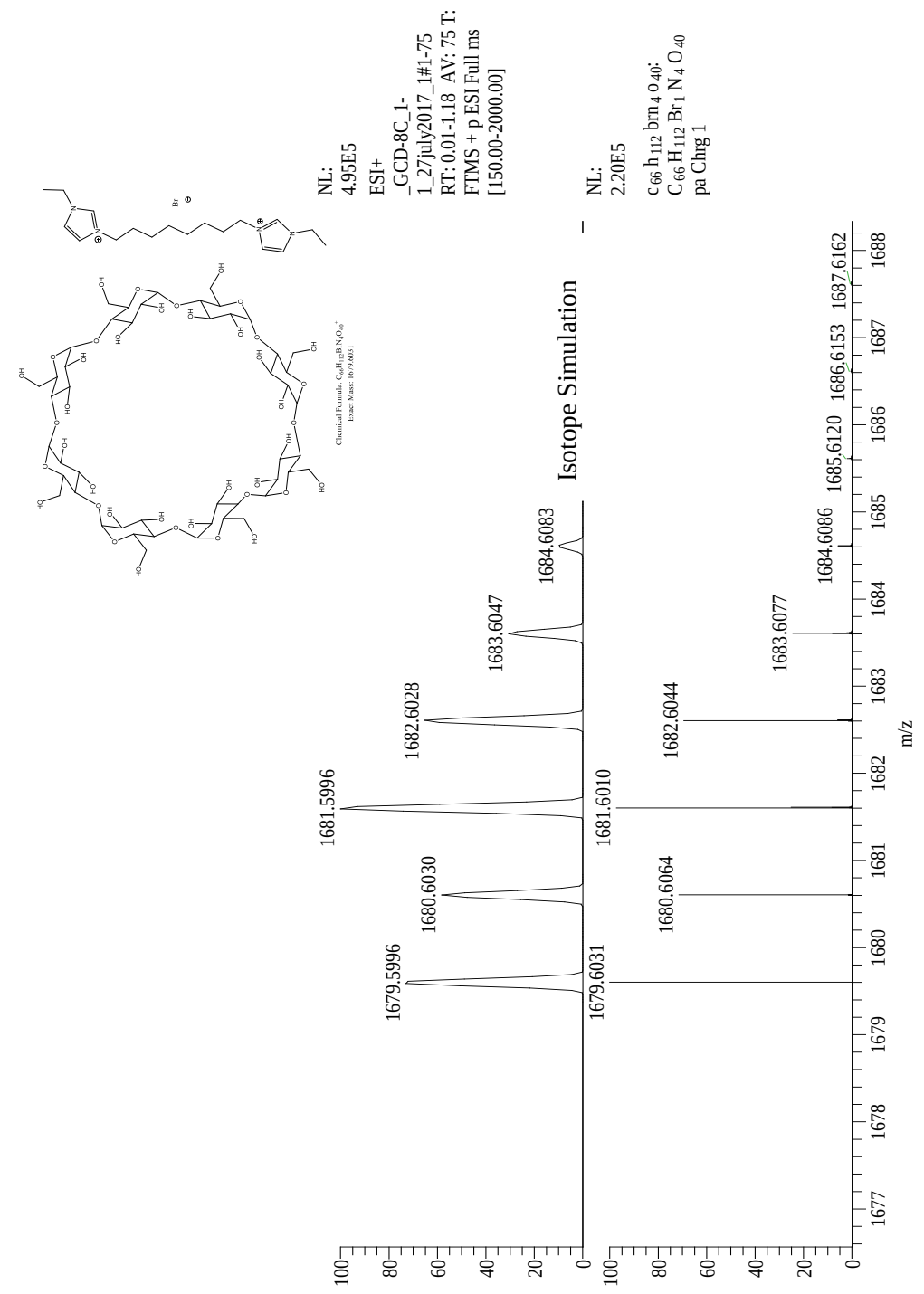

Figure 1.42: 3⊂γ-CD (ESI+, 5 uL/min, FS, 20 uM/20 uM) – m/z 1679.5996

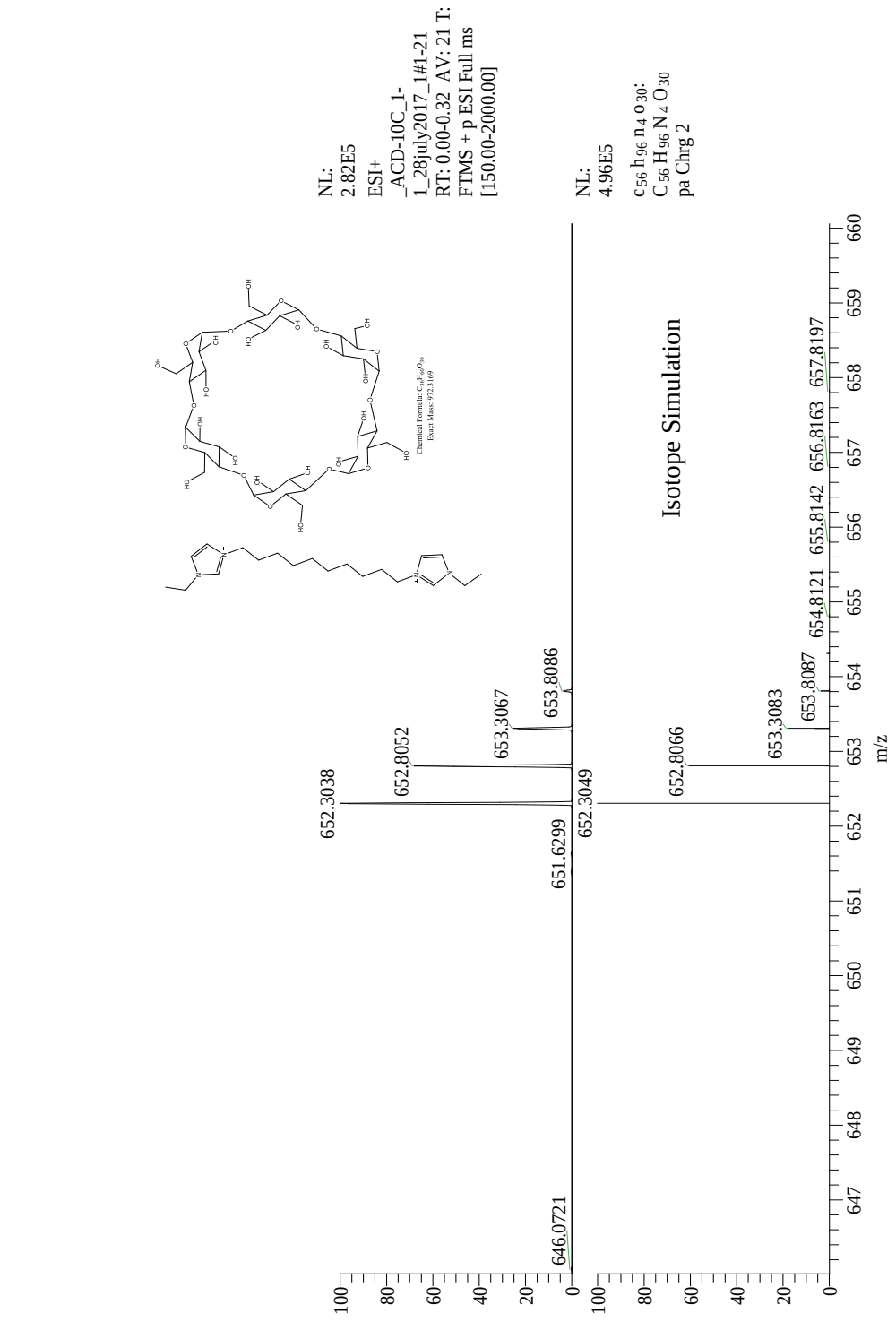

Figure 1.43: 1⊂α-CD (ESI+, 5 uL/min, FS, 20 uM/20 uM) – m/z 1707.6307

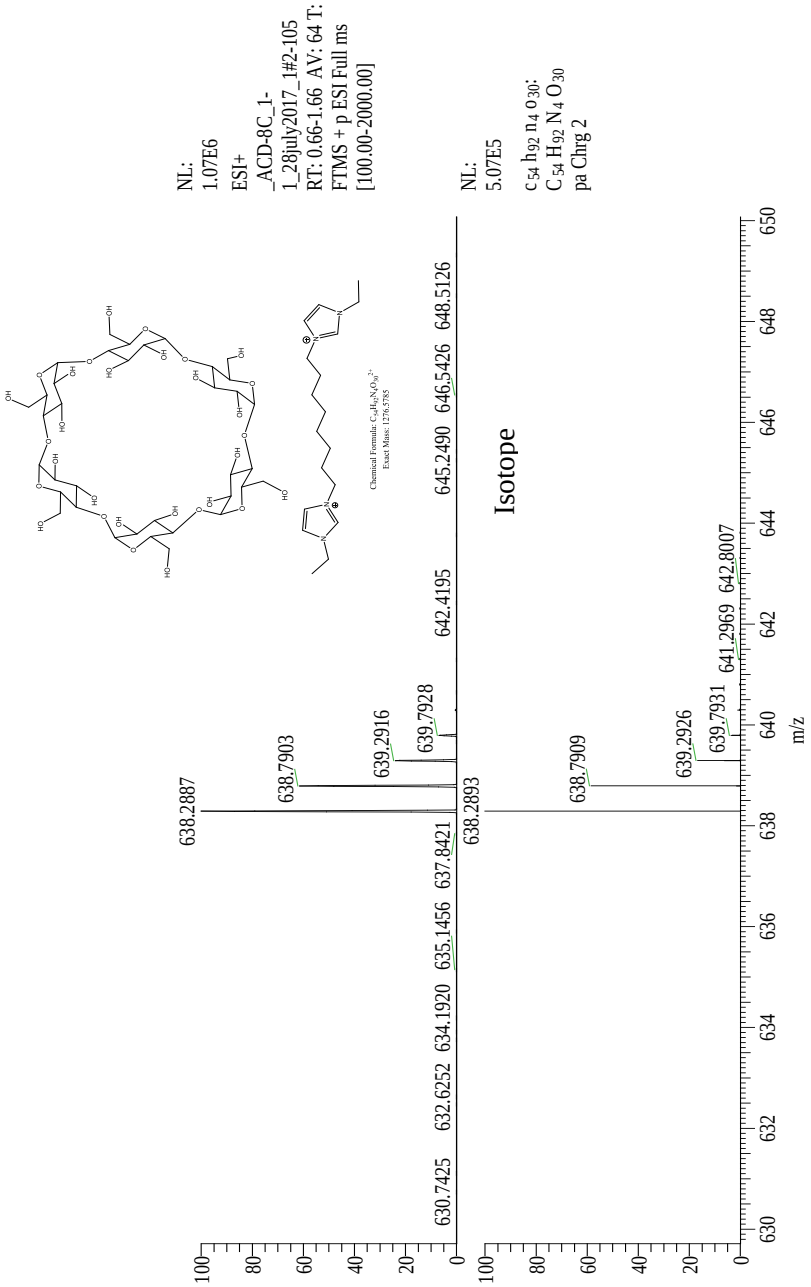

Figure 1.44: 3⊂α-CD (ESI+, 5 uL/min, FS, 20 uM/20 uM) – m/z 638.2887

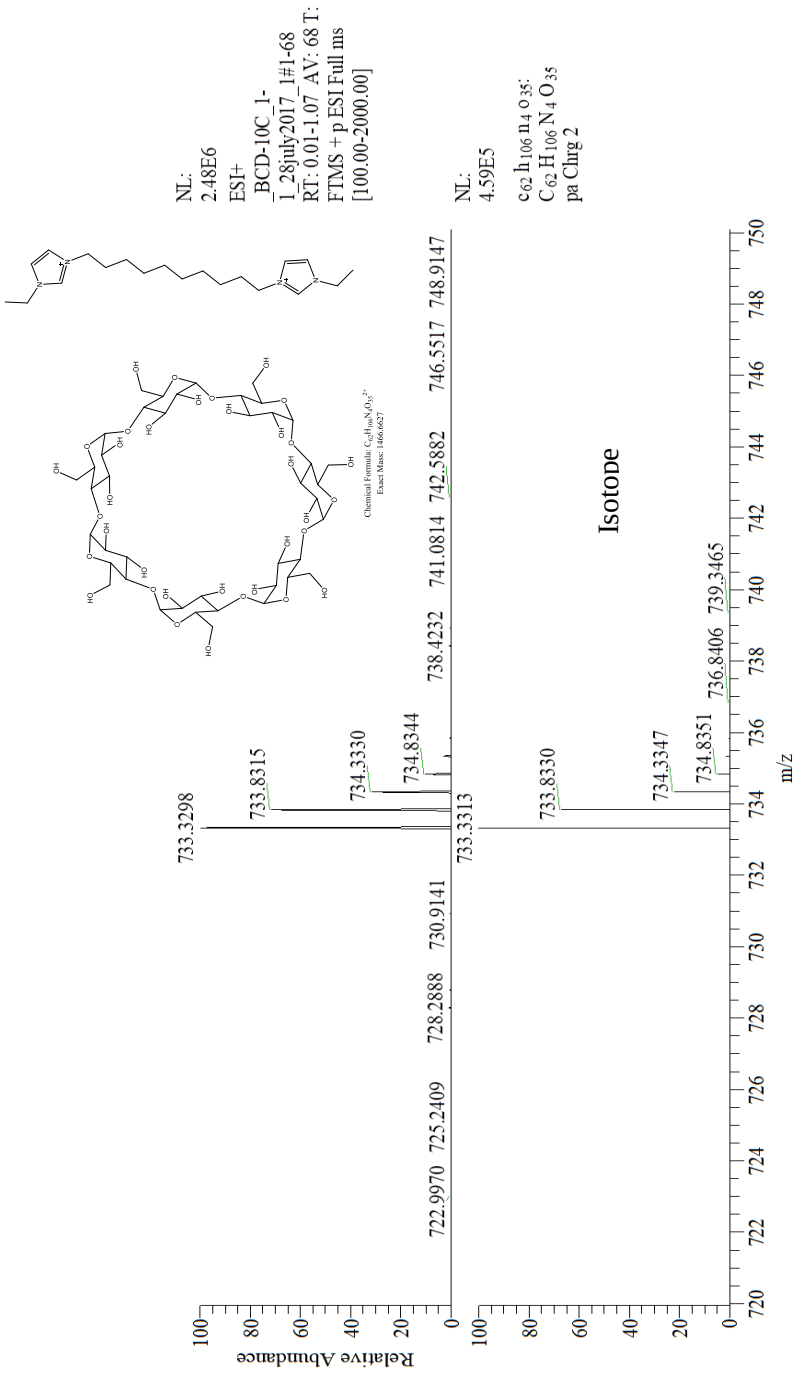

Figure 1.45: 1⊂β-CD (ESI+, 5 uL/min, FS, 20 uM/20 uM) – m/z 733.3298

Determination of association constants for guest probes and γ-CD using Isothermal Titration Calorimetry (ITC)

A 1000 mM solution of **1** and 100 mM solutions of γ-CD were made in water and plasma. Once the solutions were made, the guest solution was loaded in to the micro-syringe and the γ-CD solution was placed in the sample ampoule (2 ml). Lower concentrations of the host and guest did not provide sufficient heat flow for reliable ITC analysis. For the titration, a 1 µl/S rate and 21 injections were chosen. Except for the first injection, which was 3 µl, all the other injections were 10 µl injections. Each titration was performed for 20 minutes with a 5-minute base line. For data analysis, blank titrations were performed with addition of guest **1** to DI water and plasma without the γ-CD. The data from the blank titration were used to subtract the heat of dilutions. Once the Raw heat data was obtained, the data was processed using the online software, AFFINImeter (https://www.affinimeter.com/).

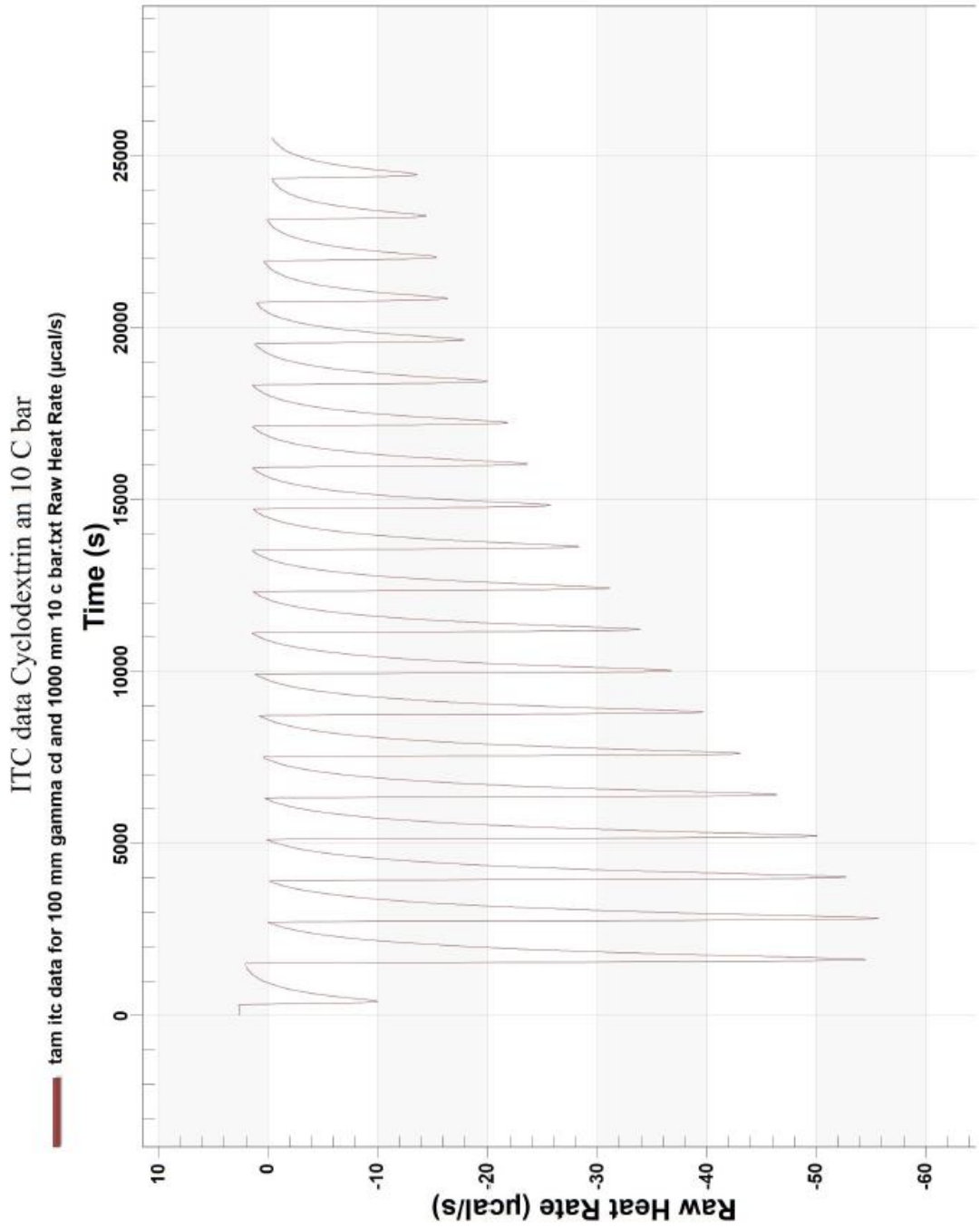

Figure 1.46: ITC of 1 with γ-CD in water

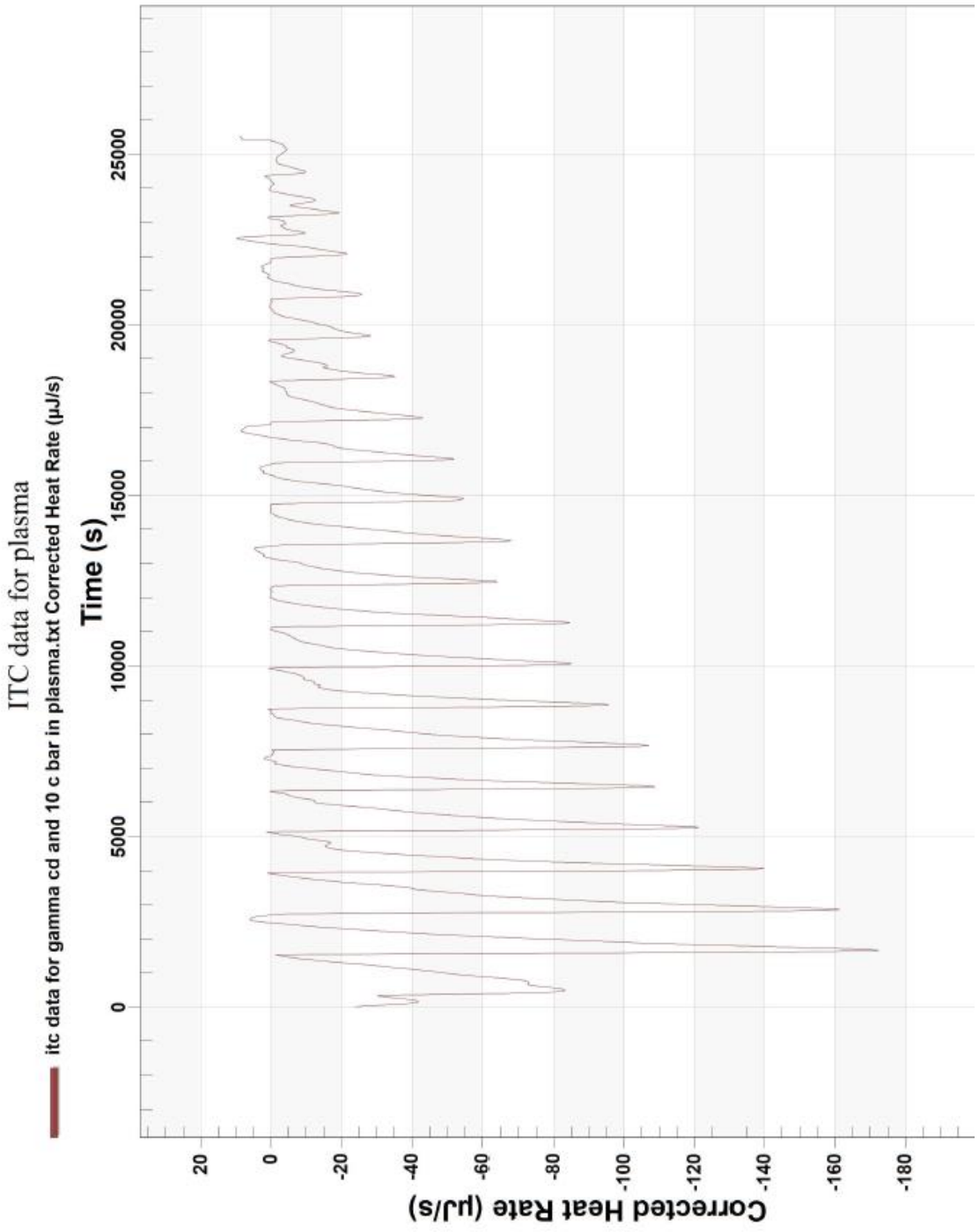

Figure 1.47: ITC of 1 with γ-CD in bovine plasma

AFFINIMETER

ITC data analysis report

v2.1608 - support@affinimeter.com

Analysis of data series #2

fit: "Ashvin" [ITC_data_for_gamma_CD_and_10_C_bar_in_water] [ID: 14688]

Experimental Settings

- Initial concentration of **M** [**M**] in the Cell: 100.000 mM
- Concentration of **A** [**A**] in the Syringe: 1000.000 mM
- Temperature: 571.3K
- Cell volume: 2 mL

Description of the Model

An *Independent Sites* model with 1 independent sets of sites has been applied.

Results

- Global χ^2: *2.24e+00*

Table 3: Correction parameters† *† fitted parameters in blue*

ΔH_{dil} [cal·mol^{-1}]	Q_{db} [cal]	r_M	r_A	r_B
0.000e+00	*0.000e+00*	(5.2030 ± 0.0327)e-01	*1.000e+00*	*1.000e+00*

Table 4: Reaction parameters† *† fitted parameters in blue*

set [#]	site		K [M^{-1}]		ΔH [cal·mol^{-1}]	
1	n(1,1)	*3*	K_A(1,1)	*1.00e+04*	ΔH_A(1,1)	*5.00e-03*

Figure 1: Fitted Isotherm and Residuals

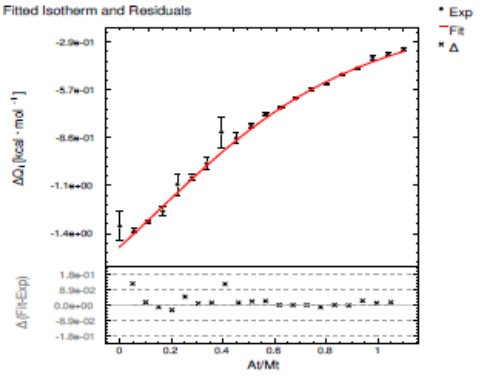

Figure 2: Contributions to the Binding Isotherm

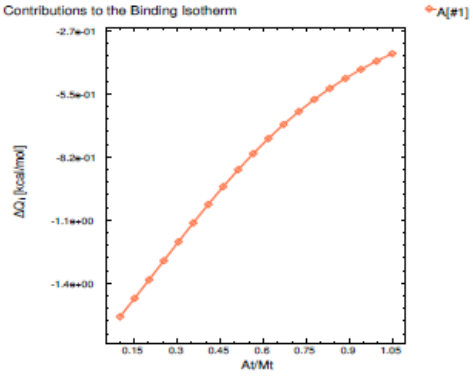

Association Constant of 1⊂γ-**CD** = 1.00 ± 0.0327 x 10^4 M^{-1}

Figure 1.48: Analysis of ITC binding data for 1 with γ-CD in water

AFFINIMETER

ITC data analysis report

v2.1608 - support@affinimeter.com

Monday, February 13, 2017

Javi Rial Rodríguez[info@affinimeter.com]

Analysis of data series #1

fit: "Ashvin" [ITC_data_for_gamma_Cd_and_10_C_bar_in_plasma] [ID: 14688]

Experimental Settings

- Initial concentration of **M** [M] in the Cell: 100.000 mM
- Concentration of **A** [A] in the Syringe: 1000.000 mM
- Temperature: 571.3K
- Cell volume: 2 mL

Description of the Model

An *Independent Sites* model with 1 independent sets of sites has been applied.

Results

- Global χ^2: ***2.24e+00***
  - χ^2 for curve [1]: ***2.84e+00***

Table 1: Correction parameters† *† fitted parameters in blue*

ΔH_{dil} [cal·mol^{-1}]	Q_{db} [cal]	r_M	r_A	r_B
0.000e+00	*0.000e+00*	(5.4913 ± 0.0928)e-01	*1.000e+00*	*1.000e+00*

Table 2: Reaction parameters† *† fitted parameters in blue*

set [#]	site		K [M^{-1}]		ΔH [cal·mol^{-1}]	
1	n(1,1)	*1.000e+00*	K_A(1,1)	(1.0114 ± 0.0592)e+02	ΔH_A(1,1)	(-3.7754 ± 0.0912)e+03

Figure 1: Fitted Isotherm and Residuals

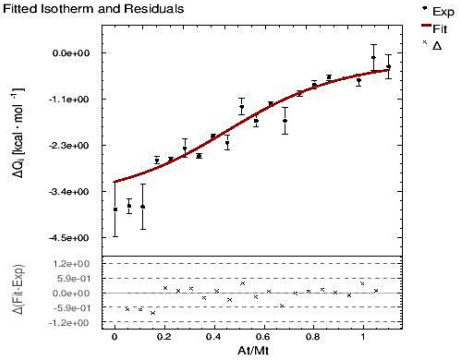

Figure 2: Contributions to the Binding Isotherm

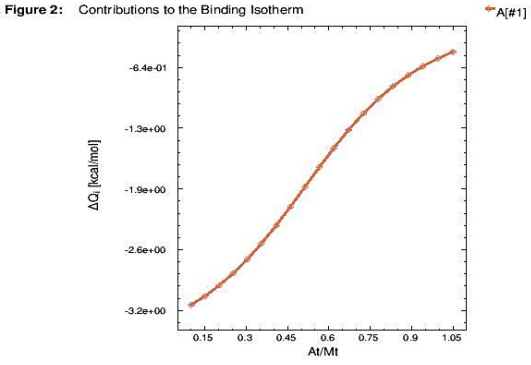

Association Constant of **1⊂γ-CD** (plasma) = 1.0114 ± 0.0592 x 10^2 M^{-1}

Figure 1.49: Analysis of ITC binding data for 1 with γ-CD in bovine plasma

A series of computational studies were performed to measure the cavity size of the pseudorotaxanes using the Spartan 16 computational chemistry package. A first minimization was performed using molecular mechanics with the MMFF force field in the gas phase. Once the minima were obtained, the same force field was used to run the simulation in water as the solvation source. After that, the semi-empirical PM3 force field was used to minimize the structure in the gas phase. This was followed using an energy minimization (PM3) using external water molecules (One water molecule of water was used per oxygen atom in the host.) to mimic the hydrophobic and hydrophilic interactions of the guest to the hydrophobic cavity of the host.

Guest / Host	Guest-1 ΔE (kcal/mol)	Guest-2 ΔE (kcal/mol)
α-CD	-132.23	-108.96
β-CD	-448.94	-433.7
γ-CD	-778.93	-722.71
CB[6]	-198.98	-174.29
CB[7]	-234.64	-210.69
CB[8]	-370.23	-338.92

Table 1-2: Calculated binding energies for pseudorotaxanes

Molecular modeling calculations were performed using Spartan 16 for all complexes as guests encapsulated in the hosts to estimate the stabilization energy obtained by complexation (which provides an indication of the relative binding constants). Above ΔE values are given in kcal/mol. The following equation was used to obtain the final values:[3]

$$\Delta E = E_{(complex)} - E_{(host)} - E_{(Guest)}$$

External water molecules (one water molecule per oxygen in the host molecule) were used to mimic the solvent environment for both the hosts and the host-guest complexes.

Table 1-3: Computed distances between guest and host for 2⊂CB6

Atom labels	C-C distance (A^o)
C32, C47	8.725
C31, C47	7.318
C20, C47	**7.369**
C34, C47	**6.039**
C18, C47	**6.557**
C17, C47	**5.805**
C19, C47	**6.511**
C15, C47	5.832

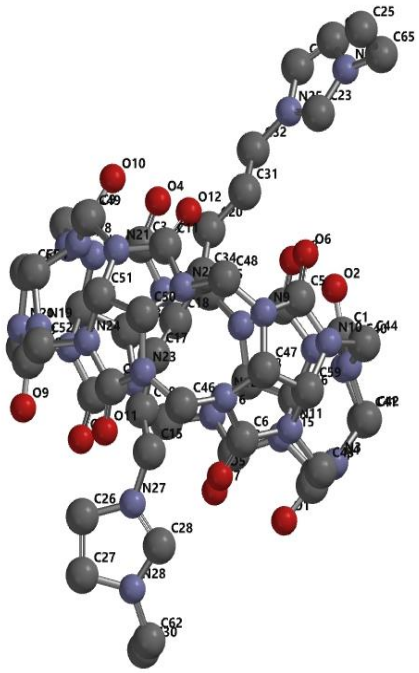

bold distances represent the atoms that are inside the host cavity

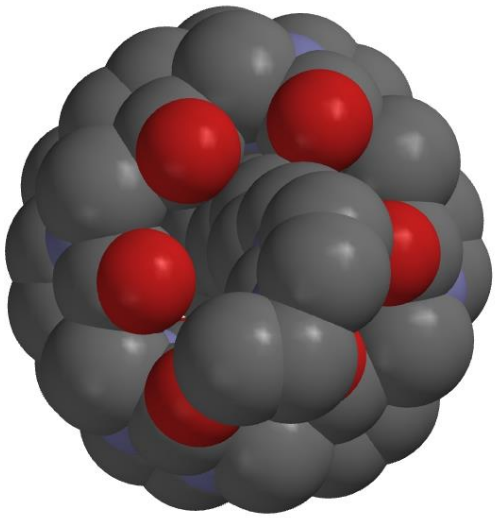

Table 1-4: Computed distances between guest and host for 1⊂CB6

Atom labels	C-C distance (A^o)
C32, C47	7.802
C31, C47	6.976
C20, C47	**5.740**
C34, C47	**5.322**
C18, C47	**4.389**
C17, C47	**4.884**
C16, C47	**4.766**
C15, C47	**6.154**
C57, C47	6.473
C13, C47	8.001

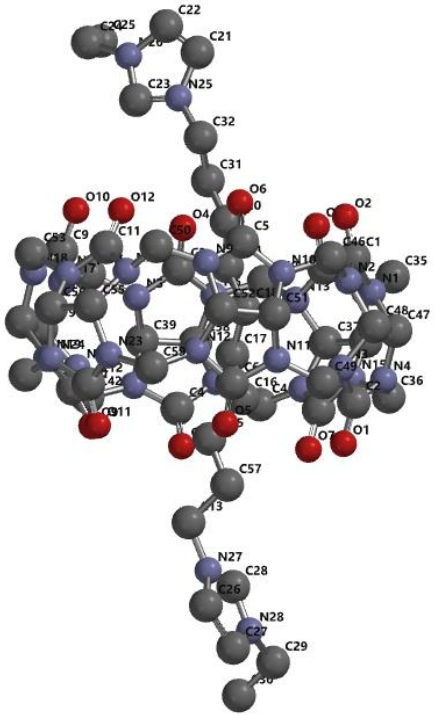

bold distances represent the atoms that are inside the host cavity

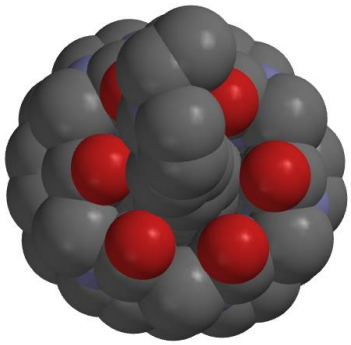

Table 1-5: Computed distances between guest and host for 2⊂CB7

Atom labels	C-C distance (A^o)
C14, C58	7.802
C13, C58	**6.976**
C11, C58	**5.740**
C9, C58	**5.322**
C4, C58	**4.389**
C5, C58	**4.884**
C3, C58	4.766
C1, C58	6.154

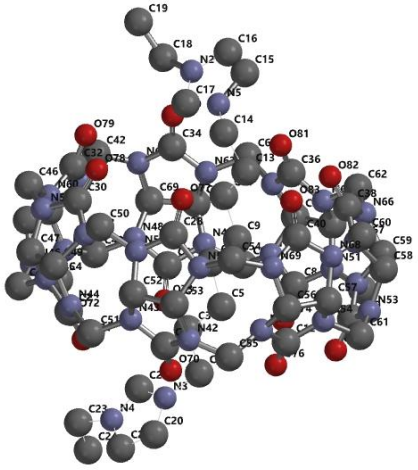

bold distances represent the atoms that are inside the host cavity

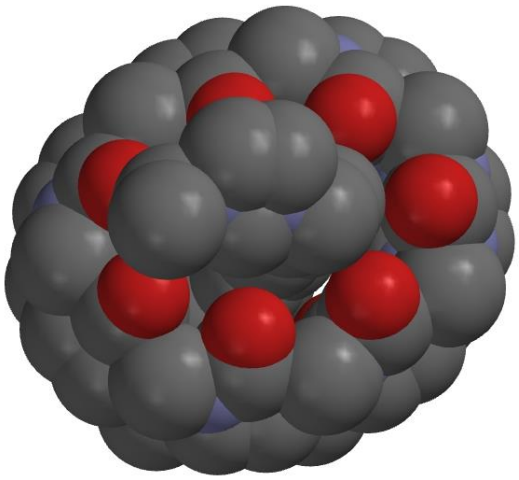

Table 1-6: Computed distances between guest and host for 1⊂CB7

Atom labels	C-C distance (A^o)
C1, C47	7.726
C3, C47	**6.481**
C5, C47	**6.161**
C7, C47	**5.075**
C9, C47	**5.333**
C11, C47	**5.256**
C13, C47	6.071
C14, C47	6.712
C25, C47	8.012
C26, C47	8.876

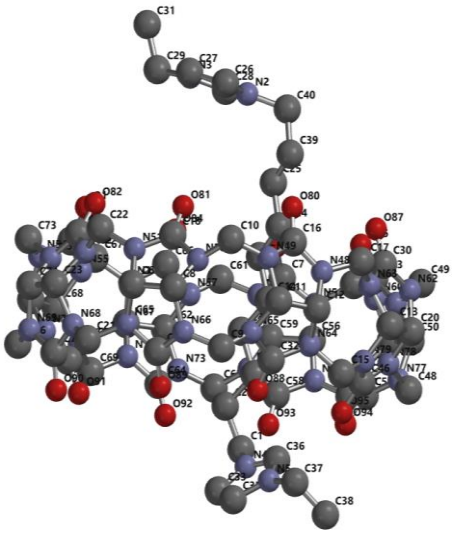

bold distances represent the atoms that are inside the host cavity

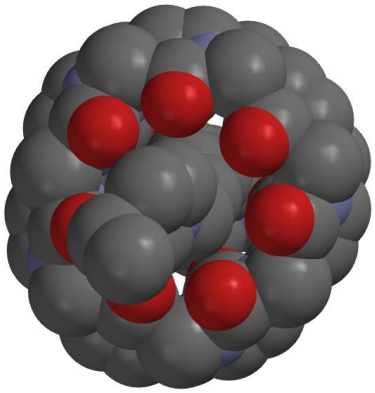

Table 1-7: Computed distances between guest and host for 2⊂CB8

Atom labels	C-C distance (A^o)
C25, C71	7.809
C24, C71	6.389
C19, C71	**6.084**
C14, C71	**5.255**
C4, C71	**5.808**
C3, C71	**5.340**
C2, C71	**6.566**
C1, C71	**6.593**

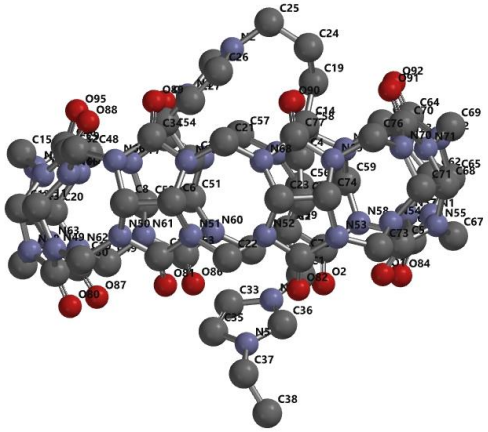

bold distances represent the atoms that are inside the host cavity

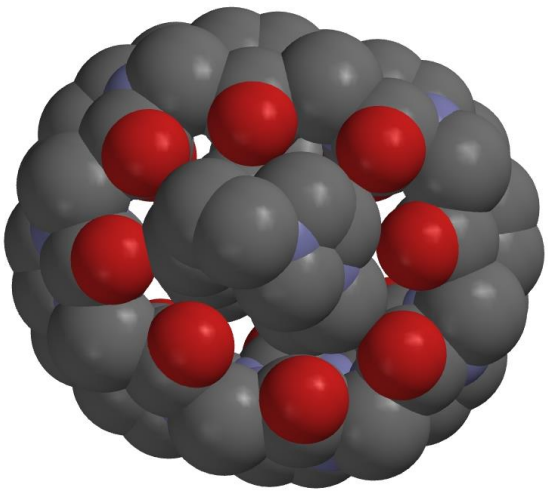

Table 1-8: Computed distances between guest and host for 1⊂CB8

Atom labels	C-C distance (A^o)
C40, C20	8.521
C39, C20	7.202
C25, C20	7.066
C24, C20	**5.895**
C19, C20	**6.276**
C14, C20	**5.438**
C4, C20	**6.455**
C3, C20	**6.089**
C2, C20	7.453
C1, C20	7.586

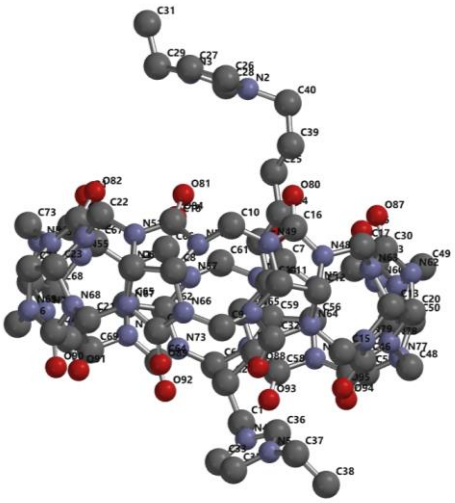

bold distances represent the atoms that are inside the host cavity

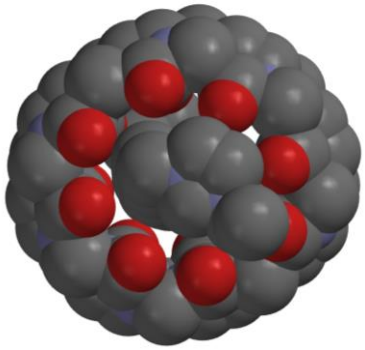

Table 1-9: Computed distances between guest and host for 2⊂α-CD

Atom labels	C-C distance (A°)
C6, C10	6.903
C5, C10	**5.739**
C4, C10	**6.250**
C3, C10	**5.493**
C2, C10	**6.404**
C7, C10	**6.458**
C18, C10	**7.366**
C19, C10	7.791

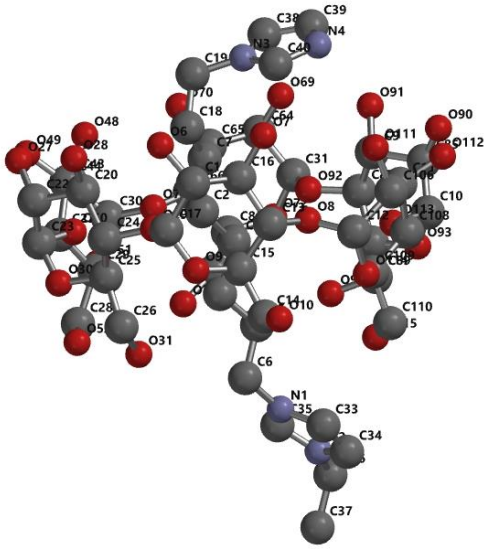

bold distances represent the atoms that are inside the host cavity

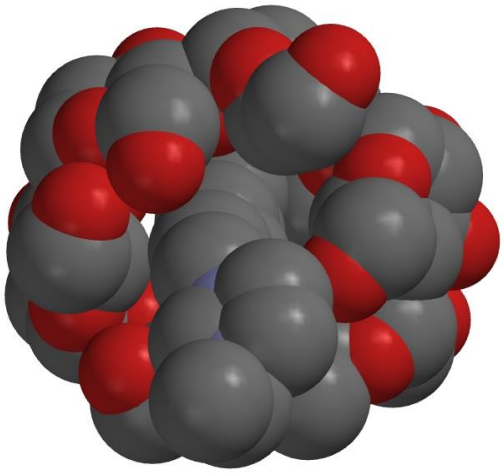

Table 1-10: Computed distances between guest and host for 1⊂α-CD

Atom labels	C-C distance (A^o)
C32, C13	8.006
C21, C13	7.552
C2, C13	6.093
C3, C13	5.953
C4, C13	4.690
C5, C13	5.155
C6, C13	4.398
C7, C13	5.408
C18, C13	5.257
C19, C13	6.569

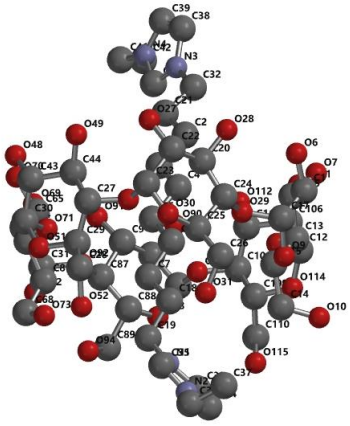

bold distances represent the atoms that are inside the host cavity

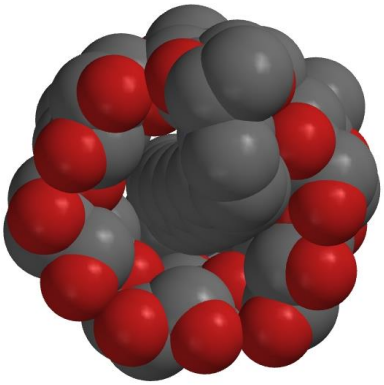

Table 1-11: Computed distances between guest and host for 1⊂α-CD

Atom labels	C-C distance (A^o)
C13, C30	6.811
C12, C30	6.102
C11, C30	**5.812**
C5, C30	**5.383**
C4, C30	**5.423**
C3, C30	**5.094**
C2, C30	**5.709**
C1, C30	**5.740**

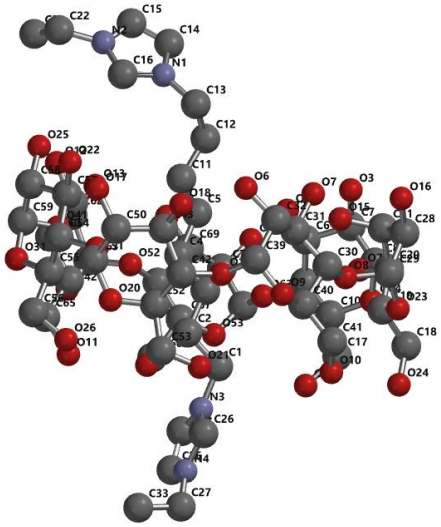

bold distances represent the atoms that are inside the host cavity

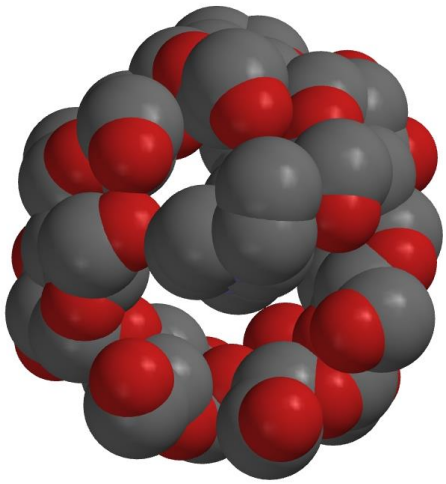

Table 1-12: Computed distances between guest and host for 1⊂β-CD

Atom labels	C-C distance (A^o)
C35, C59	7.385
C34, C59	6.2783
C13, C59	**6.664**
C12, C59	**5.892**
C11, C59	**6.763**
C5, C59	**6.527**
C4, C59	**7.629**
C3, C59	**7.812**
C2, C59	8.992
C1, C59	9.554

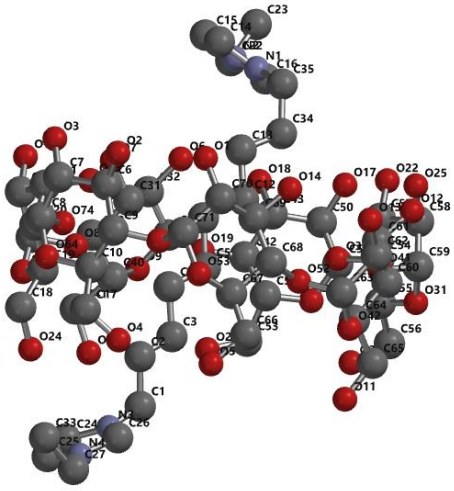

bold distances represent the atoms that are inside the host cavity

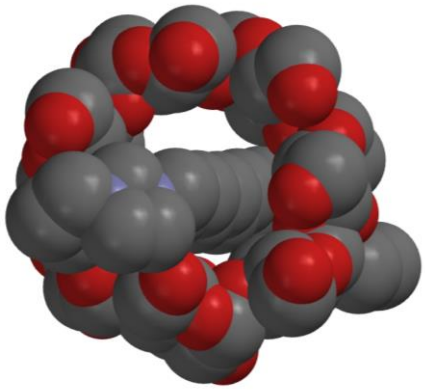

Table 1-13: Computed distances between guest and host for 2⊂γ-CD

Atom labels	C-C distance (A^o)
C2, C19	7.907
C3, C19	**7.947**
C4, C19	**9.127**
C7, C19	**9.408**
C9, C19	**10.558**
C23, C19	**10.887**
C25, C19	12.338
C33, C19	12.767

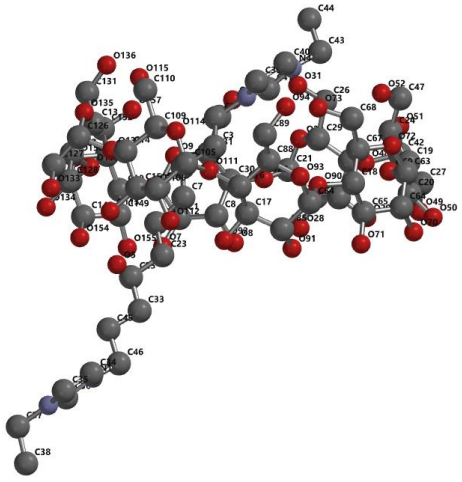

bold distances represent the atoms that are inside the host cavity

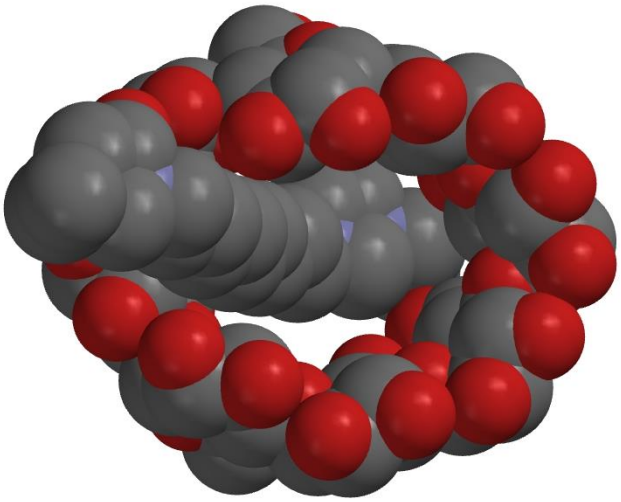

Table 1-14: Computed distances between guest and host for 1⊂γ-CD

Atom labels	C-C distance (A^o)
C2, C19	**9.347**
C3, C19	**8.737**
C4, C19	**9.309**
C7, C19	**9.223**
C9, C19	**10.032**
C23, C19	10.344
C25, C19	11.233
C33, C19	11.926
C45, C19	12.772
C46, C19	13.599

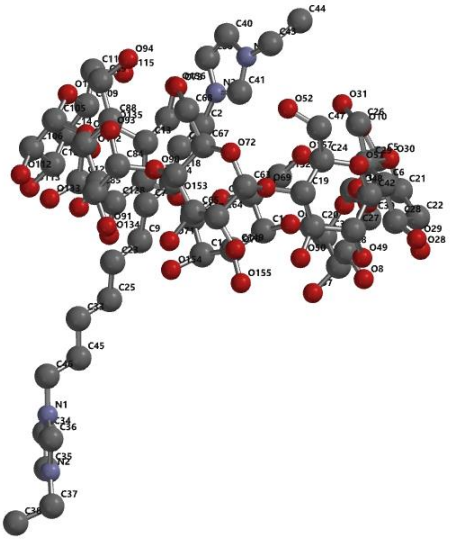

bold distances represent the atoms that are inside the host cavity

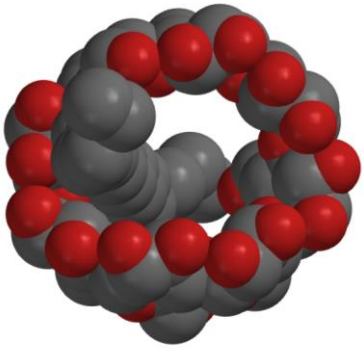

Xenon NMR studies

Naturally abundant ^{129}Xe gas was placed into a 1.0 L Tedlar bag and polarized to 60-80% via the spin exchange optical pumping (SEOP) technique using a Xemed polarizer (Xemed, Durham, NH, USA). It was then placed into a Tedlar bag which was immediately moved into a pressurized chamber within the bore of a Philips Achieva 3.0 T clinical MRI scanner to preserve its polarization. The pressure inside of the chamber was maintained between 20-45 kPa above atmospheric pressure using a pressure-sensitive ventilation device connected to a nitrogen (N_2) source, to facilitate the flow of HP ^{129}Xe gas from the Tedlar bag into the glass-fritted cell containing rotaxane solution.

Following polarization of ^{129}Xe gas, 2.5 mL of solution (50 mM) was transferred into a custom-made glass-fritted cell using a syringe. The cell containing the solution was then placed inside of a custom-made quadrature radio-frequency (RF) coil tuned to the Larmor frequency of ^{129}Xe (35.33 MHz) at 3.0 T. The Tedlar bag, already in the bore of the MRI, was then connected to the cell's inflow tube. Once connected, the pressure-stopper on the Tedlar bag was released to allow for the continuous flow of HP ^{129}Xe gas into the glass-fritted cell, which produced several microbubbles as it passed through the fine fritted disc, thereby dissolving into the solution. As HP 129Xe gas continually flowed through the glass-fritted cell, ^{129}Xe nuclear magnetic resonance (NMR) spectral data was simultaneously obtained. The concentration of ^{129}Xe at any point during the spectral acquisition was between 1-5 mM24.

All ^{129}Xe NMR spectra were acquired using a Philips Achieva 3.0 T clinical MRI scanner. Scanner software was modified for the automatic measurement of hyperpolarized chemical exchange saturation transfer (HyperCEST) depletion spectra. To saturate HP ^{129}Xe encapsulated within the rotaxane molecules, two different pre-pulse trains were used: the first consisted of 16- 30 ms 3-lobe sinc pulses, while the second consisted of 16- 30 ms sinusoidal pulses, both with 0 ms pulse intervals. To acquire each depletion spectrum, 37 free induction decay (FID)

spectra were collected at various chemical shift frequency offsets with TR = 4s. Each FID spectrum was acquired using a selective 90-degree "spredrex" excitation pulse with a 9.95 ms duration and bandwidth of 1424 Hz (40.3 ppm at 3.0 T).

The data sampling number was 2048, which corresponds to the spectral resolution of 0.44 ppm. Saturation pre-pulse frequency was automatically adjusted to range from -150 ppm to 30 ppm, where 0 ppm represents dissolved-phase ^{129}Xe, with a predetermined step before each of the subsequent excitation pulses. Offset frequency steps were 176.7 Hz, which correspond to 5 ppm at 3.0 T.

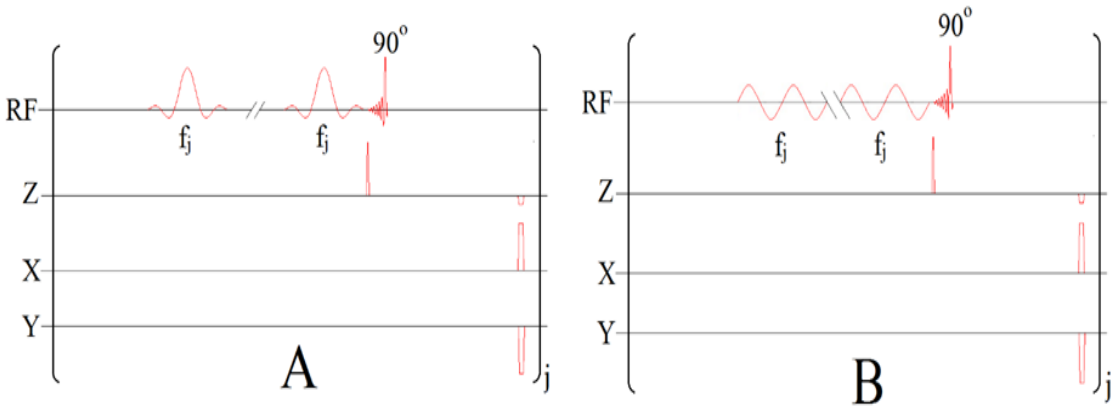

Figure 1.50: HyperCEST pulse sequence

The pulse diagrams shown above were used to prepare HyperCEST depletion spectra using different saturation pre-pulse trains including 3-lobe sinc pulses (A) and sinusoidal pulses (B). Here, fj represents the frequency of saturation pulses during FID acquisition number j. All spoiler gradients along x, y, z axis is also illustrated.

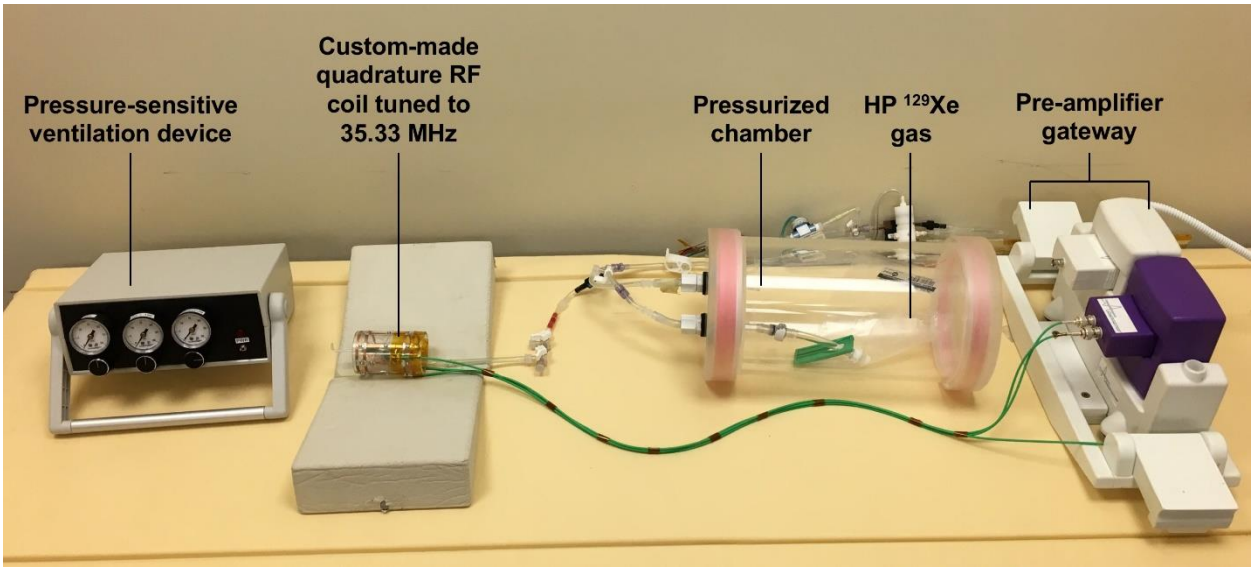

Figure 1.51: Apparatus for obtain HP Xe spectra

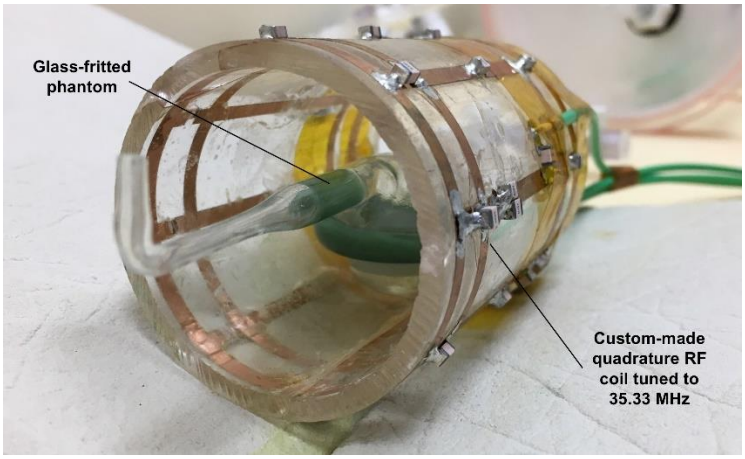

Figure 1.52: Custom-made coil and sample chamber

The image above illustrates the continuous flow of HP ^{129}Xe gas throughout the glass-fritted vessel. As depicted, once the flow of HP ^{129}Xe reaches the fine glass-fritted disc, numerous microbubbles are produced, thereby causing dissolution of HP ^{129}Xe into solution. The RF pulse is applied at the chemical shift frequency offset which corresponds to the ternary complex formed by the interaction of HP ^{129}Xe with the pseudorotaxane complex.

Cavity volume calculations

Commercially available MOE[4] software was used to calculate the free space in the host after the guest was threaded inside the CD or CB cavity, using the Assisted Model Building with Energy Refinement (AMBER) force field for energy minimizations and molecular dynamics. A custom-made active site volume script provided from MOE was used in the process. The script computationally filled the void space in the pseudorotaxane with spheres having a volume of 2.75 A^3. The volume of the cavity was calculated as the sum of the volumes of the spheres. This method is analogous to Rebek's technique for calculating the volume of a cavitand.[4]

References

(1) Zhao, N.; Lloyd, G. O.; Scherman, O. A. *Chem. Commun.* **2012**, *48*, 3070.

(2) Thordarson, P. *Chem. Soc. Rev*. **2011**, *40*, 1305–1323.

(3) Jankowski, C.; Lamouroux, C.; Jiménez-Estrada, M.; Arseneau, S.; Wagner, B. *Molecules* **2016**, *21*, 1568.

(4) Mecozzi, S.; Rebek, J. *Chem. - A Eur. J.* **1998**, *4*, 1016–1022.

(5) Molecular Operating Environment (MOE), 2013.08; Chemical Computing Group ULC 1010 Sherbooke St. West, Suite #910, Montreal, QC, Canada, H3A 2R7, 2017.

2 CHAPTER 2

Will be published in *Nature Scientific reports*

Deca methyl imidazolium pillar[5]arene as a viable contrast agent for hyperCEST 129Xe MRI

Ashvin Fernando[1], Yurii Shepelytskyi[2], Francis Hane[2], Paul Cesana[1], Adriana Mendieta[1], Alanna Wade [2], Mitchell S. Albert [3], Brenton DeBoef[1]

[2]Department of Chemistry, Lakehead University, 955 Oliver Road, Thunder Bay, Ontario P7B 5E1, Canada [3]Thunder Bay Regional Research Institute, 980 Oliver Road, Thunder Bay, Ontario P7B 5E1, Canada [1]Department of Chemistry, University of Rhode Island, 140 Flagg Road, Kingston, Rhode Island 02881, United States

Abstract

A decacationic water-soluble pillar[5]arene (P5A) possessing a non-solvated hydrophobic core has been designed and synthesized. This supramolecular host is capable of binding xenon, as evidenced by a hyperCEST depletion experiment. Fluorescence-based studies have also demonstrated that xenon binds into the cavity of the pillararene with an association constant of 4.6×10^3 M^{-1}. These data indicate that the water soluble pillararene is a potential scaffold for building targeted biosensors that can be detected by xenon-129 magnetic resonance imaging.

Introduction

There is a clear and pressing need for the development of safe magnetic resonance imaging (MRI) contrast agents. One possible alternative to the current Gd-based contrast agents, which have recently been shown to have toxicity issues, is the use of hyperpolarized xenon-129. Inhaled ^{129}Xe is non-toxic, readily distributes throughout the body, and can be easily detected using a conventional MRI instrument with a broadband coil. We have recently shown that the ^{129}Xe image of a living rat can be overlaid onto a conventional ^{1}H image to provide selective contrast. [1] The key for this work was the use of the macrocyclic contrast agent, cucurbit[6]uril (CB6), which was injected into the animal prior to the imaging experiment. The biodistribution of CB6 was imaged because the molecular host bound the inhaled ^{129}Xe *in vivo*, producing a unique localized signal in the ^{129}Xe magnetic resonance spectrum. Whereas Gd(III) ions produce image contrast in a conventional T_1-weighted MR image by reversibly binding water molecules, the macrocyclic host reversibly bound xenon atoms and this reversible binding was selectively imaged via a saturation transfer pulse sequence, hyperCEST, thus providing localized contrast. [2-5]

This seminal *in vivo* imaging experiment serves as an important proof-of-concept; however, the use of CB6 was not optimal, as it is known to bind sodium and potassium ions that are present *in vivo*, and it biodistribution cannot be changed as it is difficult to chemically modify. [6-12] Cryptophanes have also been extensively studied for their ability to bind xenon; however, they are notoriously difficult to synthesize, are not by themselves water soluble, and water-soluble derivatives such as TPCA have been recently shown to form complex aggregates in aqueous solution. [13-16]

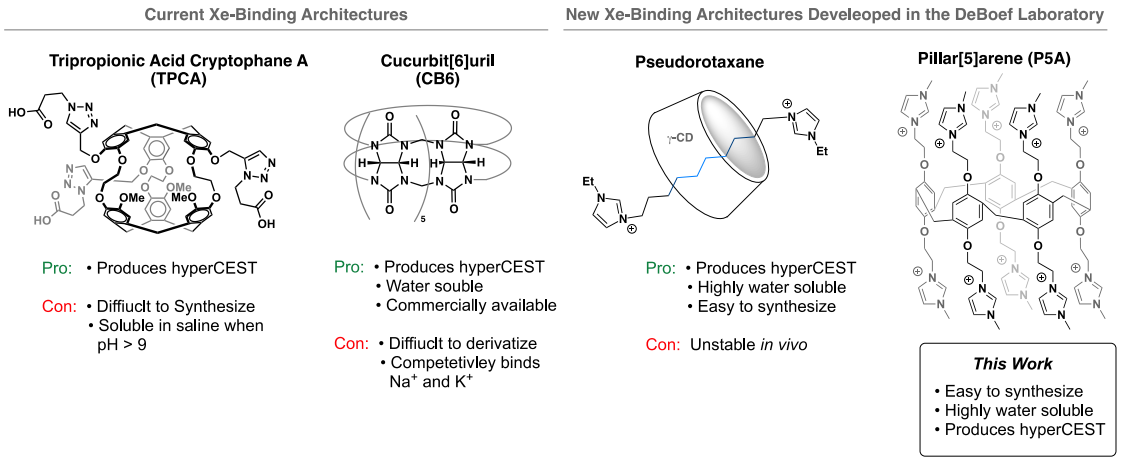

Figure 2.1: Comparison of Xe-binding hosts

We have recently focused our research efforts on the development of new supramolecular structures for binding xenon, including the development of pseudorotaxanes that form unique ternary complexes with ^{129}Xe. [17] The ideal molecular host for use in ^{129}Xe MRI would be easy to synthesize in large quantities, highly water-soluble, and would reversibly bind ^{129}Xe, as evidenced by a hyperCEST experiment. Herein, we describe the design and synthesis of a cationic pillar[5]arene macrocycle that meets all of these criteria.

Pillar[5]arenes (P5As), are pentameric macrocycles, synthesized by the templated Friedel-Crafts cyclization of hydroquinone derivatives. Since they were initially synthesized by Ogoshi a decade ago, [18] P5As have been used for a wide range of host-guest chemistry. [19,20] P5As contain a central cavity of approximately 5.8 Å^3, which is comparable to other macrocycles that have been shown to have an affinity for xenon, such as CB6 and cryptophane-A, and recently both Cohen and Schroeder have shown that P5A derivatives can interact with xenon, as evidenced by conventional ^{129}Xe NMR and by magnetization transfer experiments. [21,22] Herein, we report the design and synthesis of a P5A structure that has been optimzed for its ability to bind xenon, we then quantify its affinity for the nobel gas, and we demonstrate the first example of hyperCEST depletion for a

pillararene macrocycle, thus validating its potential as a contrast agent for ^{129}Xe MRI, and laying the necessary groundwork for subsequent *in vivo* imaging studies.

Results and discussion

We began our studies by computationally modelling a variety of P5A structures. Gas phase energy minimized structures of pillararenes were obtained using semi-empirical computations and a PM3 force field. A xenon atom was then placed outside the hydrophobic core of the P5A structure, and the energy of the system was minimized again to model the dynamics of the two species. Interestingly, the simplest P5A, which was decorated with 10 methyl groups (**4**), failed to bind xenon in this computational experiment. Additionally, P5A structures that were decorated with longer alkyl chains also failed to bind xenon (e.g. **2**). In both of these cases, the molecular dynamics experiments showed that the alkyl arms of the P5A structures preferred to fold onto themselves via hydrophobic collapse. Contrastingly, the P5A structure containing 10 cationic imidazolium groups, opened like the petals of a flower, revealing the hydrophobic core. The aforementioned gas phase molecular dynamics experiment predicted that this decacationic P5A should be an excellent candidate for binding xenon. Moreover, we predicted that this highly charged compound should be readily water soluble, making it an excellent candidate for a hyperCEST contrast agent (Scheme 1).

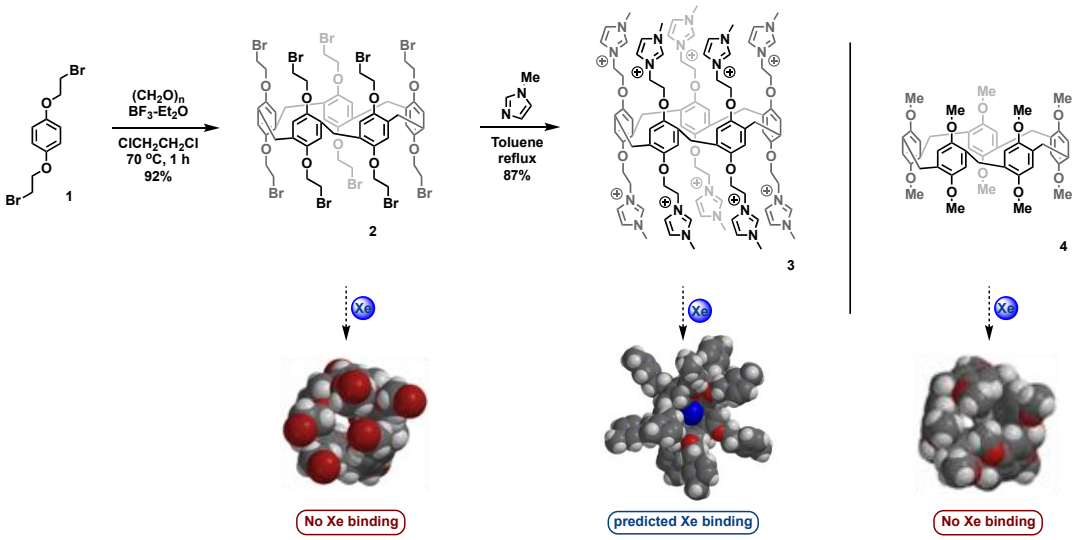

Scheme 2-1: Synthesis and computed structures of neutral and decacationic pillararenes

We further used molecular dynamics simulations in an aqueous environment to predict the binding and hydrophobicity of the host structure. These simulations were performed using 1000 iterations with 0.001 ps time step size for discretizing the equations of motion for unconstrained bond lengths, which allows free motion. The simulations were conducted in the presence of 1,830 water molecules within a P1 type cell with x, y, z distances of 90 Å, 90 Å, 90 Å (Figure 2). As before, the xenon atom was computationally placed outside the hydrophobic cavity of the P5A and was observed to rapidly associate with the hydrophobic core during the moleculear dynamics simulation, thus indicating that the cationic P5A was capable of binding a single xenon atom in aqueous solution. As shown in Figure 3, these computations prediceted that the hydrophobic core of the P5A was not a good host for water molecules, thus it was capable of binding a xenon atom with no desolvation cost.

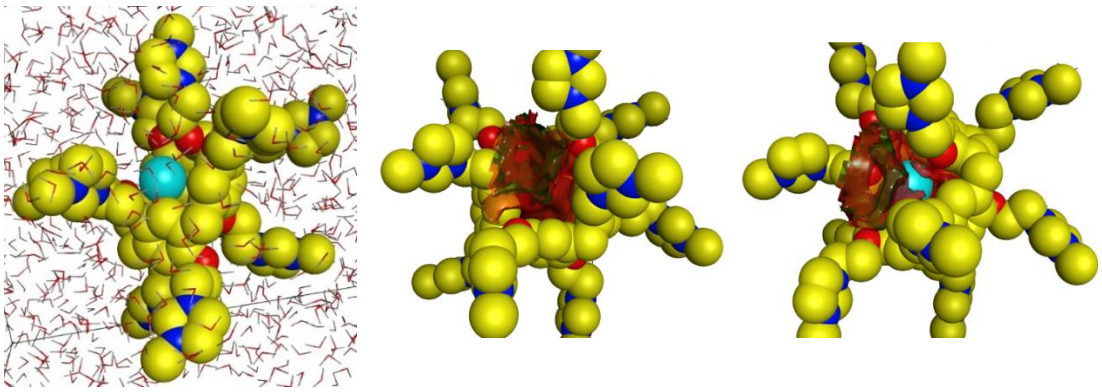

Figure 2.2: L to R: molecular dynamics simulations of Xe and 3 using 1830 water molecules; computed hydrophobic surface of **3** is shown in red; Xe binds ot the hydrophobic surface of **3**

As previously shown in the Scheme 1, the synthesis of the water-soluble P5A commenced with the Friedel-Crafts cyclization of 1,4-bis(2-bromoethoxy)benzene in dichlorethane.[26] As previously reported by Huang, this solvent is crucial for the synthesis of pillara[5]arenes because it serves as a template, allowing for high yields of the cyclic oligomer and preventing polymeric products. Subsequently, the 10 imidazolium ions were added in a single step, and the decacationic pillararene was isolated by recrystallization from methanol and diethyl ether.

^{1}H NMR spectroscopy of the pillararenes confirmed the computationally predicted structures that were previously shown (Figure 3). The decabromo-P5A (**2**) was characterized by sharp peaks in the ^{1}H NMR spectrum, indicating that its structure was rigid and compact, whereas the ^{1}H NMR spectrum of the decacationic-P5A (**3**) contained broad peaks, indicating that the charge repulsion created an open, flexible, open conformation.

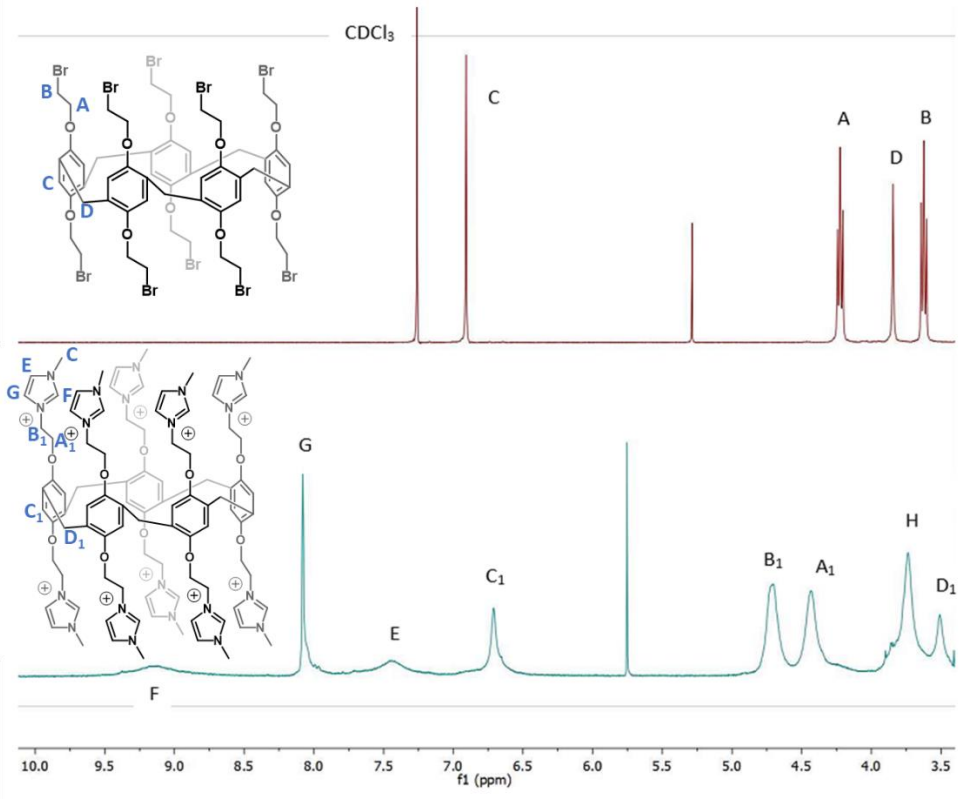

Figure 2.3: Stacked ^{1}H-NMR of **2** in $CDCl_3$ (top) and **3 in** DMSO-d_6 (bottom). Product peaks are highlighted

Fluorescence quenching by xenon provided a sensitive method for measuring Xe binding, even at substoichiometric Xe concentrations. P5As are weakly fluorescent, and titration of aqueous xenon into the a solution of **3** induced quenching. [23] (See supporting information for experimental details.) The data from the fluorescence quenching experiments was plotted using a non-linear curve fitting method for single-site binding (1:1) as described by Thordarson. [24]

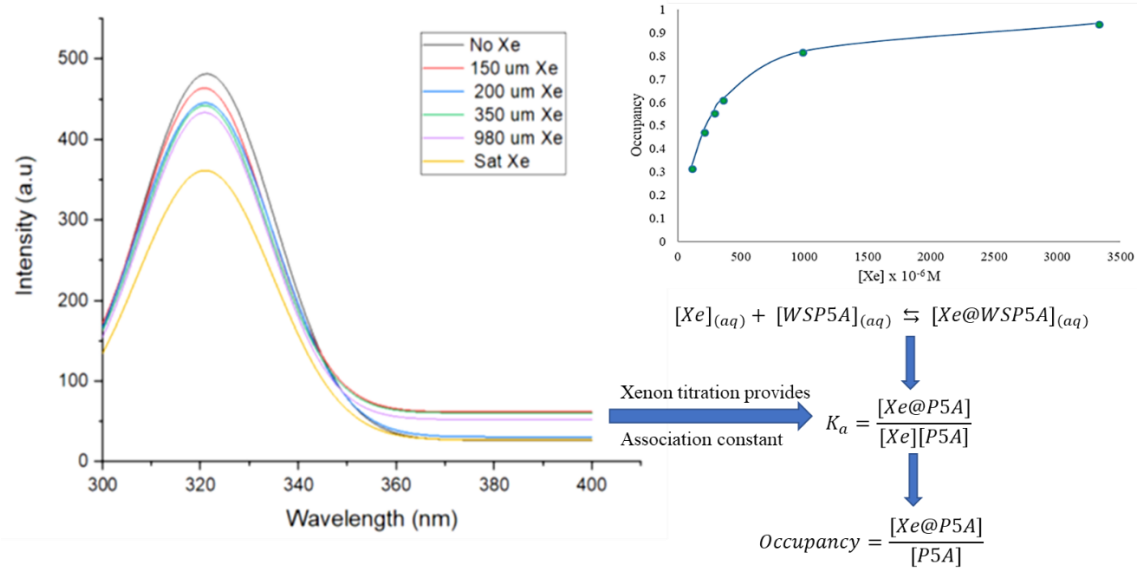

Figure 2.4: Left image; Fluorescence quenching phenomena when Xe (aq) added into a solution of WSP5A (aq) in phosphate buffer.(Gaussian curve smoothing using Origin lab software), right image; occupancy curve with respect to the concentration of Xe $_{(aq)}$ used

Dmochowski has performed similar fluorescence quenching studies for measuring the affinity of xenon for the water-soluble cryptophane shown in Figure 1, [14] reporting an association constant (K_a) of 1.7 x 10^4 M^{-1}. The association constant that we obtained for **3** was one order of magnitude lower 4.6 x 10^3 M^{-1}, but it should be noted that ^{129}Xe contrast agents do not necessarily have to bind xenon with high affinity; the hyperCEST experiment capitalizes on reversible binding of xenon in a supramolecular host. The quenching data show a maximum occupancy of 1, which is a clear illustration of single-site binding.

Finally, the potential application of **3** as a ^{129}Xe contrast agent was assessed. The z-spectrum of an aqueous solution of **3** is shown in Figure 5. The characteristic peak at -80 ppm corresponds to the key ^{129}Xe@**3** complex. The hyperCEST depletion in this experiment is 30%, which should be sufficient for imaging studies. [25] It is also likely that this result could be improved

by modifying the pre-pulse train parameters, which should allow for better depolarization of the encapsulated Xe. Importantly, these data were acquired in a Phillips Achieva 3T MRI scanner, indicating that this technology can likely be translated for preclinical and clinical imaging studies.

Determination of HyperCEST depletion of water-soluble P5A

Naturally abundant ^{129}Xe gas was polarized to 45-50% using a Xemed polarizer (Xemed, Durham, NH). 50 mg water-soluble pillar-5-arene dissolved in 4 ml of DI H_2O. 0.1 ml of DMSO was added into the sample to prevent foaming inside the glass frit cell. Then, 2.0ml of the sample was drawn into a glass frit using a syringe. The glass frit cell placed in the quadrature custom-built RF coil tuned to the Larmor frequency of ^{129}Xe at 3T (35.33 MHz). The 0.5 lL Tedlar bag filled with hyperpolarized ^{129}Xe was connected to the frit shoulder and placed in the pressure chamber, which pressurized at 24 kPa above the atmosphere. As HP ^{129}Xe flowed through the frit membrane, it produced microbubbles, which facilitated dissolution of Xe.

A Philips Achieva 3T clinical MRI scanner was used to measure all NMR spectra. The saturation pre-pulse train of 16 3-lobe sic pulses with a duration of 30 ms and with 0 ms pulse intervals was applied at various chemical shift offsets concerning the dissolved phase peak. The bandwidth of one 3-lobe sinc pulse of 30 ms duration is equal to 3 ppm. Therefore, each following pre-pulse train was applied 3 ppm apart from the frequency of the previous train. Following each saturation train, the FID spectrum was acquired. The spectral region from -150 ppm to 150 ppm was studied. The spectral bandwidth was equal to 32 kHz. The data sampling number was similar to 2048 yielding a spectral resolution of 0.44 ppm. A HyperCEST depletion spectrum was recalculated from the measured spectra at various frequency offsets from the Xe dissolved phase peak. The 129Xe NMR spectra were analyzed using MATLAB (MathWorks, Natick, MA).

The obtained HyperCest depletion spectrum was denoised using a Fast Fourier Transform Low Pass parabolic filter. The Pass Frequency was equal to 0.04 ppm-1, and the Stop Frequency was equal to 0.11 ppm-1. Following denoising, the obtained HyperCEST spectrum fitted by two peaks

of Lorentzian shapes. The processing of the HyperCEST spectrum was done in the OriginPro 2016 software (OriginLab Corp., Northampton, MA).

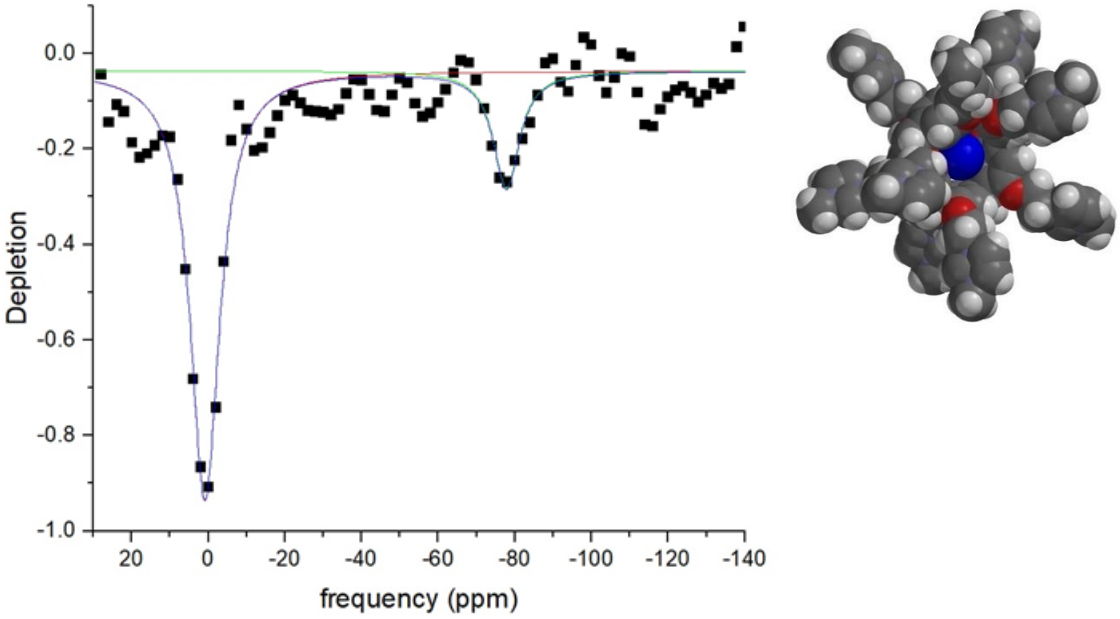

Figure 2.5: Left, HyperCEST depletion spectra for Xe binding in water-soluble pillar[5]arene. Right, energy minimized molecular model of Xe-bound P[5]A with the use of molecular dynamics.

The obtained depletion spectrum had a pillar-5-arene peak at -80 ppm. This is approximately 10 ppm upfield compared to the cucurbit[6]uril (CB6) peak position. After denoising, the peak amplitude decreased by 4%. Although the depletion was just 30 %, that is approximately 2.7 times smaller than CB6, and this supramolecular cage is a promising Xe biosensor. This result could be improved by modifying the pre-pulse train parameters which allow better depolarization of Xe inside the cage. The obtained hyperCEST depletion spectra undoubtedly show that the WSP5A host structure is reversibly encapsulating a hyper-polarized Xe atom.

Conclusions

We have successfully designed and synthesized a water-soluble pillar[5]arene that is capable of binding xenon, and we have characterized the xenon affinity by both fluorescence quenching titrations and hyperCEST. Subsequent efforts in our laboratories will be dedicated to the synthesis of functionalized P5A structures, in order to create targeted contrast agents, and the use of these new agents for *in vivo* imaging.

2.1 REFERENCES

(1) Hane, F. T.; Li, T.; Smylie, P.; Pellizzari, R. M.; Plata, J. A.; DeBoef, B.; Albert, M. S. In Vivo Detection of Cucurbit[6]uril, a Hyperpolarized Xenon Contrast Agent for a Xenon Magnetic Resonance Imaging Biosensor. *Sci. Rep*. **2017**, *7*, 41027.

(2) Schröder, L.; Lowery, T. J.; Hilty, C.; Wemmer, D. E.; Pines, A. Molecular Imaging Using a Targeted Magnetic Resonance Hyperpolarized Biosensor. *Science* **2006**, *314*, 446–449.

(3) Schröder, L. Xenon for NMR Biosensing--Inert but Alert. *Phys Med* **2013**, **29**, 3–16.

(4) Berthault, P.; Huber, G.; Desvaux, H. Biosensing Using Laser-Polarized Xenon NMR/MRI. *Progress in Nuclear Magnetic Resonance Spectroscopy* **2009**, 55, 35–60.

(5) Wang, Y.; Dmochowski, I. J. An Expanded Palette of Xenon-129 NMR Biosensors. *Acc. Chem. Res*. **2016**, 49, 2179–2187.

(6) Hane, F. T.; Smylie, P. S.; Li, T.; Ruberto, J.; Dowhos, K.; Ball, I.; Tomanek, B.; DeBoef, B.; Albert, M. S. HyperCEST Detection of Cucurbit[6]uril in Whole Blood Using an Ultrashort Saturation Pre-Pulse Train. *Contrast Media Mol. Imaging* **2016**, 11 (4), 285–290.

(7) Haouaj, El, M.; Luhmer, M.; Ko, Y. H.; Kim, K.; Bartik, K. NMR Study of the Reversible Complexation of Xenon by Cucurbituril. *J. Chem. Soc*., Perkin Trans. 2 **2001**, 804–807.

(8) Korchak, S.; Riemer, T.; Kilian, W.; Mitschang, L. Quantitative Assessment of Xenon Exchange Kinetics with Cucurbit[6]Uril in Physiological Saline. *ChemPhysChem* **2018**, 155, 157–158.

(9) Wang, Y.; Dmochowski, I. J. Cucurbit[6]uril Is an Ultrasensitive 129Xe NMR Contrast Agent. *Chem. Commun.* **2015**, 51, 8982–8985.

(10) Kim, B. S.; Ko, Y. H.; Kim, Y.; Lee, H. J.; Selvapalam, N.; Lee, H. C.; Kim, K. Water Soluble Cucurbit[6]uril Derivative as a Potential Xe Carrier for 129Xe NMR-Based Biosensors. *Chem. Commun*. (Camb.) 2008, 2756–3.

(11) Wang, Y.; Roose, B. W.; Philbin, J. P.; Doman, J. L.; Dmochowski, I. J. Programming a Molecular Relay for Ultrasensitive Biodetection Through 129Xe NMR. *Angewandte Chemie* 2015, *128*, 1765–1768.

(12) Truxal, A.; Wemmer, D. E.; Cao, L.; Isaacs, L.; Pines, A. Directly Functionalized Cucurbit[7]uril as a Biosensor for the Selective Detection of Protein Interactions by 129Xe hyperCEST NMR. *Chemistry, Eur. J*. 2019, in press.

(13) Hill, P. A.; Wei, Q.; Troxler, T.; Dmochowski, I. J. Substituent Effects on Xenon Binding Affinity and Solution Behavior of Water-Soluble Cryptophanes. *J. Am. Chem. Soc*. 2009, *131*, 3069–3077.

(14) Hill, P. A.; Wei, Q.; Eckenhoff, R. G.; Dmochowski, I. J. Thermodynamics of Xenon Binding to Cryptophane in Water and Human Plasma. *J. Am. Chem. Soc*. 2007, *129*, 9262–9263.

(15) Bai, Y.; Hill, P. A.; Dmochowski, I. J. Utilizing a Water-Soluble Cryptophane with Fast Xenon Exchange Rates for Picomolar Sensitivity NMR Measurements. *Anal. Chem*. 2012, *84*, 9935–9941.

(16) Zemerov, S. D.; Roose, B. W.; Greenberg, M. L.; Wang, Y.; Dmochowski, I. J. Cryptophane Nanoscale Assemblies Expand 129Xe NMR Biosensing. *Anal. Chem*. 2018, *90*, 7730-7738.

(17) Hane, F. T.; Fernando, A.; Prete, B. R. J.; Peloquin, B.; Karas, S.; Chaudhuri, S.; Chahal, S.; Shepelytskyi, Y.; Wade, A.; Li, T.; et al. Cyclodextrin-Based Pseudorotaxanes: Easily

Conjugatable Scaffolds for Synthesizing Hyperpolarized Xenon-129 Magnetic Resonance Imaging Agents. *ACS Omega* 2018, *3*, 677–681.

(18) Ogoshi, T.; Kanai, S.; Fujinami, S.; Yamagishi, T.-A.; Nakamoto, Y. Para-Bridged Symmetrical Pillar[5]arenes: Their Lewis Acid Catalyzed Synthesis and Host–Guest Property. J. Am. Chem. Soc. 2008, 130, 5022–5023.

(19) Xue, M.; Yang, Y.; Chi, X.; Zhang, Z.; Huang, F. Pillararenes, a New Class of Macrocycles for Supramolecular Chemistry. *Acc. Chem. Res*. 2012, *45*, 1294–1308.

(20) Ogoshi, T.; Yamagishi, T.-A.; Nakamoto, Y. Pillar-Shaped Macrocyclic Hosts Pillar[N]arenes: New Key Players for Supramolecular Chemistry. *Chem. Rev*. 2016, *116*, 7937–8002.

(21) Adiri, T.; Marciano, D.; Cohen, Y. Potential 129Xe-NMR Biosensors Based on Secondary and Tertiary Complexes of a Water-Soluble Pillar[5]arene Derivative. *Chem. Commun*. 2013, *49*, 7082–7084.

(22) Schnurr, M.; Joseph, R.; Keisar, A. N.; Kane, D. K.; Bogdanoff, N.; Schuenke, P.; Cohen, Y.; Schröder, L. High Exchange Rate Complexes of 129Xe with Water-Soluble Pillar[5]Arenes for Adjustable Magnetization Transfer MRI. *ChemPhysChem* 2019, *20* (2), 246–251.

(23) Martinho, J. M. G. Heavy-Atom Quenching of Monomer and Excimer Pyrene Fluorescence. *J. Phys. Chem*. 1989, *93*, 6687–6692.

(24) Thordarson, P. Determining Association Constants from Titration Experiments in Supramolecular Chemistry. *Chem. Soc. Rev*. 2011, *40*, 1305–1323.

(25) Mynar, J. L.; Lowery, T. J.; Wemmer, D. E.; Pines, A.; Fréchet, J. M. J. Xenon Biosensor Amplification via Dendrimer−Cage Supramolecular Constructs. *J. Am. Chem.* Soc. 2006, *128*, 6334–6335.

(26) Yao, Y.; Xue, M.; Chi, X.; Ma, Y.; He, J.; Abliz, Z.; Huang, F. *Chemical Communications* **2012**, *48* (52), 6505.

2.2 SUPPORTING INFORMATION

Deca methyl imidazolium pillar[5]arene as a viable contrast agent for hyperCEST 129Xe MRI

Experimental Section

Reagents

Substrates, including CBr_4, dry acetonitrile, dry 1,2-dichloroethane, boron trifluoride ethane, tri phenyl phosphine, methyl imidazole were purchased from Sigma-Aldrich, Fisher Scientific, and TCI chemicals. All reagents were stored under an inert atmosphere before use. Unless otherwise noted, all reactions were performed under N_2.

Instrumentation

NMR spectra were obtained using a Bruker Avance 300 MHz and 400 MHz spectrometer. Low resolution mass spectrometry was performed using a Shimadzu LRMS-2020. High resolution mass spectrometry was performed using a Thermo Scientific LTQ Orbitrap XL™ instrument. Fluorescence spectra was obtained using Shimatzu Fluorimeter and UV-Vis data was obtained via Shimatzu UV-Vis spectrometer.

Synthetic route for the synthesis of Water soluble pillar[5]arene

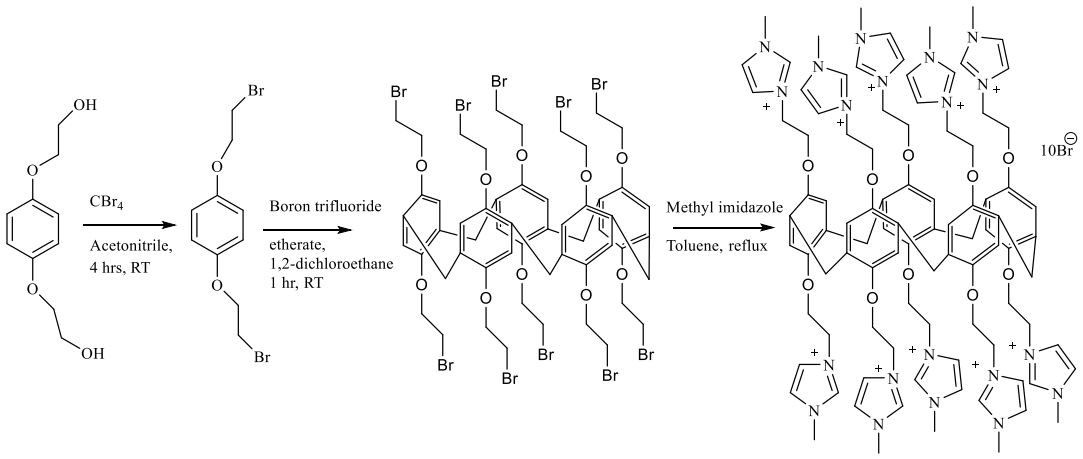

The above molecule was synthesized according to the literature procedures[1], with further optimizations and better yields.

Synthesis of brominated monomer, 1

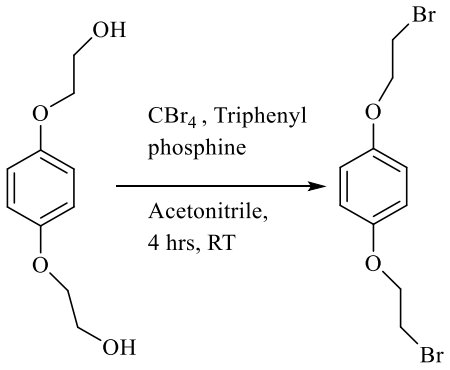

A solution of 1,4-bis(2-hydroxyethoxy)benzene (10.0 g, 50.4 mmol) and triphenylphosphine (31.5 g, 120mmol) in dry acetonitrile (250 mL) was cooled in an ice bath. Under vigorous stirring, carbon tetrabromide (39.8 g, 120 mmol) was slowly added in four portions. In every addition the solution immediately turns bright yellow and with stirring returns back to its colorless form. On the final addition the solution stays cloudy. The mixture was stirred at room temperature for 4 hours and 20 minutes. Then cold water (200 mL) was added to the reaction mixture to give white precipitation. The precipitate was collected, washed with another 200 ml of cold water followed with methanol/water (3:2, 3 × 100 mL). The collected white solids were dried under vacuum for 24 hours and used without further purification. (14.5 g, 97%). ^{1}H NMR and ^{13}C NMR was performed using $CDCl_3$. ^{1}H NMR (400 MHz, Chloroform-d) δ 6.89 (s, 4H), 4.27 (t, J = 6.3 Hz, 4H), 3.64 (t, J = 6.3 Hz, 4H). ^{13}C NMR (101 MHz, Chloroform-*d*) δ 153.5, 117.2, 68.6, 29.6.

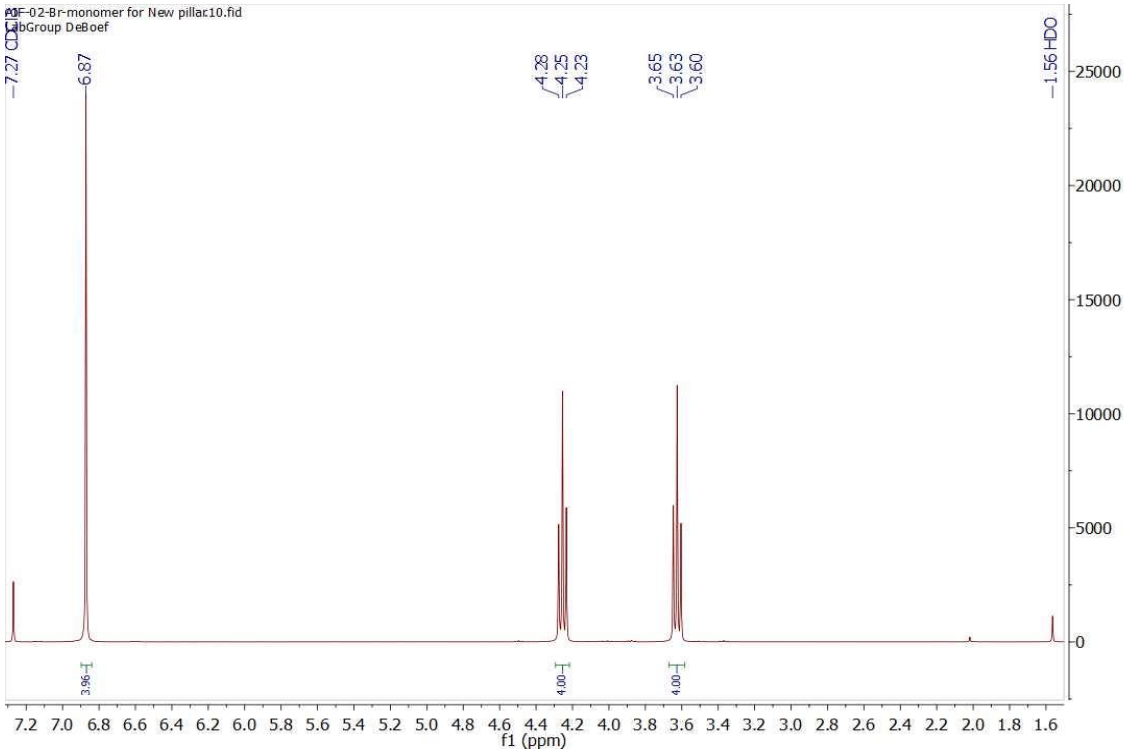

Figure 3.1: ^{1}H NMR of 1

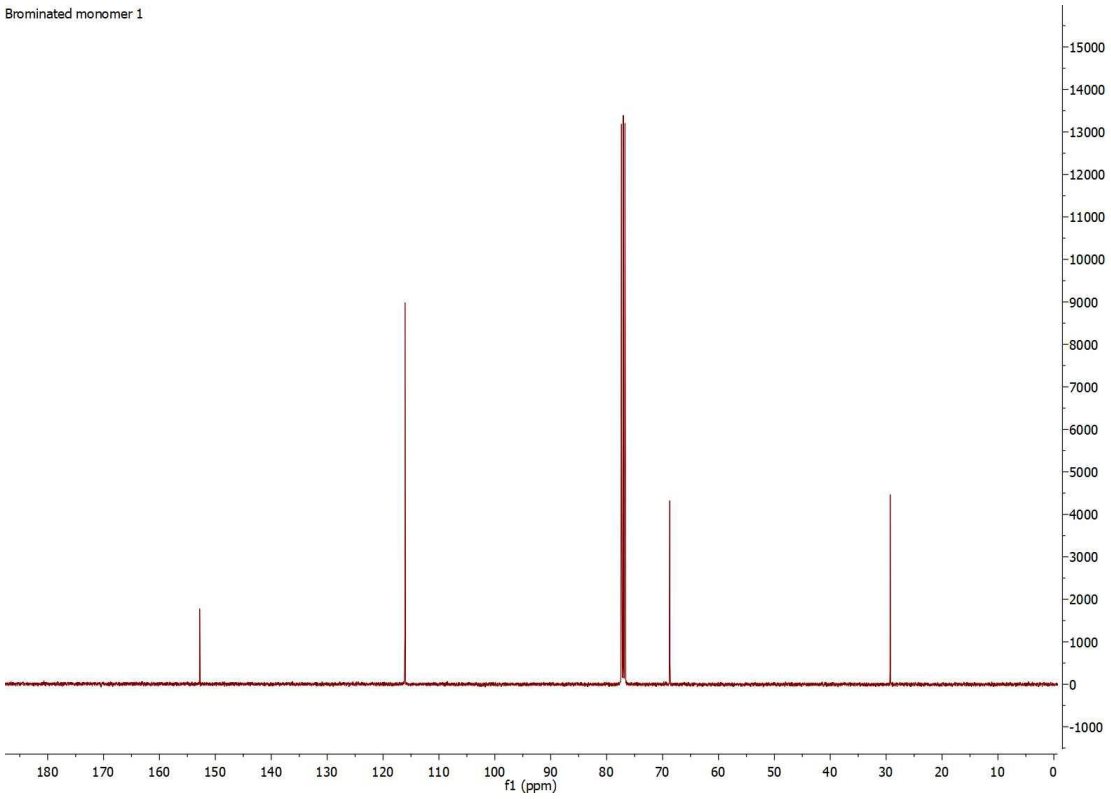

Figure 3.2: ^{13}C NMR of **1**

Synthesis of deca-brominated pillar[5]arene, 2

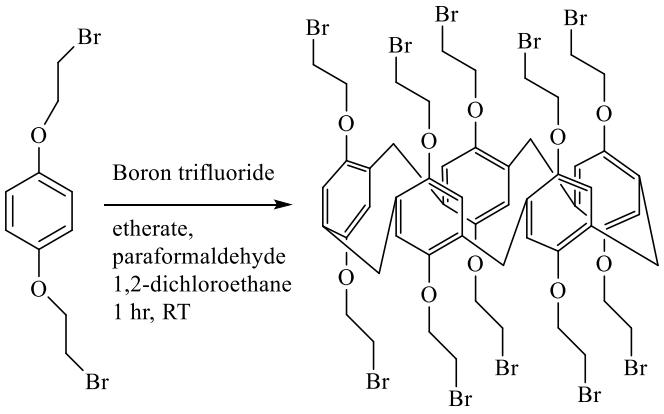

A solution of 2 (3.37 g, 11.5 mmol) and paraformaldehyde (0.349 g, 11.5 mmol) in 1,2-dichloroethane (50 mL) was cooled with ice bath. Boron trifluoride etherate (3.26 g, 23.0 mmol) was added to the solution and the mixture was stirred at room temperature for 1 hour. Between the 1 hour the reaction undergoes various color changes. All color changes are shown. The reaction mixture was then washed with water (2 × 50 mL), the further washes were done using saturated sodium bicarbonate (2 x 50 ml) and brine solution (2 x 50ml). The organic layer was dried with Na_2SO_4. The solvent was evaporated to provide a crude product. The crude product was pure; hence no further purification was needed. (yield 85%). ^{1}H NMR and ^{13}C NMR was performed using $CDCl_3$. ^{1}H NMR (400 MHz, Chloroform-d) δ 6.91 (s, 10H), 4.23 (t, J = 6.3, 5.1 Hz, 20H), 3.84 (s, 10H), 3.63 (t, J = 5.6 Hz, 20H). ^{13}C NMR (101 MHz, Chloroform-*d*) δ 149.7, 129.1, 116.1, 68.9, 30.7, 29.4.

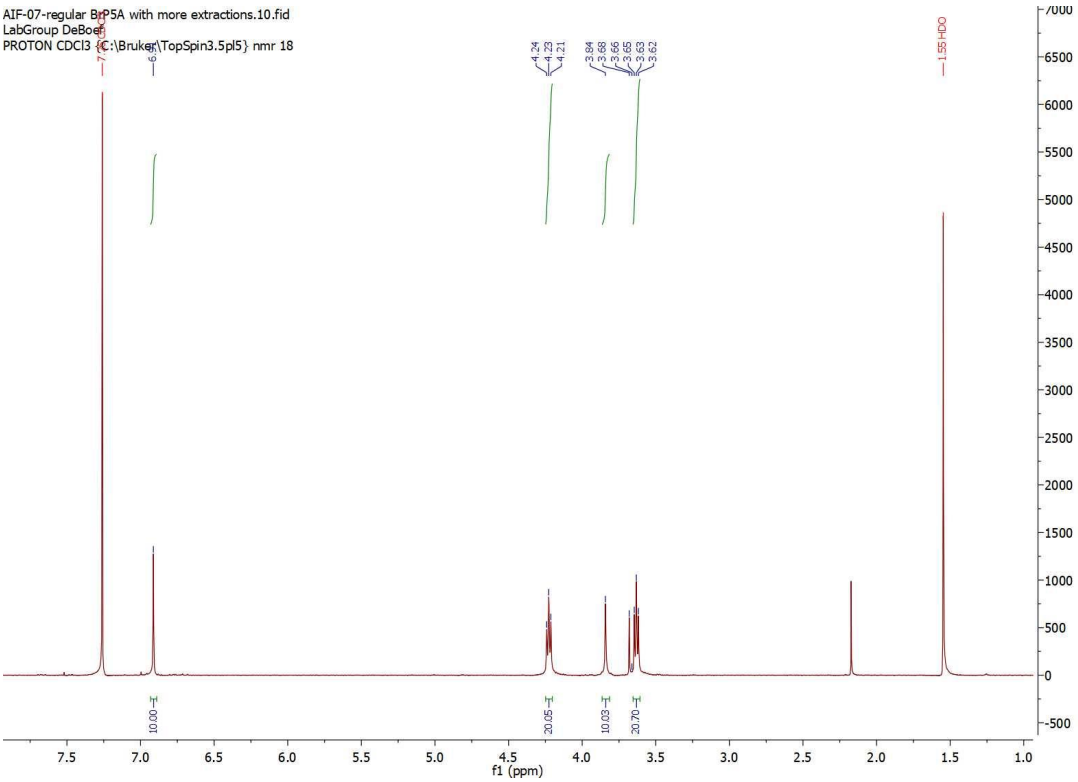

Figure 3.3: ^{1}H NMR of **2**

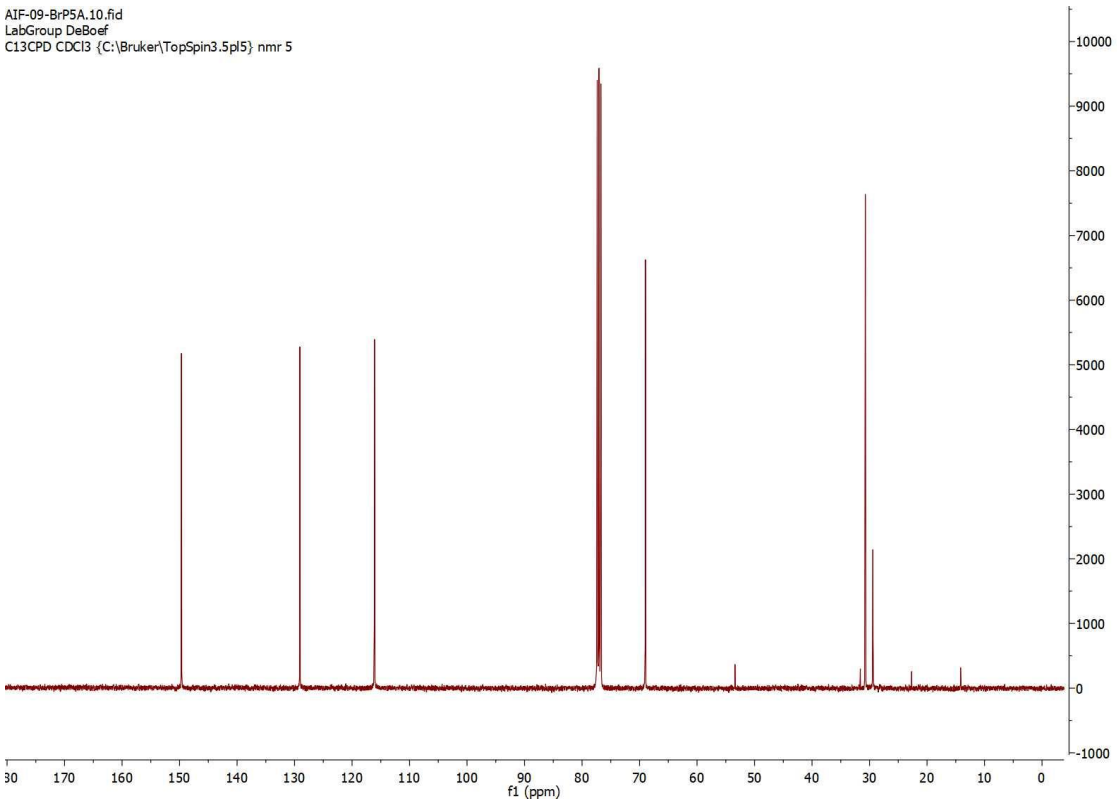

Figure 3.4: ^{13}C NMR of **2**

Synthesis of deca methyl imidazolium pillar[5]arene, 3

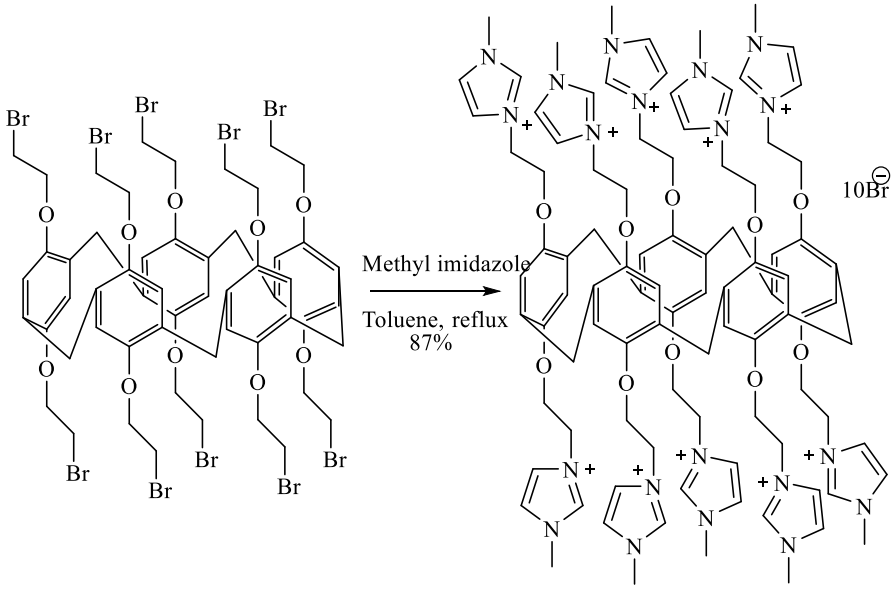

A mixture of 3 (1.68 g, 1.00 mmol) and N-methylimidazole (1.64 g, 20.0 mmol) in toluene (25 mL) was stirred in a 40 mL pressure tube at 120 ºC for 24 hours. The reaction was performed multiple times using a round bottom flask, but the reaction never worked. After cooling, the solvent was removed by evaporation and the residue was recrystallized from ethanol/diethyl ether (1:2) to give a white solid (2.1 g, 87%). ^{1}H NMR and ^{13}C NMR was performed using DMSO-d_6. ^{1}H NMR (300 MHz, DMSO-d6) δ 9.17 (br, 10H), 8.11 (s, 10H), 7.44 (br, 11H), 6.72 (br, 10H), 4.72 (br, 21H), 4.45 (br, 20H), 3.74 (br, 31H), 3.51 (br, 10H).

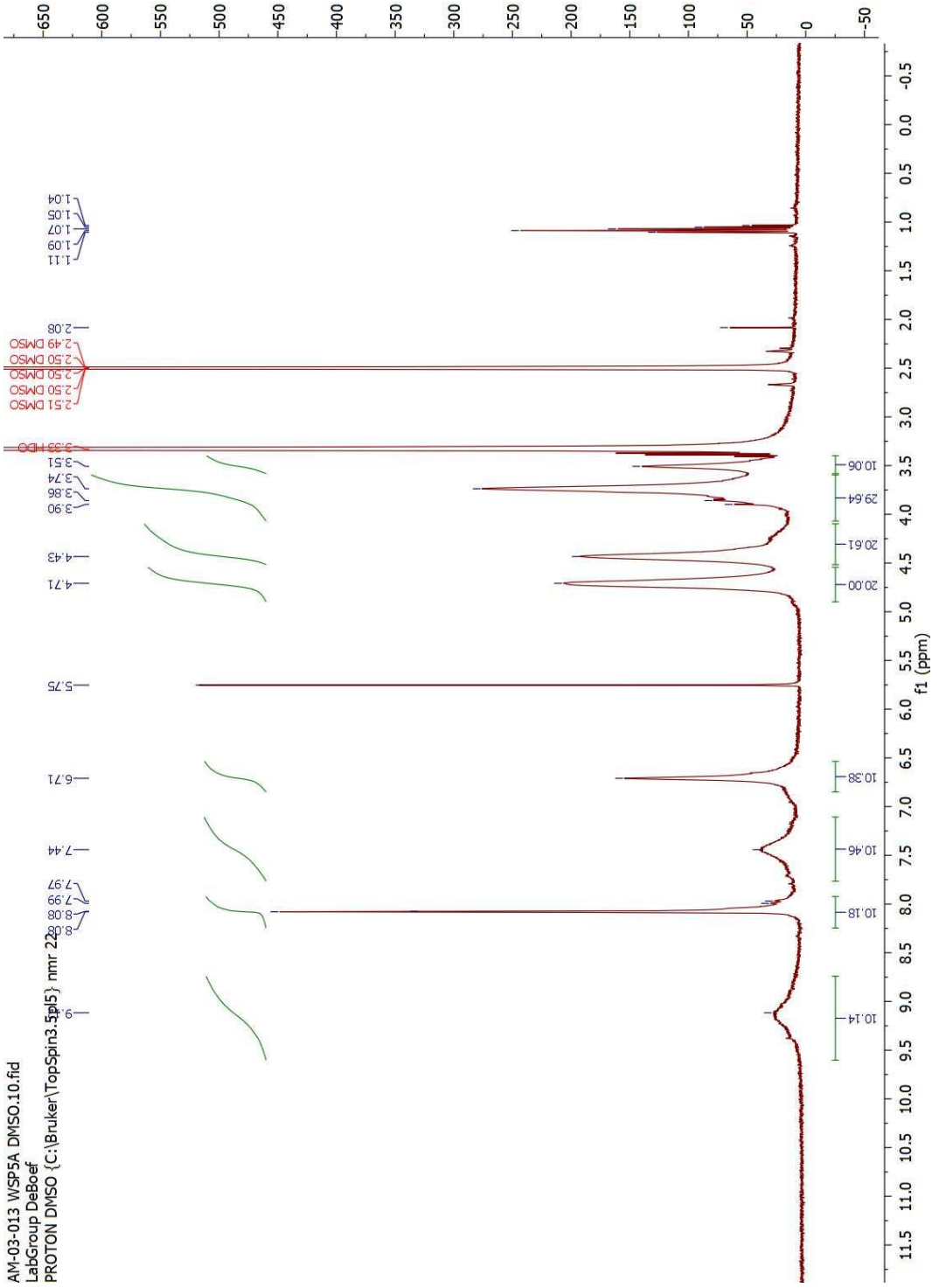

Figure 3.5: ^{1}H-NMR of **3**

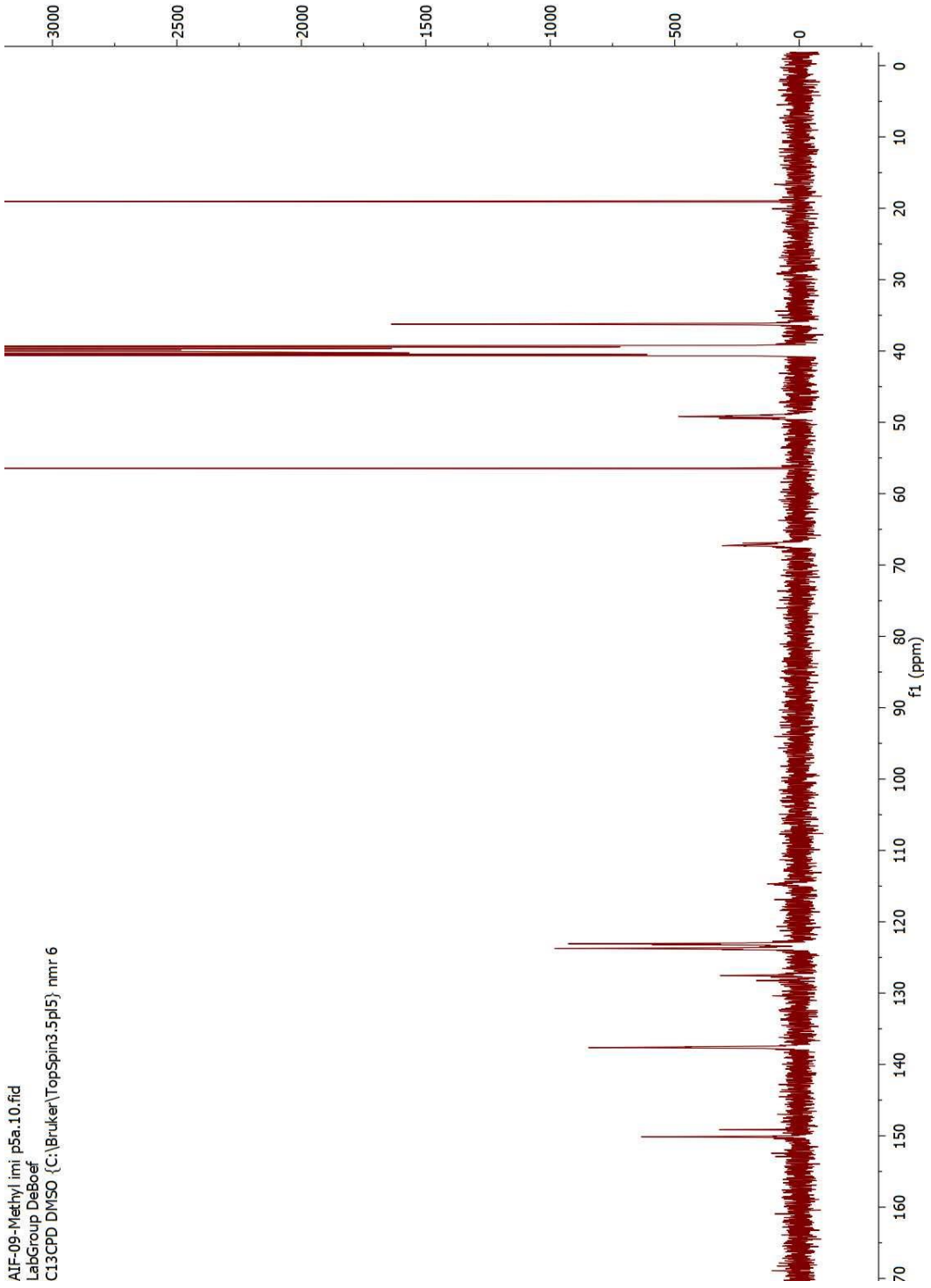

Figure 3.6: ^{13}C-NMR of **3**

Mass spectrometry of the water soluble P5A

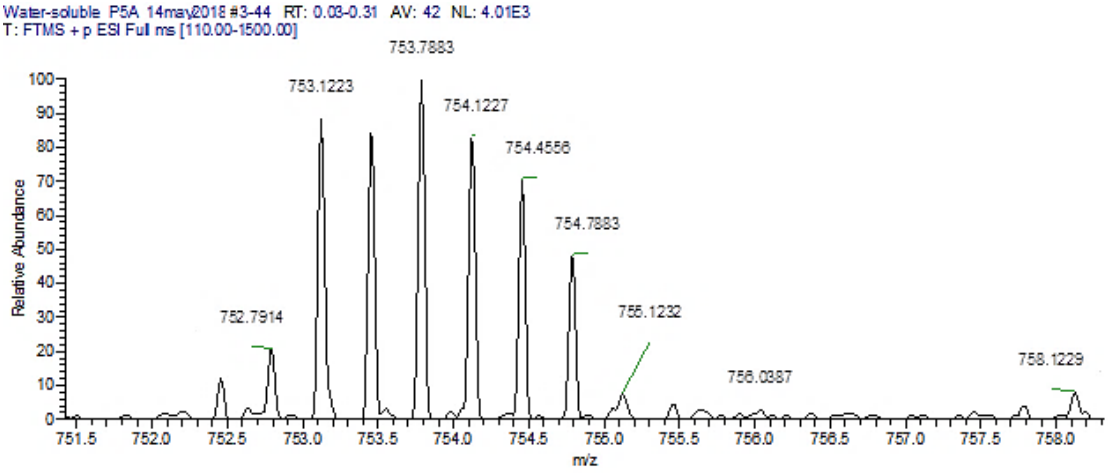

Figure 3.7: Mass spectrum of 3 for $[M - 3Br]^{3+}$ Calculated $C_{95}H_{121}O_{10}N_{20}Br_7$ 754.1270

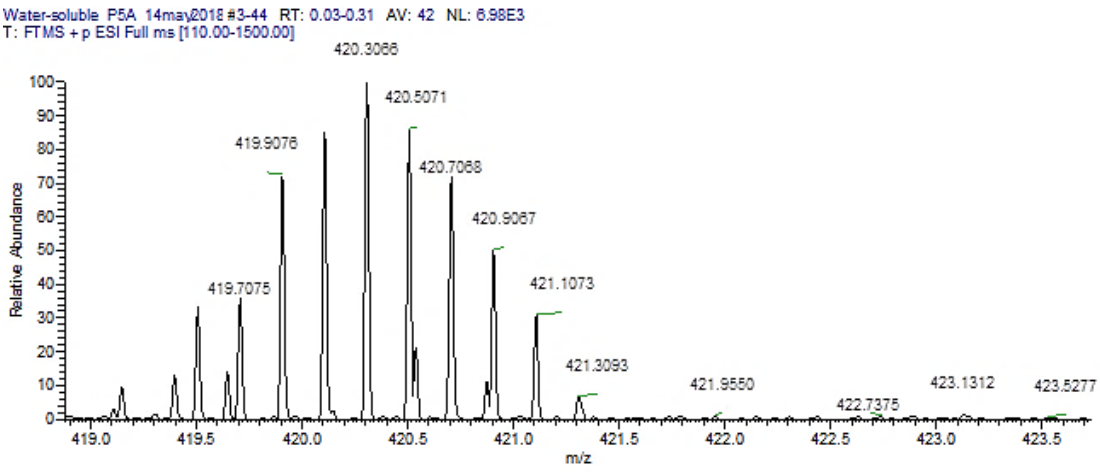

Figure 3.8: Mass spectrum of 3 for $[M - 5Br]^{5+}$ Calculated $C_{95}H_{121}O_{10}N_{20}Br_5$ 420.1090

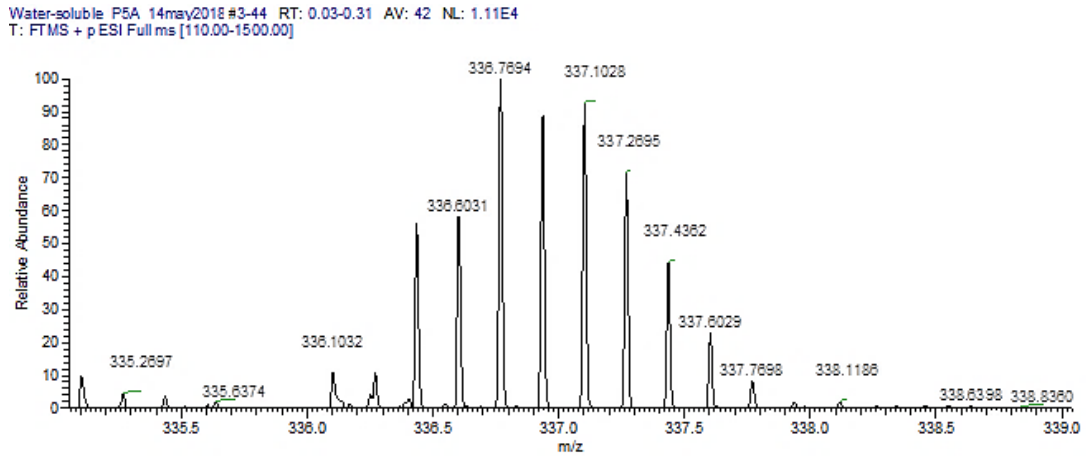

Figure 3.9: Mass spectrum of 3 for $[M - 6Br]^{6+}$ Calculated $C_{95}H_{121}O_{10}N_{20}Br_4$ 336.9378

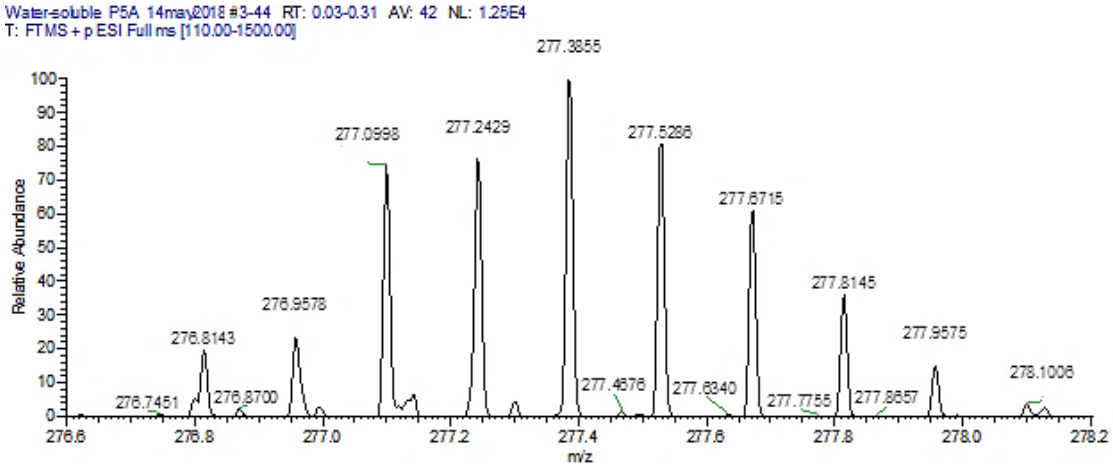

Figure 3.10: Mass spectrum of 3 for $[M - 7Br]^{7+}$ Calculated $C_{95}H_{121}O_{10}N_{20}Br_3$ 277.2442

Saturated Aqueous Xenon Solutions for Fluorescence Quenching Experiments.

Deionized water (25 ml) was added to an acid washed 50 mL round bottom flask. The flask was capped with a septum, bubbled with nitrogen for 20 minutes, and then high vacuumed through a 22-gauge needle for 5 minutes. After degassing, the needle was pushed to the bottom of the flask, and xenon was bubbled through the solution for 5 minutes. A 26-gauge needle was used to relieve excess pressure. Both needles were removed, and the solution was set aside. Next, a Chemware Tedlar™ gas sampling bag with a septum valve (6" x 6", Fisher Scientific) was connected by ¼" tubing and a three-way stopcock to both a xenon tank and a needle. The entire system was vacuumed through the needle using a separate round bottom flask, its septa, and the house vacuum line. The Tedlar bag was filled with xenon, its nozzle closed, and the three-way stopcock was removed. The needle was placed directly onto the tubing connecting the Tedlar bag, and then pierced through the septum into the headspace of the xenon solution round bottom flask. The system was placed into a 37℃ incubator for a few hours to equilibrate[2].

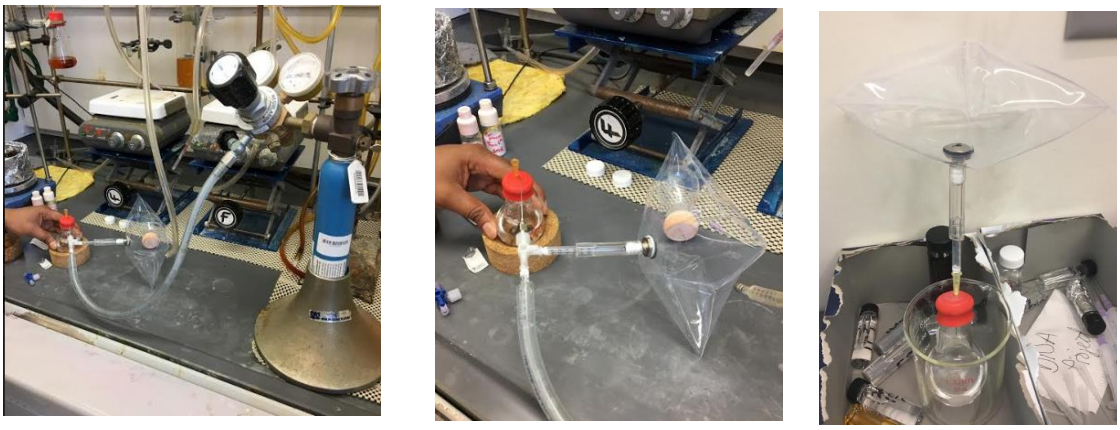

Figure 3.11: The above figures represent the experimental setup for obtaining the saturated Xe solution in DI water

WSP5A Fluorescence quenching of WSP5A with Xenon

A 5.1 x 10^{-4}M stock solution of P5A in deionized water was made using a 100 mL volumetric flask and added into a 100 mL round bottom flask with septum. The round bottom flask was bubbled with nitrogen for 5 minutes, and then high vacuumed for 5 minutes in order to degas the solution. The same dilution and degassing process was used to prepare a 1 x 10^{-3}M phosphate buffer solution. In a reduced volume cuvette with a septum seal (1.5mL, 1cm path length, Starna Cells), stock solution of P5A and phosphate buffer was added in order to dilute the P5A concentration to 15 μM at 1.5 mL. The cuvette solution was bubbled with nitrogen for 5 minutes and vacuumed for 5 minutes in order to ensure degassing. Saturated aqueous xenon was added so that the Xe concentration varied from 0 to 9.8 x 10^{-4}M through the titration at 1.5 mL total volume. The cuvette solution was allowed to equilibrate for 15 minutes in the fluorimeter before emission spectra were obtained.

Saturated xenon measurement was made by directly bubbling xenon into a degassed P5A solution in the cuvette for 5 minutes. The solution was allowed to equilibrate for 15 minutes in the fluorimeter before spectra were obtained[2]

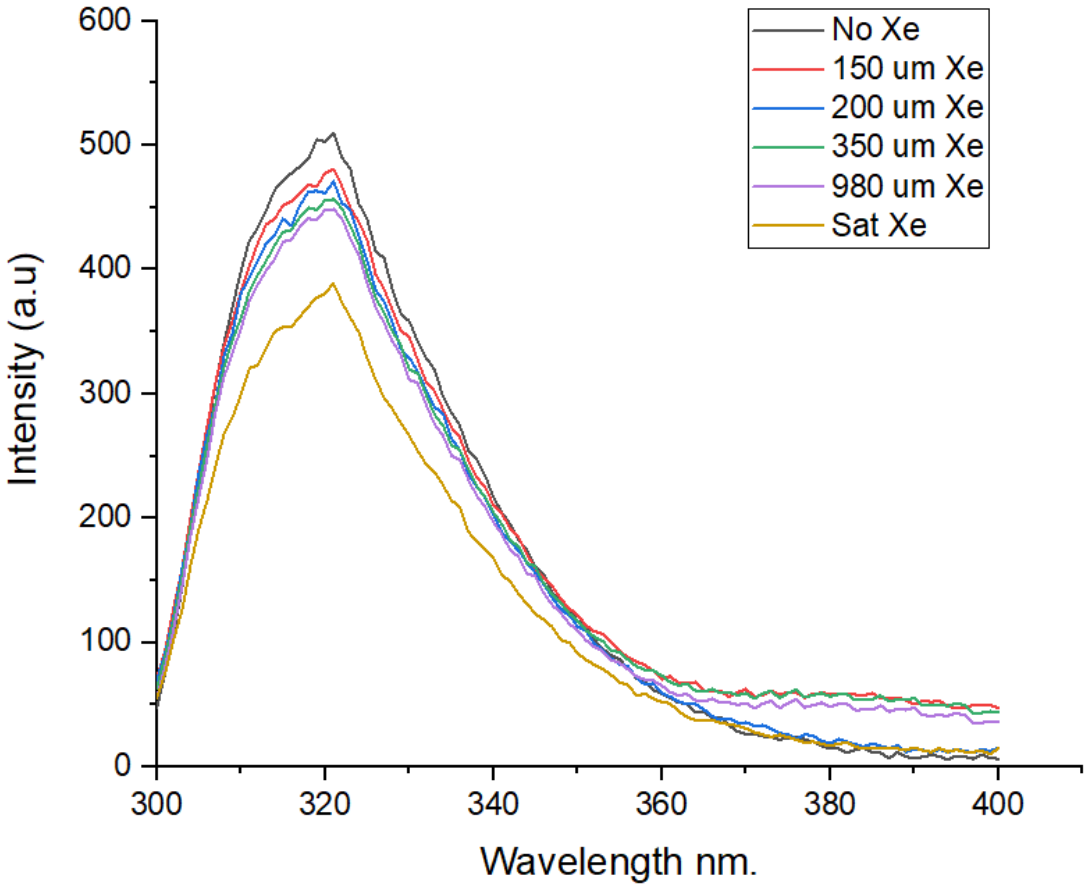

Figure 3.12: Fluorescence quenching phenomena when Xe was added in to a solution of P5A in phosphate buffer (before curve smoothening was applied)

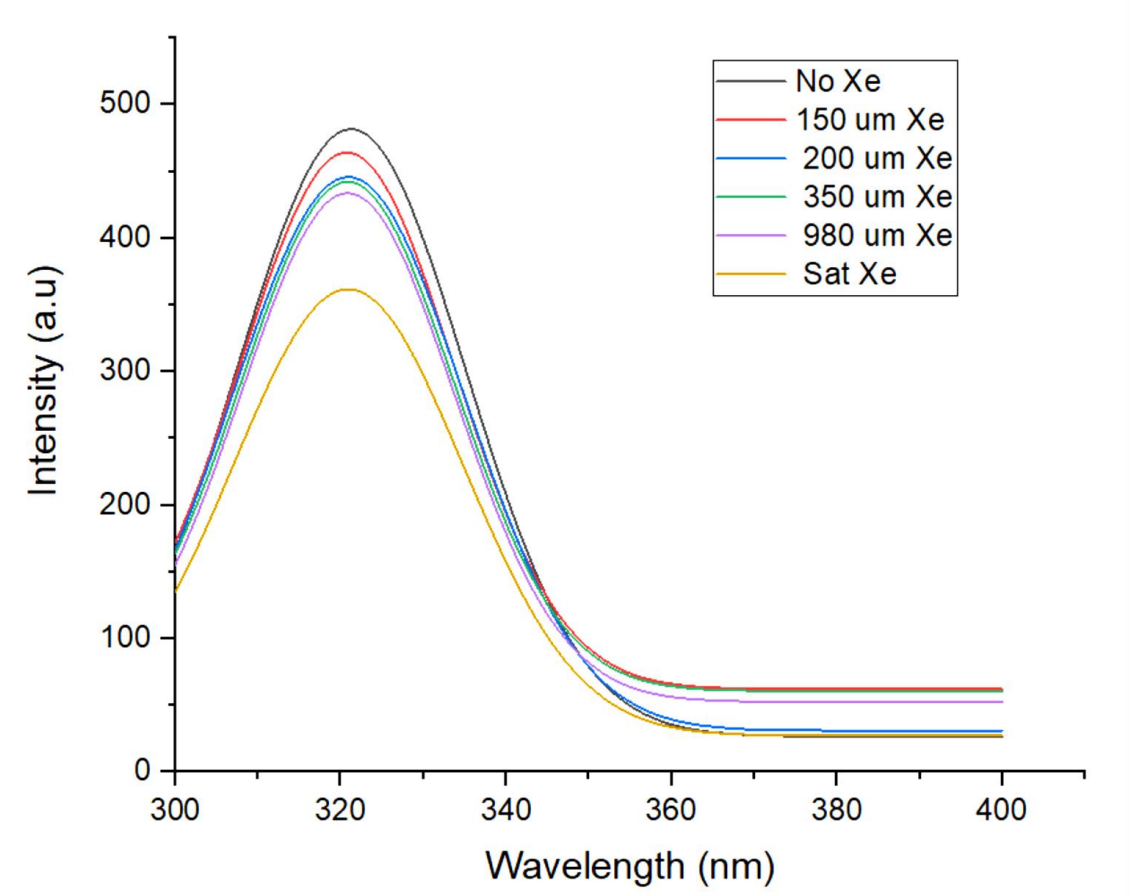

Figure 3.13: Fluorescence quenching phenomena when Xe was added in to a solution of P5A in phosphate buffer (Gaussian curve smoothing using Origin lab software)

Single site binding model (non-linear curve fit)

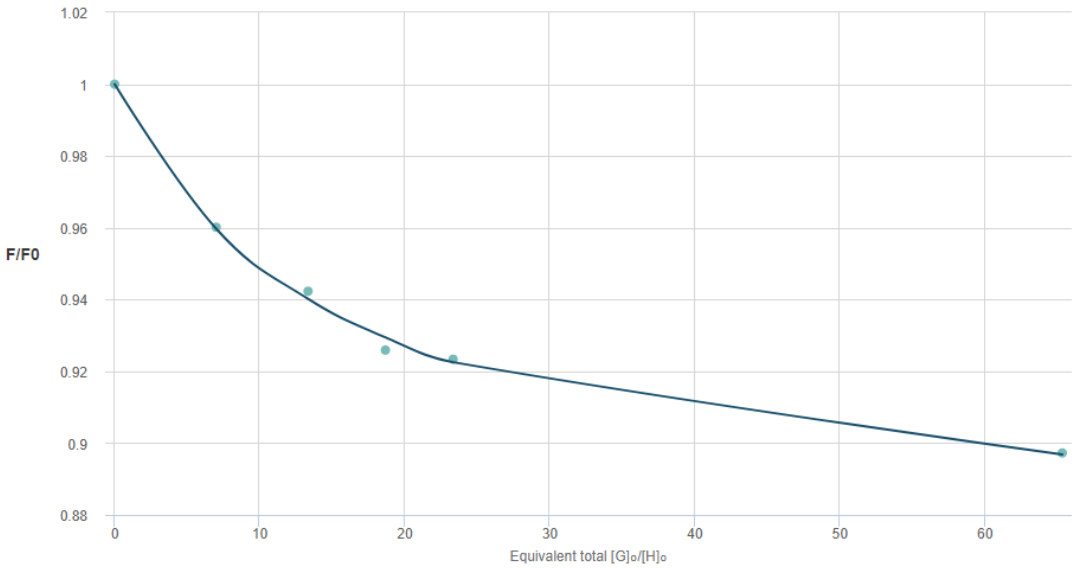

http://app.supramolecular.org/bindfit/view/ef59fc0f-0786-4811-8258-0ad6bd25392c

Details

Time to fit	0.2020 s
SSR	1.8050e-5
Fitted datapoints	6
Fitted params	2

Parameters

Parameter (bounds)	Optimised	Error
K (0 → ∞)	4694.99 M^{-1}	± 11.0469 %

Quality of fit

Fit	RMS	Covariance
F/F0	1.7344e-3	2.8639e-3
Total	**1.7344e-3**	**2.8639e-3**

Xenon Occupancy Curve for WSP5A

The fluorescence quenching of P5A is caused by the creation of a host guest complex between P5A and xenon in solution according to reaction (1):

$$(1) \quad P5A(sol'n) + Xe(sol'n) \leftrightharpoons Xe@P5A$$

The association constant, K_a, for this reaction is defined as,

$$K_a = \frac{[Xe@P5A]}{[Xe][P5A]}$$

and the occupancy of the P5A cage is defined as,

$$Occupancy = \frac{[Xe@P5A]}{[P5A]}$$

because the concentration of occupied P5A is equivalent to the concentration of xenon within the P5A. In order to determine the concentration of occupied P5A, an ICE table for reaction (1) must be developed (shown below), where Y represents the initial concentration of free xenon in solution.

	P5A	Xe	Xe@P5A
Initial	$15x10^{-6}$M	Y	0
Change	-X	-X	X
Equilibrium	$15x10^{-6}$M - X	Y-X	X

Substituting the equilibrium concentrations shown above in the ICE table equivalent to the known K_a, $4.7x10^{3}M^{-1}$, the concentration of bound xenon, represented as X in the ICE table, can be determined.

$$K_a = \frac{[X]}{[Y-X][15x10^{-6}M]} = 4.7x10^{3}M^{-1}$$

The X values were determined for each xenon solution concentration titrated and shown in the table below. Then, they were graphed as a function of xenon solution concentration, and the occupancy curve was developed.

[Xe] soln (M)	Occupancy
$1.05x10^{-4}$	0.318
$2.80x10^{-4}$	0.558
$3.50x10^{-4}$	0.613
$2.00x10^{-4}$	0.473
$9.80x10^{-4}$	0.818
$3.32x10^{-3}$	0.939

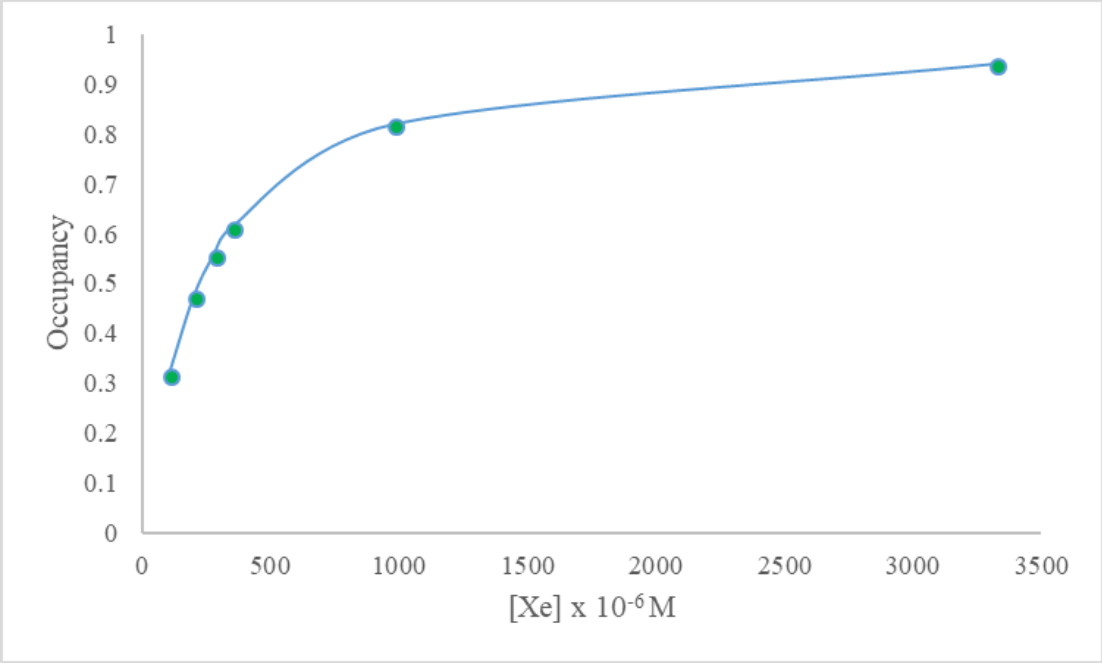

Figure 3.14: Occupancy curve for WSPA

Xenon NMR studies

Naturally abundant ^{129}Xe gas was placed into a 1.0 L Tedlar bag and polarized to 60-80% via the spin exchange optical pumping (SEOP) technique using a Xemed polarizer (Xemed, Durham, NH, USA). It was then placed into a Tedlar bag which was immediately moved into a pressurized chamber within the bore of a Philips Achieva 3.0 T clinical MRI scanner to preserve its polarization. The pressure inside of the chamber was maintained between 20-45 kPa above atmospheric pressure using a pressure-sensitive ventilation device connected to a nitrogen (N2) source, to facilitate the flow of HP ^{129}Xe gas from the Tedlar bag into the glass-fritted cell containing rotaxane solution.

Following polarization of ^{129}Xe gas, 2.5 mL of solution (50 mM) was transferred into a custom-made glass-fritted cell using a syringe. The cell containing the solution was then placed inside of a custom-made quadrature radio-frequency (RF) coil tuned to the Larmor frequency of ^{129}Xe (35.33 MHz) at 3.0 T. The Tedlar bag, already in the bore of the MRI, was then connected to the cell's inflow tube. Once connected, the pressure-stopper on the Tedlar bag was released to allow for the continuous flow of HP ^{129}Xe gas into the glass-fritted cell, which produced several microbubbles as it passed through the fine fritted disc, thereby dissolving into the solution. As HP 129Xe gas continually flowed through the glass-fritted cell, ^{129}Xe nuclear magnetic resonance (NMR) spectral data was simultaneously obtained. The concentration of ^{129}Xe at any point during the spectral acquisition was between 1-5 mM24.

All ^{129}Xe NMR spectra were acquired using a Philips Achieva 3.0 T clinical MRI scanner. Scanner software was modified for the automatic measurement of hyperpolarized chemical exchange saturation transfer (HyperCEST) depletion spectra. To saturate HP ^{129}Xe encapsulated within the rotaxane molecules, two different pre-pulse trains were used: the first consisted of 16- 30 ms 3-lobe sinc pulses, while the second consisted of 16- 30 ms sinusoidal pulses, both with 0 ms pulse intervals. To acquire each depletion spectrum, 37 free induction decay (FID)

spectra were collected at various chemical shift frequency offsets with TR = 4s. Each FID spectrum was acquired using a selective 90-degree "spredrex" excitation pulse with a 9.95 ms duration and bandwidth of 1424 Hz (40.3 ppm at 3.0 T).

The data sampling number was 2048, which corresponds to the spectral resolution of 0.44 ppm. Saturation pre-pulse frequency was automatically adjusted to range from -150 ppm to 30 ppm, where 0 ppm represents dissolved-phase ^{129}Xe, with a predetermined step before each of the subsequent excitation pulses. Offset frequency steps were 176.7 Hz, which correspond to 5 ppm at 3.0 T.

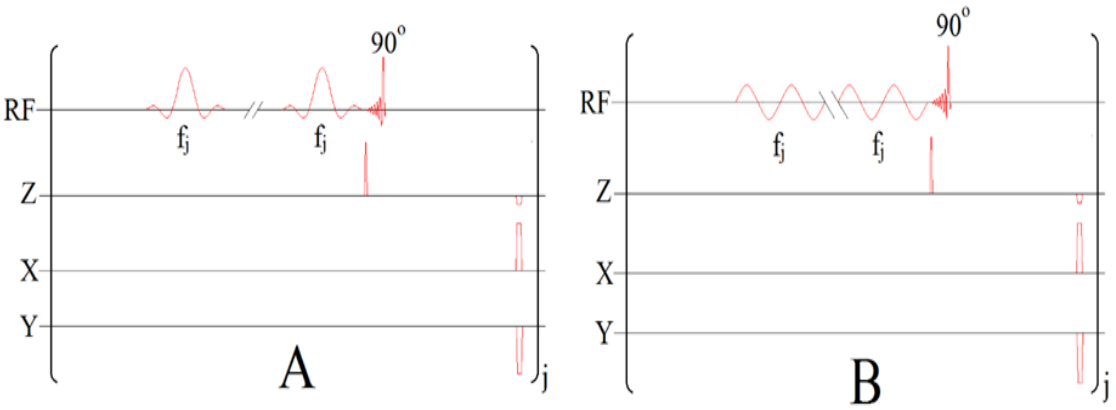

The pulse diagrams shown above were used to prepare HyperCEST depletion spectra using different saturation pre-pulse trains including 3-lobe sinc pulses (A) and sinusoidal pulses (B). Here, fj represents the frequency of saturation pulses during FID acquisition number j. All spoiler gradients along x, y, z axis are also illustrated.

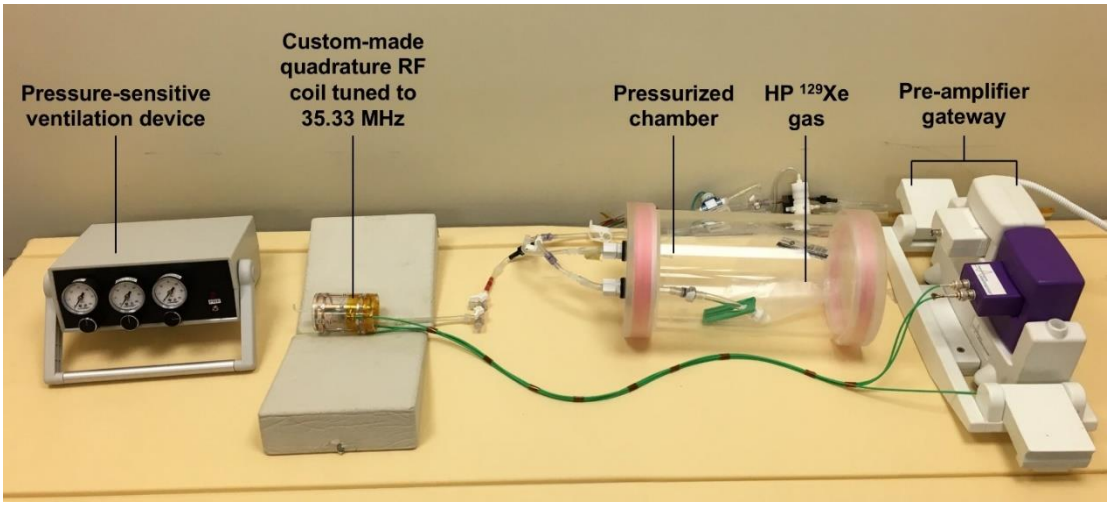

Above setup was used to obtain the Xe-spectra and to obtain the final depletion spectra.

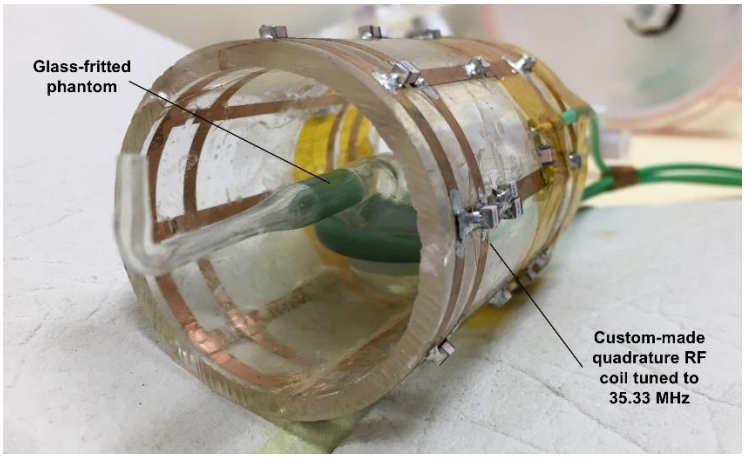

The image above illustrates the continuous flow of HP ^{129}Xe gas throughout the glass-fritted vessel. As depicted, once the flow of HP ^{129}Xe reaches the fine glass-fritted disc, numerous microbubbles are produced, thereby causing dissolution of HP ^{129}Xe into solution. The RF pulse is applied at the chemical shift frequency offset which corresponds to the ternary complex formed by the interaction of HP ^{129}Xe with the WSP5A solution.

References

(1) Yao, Y.; Xue, M.; Chi, X.; Ma, Y.; He, J.; Abliz, Z.; Huang, F. *Chem. Commun.* **2012**, *48* (52), 6505–6507.

(2) Hill, P. A.; Wei, Q.; Eckenhoff, R. G.; Dmochowski, I. J. *J. Am. Chem. Soc.* **2007**, *129* (30), 9262–9263.

3 CHAPTER 3

Will be submitted to *Organic letters*

Efficient Synthesis of β-cyclodextrin and γ-cyclodextrin-based rotaxanes via Diels-Alder End-Capping

Ashvin I. Fernando, John Christy, Brianna Peloquin, Paul Cesana, Samantha Donahue, Brenton DeBoef*

Department of Chemistry, University of Rhode Island, 140 Flagg Road, Kingston, Rhode Island 02881, United States

ABSTRACT

A versatile, three component, one-pot synthesis of β and γ cyclodextrin-based rotaxanes has been developed, and the novel supramolecular products have been characterized. The key, end-capping Diels-Alder reaction can be used to synthesize 1:1, 1:2 and 2:1 rotaxane structures. The syntheses can be performed on gram-scale, resulting in high yields of pure rotaxane products.

Mechanically interlocked supramolecular complexes, such as catenanes and rotaxanes, are currently used in a wide variety of applications, including catalysis, drug delivery, hydrogel formations, and molecular devices/machines[1].

Our interest in the field of mechanically interlocked compounds originated from our recent synthesis of pseudo-rotaxanes that contain hydrophobic cavities[2]. We found that pseudorotaxanes made of a linear alkane guest and γ-cyclodextrin as a host could form ternary complexes with xenon, and these complexes could be detected using a CEST pulse sequence in a clinical MRI. We envision this as a possible platform for the development of xenon-129 MRI biosensors, but rotaxanes that contain hydrophobic cavities could also be used for a variety of other applications involving the capture of environmental analytes or drug delivery[3]. However, to improve the stability and biocompatibility of the supramolecular framework, we commenced a synthetic campaign towards the synthesis of end-capped rotaxane structures that contained a hydrophobic cavity.

One of the classic methods for synthesis of rotaxanes involves the threading of a linear molecular guest through a cyclic macromolecular host[4]. This association is then followed by a rapid and quantitative reaction at the two termini of the molecular thread, creating large stoppers on the ends of the guest and thus preventing dissociation[5]. Common end-capping schemes for rotaxane synthesis use coupling or click-type reactions that attach bulky end groups because these reactions are generally fast, high-yielding and can be performed in a variety of solvents[6]. Herein, we present an efficient and general process for the synthesis of cyclodextrin-based rotaxanes using a 4+2 cycloaddition as the end-capping step. The method can be used to synthesize rotaxanes having a host: guest ratio of 1:1, 2:1, or 1:2 in high yields and high purities. The 1:1 and 2:1 (host: guest) rotaxanes contain a sizeable hydrophobic cavity that can be used for the formation of ternary complexes with hydrophobic molecular payloads.

As shown in Scheme 1, a linear host compound containing terminal anthracene **1** rapidly formed pseudo-rotaxane complexes with β- and γ-cyclodextrins in toluene. The pseudo-rotaxanes then underwent efficient end-capping cycloadditions with the furan protected maleimide, **2**.

Three classes of rotaxanes were synthesized, one with a single CD host and a guest (1:1), one rotaxane with two CD's and one guest (1:2) and one rotaxane with a single CD with two guests (2:1). The formation of these various rotaxanes was easily verified by integrating the ^{1}H NMR.

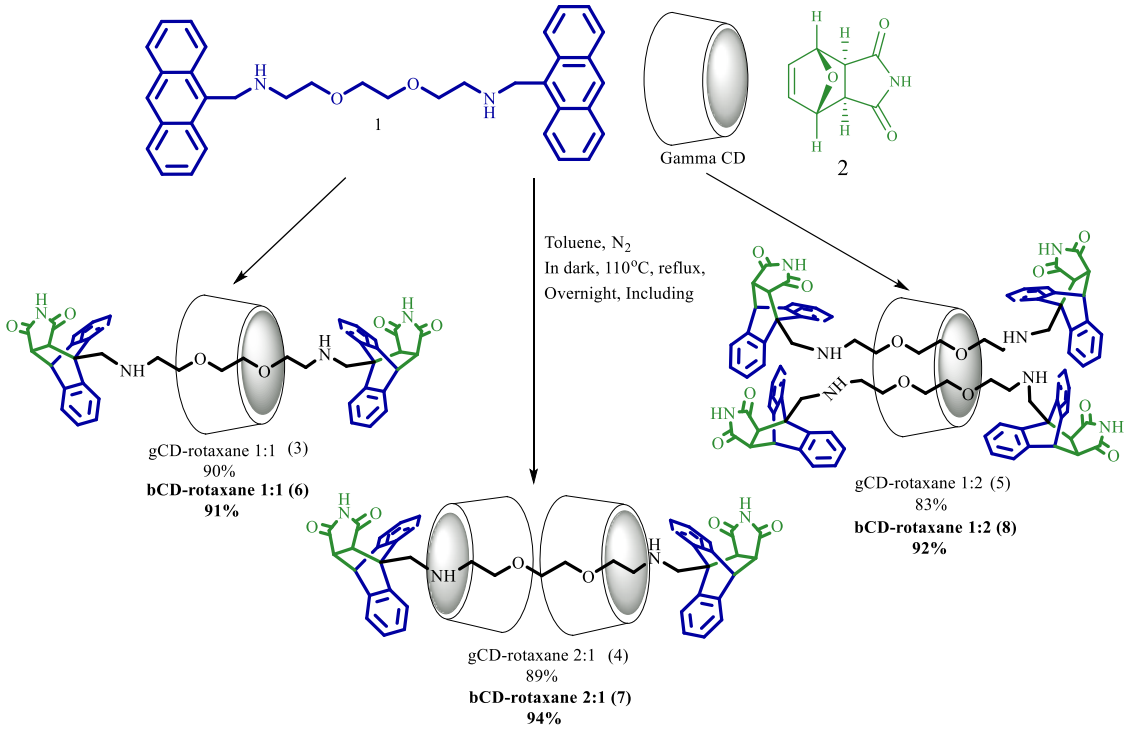

Scheme 3-1: Reaction scheme for the complete synthesis of γ-CD rotaxane 1:1 and γ-CD rotaxane 1:2

The rotaxanes mentioned above were obtained through the reaction of **1** with γ-CD or β-CD in the proper stoichiometric amounts. To achieve the final rotaxane, first **1** was mixed with γ-CD and toluene was added. The complete solution was sonicated for 15 minutes and was stirred at 80-90 °C for 1 hour to accommodate the threading of the **1** into the hydrophobic γ-CD cavity. Increased temperature usage allows more hydrophobic interactions with the γ-CD cavity[7].

Additionally, the oxygens on **1** tend to form hydrogen bonding interactions with the hydroxy groups in the cavity of the γ-CD. The formation of this inclusion complex can be observed by the appearance of turbidity in the reaction mixture. Similar observations have been reported with the formation of poly-pseudo rotaxanes[8] and have been attributed to their aggregation via intermolecular hydrogen bonds.

The association constant for **1** and γ-CD was found out to be 2.5 (±0.15) x 10^3 M^{-1} using NMR titrations. Complexation between **1** and γ-CD was monitored through ^{1}H-NMR as shown in figure S58. The main observation in 1H-NMR was shifting of the alkane hydrogens caused by the shielding that occurred when the complex formed. Once the complexation was completed (which takes approximately 1 hour) dienophile **8** was added to the reaction. The mixture was then stirred in the dark at reflux for 18 hours.

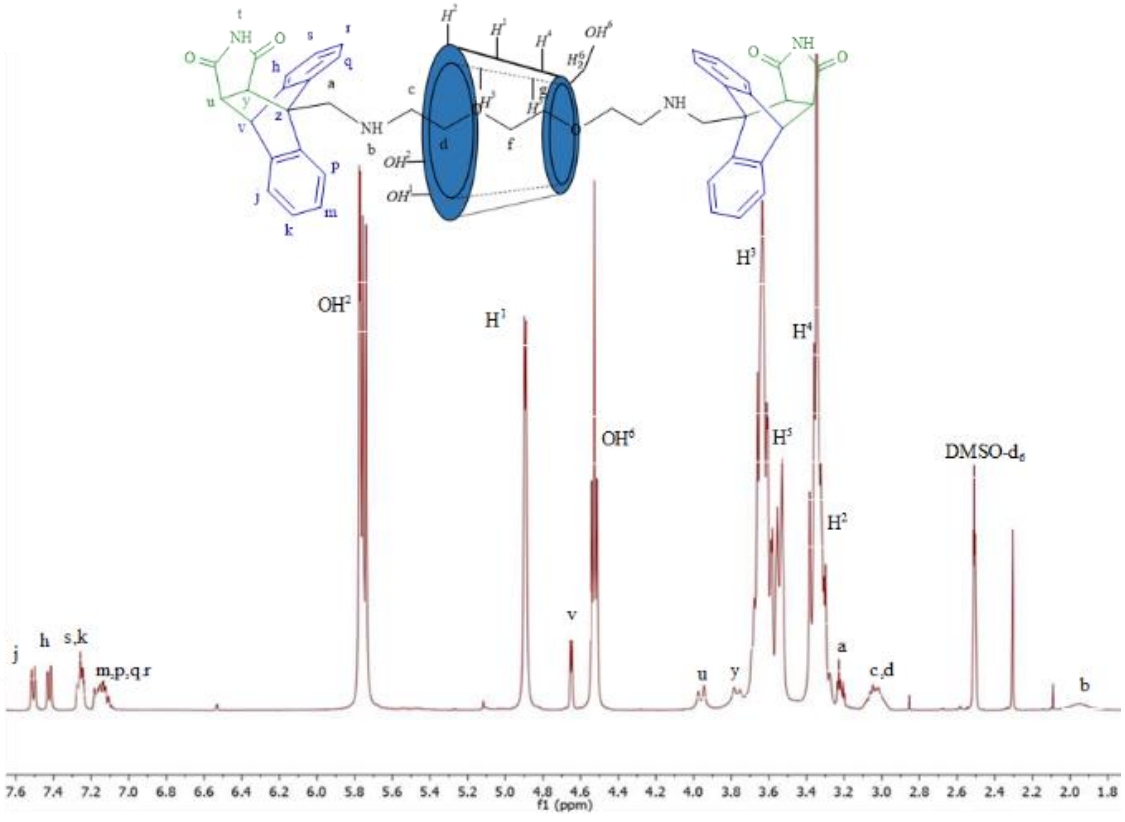

Figure 3.1: ^{1}H-NMR of 3 (400 MHz, DMSO-d_6)

The completion of the reaction was physically observed by the change in colors of the reaction, due to the loss of conjugation in the anthracene. The final rotaxanes (**3**, **4** and **5**) were obtained by vacuum evaporation of the excess toluene and placed under high vacuum overnight. As shown in scheme 2 the same method can be employed to form rotaxane structures containing small molecule affinity tags (e.g. **7**). The synthesis of dienophile-affinity tag conjugate is a straight forward S_N2 reaction, allowing for a wide variety chemical probes to be attached to the rotaxane core for potential application as drug delivery or molecular imaging agents. In addition, the reaction was performed on gram scale and the reaction yields remain the same, proving that reaction can be scaled up with ease.

Interestingly, the structure of the molecular thread proved to be critical for the formation of the rotaxanes. When the same reaction that is shown in Figure 1 was performed on a diene like 1, but containing a 12-carbon central chain, no rotaxane products were observed. This indicates that hydrogen bonding between the interior hydroxyl groups of the CD and the oxygens in the ethylene glycol chain may play a crucial role in the formation of rotaxanes **3**-**7**. These types of associations are found in cucurbit[n]urils based click chemistry.[9] As shown in Scheme 1, in the presence of γ-CD the double Diels Alder reaction produced an overall yield of 90% for the rotaxane **3**, whereas the same reaction in the absence of γ-CD, produced only a 45% of the double Diels-Alder product(not shown). We hypothesize that the excellent yields for **3**-**7** are an example of cooperative capture synthesis, where the cyclodextrin acts as a cofactor that preorganizes the reagents for the Diels-Alder reaction, leading to increased reaction efficiency.[11]

The Rotaxanes **3**-**5**were characterized using ^{1}H-NMR and 2-D NMR, as well as high-resolution mass spectroscopy. The use of DMSO as an NMR solvent has been shown to prevent the formation of any inclusion compounds with CDs. Thus indicating that the interlocked structure produced are stable rotaxanes, as opposed to labile inclusion complexes[10].

The dienophile guest **1** contains a distinguishable singlet in the aromatic region arising from the proton in the middle of the anthracene core. This singlet moves from the aromatic region of the spectrum after the Diels-Alder reaction. In addition, two small singlets coupled to each other arise from the newly formed C-C bond (labeled as U-V in Figure 1). The doublet near 4.7 ppm corresponds to the Z-hydrogen which is directly coupled to the new U-V bond. This provides significant proof that the Diels-Alder reaction took place, in the presence of γ-CD. Similar NMR evidence is equally seen in β-CD based rotaxane systems.

As shown in Figure 1, the ethylene protons in the guest were shifted downfield, indicating that they are located inside the host's cavity. Additionally, the peaks of both the cyclodextrins or the guest protons are not subjected to peak broadening which designates that the molecule formed here is a one single inter-locked rotaxane molecule, not an inclusion complex. The most conclusive evidence demonstrating the formation of the rotaxane is shown in the 2D ROESY spectra of **3**. The cross peaks are shown in Figure 2 corresponds to the ethylene protons of the guest molecule that are correlated with H-3 and H-5 protons of the γ-CD which are found inside the hydrophobic cavity. Similar ROE cross peaks were observed for β-CD based rotaxanes.

The control reaction, in which a guest that contained Diels-Alder adducts was mixed with γ-CD, did not produce these cross peaks. This demonstrates that the synthesis is shown previously in Scheme 2 and 3 forms stable rotaxanes. While the anthracene moieties are still small enough to pass through the center of the CD, the Diels-Alder adducts are too bulky for the guest to de-thread, once it is interlocked.

Additionally, an NOE correlation was observed, corresponding to the N-H present in the guest and the OH2 proton of the γ-CD that lies on the outer rim of the γ-CD (See supporting info). This indicates that the cyclodextrin is situated between the boundaries of the two amines present in the guest.

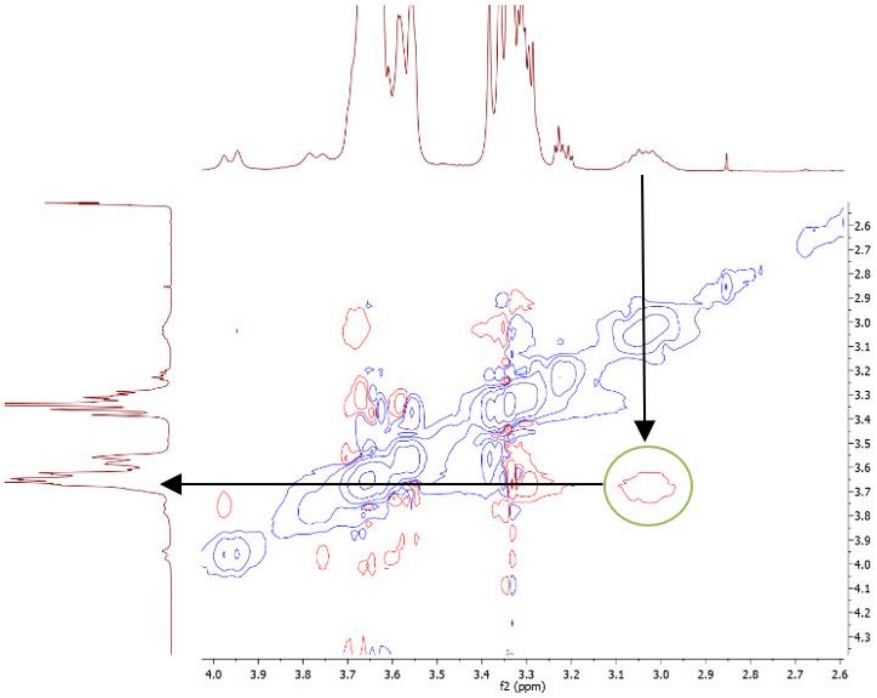

Figure 3.2: ROESY NMR of 3 (400 MHz, DMSO-d_6). The arrows point towards the regions of H3 and H5 protons NOE correlation with C-D protons of the guest molecule. Mixing time = 500 ms

Comparable correlations were seen for the Rotaxane with ThT groups, **10**. **7** was successfully synthesized with a yield of 85%. Furthermore, we have synthesized similar 1:1, 1:2 and 2:1 rotaxanes using β-cyclodextrin as a host-structure, similar characterizations were acquired along with mass spectroscopy to confirm their structures.

Analysis of large rotaxanes which exceed 2000 Da were analyzed using a Waters Synapt G2 HDMS mass spectrometer with resolution of 1000, in the mass range of 100 to 5000 m/z. Mass specta for compounds **3**, **4** and **5** were obtained via lower capillary voltages, while higher capillary voltages were used for **10** which is a much larger and heavier compound. The usage of more power was due to fragmentation requires more power.

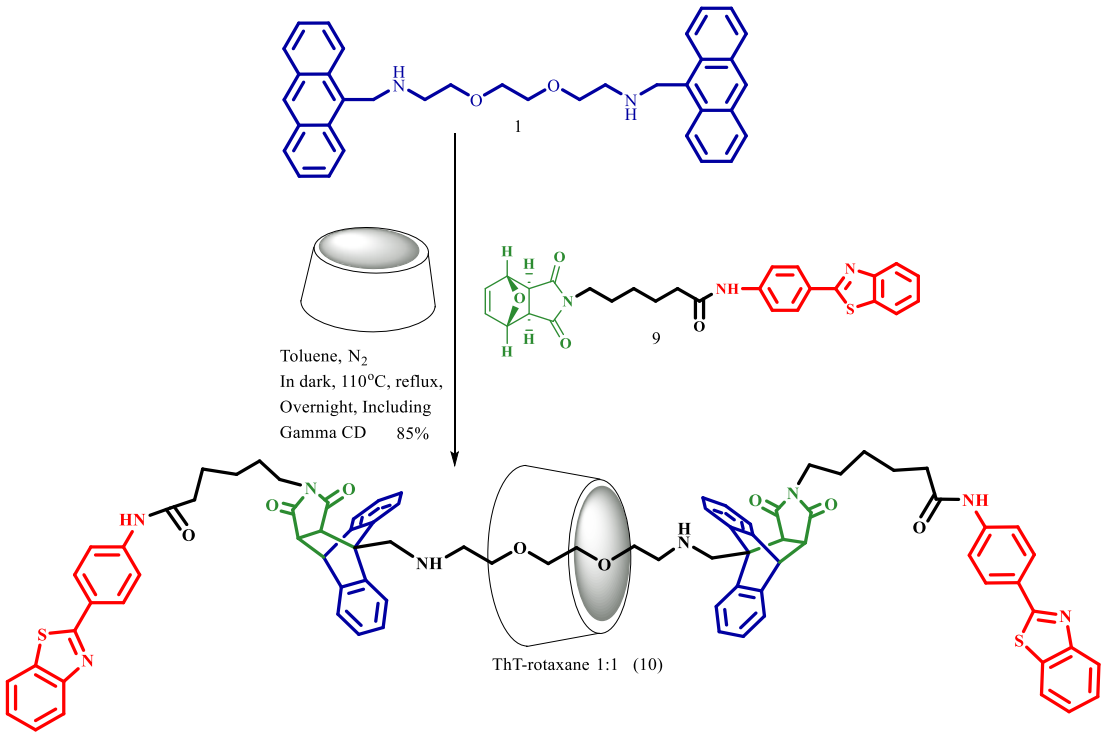

Scheme 3-2: Reaction scheme for the complete synthesis of ThT-rotaxane 1:1 and ThT-rotaxane 1:2

We can observe signals with isotopic pattern and mass accuracy for the expected **3** with two charges $[M+2H]^{2+}$ monoisotopic m/z 1010.3765 (2.67 ppm) for the for the formula $C_{92}H_{122}O_{46}N_4$. The spectrum also has signals related to $[M+H]^{+}$ monoisotopic m/z 2019.7424 (1.04 ppm). In the same m/z region signals are observed for a non-covalent dimer $[2M+2H]^{+}$.

For 4 The mass spectrum shows a base peak with 1959.0930 Zooming into this region we could observe signals with isotopic pattern and mass accuracy for the expected compound with two charges $[M+2H]^{2+}$ monoisotopic m/z 1658.5902 (3.07 ppm) for the for the formula $C_{140}H_{202}O_{86}N_4$.

The spectrum for **7** shows signals with mass accuracy and isotopic pattern for $[M+2H]^{2+}$. The monoisotopic m/z 1980.6952 has -1,87 ppm mass accuracy for the theoretical m/z of **7**. Reason for this behavior is that higher voltages must be used for fragmentation, which results in losing the molecular ion peak, but the monoisotopic m/z confirms that the rotaxane is present. The above-

mentioned mass spectroscopy data proves that the rotaxanes were stable and formed as mentioned in scheme **1** and **2**. Furthermore, β-CD based rotaxanes shows mass adducts that matches the theoretical mass adducts, hence we can conclude that both rotaxanes types were successfully synthesized.

Computational studies were performed using commercially available MOE software. The same software was used to design the supramolecular compounds in 3-D space, energy minimizations, dynamics, and docking. Energy minimizations were conducted using the MMFX94 force field22, with an R-field of 1.80. A unit cell was created around the molecule with a cell size of 43.321 Å in x, y, z directions. Rigid water molecules were chosen, with a gradient of 0.001 RMS kcal/mol/Å.

Complex name	$\Delta E_{Complex}$ (stabilization energy) / [kcal/mol]	ΔG binding (final docking score) / [kcal/mol]
1 and γ-CD (1:1)	-8.0068	-6.9883
1 and γ-CD (2:1)	-8.5634	-8.2360
3	-15.6887	-9.7994
4	-17.6590	-8.1153
10	-33.2087	-8.8183

Table 3-1: Stabilization energies and docking scores of complexes

As given in table 1, the molecular dynamics data confirms that **7** has the lowest negative ΔE Complex which means that **7** has the highest stability. Docking results further explained the reason behind this. After docking the ThT rotaxane into the γ-CD cavity. The complex arranged in a very orderly manner wrapping around the CD cavity as given in figure 3 which explains the low $\Delta E_{Complex}$ due to high ordered packing.

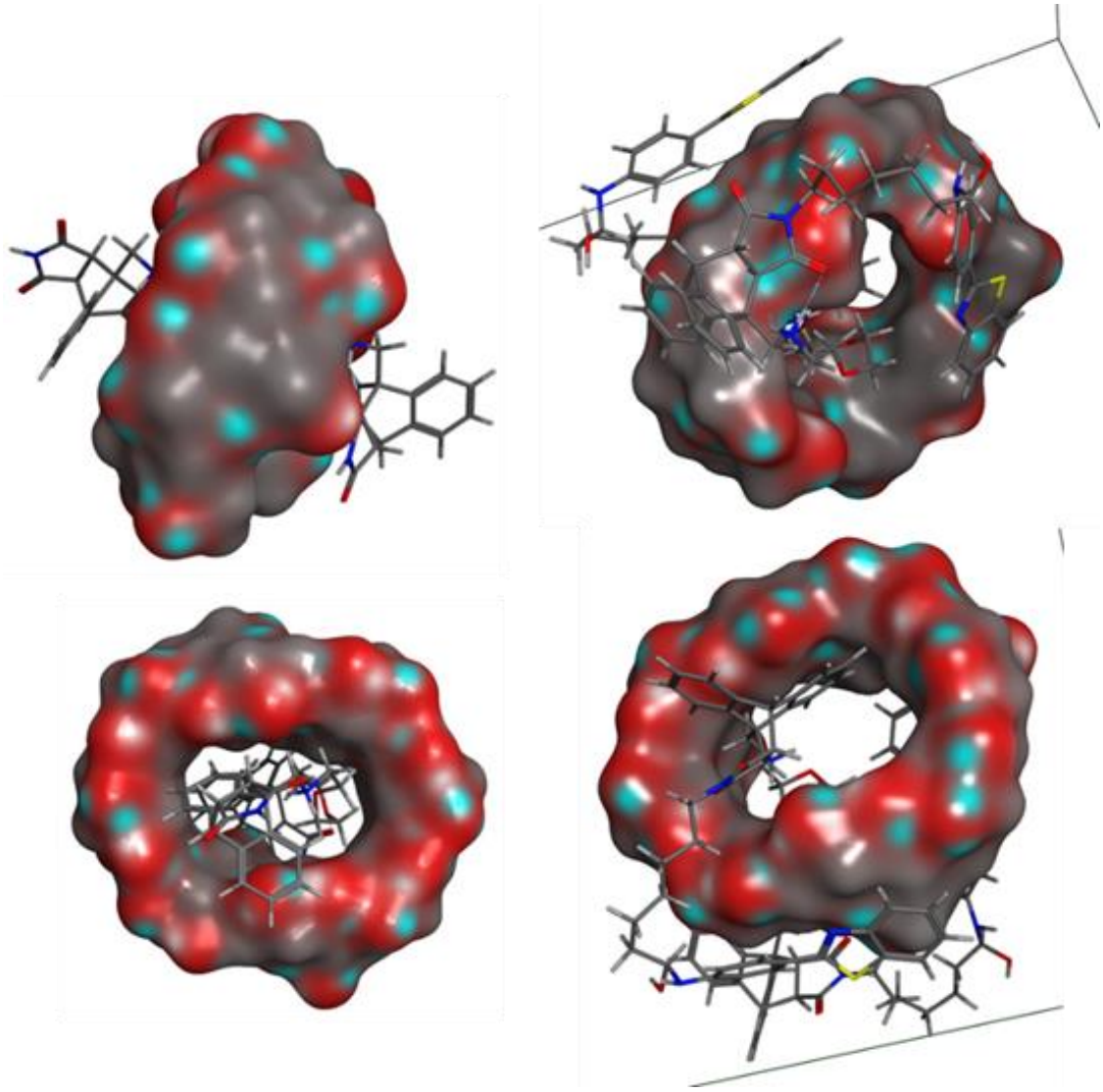

Figure 3.3: Images of 3 (to the left) and 10 (to the right) after docking using MOE software, the surfaces represent the hydrophobic surface of the cyclodextrin and the ligand placement inside the hydrophobic centroid

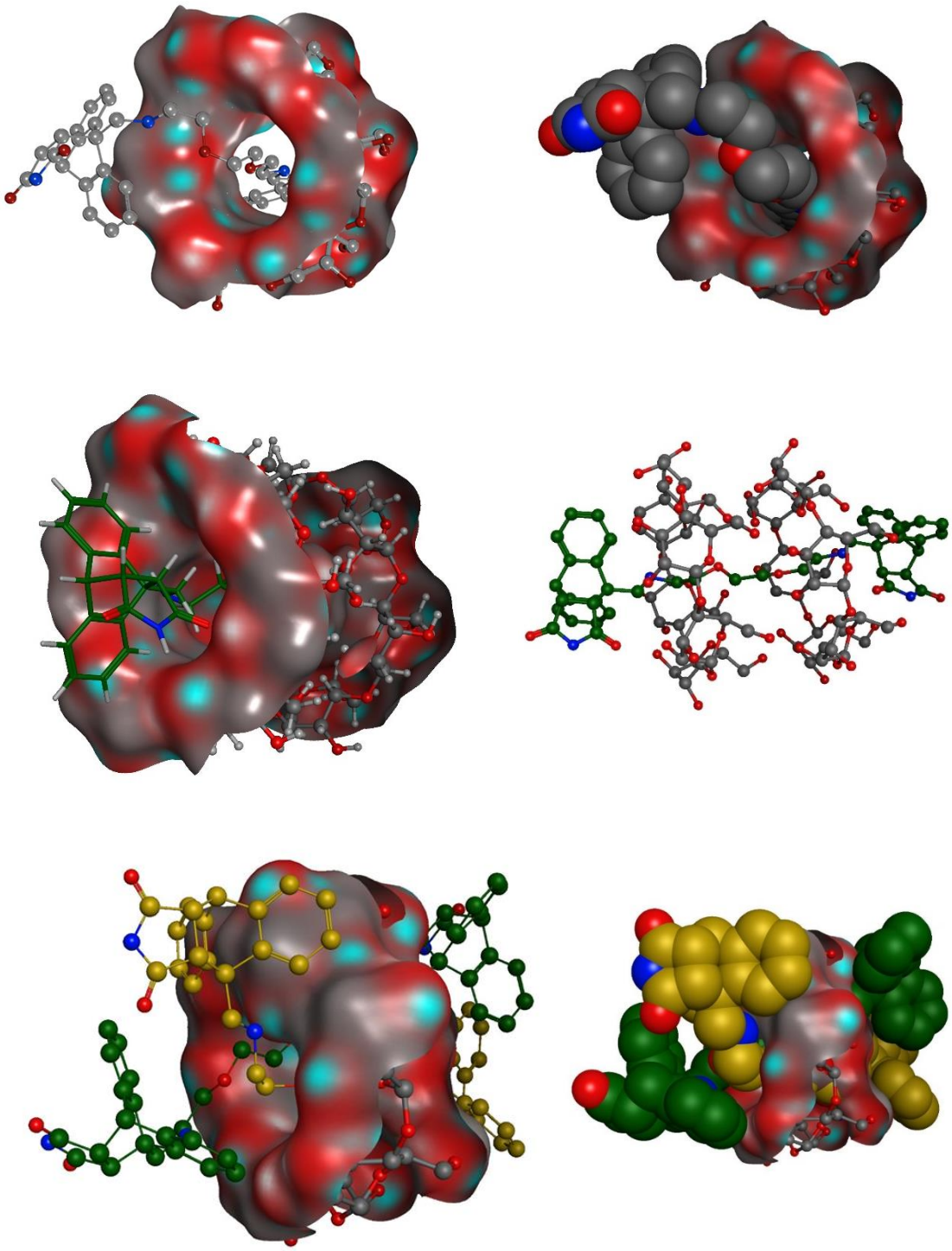

Figure 3.4: from top to bottom, energy minimized molecular models of γ-CD rotaxane 1:1, γ-CD rotaxane 2:1 and γ-CD rotaxane 1:2

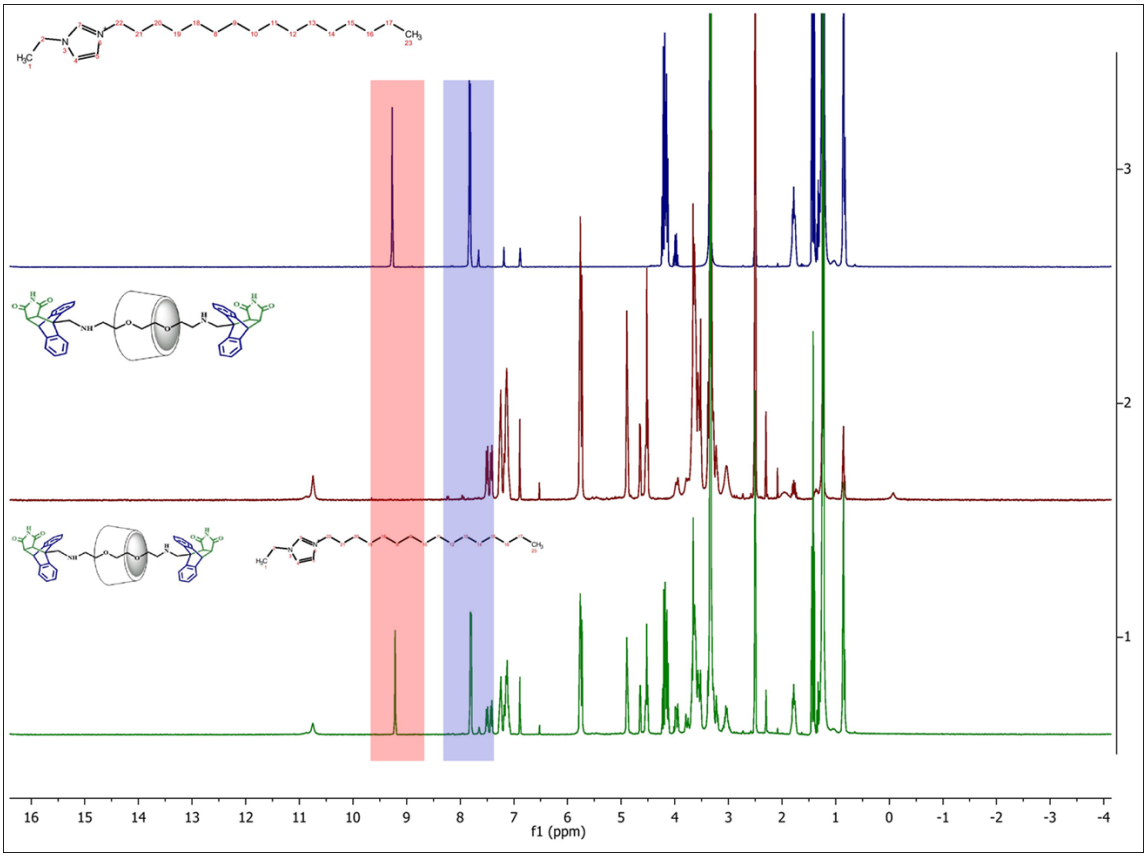

Figure 3.5: Stacked image of methylimidazolium guest, 1:1 γ-CD rotaxane and complexation of the host and the guest in 1:1 ratio

A 16-Carbon aliphatic bar with an imidazole polar head-group was chosen as a molecular mimic to "Perifosine" to examine the binding properties of the Rotaxane complex. Similar compounds in the literature exhibit the ability to stabilize charged species in DMSO due to stabilization by etheric oxygens at the center of the bar threaded inside the cyclodextrin. Given in figure 5 are the NMR spectra supporting this conclusion, showing shielding of the charged Imidazole head-group and nearby protons indicating inclusion of the head-group into the rotaxane complex in DMSO. We further hypothesize that in aqueous solution, hydrophobic interactions will predominate, and drive the aliphatic chain to enter the complex instead of the head-group. Imidazole functionalization of other molecules may provide a facile method of functionalizing guest molecules that do not interact with the rotaxane host complex in their native state.

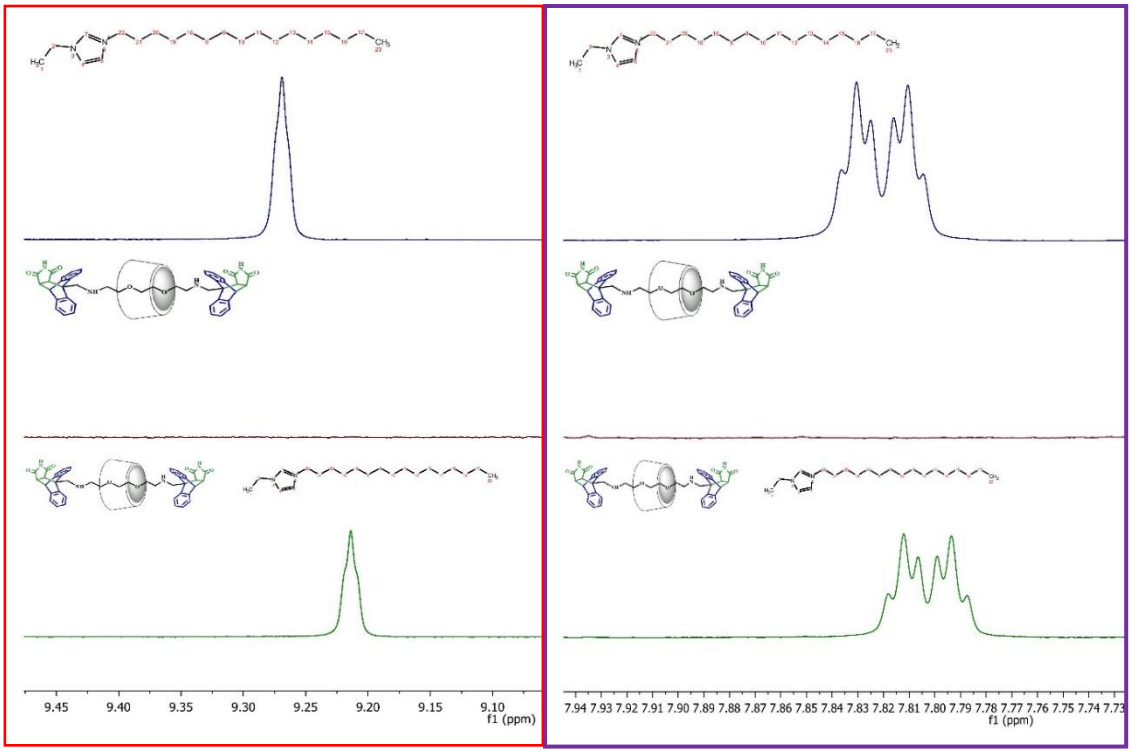

Figure 3.6: The expanded in images of the imidazole ^{1}H NMR peaks displaying the shielding effect of these peaks in the presence of the 1:1 rotaxane system showing that the cavity itself is exhibiting the hydrophilic effects

In addition, we used this same guest to perform an NMR titration to investigate the association of the guest inside the host cavity. With the increased addition of the guest, the imidazole peaks shifted further towards de-shielding side showing that the polar headgroup is indeed inside the cavity of the γ-CD rotaxane. We did not observe the same change in the aliphatic non-polar tail end. The NMR titrations for 16-C ethyl imidazolium chain and the γ-CD rotaxane 1:1 showed an association constant of $4.98 \pm 0.013 \times 10^{3}\ M^{-1}$.

The cavity space inside the γ-CD rotaxane is not enough to achieve 1:2 binding. This is further confirmed from the computational modeling seen on figure 4.

Conclusion

We have discovered a new efficient method of synthesizing rotaxane with ease and high yields. These rotaxanes can also be easily functionalized using SN_2 chemistry. Furthermore, we have shown that these rotaxanes can be potentially used in drug delivery systems to carry small molecule payloads that consist of charged species. In addition, structures **3**-**7** can be used as a useful tool to add other different drugs and targets depending on the disease which it is targeted.

3.1 REFERENCES

(1) Stoddart, J. F. Mechanically Interlocked Molecules (MIMs)-Molecular Shuttles, Switches, and Machines (Nobel Lecture). *Angew. Chemie Int. Ed.* **2017**, 11094–11125. https://doi.org/10.1002/anie.201703216.

(2) Hane, F. T.; Fernando, A.; Prete, B. R. J.; Peloquin, B.; Karas, S.; Chaudhuri, S.; Chahal, S.; Shepelytskyi, Y.; Wade, A.; Li, T.; et al. Cyclodextrin-Based Pseudorotaxanes: Easily Conjugatable Scaffolds for Synthesizing Hyperpolarized Xenon-129 Magnetic Resonance Imaging Agents. *ACS Omega* **2018**, *3* (1), 677–681. https://doi.org/10.1021/acsomega.7b01744.

(3) Pairault, N.; Barat, R.; Tranoy-Opalinski, I.; Renoux, B.; Thomas, M.; Papot, S. Rotaxane-Based Architectures for Biological Applications. *Comptes Rendus Chim.* **2016**, *19* (1–2), 103–112. https://doi.org/10.1016/j.crci.2015.05.012.

(4) Xue, M.; Yang, Y.; Chi, X.; Yan, X.; Huang, F. Development of Pseudorotaxanes and Rotaxanes: From Synthesis to Stimuli-Responsive Motions to Applications. *Chem. Rev.* **2015**, *115* (15), 7398–7501. https://doi.org/10.1021/cr5005869.

(5) Jimenez, R.; Martin, C.; Lopez-Cornejo, P. Formation of a Rotaxane from the End-Capping Process of a Pseudorotaxane. Effects of the Solvent. *J. Phys. Chem. B* **2008**, *112* (37), 11610–11615. https://doi.org/10.1021/jp804918t.

(6) Thibeault, D.; Morin, J. F. Recent Advances in the Synthesis of Ammonium-Based Rotaxanes. *Molecules* **2010**, *15* (5), 3709–3730. https://doi.org/10.3390/molecules15053709.

(7) Ross, P. D.; Rekharsky, M. V. Thermodynamics of Hydrogen Bond and Hydrophobic Interactions in Cyclodextrin Complexes. *Biophys. J.* **1996**, *71* (4), 2144–2154.

https://doi.org/10.1016/S0006-3495(96)79415-8.

(8) Lee, S. C.; Choi, H. S.; Ooya, T.; Yui, N. Block-Selective Polypseudorotaxane Formation in PEI-b-PEG-b-PEI Copolymers via PH Variation. *Macromolecules* **2004**, *37* (20), 7464–7468. https://doi.org/10.1021/ma048666r.

(9) Finbloom, J. A.; Slack, C. C.; Bruns, C. J.; Jeong, K.; Wemmer, D. E.; Pines, A.; Francis, M. B.; Shen, C.; New, E. J.; Major, J. L.; et al. Rotaxane-Mediated Suppression and Activation of Cucurbit[6]Uril for Molecular Detection by ^{129} Xe HyperCEST NMR. *Chem. Commun.* **2016**, *52* (15), 3119–3122. https://doi.org/10.1039/C5CC10410F.

(10) Fredy, J. W.; Scelle, J.; Ramniceanu, G.; Doan, B.-T.; Bonnet, C. S.; Tóth, É.; Ménand, M.; Sollogoub, M.; Vives, G.; Hasenknopf, B. Mechanostereoselective One-Pot Synthesis of Functionalized Head-to-Head Cyclodextrin [3]Rotaxanes and Their Application as Magnetic Resonance Imaging Contrast Agents. *Org. Lett.* **2017**, acs.orglett.7b00153. https://doi.org/10.1021/acs.orglett.7b00153.

(11) Hou, X.; Ke, C.; Stoddart, F. *J. Chem.Soc.Rev*.,**2016**,*45*,3766—3780.

3.2 SUPPORTING INFORMATION

Efficient Synthesis of β-cyclodextrin and γ-cyclodextrin based rotaxanes via Diels-Alder End-Capping

Experimental Section

Reagents

Substrates mentioned in the supplementary information were purchased from Sigma-Aldrich, Fisher Scientific, and TCI chemicals. All reagents were stored under an inert atmosphere before use. Unless otherwise noted, all reactions were performed under N_2.

Instrumentation

NMR spectra were obtained using a Bruker Avance 300 MHz and 400 MHz spectrometers. Low resolution mass spectrometry was performed using a Shimadzu LRMS-2020. High resolution mass spectrometry was performed using a Thermo Scientific LTQ Orbitrap XL™ instrument

Synthesis of Thioflavin analog

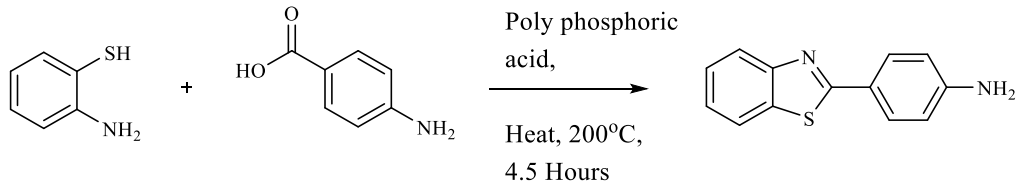

p-Amino Benzoic Acid (2.74 g, 20.0 mmol) and 2-Aminothiophenol (2.14 ml, 20.0 mmol) were dissolved in (21.03 g, 250.00 mmol) polyphosphoric acid. The mixture was Heated at 200°C and stirred for 4.5 hours. After cooling, 10% Na_2CO_3 was slowly poured into solution. This resulted in a greenish mixture. This solution was stirred until gas evolution was completed. Next, the solution was filtered using vacuum filtration. The solid was washed with water (3x50mL) and recrystallized with MeOH and H_2O to give the final product. The yield was 70%. ^{1}H-NMR was performed using DMSO-d_6. The literature-based procedure was followed[1]. LRMS ESI (m/z): [M+H] calculated for $C_{13}H_{10}N_2S$ 227.06, observed 227.05. ^{1}H NMR (400 MHz, DMSO-d_6) δ 8.02 (d, J = 8.0, 1.1 Hz, 1H), 7.90 (d, J = 8.0 Hz, 1H), 7.76 (t, J = 8.7 Hz, 2H), 7.45 (d, J = 7.7 Hz, 1H), 7.34 (d, J = 7.7 Hz, 1H), 6.67 (d, J = 8.6 Hz, 2H), 5.88 (br, 2H).

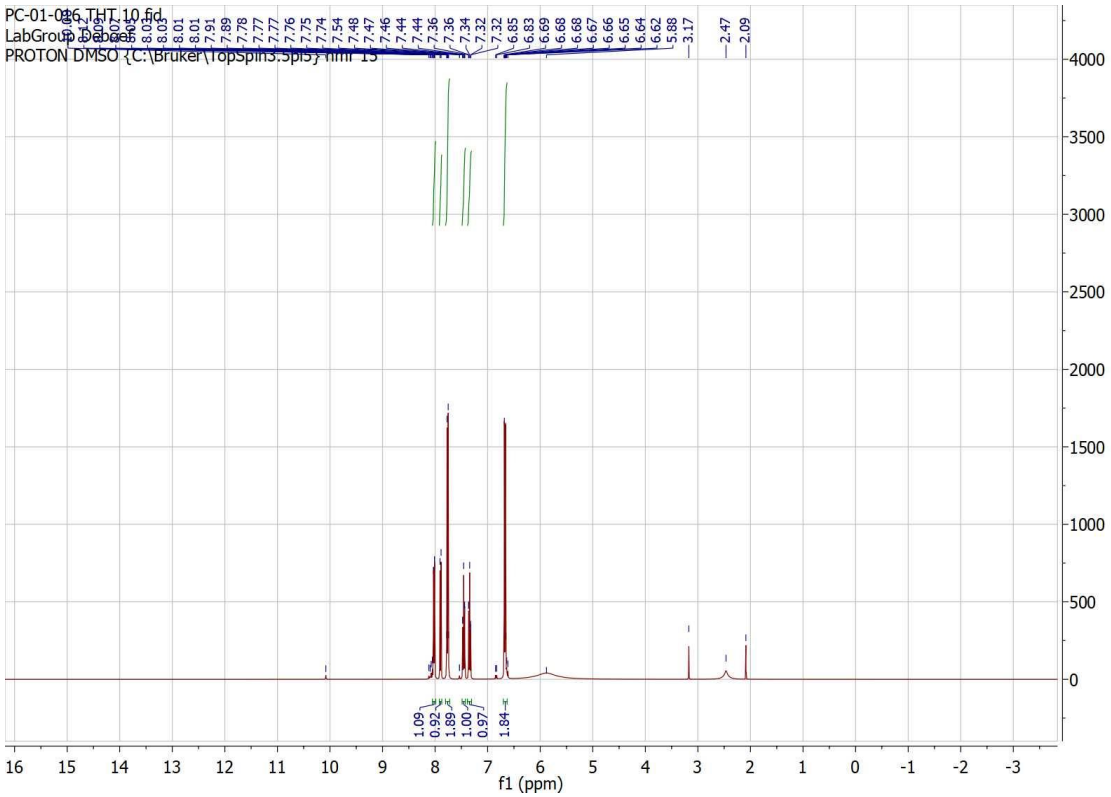

Figure 3.7: ^{1}H NMR of Thioflavin analog

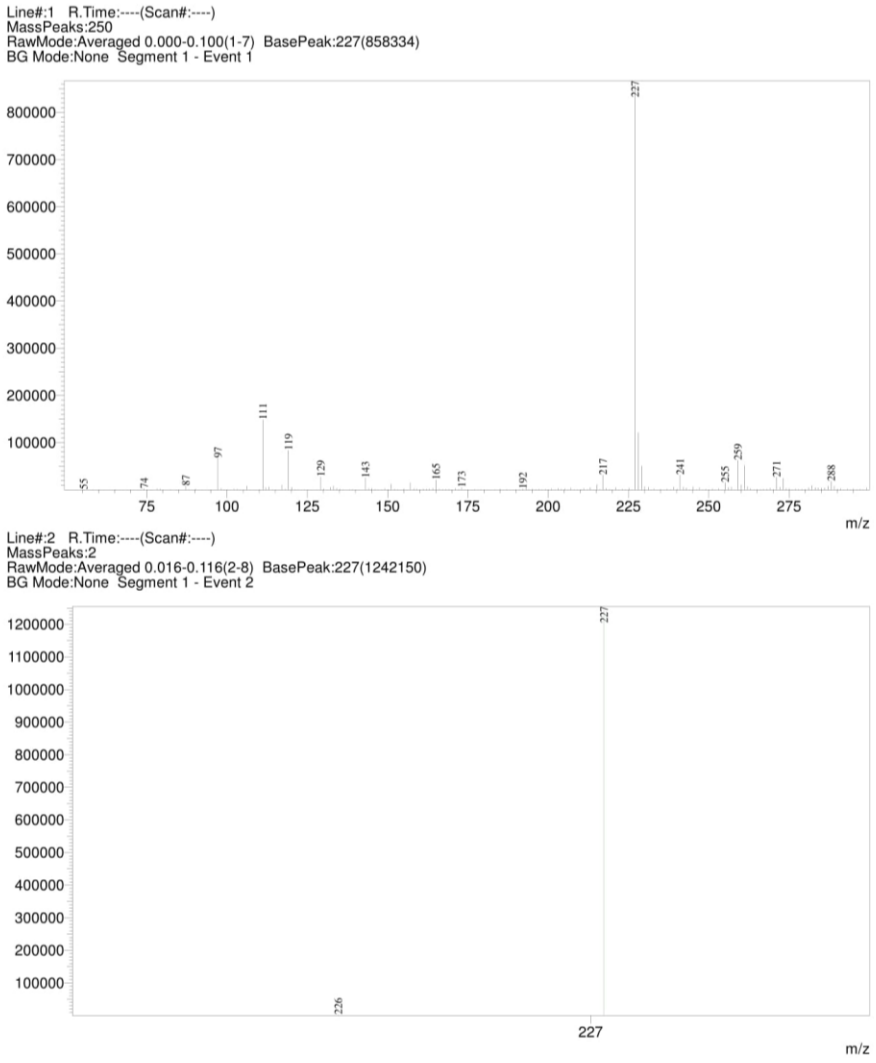

Figure 3.8: Mass spectrum of Thioflavin analog

Synthesis of Thioflavin analog based linker

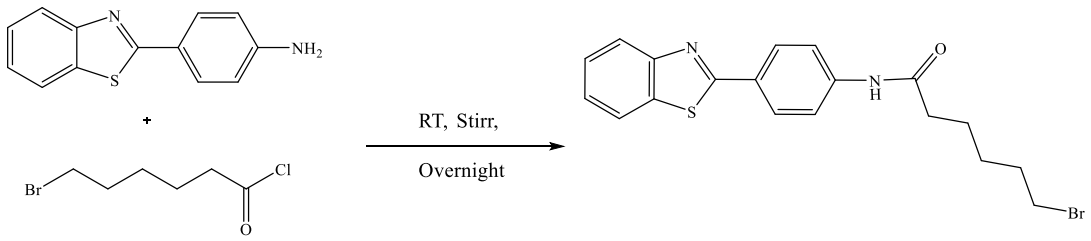

ThT-NH_2 (452.6 mg, 2.00 mmol) was dissolved in 20 ml of anhydrous CH_2Cl_2. To this mixture 6-Bromohexonoyl chloride (305.0 µl, 2.00 mmol) was added drop wisely. The reaction was performed inside a glove box under Nitrogen atmosphere. The reaction mixture was stirred overnight at room temperature. The reaction was monitored by TLC. After overnight stirring, the mixture was poured into several centrifuge tubes and centrifuged at 6000 rpm for 15 minutes. Once centrifugation was completed, the supernatant was discarded. CH_2Cl_2 was added into the remaining precipitate and centrifuged again. Once again, the supernatant was discarded, and this was done for two more times with a total of three washes with CH_2Cl_2. Finally, the remaining precipitate was dissolved in deuterated $CDCl_3$ and centrifuged, and the precipitate was collected with the removal of $CDCl_3$. ($CDCl_3$ was used to remove the CH_2Cl_2 peak from the spectra.) This was subjected to overnight vacuum. The product was further purified using automated flash chromatography. The reaction yielded 59%. ^{1}H-NMR and ^{13}C-NMR were performed using DMSO-d_6. LRMS ESI (m/z): [M+H] calculated for $C_{19}H_{19}BrN_2OS$ 403.05, observed 403.05. ^{1}H NMR (400 MHz, DMSO-d_6) δ 10.25 (s, 1H), 8.12 (dd, *J* = 8.0, 1.2 Hz, 1H), 8.03 (td, *J* = 8.7, 7.8, 2.5 Hz, 3H), 7.80 (dd, *J* = 8.8, 2.6 Hz, 2H), 7.53 (ddd, *J* = 8.3, 7.2, 1.3 Hz, 1H), 7.43 (ddd, *J* = 8.3, 7.2, 1.2 Hz, 1H), 3.64 (q, *J* = 6.6 Hz, 1H), 3.55 (t, *J* = 6.7 Hz, 1H), 2.38 (t, *J* = 7.4 Hz, 2H), 1.80 (dm, *J* = 34.0, 7.5, 7.0, 6.8 Hz, 2H), 1.68 – 1.58 (m, *J* = 7.5 Hz, 2H), 1.44 (t, *J* = 8.2, 7.1 Hz, 2H). ^{13}C NMR (101 MHz, DMSO-d_6) δ 172.0, 167.5, 154.1, 142.6, 134.7, 128.5, 127.8, 127.0, 125.7, 123.0, 122.7, 119.6, 45.8, 36.8, 35.5, 32.5, 27.7, 26.4, 24.7.

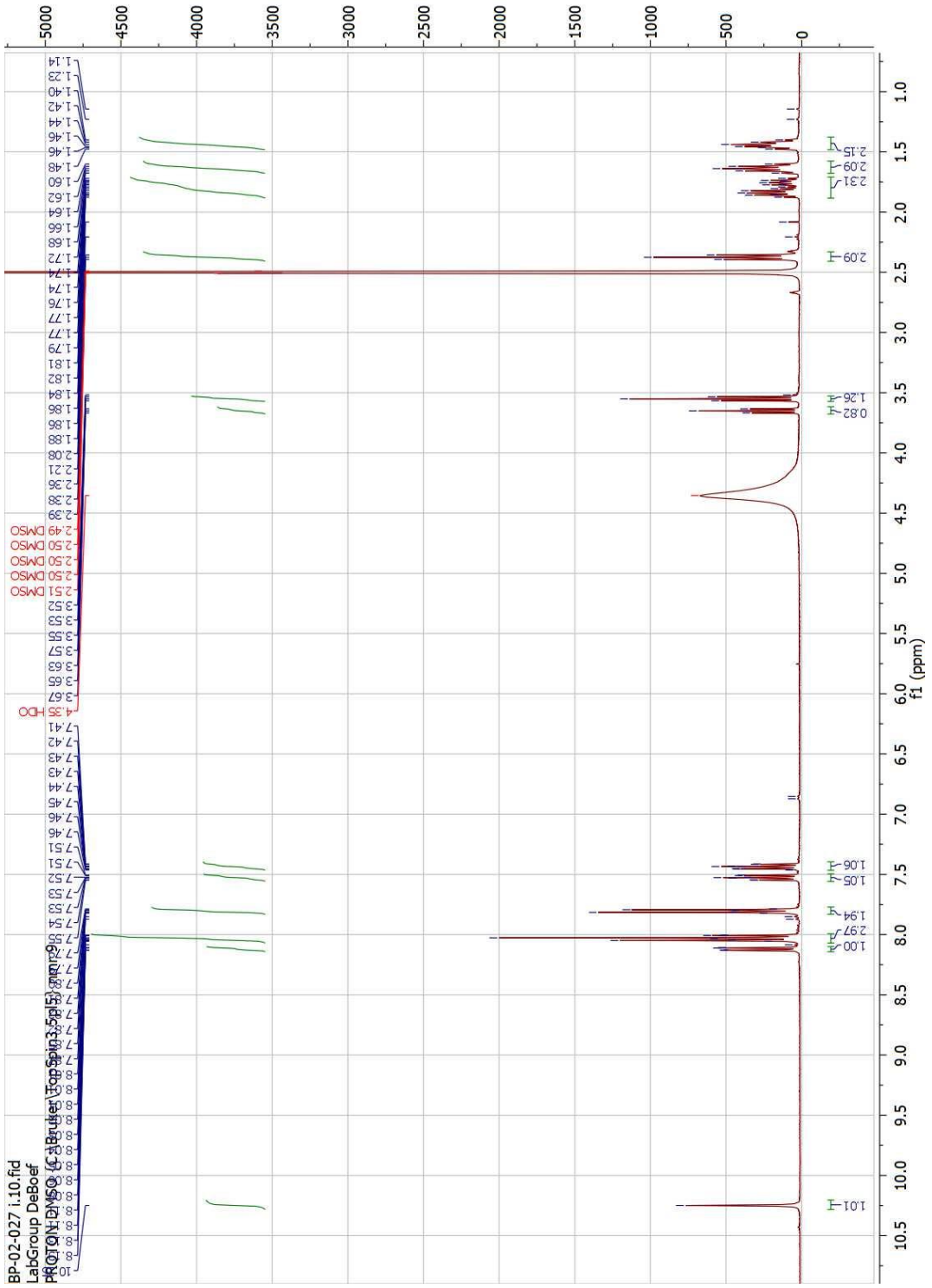

Figure 3.9: ^{1}H NMR of Thioflavin analog based linker

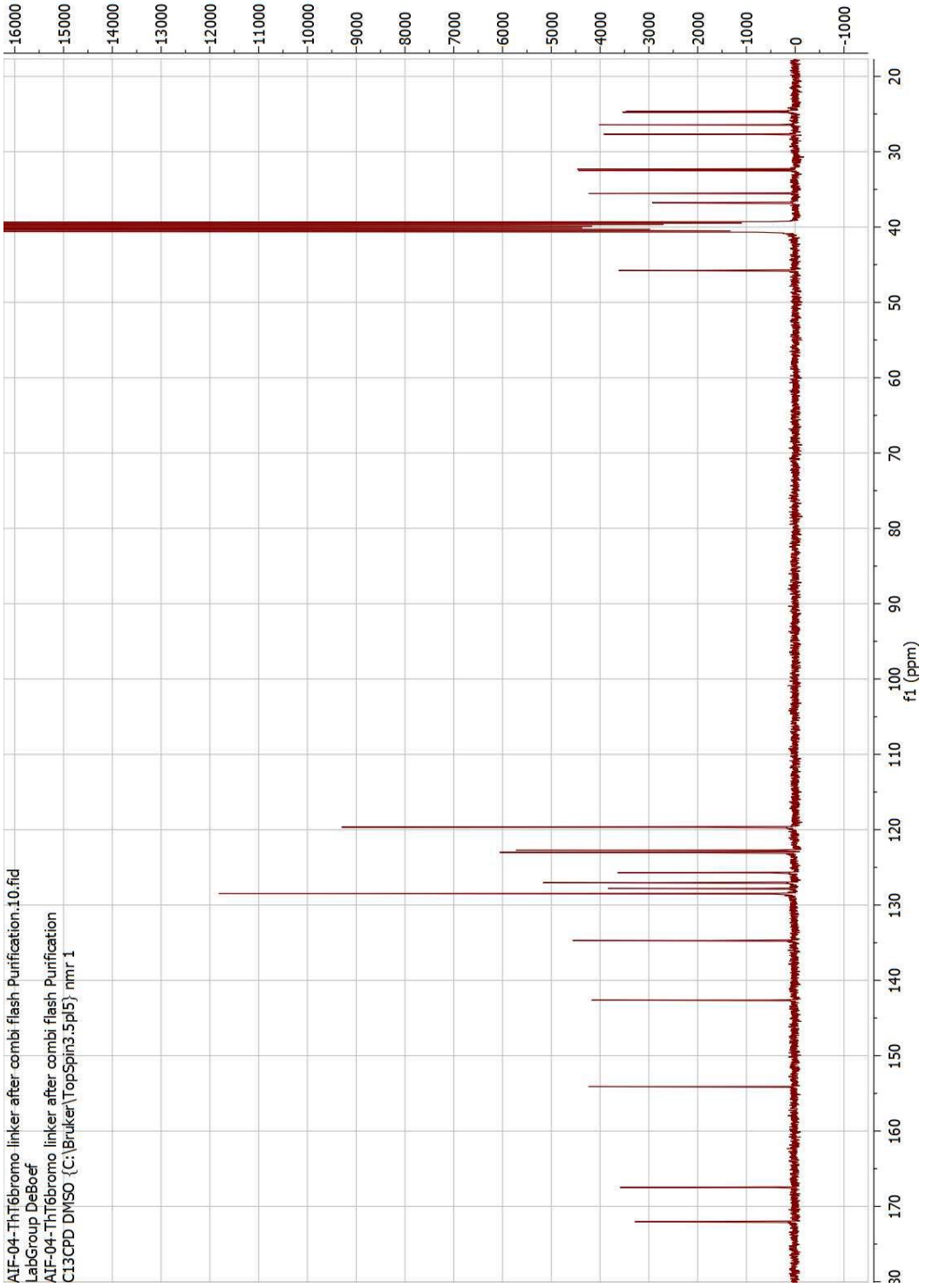

Figure 3.10: ^{13}C NMR of Thioflavin analog based linker

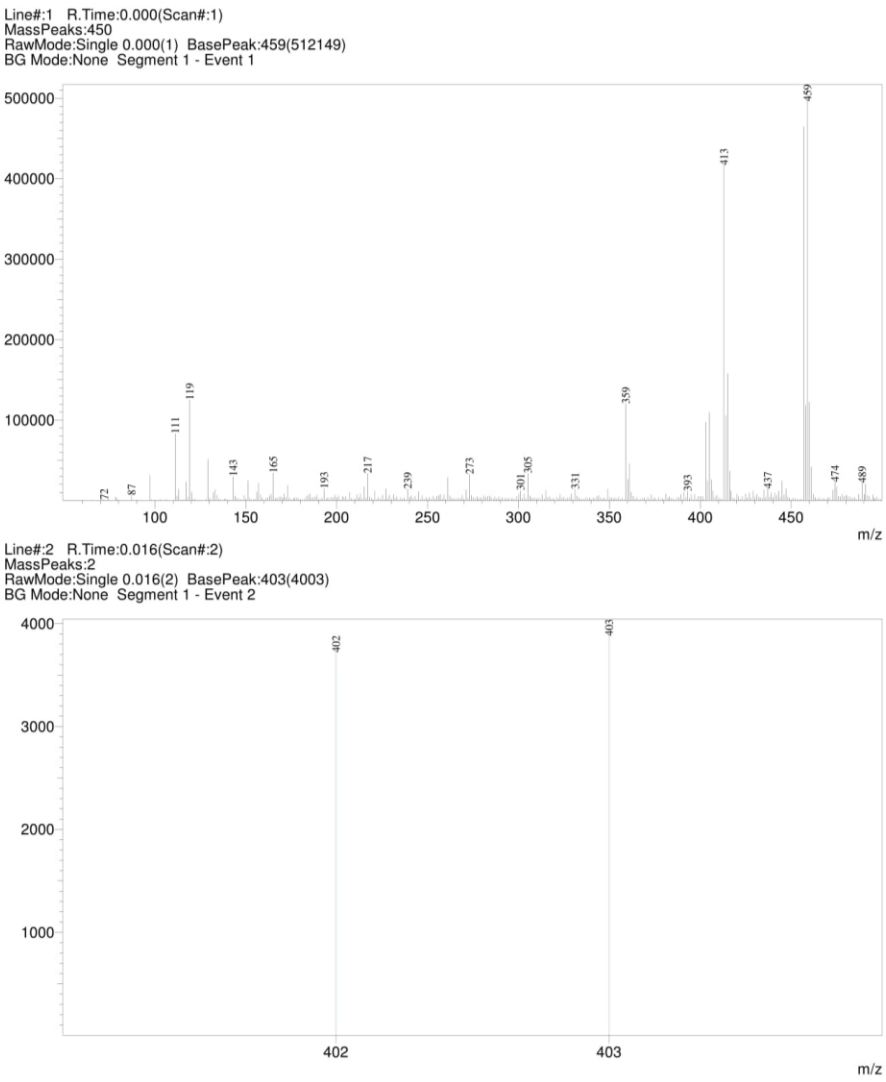

Figure 3.11: Mass spectrum of Thioflavin analog based linker

Synthesis of 9

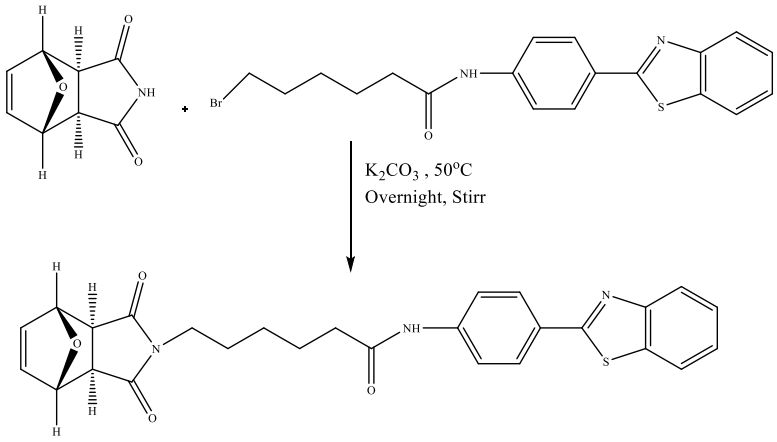

Furan protected maleimide (330.3 mg, 2.00 mmol) and ThT-6-Br (403.3 mg, 1.00 mmol) was dissolved in 10 mL of dry DMF. Next K_2CO_3 (290.2 mg, 2.10 mmol) was added and into the mixture. This mixture was heated to 50 ºC for overnight. The literature method only suggested heating for three hours, but this tends to give a mixture of starting materials and product, but letting it react for overnight helps to get the product exclusively. The mixture was then dissolved in 50 mL diethyl ether and washed with 5% HCl, followed by water to remove excess DMF. The organic layer was then dried with magnesium sulfate and subjected to rotatory evaporator until dryness. The product was further purified using automated flash chromatography. The method is given below. LRMS ESI (m/z): [M+H] calculated for $C_{27}H_{25}N_3O_4S$ 488.16, observed 488.15. ^{1}H NMR (300 MHz, DMSO-d_6) δ 10.20 (s, 1H), 8.15 – 8.09 (m, 1H), 8.06 – 7.99 (m, 3H), 7.79 (td, *J* = 8.8, 8.8, 5.4 Hz, 2H), 7.53 (ddd, *J* = 8.3, 7.2, 1.4 Hz, 1H), 7.43 (ddd, *J* = 8.4, 7.2, 1.3 Hz, 1H), 6.54 (s, 2H), 5.12 (s, 2H), 3.36 (t, *J* = 7.1 Hz, 2H), 2.91 (s, 2H), 2.33 (t, *J* = 7.4 Hz, 2H), 1.60 (p, *J* = 7.5 Hz, 2H), 1.48 (p, *J* = 7.2 Hz, 2H), 1.25 (p, *J* = 9.7, 8.9 Hz, 2H). ^{13}C NMR (101 MHz, DMSO-d_6) δ 178.3, 176.9, 172.1, 172.1, 167.5, 162.8, 154.1, 142.6, 136.9, 134.7, 128.4, 127.7, 127.0, 125.7, 123.0, 122.6, 119.6, 48.9, 47.5, 45.7, 38.2, 36.7, 36.2, 34.7, 32.3, 31.2, 27.4, 26.4, 26.1, 24.9, 24.7.

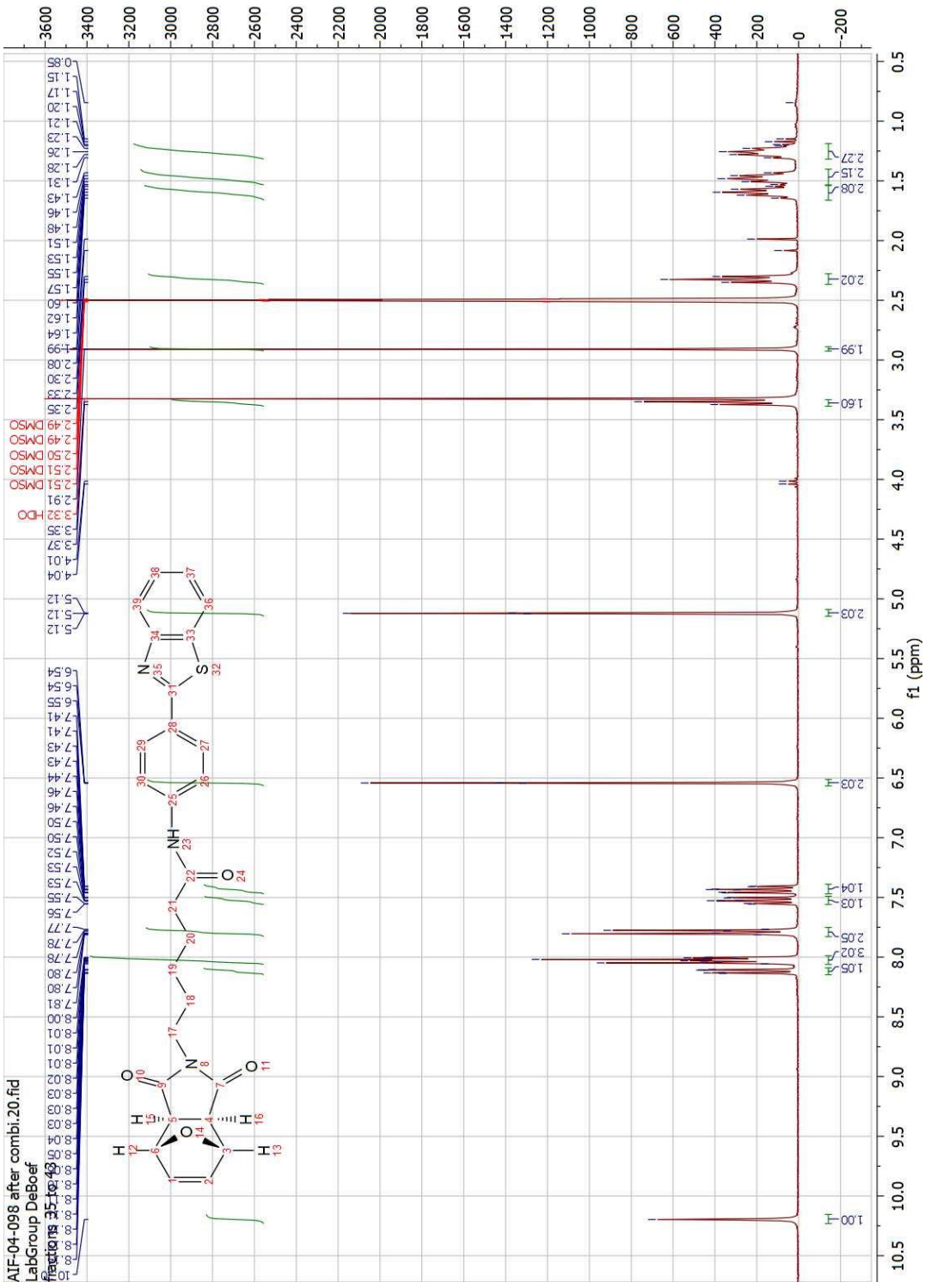

Figure 3.12: ^{1}H NMR of **9**

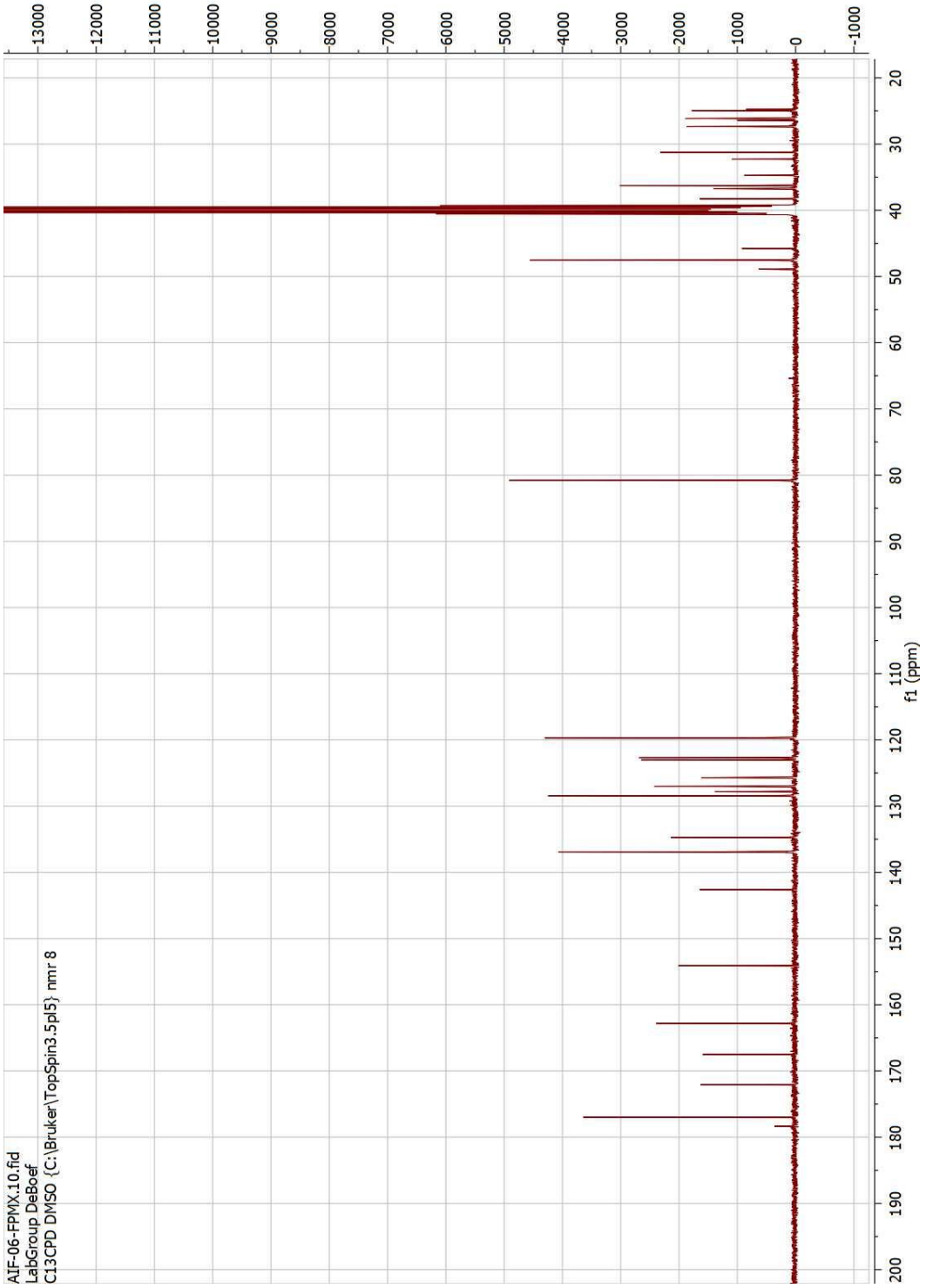

Figure 3.13: ^{13}C NMR of **9**

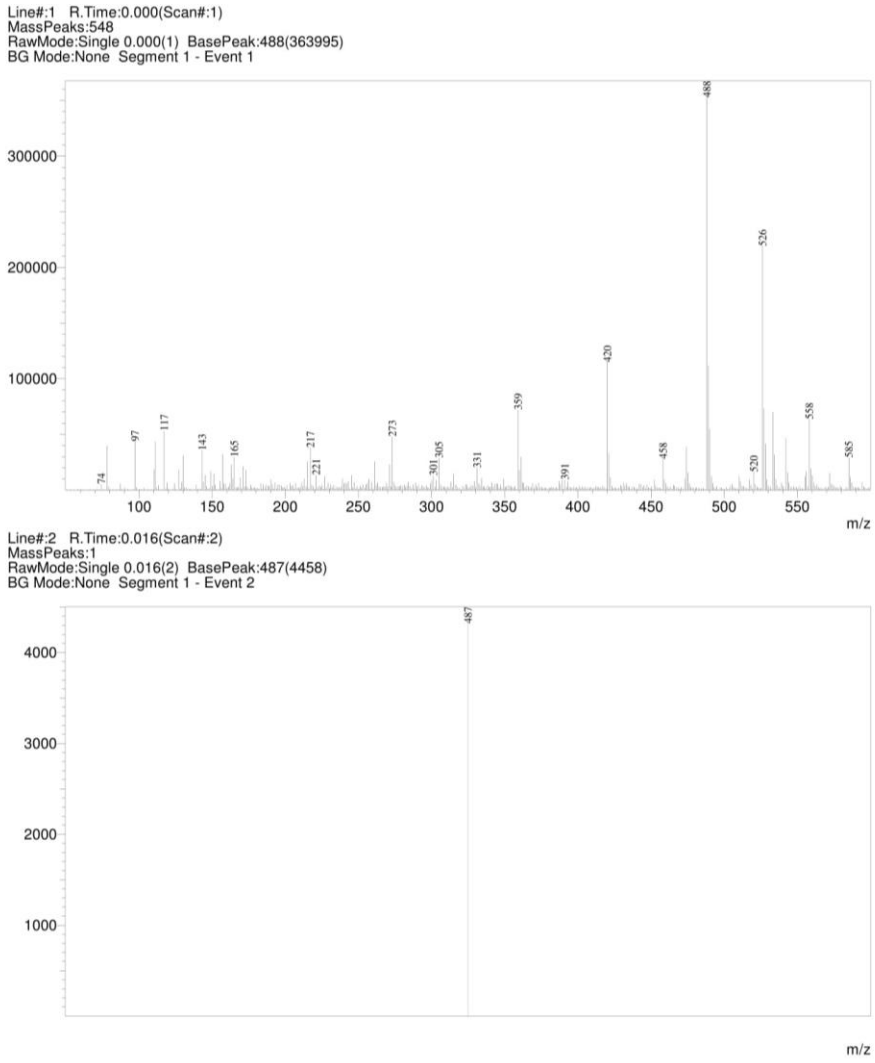

Figure 3.14: Mass spectrum of **9**

Synthesis of 2

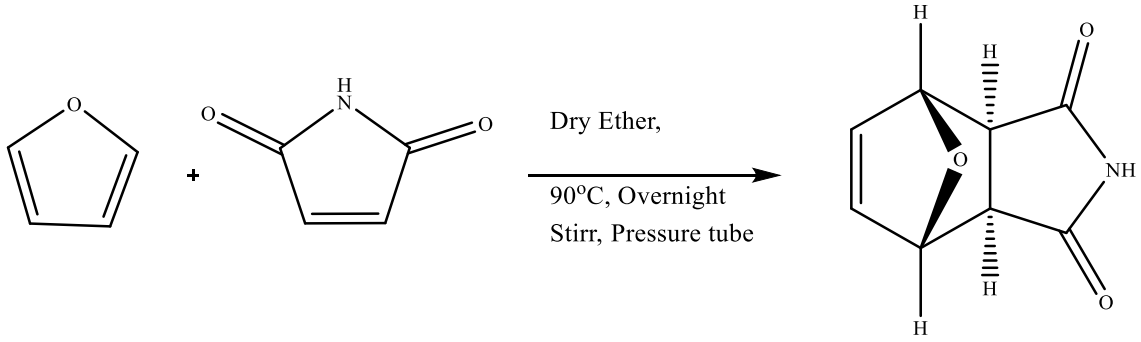

Maleimide (1.33g, 13.73 mmol) and furan (1.50 ml, 20.66 mmol) were dissolved in 10 mL diethyl ether in a sealed tube and heated to 90-100 °C for 12 hours. The 3, 6-Endoxo-Δ4-tetrahydrophthalhide (furan-masked maleimide) precipitated as a white solid after cooling the mixture to room temperature. The product was then filtered, washed with 3x10mL cold diethyl ether to remove the unreacted maleimide, giving rise to a yield of 6.04g (89%). The NMR spectra indicate that the product is exclusively the exo isomer. ^{1}H-NMR and ^{13}C-NMR were performed using DMSO-d_6. LRMS ESI (m/z): [M+H] calculated for $C_8H_7NO_3$ 165.04, observed 165.04. ^{1}H NMR (300 MHz, DMSO-d_6) δ 11.15 (br, 1H), 6.52 (d, J = 0.9 Hz, 2H), 5.11 (t, J = 0.9 Hz, 2H), 2.85 (s, 2H). ^{13}C NMR (101 MHz, DMSO-d_6) δ 178.3, 136.9, 80.8, 48.9.

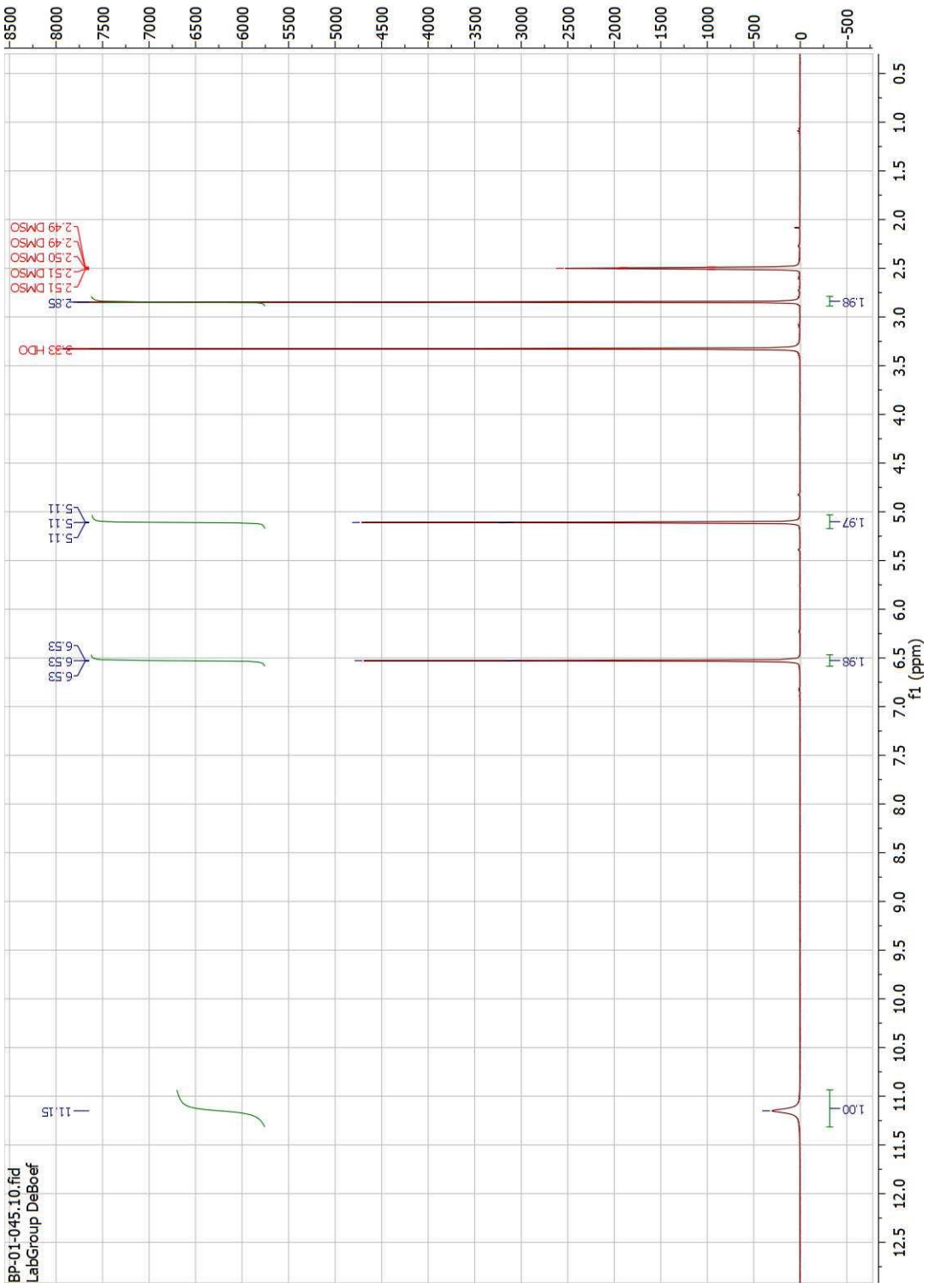

Figure 3.15 : ^{1}H NMR of **2**

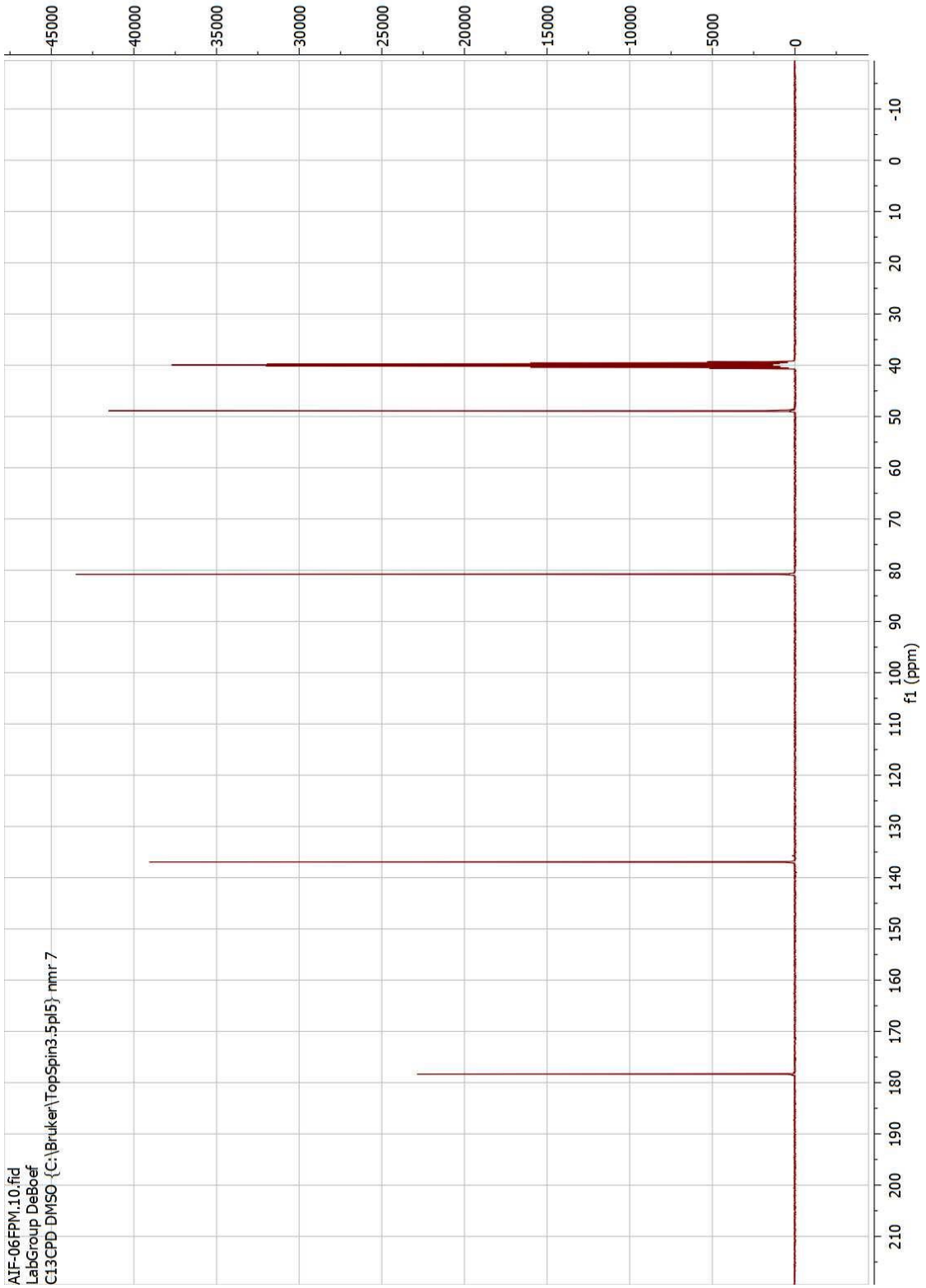

Figure 3.16: ^{13}C NMR of **2**

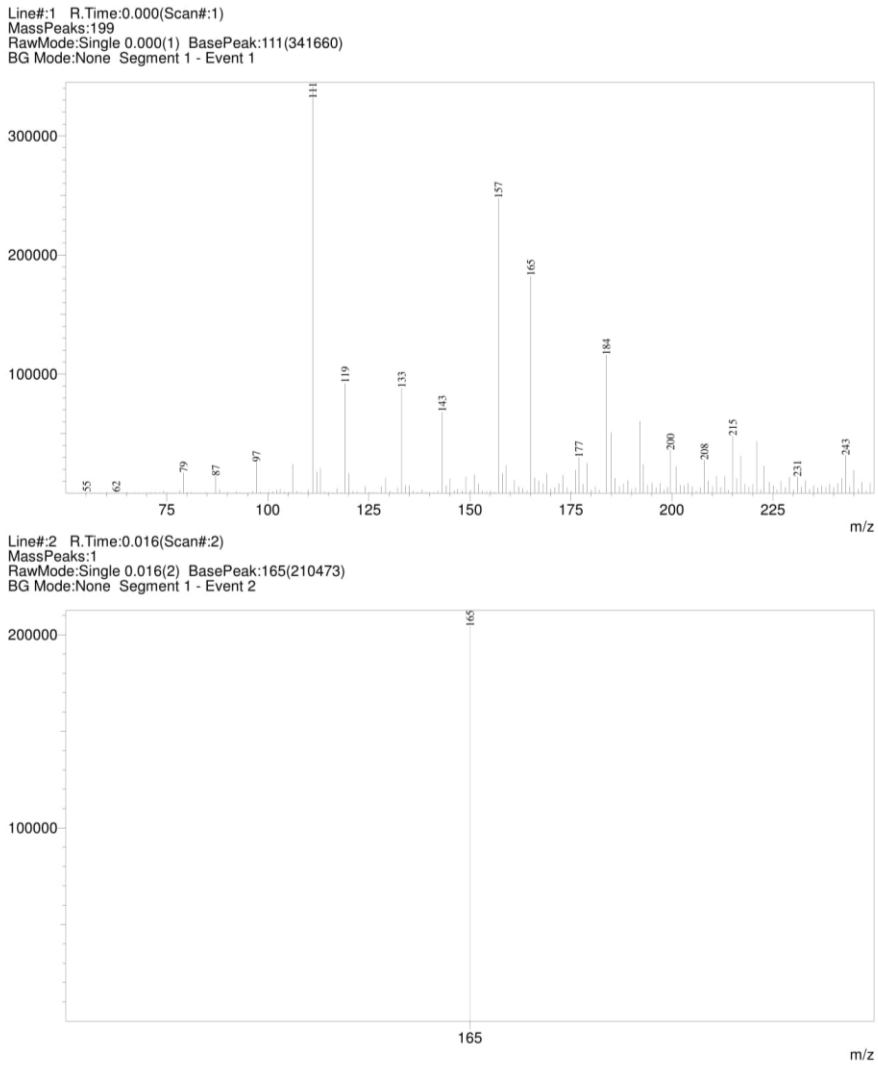

Figure 3.17: Mass spectrum of **2**

Synthesis of imine 1

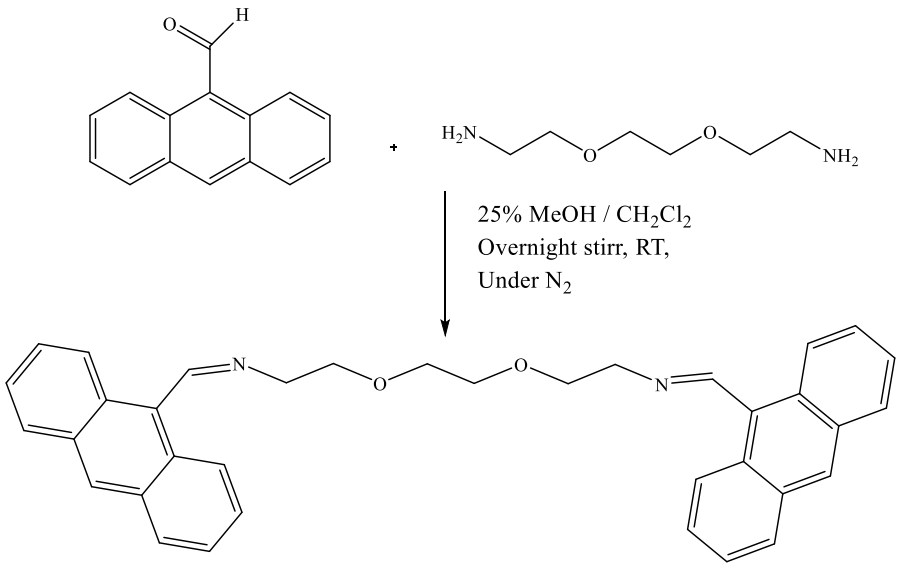

To a stirred solution of 2,2′-(Ethylenedioxy)bis(ethylamine) (730.0 µl, 5.00 mmol) in 25% MeOH/CH_2Cl_2 (10 mL), was added a solution of 9-anthraldehyde (2.16 g, 10.5 mmol) in 25% MeOH/CH_2Cl_2 (10 mL) under N_2. The mixture was stirred at room-temperature overnight until the imine formation was complete (monitored by TLC). The solvent was evaporated under vacuum to give the crude imine product as a yellow solid, which was used for reduction without further purification. Reaction yield was 96%. ^{1}H-NMR was performed using DMSO-d_6. HRMS ESI (m/z): [M+H] calculated for $C_{36}H_{33}N_2O_2$ 525.2542, observed 525.2485. ^{1}H NMR (300 MHz, DMSO-d_6) δ 9.31 (d, J = 1.4 Hz, 2H), 8.62 (s, 2H), 8.55 – 8.45 (m, 4H), 8.14 – 8.04 (m, 4H), 7.57 – 7.47 (m, 8H), 3.97 (t, J = 5.8 Hz, 4H), 3.87 (t, J = 5.4 Hz, 4H), 3.35 (s, 2H), 3.18 (s, 3H).

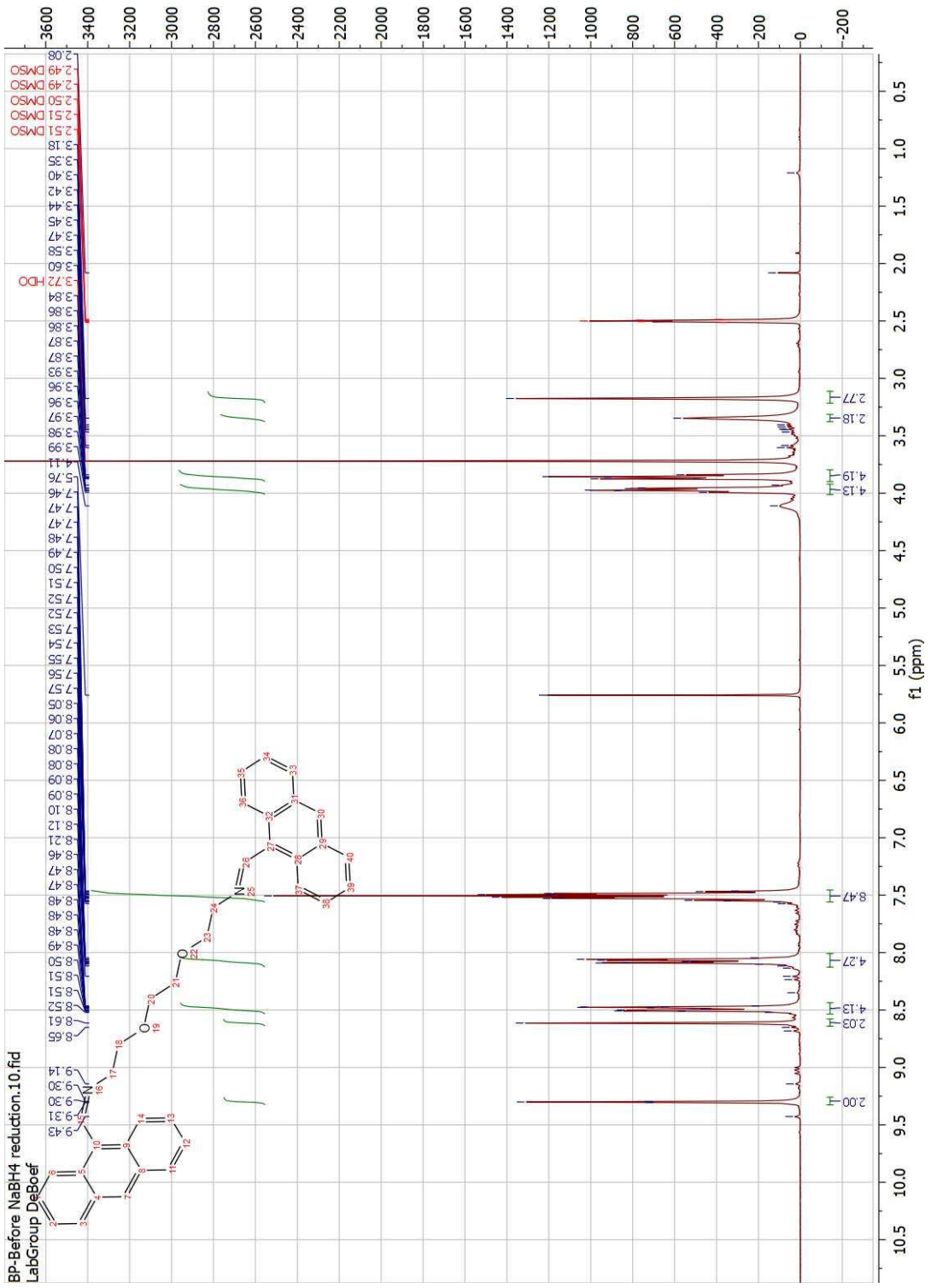

Figure 3.18: ^{1}H NMR of imine **1**

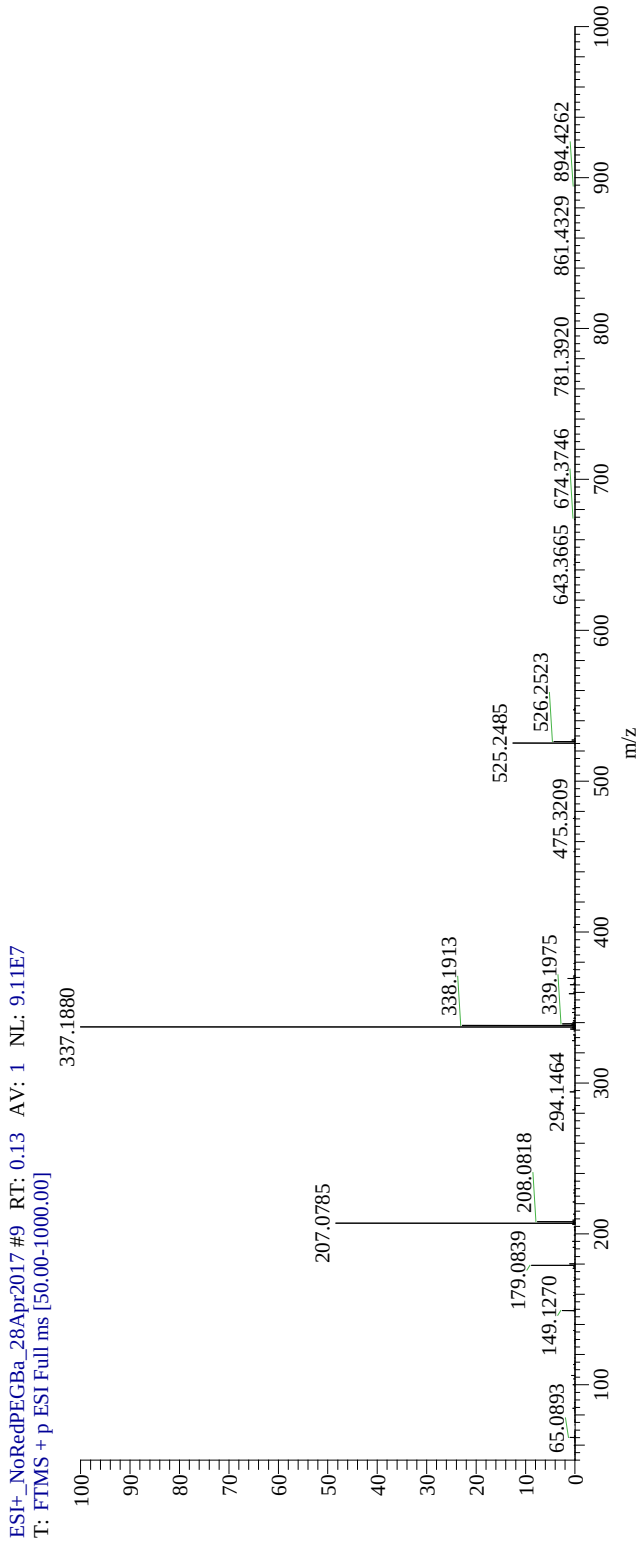

Figure 3.19: Mass spectrum of imine **1**

Synthesis of 1

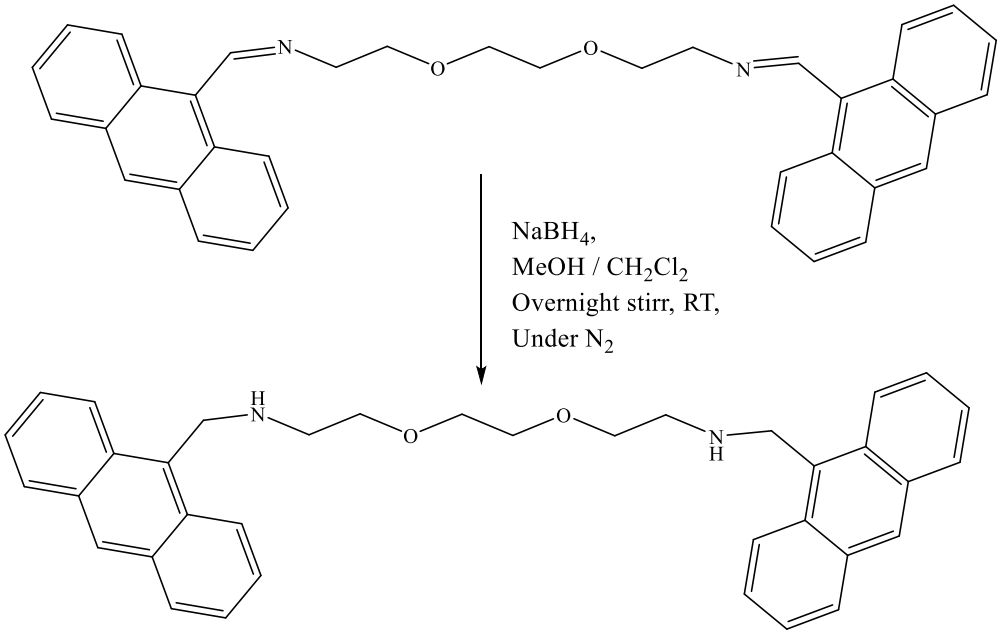

$NaBH_4$ (3 equiv.) was added in small portions to the solution of crude imine (1 equiv.) in 1:1 CH_3OH: CH_2Cl_2 (20 mL) at 0°C. The mixture was stirred at room temperature overnight, then concentrated under vacuum. The residue was dissolved in CH_2Cl_2 (50 mL) and washed three times with 50mLof aqueous Na_2CO_3 (pH=10). The organic layer was separated, dried over anhydrous Na_2SO_4, filtered, and concentrated under vacuum to provide the secondary amines. Reaction yield was 90%. ^{1}H-NMR and ^{13}C-NMR were performed using DMSO-d_6. HRMS ESI (m/z): [M+H] calculated for $C_{36}H_{36}N_2O_2$ 529.2855, observed 529.2794. ^{1}H NMR (300 MHz, DMSO-d_6) δ 8.50 (s, 2H), 8.40 – 8.31 (m, 4H), 8.05 (dd, J = 7.7, 2.0 Hz, 4H), 7.55 – 7.44 (m, 8H), 4.58 (s, 4H), 3.49 (t, J = 5.6 Hz, 8H), 2.82 (t, J = 5.6 Hz, 4H), 2.03 (br, 2H). ^{13}C NMR (101 MHz, DMSO-d_6) δ 135.0, 132.7, 131.5, 130.3, 129.2, 127.0, 126.3, 125.5, 125.1, 70.5, 70.1, 49.3, 45.2.

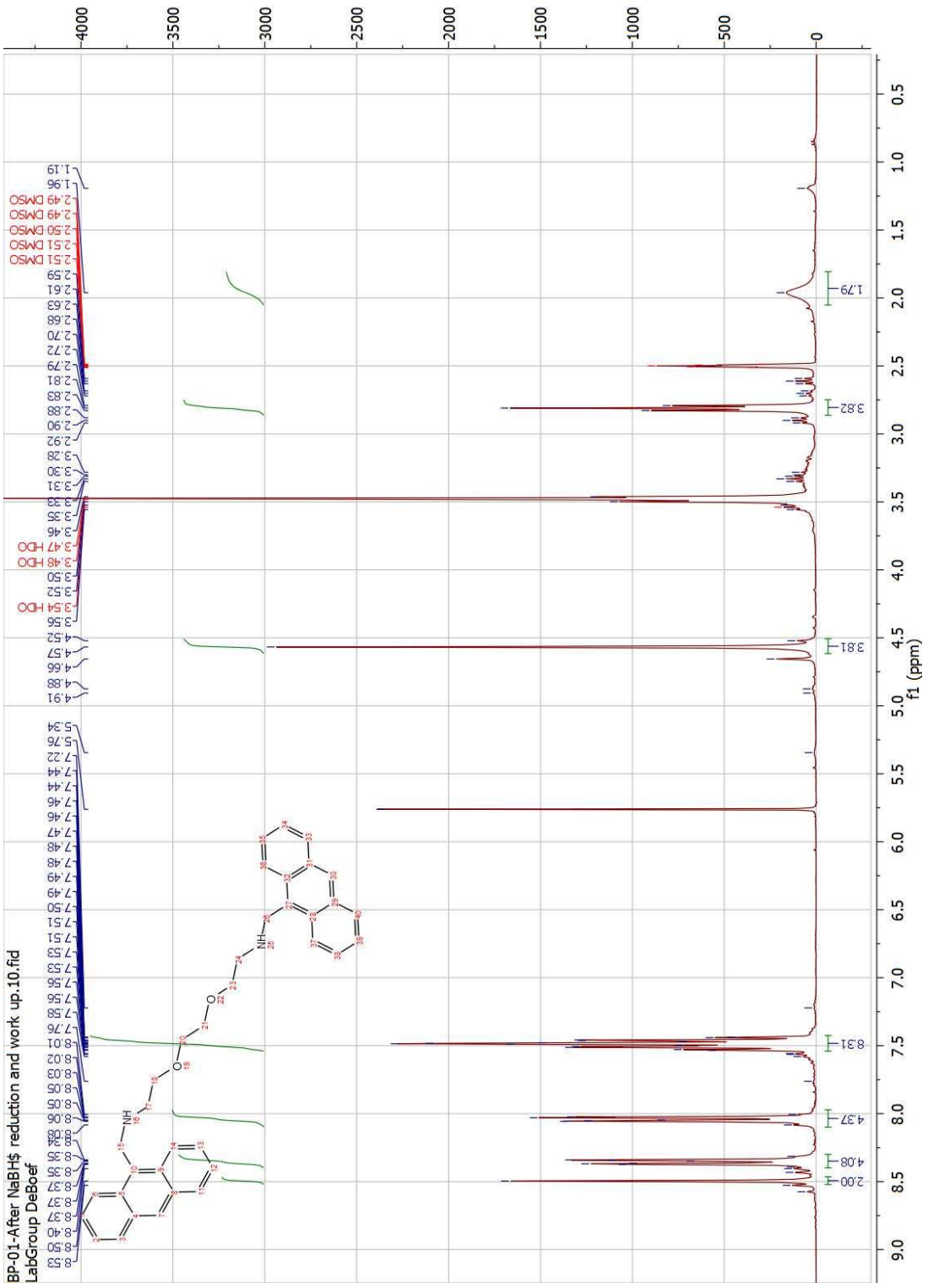

Figure 3.20: ^{1}H NMR of **1**

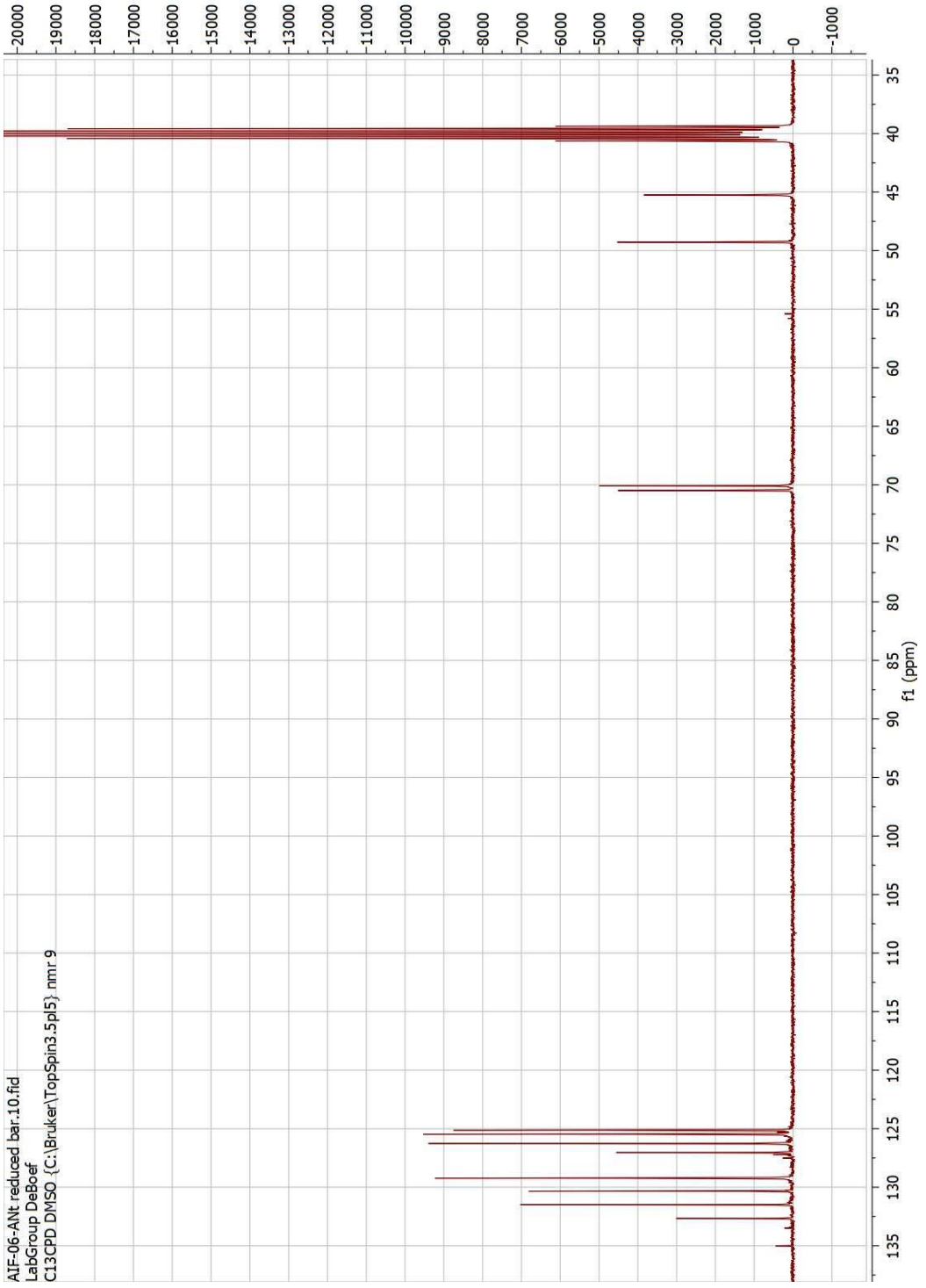

Figure 3.21: ^{13}C NMR of **1**

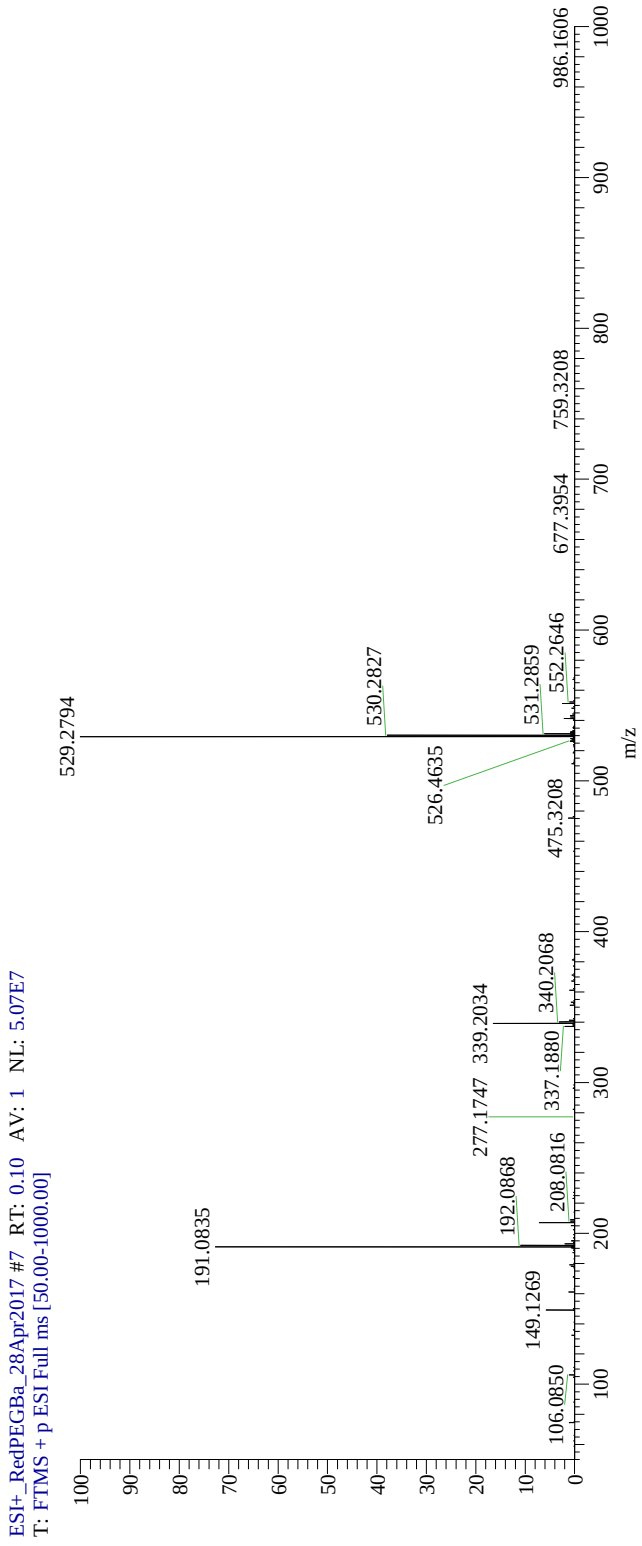

Figure 3.22: Mass spectrum of **1**

Diels alder reaction with 1 and 2 [without γ-CD]

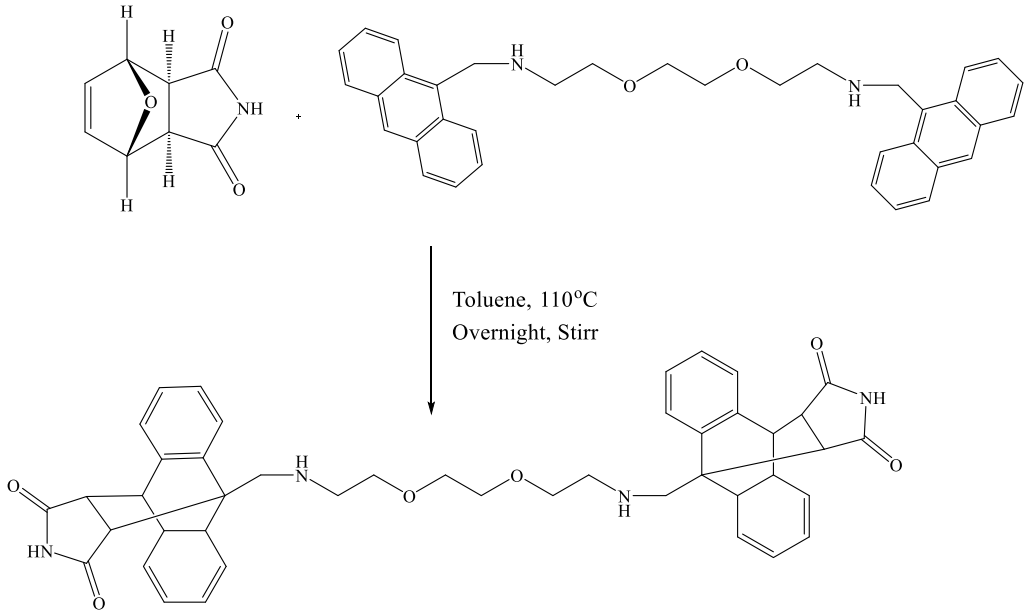

8 (2.2 equiv.) and **4** (1 equiv.) was mixed in 20 ml of Toluene. This reaction mixture was refluxed at 110°C for overnight. Physical observation of the formation of Diels-alder adduct was observed by the change of colors from yellow solution to white with precipitate. Next, the reaction mixture was subjected for rotary evaporation until dryness and dried overnight under high vacuum. Reaction yield was 45%. ^{1}H-NMR and ^{13}C-NMR were performed using DMSO-d_6. HRMS ESI (m/z): [M+H] calculated for $C_{44}H_{46}N_4O_6$ 723.3081, observed 723.3083. ^{1}H NMR (400 MHz, DMSO-d_6) δ 10.68 (br, 2H), 7.50 (dd, *J* = 7.3, 1.5 Hz, 2H), 7.42 (dd, *J* = 6.9, 1.7 Hz, 2H), 7.25 (ddd, *J* = 7.0, 4.0, 1.9 Hz, 5H), 7.13 (dddt, *J* = 12.6, 8.7, 5.1, 1.5 Hz, 9H), 4.65 (d, *J* = 3.3 Hz, 2H), 3.95 (d, *J* = 12.3 Hz, 2H), 3.76 (d, *J* = 12.3 Hz, 2H), 3.66 (d, *J* = 6.3 Hz, 7H), 3.28 (dd, *J* = 8.7, 3.1 Hz, 2H), 3.24 – 3.20 (m, 2H), 3.09 – 2.95 (m, 4H), 2.30 (s, 2H), 1.95 (br, 2H). ^{13}C NMR (101 MHz, DMSO-d_6) δ 178.4, 177.9, 143.5, 141.2, 140.4, 129.4, 128.7, 126.8, 126.6, 126.3, 125.2, 124.3, 124.1, 122.8, 70.3, 50.0, 49.1, 48.5, 47.2, 45.0.

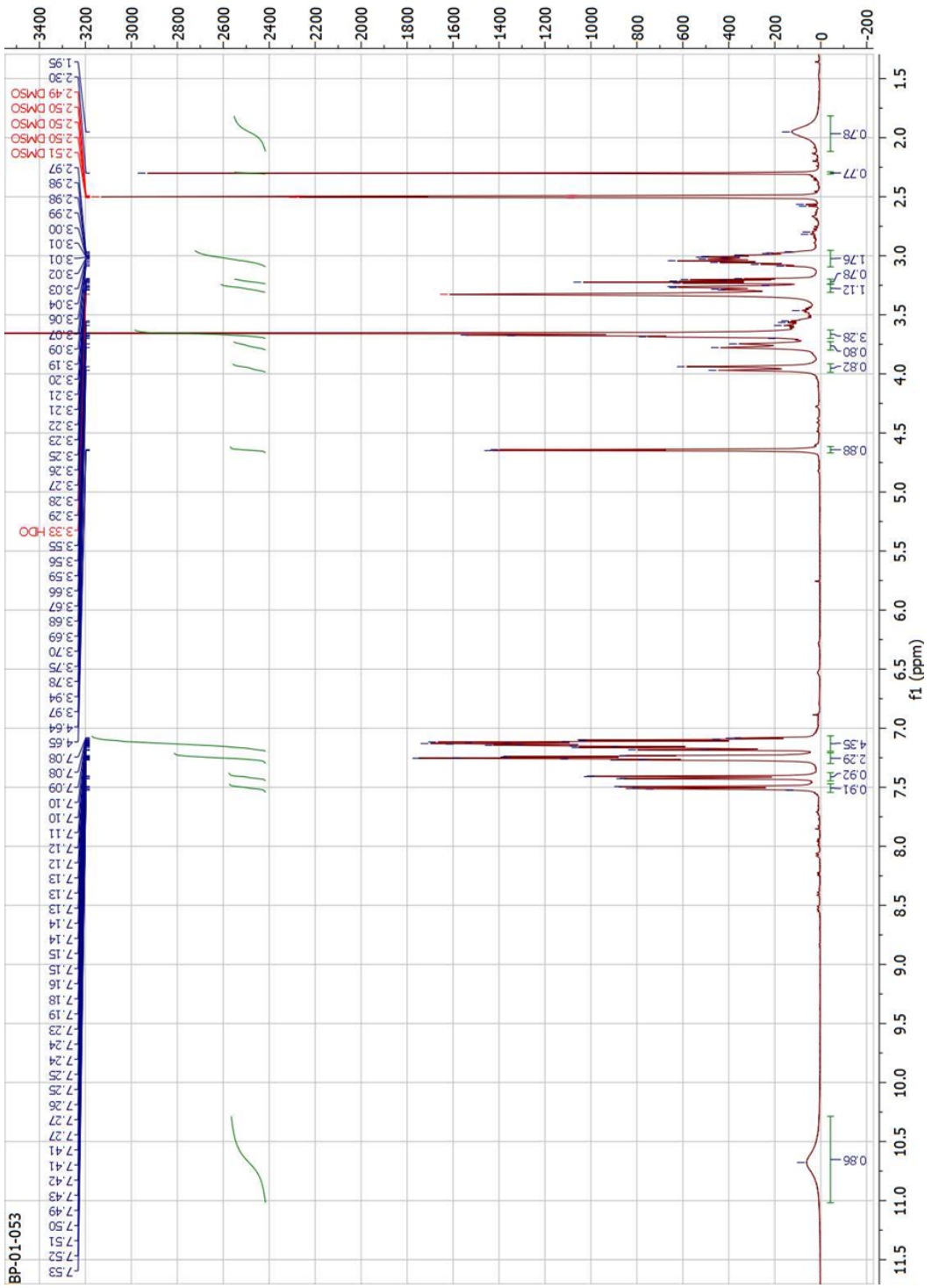

Figure 3.23: ^{1}H NMR of reaction with **1** and **2** [without γ-CD]

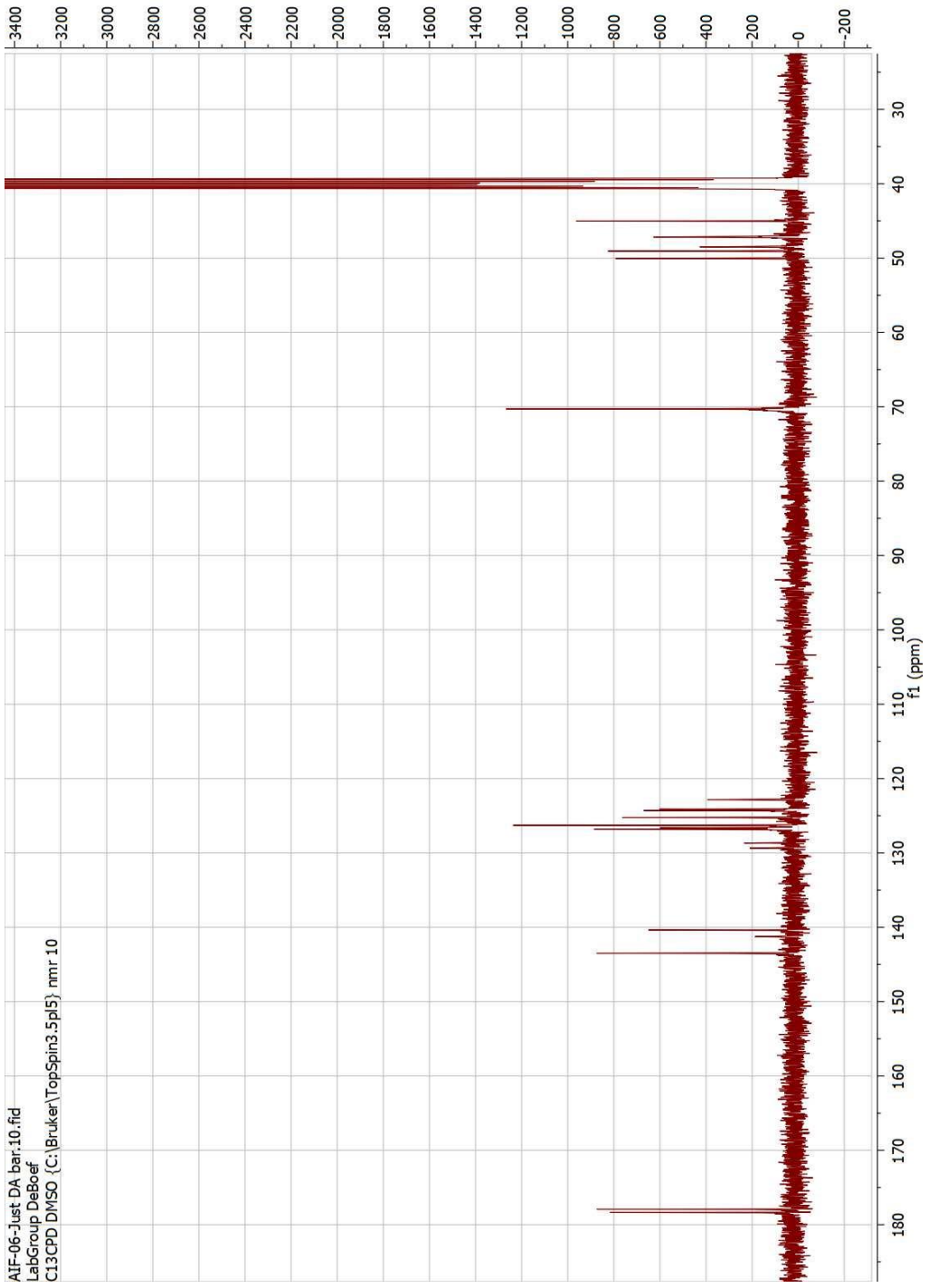

Figure 3.24: ^{13}C NMR of reaction with **1** and **2** [without γ-CD]

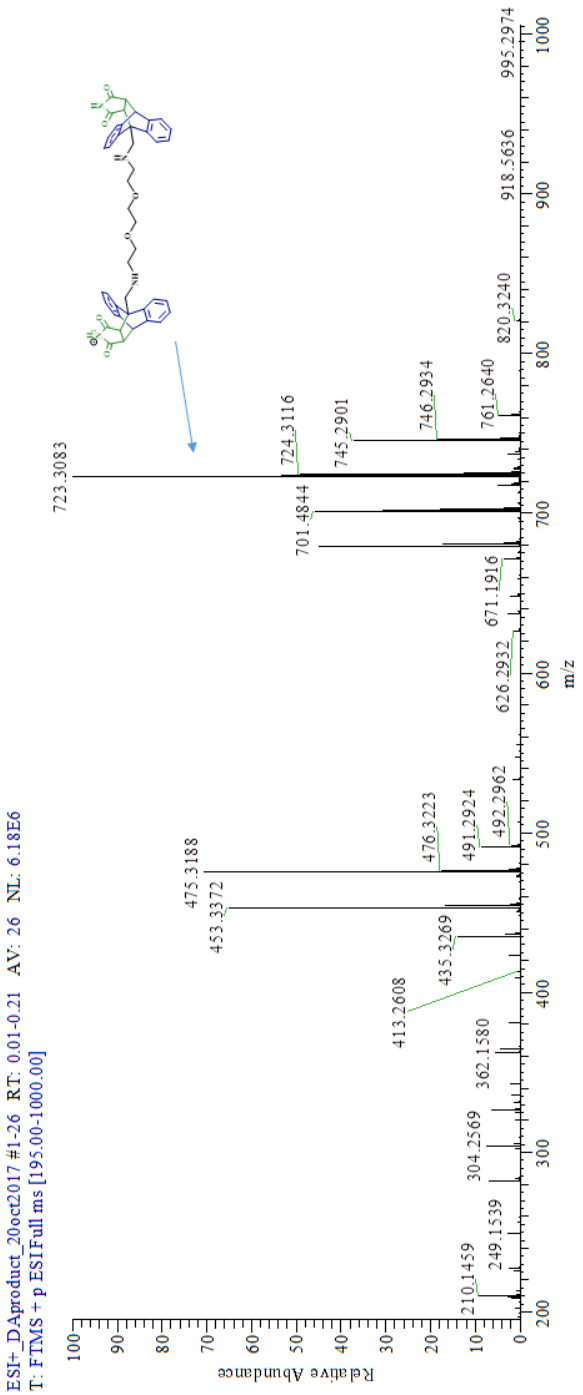

Figure 3.25: Mass spectrum of reaction with **1** and **2** [without γ-CD]

Synthesis of 3, 4 and 5

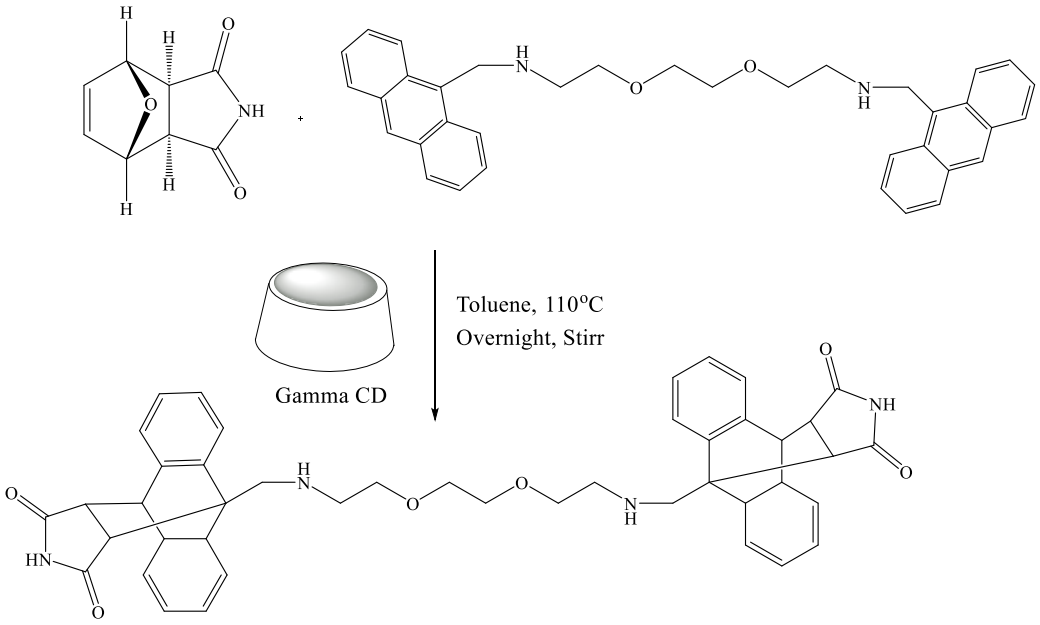

γ-CD (1 equiv.) and **4** (1 equiv.) was mixed in 20 ml of Toluene. This reaction mixture was ultrasonicated for 15 minutes. Then it was heated at 80°C for another 15 minutes. To this solution **8** (2.4 equiv.) was added and the complete reaction mixture was refluxed at 110°C for overnight. Physical observation of the formation of Diels-alder adduct was observed by the change of colors from yellow solution to white with precipitate. Next, the reaction mixture was subjected for rotary evaporation until dryness and dried overnight under high vacuum. By changing the addition equivalents to 1 or 2 of the γ-CD, it was possible to obtain 1 or 2 CDs on the thread. Reaction yield was 90%, 89% and 83% in the order of 1:1, 1:2 and 2:1. ^{1}H-NMR, ^{13}C-NMR and ROESY NMR was performed using DMSO-d_6.

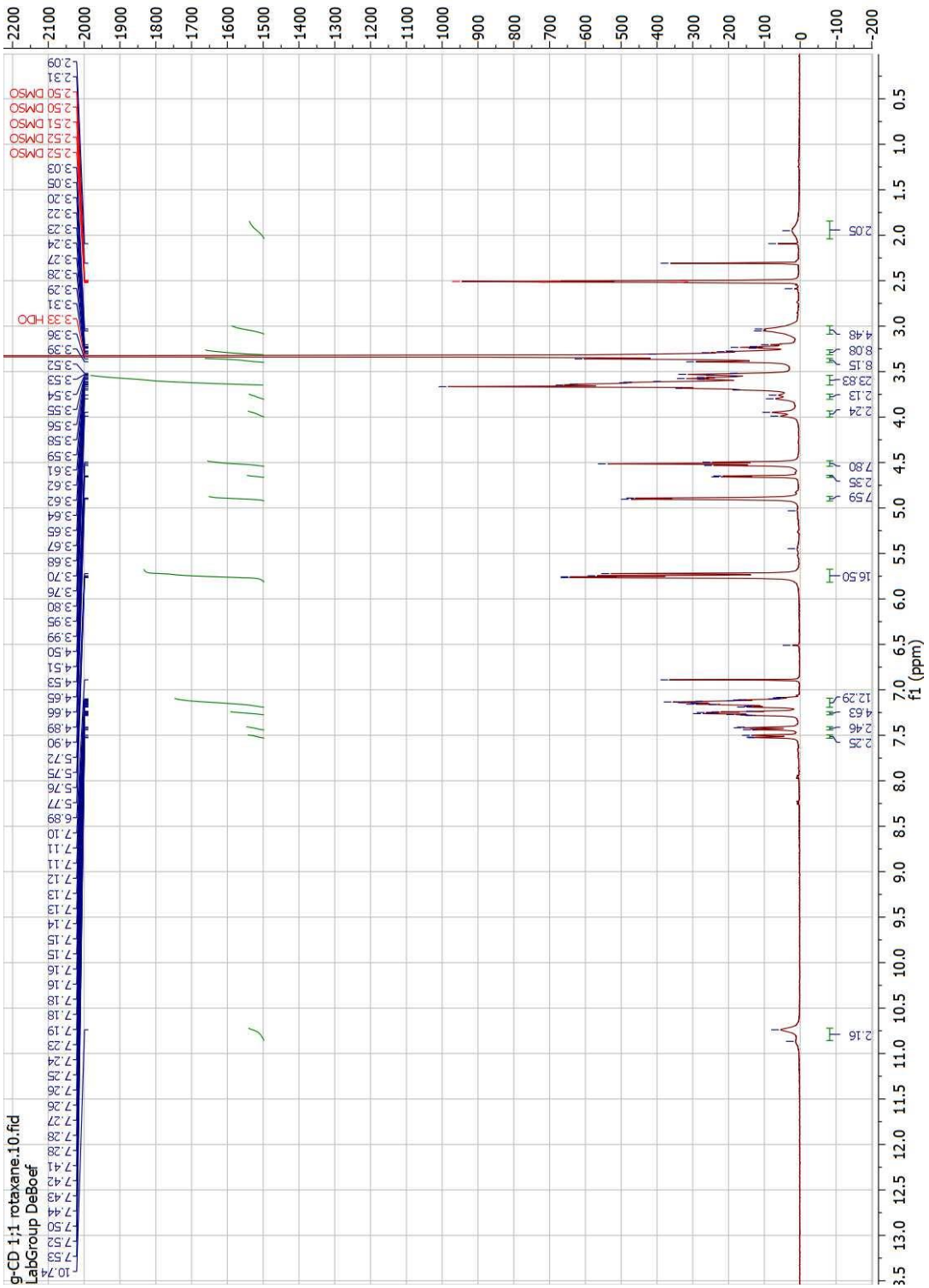

Figure 3.26: ^{1}H NMR of **3**

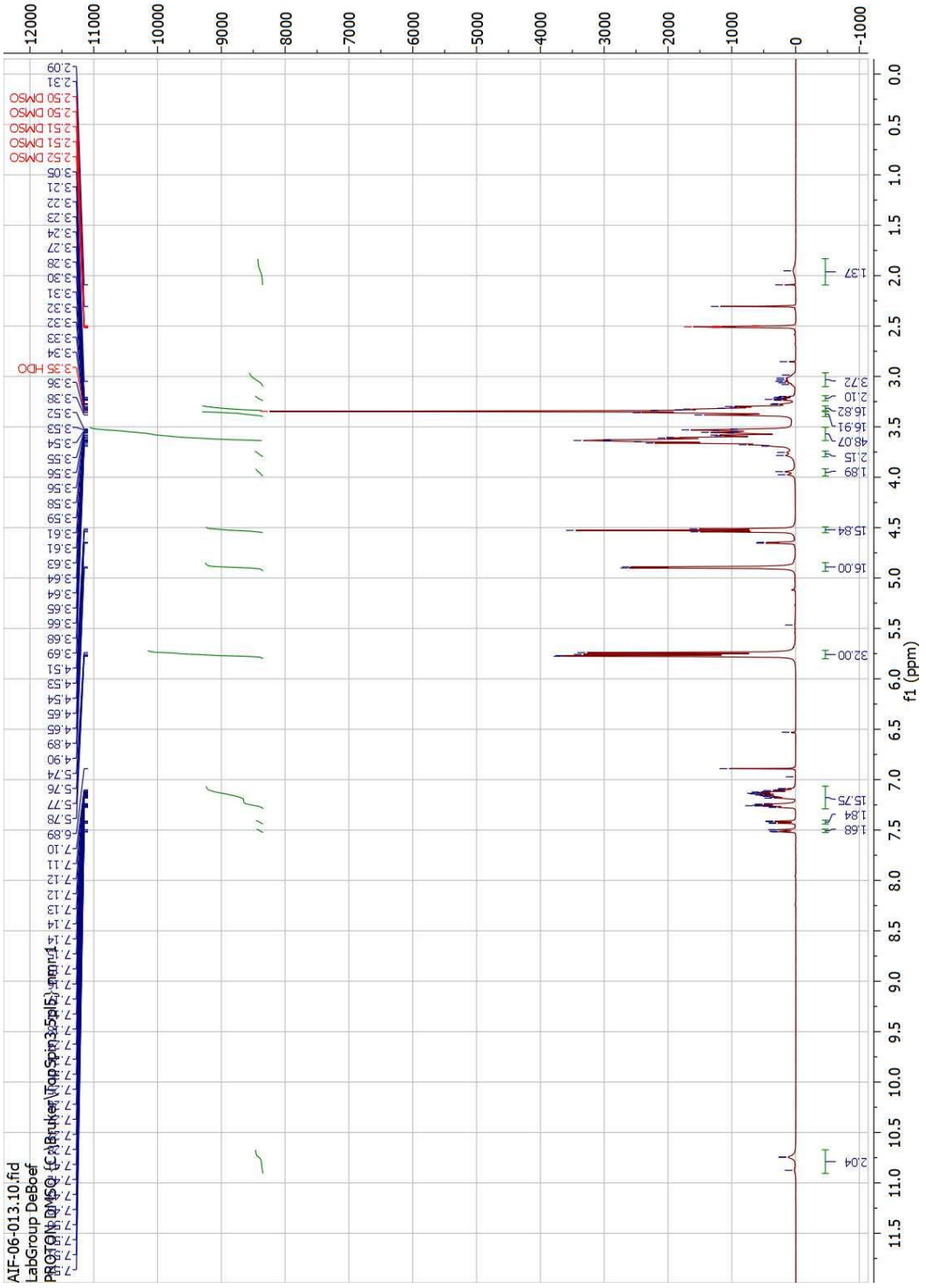

Figure 3.27: ^{1}H NMR of **4**

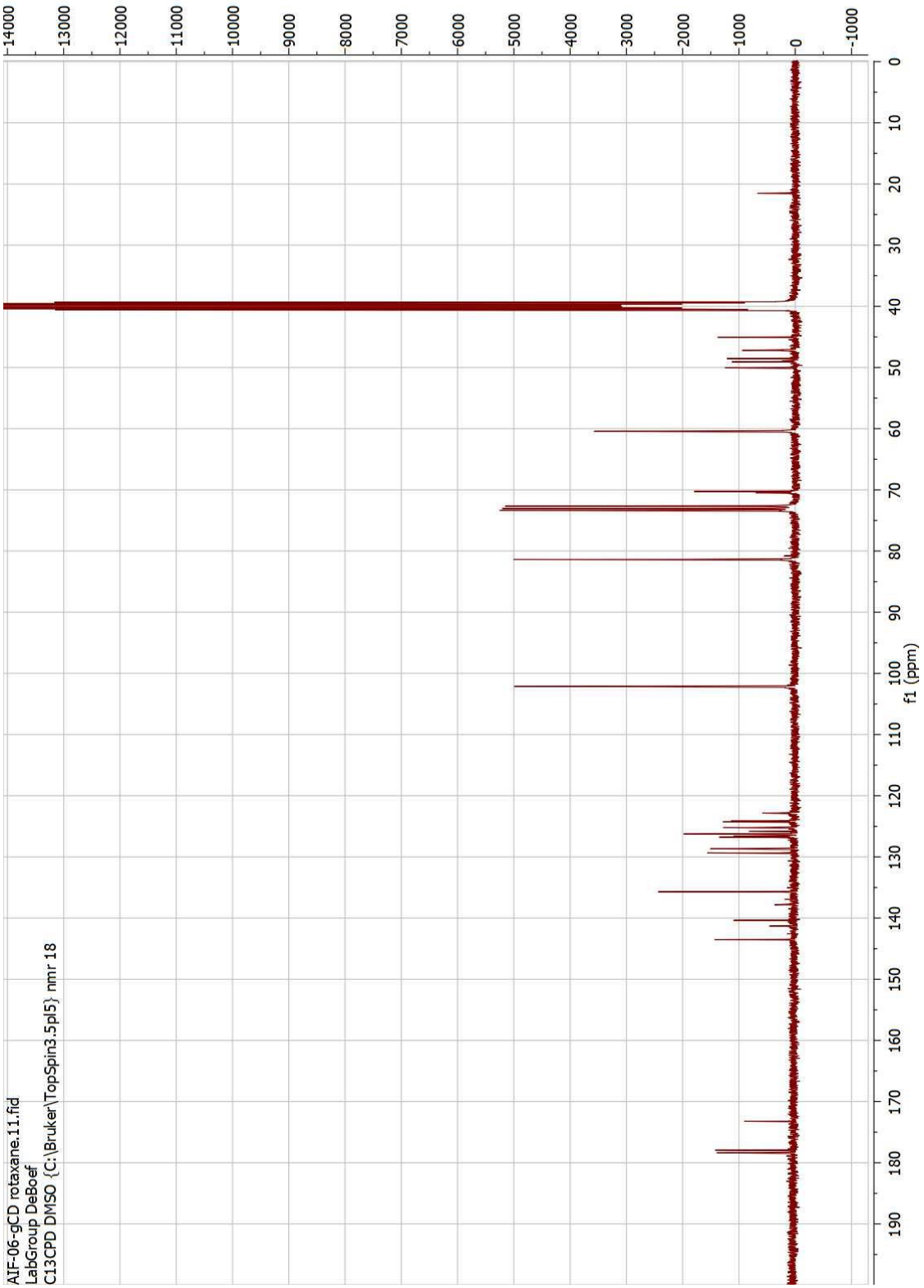

Figure 3.28: ^{13}C NMR of **3**

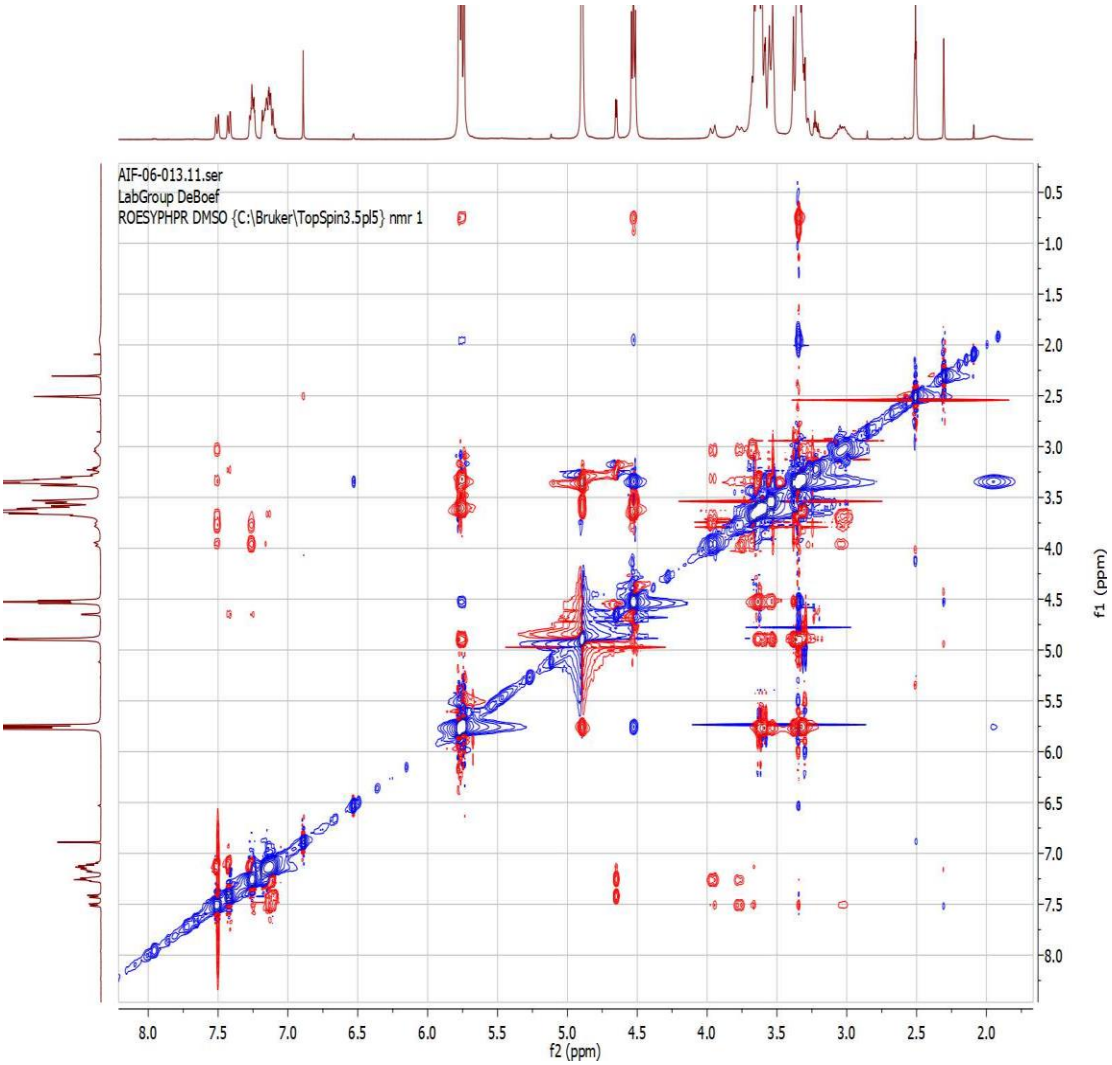

Figure 3.29: ROESY NMR of **3**, with a mixing time 500 ms

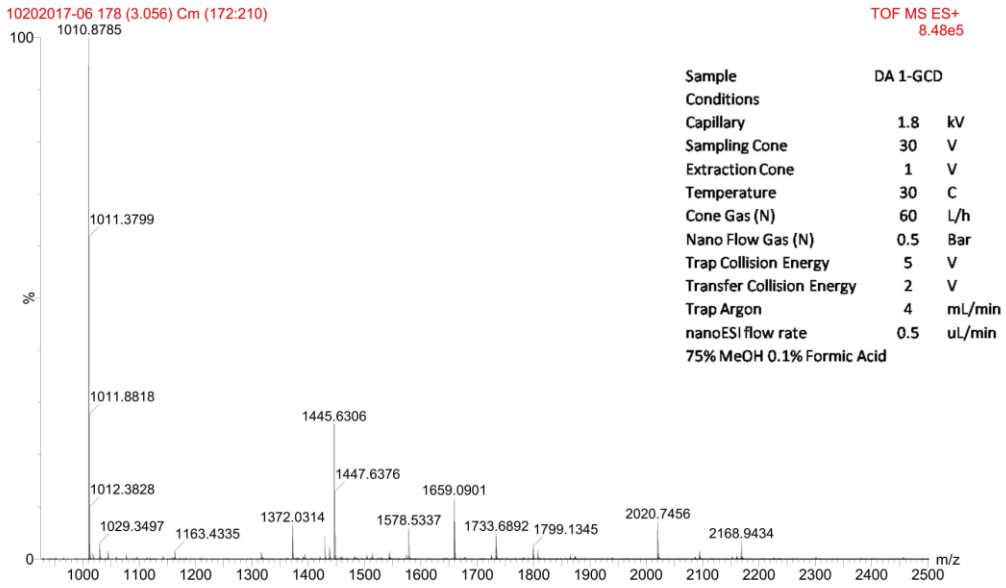

Figure 3.30: Complete mass spectrum of **3**

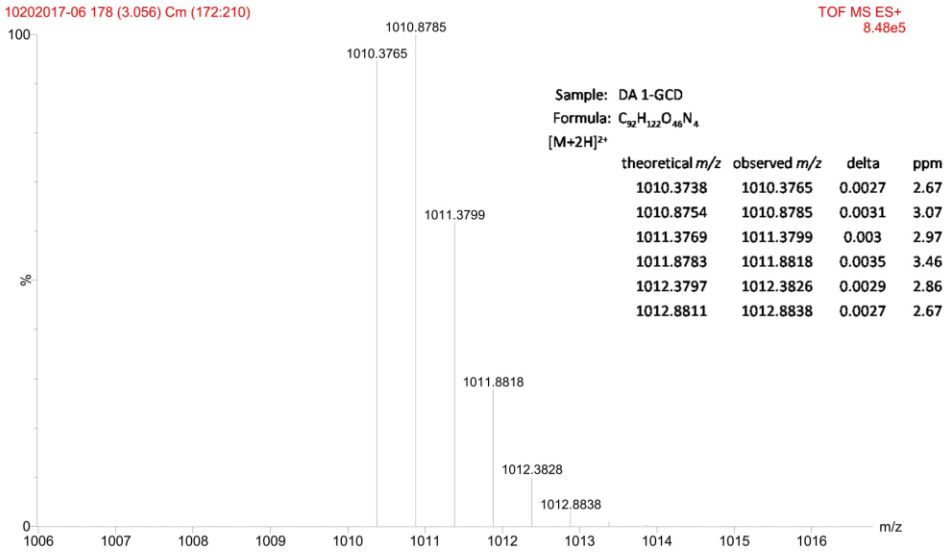

Figure 3.31: mass spectrum of 3 at the range of 1006 – 1016 m/z

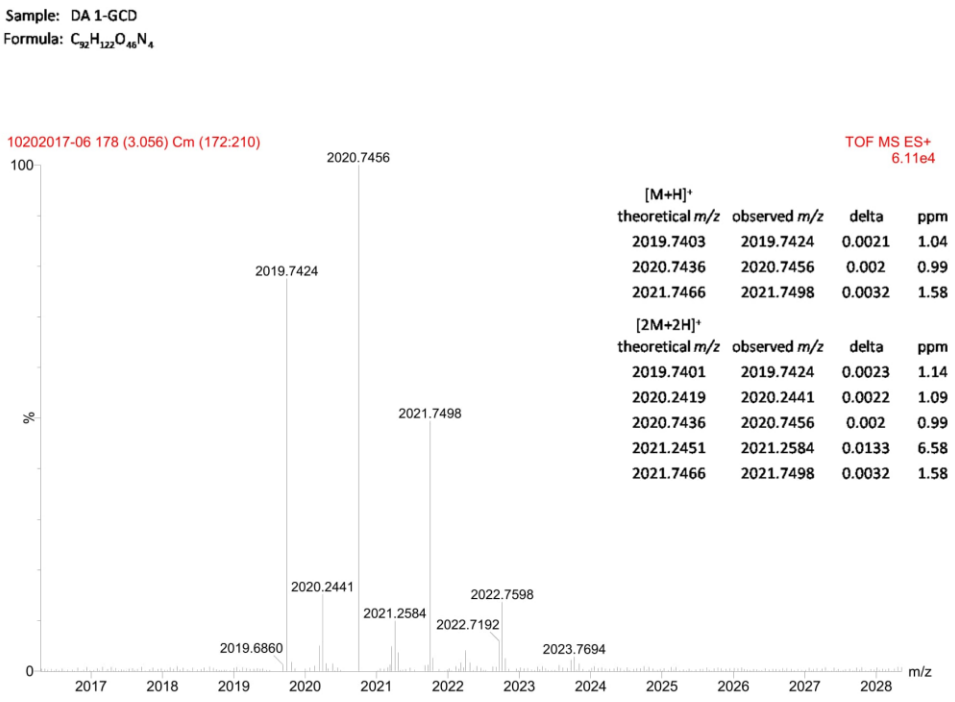

Figure 3.32: mass spectrum of 3 at the range of 2017 – 2028 m/z

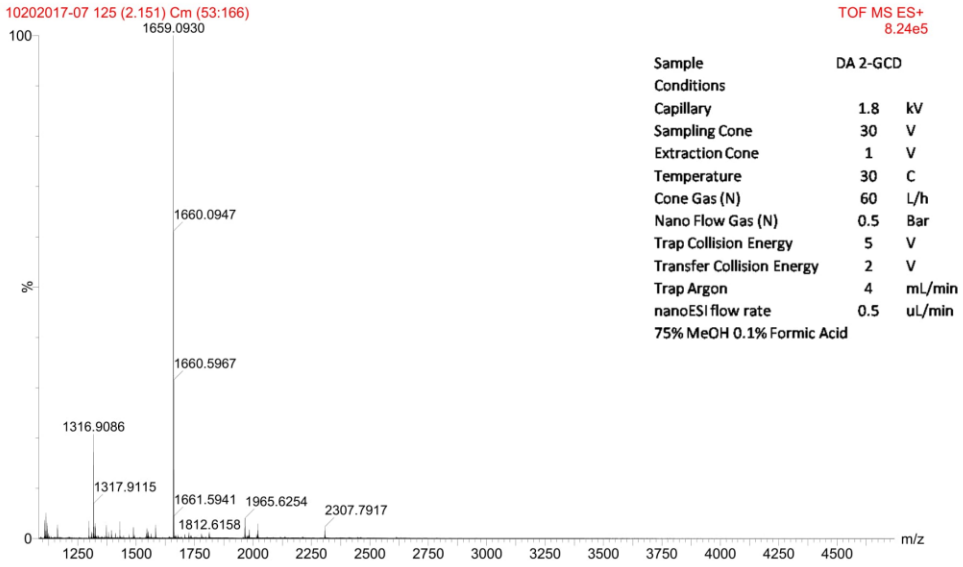

Figure 3.33: Complete mass spectrum of **4**

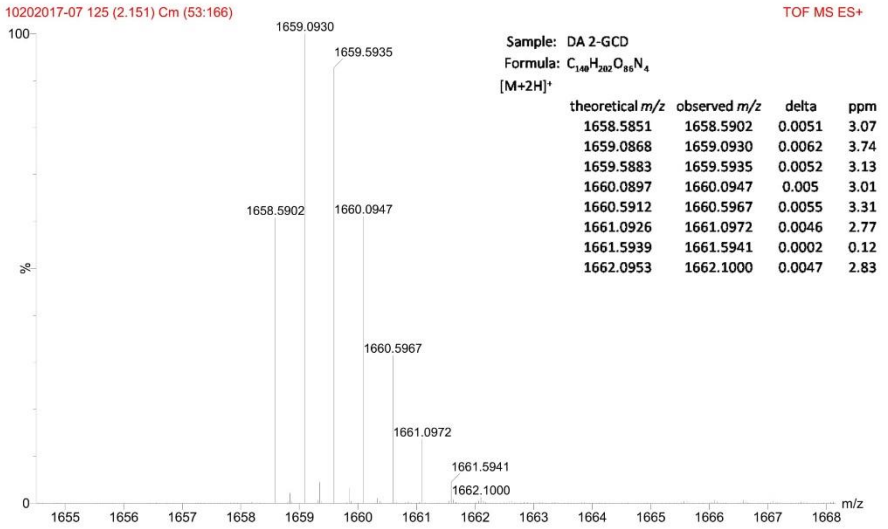

Figure 3.34: mass spectrum 4 at the range of 1655-1668 m/z

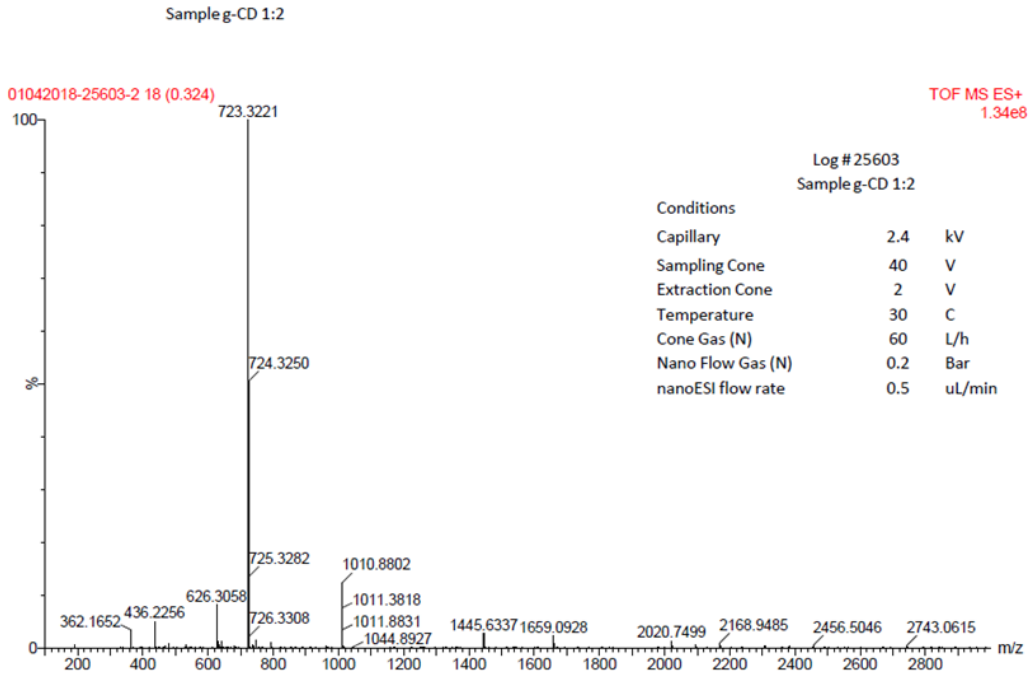

Figure 3.35: Complete mass spectrum of 5

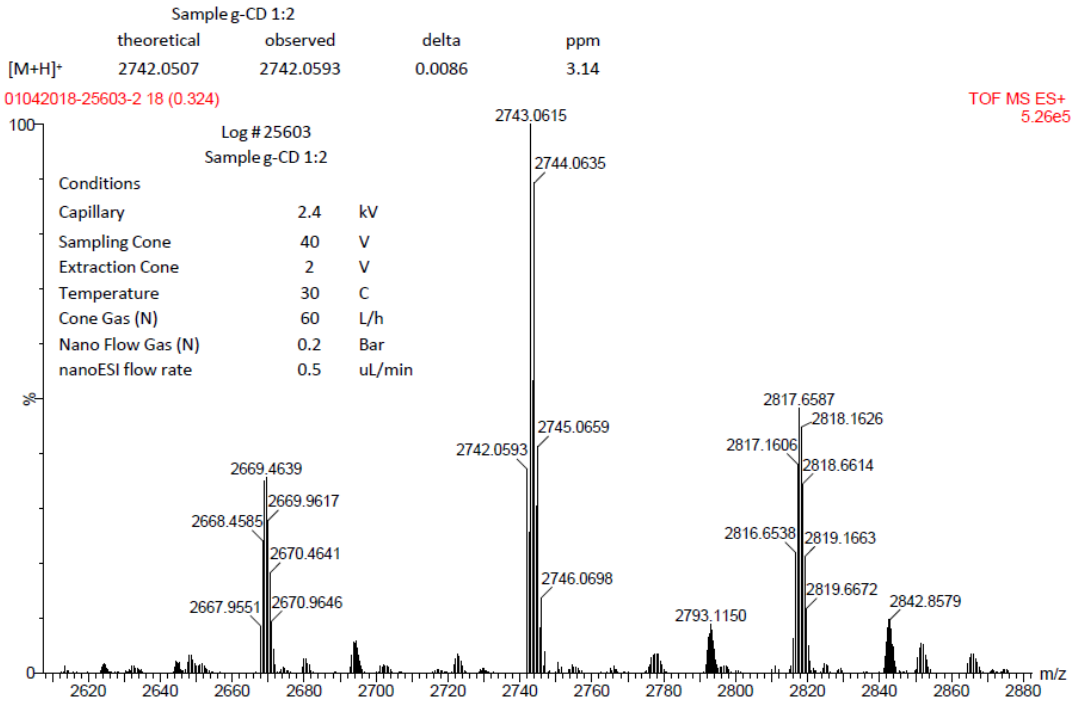

Figure 3.36: mass spectrum of 5 at the range of 2620 - 2880 m/z

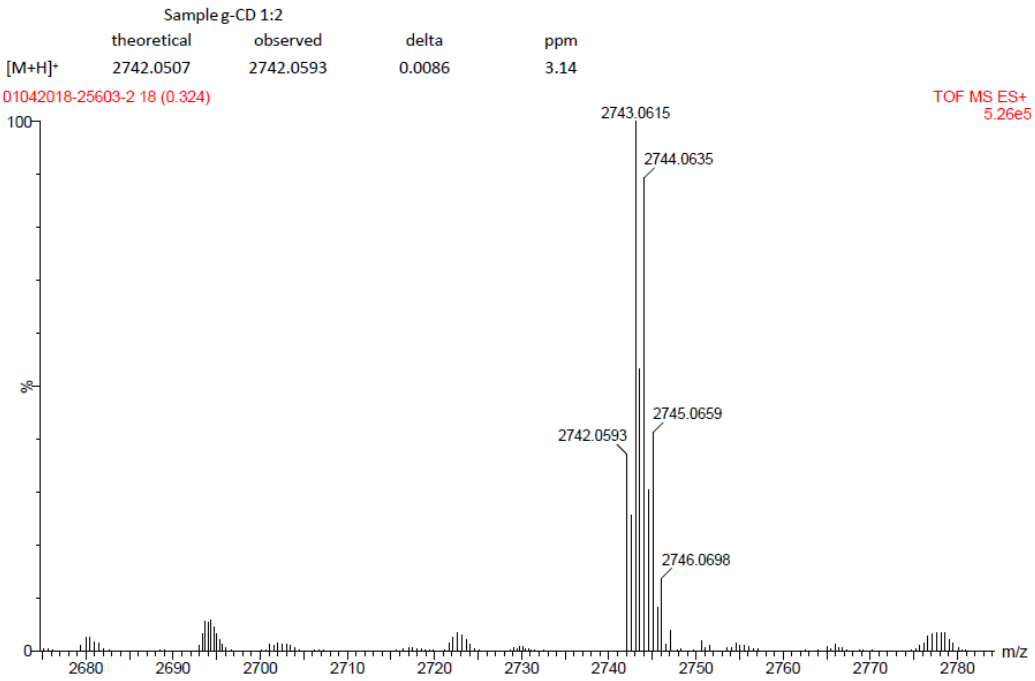

Figure 3.37: mass spectrum of 5 at the range of 2680 - 2780 m/z

Synthesis of 6,7 and 8

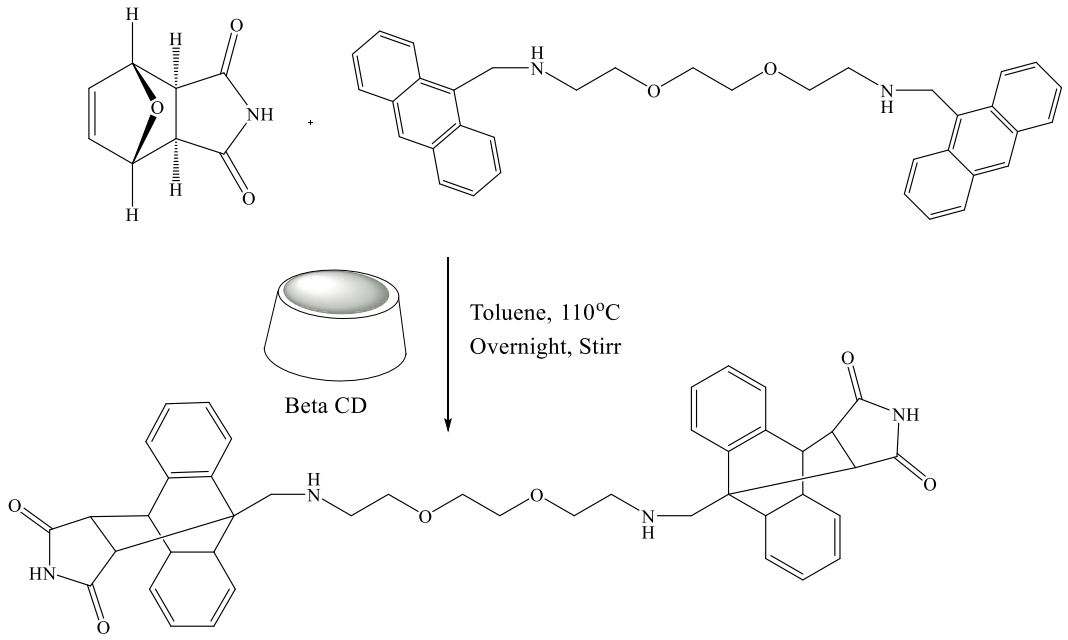

β-CD (1 equiv.) and **4** (1 equiv.) was mixed in 20 ml of Toluene. This reaction mixture was ultrasonicated for 15 minutes. Then it was heated at 80°C for another 15 minutes. To this solution **8** (2.4 equiv.) was added, and the complete reaction mixture was refluxed at 110°C for overnight. Physical observation of the formation of Diels-alder adduct was observed by the change of colors from yellow solution to white with precipitate. Next, the reaction mixture was subjected for rotary evaporation until dryness and dried overnight under high vacuum. By changing the addition equivalents to 1 or 2 of the β-CD, it was possible to obtain 1 or 2 CDs on the thread, resulting 1:2 and 2:1 rotaxanes. Reaction yield was 91%, 92%, 94% in the order of 1:1, 1:2 and 2:1. ^{1}H-NMR, ^{13}C-NMR and ROESY NMR was performed using DMSO-d_6.

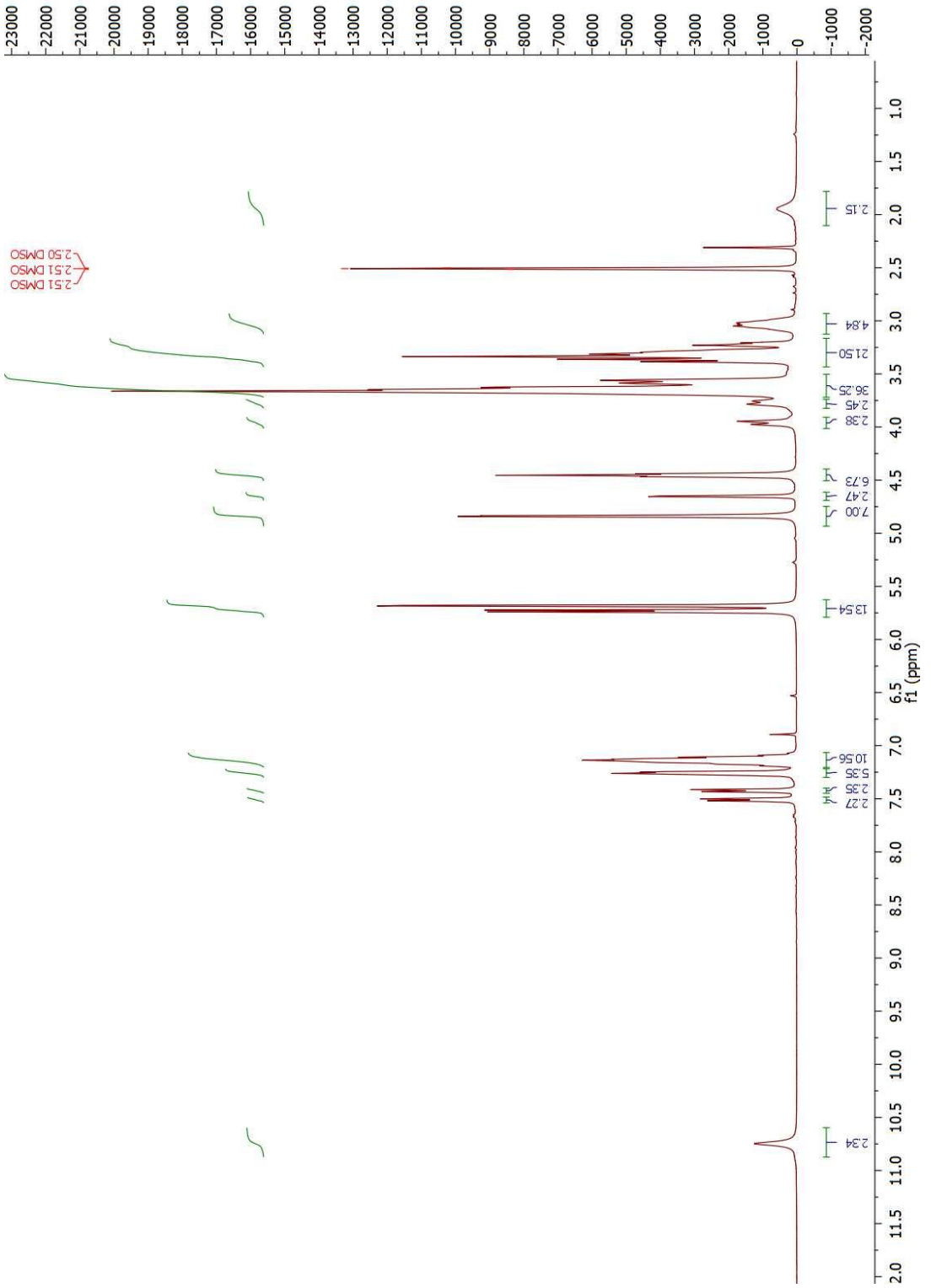

Figure 3.38: ^{1}H NMR for **6**

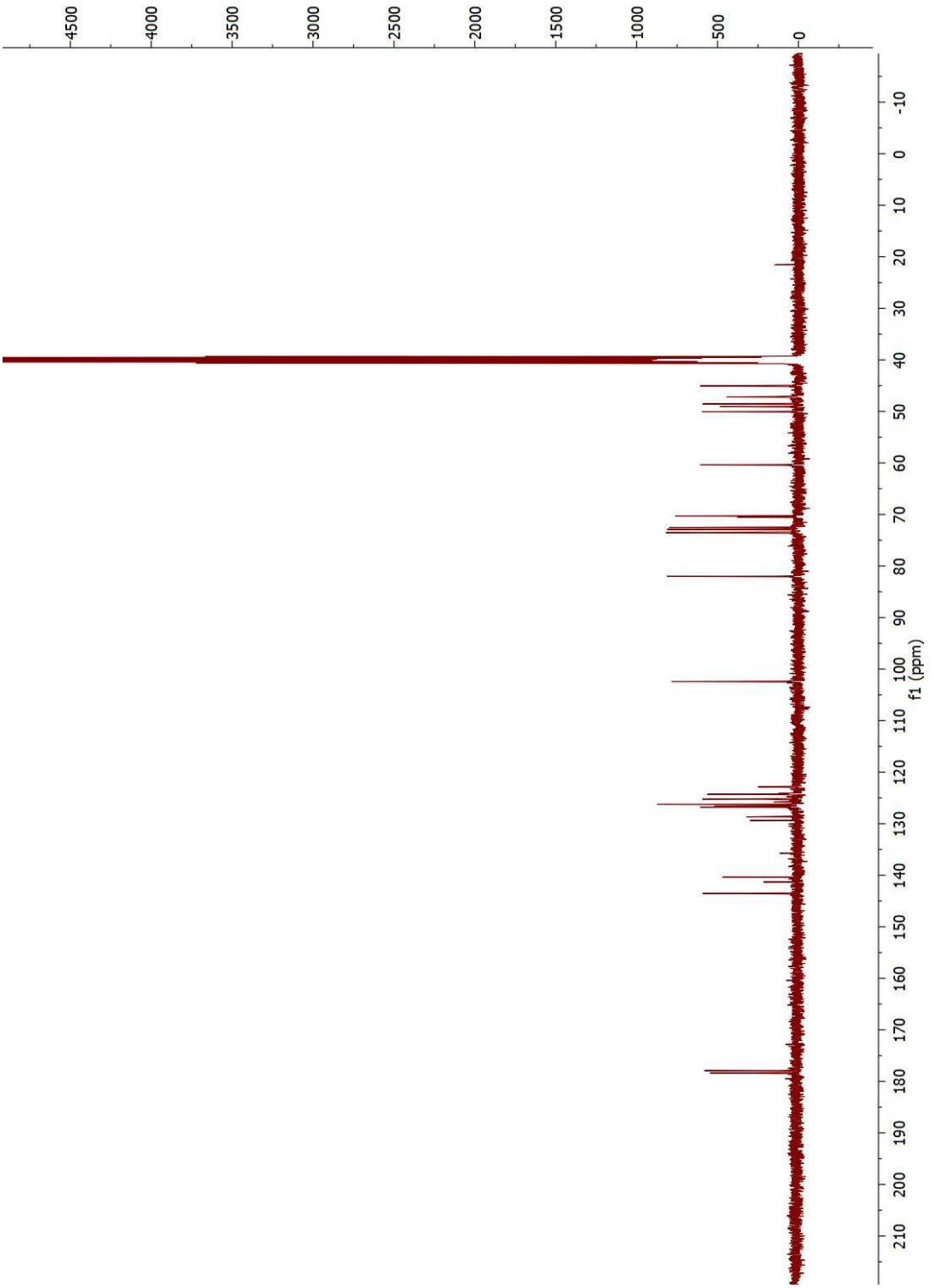

Figure 3.39: ^{13}C NMR for **6**

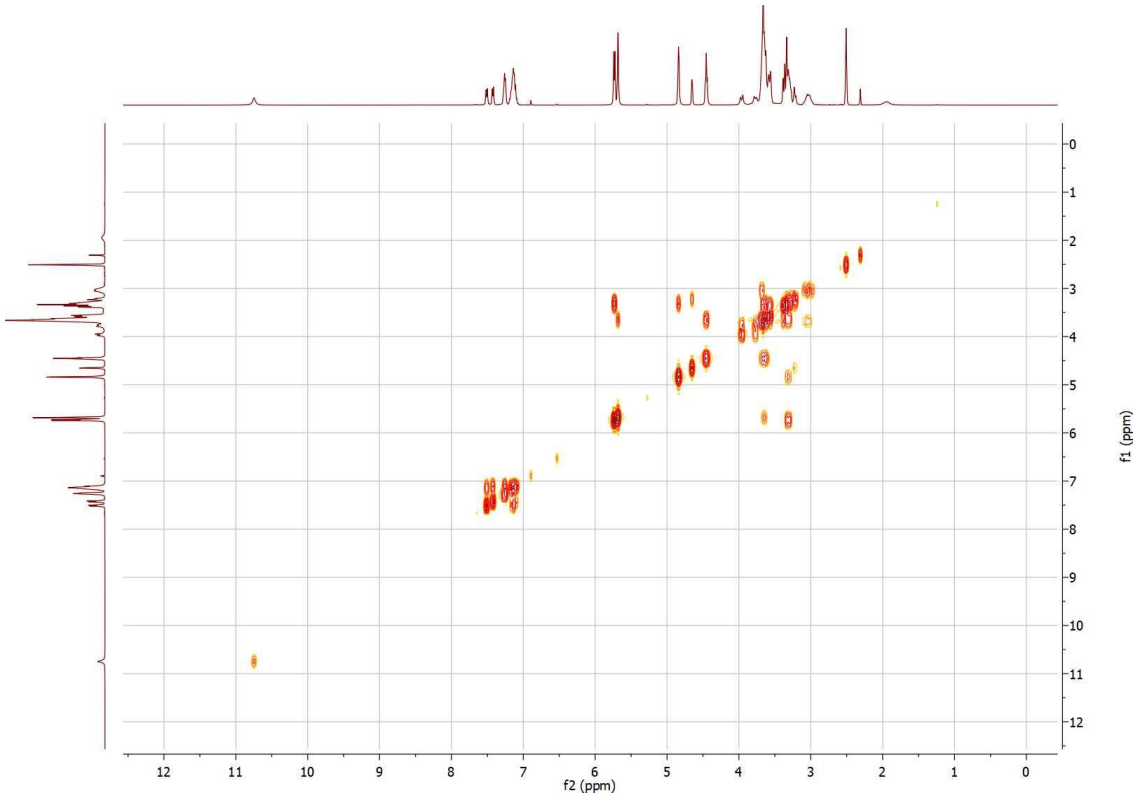

Figure 3.40: COSY spectrum for **6**

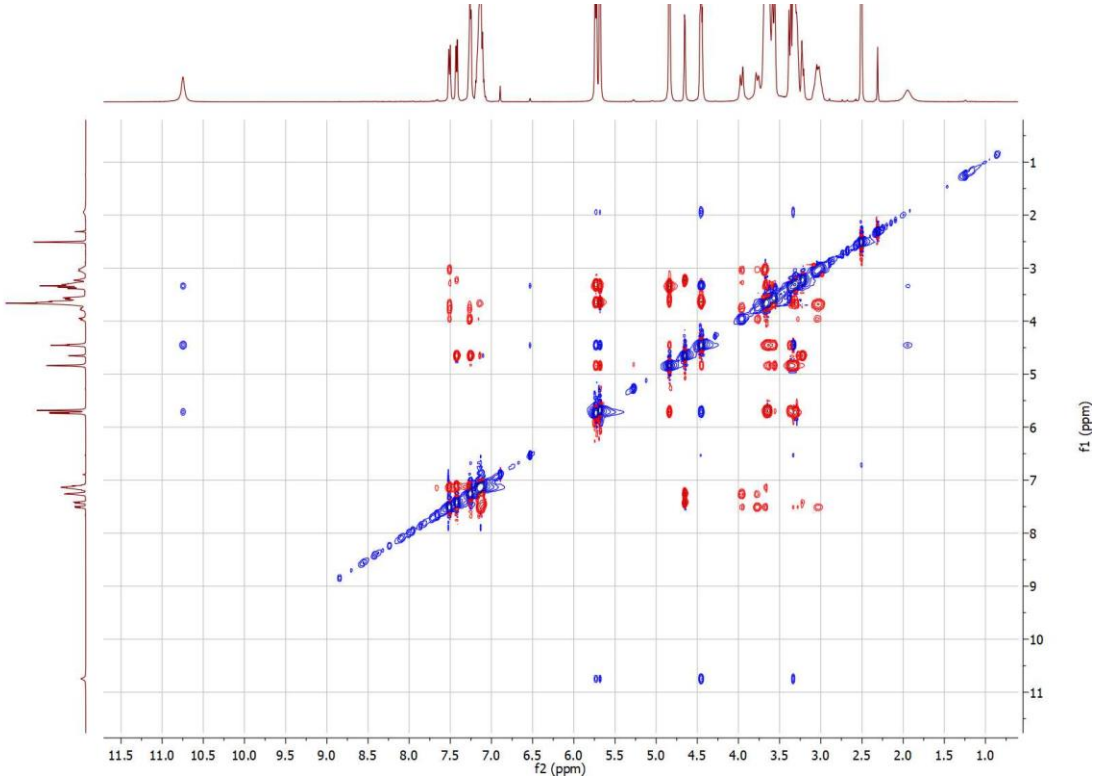

Figure 3.41: ROESY spectrum for **6**, with a mixing time of 500 ms

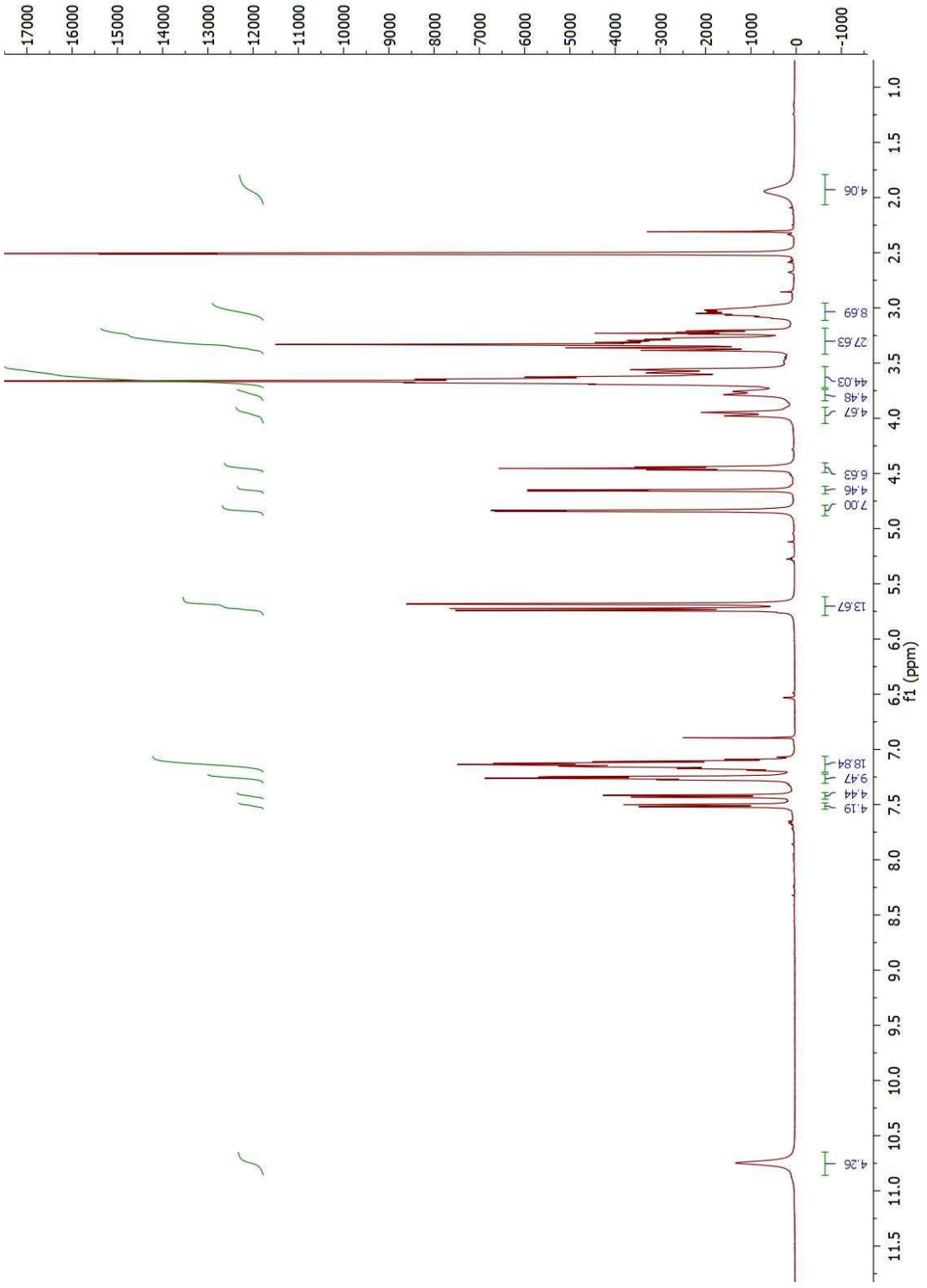

Figure 3.42: ^{1}H NMR of **8**

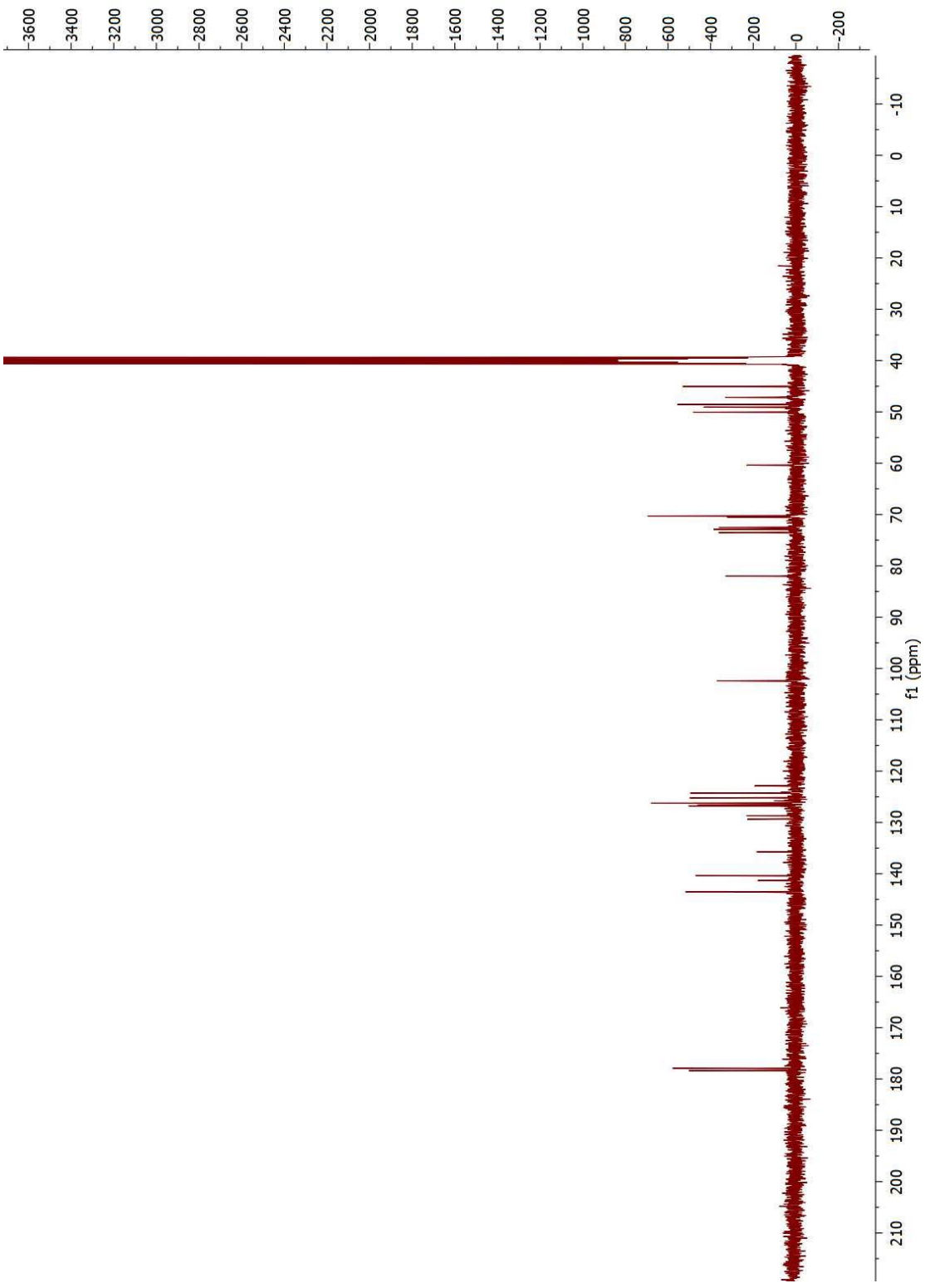

Figure 3.43: ^{13}C NMR of **8**

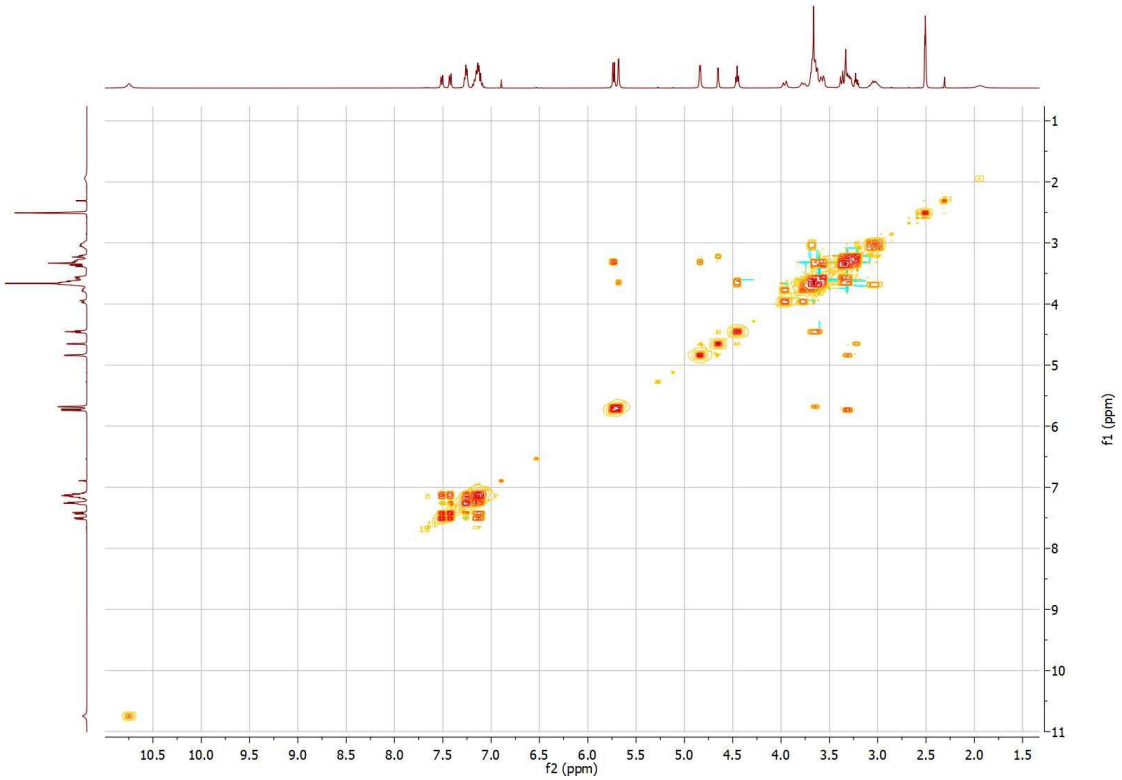

Figure 3.44: The COSY spectrum of **8**

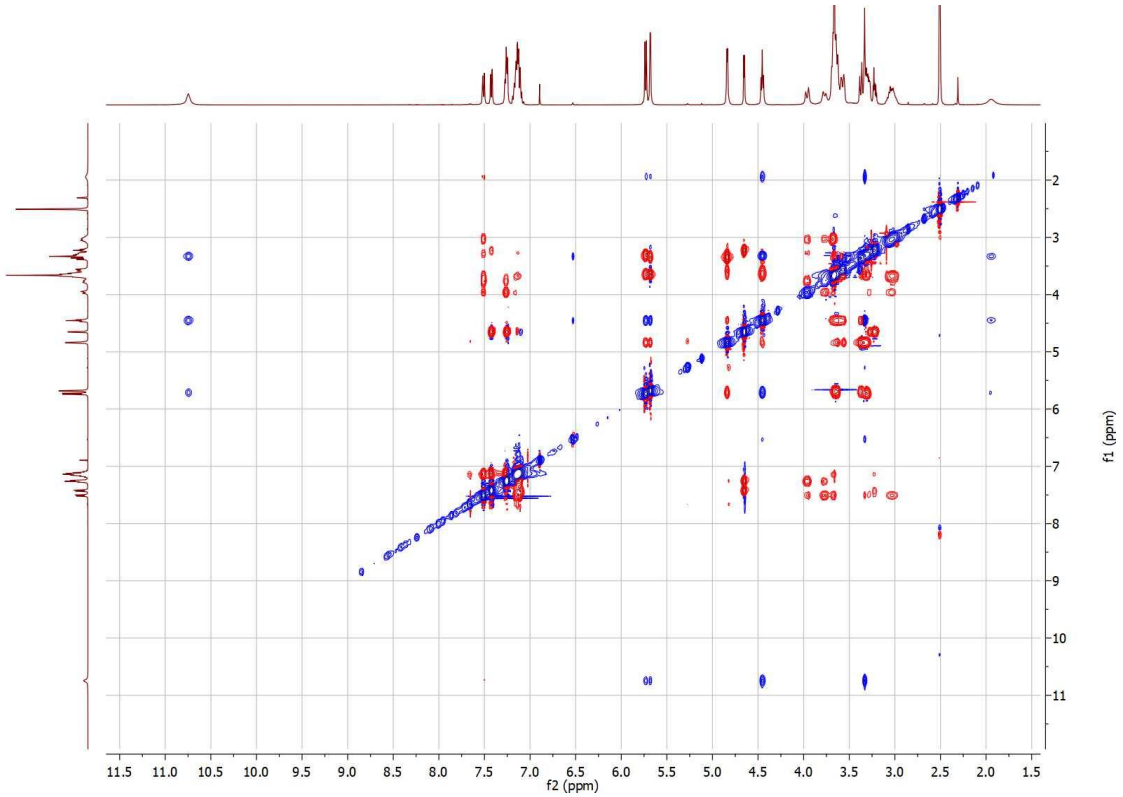

Figure 3.45: ROESY spectrum of 8, with a mixing time of 500 ms

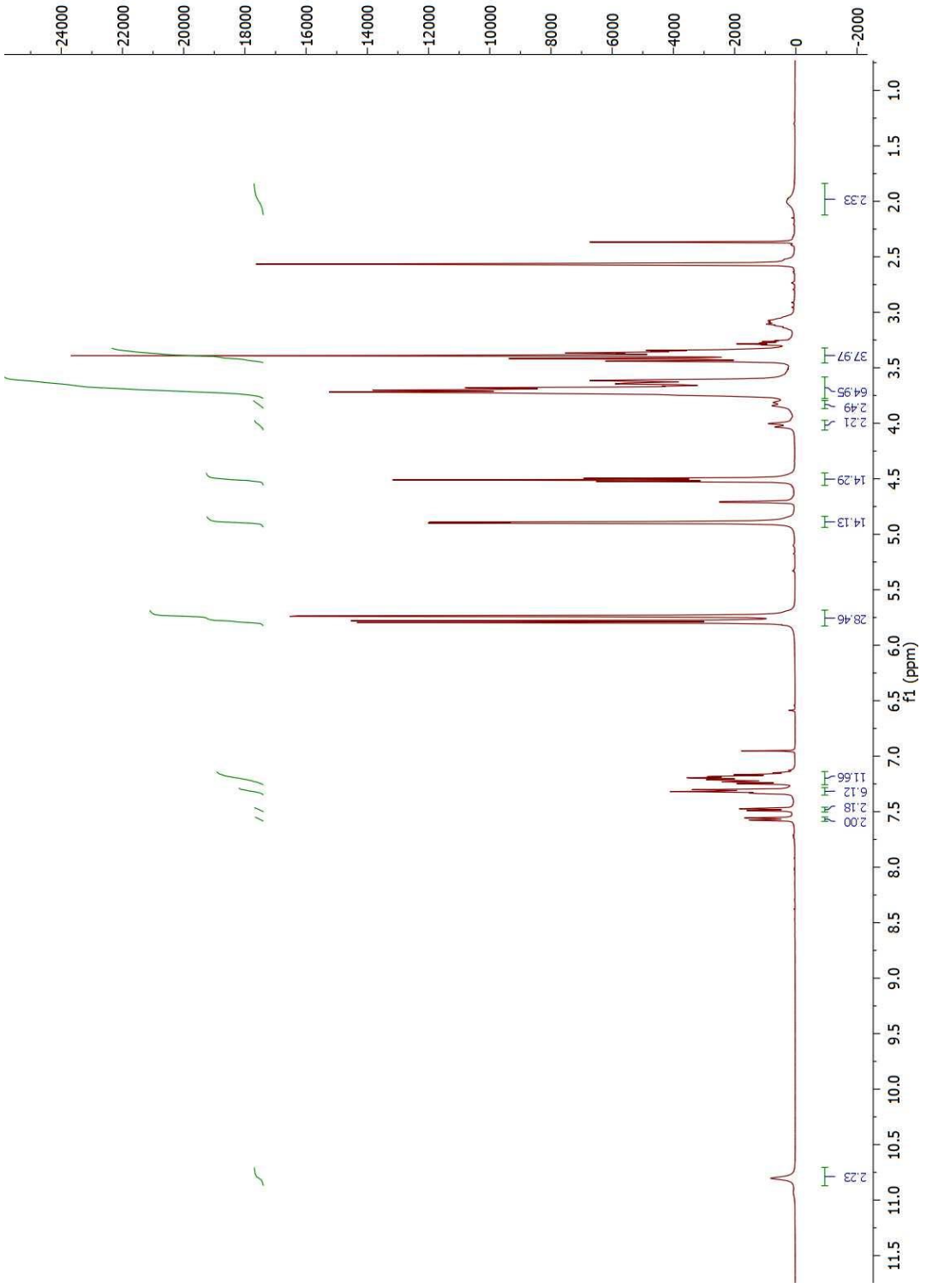

Figure 3.46: ^{1}H NMR of **7**

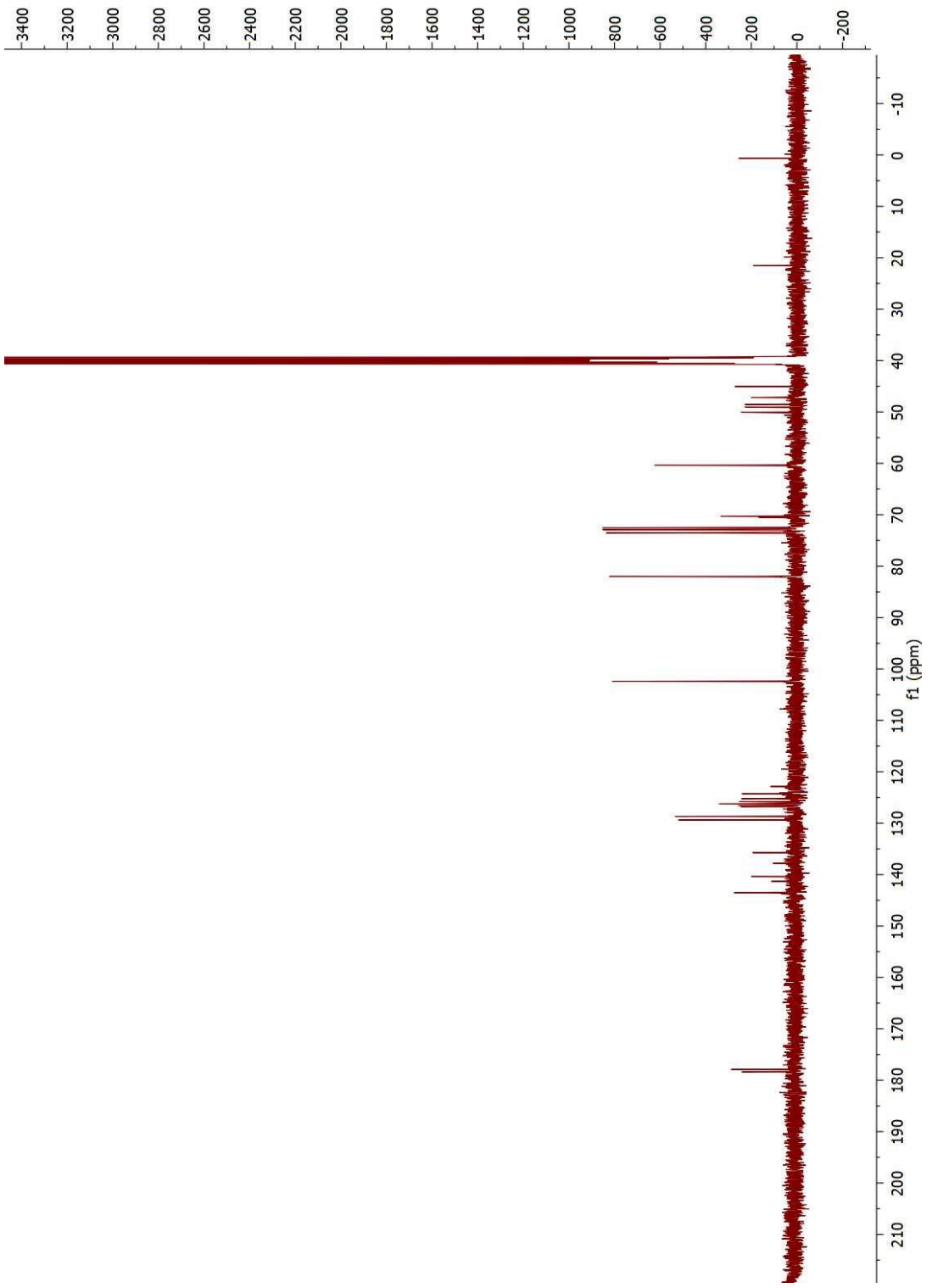

Figure 3.47: ^{13}C NMR of **7**

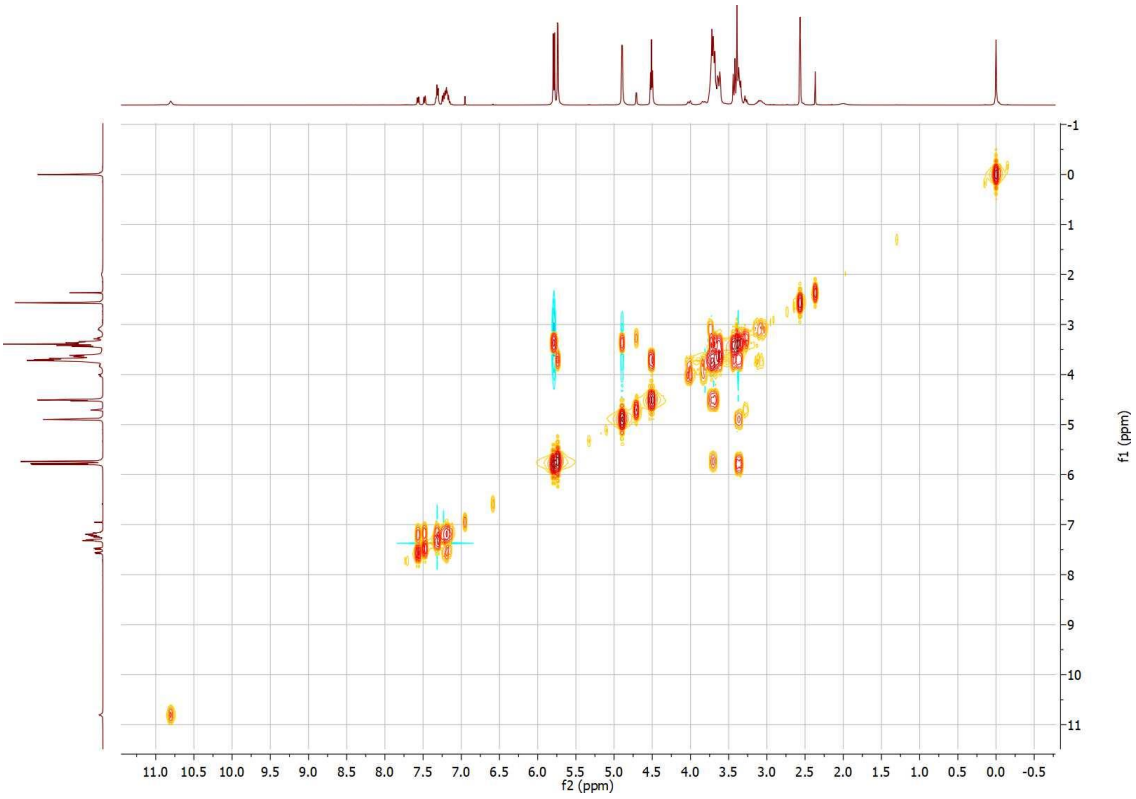

Figure 3.48: COSY of **7**

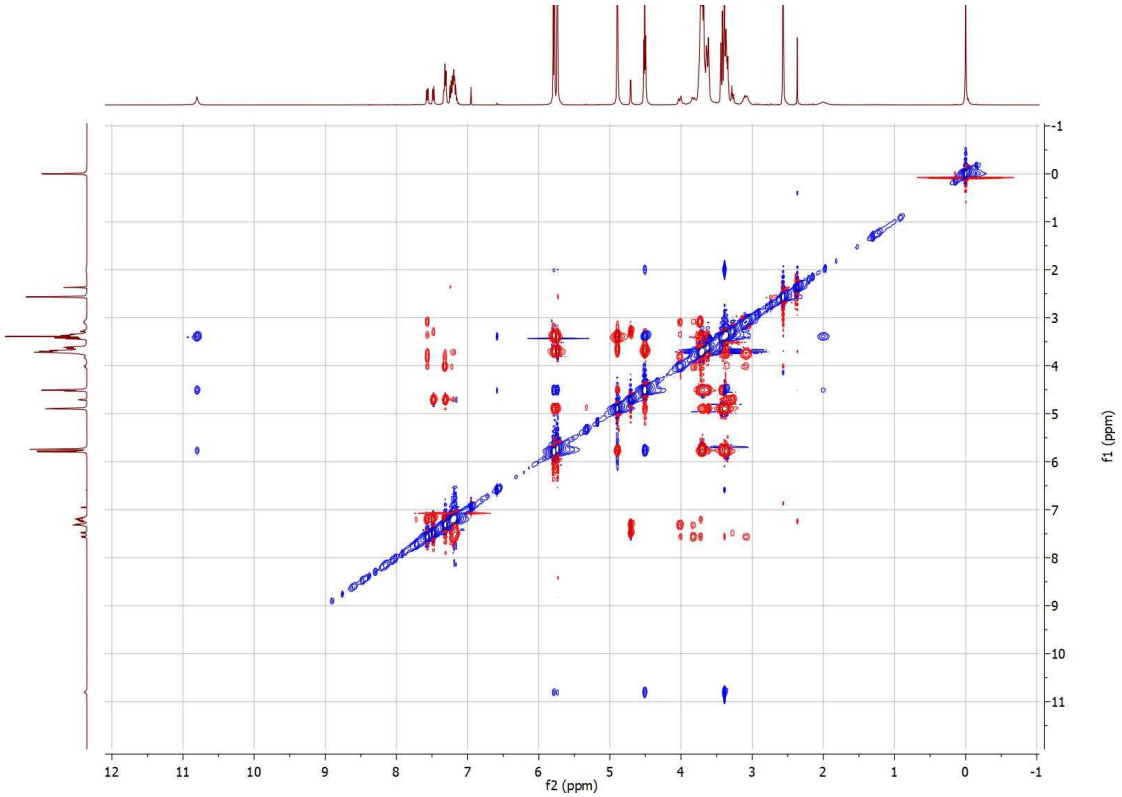

Figure 3.49: ROESY of **7**, with a mixing time of 500 ms

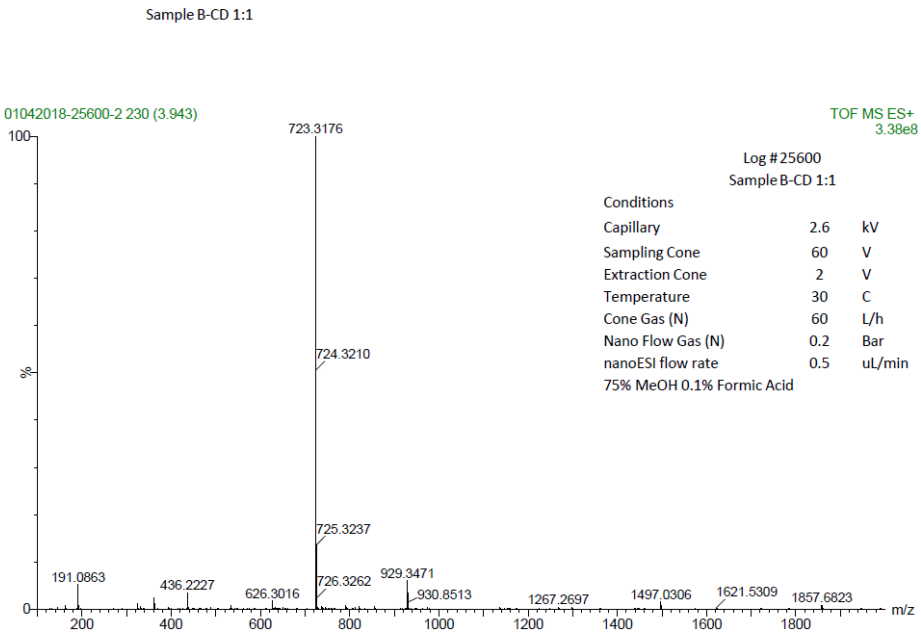

Figure 3.50: Complete mass spectrum of **6**

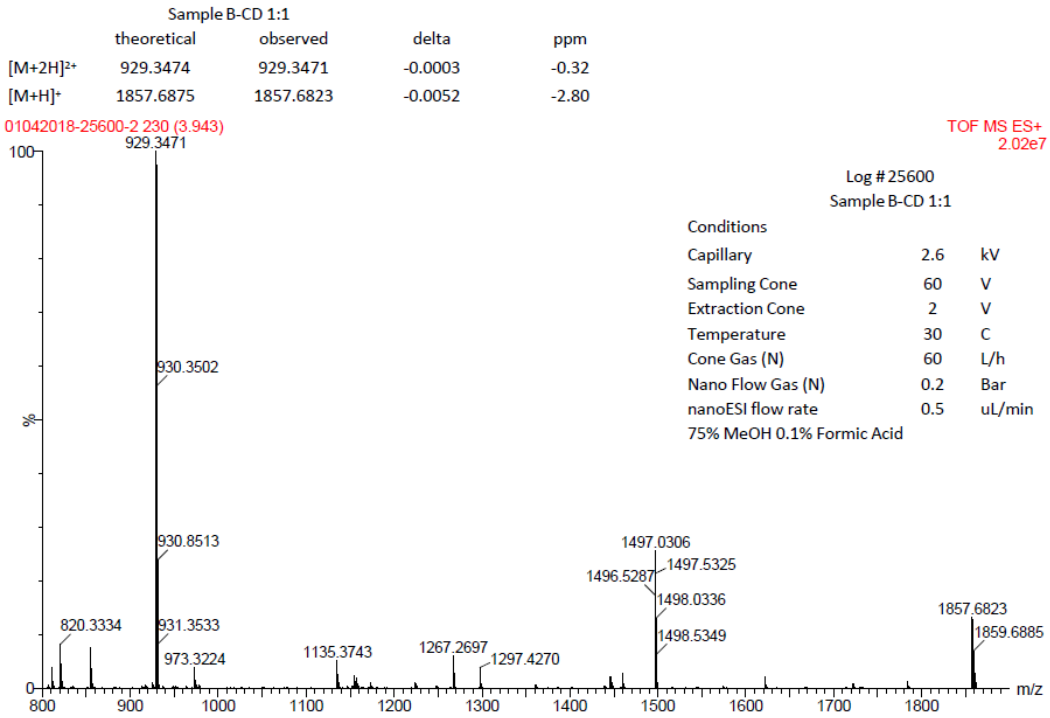

Figure 3.51: mass spectrum of 6 at the range of 800 – 1800 m/z

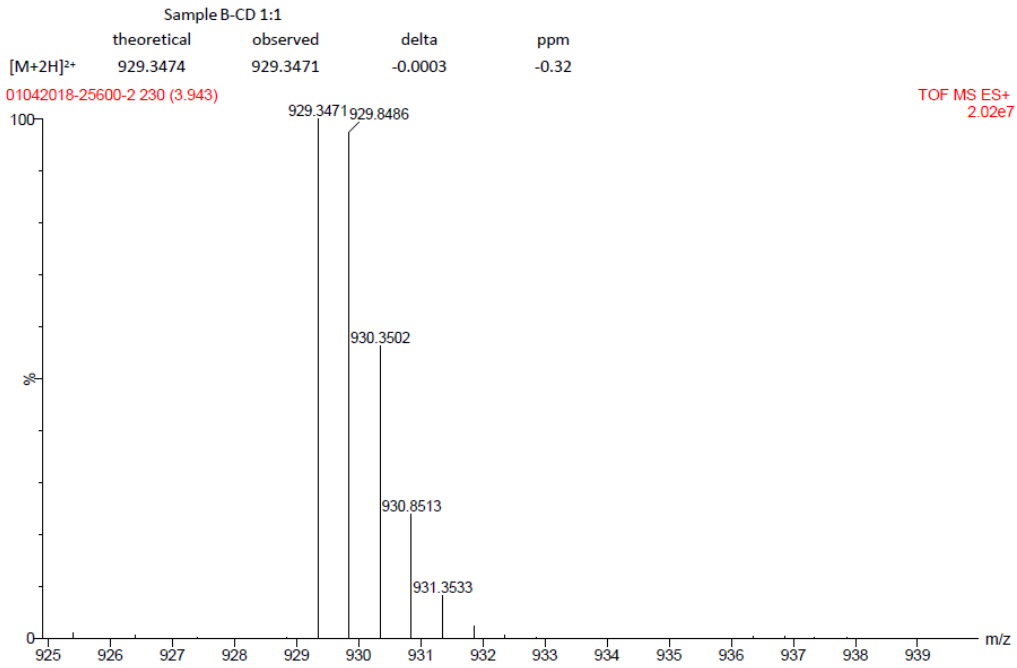

Figure 3.52: mass spectrum of **6** at the range of 925 – 939 m/z

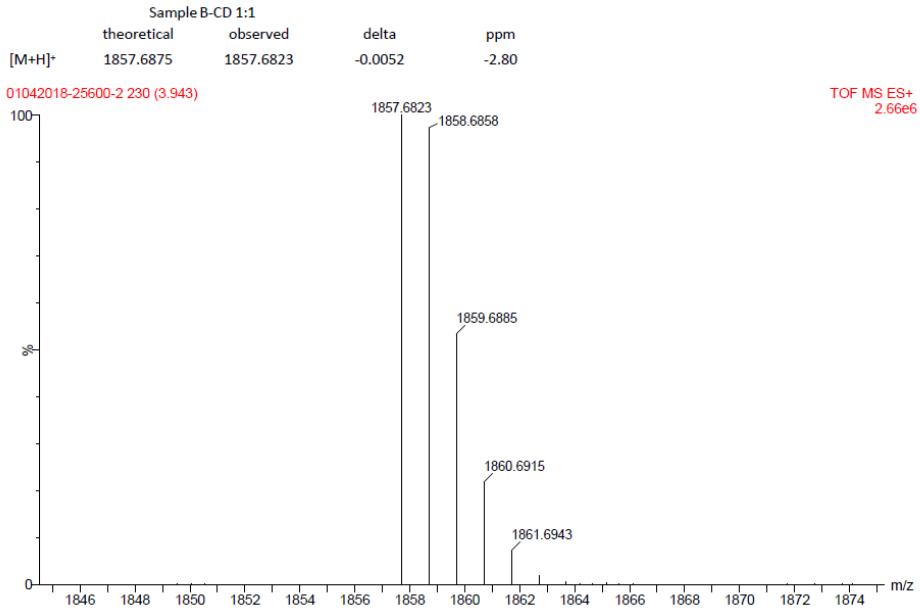

Figure 3.53: mass spectrum of **6** at the range of 1846 - 1874 m/z

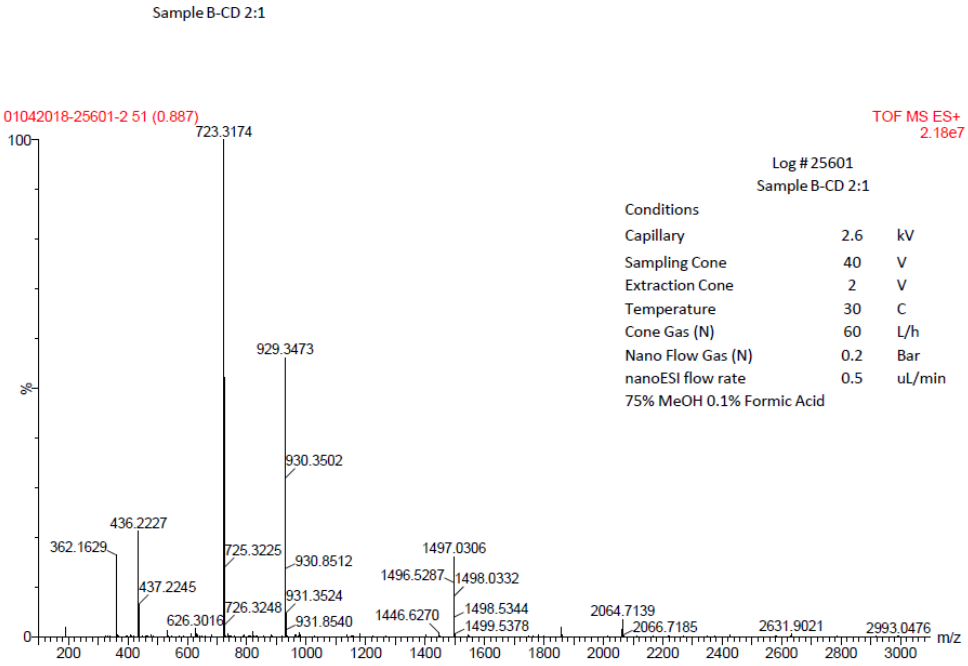

Figure 3.54: Complete mass spectrum of 7

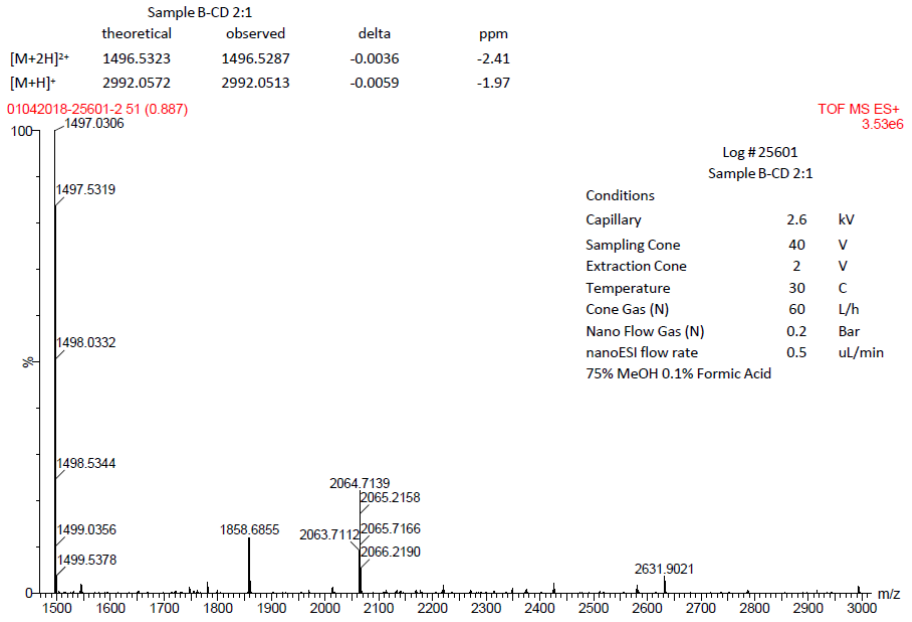

Figure 3.55: mass spectrum of 7 at the range of 1500 - 3000 m/z

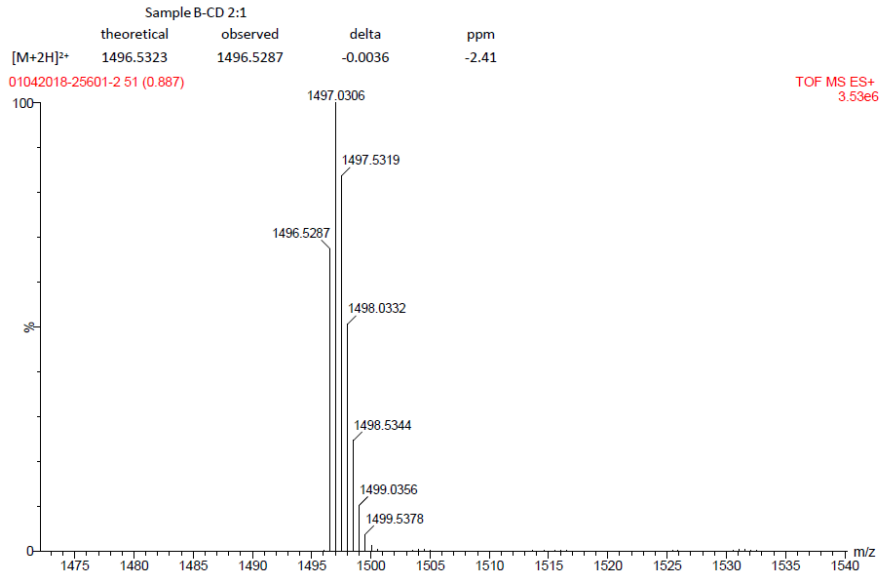

Figure 3.56: mass spectrum of **7** at the range of 1475 - 1540 m/z

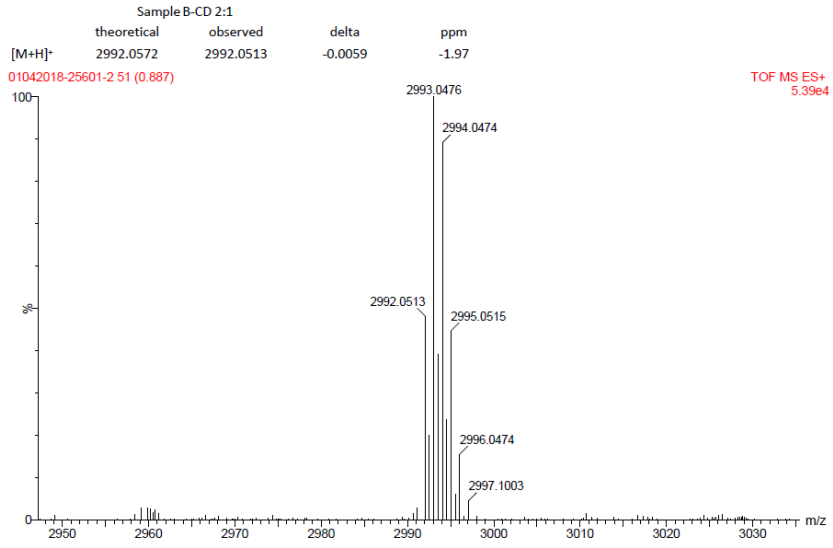

Figure 3.57: mass spectrum of **7** at the range of 2950 - 3030 m/z

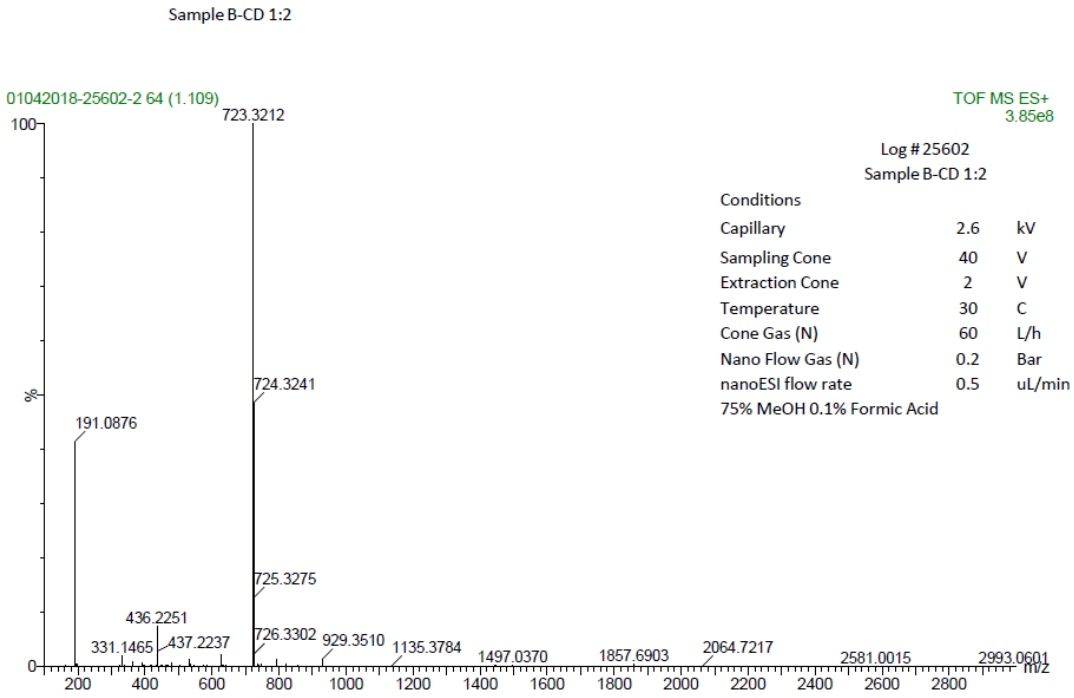

Figure 3.58: Complete mass spectrum of **8**

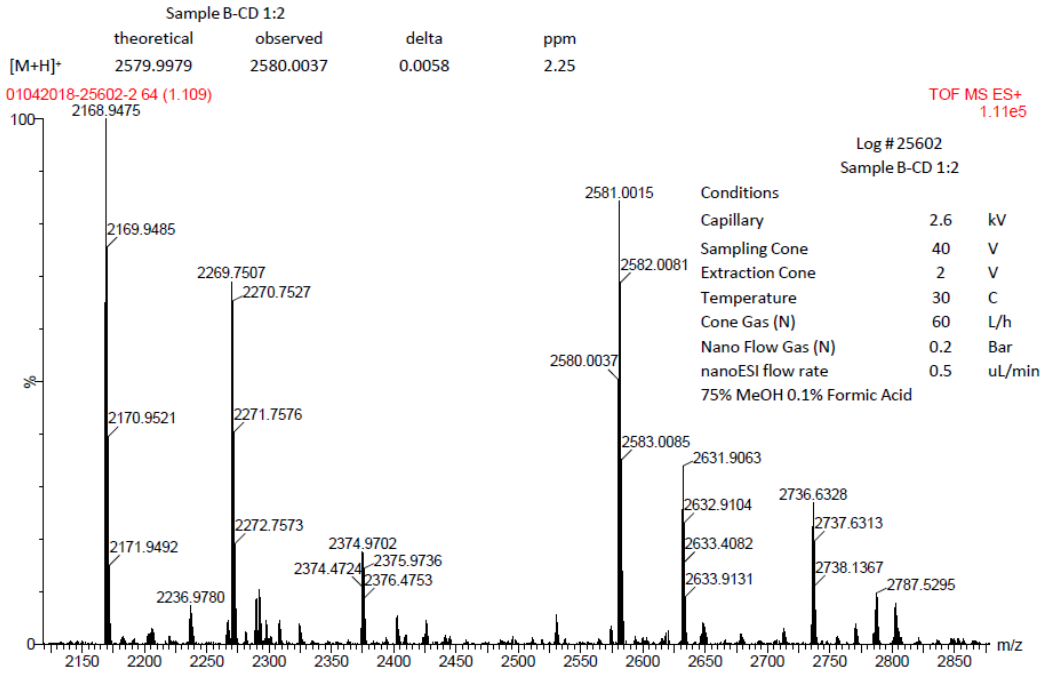

Figure 3.59: mass spectrum of **8** at the range of 2150 - 2850 m/z

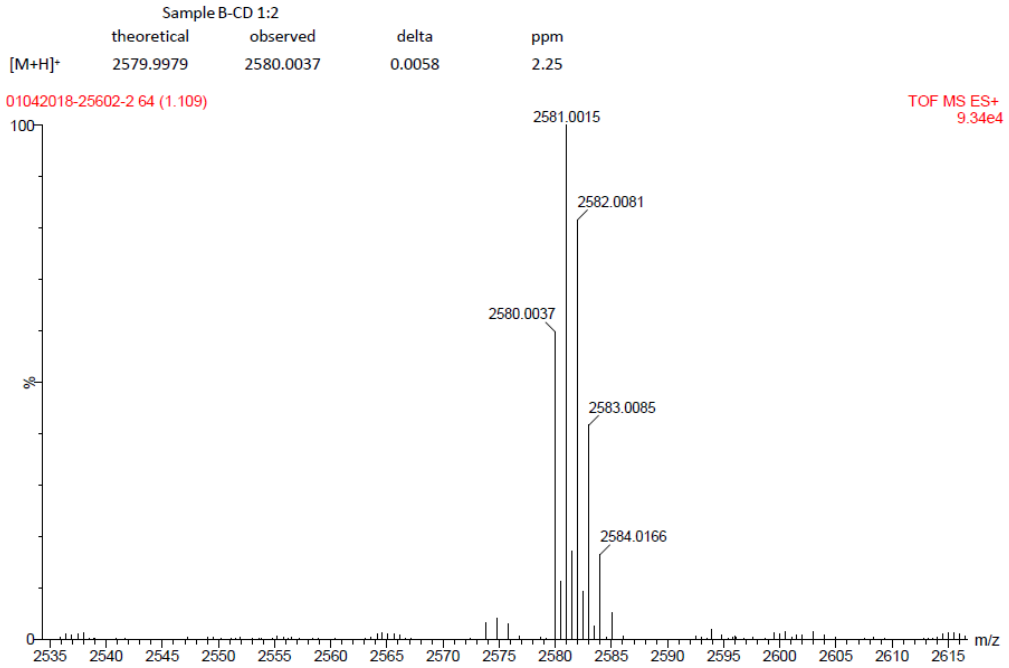

Figure 3.60: mass spectrum of **8** at the range of 2535 - 2615 m/z

Synthesis of 10 and 11

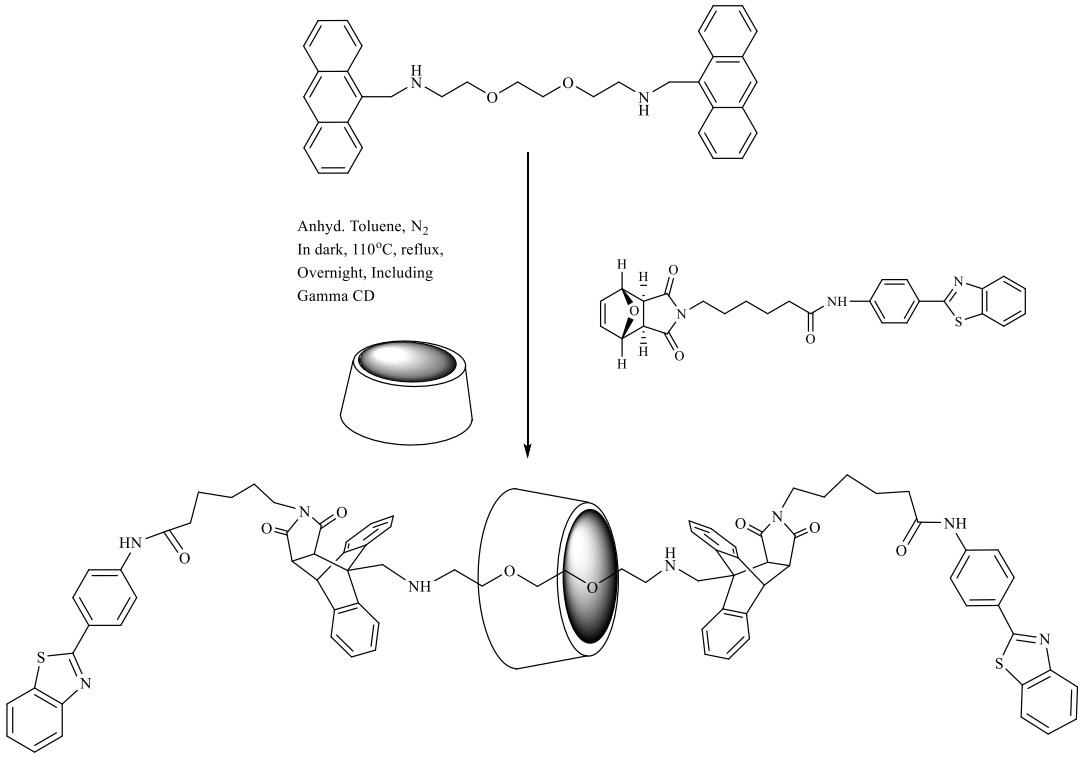

γ-CD (1 equiv.) and **4** (1.1 equiv.) was mixed in 20 ml of Toluene. This reaction mixture was ultrasonicated for 15 minutes. Then it was heated at 80°C for another 15 minutes. To this solution **8** (2.4 equiv.) was added the complete reaction mixture was refluxed at 110°C for overnight. Physical observation of the formation of Diels-alder adduct was observed by the change of colors from yellow solution to white with precipitate. Next, the reaction mixture was subjected for rotary evaporation until dryness and dried overnight under high vacuum. By changing the addition equivalents to 1 or 2 of the γ-CD, it was possible to obtain 1 or 2 CDs on the thread. Reaction yield was 85%. ^{1}H-NMR, ^{13}C-NMR and ROESY NMR was performed using DMSO-d_6.

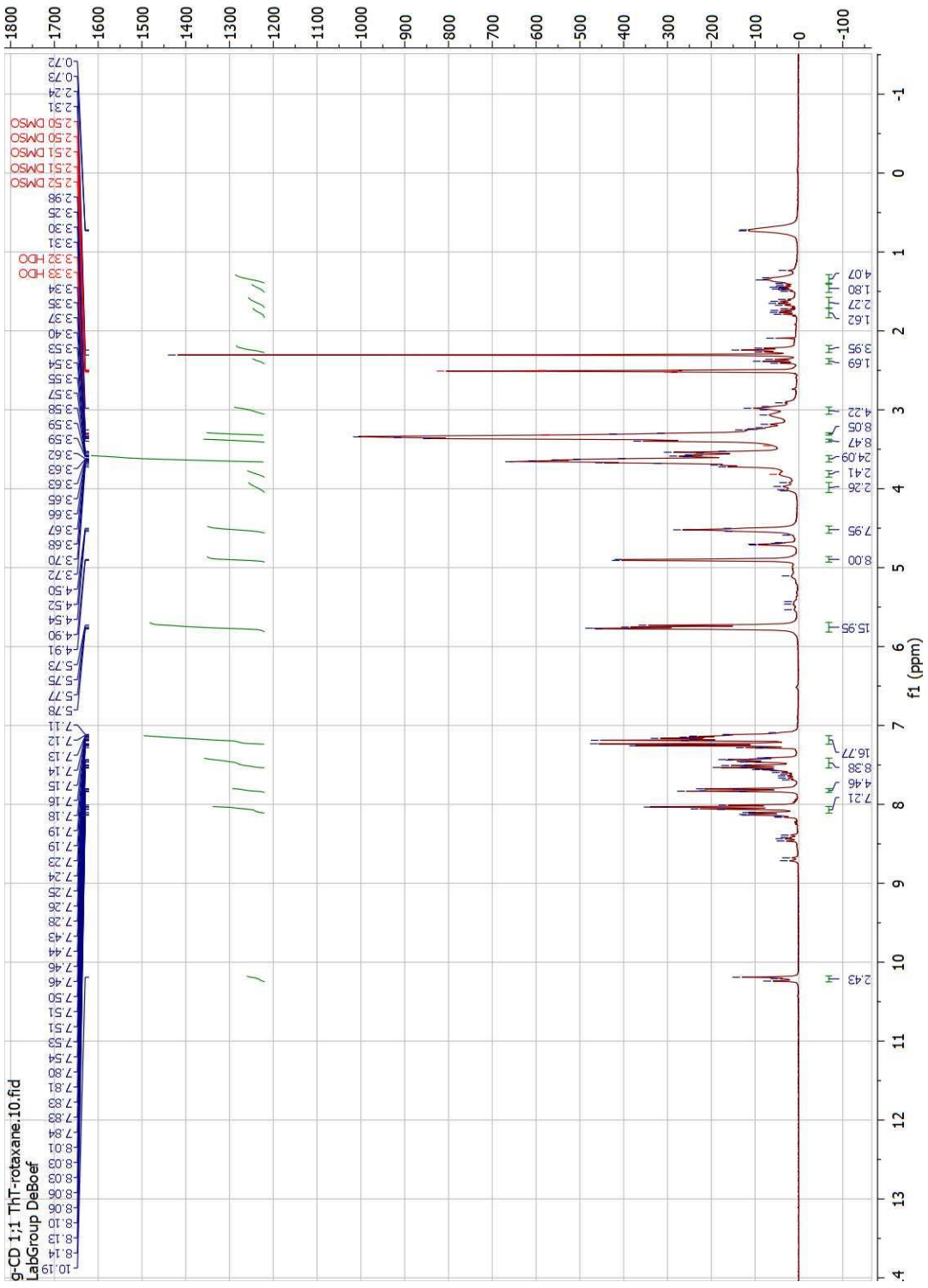

Figure 3.61: ^{1}H NMR of **10**

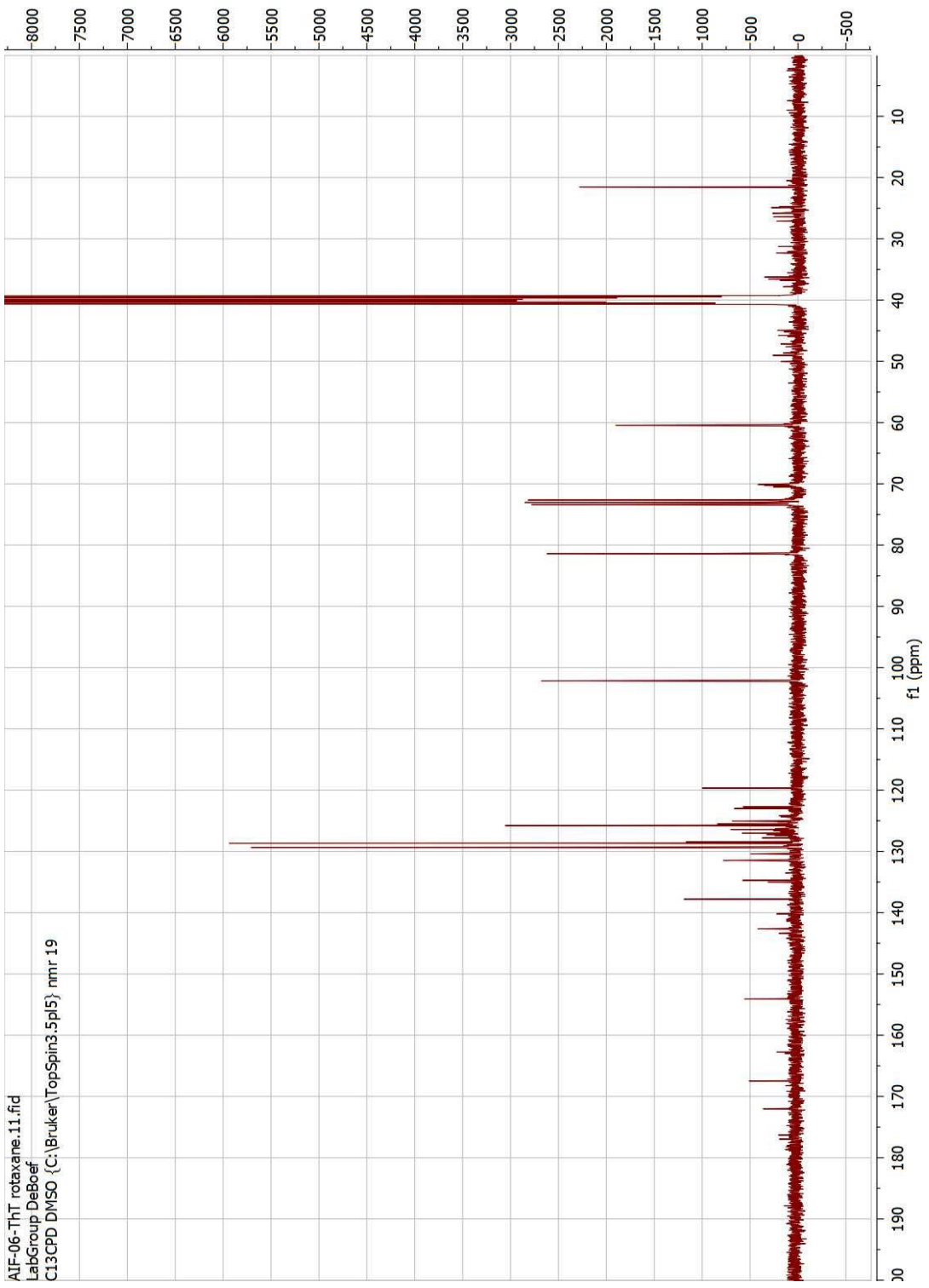

Figure 3.62: ^{13}C NMR of **10**

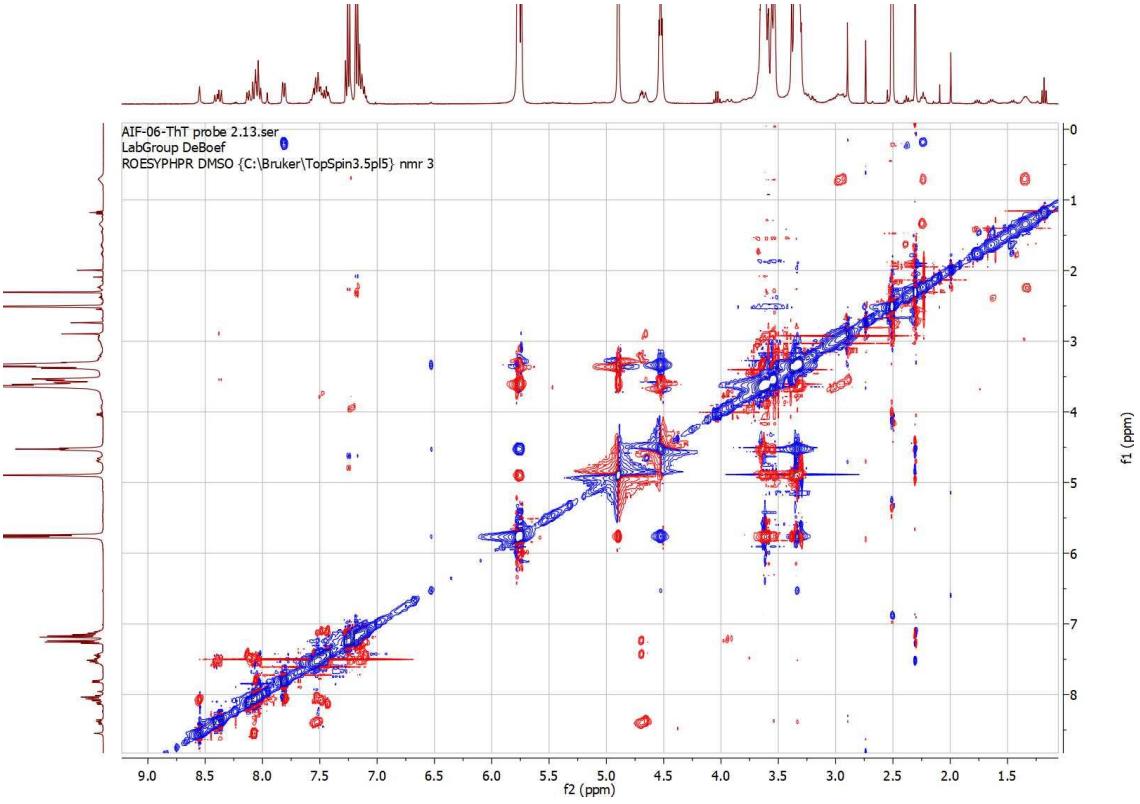

Figure 3.63: ROESY spectrum of **10**

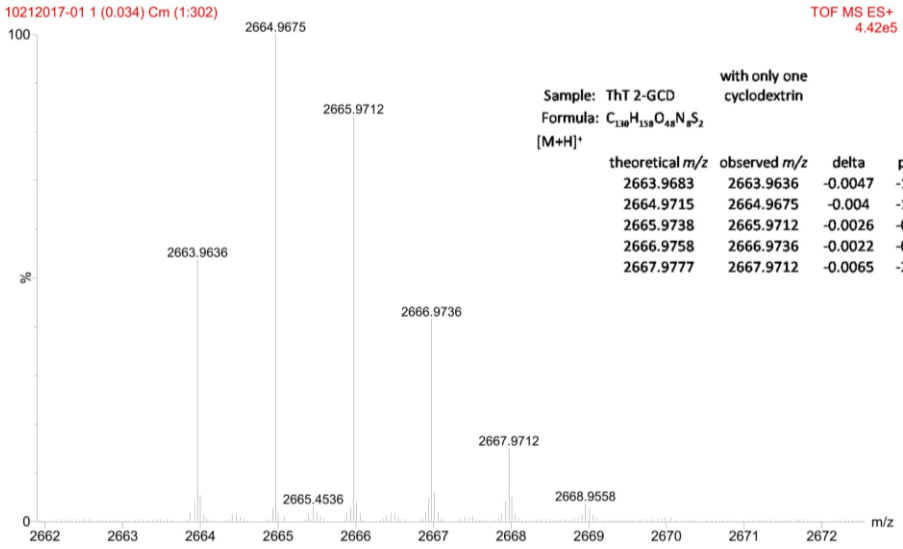

Figure 3.64: mass spectrum of **10**

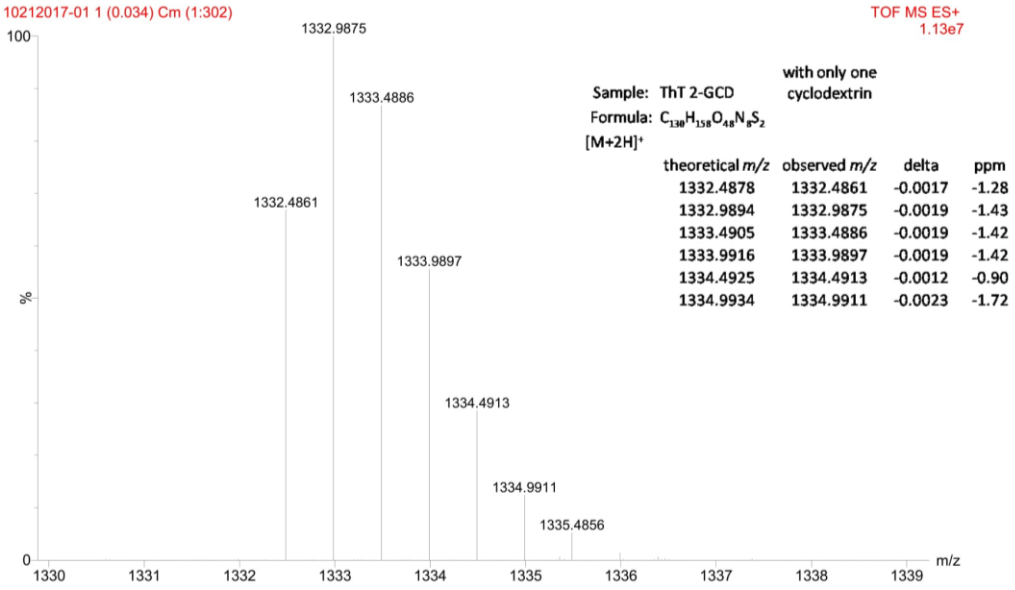

Figure 3.65: mass spectrum of **10**

NMR titration of 1 and γ-CD

The NMR titration experiments were conducted per the following procedures.[2] The host CD concentrations were kept constant while the guest concentration was increased periodically. Stock solutions of 20 mM host (cyclodextrin) and 60 mM guest were prepared. A series of NMR samples were made in 5 mm NMR tubes. The series ranged from 10 mM to 80 mM. All samples were prepared and heated for 3 minutes at 80 ^{o}C and cooled to room temperature. The NMR was performed at 300K (Room temperature). The guest protons were monitored. Data was processed using an Excel spreadsheet using the equation shown below and fitting the data. The plots are shown below. The data was evaluated using the "OpenDataFit" website which is an online free fitting program found at supramolecular.org.[2] The two different analysis methods provided similar results.

The following equation was used to calculate the association constant:

$$\Delta\delta = \left(\frac{\Delta\delta_{max}}{2[H_0]}\right) + \{[H_0] + [G_0] + \frac{1}{K} - ((\left([H_0] + [G_0] + \frac{1}{K}\right)^2 - 4[H_0]\Big[G_0]\Big)^{\frac{1}{2}}\}$$

where Δδ = change in chemical shift, $[H_0]$ = Initial Host concentration, $[G_0]$ = Initial concentration, and K = association constant. Δδ was plotted as a function of the guest concentration.

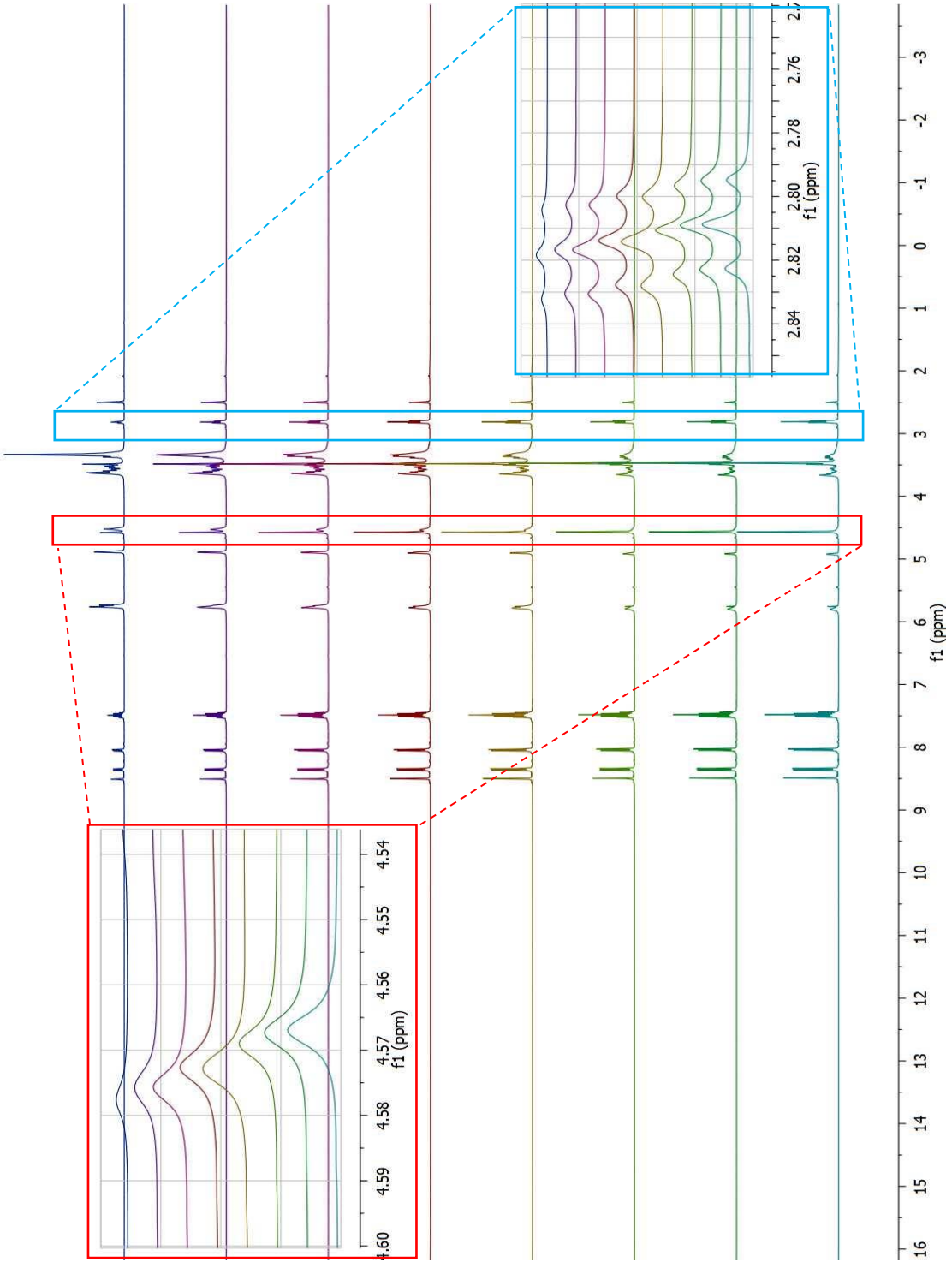

Figure 3.66: NMR titration with 1 and γ-CD

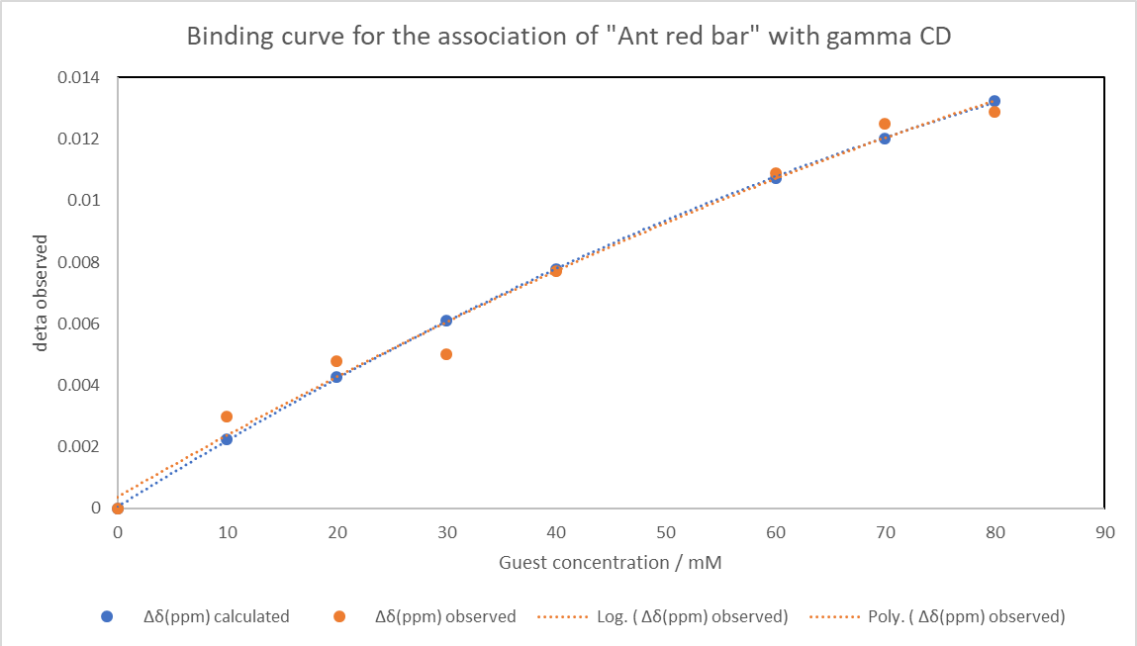

Figure 3.67: Binding curve for **1** and γ-CD

Computational studies were performed using commercially available Spartan 16 and Molecular operating environment (MOE) software. Spartan was used to design the supramolecular compounds in 3D space. Energy minimizations, dynamics and docking were performed using MOE. Energy minimizations were conducted using the MMFX94 force field,[20] with an R-field of 1.80. A unit cell was created around the molecule with a cell size of 43.321 Å in x, y, z directions. The periodic system was used to perform the calculations. Rigid water molecules were chosen, with a gradient of 0.001 RMS kcal/mol/Å.[02]

The energy minimized structure was prepared for docking by using the built-in prep tool named as "quick-prep." This tool fixes errors present in the molecule such as adding missing hydrogens and charges. This molecule was further subjected to molecular simulations via NPA (Nose-Poincare-Anderson equation) method[21], which is the most correct and most sensitive method used by the MOE software. All simulations were performed inside the unit cell, with water surrounding water molecules at a temperature of 300K.

The guest was manually selected to dock the guest inside the CD cavity. This made the CD as the host receptor. The site finder tool was used to place dummy atoms inside the hydrophobic cavity of the CD. This was done to optimize the docking procedure. The unit cell mentioned above was maintained with its initial parameters at the docking stage to mimic the solvent effect. Triangle matcher was used as the docking placement methodology while London dG was selected as the initial scoring methodology. A number of 50 poses were passed to the refinement step. Rigid receptor post-placement refinement was used with GBVI/WSA as the final scoring method. The lowest negative number for final docking score was chosen as the final values.

Figure 3.68: Computational modeling for **4** and one γ-CD molecule

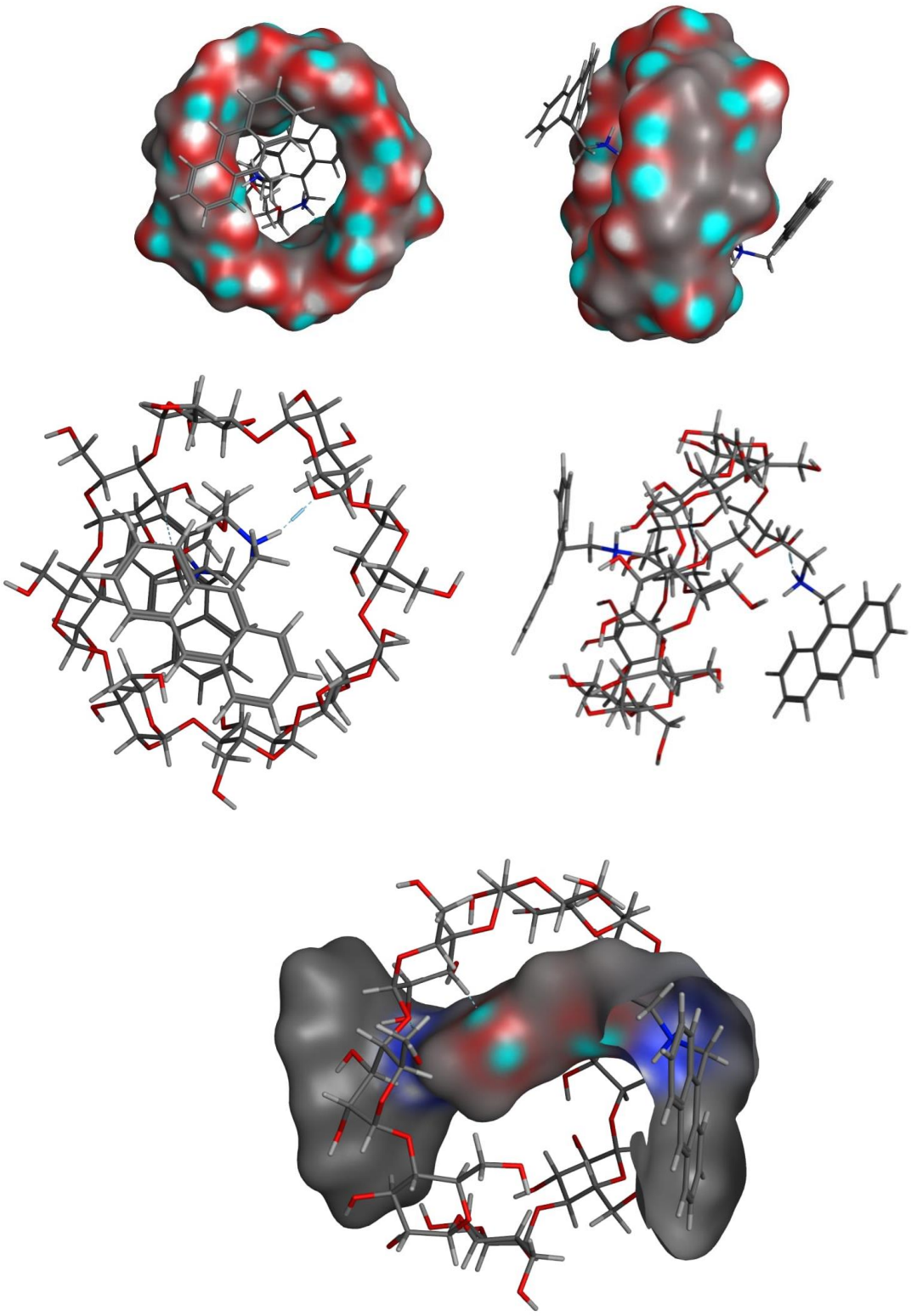

Figure 3.69: Computational modeling for **3**

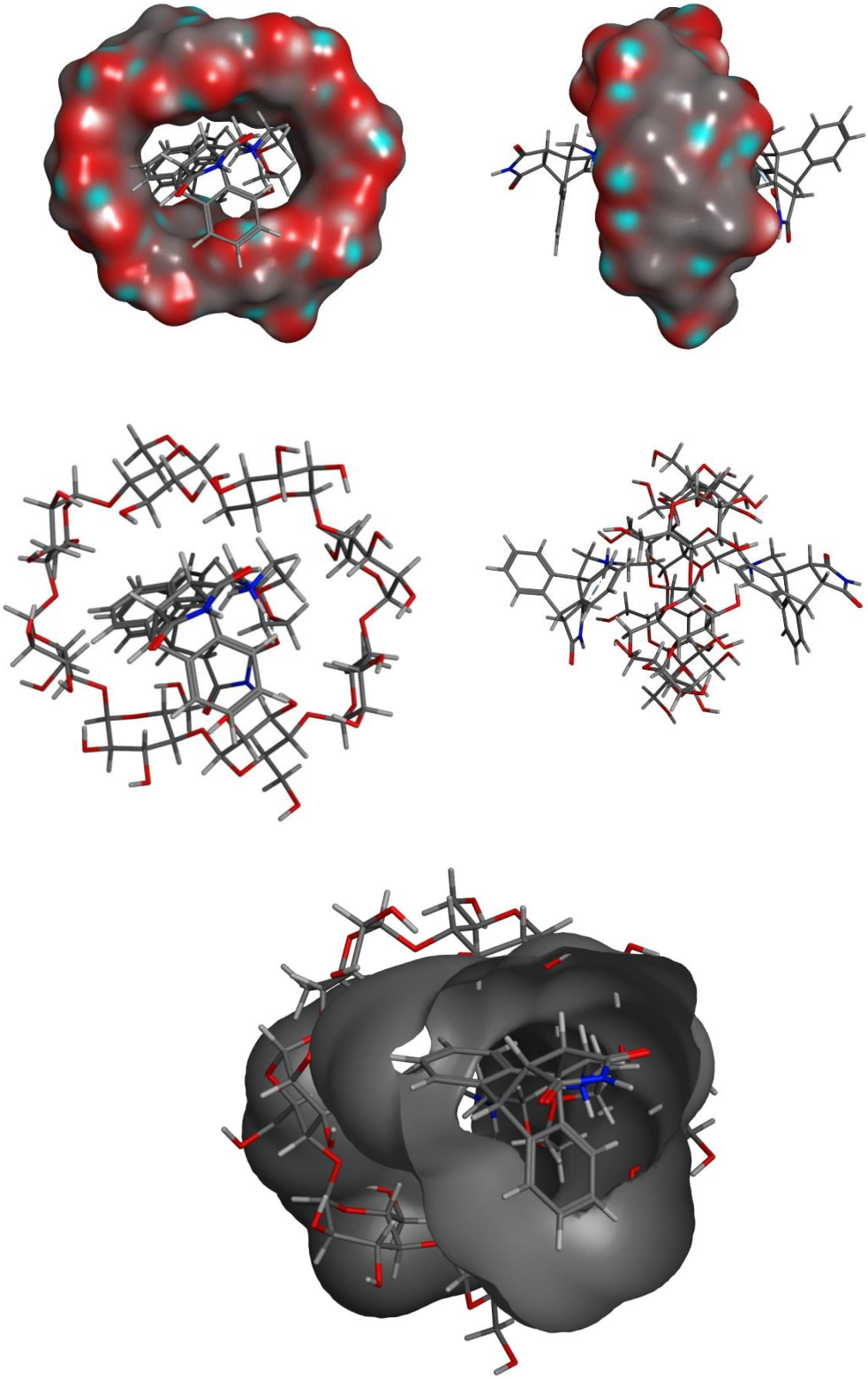

Figure 3.70: Computational modeling for **10**

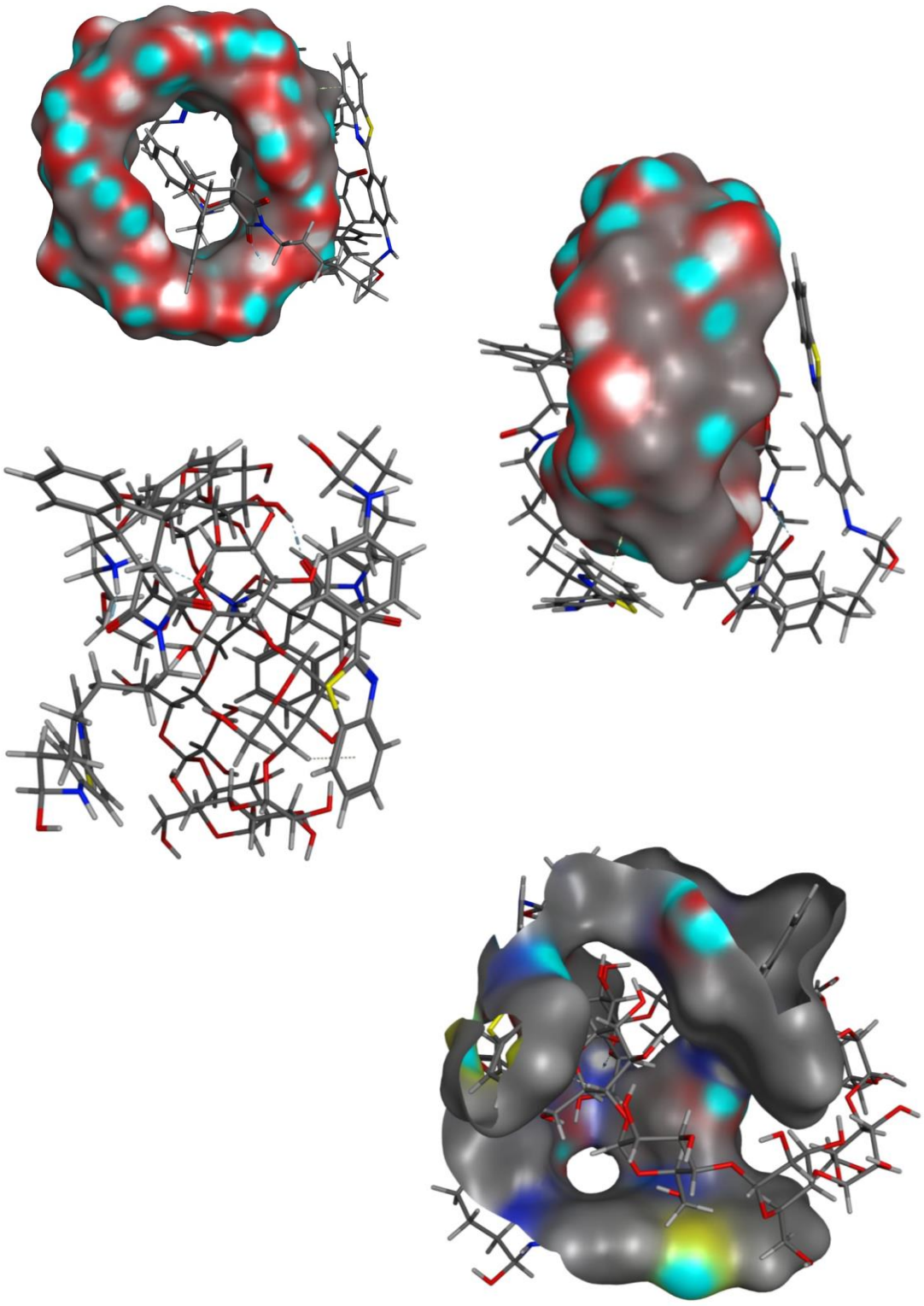

Figure 3.71: Computational modeling for **1** and **2** γ-CD molecules

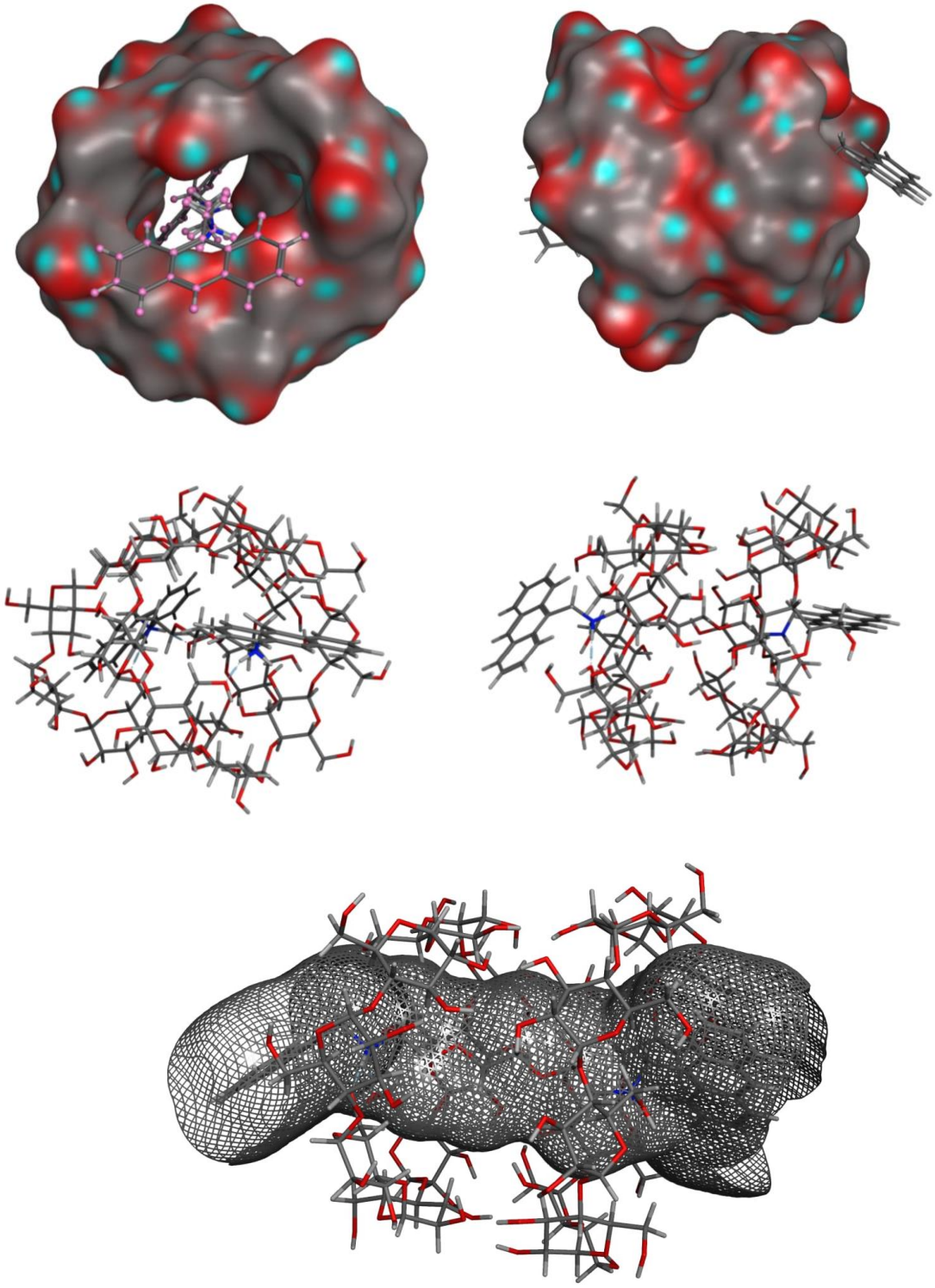

Figure 3.72: Computational modeling for **4**

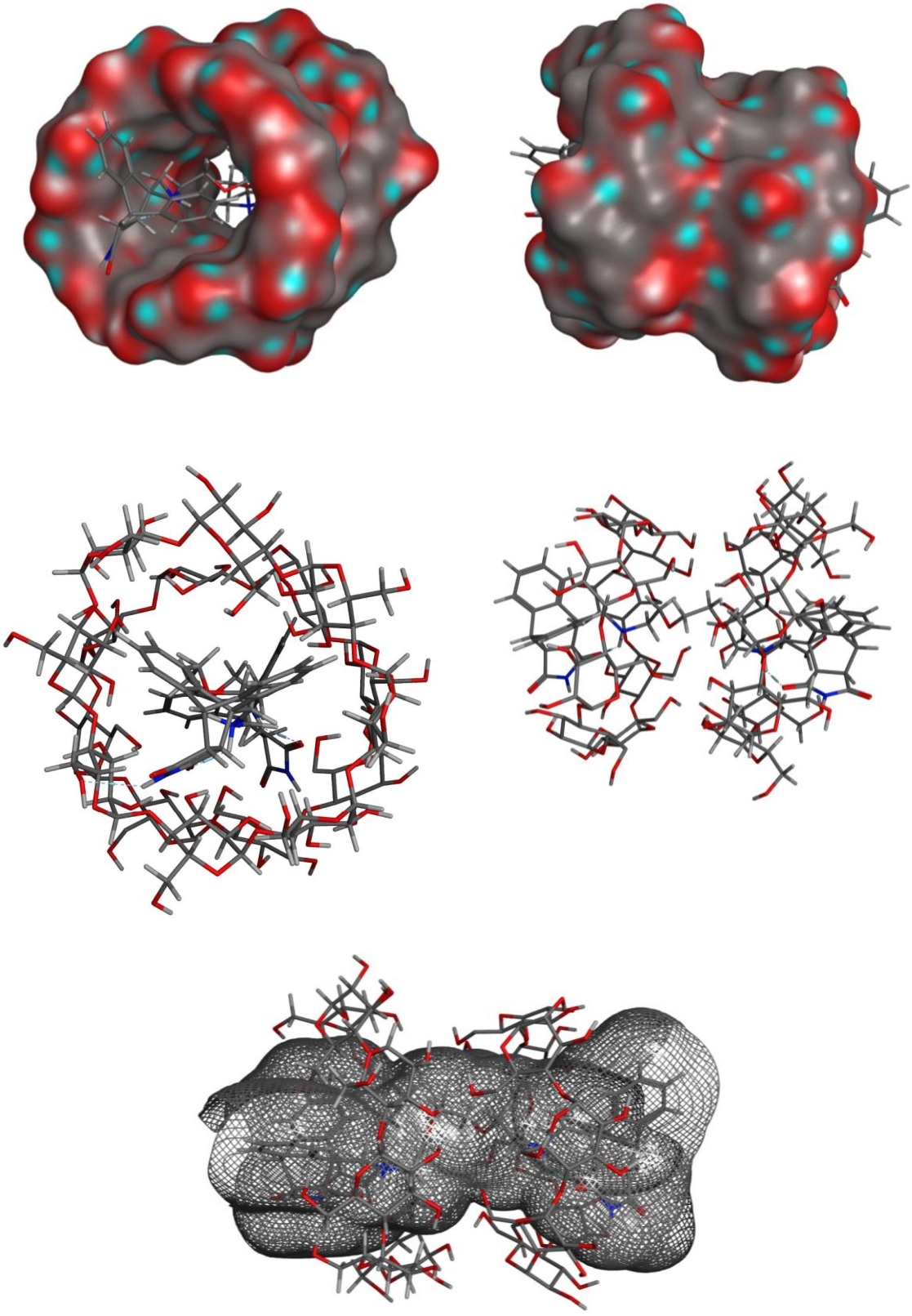

Figure 3.73: Computational modeling for **11** (ThT based γ-CD rotaxane 2:1)

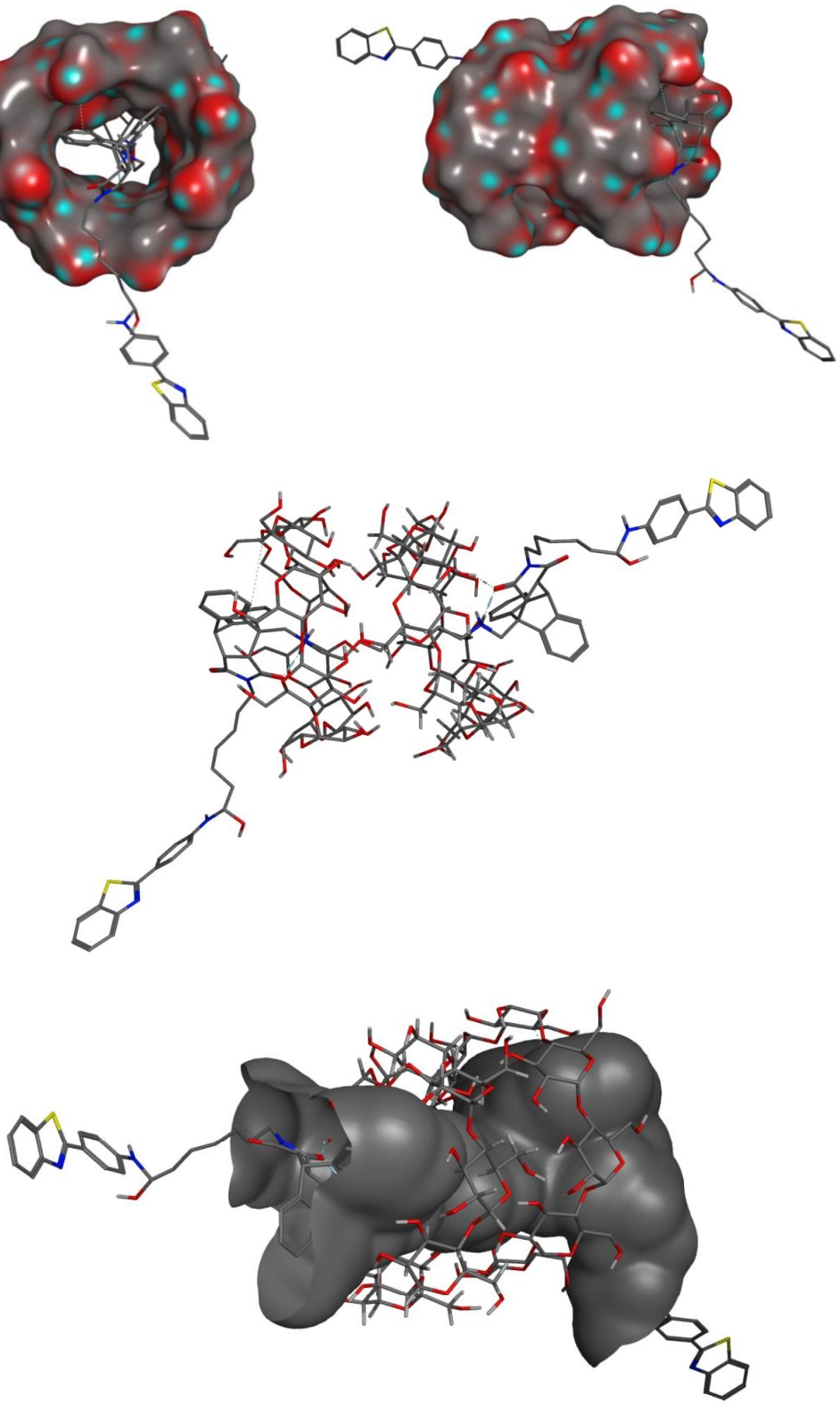

References

(1) Jung, S. J.; Park, Y. D.; Park, J. H.; Yang, S. D.; Hur, M. G.; Yu, K. H. *Med. Chem. Res.* **2013**, *22* (9), 4263.

(2) Thordarson, P. *Chem. Soc. Rev.* **2011**, *40* (3), 1305.

4 CHAPTER 4

Will be published in *Chemical Communications*

A fluorescent pillar[5]arene based molecular switch

Ashvin I. Fernando, Paul Cesana, Adriana Mendieta, Cassandra Chartier, Al Bach , Brenton DeBoef*

Department of Chemistry, University of Rhode Island, 140 Flagg Road, Kingston, Rhode Island 02881, United States

Abstract

The synthesized novel Thioflavin-appended pillararene structure can switch from a folded, intercalated form to an open form via a change of temperature or in response to a chemical analyte. This unique behavior was studied using 1D and 2D NMR spectroscopy, fluorescence spectroscopy, and computational modeling. In synthesizing the novel structure, new reaction conditions with higher yields for the synthesis and functionalization of copillararenes were developed. The dual-functionalized pillararene is a unique molecular switch that can be used to bind analyts in it hydrophobic cavity, producing a signal that can be easily detected by NMR for fluoroescence spectroscopy.

Introduction

Despite the relatively short time since their discovery, pillararenes have been widely used in applications ranging from molecular machines[1] to drug delivery.[2] These barrel-shaped macrocyclic structures were first reported by Ogoshi and coworkers.[3] When compared with other supramolecular structures, pillararenes are far more versatile and robust due to their ease of functionalization and synthesis.[4] Our group became interested in the chemistry of pillararenes as part of our efforts to design and discover molecular structures that are capable of binding xenon,[5] which can be used as molecular contrast agents for ^{129}Xe MRI.[6] During the course of these studies we have optimized the conditions by which co-pillararenes (Co-P5A) can be synthesized and functionalized. Herein, we report these synthetic advances and their application to the development of a novel molecular switch that can be used as a fluorescent sensor.

Results and discussion

The synthesis of the Co-P5A commenced using monomers containing bromoethyl and propargyl groups (**1** and **2**). These two monomers were mixed in a series stoichiometries and Lewis acids. Numerous co-P5A syntheses have been published using an excess of the brominated monomer, usually 10:1,[10] but in our hands, the yield for the Co-P5A increased 10-fold when the ratio was lowered to 5:1. The only side product that we obtained was the per-brominated P5A (See Supporting Information for details).

Subsequent functionalization of **3** via copper-catalyzed azide-alkyne cycloaddition also proved to be unfruitful by a variety of common reaction conditions. Molecular modeling indicated that the barrel-shaped structure of **3** was closed on the top and bottom, as the flexible bromyethyl and propargyl appendages bent towards the hydrophobic cores. We hypothesized that the insertion of a guest molecule into the macrocycle could force the propargyl group into a solvent-exposed position. This hypothesis was supported by computational modelling and was verified experimentally. Simply switching the solvent from *tert*-butanol or dichloromethane to 1,2-dichloroethane, a solvent that is known to fit into the inner core of pillararene structures, increased the yield of the cycloaddition from 0% to 80% (Scheme 4-1).

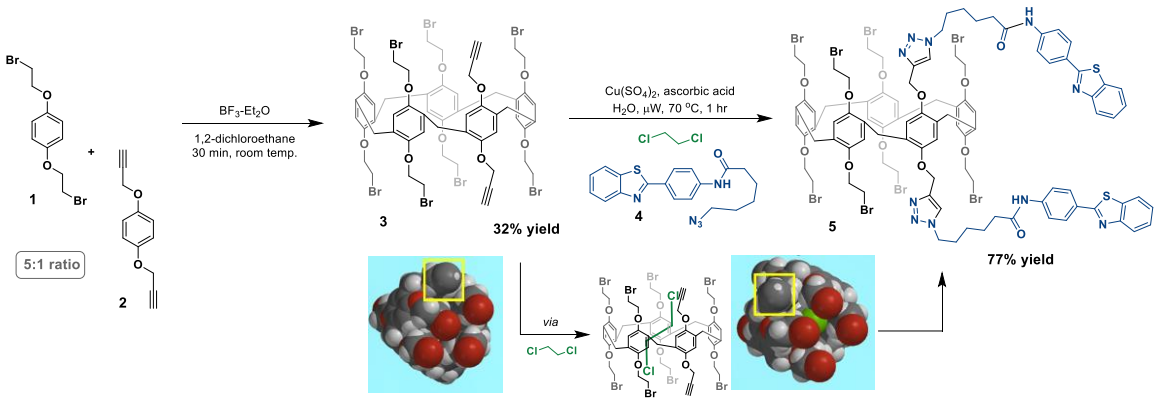

Figure 4.1: Optimized synthesis of functionalized co-pillararenes. (Molecular modeling images with propargyl group highlighted.)

We chose to append two thioflavin T (ThT) molecules to the P5A core using a flexible six-carbon linker. ThT is a fluorescent dye that is widely used for its ability to bind the β-amyloid plaques that are associated with Alzheimer's disease. However, the properties that were the most essential for the design of our molecular switch were ThT's linear structure and its fluorescent properties. Following the synthesis of the difunctionalized pillararene, **5**, we observed that formed a unique self-inclusion structure, where one of the pendant ThT-terminated "arms" was threaded through the core of the P5A (Figure 4-1)

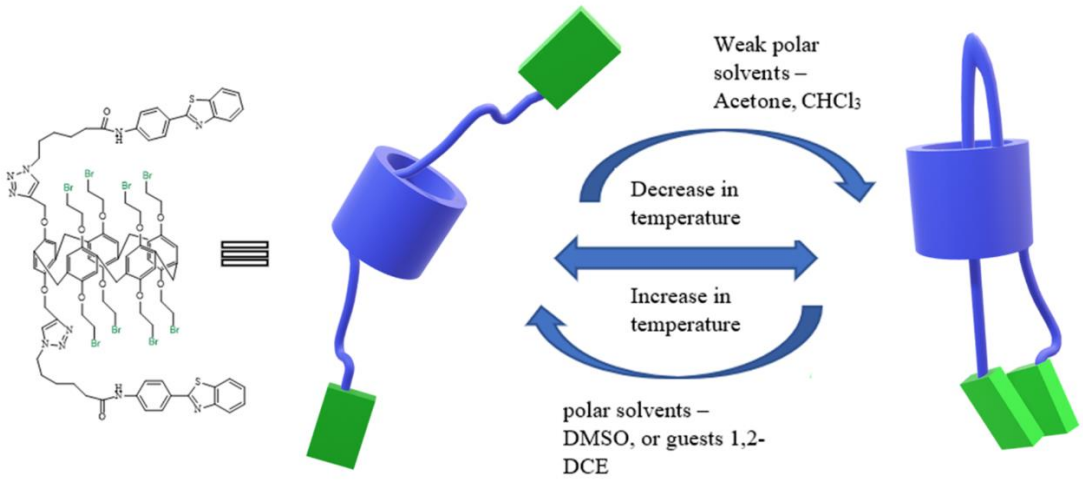

Figure 4.2: Cartoon representation of the self-inclusion behavior with the change of conditions

The inclusion behavior of ThT-pillararene was first studied via ^{1}H NMR spectroscopy in different solvents (Figures 4.4). In the ^{1}H NMR spectra, the unique upfield chemical shifts between -0.5 and -2.5 ppm correponds to the protons in the linker arm group connecting the ThT linker to the pillararene (Light blue region). This indicates the inclusion of the linker connected to the ThT group into the cavity of the P5A, which resulted in the formation of the inclusion structure ThT-CoP5A. Similar upfield shift phenomena were also observed from the spectrum using acetone-d_6 as the solvent. However, the signals of the protons of ThT-pillararene in ^{1}H NMR spectra was in the positive chemical shift range in strong polar solvents, such as DMSO-d_6, which meant that the

inclusion behavior of ThT-CoP5A was destroyed in DMSO-d_6. This type of behavior has been previously shown by Wu and his co-workers[9].

This was further investigated using the molecular dynamics studies using MOE computational software. Firstly a flexible assignment scan was conducted to find out if molecular dynamics could result in a structure with a self-inclusion. The scan gave us a flexible assignment showing the self-inclusion assignment. Next, a unit cell was created to accommodate the self-inclusion complex in the inclusion stage and DMSO-d_6 was used as a solvent, and multiple molecular dynamic iterations were carried out. From the results, it was evident that DMSO-d_6 pushes the ThT and the linker arm due to binding of DMSO inside the P5A cavity. The same control study was performed using the $CDCl_3$ as the solvent, the inclusion remains inside with no release of the linker arm with ThT.

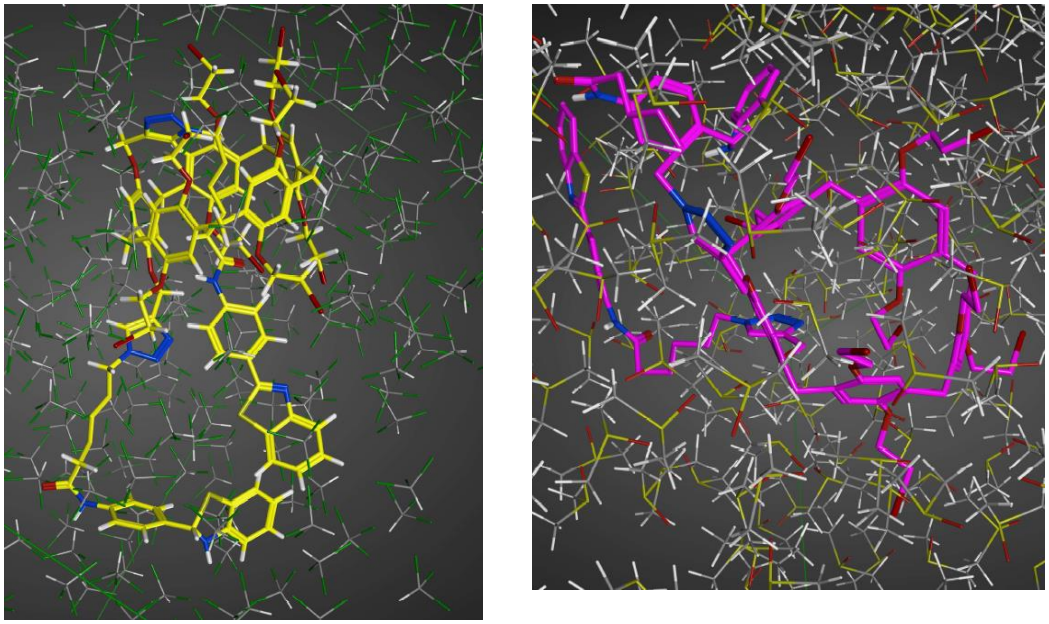

Figure 4.3: L to R, ThT Co-P5A in a simulated environment surrounded with CHCl3 molecules (Self-inclusion form), ThT Co-P5A in a simulated environment surrounded with DMSO molecules (Free-form)

To investigate whether the inclusion behavior was intramolecular or intermolecular, host-guest interaction between just the ThT azido linker and Co-P5A was firstly studied by themselves. This experiment was used as a control study to show the unique self-inclusion behavior present in the product itself. As shown in Figure S4.48 and S4.49 in the supplementary information, the ^{1}H NMR spectra of Co-P5A with the addition of different equivalents of ThT azido linker showed that the chemical shifts of the linker arm gradually shifted upfield with the increase of the ThT azido linker, exhibiting a fast exchange process within the NMR timescale. The most visible observation from this titration is that with the addition the chemical shifts corresponding to the linear arms became broader, which suggests that binding does take place. This broadening is not seen in the aromatic range of the linker, indicating that the linker arm protons do indeed bind in the cavity of

the Co-P5A. The linker arm protons have five distinguishable peak areas which range from ppm of 3.27, 2.38, 1.75, 1.62 and 1.44. These chemical shifts were then moved up field with the addition of ThT linker to ppm ranges of 3.11, 2.32, 1.66, 1.522 and 1.39. This means that there is only a slightly upfield shift around 0.16 ppm of these linker arm protons.

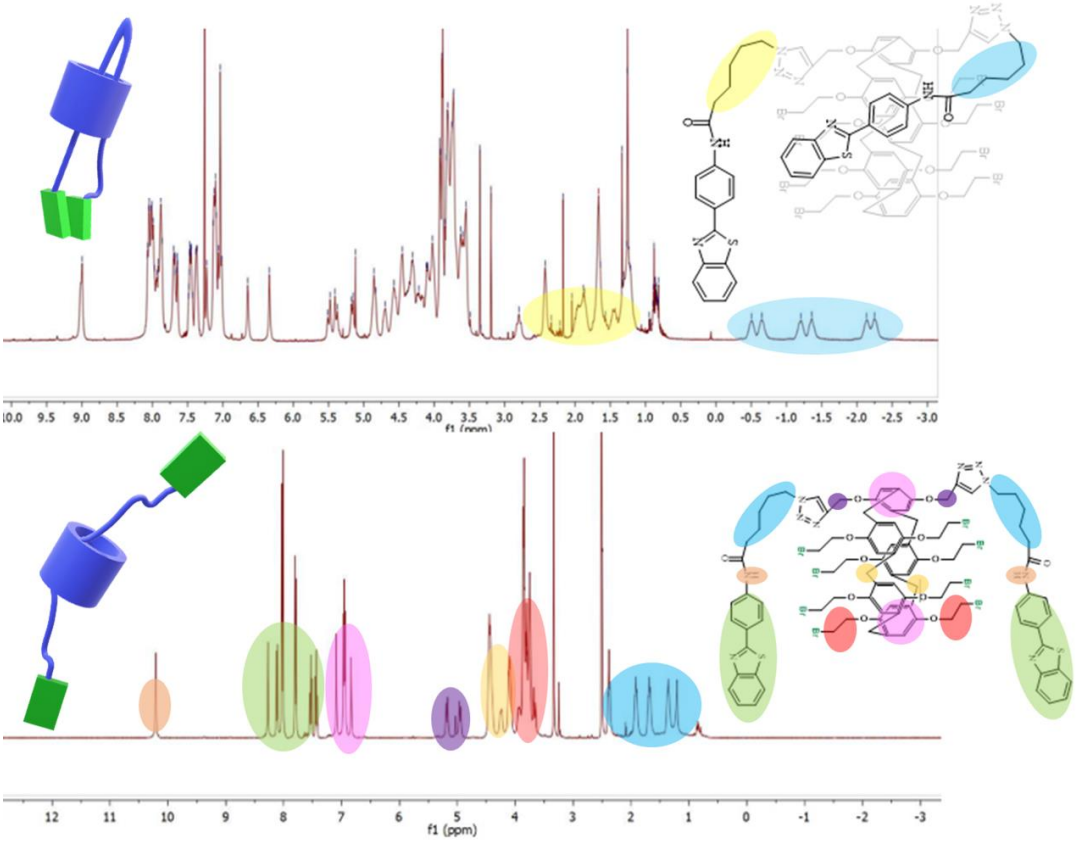

Figure 4.4: Top, ThT based CoP5A in CDCl3 and bottom, ThT based CoP5A in DMSO-d_6

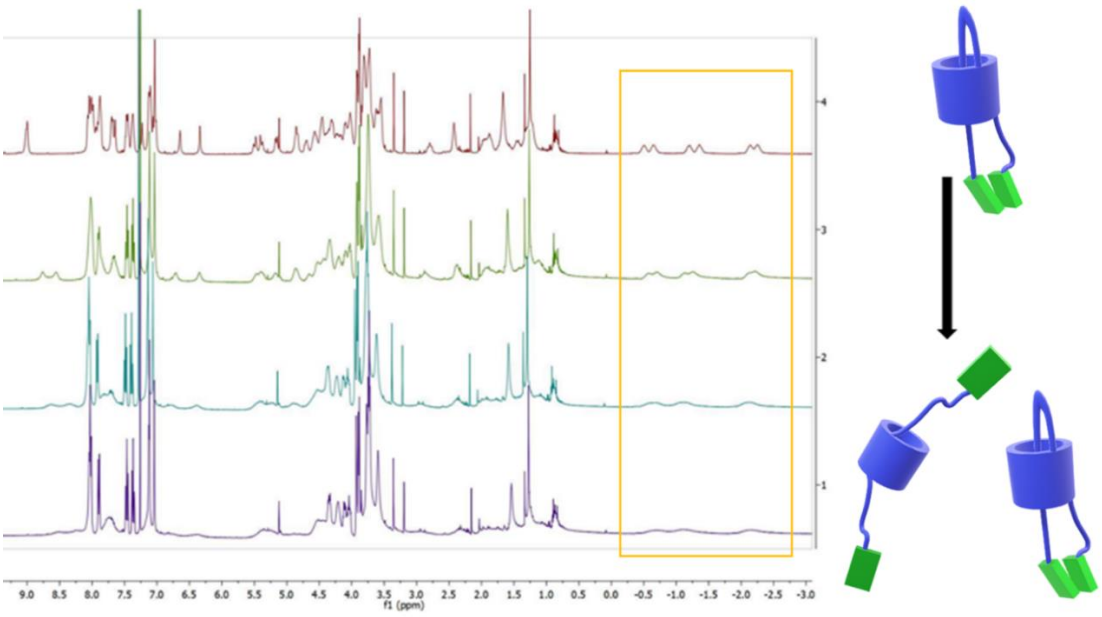

Figure 4.5: Temperature study of ^{1}H-NMR of ThT-CoP5A in $CDCl_3$

As the concentration increased, the proton resonances did not exhibit apparent changes even at high concentration levels of 500 mM, which almost reaches the saturation level of the ThT linker. As a result, the interaction between ThT azido linker and Co-P5A was weak. This confirms that the ThT-CoP5A molecule is indeed occurred due to intramolecular forces, this further confirmed that with the increase in ThT azido linker no negative chemical shift peaks were observed (seen when the self-inclusion takes place).

Moreover, variable concentration ^{1}H NMR spectroscopy of ThT-CoP5A in $CDCl_3$ was carried out to monitor the stability of the self-inclusion complex. It was found that the aggregates formed by ThT-CoP5A were stable even in very dilute $CDCl_3$ solution (1 mM) and still showed the negative chemical shifts. This points out that these interactions that are formed are strong and stable.

In addition, we conducted a variable temperature ^{1}H NMR spectroscopy. This was conducted to show that with heat the self-inclusion complex unwraps to form the free form. As

seen in figure 6, where the up-field peaks which were showing three doublets start to disappear slowly and the peaks of the spectra become sharper showing the release of the ThT-linker arm. However, we can still see that the up-field peaks do not disappear even after heating to 60 °C showing that a specific population of the Self-inclusion complexes still exists. Also, we reversed the temperature letting the sample gradually cool down, to show that the final product does not undergo decomposition at an elevated temperature (60 °C). This shows the stability under varying temperatures. The stability at 30 – 40 °C is important, allowing us to use the ability of self-inclusion of this molecule in a biological system.

^{1}H NMR COSY, ROESY, and TOCSY experiments were performed to investigate the binding of the linker arm further and show that one of the linker arms exists in the free form and the other stays at the self-inclusion form. The ROESY data shows that these movements are taking place in equilibrium in liquid form. The diagonal peaks (light green box) at the negative chemical shifts corresponds to the linker arm protons that are inside the cavity of the P5A, while the peaks below (light blue box) those represents the other linker arm protons that are outside the cavity. Presence of these two different sets of signals for the same linker arms implies that these protons are in chemical exchange.

Furthermore, these outside protons have direct ROE correlations with 1.85, 1.55 and 1.19 chemical shift peaks which confirms that these are the linker arm protons that is situated outside the cavity of P5A. Also, the negative peaks at -1.37 and -0.66 show ROE correlations to the aromatics of the P5A. Similar ROE peaks are seen from the negative chemical shifts to the methylene groups of P5A structure. Also, through TOCSY studies we were able to pinpoint the directionality of the linker arm bound to the cavity with respect to its chemical shifts -1.18, -2.38, -3.62, -3.25, -1.64 and -0.87 ppm. This pattern points out that the highest upfield chemical shifts are from the protons that are fully encapsulated within the cavity, while the others are exposed

outside. Therefore, we conclude that a stable pseudorotaxane system was formed in chloroform solvent.

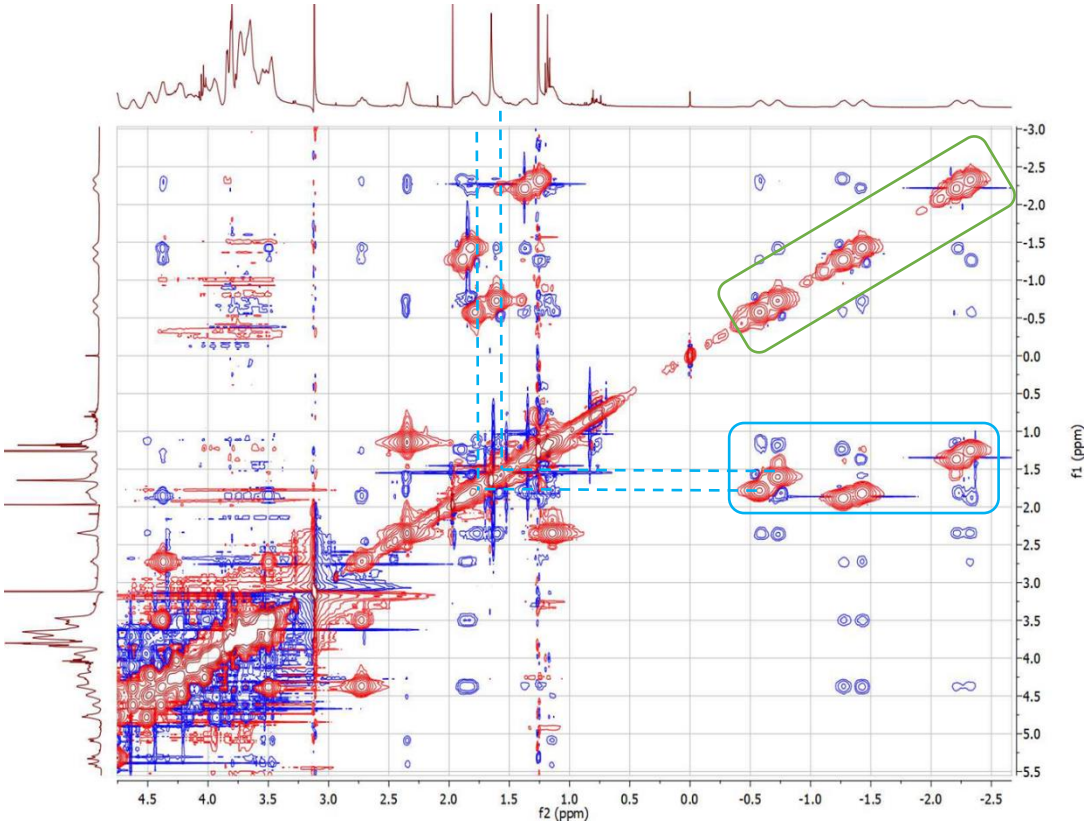

Figure 4.6: ROESY spectrum of ThT Co-P5A in $CDCl_3$

Subsequently, we attempted to investigate the dynamic behavior of this self-assembled ThT Co-P5A. As mentioned earlier, the effect of solvent polarity on this disassembly process was investigated. It was found that, with the increase of the solvent polarity by gradually adding DMSO-d_6 or 1,2-dichloroethane into the $CDCl_3$ solution of ThT-CoP5A, the negative chemical shifts for the linker arm present in th self-inclusion structure disappeared gradually. This observation suggested that the self-inclusion structure was gradually destroyed, presenting a slow exchange process within the NMR timescale. When the ratio of the mixture DMSO-d_6/$CDCl_3$ was raised to 1: 1 (v/v), most of the self-inclusion structure was switched into the free form. This was shown to be true to both solvents DMSO and 1,2-DCE (See supporting info for spectra).

Next, we studied competitive binding using fluorescence as shown in figure 6. ThT moieties are known to be fluorescent. Hence the overall molecule has a moderate fluorescence activity. This can be used to show the unwinding of the linker. Furthermore, we performed another titration experiment that refers to the addition of DMSO into the self-assembled structure in $CDCl_3$ to observe any changes in the fluorescence emission, due to the thioflavin moieties on the CoP5A results in fluorescence emission. This led to us to observe an increase in fluorescence emission with an addition of DMSO. As seen on the figure with the addition of the DMSO, a new band at 385 nm appeared which was not observed when no DMSO was present. We hypothesize that this new fluorescence signal corresponds to the open non-included complex.

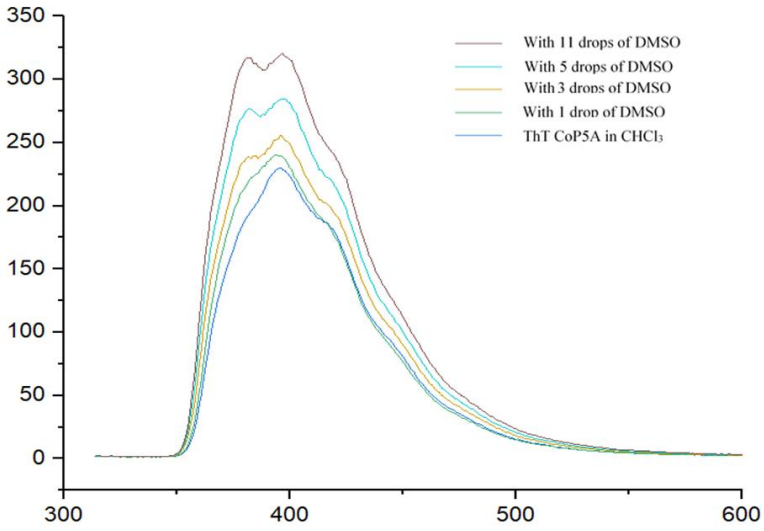

Figure 4.7: Fluorescence emission spectra of ThT self-assembled CoP5A, with the addition of DMSO. The excitation wavelength used was 304 nm

Furthermore, it is known that P5A has the tendency to bind small organic compounds such as adiponitrile inside its hydrophobic cavity. We gradually titrated this linear guest into a solution of ThT-CoP5A in $CDCl_3$ (the self-included complex). As soon as the guest was added, a new broad upfield peak started to form , corresponding to included adiponitrile, and the self-inclusion peaks started to disappear (Figure 4.9).

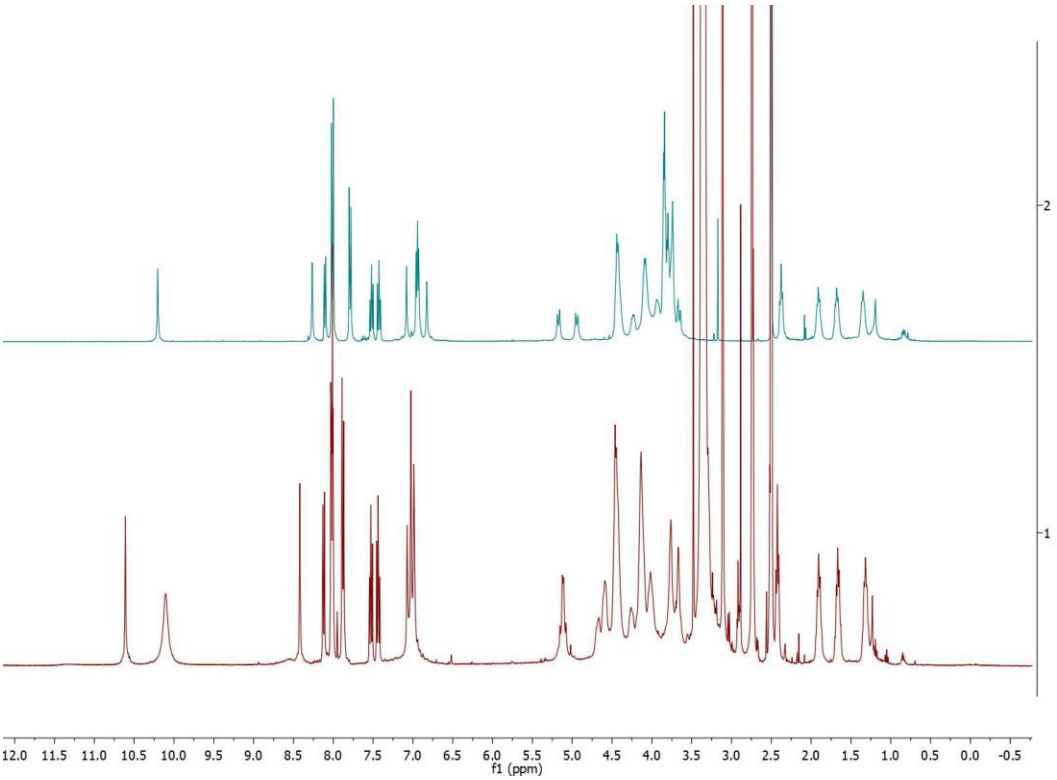

Figure 4.8: Stacked ^{1}H NMR of the non-water soluble and water-soluble ThT CoP5A

Once the self-inclusion phenomena were fully investigated, we focused on synthesizing a water-soluble version of the ThT-CoP5A (Figure 4.8). This was achieved by adding Me_3N and heating at 100 °C for 48 hours. Surprisingly, once the bromide groups are converted to ammonium ions, no inclusion phenomena were observed. This could be attributed to steric hindrance to the upper and lowers rims of the pillararene, but it could also simple be the consequence of the aqueous solvent, as we have previously shown that the polarity and size of the solvent can switch the ThT-Co-P5A from its included to open forms.

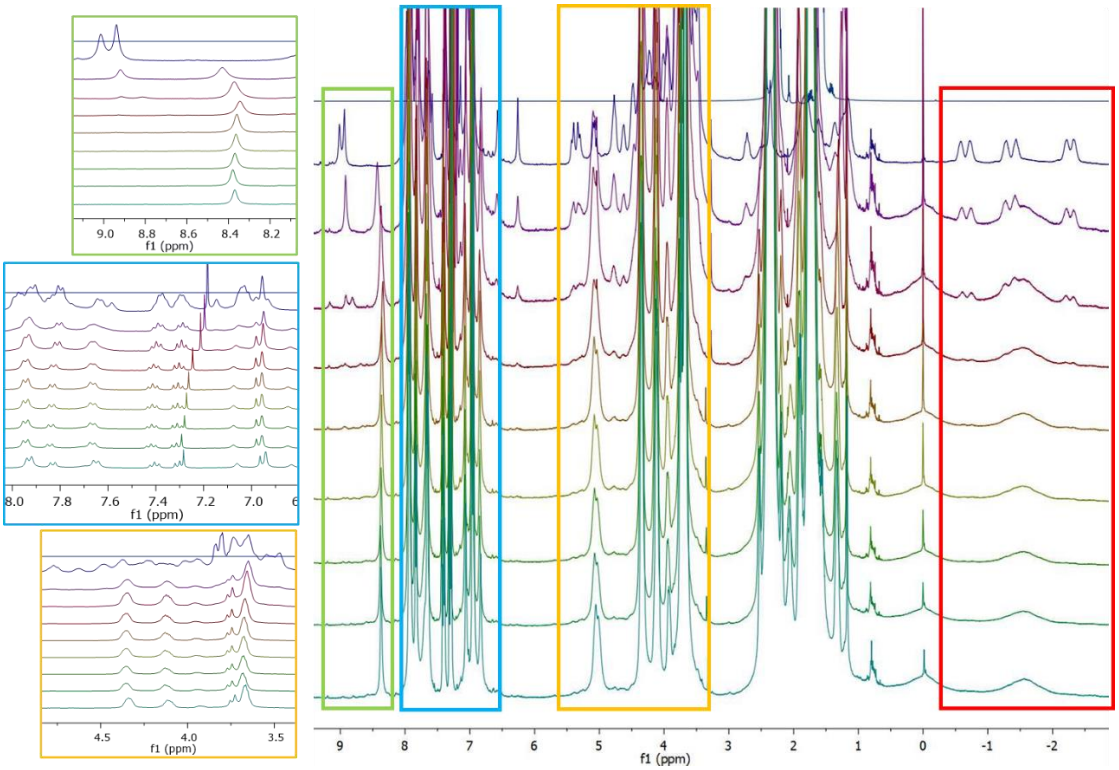

Figure 4.9: Titration of Adiponitrile in to ThT-CoP5A in CDCl3 at 298K, the boxes show zoomed images of the area, except red box indicates the binding of adiponitrile in the cavity of the ThT Co-P5ATitration of Adiponitrile in to ThT-CoP5A in $CDCl_3$ at 298K, the boxes show zoomed images of the area, except red box indicates the binding of adiponitrile in the cavity of the ThT Co-P5A

Conclusions

We have successfully synthesized a novel switchable pillar[5]arene structure that can be switched from closed to open with temperature and polar solvents. This switchable pillar[5]arene can be used as a molecular switch in applications.

4.1 REFERENCES

(1) Balzani, V.; Pez, Ä.; Stoddart, J. F. Molecular Machines. **1998**, *31* (7), 405–414. https://doi.org/10.1021/ar970340y.

(2) Yu, G.; Yu, W.; Mao, Z.; Gao, C.; Huang, F. A Pillararene-Based Ternary Drug-Delivery System with Photocontrolled Anticancer Drug Release. **2015**, No. 8, 919–925. https://doi.org/10.1002/smll.201402236.

(3) Ogoshi, T.; Kanai, S.; Fujinami, S.; Yamagishi, T. A.; Nakamoto, Y. Para-Bridged Symmetrical Pillar[5]Arenes: Their Lewis Acid Catalyzed Synthesis and Host-Guest Property. *J. Am. Chem. Soc.* **2008**, *130* (15), 5022–5023. https://doi.org/10.1021/ja711260m.

(4) Ogoshi, T.; Yamagishi, T.; Nakamoto, Y. Pillar-Shaped Macrocyclic Hosts Pillar [n] Arenes : New Key Players for Supramolecular Chemistry. **2016**. https://doi.org/10.1021/acs.chemrev.5b00765.

(5) Hane, F. T.; Fernando, A.; Prete, B. R. J.; Peloquin, B.; Karas, S.; Chaudhuri, S.; Chahal, S.; Shepelytskyi, Y.; Wade, A.; Li, T.; et al. Cyclodextrin-Based Pseudorotaxanes: Easily Conjugatable Scaffolds for Synthesizing Hyperpolarized Xenon-129 Magnetic Resonance Imaging Agents. *ACS Omega* **2018**, *3* (1), 677–681. https://doi.org/10.1021/acsomega.7b01744.

(6) Zamberlan, F.; Lesbats, C.; Rogers, N. J.; Krupa, J. L.; Pavlovskaya, G. E.; Thomas, N. R.; Faas, H. M.; Meersmann, T. Molecular Sensing with Hyperpolarized 129 Xe Using Switchable Chemical Exchange Relaxation Transfer. *ChemPhysChem* **2015**, *16* (11), 2294–2298. https://doi.org/10.1002/cphc.201500367.

(7) Reinke, A. A.; Gestwicki, J. E. NIH Public Access. *Chem Biol Drug Des* **2012**, *77* (6),

399–411. https://doi.org/10.1111/j.1747-0285.2011.01110.x.Insight.

(8) Chatani, E.; Inoue, R.; Imamura, H.; Sugiyama, M.; Kato, M.; Yamamoto, M.; Nishida, K.; Kanaya, T. Early Aggregation Preceding the Nucleation of Insulin Amyloid Fibrils as Monitored by Small-Angle X-Ray Scattering. *Sci. Rep.* **2015**, *5* (July), 15485. https://doi.org/10.1038/srep15485.

(9) Wu, X.; Ni, M.; Xia, W.; Hu, X. Y.; Wang, L. A Novel Dynamic Pseudo[1]Rotaxane Based on a Mono-Biotin-Functionalized Pillar[5]Arene. *Org. Chem. Front.* **2015**, *2* (9), 1013–1017. https://doi.org/10.1039/c5qo00159e.

(10) Yao, Y.; Xue, M.; Chi, X.; Ma, Y.; He, J.; Abliz, Z.; Huang, F. *Chemical Communications* **2012**, *48* (52), 6505.

4.2 SUPPORTING INFORMATION

A switchable pillar[5]arene based dual-arm self-assembly

Experimental section

Reagents

Substrates, hydroquinone, boron trifluoride etherate, 1,2 dichloroethane, dichloromethane, DMF, sodium azide, $CuSO_4$. $5H_2O$, sodium ascorbate, tri methyl amine, CBr_4, methanol, acetonitrile,

were purchased from Sigma-Aldrich, Fisher Scientific, and TCI chemicals. All reagents were stored under an inert atmosphere before use. Unless otherwise noted, all reactions were performed under N_2.

Instrumentation

NMR spectra were obtained using a Bruker Avance 300 MHz and 400 MHz spectrometers. Low-resolution mass spectrometry was performed using a Shimadzu LRMS-2020. High-resolution mass spectrometry was performed using a Thermo Scientific LTQ Orbitrap XL™ instrument. Isothermal calorimetry was performed using TA Instruments TAM III™ instrument, Fluorescence spectrometer and UV-Vis spectrometer

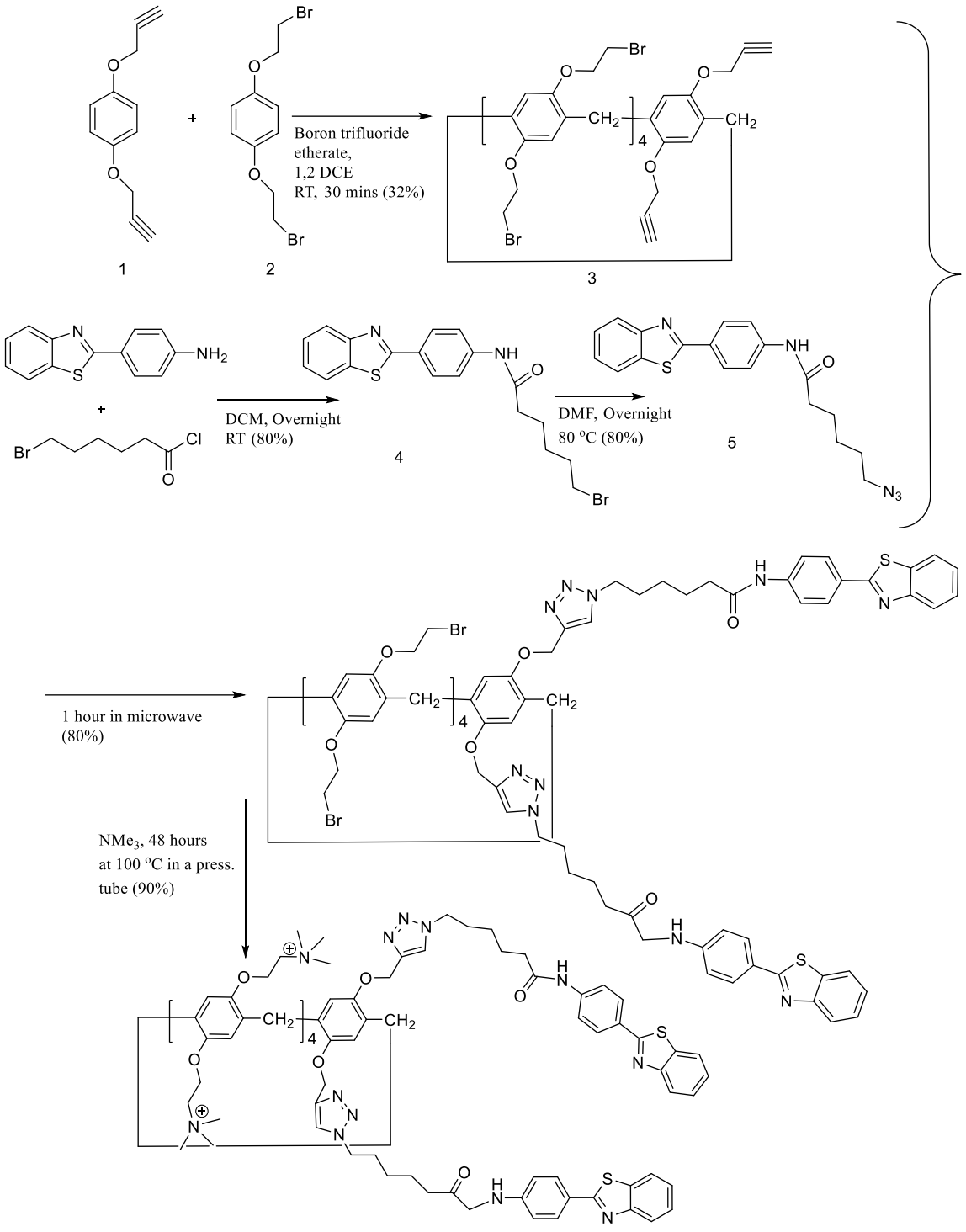

Scheme 4-1: The complete synthetic scheme of synthesis of dual-ThT appended Co-P5A

Synthesis of Brominated monomer

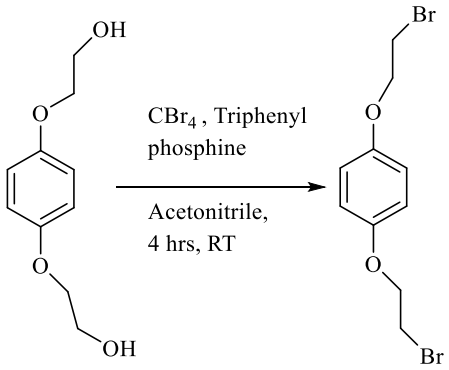

A solution of 1,4-bis(2-hydroxyethyl)benzene (10.0 g, 50.4 mmol) and triphenylphosphine (31.5 g, 120mmol) in dry acetonitrile (250 mL) was cooled in an ice bath. While vigorous stirring, carbon tetrabromide (39.8 g, 120 mmol) was slowly added in four portions. In every addition, the solution immediately turns in to bright yellow and with futher stirring returns to its colorless form. On the final addition, the solution stays cloudy. The mixture was stirred at room temperature for 4 hours and 20 minutes. Then cold water (200 mL) was added to the reaction mixture to give white precipitation. This collected precipitate was washed with another 200 ml of cold water and methanol/water wash. (3:2, 3 × 100 mL). The collected white solids were dried under vacuum for 24 hours and used without further purification. (14.5 g, 97%). ^{1}H NMR and ^{13}C NMR were performed using $CDCl_3$. ^{1}H NMR (400 MHz, Chloroform-d) δ 6.89 (s, 4H), 4.27 (t, J = 6.3 Hz, 4H), 3.64 (t, J = 6.3 Hz, 4H). ^{13}C NMR (101 MHz, DMSO-d_6) δ 154.2, 118.3, 69.7, 29.8

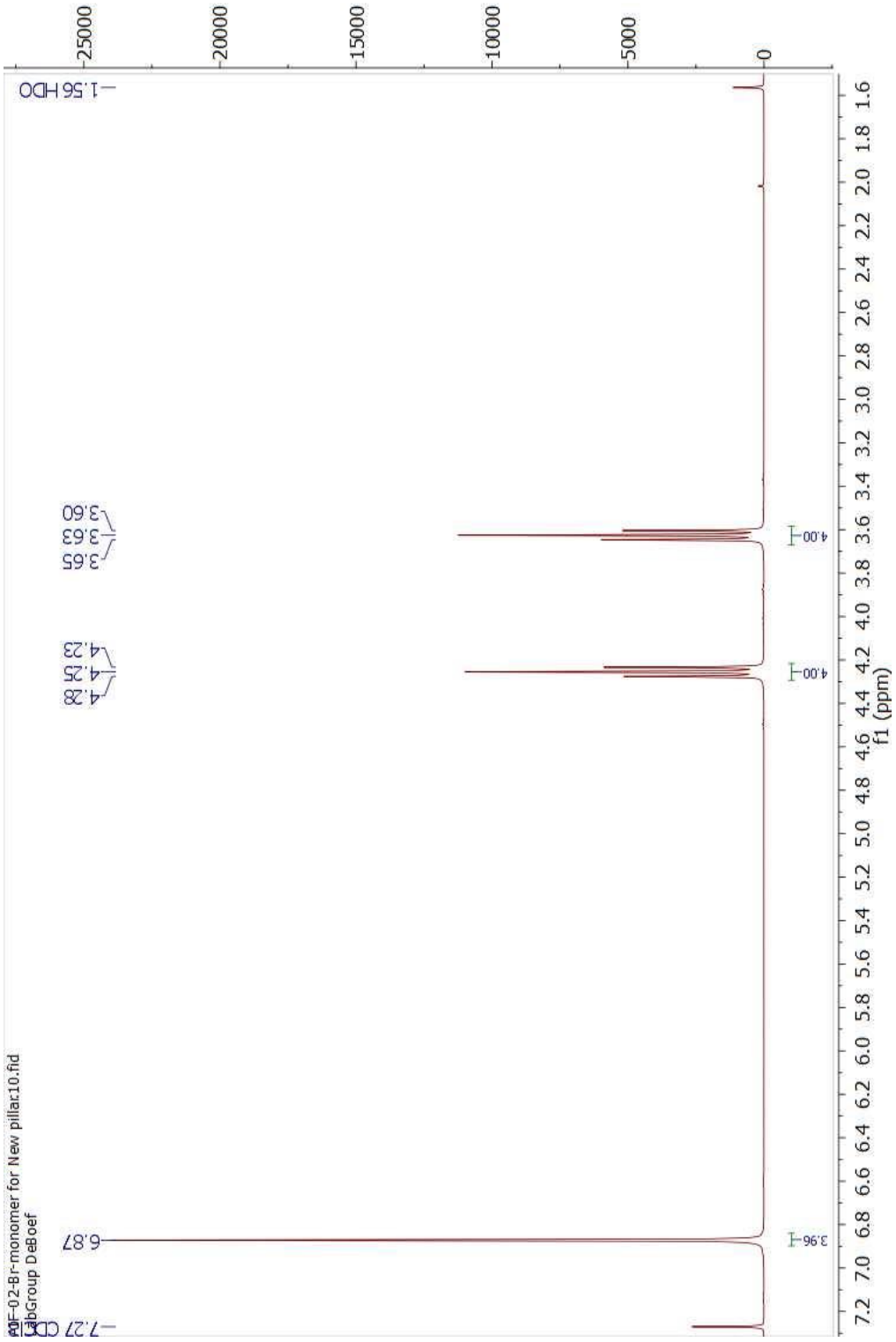

Figure 4.10: ^{1}H NMR of Brominated monomer

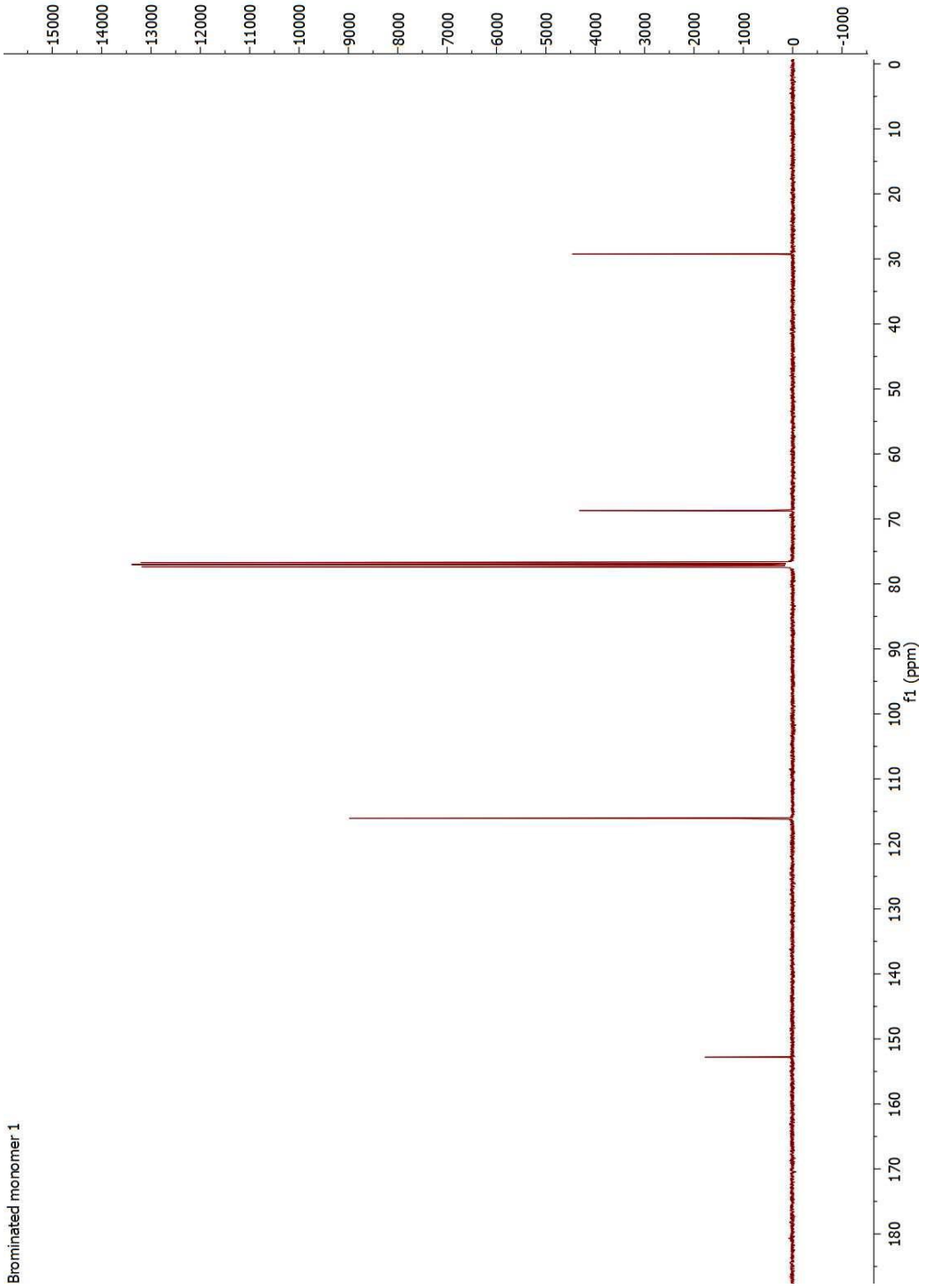

Figure 4.11: ^{13}C-NMR of Brominated monomer

Synthesis of proapargylated monomer

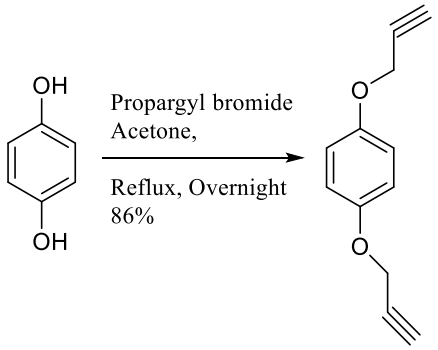

Hydroquinone, anhydrous potassium carbonate was added into solution of acetonitrile. Then the reaction mixture containing RBF was placed on an ice bath. Next, the propargyl bromide was added in drop wisely. Then, the reaction solution was stirred 20 hours at 60 °C. Once the reaction was completed, the solvent was removed via rotary evaporation. Dichloromethane (100 ml) was added into the RBF, and this was transferred into a separatory funnel for further washes. Washing steps were conducted using 2.5 M NaOH (3 x 100 ml) followed with DI water (3 x 100 ml) and finally with brine (2 x 100 ml). Then the DCM layer was collected and dried over anhydrous sodium sulfate. The final mixture was subjected to dry loaded automated flash chromatography. ^{1}H NMR and ^{13}C NMR were performed using $CDCl_3$. ^{1}H NMR (400 MHz, DMSO-d6) δ 6.95 (s, 4H), 4.74 (d, J = 2.5 Hz, 4H), 3.53 (t, J = 2.4 Hz, 2H). ^{13}C NMR (101 MHz, DMSO-d_6) δ 147.6, 111.3, 74.1, 70.6, 51.7.

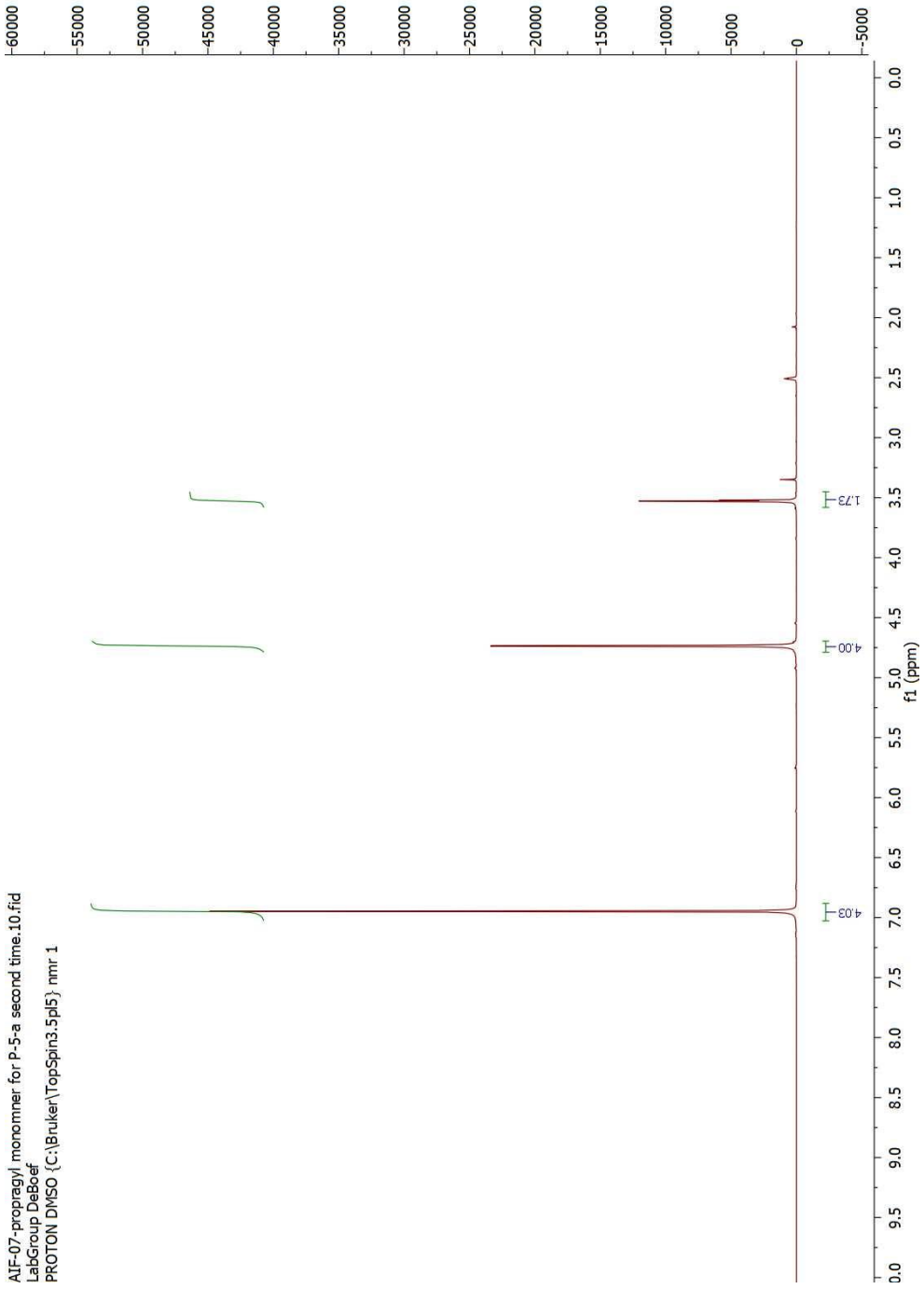

Figure 4.12: ^{1}H-NMR of proapargylated monomer

Synthesis of Co-pillar[5]arene

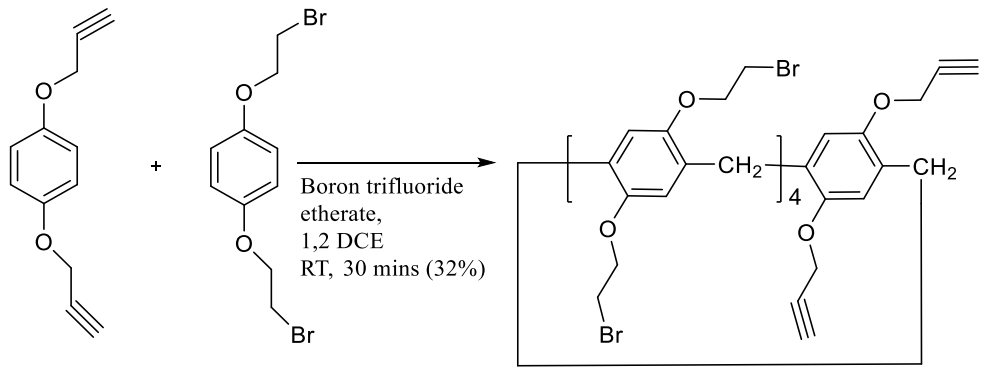

Brominated monomer, proapargylated monomer, and paraformaldehyde were added into an RBF charged with 1,2-dichloroethane. Next, the boron trifluoride etherate was added in dropwise at room temperature. The reaction mixture was left to stir at room temperature for 30 minutes. Subsequently, 20 ml of methanol was added after the 30 minutes to quench the reaction. The resulting solution was evaporated using the rotary evaporator. To the dried mixture, 20 ml of DCM was added, which was then transferred into a separatory funnel for further washing. Washing steps were conducted using 10% (m/v) sodium bicarbonate (2 x 10 ml) which was followed with 10 ml DI water wash. The collected DCM layer was evaporated and the directly subjected into dry loaded automated flash chromatography. ^{1}H NMR and ^{13}C NMR were performed using $CDCl_3$. ^{1}H NMR (400 MHz, Chloroform-d) δ 6.84 (s, 2H), 6.81 – 6.77 (m, 6H), 6.69 (s, 2H), 4.51 (d, J = 2.4 Hz, 4H), 4.18 – 4.05 (m, 17H), 3.80 – 3.73 (m, 10H), 3.53 (dtd, J = 21.0, 5.7, 2.3 Hz, 17H), 2.13 (t, J = 2.4 Hz, 2H). ^{13}C NMR (101 MHz, Chloroform-*d*) δ 149.73, 149.70, 149.6, 149.3, 129.4, 129.1, 129.0, 128.9, 116.2, 116.1, 115.9, 115.8, 115.6, 79.2, 74.9, 69.1, 69.1, 68.9, 68.9, 68.7, 30.6, 30.5, 30.4, 29.8, 29.7, 29.4.

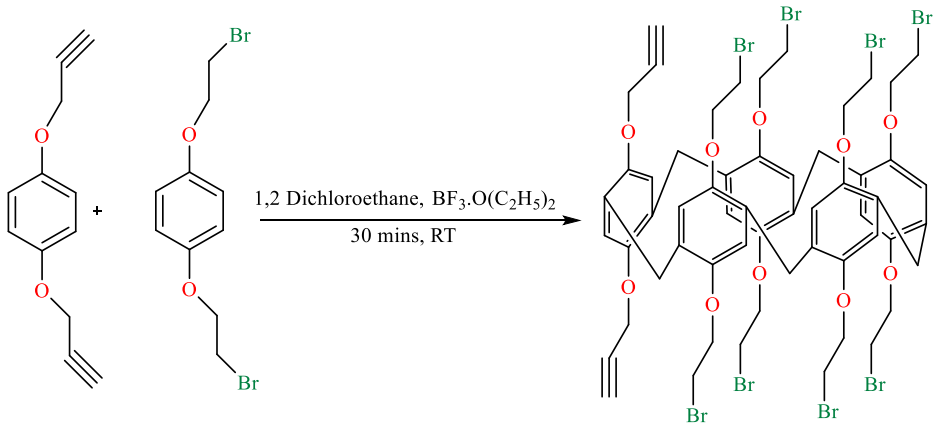

Equivalents of propargyl monomer	Equivalents of brominated monomer	Lewis acid	% yield
1	4	$BF_3.O(C_2H_5)_2$	24
1	5	$BF_3.O(C_2H_5)_2$	32
1	7	$BF_3.O(C_2H_5)_2$	14
1	8	$BF_3.O(C_2H_5)_2$	5
1	10	$BF_3.O(C_2H_5)_2$	3
1	8	$FeCl_3$	No rxn
1	10	$FeCl_3$	No rxn

Table 4-1: The data represents the yields that were obtained with the change of the brominated monomer equivalents and the type of Lewis acid

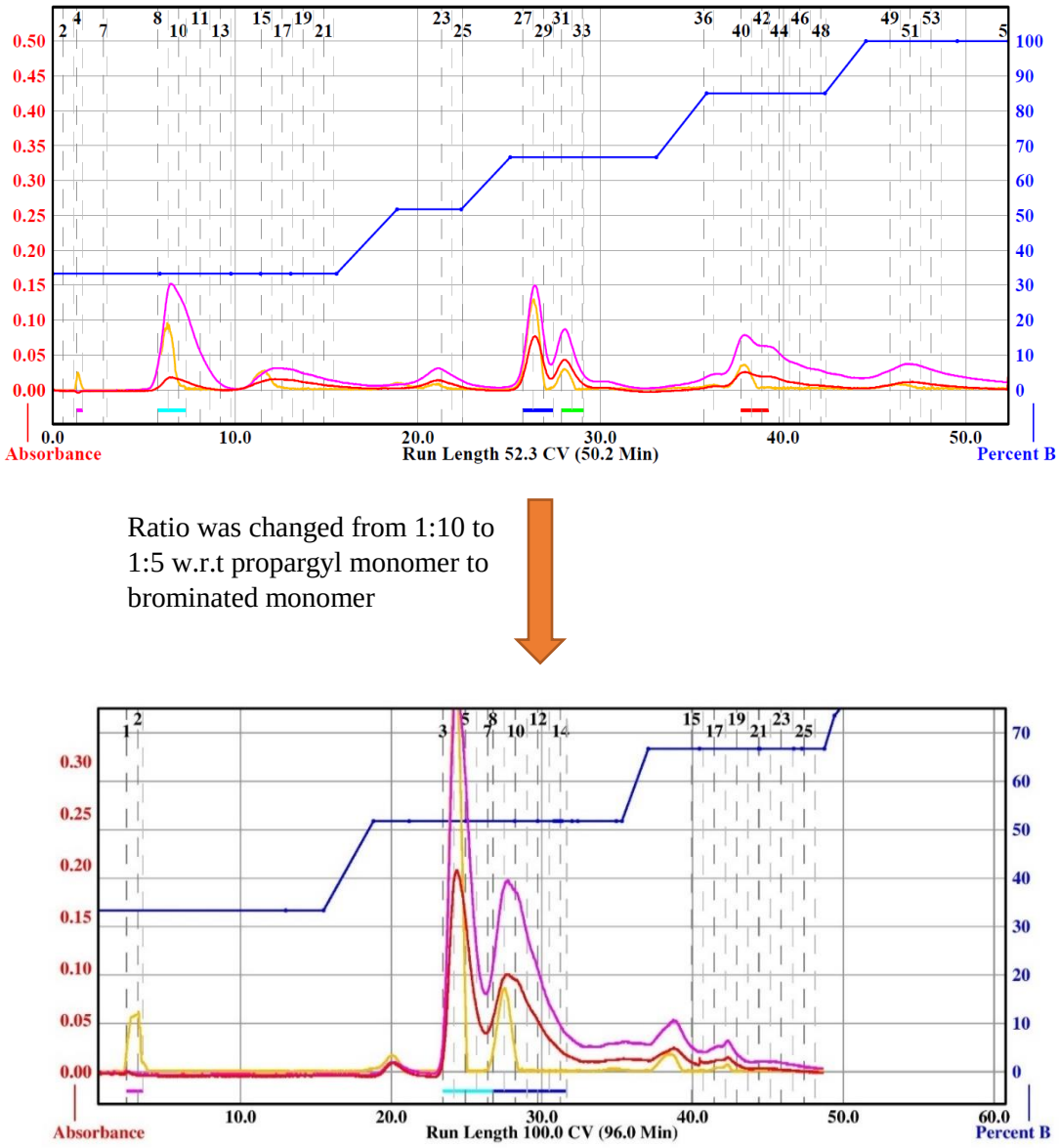

Figure 4.13: Top: the flash chromatogram of the 1:10 equivalents in hexane/dichloromethane solvent system. Peaks correspond to products that were recovered. Bottom: flash chromatogram of the 1:5 equivalents in hexane/dichloromethane solvent system

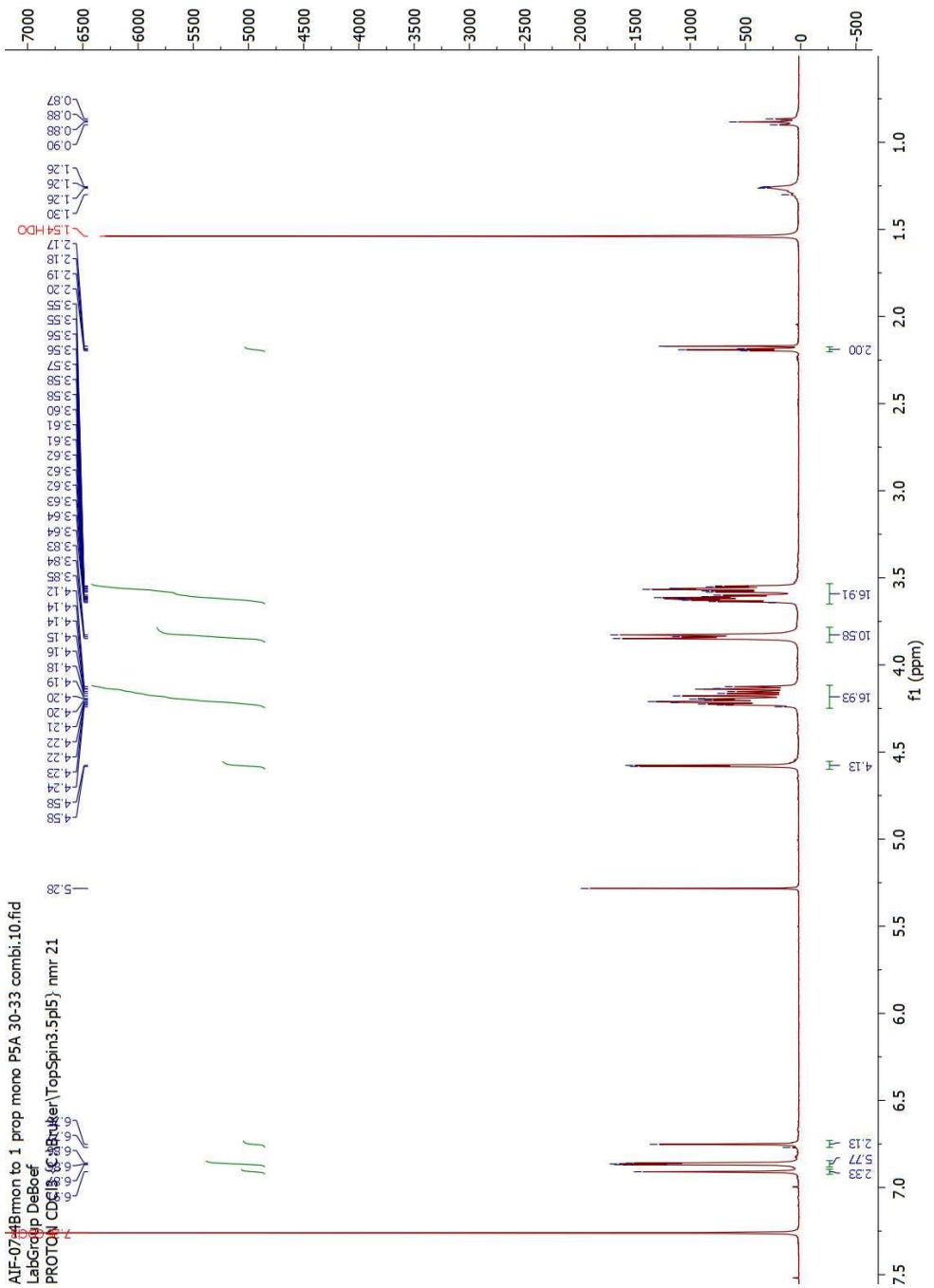

Figure 4.14: ^{1}H-NMR of Co-pillar[5]arene

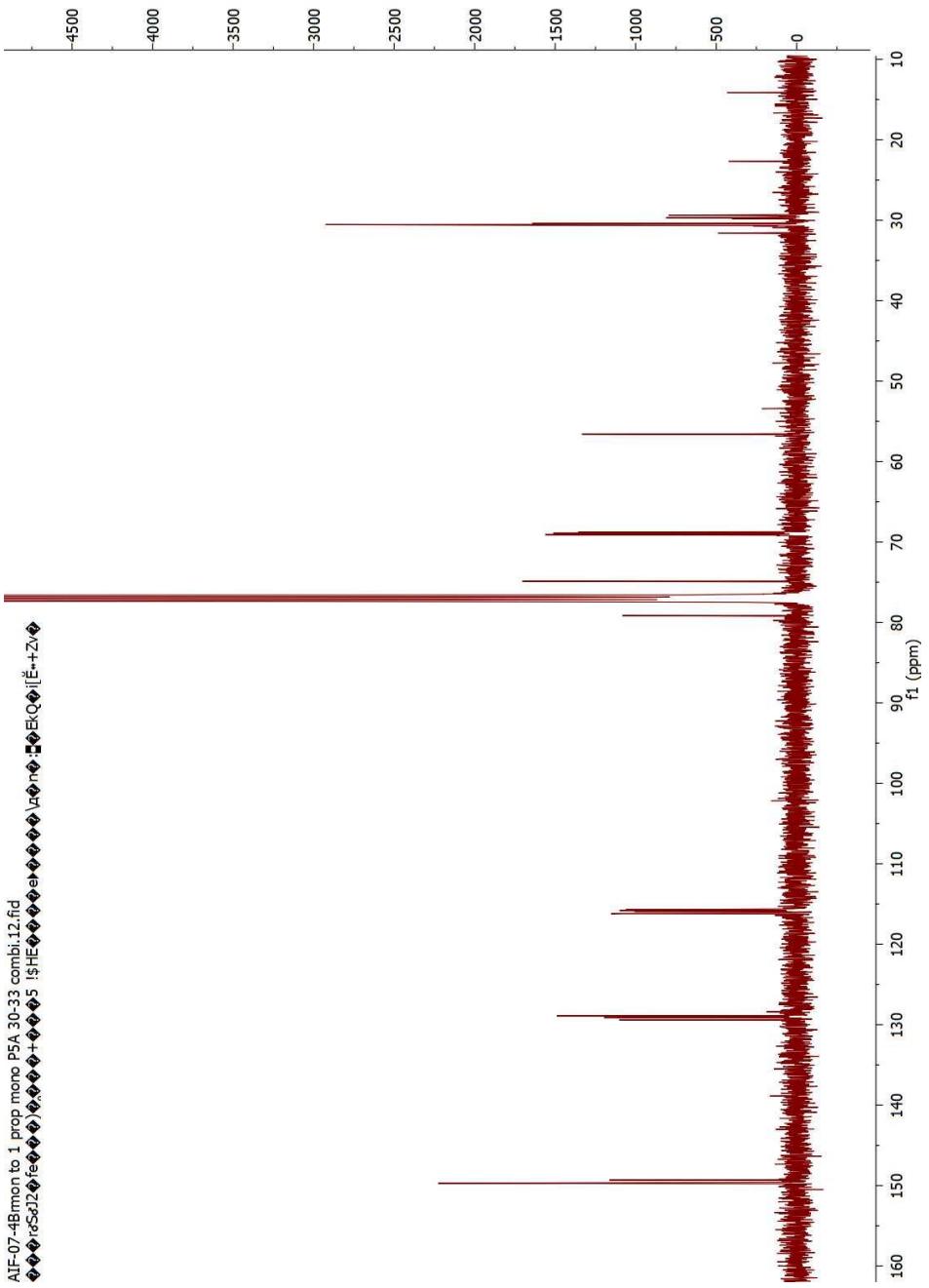

Figure 4.15: ^{13}C-NMR of Co-pillar[5]arene

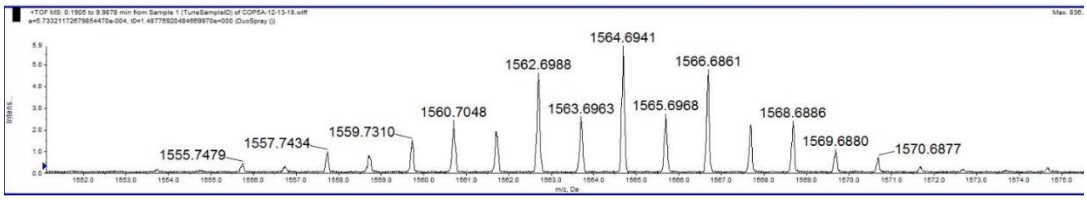

Figure 4.16: Mass spectrum of Co-pillar[5]arene

Synthesis of Thioflavin

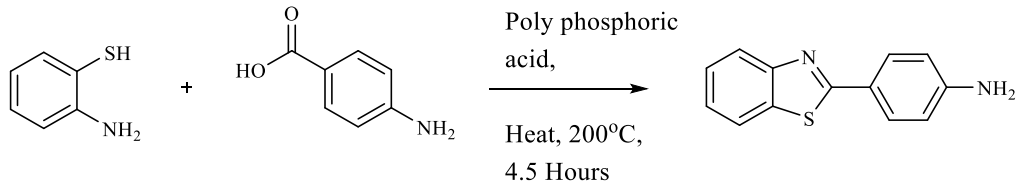

p-Amino Benzoic Acid (2.74 g, 20.0 mmol) and 2-Aminothiophenol (2.14 ml, 20.0 mmol) was dissolved in (21.03 g, 250.00 mmol) polyphosphoric acid. The mixture was heated at 200°C and stirred for 4.5 hours. After cooling, 10% Na_2CO_3 was slowly poured into solution. This resulted in a greenish mixture. This solution was stirred until gas evolution was completed. Next, the solution was filtered using vacuum filtration. The solid was washed with water (3x50mL) and recrystallized with MeOH and H_2O to give the final product. The yield was 70%. ^{1}H-NMR was performed using DMSO-d_6. Literature-based procedure was followed[1]. LRMS ESI (m/z): [M+H] calculated for $C_{13}H_{10}N_2S$ 227.06, observed 227.05. ^{1}H NMR and ^{13}C NMR were performed using DMSO-d_6. ^{1}H NMR (400 MHz, DMSO-d_6) δ 8.02 (d, *J* = 8.0, 1.1 Hz, 1H), 7.90 (d, *J* = 8.0 Hz, 1H), 7.76 (t, *J* = 8.7 Hz, 2H), 7.45 (d, *J* = 7.7 Hz, 1H), 7.34 (d, *J* = 7.7 Hz, 1H), 6.67 (d, *J* = 8.6 Hz, 2H), 5.88 (br, 2H).

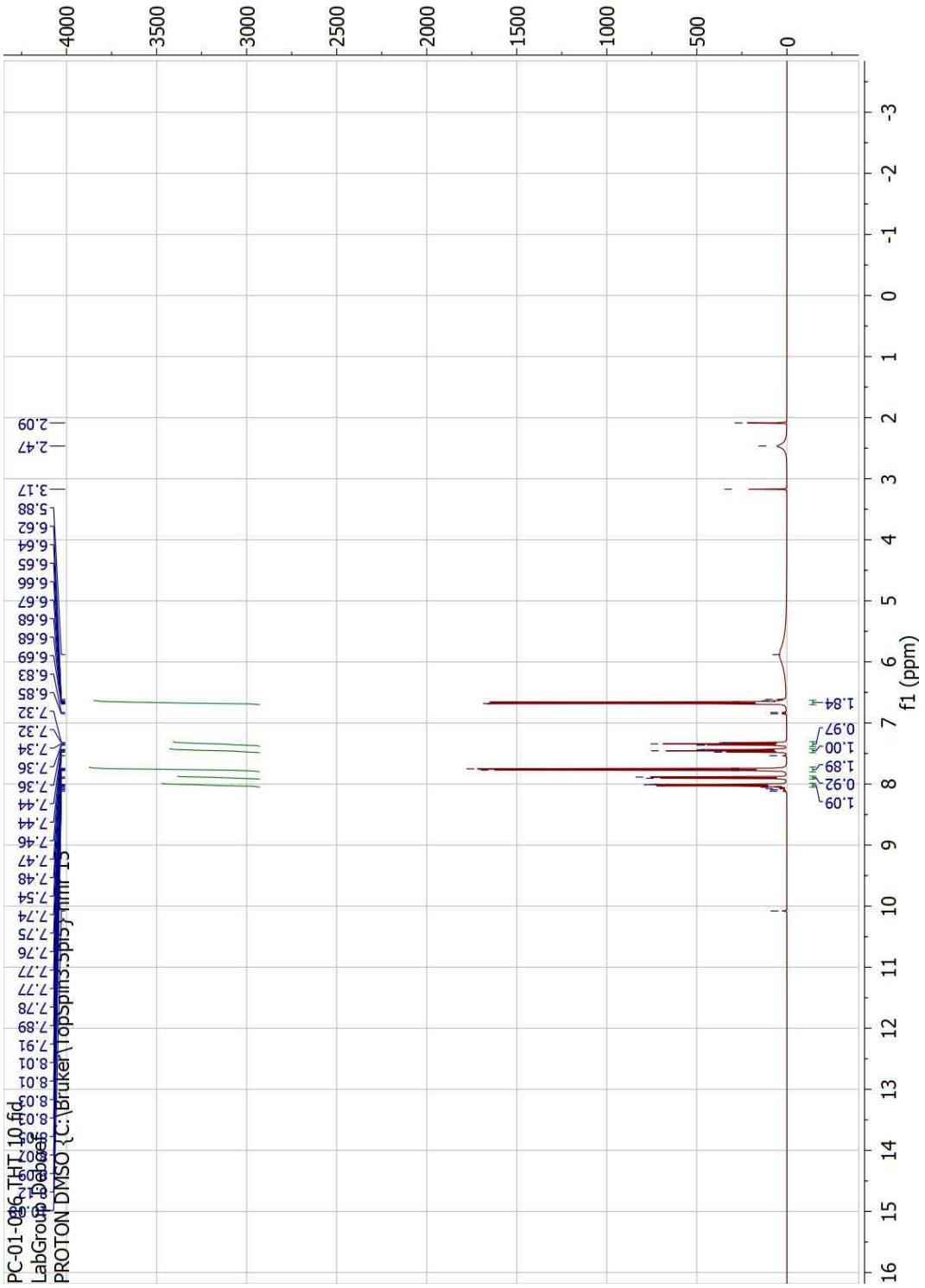

Figure 4.17: ^{1}H NMR of Thioflavin

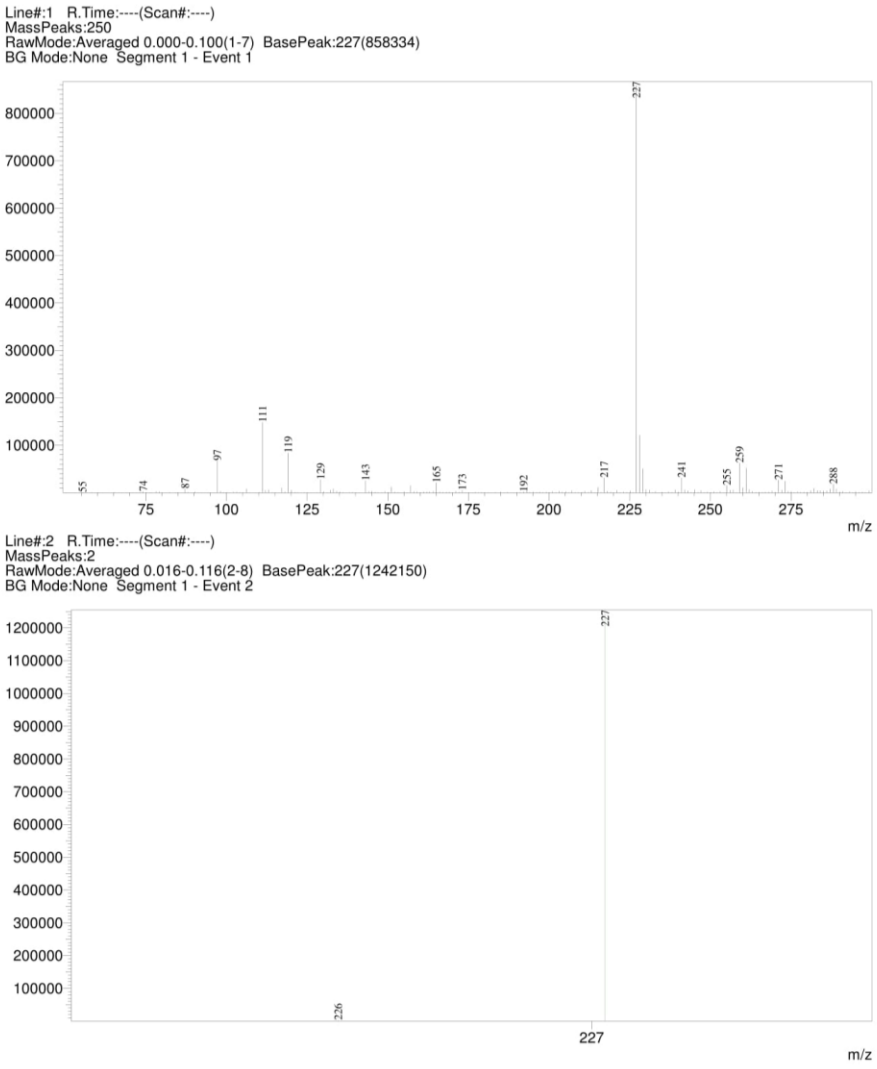

Figure 4.18: Mass spectrum of Thioflavin

Synthesis of Thioflavin-6-Br linker

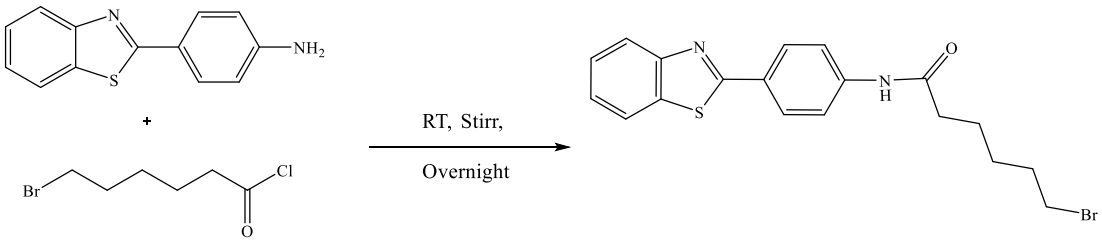

ThT-NH_2 (452.6 mg, 2.00 mmol) was dissolved in 20 ml of anhydrous CH_2Cl_2. To this mixture 6-Bromohexonoyl chloride (305.0 µl, 2.00 mmol) was added drop wisely. The reaction was performed inside the glove box with a Nitrogen atmosphere. The reaction mixture was stirred overnight at room temperature. The reaction was monitored by TLC. After overnight stirring the mixture was poured into several centrifuge tubes and centrifuged for 15 minutes at 6000 rpm. Once centrifugation was completed, the supernatant was discarded. CH_2Cl_2 was added into the remaining precipitate and centrifuged again. Once again, the supernatant was discarded, and this was done for two more times with a total of three washes with CH_2Cl_2. Finally, the remaining precipitate was dissolved in deuterated $CDCl_3$ and centrifuged, and the precipitate was collected with the removal of $CDCl_3$. ($CDCl_3$ was used to remove the CH_2Cl_2 peak from the spectra.) This was subjected to overnight vacuum. The product was further purified using automated flash chromatography. The reaction yielded 59%. ^{1}H-NMR and ^{13}C-NMR were performed using DMSO-d_6. ^{1}H NMR (400 MHz, DMSO-d_6) δ 10.25 (s, 1H), 8.12 (dd, *J* = 8.0, 1.2 Hz, 1H), 8.03 (td, *J* = 8.7, 7.8, 2.5 Hz, 3H), 7.80 (dd, *J* = 8.8, 2.6 Hz, 2H), 7.53 (ddd, *J* = 8.3, 7.2, 1.3 Hz, 1H), 7.43 (ddd, *J* = 8.3, 7.2, 1.2 Hz, 1H), 3.64 (q, *J* = 6.6 Hz, 1H), 3.55 (t, *J* = 6.7 Hz, 1H), 2.38 (t, *J* = 7.4 Hz, 2H), 1.80 (dm, *J* = 34.0, 7.5, 7.0, 6.8 Hz, 2H), 1.68 – 1.58 (m, *J* = 7.5 Hz, 2H), 1.44 (t, *J* = 8.2, 7.1 Hz, 2H).LRMS ESI (m/z): [M+H] calculated for $C_{19}H_{19}BrN_2OS$ 403.05, observed 403.05

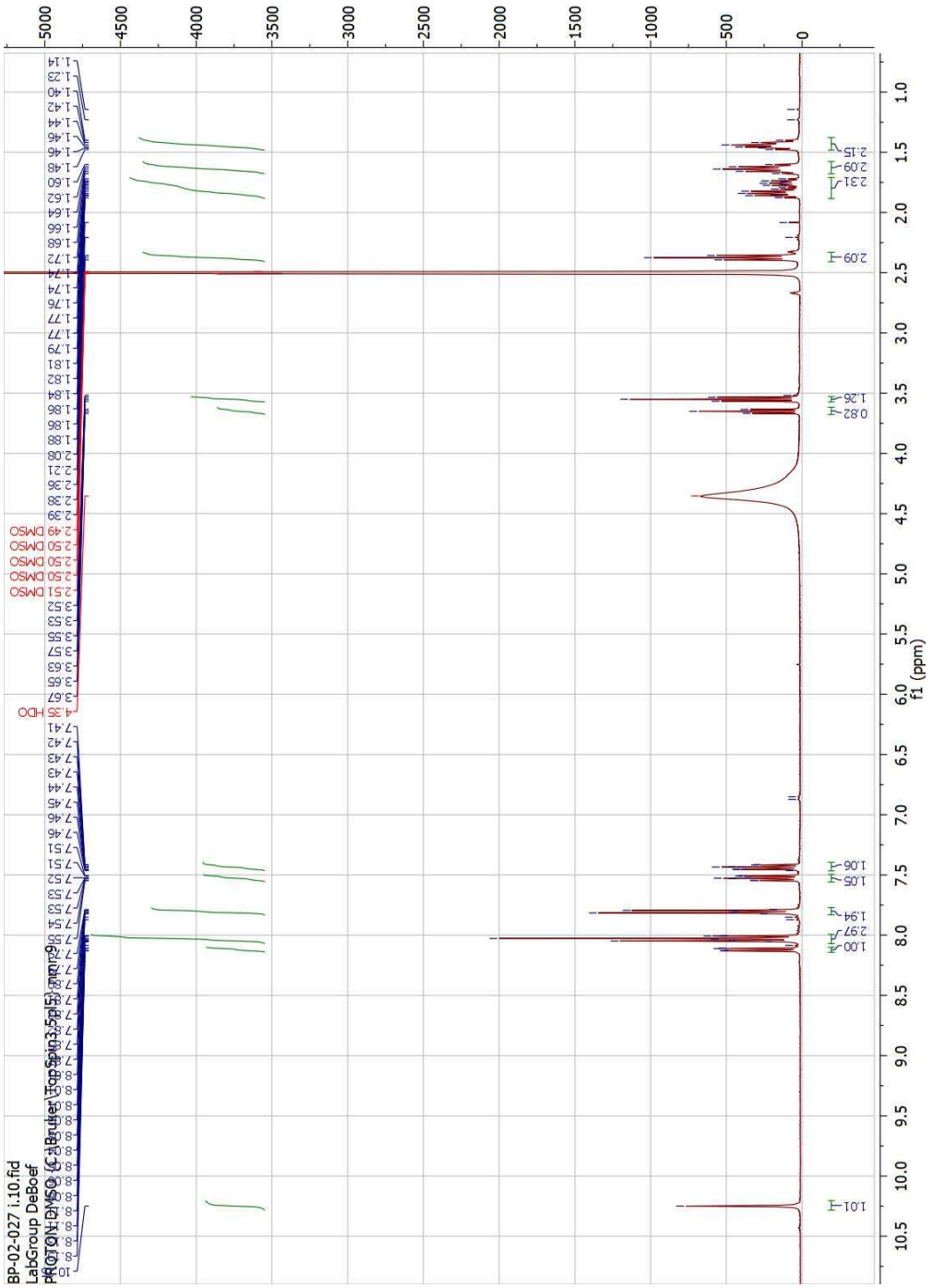

Figure 4.19: ^{1}H NMR of Thioflavin-6-Br linker

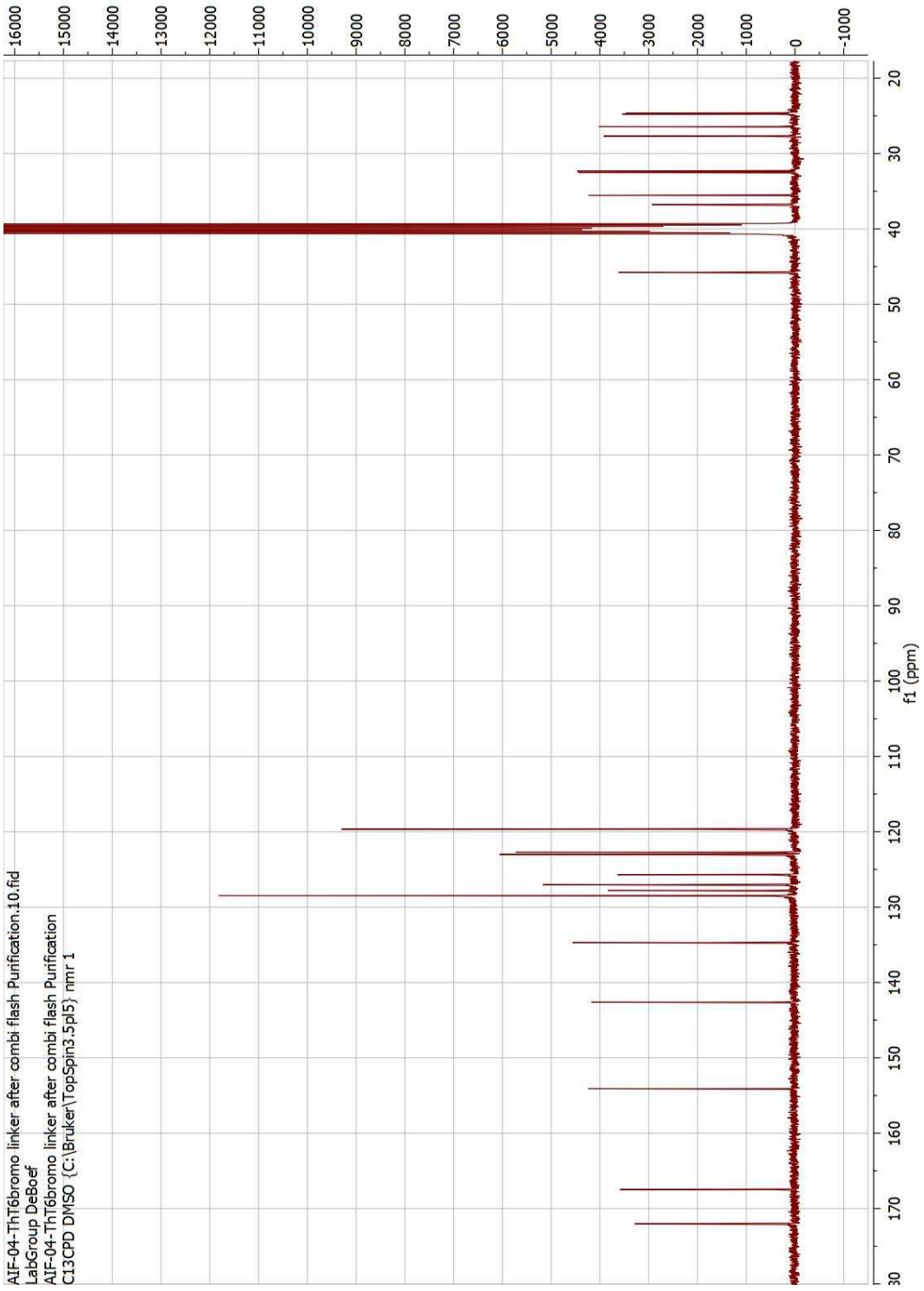

Figure 4.20: ^{13}C NMR of Thioflavin-6-Br linker

Synthesis of Thioflavin-6-azide

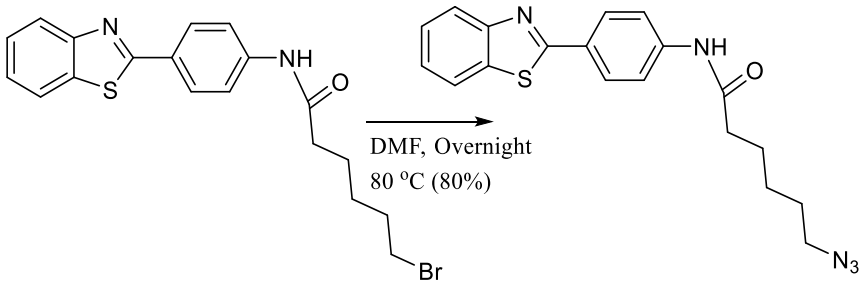

ThT-6-Br (1 equiv.) was dissolved in anhydrous DMF 30 ml and to this solution Sodium azide (4 equiv.) was added. This reaction mixture was stirred at 80 °C for 12 hours. The resulted reaction mixture was quenched by adding 150 ml of DI water and the extraction with ethyl acetate (3 x 100ml). The collected organic layer was dried over anhydrous sodium sulfate and subjected to dry loaded automated flash chromatography. ^{1}H NMR was performed using DMSO-d_6. ^{1}H NMR (300 MHz, DMSO-d6) δ 10.23 (s, 1H), 8.16 – 8.11 (m, 1H), 8.08 – 8.01 (m, 3H), 7.84 – 7.78 (m, 2H), 7.54 (ddd, J = 8.3, 7.2, 1.4 Hz, 1H), 7.44 (ddd, J = 8.3, 7.2, 1.3 Hz, 1H), 3.37 (t, J = 6.8 Hz, 2H), 2.38 (t, J = 7.3 Hz, 2H), 1.60 (dq, J = 18.5, 7.2 Hz, 4H), 1.46 – 1.32 (m, 2H). ^{13}C NMR (101 MHz, DMSO-d_6) δ 172.1, 167.5, 154.1, 142.6, 134.7, 128.5, 127.8, 127.0, 125.7, 123.0, 122.7, 119.6, 50.9, 36.8, 28.5, 26.3, 25.0.

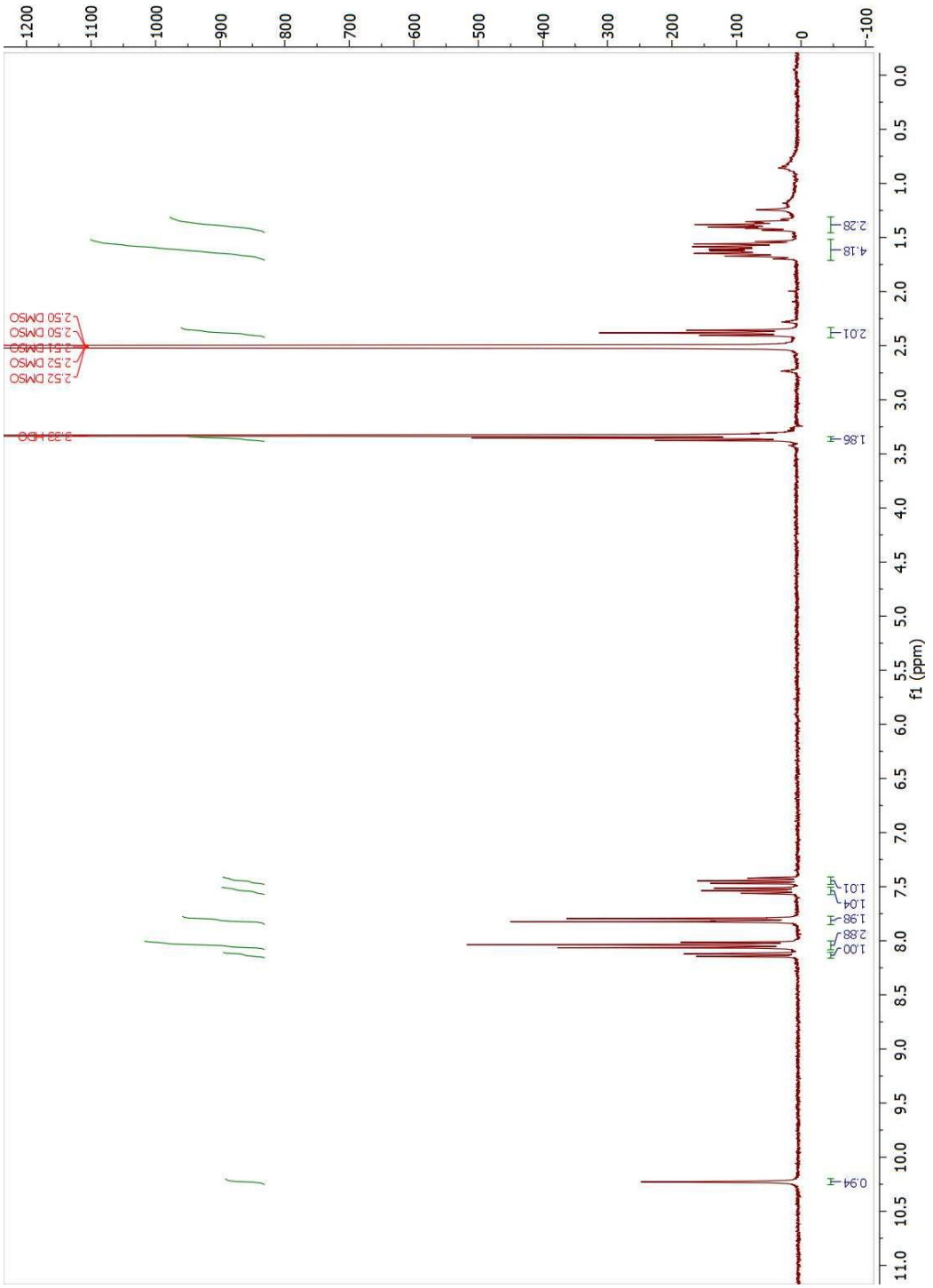

Figure 4.21: ^{1}H NMR of Thioflavin-6-azide linker

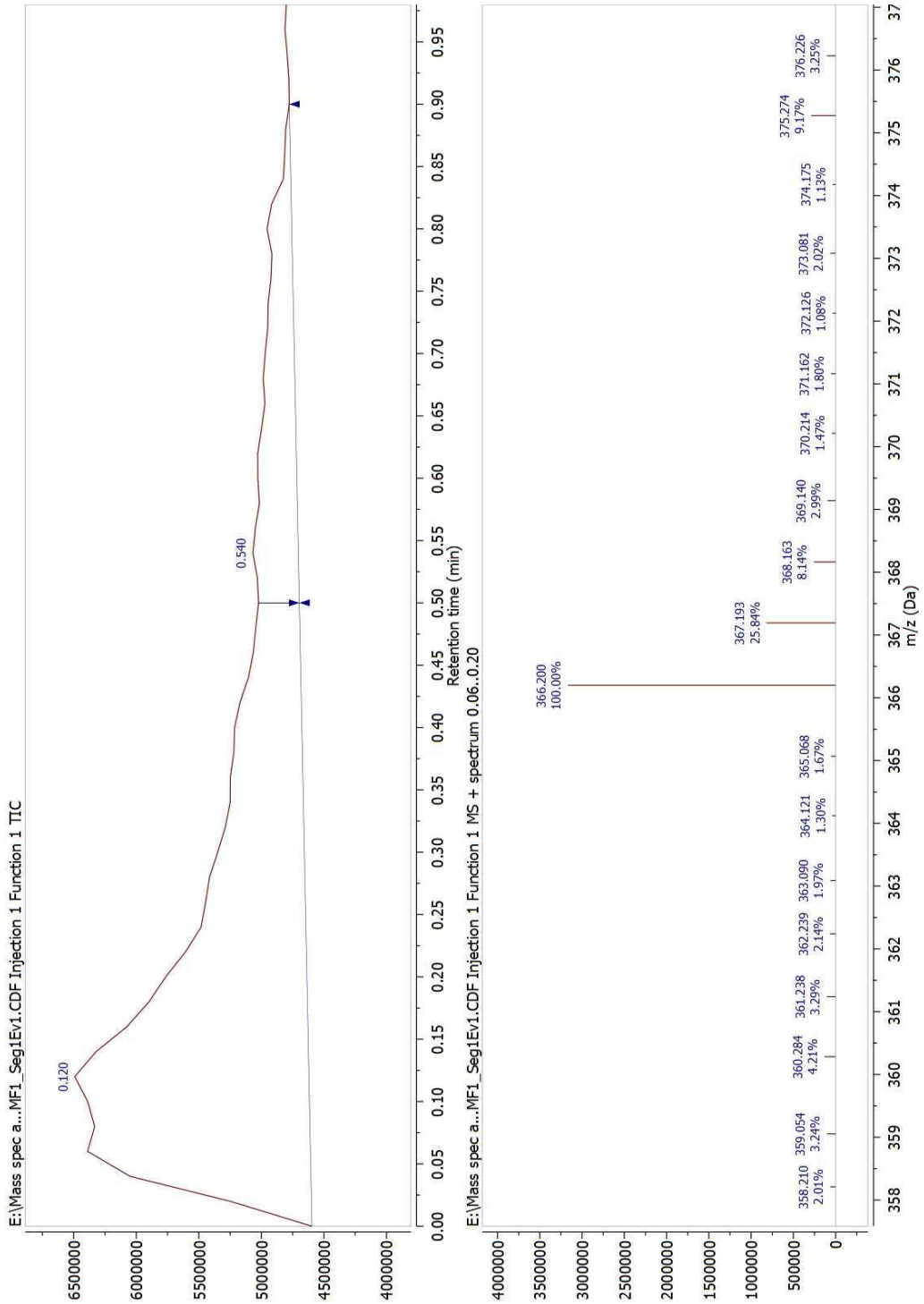

Figure 4.22: Mass spectrum of Thioflavin-6-azide linker

Synthesis of ThT-CoP5A

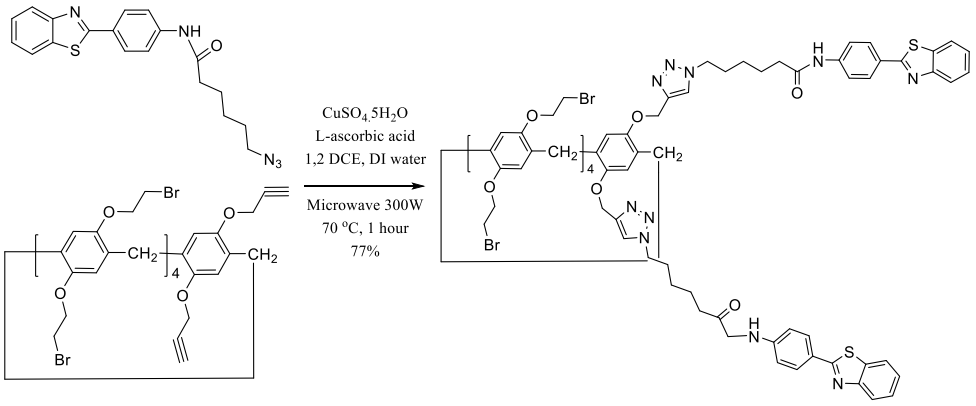

Co-P5A (46.3 mg) , ThT-6N3 (23.8 mg), CuSO4.5H2O (25.0 mg) and L-ascorbic acid (20.1 mg) was added in to a 10 ml microwave vial, to this vial 2 ml of 1,2-DCE was added in, which was followed up with 2 ml of ultra-pure water. Next this reaction mixture was subjected to 300 W microwave power at 70 °C for 1 hour in a microwave with stirring. The resulting mixture was the transferred in to a separatory funnel. DI water 10 ml was added in to the same funnel and extraction was performed with 3 x 10 ml DCM. The collected DCM layer was dried over anhydrous sodium sulfate and subjected to dry loaded automated flash chromatography for purification. ^{1}H NMR and ^{13}C NMR was performed using DMSO-d_6 and $CDCl_3$. ^{1}H NMR (400 MHz, DMSO-d_6) δ 10.21 (s, 2H), 8.27 (s, 2H), 8.11 (dd, J = 8.0, 1.1 Hz, 2H), 8.06 – 7.95 (m, 6H), 7.84 – 7.75 (m, 4H), 7.53 (ddd, J = 8.2, 7.2, 1.3 Hz, 2H), 7.47 – 7.39 (m, 2H), 7.09 (s, 2H), 7.01 – 6.90 (m, 6H), 6.83 (s, 2H), 5.18 (d, J = 11.3 Hz, 2H), 4.95 (d, J = 11.1 Hz, 2H), 4.44 (q, J = 8.0, 7.5 Hz, 9H), 4.30 – 4.19 (m, 3H), 4.09 (dq, J = 11.5, 5.7 Hz, 10H), 3.88 – 3.74 (m, 21H), 2.38 (t, J = 7.3 Hz, 4H), 1.92 (p, J = 7.1 Hz, 4H), 1.69 (p, J = 7.4 Hz, 4H), 1.36 (p, J = 7.8 Hz, 4H). ^{13}C NMR (101 MHz, DMSO-d_6) δ 171.9, 167.5, 154.1, 149.4, 149.3, 149.3, 143.6, 142.6, 134.7, 129.0, 128.9, 128.7, 128.7, 128.4, 127.8, 127.0, 125.6, 124.4, 123.0, 122.7, 119.6, 115.6, 115.1, 79.8, 79.5, 79.1, 69.2, 69.1, 68.7, 62.3, 49.7, 36.7, 32.9, 32.7, 30.2, 29.5, 28.8, 26.0, 24.8.

Reagents	Rxn conditions	
$CuSO_4$. $5H_20$, ascorbic acid	1:1 H_20 / DCM 24 h	No rxn
$CuSO_4$. $5H_20$, ascorbic acid	1:1 H_20 / DCM 80 °C , Overnight	No rxn
$CuSO_4$. $5H_20$, ascorbic acid	DMF, 60 °C, Overnight	No rxn
$CuSO_4$. $5H_20$, ascorbic acid	DMF, 80 °C, Overnight	No rxn
1M $CuSO_4$ solution, Cu solid	1:1 H_20 / *t*-BuOH 80 °C, 24 h	No rxn
1M $CuSO_4$ solution, Cu solid	1:1 H_20 / *t*-BuOH 80 °C, 3 days	No rxn
1M $CuSO_4$ solution, Cu solid, ascorbic acid	1:1 H_20 / *t*-BuOH 80 °C, 3 d	No rxn
$CuSO_4$. $5H_20$, ascorbic acid	DMF, 80 °C, 30 mins Microwave, 150W	No rxn
1M $CuSO_4$ solution, Cu solid, ascorbic acid	1:1 H20 / *t*-BuOH, Microwave, 150W, 30 mins	No rxn

Table 4-2: Various click reaction conditions that were used during the screening process of identifying the correct reaction conditions for the ThT-based CoP5A synthesis

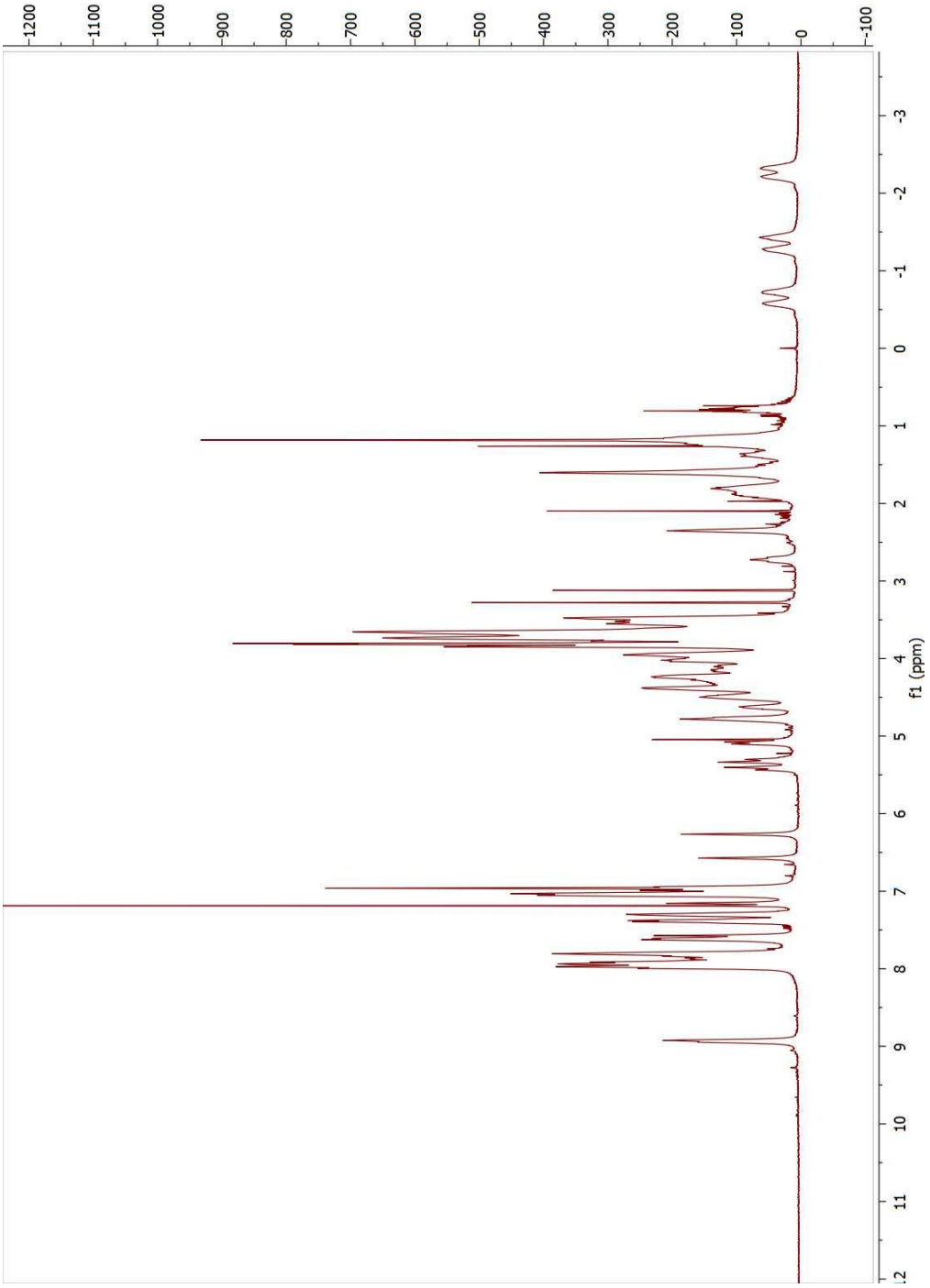

Figure 4.23: ^{1}H-NMR of ThT-CoP5A in $CDCl_3$

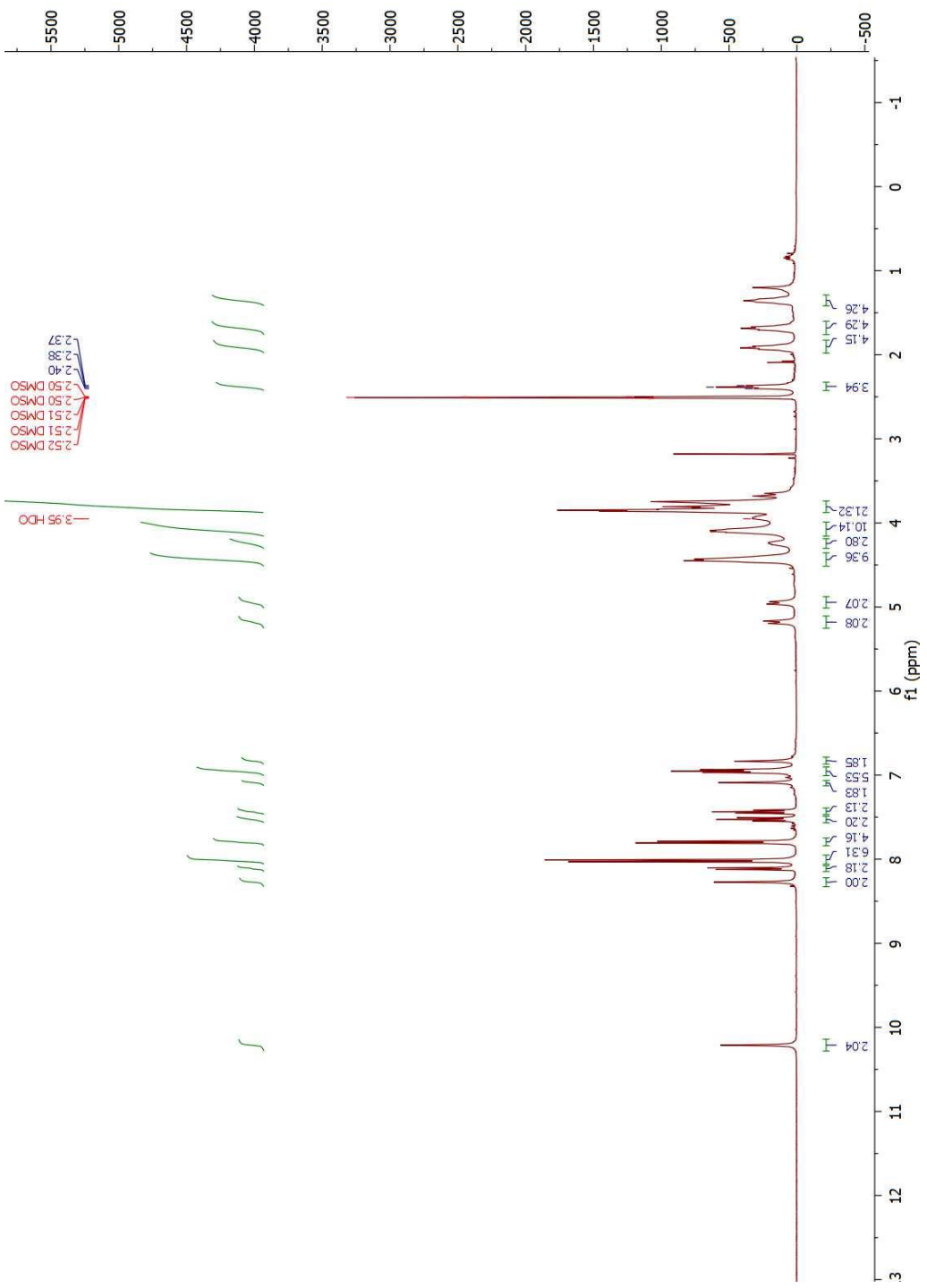

Figure 4.24: ^{1}H-NMR of ThT-CoP5A in DMSO-d_6

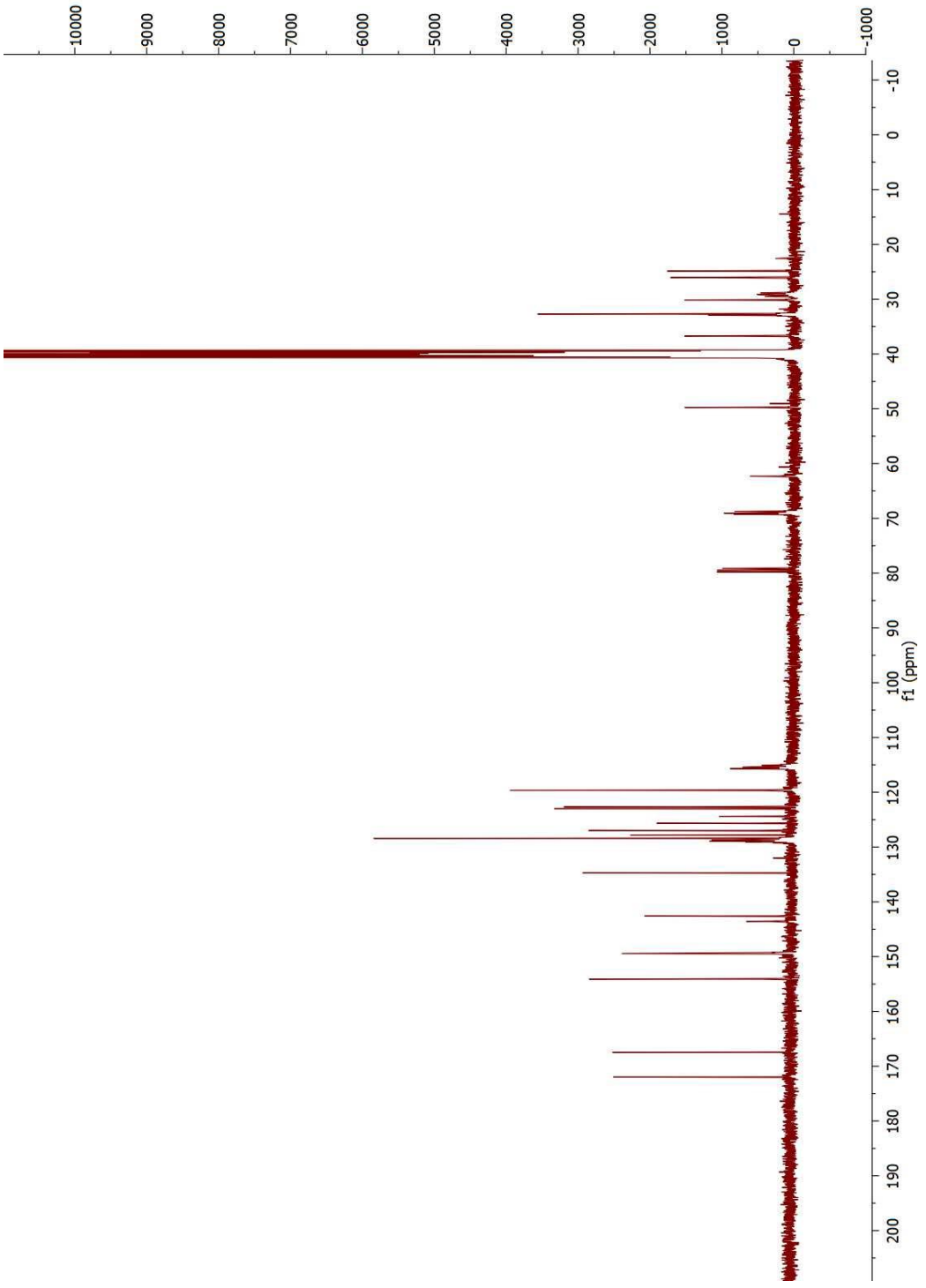

Figure 4.25: ^{13}C-NMR of ThT-CoP5A in DMSO-d_6

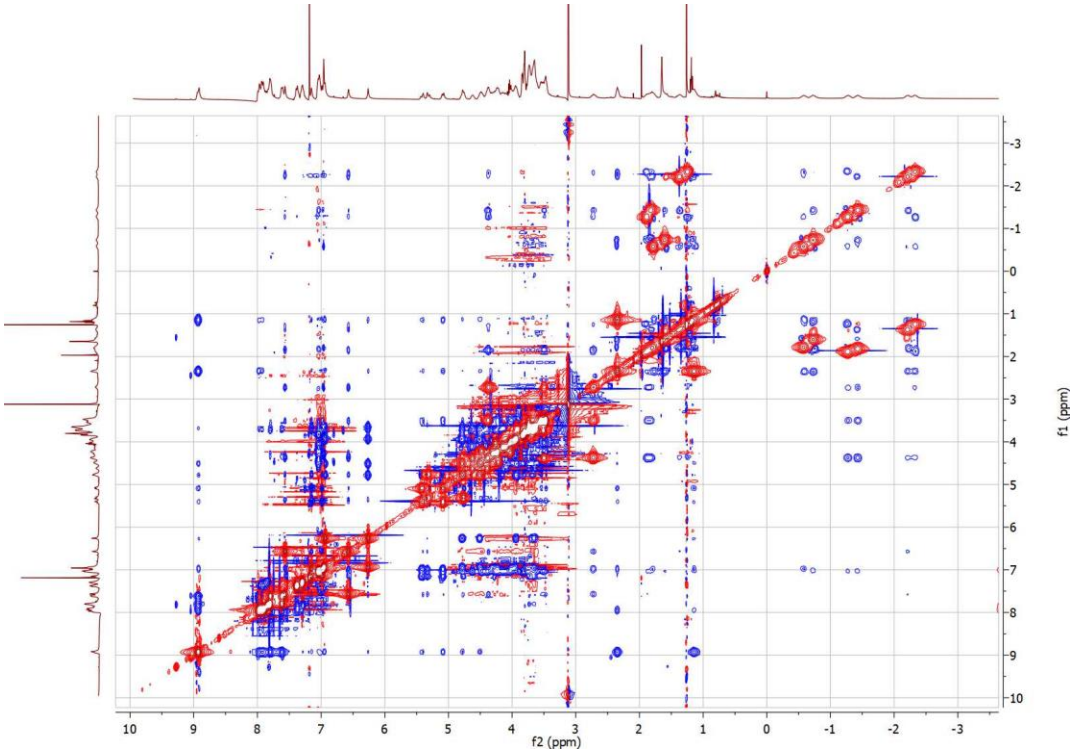

Figure 4.26: ROESY spectra of ThT-CoP5A in $CDCl_3$

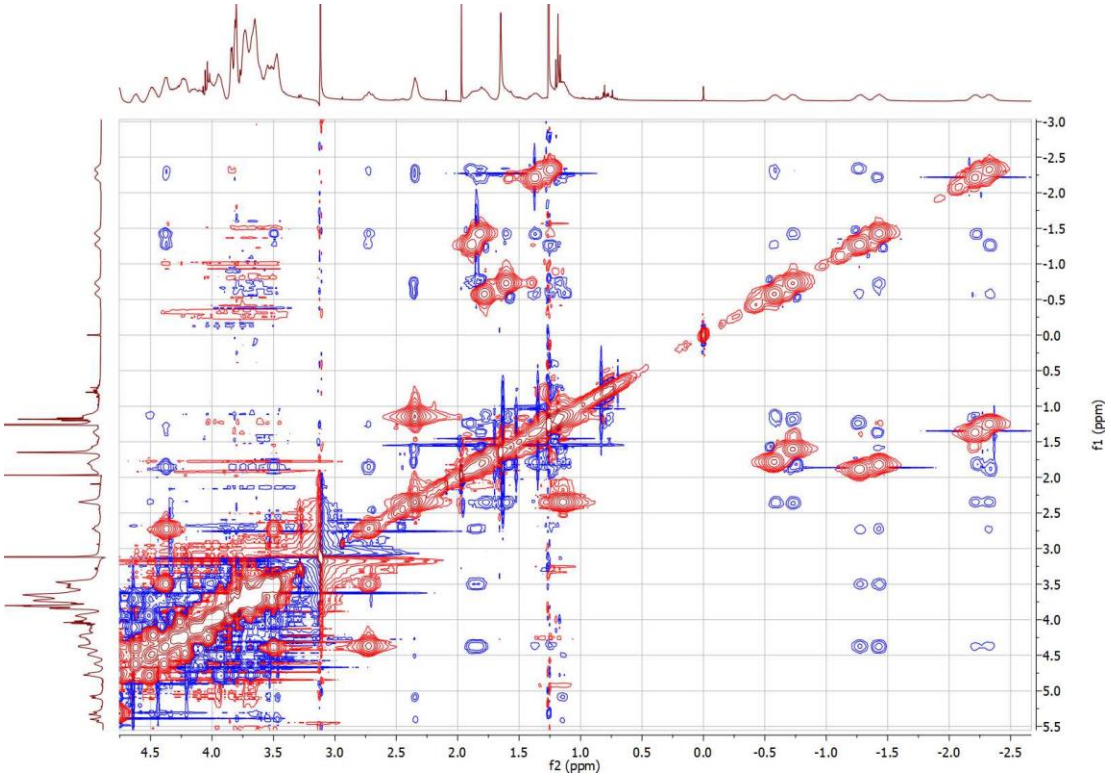

Figure 4.27: Zoomed image of ROESY spectra of ThT-CoP5A in $CDCl_3$

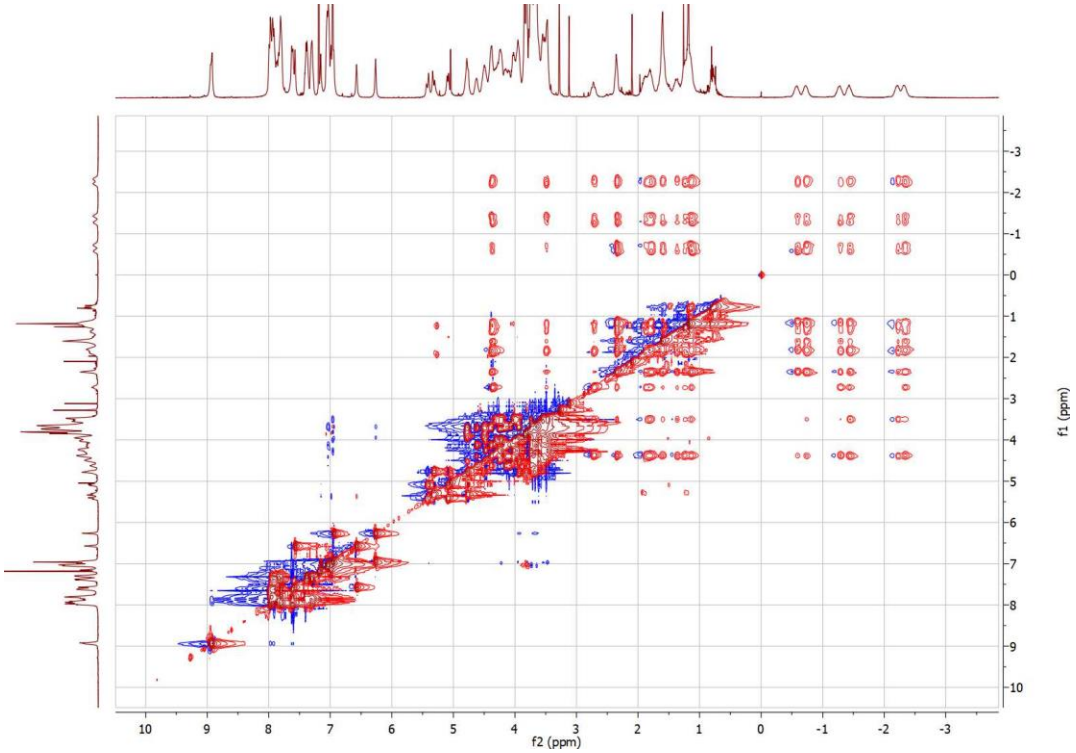

Figure 4.28: TOCSY spectra of ThT-CoP5A in $CDCl_3$

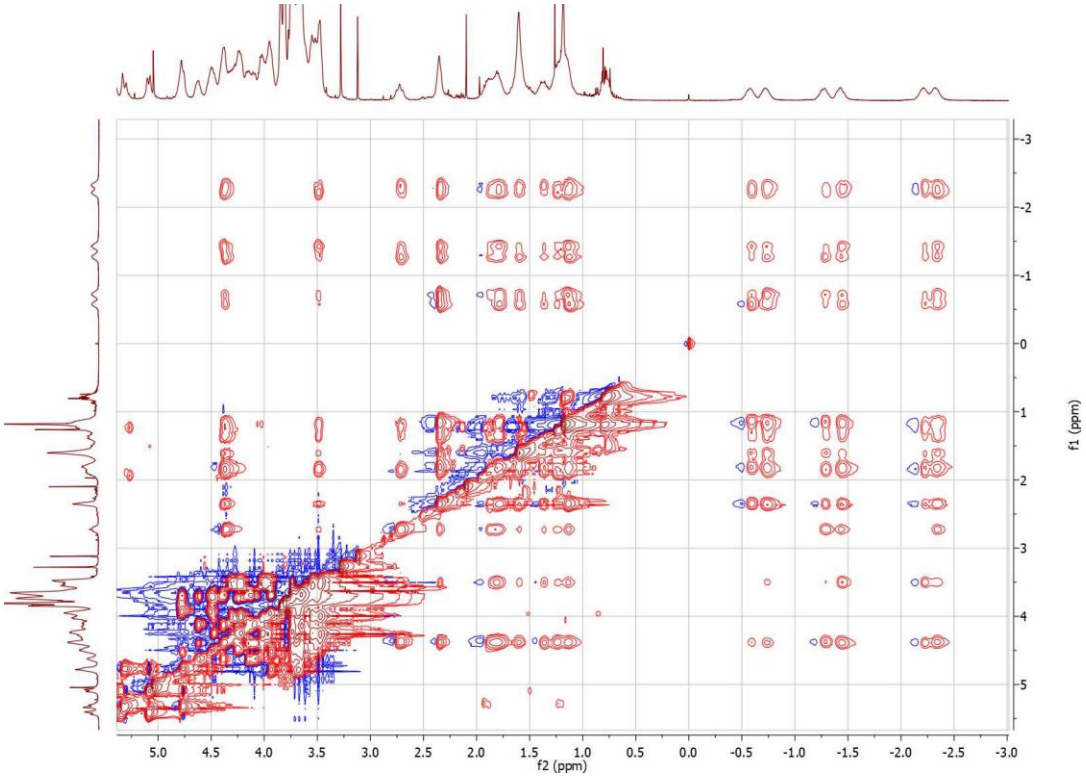

Figure 4.29: Zoomed image of TOCSY spectra of ThT-CoP5A in $CDCl_3$

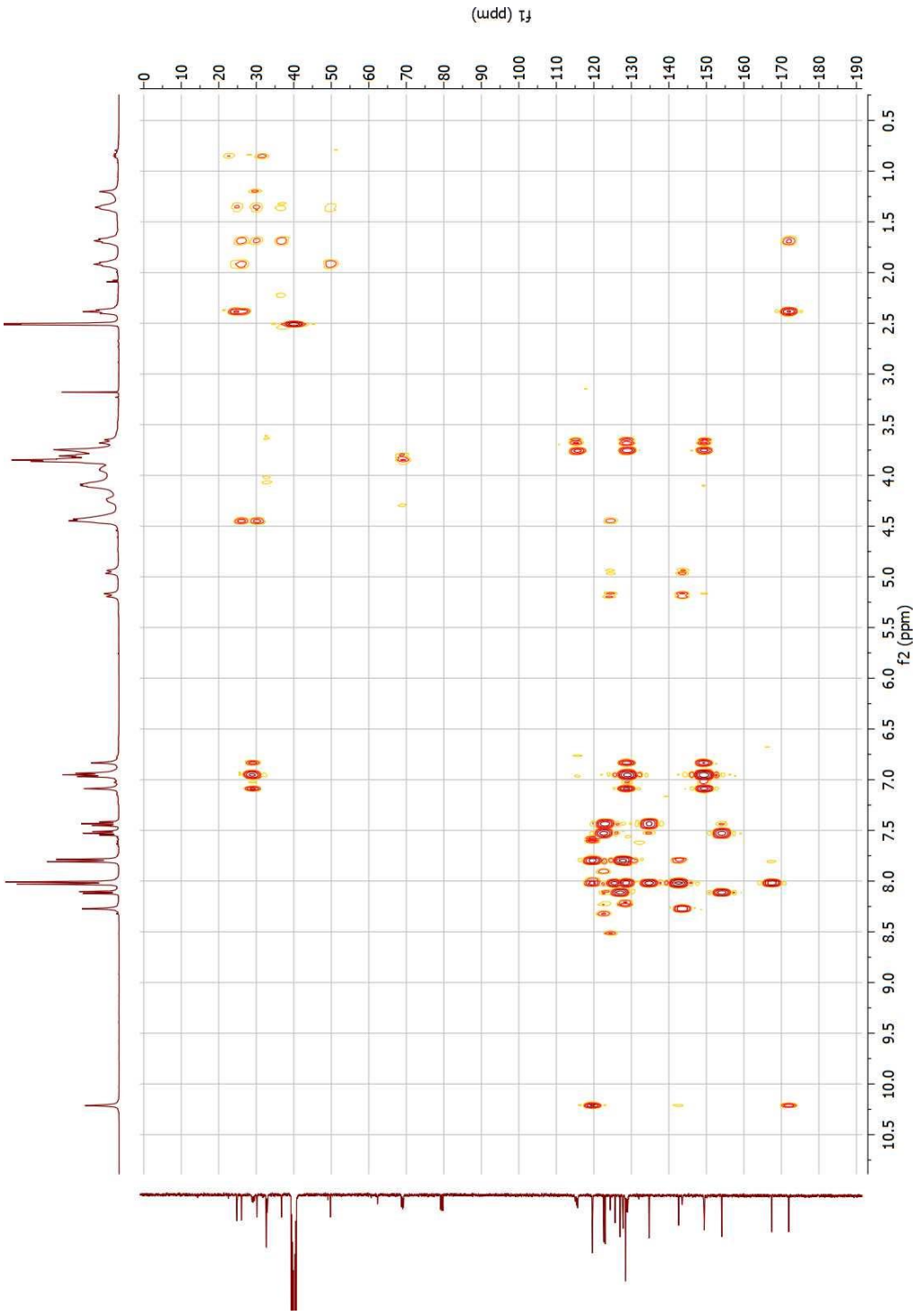

Figure 4.30: HMBC spectra of ThT-CoP5A in DMSO-d_6

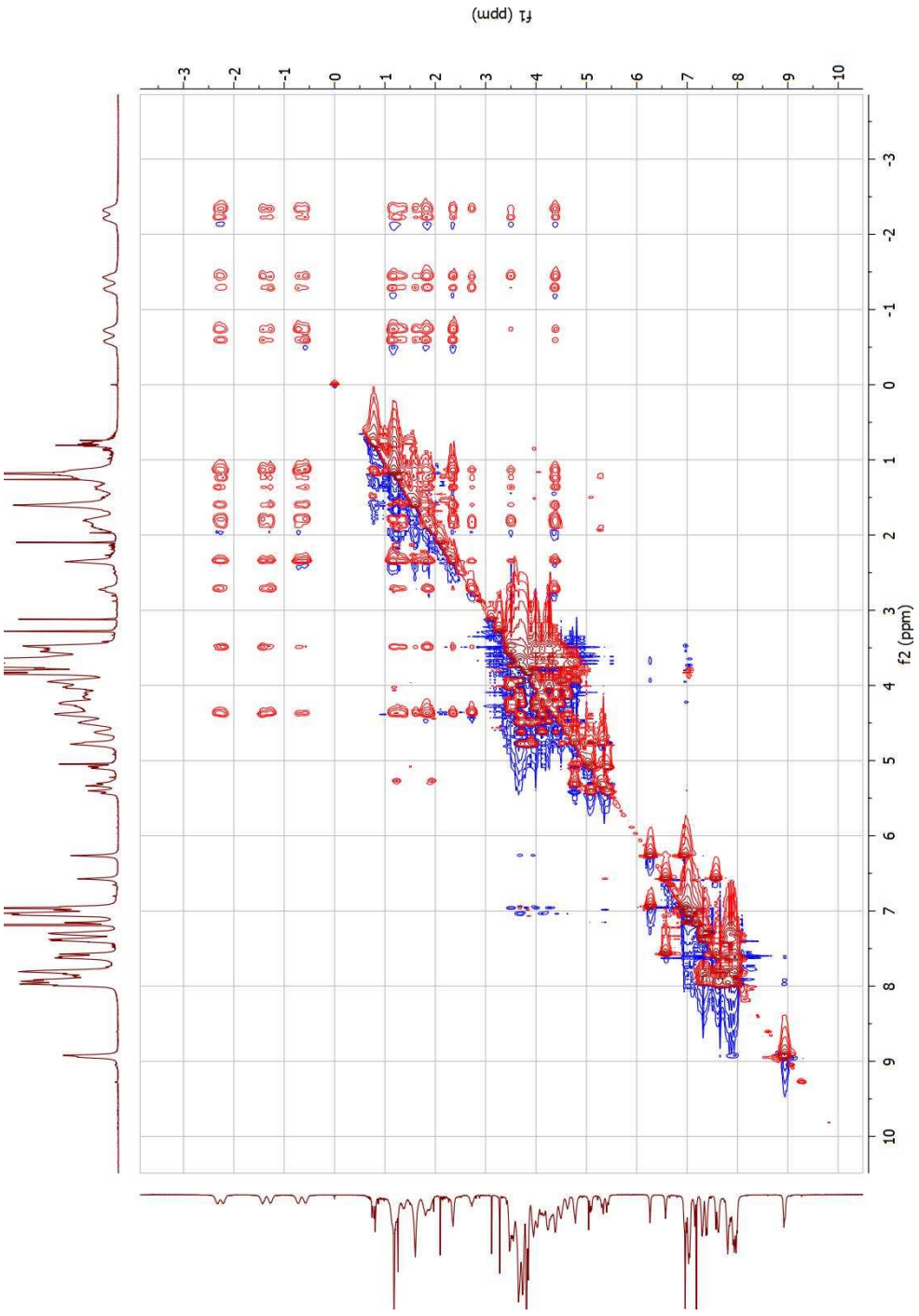

Figure 4.31: TOCSY spectra of ThT-CoP5A in $CDCl_3$

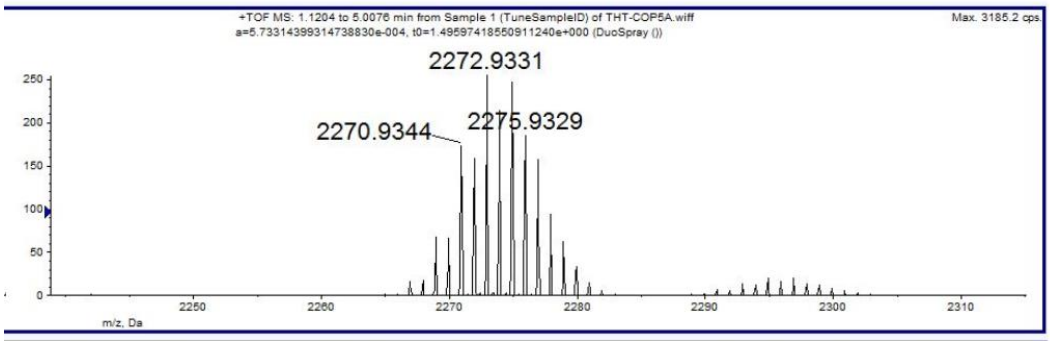

Figure 4.32: Mass spectra of ThT-CoP5A in methanol

Synthesis of water soluble ThT Co-P5A

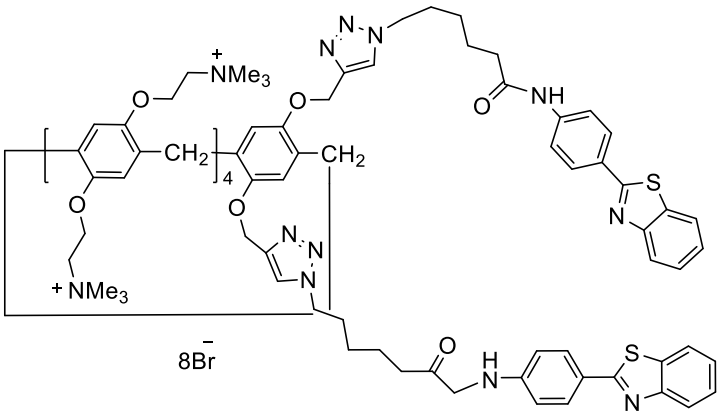

ThT-CoP5A (143. 2 mg) was mixed with tri methylamine (250 ul) to this 1 ml CHCl3 and 2 ml ethanol was added. All these was added into a pressure tube. This reaction mixture was then heated at 100 °C for 48 hours with stirring. After the 48 hours, the reaction mixture was cooled to room temperature, and the solvent was evaporated. To the dried mixture, 5 ml of ultra-pure water was added, and any resulting precipitate was filtered using Whatman 40 filter paper. The final filtered solution was cooled in a -20 °C refrigerator and then freeze-dried to obtain the final dried product. ^{1}H NMR and ^{13}C NMR were performed using DMSO-d_6. ^{1}H NMR (400 MHz, DMSO-d6) δ 10.61 (s, 2H), 8.42 (s, 2H), 8.15 – 8.09 (m, 2H), 8.05 – 7.98 (m, 6H), 7.91 – 7.84 (m, 4H), 7.53 (ddd, J = 8.3, 7.2, 1.3 Hz, 2H), 7.44 (ddd, J = 8.3, 7.2, 1.2 Hz, 2H), 7.14 – 6.89 (m, 10H), 5.20 – 5.04 (m, 4H), 4.75 – 4.35 (m, 20H), 4.08 (d, J = 47.9 Hz, 19H), 3.72 (d, J = 38.1 Hz, 11H), 3.23 (s, 87H), 2.42 (t, J = 7.3 Hz, 4H), 1.89 (p, J = 7.2 Hz, 4H), 1.67 (p, J = 7.6 Hz, 4H), 1.32 (p, 4H). ^{13}C NMR (101 MHz, DMSO-d_6) δ 172.2, 167.5, 154.1, 149.5, 149.3, 142.7, 134.7, 128.7, 128.4, 127.7, 127.1, 125.7, 123.0, 122.7, 119.6, 57.8, 54.9, 54.8, 54.8, 53.6, 53.5, 49.8, 44.4, 36.6, 34.6, 30.0, 25.9, 24.8.

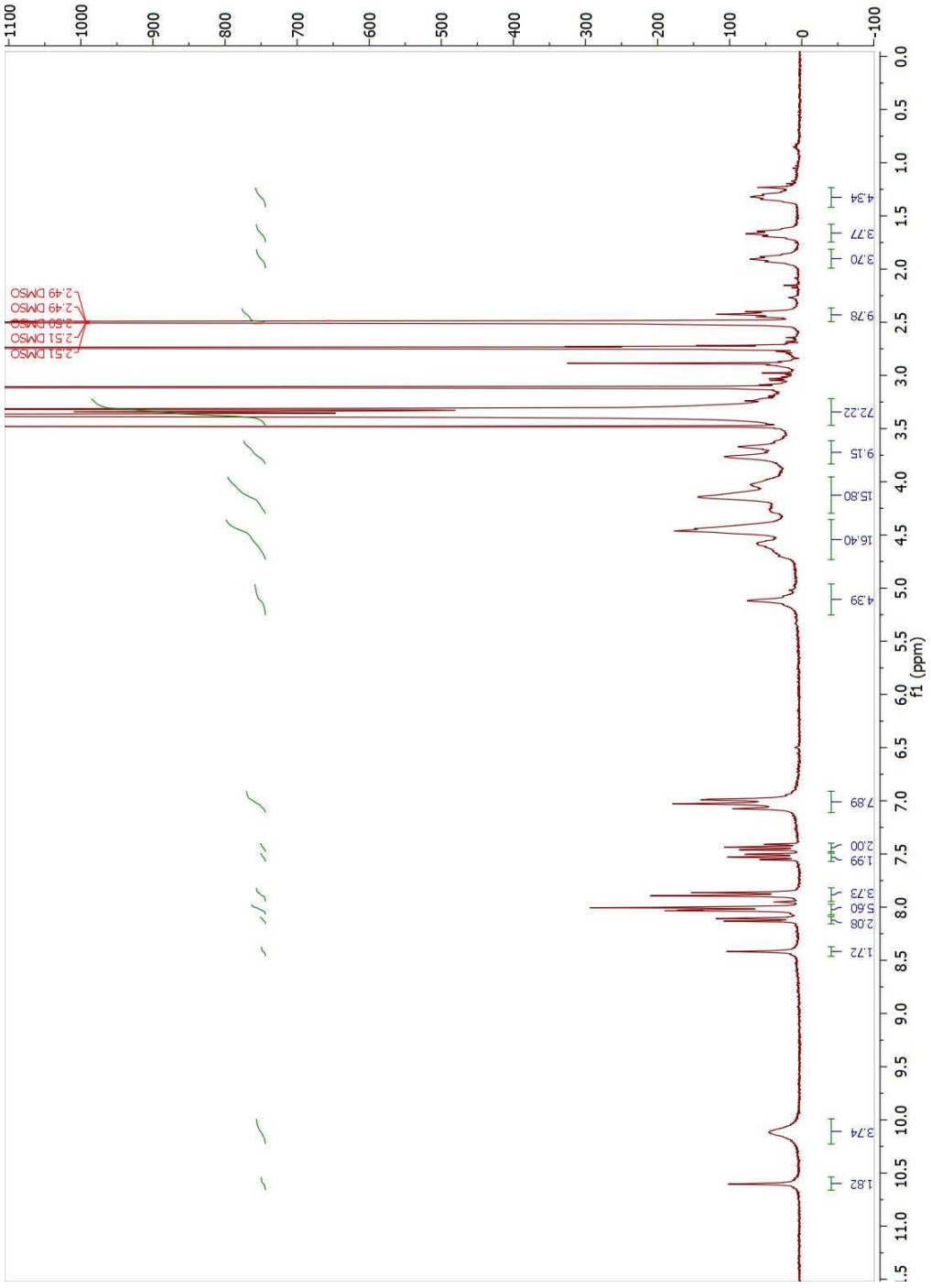

Figure 4.33: ^{1}H-NMR of water-soluble ThT-CoP5A in DMSO-d_6

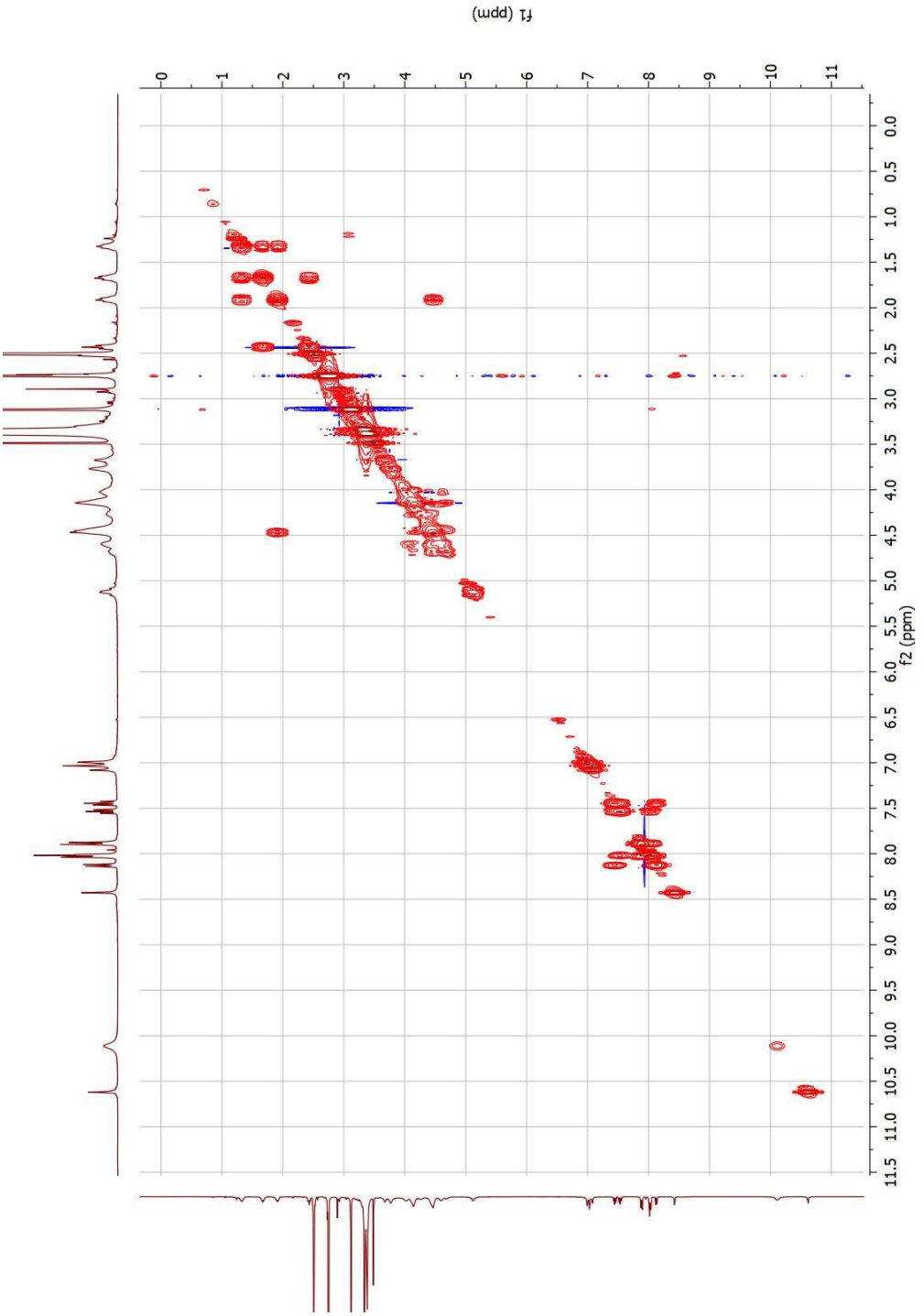

Figure 4.34: COSY spectrum of water soluble ThT-CoP5A in DMSO-d_6

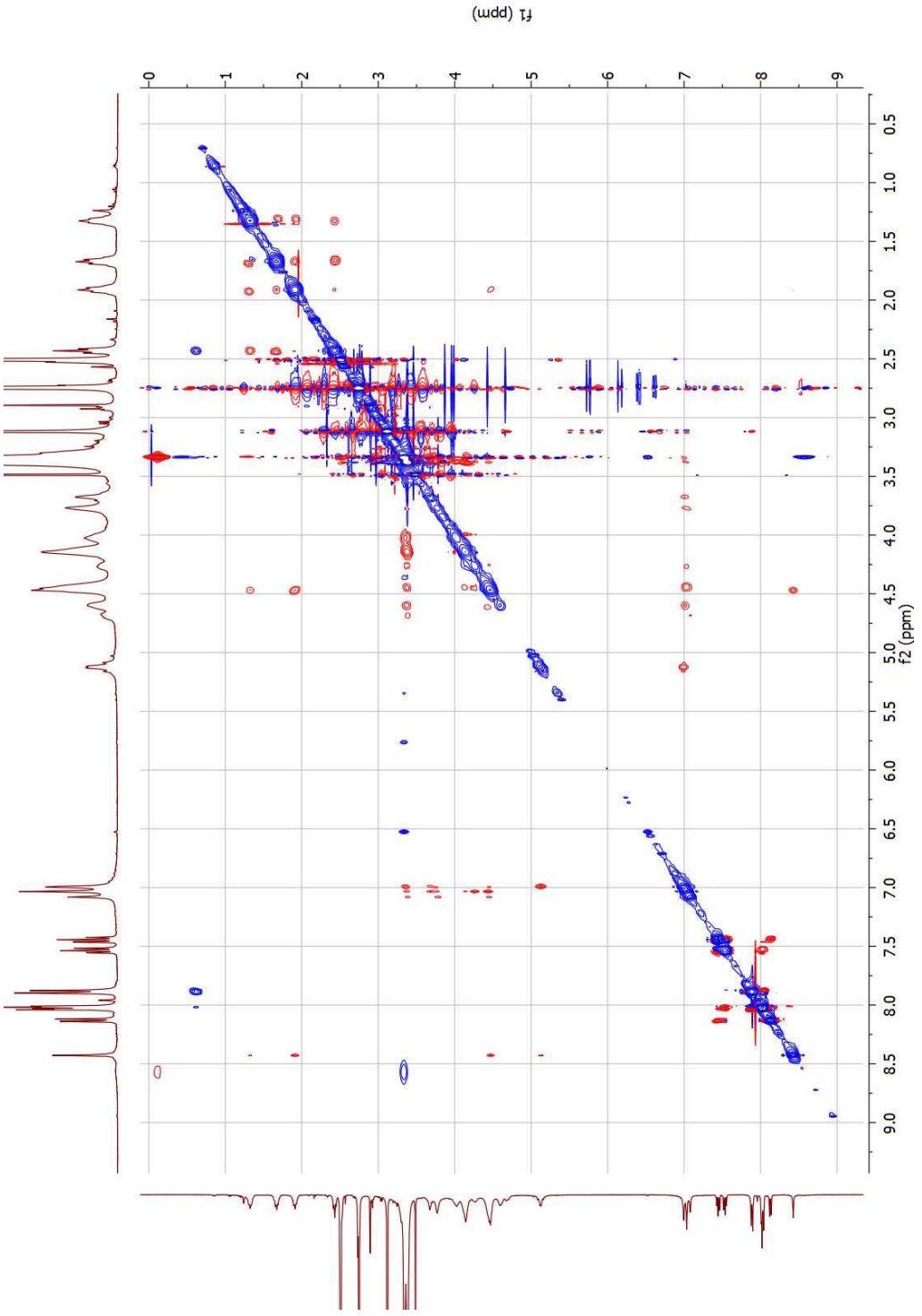

Figure 4.35: ROESY spectrum of water soluble ThT-CoP5A in DMSO-d_6

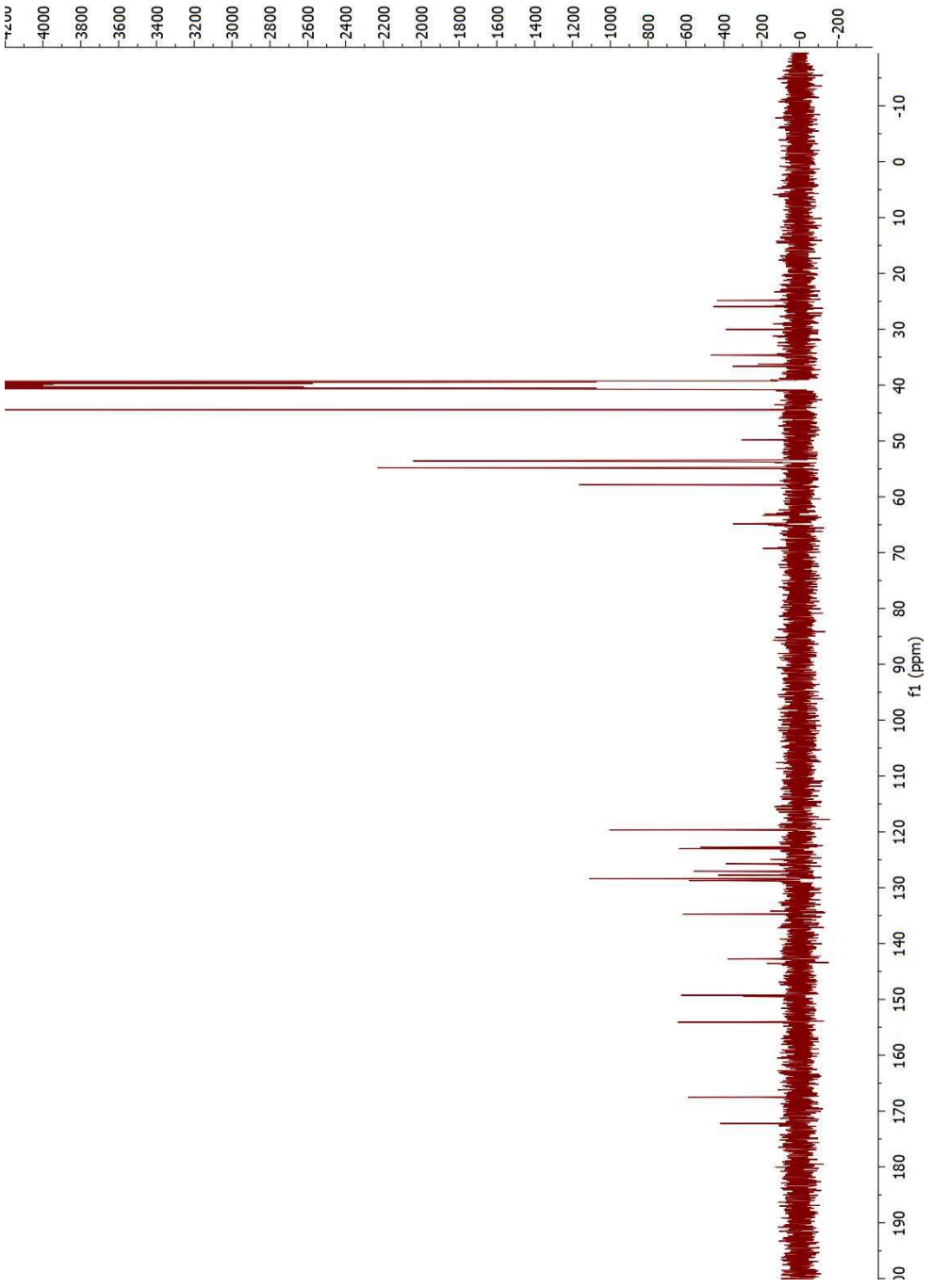

Figure 4.36: ^{13}C NMR spectrum of water soluble ThT-CoP5A in DMSO-d_6

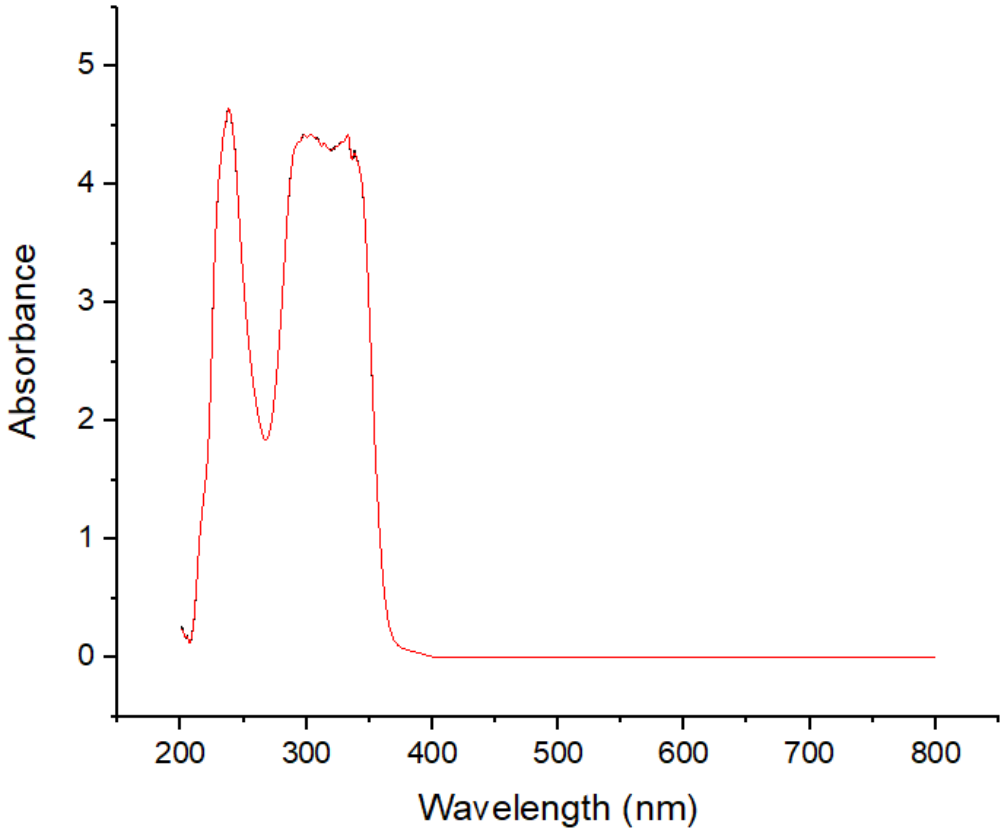

Figure 4.37: Absorbance curve for ThT-CoP5A in chloroform

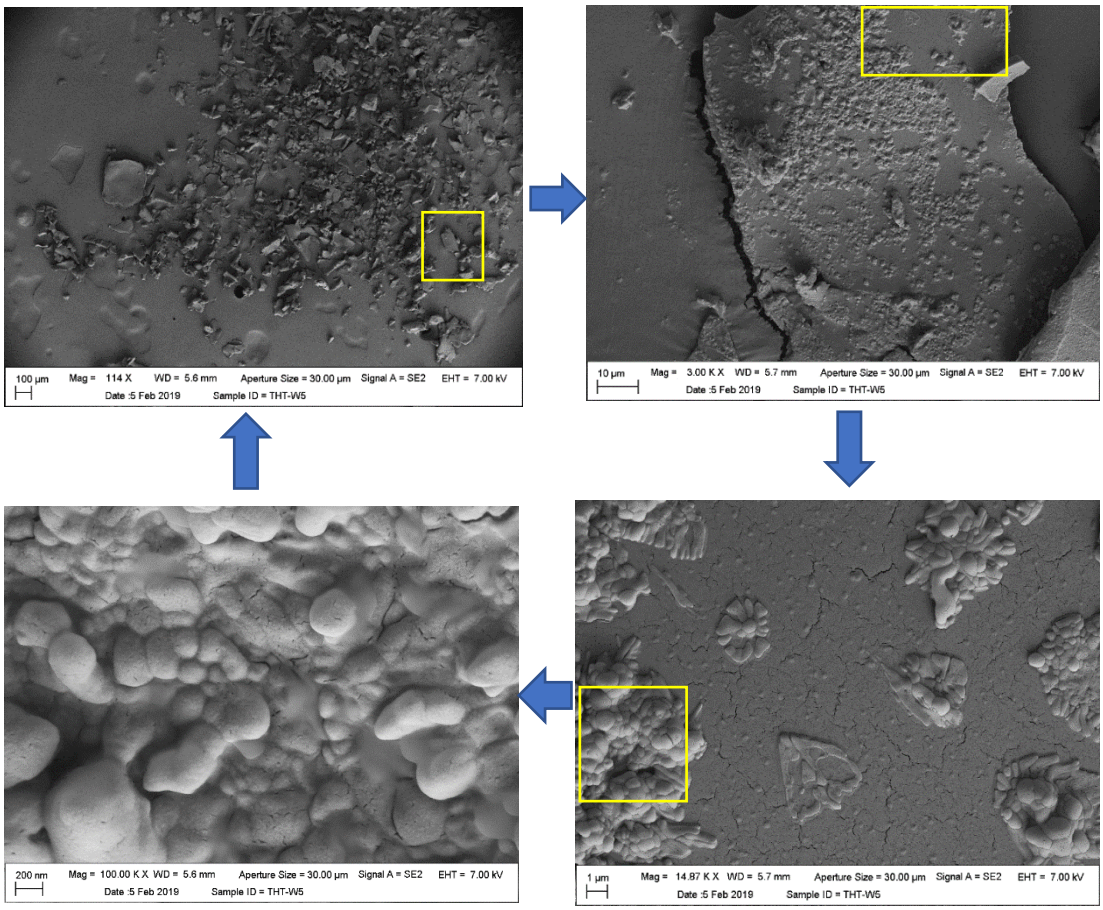

Figure 4.38: SEM images, as indicated from the arrows each one represents the increase of the level of magnification and decrease of the particle size ranging from 100 µm to 200 nm. The yellow boxes indicate the area that was zoomed in. The sample was loaded on to a platform and then it was gold spluttered. This gold spluttered surface was used to observe the surface in its dried form under vacuum.

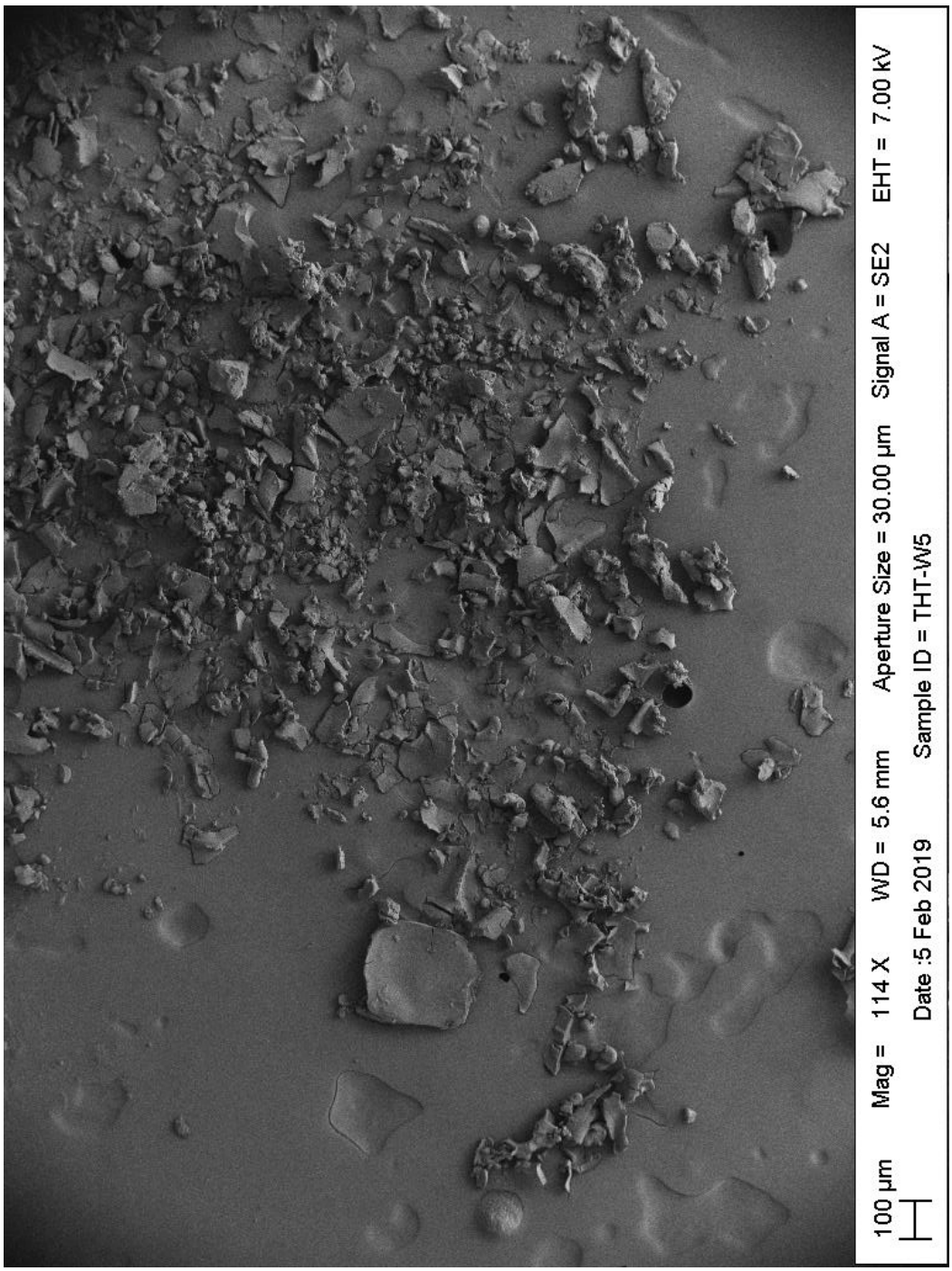

Figure 4.39: SEM image of ThT-CoP5A at 100 µm level

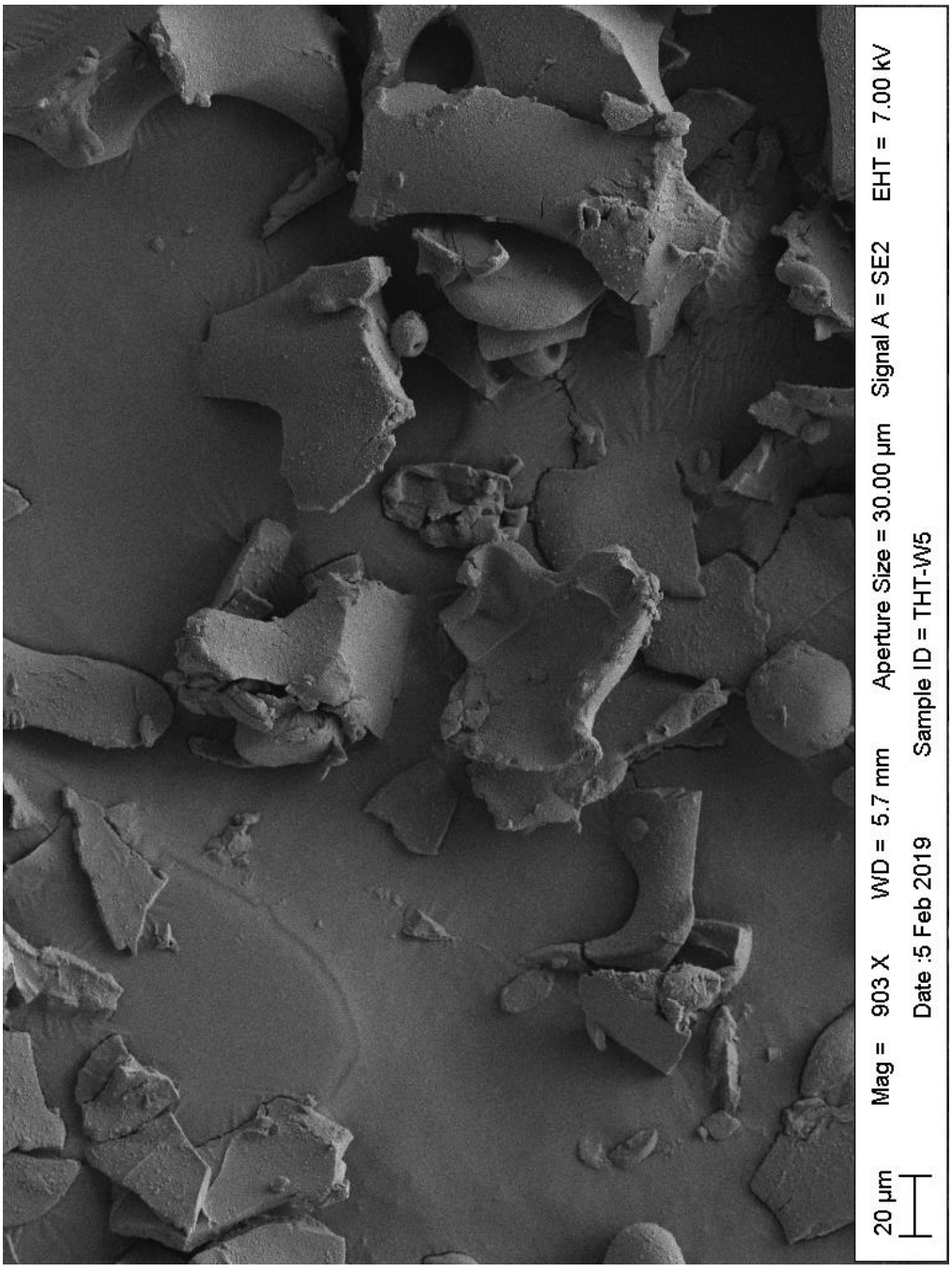

Figure 4.40: SEM image of ThT-CoP5A at 20 µm level

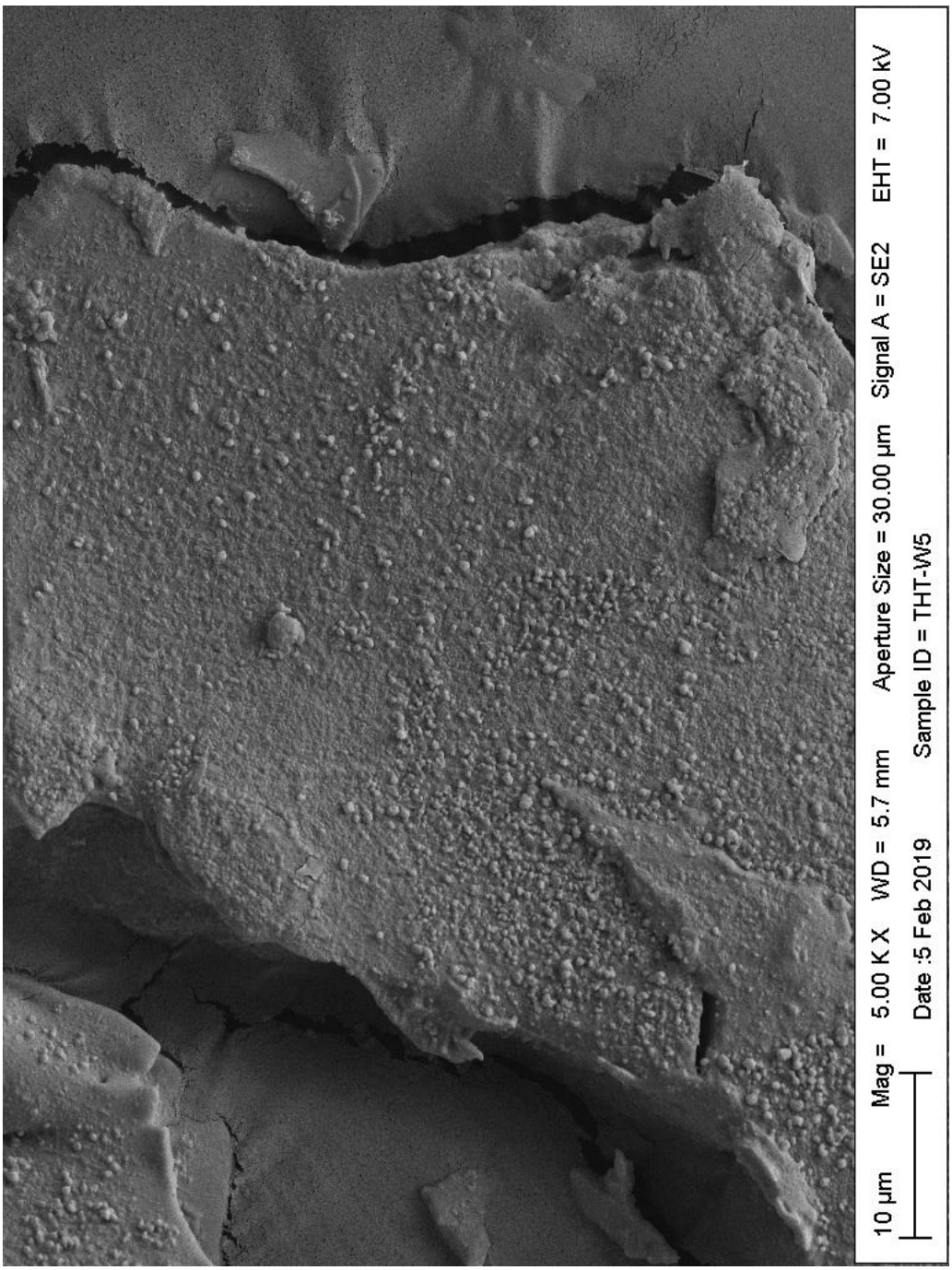

Figure 4.41: SEM image of ThT-CoP5A at 10 µm level

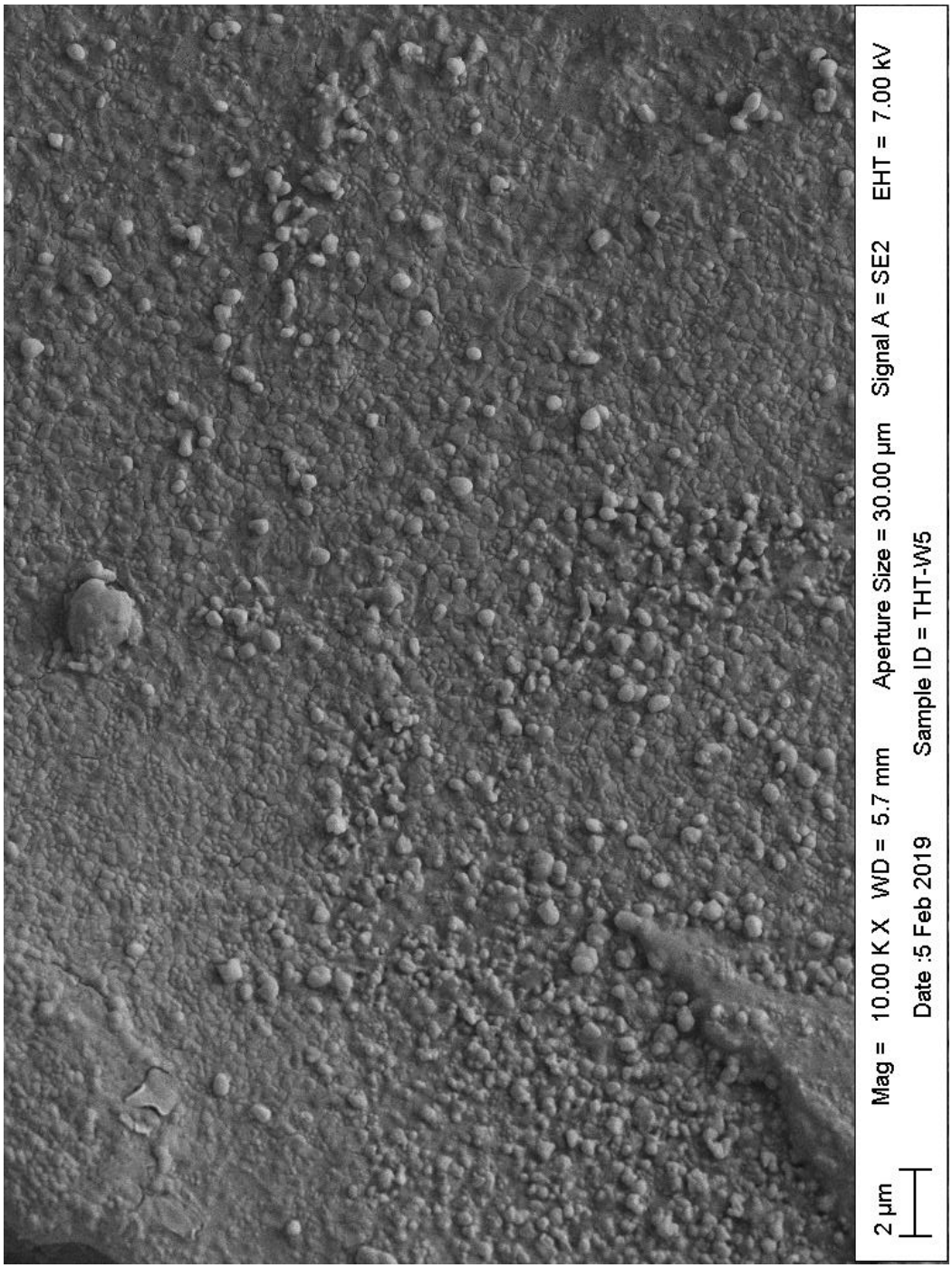

Figure 4.42: SEM image of ThT-CoP5A at 2 µm level

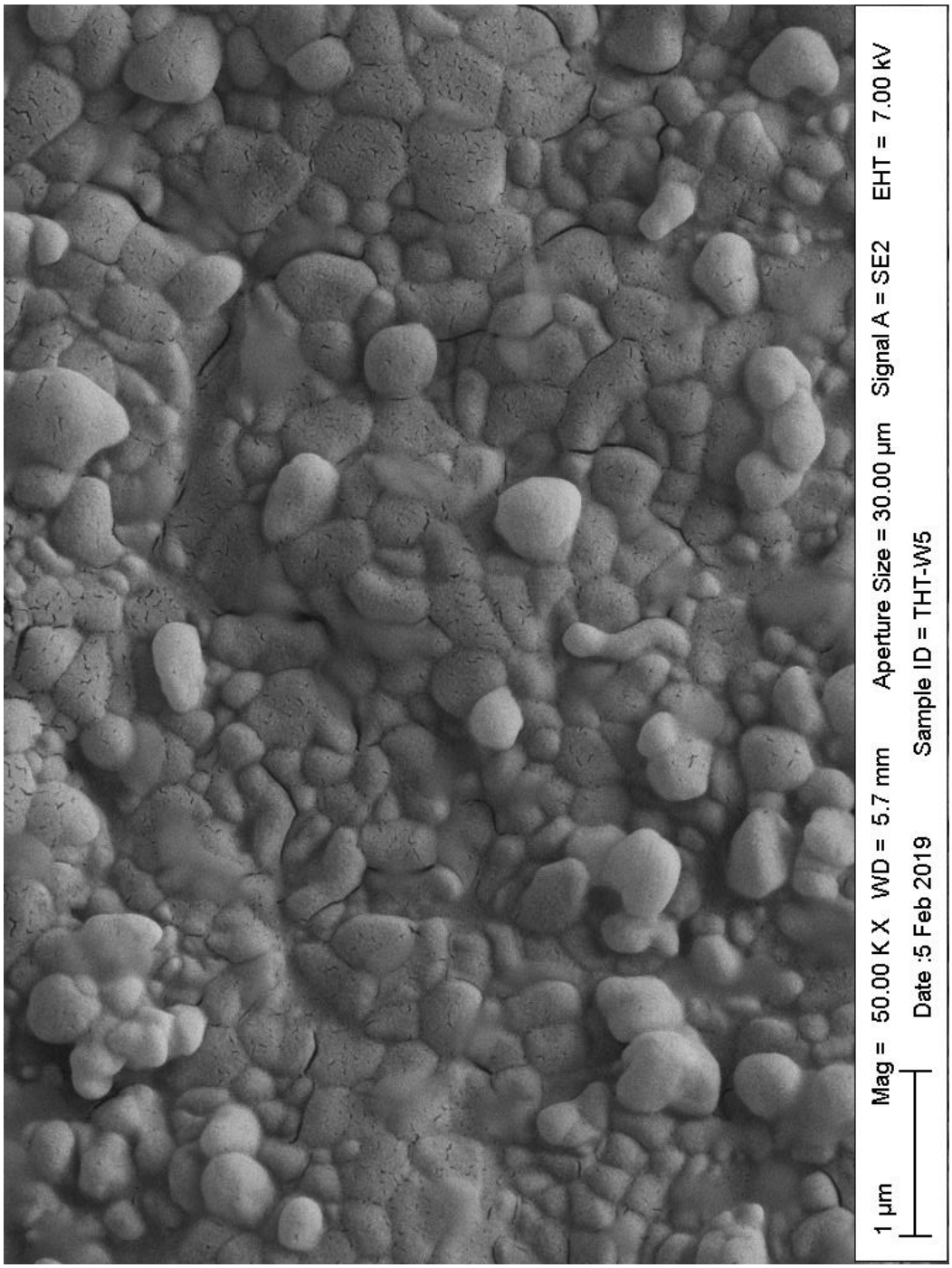

Figure 4.43: SEM image of ThT-CoP5A at 1 µm level

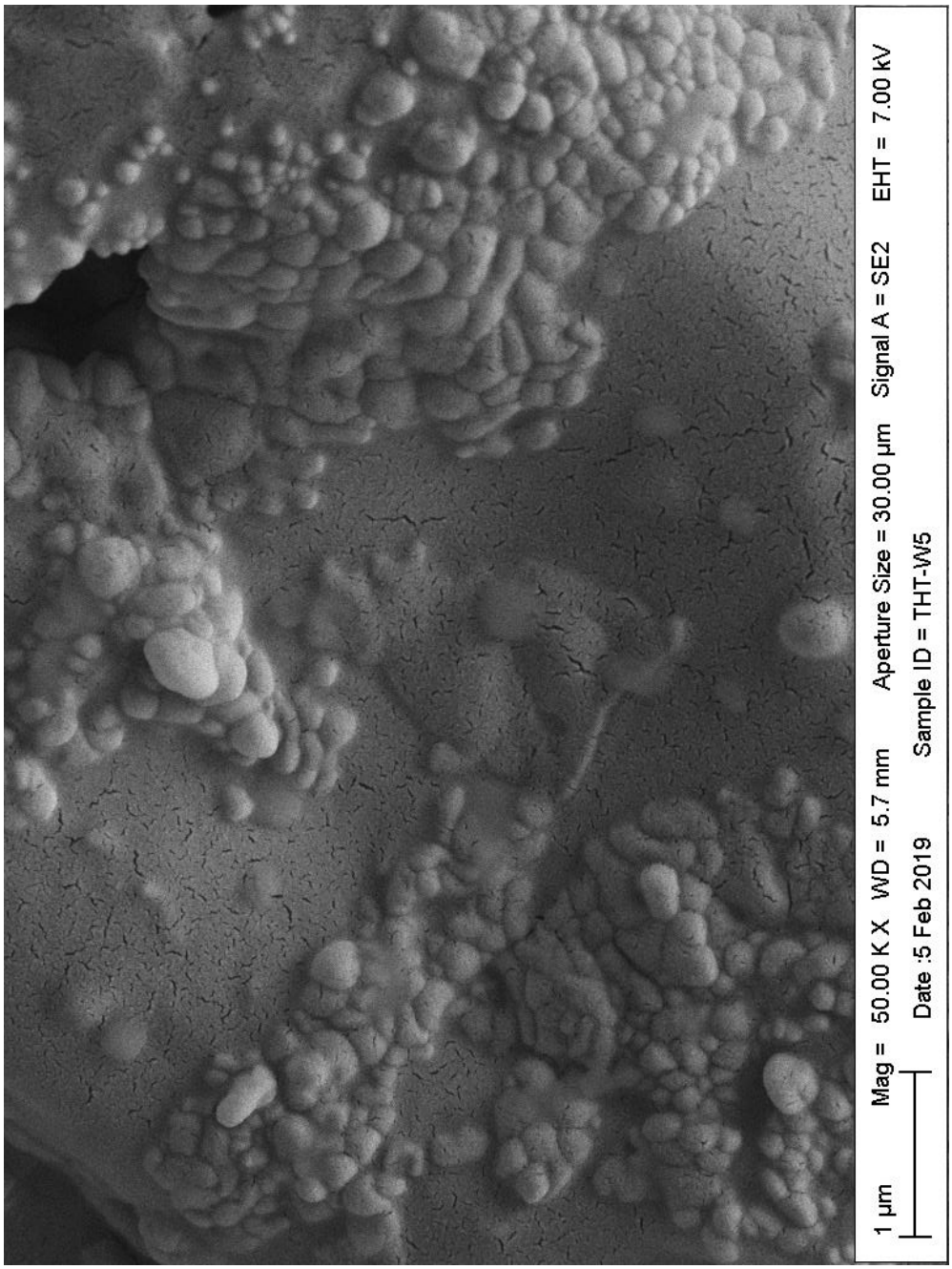

Figure 4.44: SEM image of ThT-CoP5A at 1 µm level

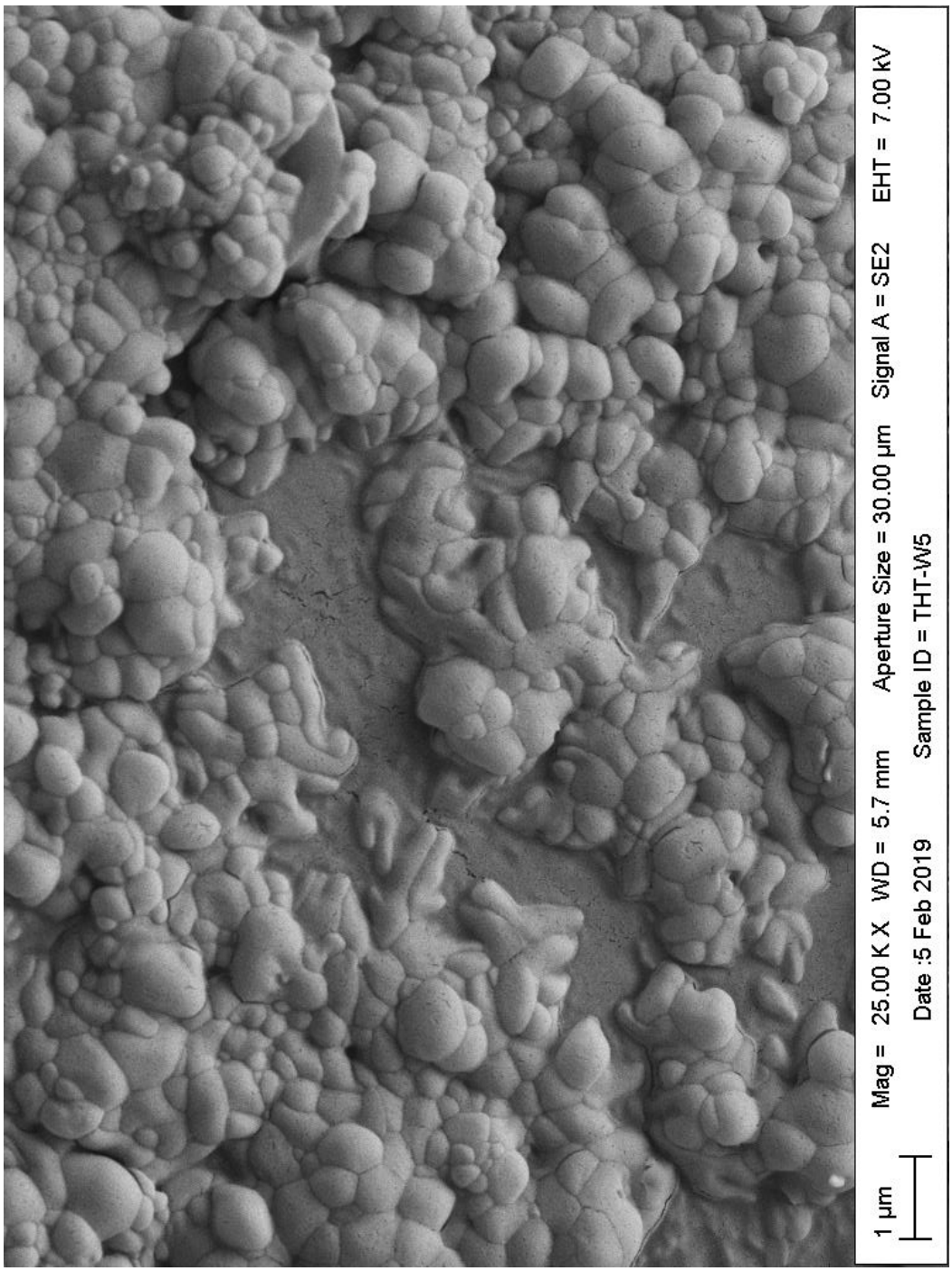

Figure 4.45: SEM image of ThT-CoP5A at 1 µm level

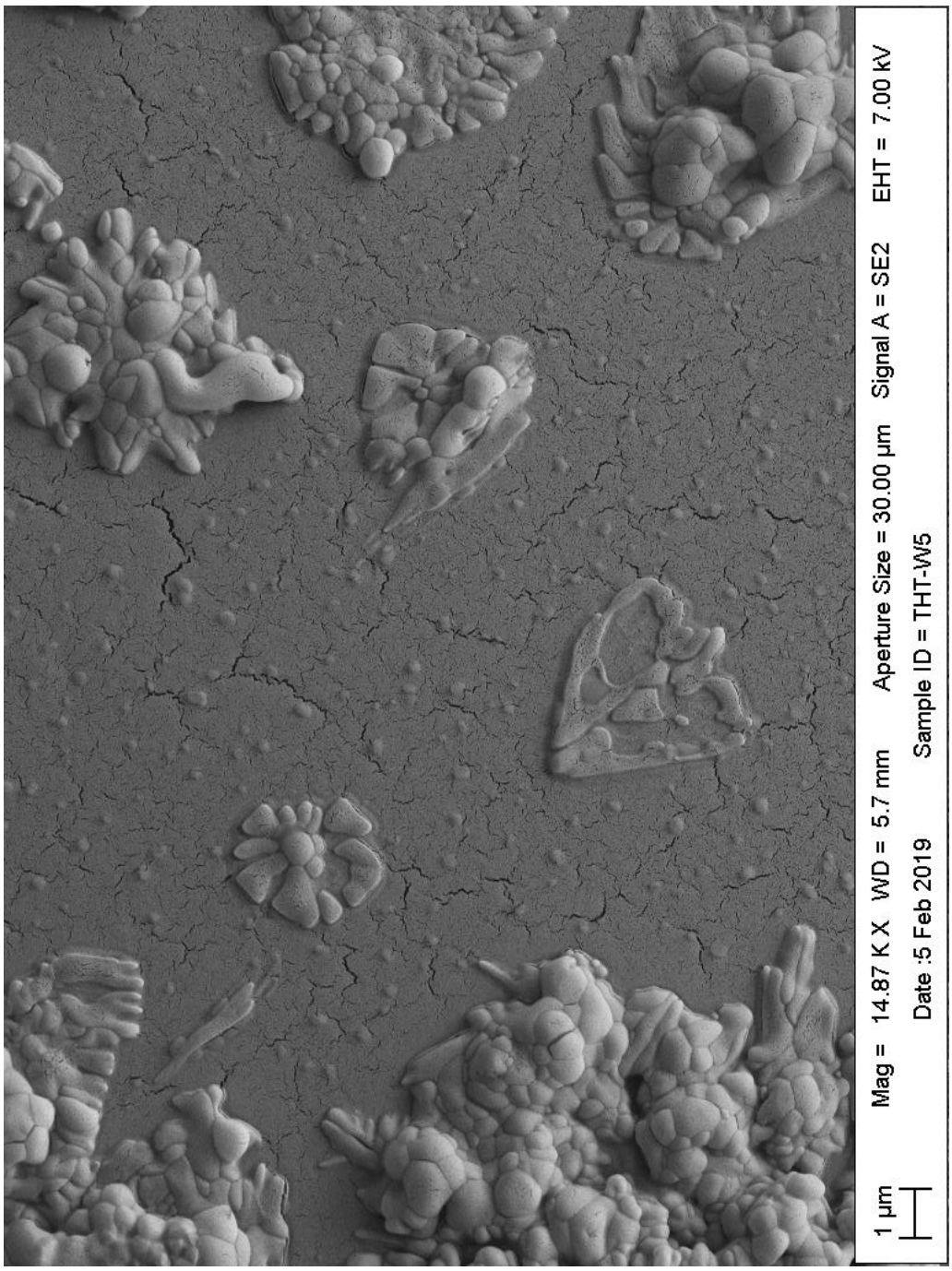

Figure 4.46: SEM image of ThT-CoP5A at 1 µm level

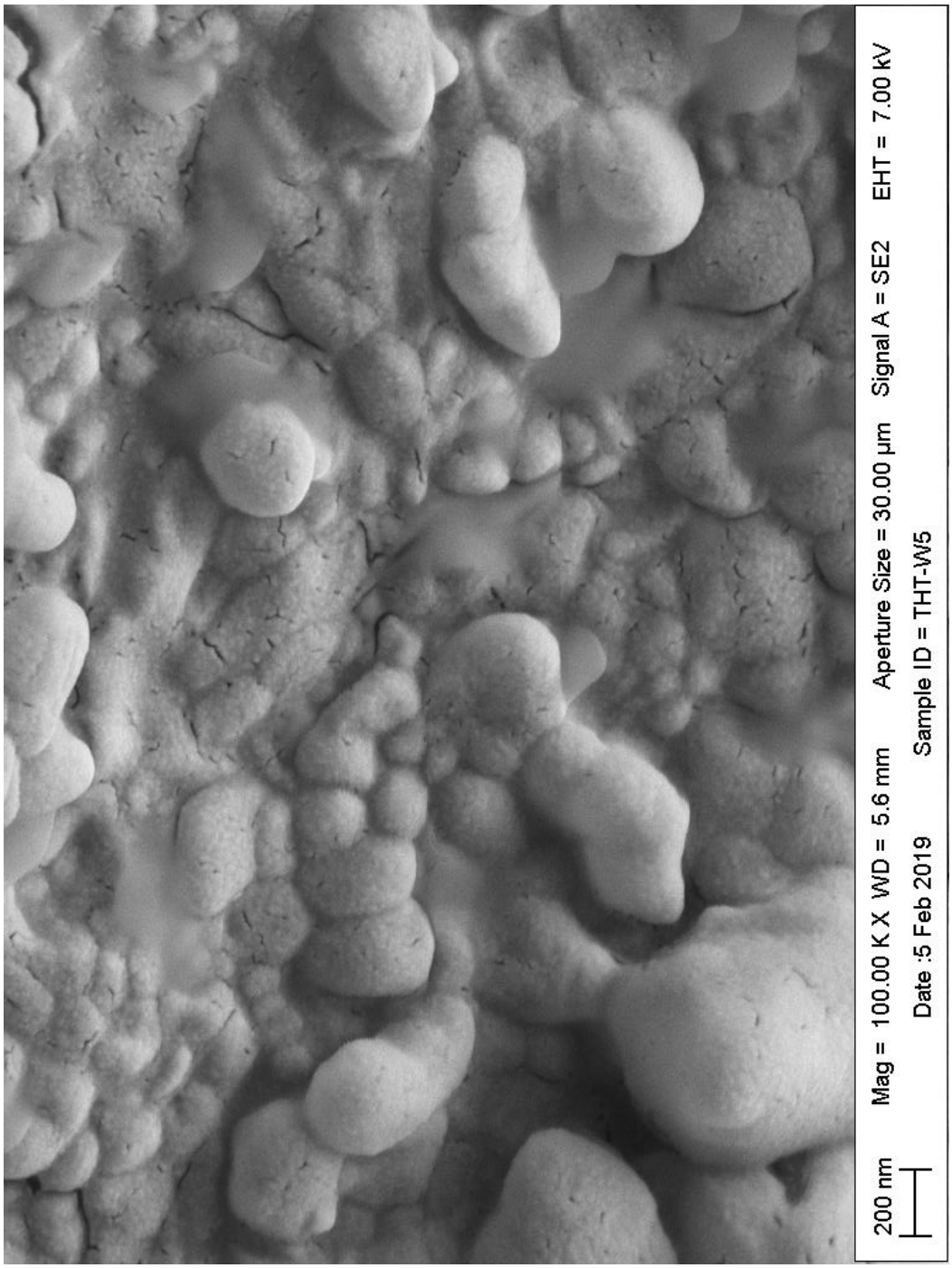

Figure 4.47: SEM image of ThT-CoP5A at 1 µm level

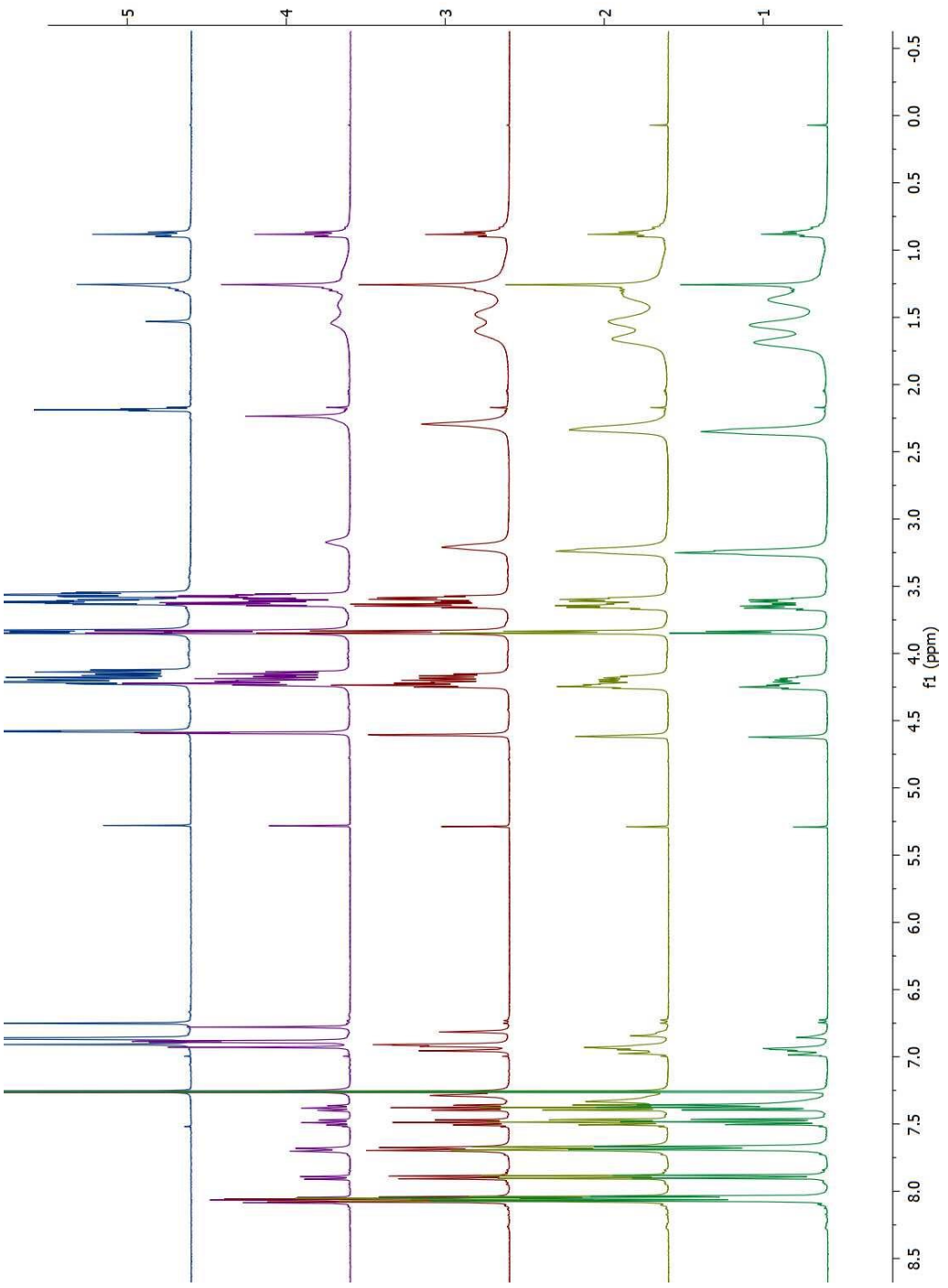

Figure 4.48: Titration of ThT-6-azide to a solution of CoP5A in $CDCl_3$ solvent

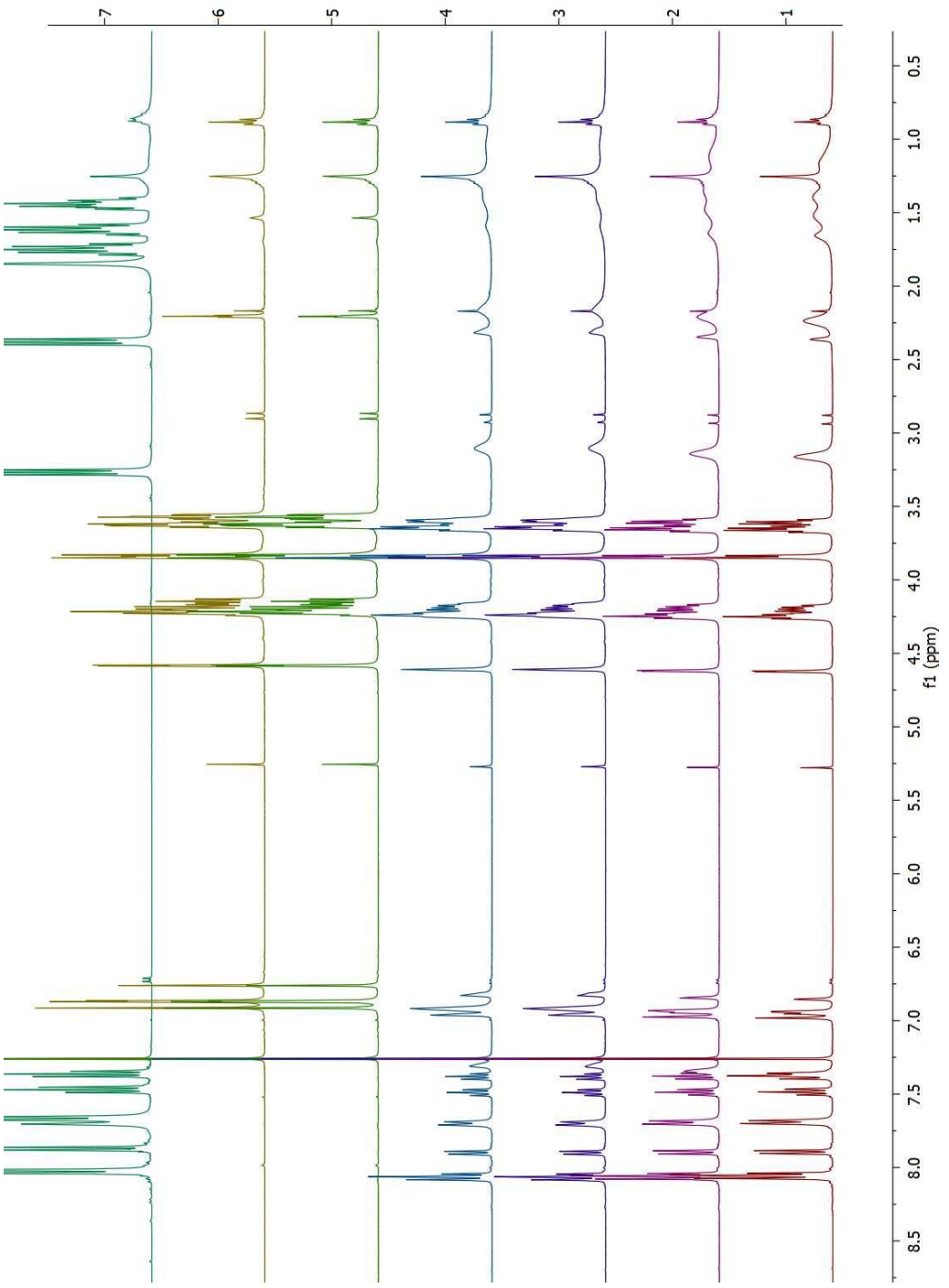

Figure 4.49: Titration of ThT-6azide to a solution of CoP5A in $CDCl_3$

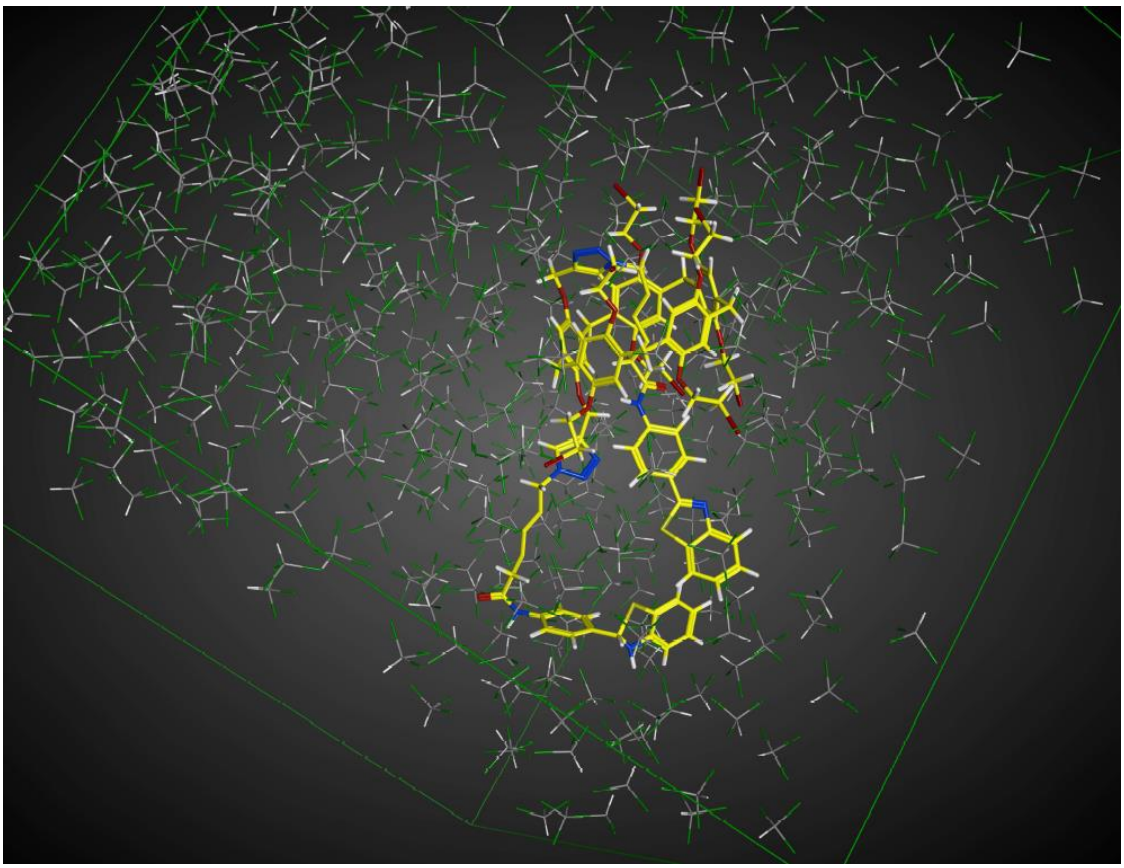

Figure 4.50: Computational model after molecular dynamics in $CHCl_3$ solvent system.

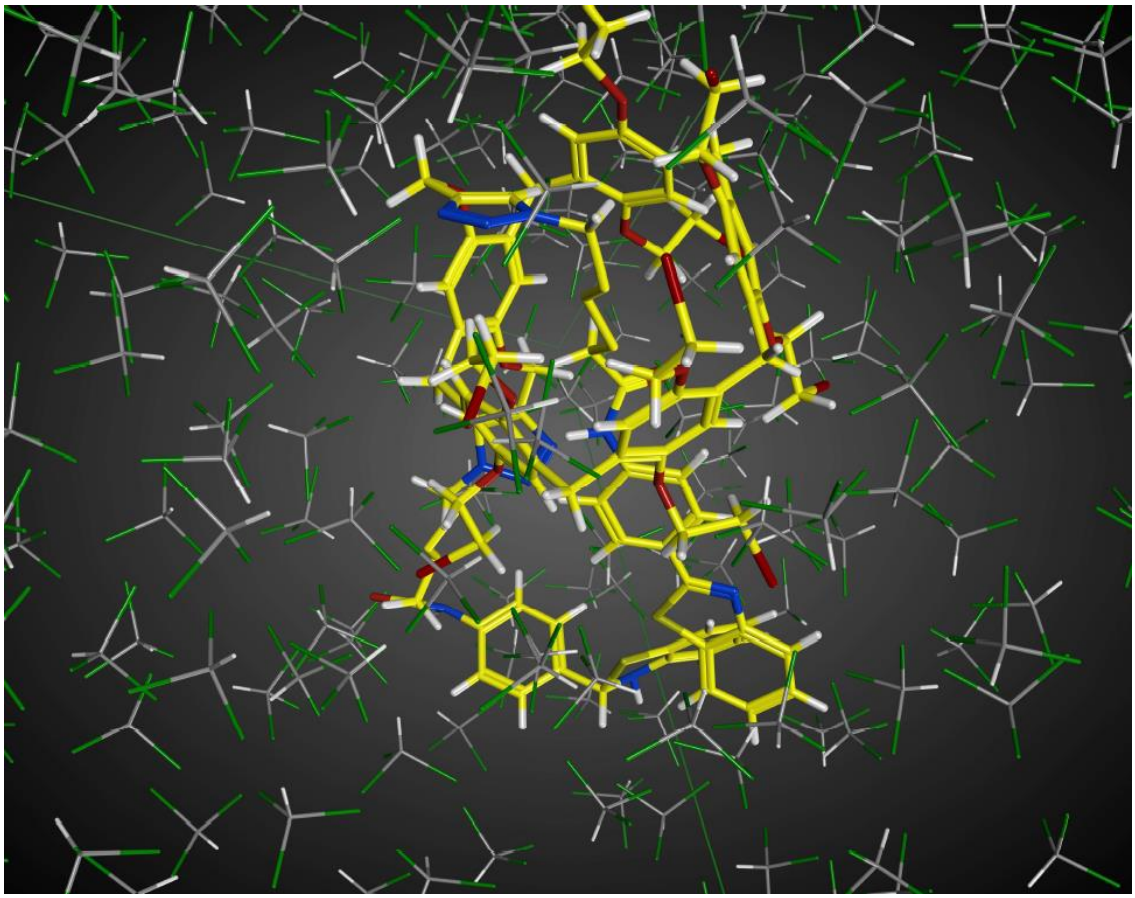

Figure 4.51: Zoomed image of the Computational model after molecular dynamics in $CHCl_3$ solvent system.

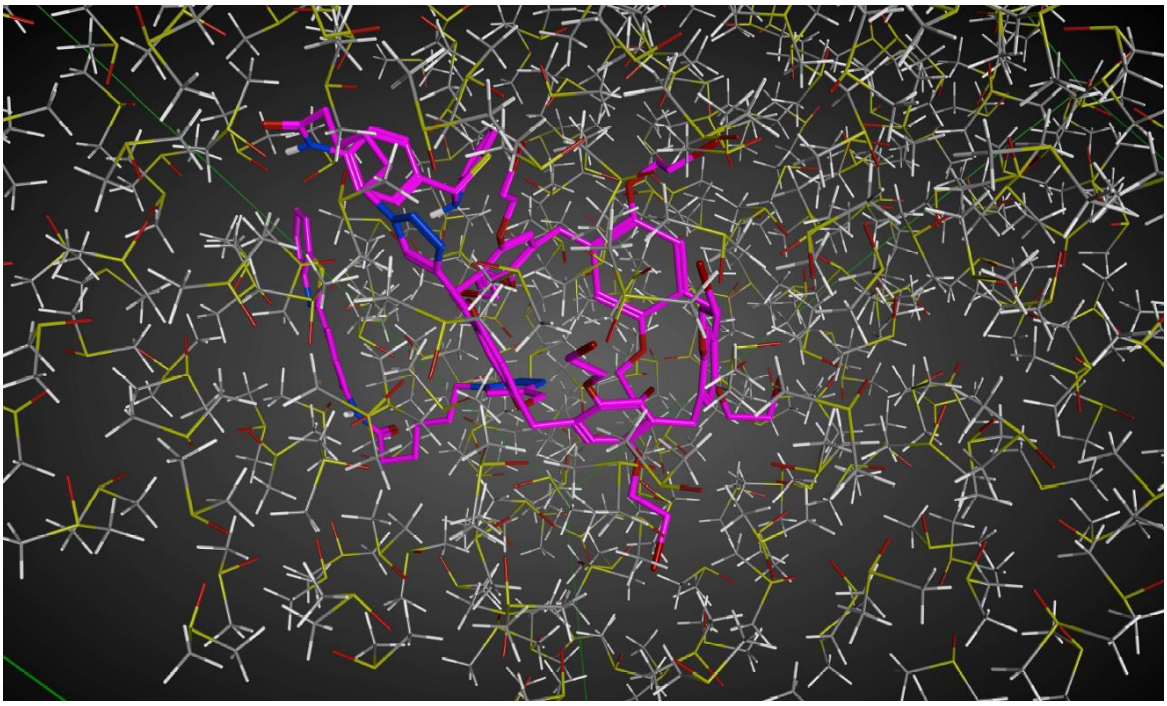

Figure 4.52: Computational model after molecular dynamics in DMSO solvent system

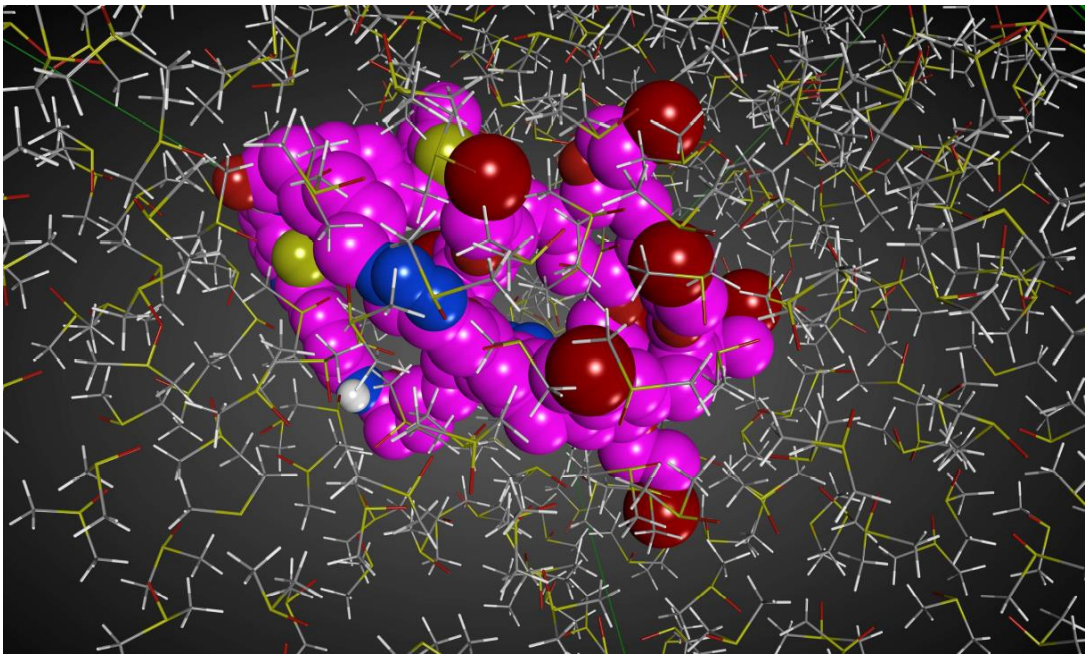

Figure 4.53: Computational model after molecular dynamics in DMSO solvent system. (Space filling model)

5 CHAPTER 5

Will be submitted to *Supramolecular chemistry*

Cationic Pillararenes: Porous Single Molecules for Binding Toxicants in Aqueous Media

Ashvin I Fernando, Teresa Mako, Adelaide Levenson, Paul Cesana, Adriana Mendieta, Mindy Levine, Brenton DeBoef

Department of Chemistry, University of Rhode Island, 140 Flagg Road, Kingston, Rhode Island 02881, United States

Abstract

The ability to detect biologically relevant small molecules with high levels of selectivity, sensitivity and broad applicability for a variety of analytes in a variety of complex environments is an essential goal in bioanalytical chemistry. Methods to achieve such detection vary widely and include the use of electrochemical, spectroscopic, and visible read-out signals. The purpose of supramolecular chemistry to accomplish such detection has many notable advantages, including straightforward tunability, high general applicability, and ease of modification of every component. Reported herein is the use of supramolecular chemistry of pillar[5]arenes to accomplish precisely such detection. A variety of pillar[5]arenes has been synthesized and analyzed for their applicability toward small molecule detection schemes. Water-soluble pillar[5]arenes functionalized with cationic linker arms have been found to bind small molecule toxicants in their hydrophobic cavities with association constants on the orders of 10^5 and 10^6 M^{-1}. With the use of exchange resins, cationic pillar[5]arenes could be removed from solution along with their encapsulated guests, allowing for potential application to water purification systems.

Introduction

The development of methods for the selective removal of highly toxic organic pollutants from aqueous environments is a pressing research need with significant implications in public health,[1] environmental legislation,[2] and biological sciences.[3,4] Many existing methods for such removal suffer from significant drawbacks, including lack of selectivity in toxicant removal,[5] introduction of toxic removal agents in order to remove the targeted pollutants,[6] inefficient toxicant removal performance,[7] and lack of recyclability of the removal agents.[8] These drawbacks are particularly significant for compounds that are highly environmentally persistent, which means that such compounds will remain in the environment for several years after an initial contamination event unless actively removed, as well as for compounds that lack clear detectable signatures,[9] including visible colour and/or high luminescence, which means that their continued presence in the environment is challenging to detect.

Previous work from our research groups has reported extensive results using cyclodextrin-based systems for highly effective toxicant detection and medical imaging applications.[10,11,12] Some work in synthetically-modified cyclodextrins,[13-15]modified curcubiturils,[16] and fully synthetic all-organic macrocycles[17,18] has also been reported, but the utility of such materials in small molecule binding and sequestration has not been fully explored. The highly efficient removal of micropollutants using insoluble cyclodextrin polymers cross-linked with rigid aromatic groups has been reported by Dichtel and co-workers.[19,20] While this material was highly effective at pollutant capture in both air and water,[21] it required anhydrous conditions and a multi-day reaction time to synthesize the porous polymer in 45% isolated yield. Moreover, the use of an insoluble material for pollutant removal rather than the soluble macrocycle reported herein comes with additional trade-offs in terms of detailed material characterization, as well as rationally-guided opportunities for further tunability and structural optimization.

Compared to cyclodextrin-based systems, pillararenes are relatively new, with the first reported pillararene synthesized by Ogoshi and co-workers in 2008.[22] These macrocycles, which are formed from the condensation reaction of a 1,4-dialkoxybenzene with paraformaldehyde, and generally form the thermodynamically favored 5-membered cyclic oligomer, termed a pillar[5]arene,[23] having symmetrical, rigid, pillar-like cavities,[24] The electronic and steric properties of pillararenes can be tuned via judicious choice of dialkylhydroquinone starting material, although overall highly electron-rich structures are obtained.[25] As a result, pillar[5]arenes are well-suited to bind electron deficient small molecule guests in their interior cavities,[26] with binding constants between 10^3 and 10^5 M^{-1} generally obtained.[27] Examples of small molecule guests include biologically relevant analytes such as methionine,[28] tryptophan,[29] and adenosine triphosphate (ATP),[30] with the pillararenes in those cases bearing cationic groups that facilitate aqueous solubility.

Despite the significant advances in pillararene syntheses and applications that have been reported in recent years, the use of pillararenes for environmental remediation applications such as purification of contaminated water has been only rarely reported. This is true despite the fact that pillararene-induced binding of environmentally relevant analytes has strong potential to facilitate such environmental remediation, provided that there is a mechanism to remove the analytes of interest after binding in the pillararene is achieved. Such analytes include polycyclic aromatic hydrocarbons (PAHs),[31] polyfluorooctanoic acid (PFOA),[32] aromatic pesticides,[33] pharmaceutical drugs such as Tylenol and Advil,[34] and plasticizers such as phthalate esters,[35] all of which have been found in aqueous environments and have the potential to induce deleterious health effects.[36]

Reported herein is the use of a newly synthesized cationic pillar[5]arene to bind a broad variety of small molecule organic analytes, including several of the analytes listed above, with strong binding constants up to 10^9 M^{-1} observed. This macrocyclic host demonstrates good generality for a range of analytes as well as high aqueous solubility due to its cationic pendant groups, which facilitates its usage in water purification efforts. Moreover, the ability to use cationic

exchange resins to remove the cationic pillar[5]arene after binding the analyte, which facilitates practical water purification efforts, is also demonstrated, as are comparisons to a neutral pillar[5]arene host. Computational efforts are invoked to explain the observed experimental data and overall trends.

Results and Discussion

The water-soluble pillar[5]arene host was synthesized with an 80% overall yield over three steps. The first step of the synthesis consisted of bromination of *para*-hydroquinone to form the dialkoxyether monomer **1**, followed by cyclization using boron trifluoride etherate as a Lewis acid to promote the desired cyclization in a solution of 1,2-dichloroethane, which serves as both the bulk solvent and as the molecular template for the macrocyclization to form pillar[5]arene **2**. A subsequent substitution using *N*-methylimidazole provided the decacationic pillar[5]arene **3** in an 81% yield over two steps.[37,38]

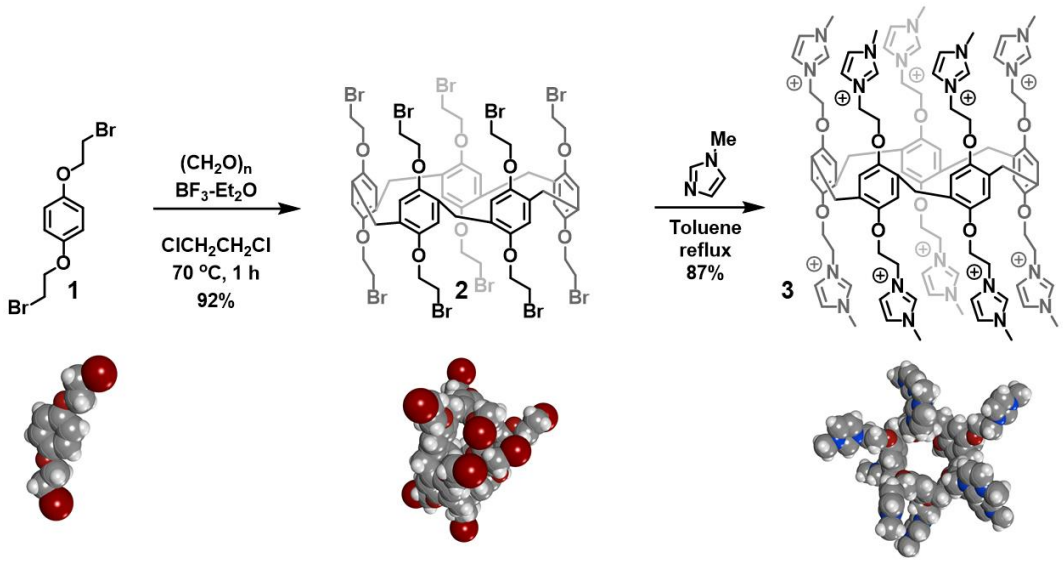

Figure 5.1: Illustration of the synthesis of pillar[5]arene 3 via cyclization of monomer 1 in the presence of dichloroethane solvent, followed by nucleophilic substitution of the terminal bromine moieties on compound 2.Three-dimensional structures underneath the reaction scheme show energy-minimized molecular conformations.

Molecular mechanics calculations predicted that compound **3** has a unique structure with a central cavity (Figure 1), which is readily accessible due to the repulsion created by the ten positive charges on the ethylene arms. Pillararene **3**'s hydrophobic core, flexible aperture, and high water solubility make it a great candidate for binding a wide variety of small organic molecules in aqeous media. Furthermore, the imidazolium cations that are present at the termini have the potential to participate in π-π[39] or cation-π[40] interactions. Consequently, we predicted that **3** could accommodate different types of toxicants with a broad variety of sizes, electronics, and other structural components.

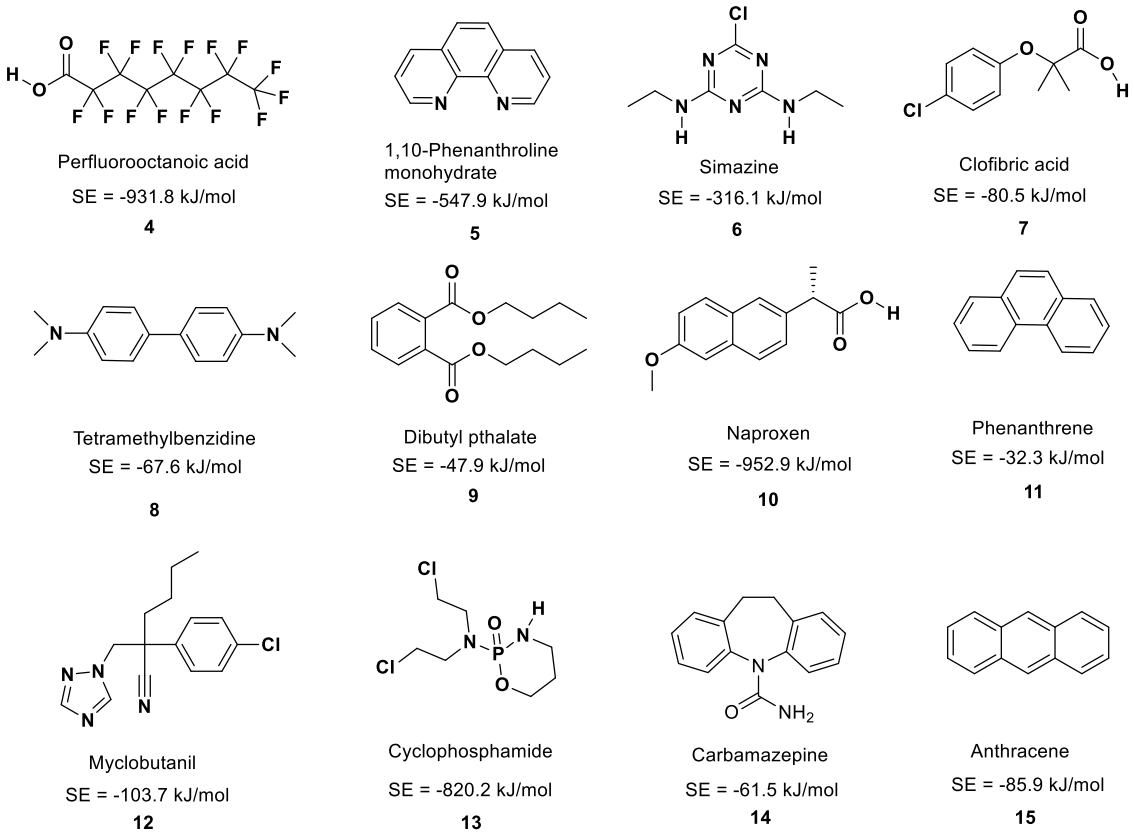

Figure 5.2: Array of toxicants and small molecules that were used in the binding study with supramolecular host 3, with calculated stabilization energies of the toxicants upon binding in host 3 (obtained via Spartan 16) shown.The values given represents the stabilization energy for the final complex formation between the toxicant and **3.** The equation used is $\Delta\Delta H\ (\text{stabilation energy}) = \Delta H\ (\mathbf{3} + \text{guest}) - \Delta H(\mathbf{3}) - \Delta H(\text{guest})$. Top - Cartoon image represents the binding phenomena taking place between **3** and the toxicants.

Computational Investigations

Pillararene **3** has a calculated internal diameter of 9 Å and an outer diameter of 11 Å. The diameters of toxicants **4-15** in this study ranged from 7 Å to 11.5 Å, which means that most of them should be able to fit in the cavity of the supramolecular host. Furthermore, docking studies performed using supramolecular host **3** and toxicants **4-15** resulted in calculated stabilization energies and docking scores (Table 1) that highlight the favourability of supramolecular complexation.

As shown in Table 1, the most favourable stabilization energy (largest negative value) corresponds to the binding of naproxen (analyte **10**), a pharmaceutical drug with some associated toxicity, likely as a result of the good complementary fit between the analyte and the supramolecular cavity (Figure 3A). This is also true for other molecules such as PFOA (Figure 3B), cyclophosphamide (Figure 3C), and 1,10-phenanthroline (Figure 3D), all of which appear to be using the majority of the interior space and all of which have key favourable interactions. More generally, the uniformly negative stabilization energies obtained for all toxicants in the supramolecular host **3** indicate that all complexes should spontaneously form in aqueous media. Of note, toxicants such as 1,10-phenanthroline were bound more towards the outer portal of the host (Figure 3D), which generally displayed weaker binding compared to binding that was deeper in the interior cavity.

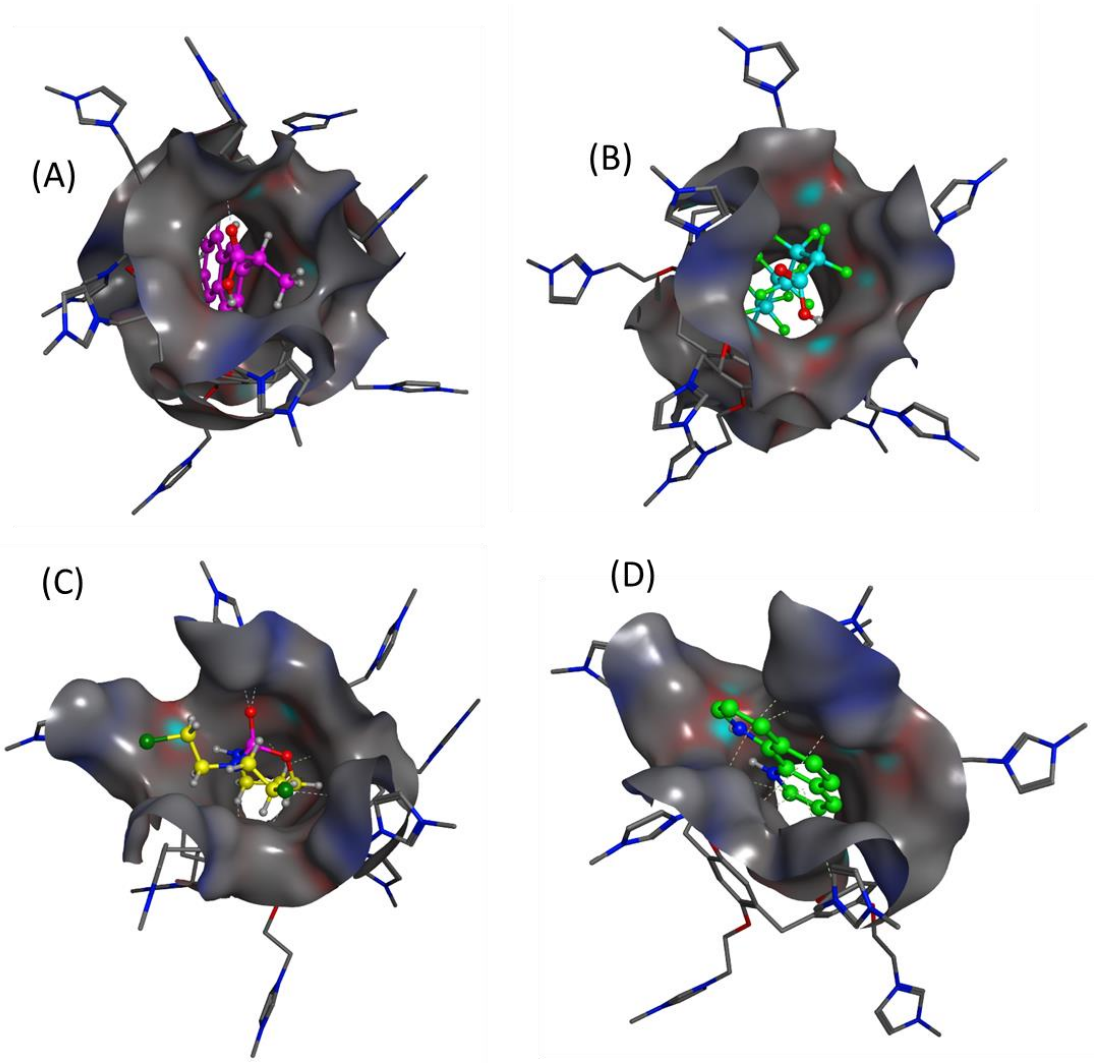

Figure 5.3: Computed images of analytes docked in macrocycle 3. (A) Naproxen; (B) PFOA; (C) Cyclophosphamide; and (D) 1,10-Phenanthroline

NMR Spectroscopy

Additionally, ^{1}H NMR spectroscopy investigations provided structural insight into the host: guest complex, with shifts observed in the peaks that correspond to the interior protons of host **3** and the methylene protons on the imidazolium-terminated side chains (Figure 4). Similarly, ^{19}F NMR spectroscopy (Figure 5) demonstrated broadening of the fluorine signal that corresponds to the PFOA analyte **4** in the presence of the pillararene host, indicating restricted conformational freedom as a result of host-guest inclusion.

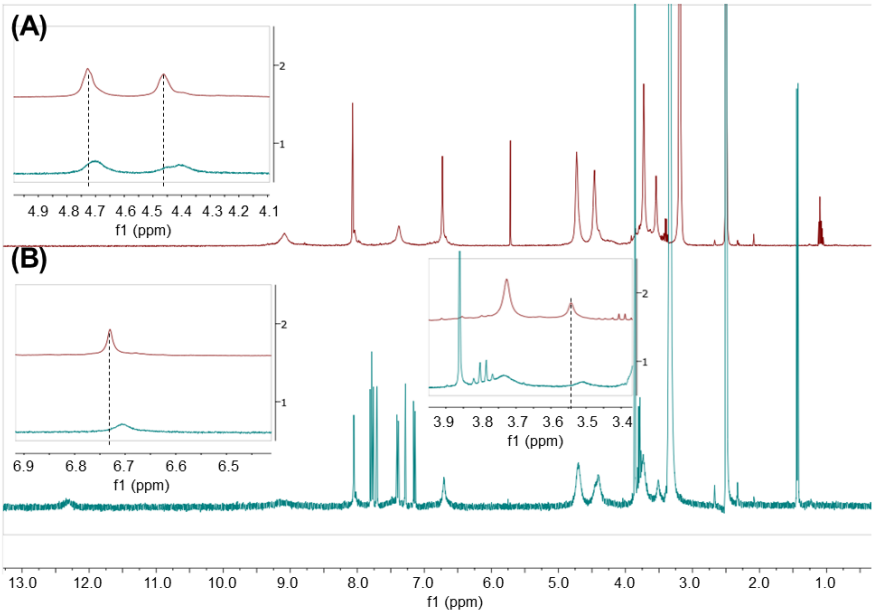

Figure 5.4: [1]H NMR spectra of: (A) macrocycle 3; and (B) macrocycle 3 and naproxen 10 in a 1:1 molar ratio. The concentrations of the guest and host were 10 mM each

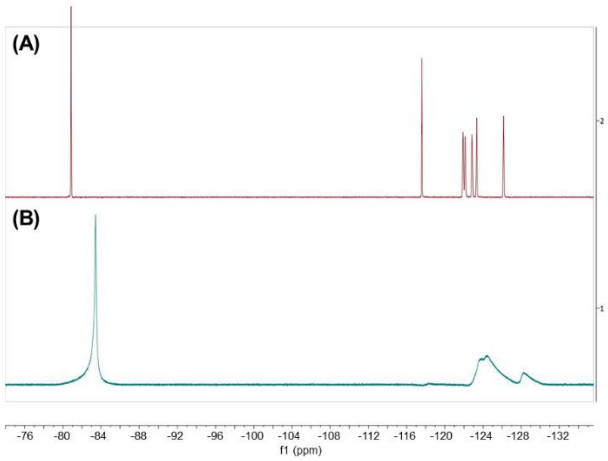

Figure 5.5: Fluorine NMR spectra of: (A) Perfluorooctanoic acid (PFOA); and (B) complex between PFOA and supramolecular host 3

Fluorescence Spectroscopy of Inclusion Complexes

Fluorescence studies were undertaken to elucidate the binding modes and affinities of the small molecule toxicants shown in Figure 2. The results of analyte binding inside cationic pillararene **3** are summarized in Table 2, with selected results highlighted in Figures 6 and 7. These studies showed that most of the analytes formed 1:1 association complexes both in phosphate buffered saline (PBS) as well as in DMSO. The compounds that formed 1:2 complexes in PBS included clofibric acid, myclobutanil, and 1,10-phenanthroline, with only 1,10-phenanthroline maintaining the 1:2 complex in DMSO as well. Of note, both clofibric acid and myclobutanil contain a chlorine-substituted benzene ring with the chlorine in the para-position relative to the rest of the structure. *Para*-chlorobenzene structures have been shown in the literature to bind strongly in pillararene structures,[41] and the relatively small size of this structure allows for the inclusion of two small molecule guests simultaneously. Simazine formed an unusual 2:1 complex, likely due to the ability of the amine substituents to associate with two different pillararene hosts simultaneously. The fact that phenanthroline formed a 1:2 complex is likely due to the ability of the heterocyclic aromatic architecture to form strong π-stacked association complexes, in accordance with literature precedent.[42,43]

Compound number	**Host:Guest Stoichiometry**	**Association Constant in water (M^{-1})**	**Association constant in DMSO (M^{-1})**
Anthracene	1:1	$7.18\ (0.0001) \times 10^{5}$	N/A
Carbamazepine	1:1	$1.06\ (0.12) \times 10^{5}$	N/A
Clofibric acid	1:2	$K_{a1} = 6.34\ (1.27) \times 10^{6}$ $K_{a2} = 4.77\ (0.32) \times 10^{5}$	N/A
Cyclophosphamide	1:1	$1.33\ (0.19) \times 10^{6}$	$2.17\ (0.35) \times 10^{5}$
Dibutylphtalate	1:1	$5.67\ (0.97) \times 10^{5}$	$3.32\ (0.45) \times 10^{5}$
Myclobutanil	1:2	$K_{a1} = 5.10\ (0.92)$ $K_{a2} = 2.62\ (0.0044) \times 10^{10}$	N/A
N,N,N,N - tetramethylbenzidine	1:1	$1.62\ (0.12) \times 10^{6}$	N/A
Naproxen	1:1	$6.51\ (0.911) \times 10^{3}$	N/A
PFOA	1:1	$1.13\ (0.13) \times 10^{6}$	$2.44\ (0.17) \times 10^{4}$
Phenanthrene	1:1	$2.32\ (0.02) \times 10^{4}$	$8.10\ (1.80) \times 10^{3}$
1,10-Phenothroline	1:2	N/A	$K_{a1} = 4.40\ (0.027) \times 10^{5}$ $K_{a2} = 2.67\ (0.24) \times 10^{4}$
Simazine	2:1	$K_{a1} = 1.37\ (0.22) \times 10^{10}$ $K_{a2} = 6.47\ (1.42) \times 10^{9}$	$K_{a1} = 7.52\ (0.001) \times 10^{11}$ $K_{a2} = 6.47\ (0.42) \times 10^{4}$

Table 5-1: Association constants obtained from fluorescence titrations

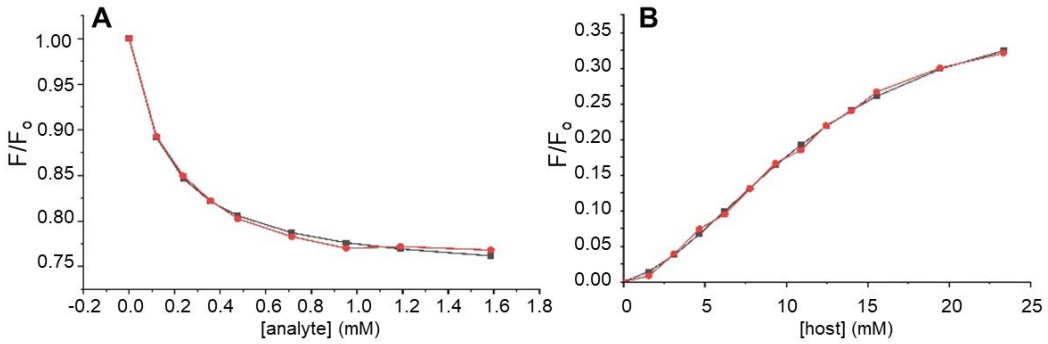

Figure 5.6: Sample fluorescence titrations of analytes with cationic host 3 used to determine binding constants: (A) with simazine guest; and (B) with phenanthrene guest. The black line represents the calculated values and the red line represents the experimentally determined values

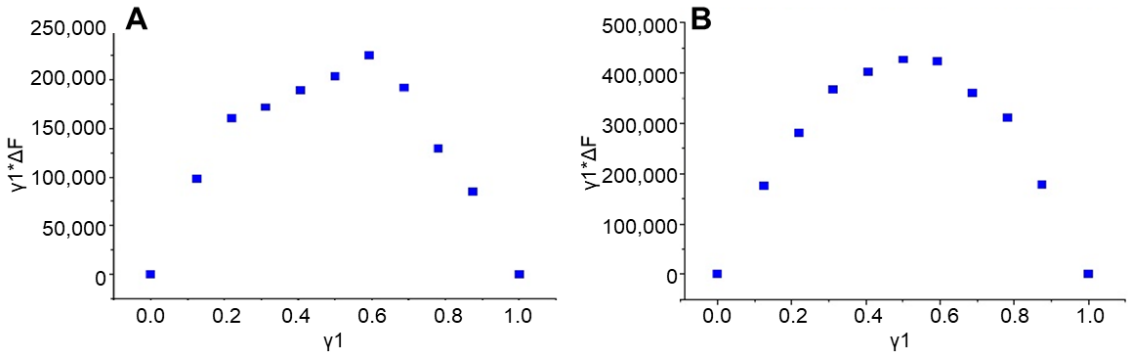

Figure 5.7: Job's plot analysis of binding of cationic host 3 with: (A) anthracene and (B) phenanthrene small molecule guests

Interestingly, we synthesized a neutral pillar[5]arene that contains ten propargyl groups as a control to compare with the cationic structure of supramolecular host **3**. In the control case, most of the toxicants formed 1:2 complexes with the propargyl-substituted host, likely as a result of the fact that the alkynes extend the size of the hydrophobic cavity and facilitate the binding of multiple guest molecules.[44] Moreover, cationic host **3** is likely to suffer from charge repulsion, either via

self-repulsion or via repulsion with cationic small molecule guests.[1] This charge repulsion, in turn, leads to more 1:1 complexation than any other binding stoichiometry.

Moreover, pillararene **3** showed the strongest binding to simazine in aqueous solution, with a 10^{10} M^{-1} binding constant observed (for binding the first equivalent of toxicant), and myclobutanil, with a 10^{10} M^{-1} binding constant observed (for binding a second equivalent of toxicant). These binding constants are four orders of magnitude higher than the next highest strength constants, seen for clofibric acid, cyclophosphamide, *N,N,N',N'*-tetramethylbenzidine, perfluorooctanoic acid, and 1,10-phenanthroline, all of which displayed association constants on the order of 10^6 M^{-1}. A structural comparison between the two strongest binding guests indicates high levels of electron deficiency for both simazine and myclobutanil. Although other analytes also show moderate to significant electron deficiencies, the highly aminated structures of myclobutanil and simazine provide additional benefits for association with a cationic supramolecular host, with the nitrogen atoms able to associate with the cationic charge. The weakest binding guests, phenanthrene (10^4 M^{-1}) and naproxen (10^3 M^{-1}), have much higher electron density, which disfavours binding inside the pillararene host.

Switching the solvent to DMSO resulted in decreases in host: guest association complexes, with a reduction in binding affinity of up to three orders of magnitude observed (simazine in PBS = 10^{10} M^{-1}; in DMSO = 10^7 M^{-1}). The decreased binding affinity in non-aqueous environments means that the likely mechanism of binding is via hydrophobic association and that switching to non-aqueous solvents results in decreasing the energetic favorability of such association. Literature precedent strongly supports the notion of hydrophobically-driven binding in pillararene architectures, as well as the fact that switching to non-aqueous solvents reduces the favorability of hydrophobically-driven inclusion.

Finally, linear discriminant analysis of the experimentally obtained binding constants revealed 100% differentiation between the different toxicants (Figure 8), with clustering between structurally similar analytes observed. For example, anthracene, 1,10-phenanthroline and

phenanthrene all grouped near each other due to similarities in their planar, polycyclic aromatic core. The only fluorinated analyte, PFOA, was found to be separate on the graph from the other analytes investigated. Such separation among different analytes, even those with high degrees of structural similarity, highlight the potential of this method to enable selective toxicant detection capabilities.

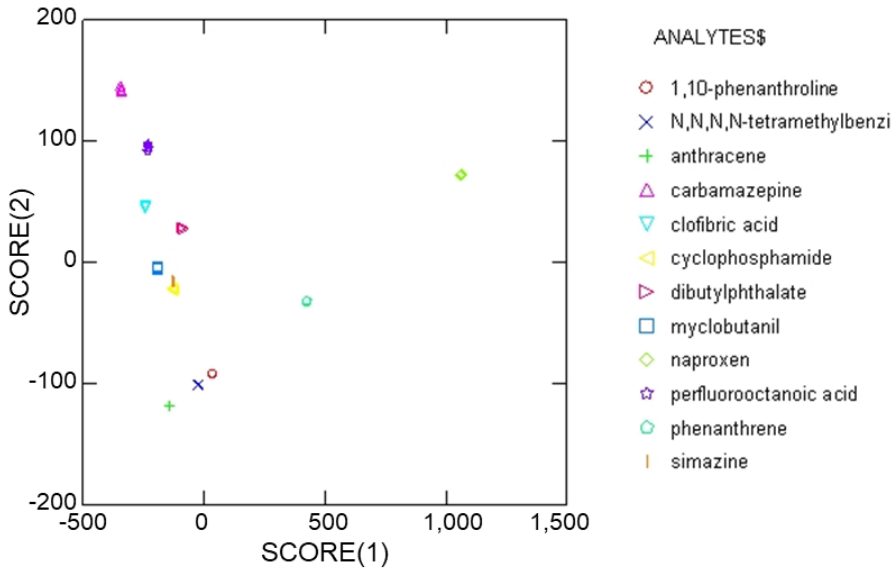

Figure 5.8: Linear discriminant analysis of analyte-induced responses upon binding in cationic host 3

Finally, we have shown that pillararene host **3** can be removed by a cation exchange resin after it binds the toxicant small molecule guests (Figure 9).

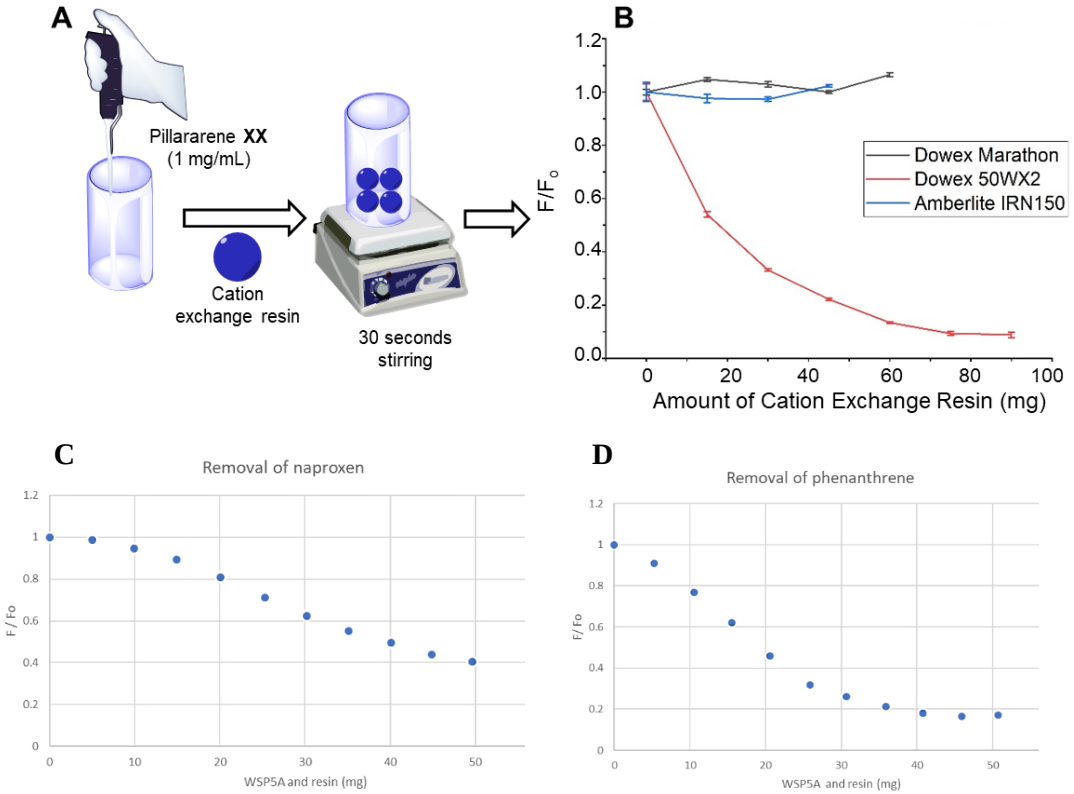

Figure 5.9: (A) Schematic illustration of removal of toxicant-bound pillararene with cationic exchange resin; (B) Quantitative assessment of the amount of 3 that was removed by different cation resin types.The black line represents Dowex Marathon resin, the red line represents Dowex 50WX2 resin, and the blue line represents Amberlite IRN150 resin. (C) Quantitative assessment of the amount of naproxen removed after treatment of **3** with resin and (D) Quantitative assessment of the amount of phenanthrene removed after treatment of **3** with resin

As seen on figure 9 we were able to successfully remove naproxen and phenanthrene from an aqueous solution using WSP5A as the capture agent and exchange resin as a removal agent, to remove the whole guest encapsulated 3 from the aqueous solution with ease.

Conclusion

The ability to use rationally designed supramolecular hosts such as pillararene **3** for the removal of toxic compounds from contaminated aqueous environments has significant potential advantages, provided that the removal can occur with high efficacy for toxic compounds and broad relevance for a variety of potential contaminants, and that the contaminants can be removed from the aqueous solution following binding. The results reported herein constitute significant progress towards achieving this goal, through the development of polycationic pillararene host **3,** using computational and experimental results to understand its binding to a variety of small molecule toxicants, and then demonstrating the practical relevance of such systems via the use of cationic exchange resins to remove the complex after toxicant binding. Current efforts in our laboratory are focused on the development of practical environmental remediation systems based on such technology, and on developing other effective supramolecular systems based on the progress reported herein. The results of these and other investigations will be reported in due course.

5.1 REFERENCES

(1) Miner, K. R.; Bogdal, C.; Pavlova, P.; Steinlin, C.; Kreutz, K. J. Quantitative Screening Level Assessment of Human Risk from PCBs Released in Glacial Meltwater: Silvretta Glacier, Swiss Alps. Ecotoxicol. Environ. Safety 2018, 166, 251-258.

(2) Bieber, S.; Rauch-Williams, T.; Drewes, J. E. An Assessment of International Management Strategies for CECs in Water. ACS Symposium Series 2016, 1241, 11-22.

(3) Kanupuru, S.; Kumari, J. P. Impact of Lead on Environment and Human Health -A Review. World J. Pharmaceutical Res. 2016, 5, 531-554.

(4) Guo, X.; Feng, C. Biological Toxicity Response of Asian Clam (Corbicula fluminea) to Pollutants in Surface Water and Sediment. Sci. Total Environ. 2018, 631-632, 56-70.

(5) Sajid, M.; Nazal, M. K.; Ihsanullah; Baig, N.; Osman, A. M. Removal of Heavy Metals and Organic Pollutants from Water Using Dendritic Polymers Based Adsorbents: A Critical Review. Separation Purification Technol. 2018, 191, 400-423.

(6) Sivrioglu, O.; Yonar, T. Determination of the Acute Toxicities of Physicochemical Pretreatment and Advanced Oxidation Processes Applied to Dairy Effluents on Activated Sludge. J. Dairy Sci. 2015, 98, 2337-2344.

(7) Wang, J.; Zhuang, S. Removal of Various Pollutants from Water and Wastewater by Modified Chitosan Adsorbents. Critical Rev. Environ. Sci. Technol. 2017, 47, 2331-2386.

(8) Zhang, L.; Shan, B.; Yang, H.; Wu, D.; Zhu, R.; Nie, J.; Cao, R. A New Heterogeneous Photocatalyst Based on Wells-Dawson Polyoxometalate and Nickel Coordination Compounds: Synthesis, Structure and Property. RSC Adv. 2015, 5, 23556-23562.

(9) Vivek, J. P.; Berry, N. G.; Zou, J.; Nichols, R. J.; Hardwick, L. J. In Situ Surface-Enhanced Infrared Spectroscopy to Identify Oxygen Reduction Products in Nonaqueous Metal-Oxygen Batteries. J. Phys. Chem. C 2017, 121, 19657-19667.

(10) DiScenza, D. J.; Lynch, J.; Feder, E.; Levine, M. Detection of Bisphenol A and

Derivatives in Human Urine via Cyclodextrin-Promoted Fluorescence Modulation. Anal. Methods 2018, 10, 3783-3790.

(11) DiScenza, D. J.; Lynch, J.; Miller, J.; Verderame, M.; Levine, M. Detection of Organochlorine Pesticides in Contaminated Marine Environments via Cyclodextrin-Promoted Fluorescence Modulation. ACS Omega 2017, 2, 8591-8599.

(12) Hane, F. T.; Fernando, A.; Prete, B. R. J.; Peloquin, B.; Karas, S.; Chaudhuri, S.; Chahal, S.; Shepelytskyi, Y.; Wade, A.; Li, T.; DeBoef, B.; Albert, M. S. Cyclodextrin-based Pseudorotaxanes: Easily Conjugatable Scaffolds for Synthesizing Hyperpolarized Xenon-129 Magnetic Resonance Imaging Agents. ACS Omega 2018, 3, 677–681.

(13) Chaudhuri, S.; DiScenza, D. J.; Verderame, M.; Cromwell, B.; Levine, M. Colorimetric Detection of Polycyclic Aromatic Hydrocarbons Using Supramolecular Cyclodextrin Dimer-Squaraine Constructs. Supramol. Chem. 2019, 31, 211-219.

(14) Chaudhuri, S.; DiScenza, D. J.; Smith, B.; Yocum, R.; Levine, M. Array-Based Detection of Isomeric and Analogous Analytes Employing Synthetically Modified Fluorophore Attached β-Cyclodextrin Derivatives. New J. Chem. 2017, 41, 14431-14437.

(15) Chaudhuri, S.; Verderame, M.; Mako, T. L.; Bandara, Y. M. N. D. Y.; Fernando, A. I.; Levine, M. Synthetic β-Cyclodextrin Dimers for Squaraine Binding: Effect of Host Architecture on Photophysical Properties, Aggregate Formation and Chemical Reactivity. Eur. J. Org. Chem. 2018, 2018, 1964-1974

(16) Hane, F. T.; Li, T.; Smylie, P.; Pellizzari, R. M.; Plata, J. A.; DeBoef, B.; Albert, M. S. In Vivo Detection of Cucurbit[6]uril, a Hyperpolarized Xenon Contrast Agent for a Xenon Magnetic Resonance Imaging Biosensor. Sci. Reports 2017, 7, 41027.

(17) Radaram, B.; Potvin, J.; Levine, M. Highly Efficient Non-Covalent Energy Transfer in All-Organic Macrocycles. Chem. Commun. 2013, 49, 8259-8261

(18) Radaram, B.; Levine, M. Rationally Designed Supramolecular Organic Hosts for Benzo[a]pyrene Binding and Detection. Eur. J. Org. Chem. 2015, 2015, 6194-6204.

(19) Xiao, L.; Ling, Y.; Alsbaiee, A.; Li, C.; Helbling, D. E.; Dichtel, W. R. β-Cyclodextrin Polymer Network Sequesters Perfluorooctanoic Acid at Environmentally Relevant Concentrations. J. Am. Chem. Soc. 2017, 139, 7689-7692.

(20) Alsbaiee, A.; Smith, B. J.; Xiao, L.; Ling, Y.; Helbling, D. E.; Dichtel, W. R. Rapid Removal of Organic Micropollutants from Water by a Porous β-Cyclodextrin Polymer. Nature 2016, 529, 190-194.

(21) Alzate-Sanchez, D. M.; Smith, B. J.; Alsbaiee, A.; Hinestroza, J. P.; Dichtel, W. R. Cotton Fabric Functionalized with a β-Cyclodextrin Polymer Captures Organic Pollutants from Contaminated Air and Water. Chem. Mater. 2016, 28, 8340-8346.

(22) Ogoshi, T.; Kanai, S.; Fujinami, S.; Yamagishi, T.-a.; Nakamoto, Y. Para-Bridged Symmetrical Pillar[5]arenes: Their Lewis Acid Catalyzed Synthesis and Host-Guest Property. J. Am. Chem. Soc. 2008, 130, 5022-5023.

(23) Ogoshi, T.; Yamagishi, T.-a.; Nakamoto, Y. Pillar-Shaped Macrocyclic Hosts Pillar[n]arenes: New Key Players for Supramolecular Chemistry. Chem. Rev. 2016, 116, 7937-8002.

(24) Boehmer, V. Calixarenes Macrocycles with (Almost) Unlimited Possibilities. Angew. Chem. Int. Ed. 1995, 34, 713-745.

(25) Wu, J.-R.; Yang, Y.-W. New Opportunities in Synthetic Macrocyclic Arenes. Chem. Commun. 2019, 55, 1533-1543.

(26) Wang, Y.; Ping, G.; Li, C. Efficient Complexation Between Pillar[5]arenes and Neutral Guests: From Host-Guest Chemistry to Functional Materials. Chem. Commun. 2016, 52, 9858-9872.

(27) Park, C.; Kim, K. T. Pillar[n]arenes and Other Cavitands: Aspects of Complex Thermodynamics. Chinese J. Chem. 2015, 33, 311-318.

(28) Lin, Q.; Liu, L.; Zheng, F.; Mao, P.-P.; Liu, J.; Zhang, Y.-M.; Yao, H.; Wei, T.-B. A Water-Soluble Pillar[5]arene-Based Chemosensor for Highly Selective and Sensitive

Fluorescence Detection of L-Methionine. RSC Adv. 2017, 7, 34411-34414.

(29) Wei, T.-B.; Chen, J.-F.; Cheng, X.-B.; Li, H.; Han, B.-B.; Zhang, Y.-M.; Yao, H.; Lin, Q. A Novel Functionalized Pillar[5]arene-Based Selective Amino Acid Sensor for L-Tryptophan. Org. Chem. Frontiers 2017, 4, 210-213.

(30) Yu, G.; Zhou, J.; Shen, J.; Tang, G.; Huang, F. Cationic Pillar[6]arene/ATP Host-Guest Recognition: Selectivity, Inhibition of ATP Hydrolysis, and Application in Multidrug Resistance Treatment. Chem. Sci. 2016, 7, 4073-4078.

(31) Meng, Y.; Liu, X.; Lu, S.; Zhang, T.; Jin, B.; Wang, Q.; Tang, Z.; Liu, Y.; Guo, X.; Zhou, J.; Xi, B. A Review on Occurrence and Risk of Polycyclic Aromatic Hydrocarbons (PAHs) in Lakes of China. Sci. Total Environ. 2019, 651, 2497-2506.

(32) Ghisi, R.; Vamerali, T.; Manzetti, S. Accumulation of Perfluorinated Alkyl Substances (PFAS) in Agricultural Plants: A Review. Environ. Res. 2019, 169, 326-341.

(33) Khanna, R.; Gupta, S. Agrochemicals as a Potential Cause of Ground Water Pollution: A Review. Int. J. Chem. Studies 2018, 6, 1-6.

(34) Aljeboree, A. M.; Alshirifi, A. N. Adsorption of Pharmaceuticals as Emerging Contaminants from Aqueous Solutions on to Friendly Surfaces such as Activated Carbon: A Review. J. Pharmaceutical Sci. Res. 2018, 10, 2252-2257.

(35) Gao, D.; Li, Z.; Wang, H.; Liang, H. An Overview of Phthalate Acid Ester Pollution in China Over the Last Decade: Environmental Occurrence and Human Exposure. Sci. Total Environ. 2018, 645, 1400-1409.

(36) Choudri, B. S.; Charabi, Y.; Ahmed, M. Effects of Pollution on Freshwater Organisms. Water Environ. Res. 2018, 90, 1723-1747.

(37) Santra, S.; Kovalev, I. S.; Kopchuk, D. S.; Zyryanov, G. V.; Majee, A.; Charushin, V. N.; Chupakhin, O. N. Role of Polar Solvents for the Synthesis of Pillar[6]arenes. RSC Adv. 2015, 5, 104284-104288.

(38) Meyer, D.; Strassner, T. 1,2,4-Triazole-Based Tunable Aryl/Alkyl Ionic Liquids. J. Org.

Chem. 2011, 76, 305-308.

(39) Jebur, M.; Sengupta, A.; Chiao, Y.-H.; Kamaz, M.; Qian, X.; Wickramasinghe, R. Pi Electron Cloud Mediated Separation of Aromatics Using Supported Ionic Liquid (SIL) Membrane Having Antibacterial Activity. J. Membrane Sci. 2018, 556, 1-11.

(40) Wang, Y.-L. Competitive Microstructures Versus Cooperative Dynamics of Hydrogen Bonding and π-Type Stacking Interactions in Imidazolium Bis(oxalato)borate Ionic Liquids. J. Phys. Chem. B 2018, 122, 6570-6585.

(41) Zhang, Y.; Lv, Q.; Qi, M.; Cai, Z. Performance of Permethyl Pillar[5]arene Stationary Phase for High-Resolution Gas Chromatography. J. Chromatography A 2017, 1496, 115-121.

(42) Du, X.; Fan, R.; Wang, X.; Qiang, L.; Wang, P.; Gao, S.; Zhang, H.; Yang, Y.; Wang, Y. Combined Effect of Hydrogen Bonding and π···π Stacking Interactions in the Assembly of Indium(III) Metal-Organic Materials: Structure-Directing and Aggregation-Induced Emission Behavior. Crystal Growth & Design 2015, 15, 2402-2412.

(43) An, C.; Guo, X.; Baumgarten, M. Highly Ordered Phenanthroline-Fused Azaacene. Crystal Growth & Design 2015, 15, 5240-5245.

(44) Aime, S.; Gianolio, E.; Arena, F.; Barge, A.; Martina, K.; Heropoulos, G.; Cravotto, G. New Cyclodextrin Dimers and Trimers Capable of Forming Supramolecular Adducts with Shape-Specific Ligands. Org. Biomolecular Chem. 2009, 7, 370-379.

(45) Jannuzzi, S. A. V.; Martins, B.; Felisberti, M. I.; Formiga, A. L. B. Supramolecular Interactions between Inorganic and Organic Blocks of Pentacyanoferrate/Poly(4-vinylpyridine) Hybrid Metallopolymer. J. Phys. Chem. B 2012, 116, 14933-14942.

5.2 SUPPORTING INFORMATION

Cationic Pillararenes: Porous Single Molecules for Binding Toxicants in Aqueous Media

Reagents

Substrates, including CBr_4, dry acetonitrile, dry 1,2-dichloroethane, boron trifluoride etherate, triphenylphosphine, methylimidazole were purchased from Sigma-Aldrich, Fisher Scientific, and TCI chemicals. All reagents were stored under an inert atmosphere before use. Unless otherwise noted, all reactions were performed under N_2.

Instrumentation

NMR spectra were obtained using Bruker Avance 300 MHz and 400 MHz spectrometers. Low-resolution mass spectrometry was performed using a Shimadzu LRMS-2020. High-resolution mass spectrometry was performed using a Thermo Scientific LTQ Orbitrap XL™ instrument. UV-Vis spectra was obtained via Shimadzu UV-Vis spectrophotometer, and Fluorescence spectra was obtained via Shimadzu Fluorimeter.

The synthetic route for the synthesis of Water-soluble pillar[5]arene

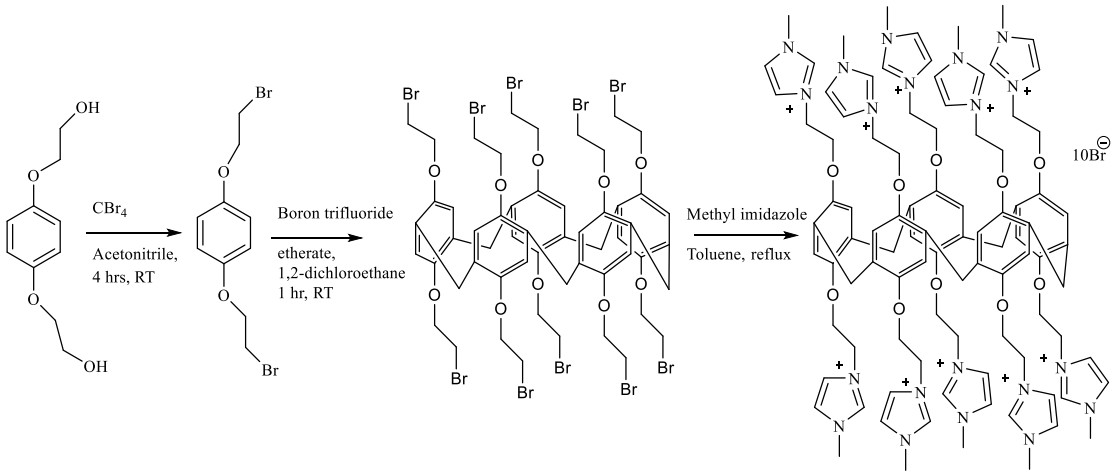

The above molecule was synthesized according to the literature procedures[1], with further optimizations and better yields.

[In the UV-Vis, fluorescence spectra and jobs plot WSP5A is mentioned as PA1 and the neutral proapargylated is mentioned as PA2]

Synthesis of guest molecules

Synthesis of brominated monomer, 1

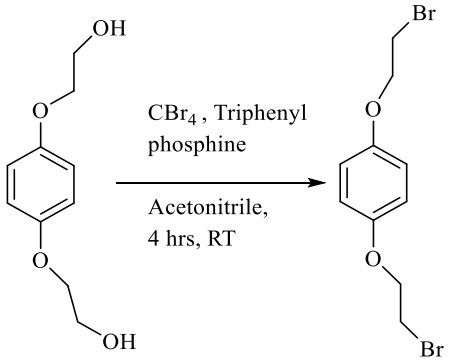

A solution of 1,4-bis(2-hydroxyethyl)benzene (10.0 g, 50.4 mmol) and triphenylphosphine (31.5 g, 120mmol) in dry acetonitrile (250 mL) was cooled in an ice bath. Under vigorous stirring, carbon tetrabromide (39.8 g, 120 mmol) was slowly added in four portions. In every addition, the solution immediately turns bright yellow and with stirring returns to its colorless form. On the final addition, the solution stays cloudy. The mixture was stirred at room temperature for 4 hours and 20 minutes. Then cold water (200 mL) was added to the reaction mixture to give a white precipitate. The precipitate was collected, washed with another 200 ml of cold water followed with methanol/water (3:2, 3 × 100 mL). The collected white solids were dried under vacuum for 24 hours and used without further purification. (14.5 g, 97%). ^{1}H NMR and ^{13}C NMR was performed using $CDCl_3$. ^{1}H NMR (400 MHz, Chloroform-d) δ 6.89 (s, 4H), 4.27 (t, J = 6.3 Hz, 4H), 3.64 (t, J = 6.3 Hz, 4H).

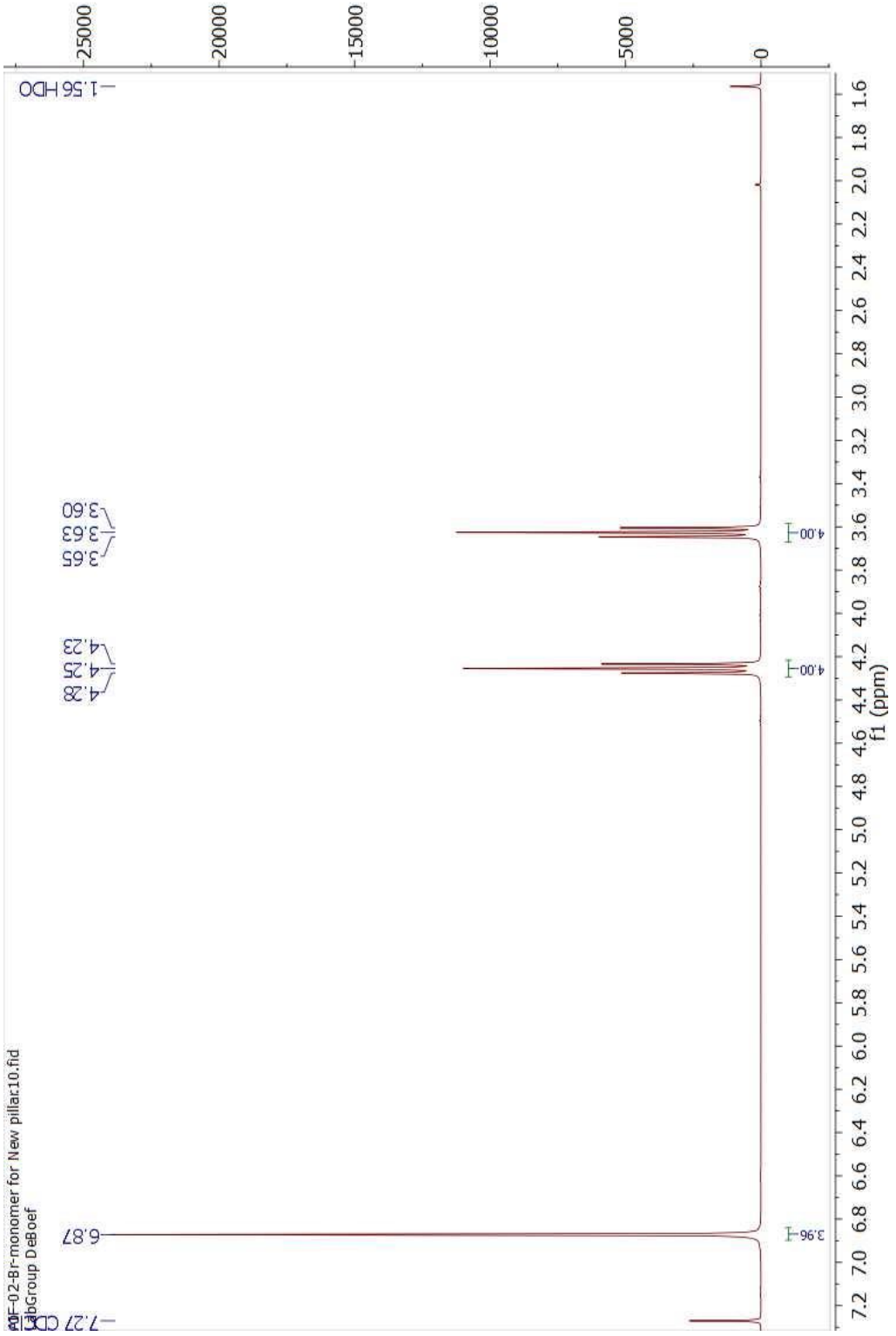

Figure 5.10: ^{1}H NMR of brominated monomer

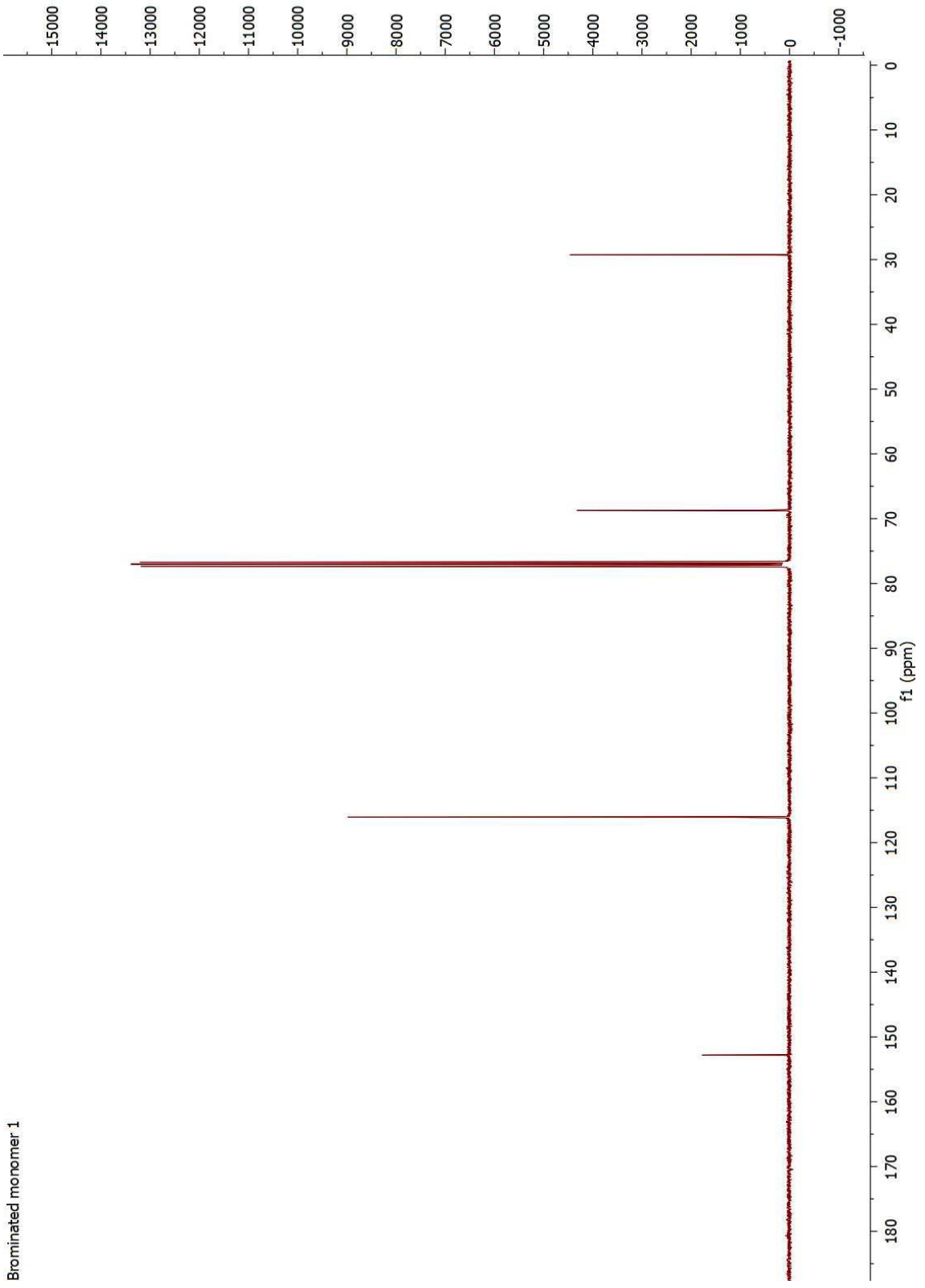

Figure 5.11: ^{13}C NMR of 1

Synthesis of deca-brominated pillar[5]arene, 2

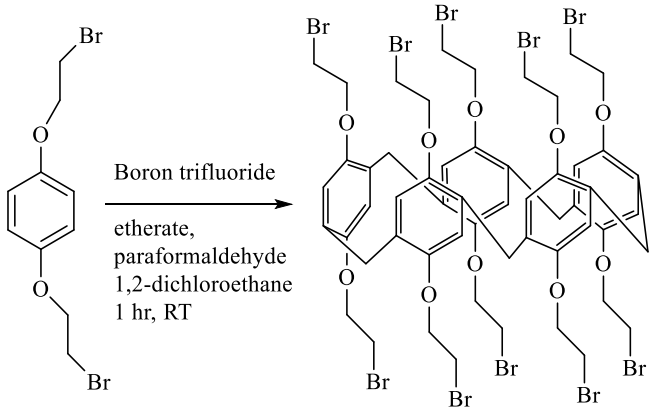

A solution of brominated monomer (3.37 g, 11.5 mmol) and paraformaldehyde (0.349 g, 11.5 mmol) in 1,2-dichloroethane (50 mL) was cooled with an ice bath. Boron trifluoride etherate (3.26 g, 23.0 mmol) was added to the solution, and the mixture was stirred at room temperature for 1 hour. During the 1 hour, the reaction undergoes various color changes. This reaction mixture was washed with DI water (2 × 50 mL), saturated sodium bicarbonate (2 x 50 ml) and brine solution (2 x 50ml). The organic layer was dried with anhydrous Na_2SO_4. The solvent was evaporated to provide a crude product. The crude product was pure; hence no further purification was required. (yield 85%). ^{1}H NMR and ^{13}C NMR were performed using $CDCl_3$. ^{1}H NMR (400 MHz, Chloroform-d) δ 6.91 (s, 10H), 4.23 (t, J = 6.3, 5.1 Hz, 20H), 3.84 (s, 10H), 3.63 (t, J = 5.6 Hz, 20H).

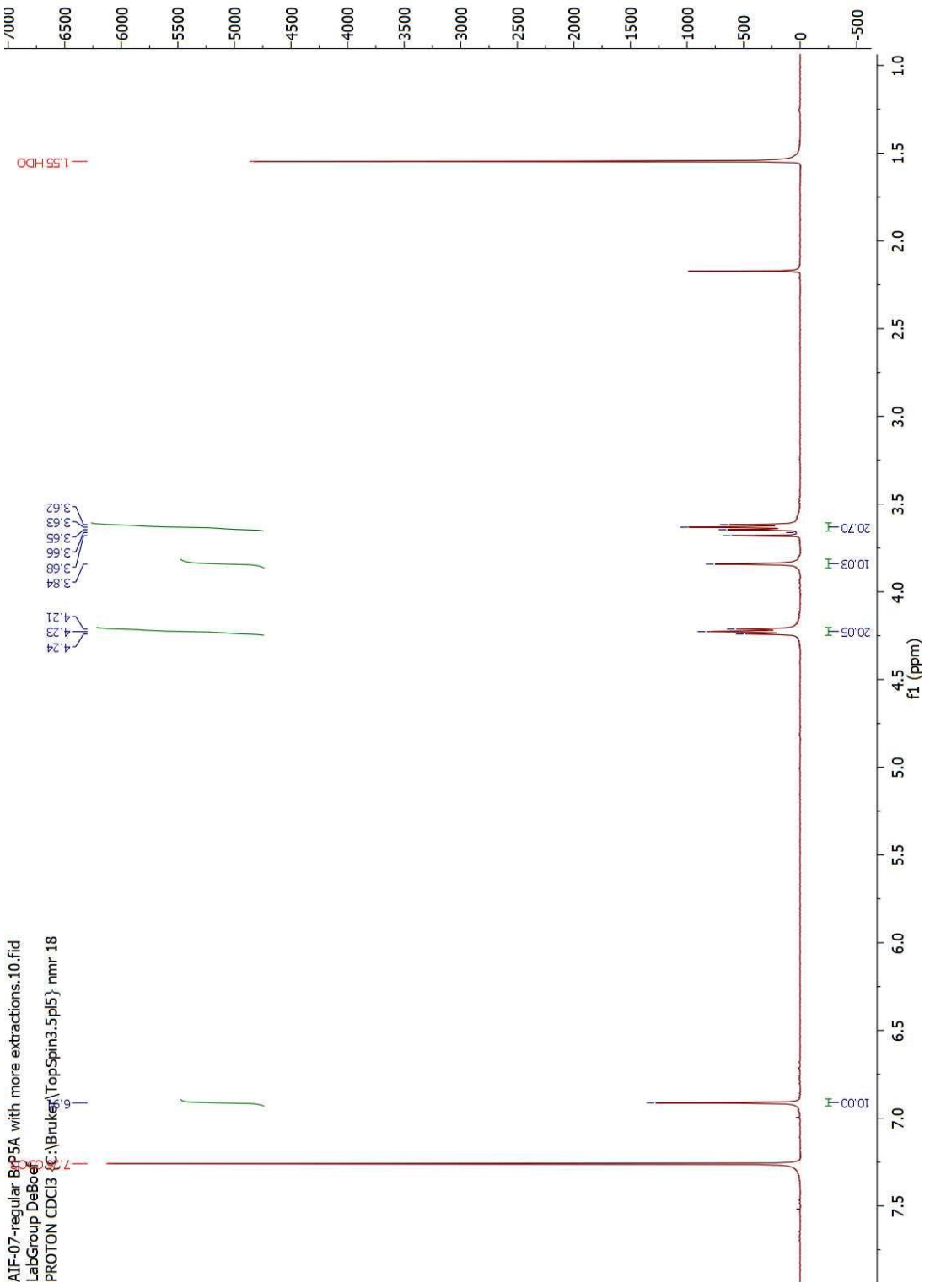

Figure 5.12: ^{1}H NMR of Brominated pillar[5]arene **2**

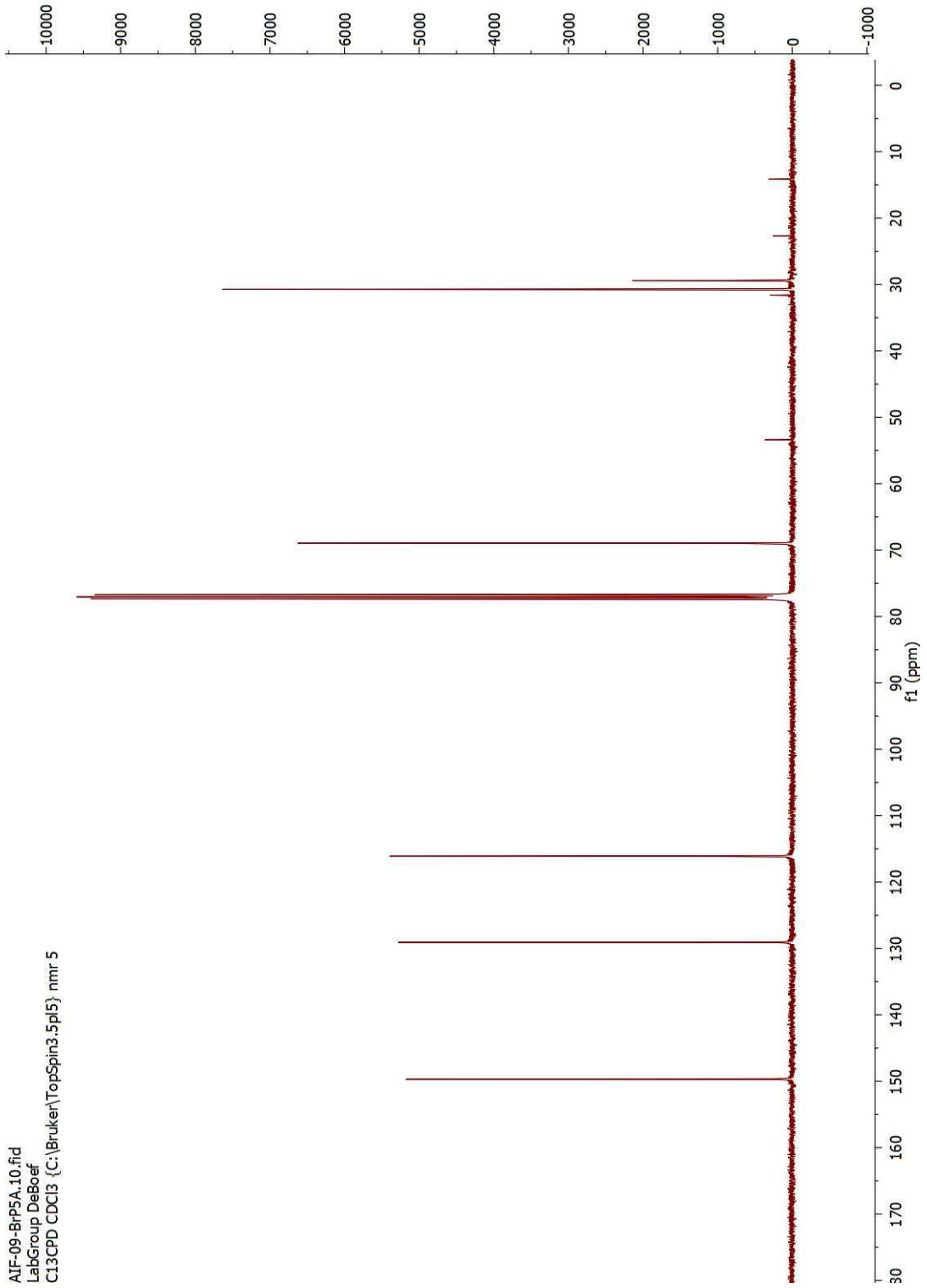

Figure 5.13: ^{13}C NMR of Brominated pillar[5]arene **2**

Synthesis of deca methyl imidazolium pillar[5]arene, 3

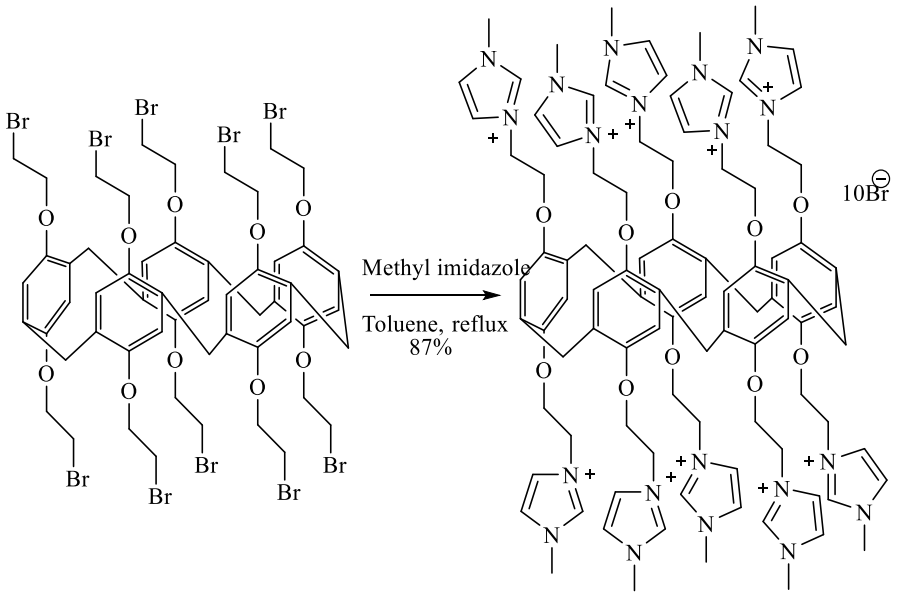

A mixture of brominated pillar[5]arene (1.68 g, 1.00 mmol) and N-methylimidazole (1.64 g, 20.0 mmol) in toluene (25 mL) was stirred in a 40 mL pressure tube at 120 ºC for 24 hours. The reaction was performed multiple times using a round bottom flask, but the reaction never worked. After cooling, the solvent was subjected to rotaroy evaporation of the solvent and the residue was then dissolved in ethanol and diethylether was added to crash the solid material out of the ethanol solution. This white precipitate consisting solution was further cooled for 24 hours and then filtered and collected as a off white product. (2.1 g, 87%). ^{1}H NMR and ^{13}C NMR were performed using DMSO-d_6. ^{1}H NMR (300 MHz, DMSO-d_6) δ 9.17 (br, 10H), 8.11 (s, 10H), 7.44 (br, 11H), 6.72 (br, 10H), 4.72 (br, 21H), 4.45 (br, 20H), 3.74 (br, 31H), 3.51 (br, 10H).

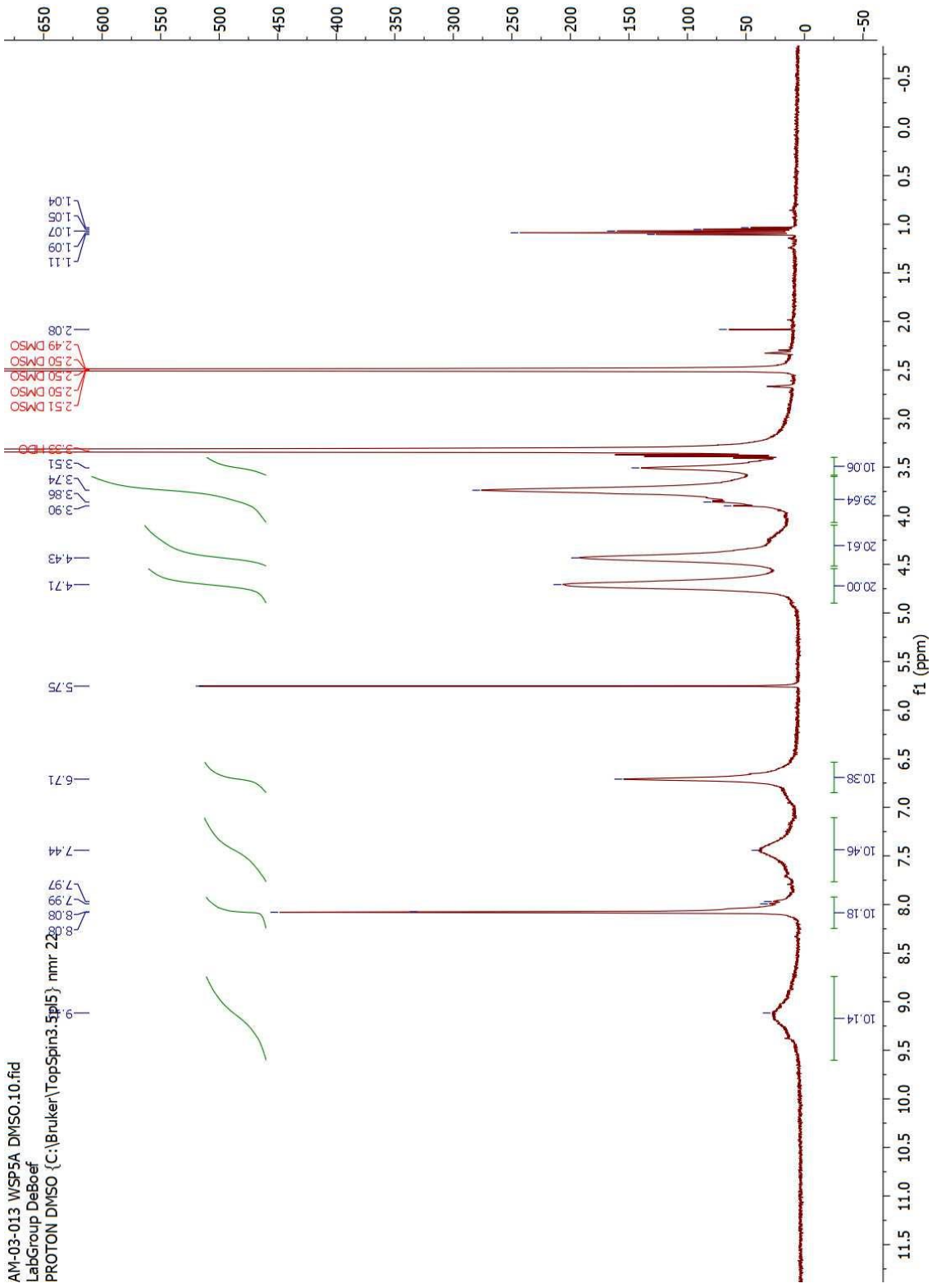

Figure 5.14: ^{1}H-NMR of **3**

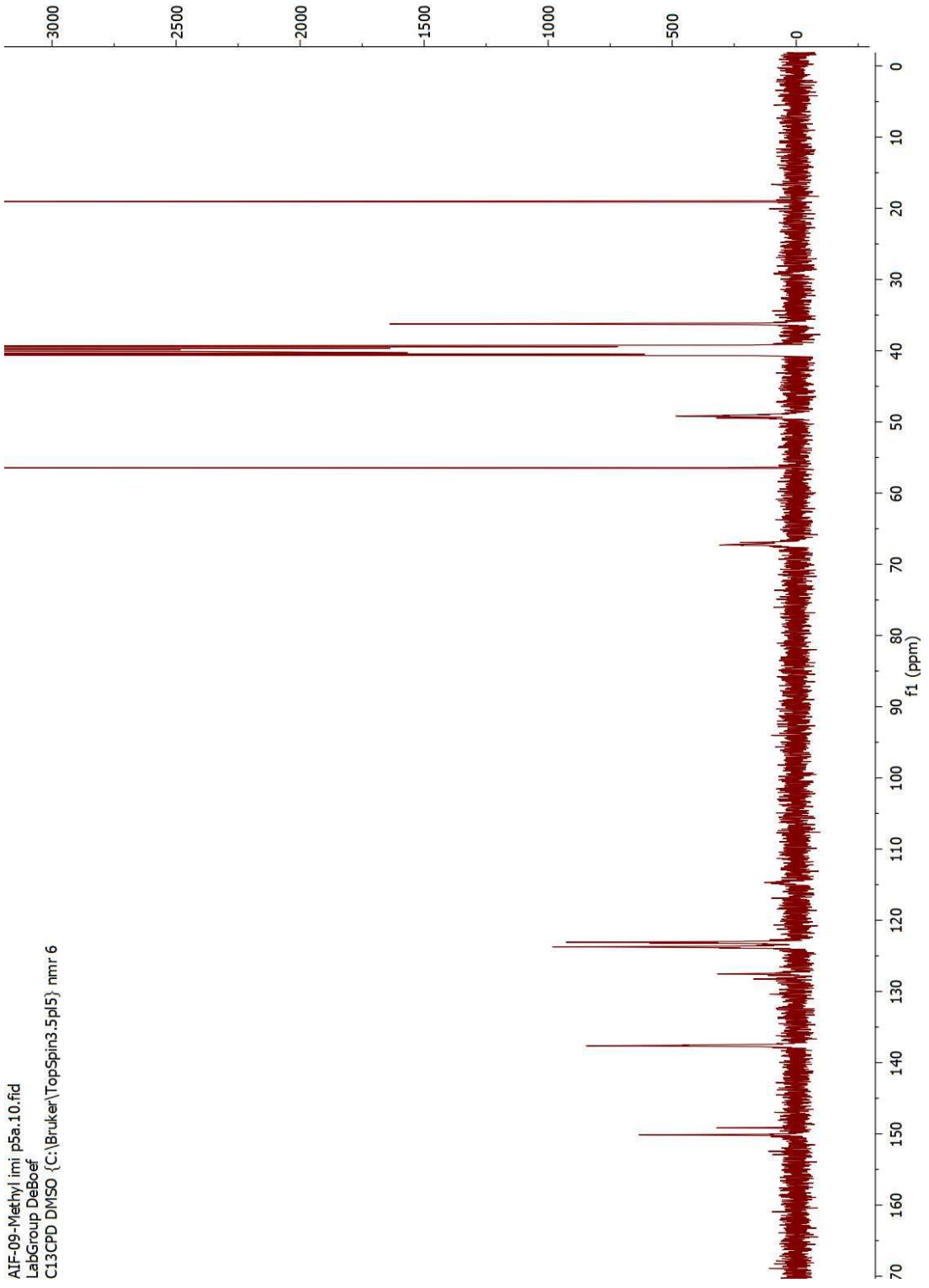

Figure 5.15: ^{13}C-NMR of **3**

Mass spectrometry of the water soluble P5A

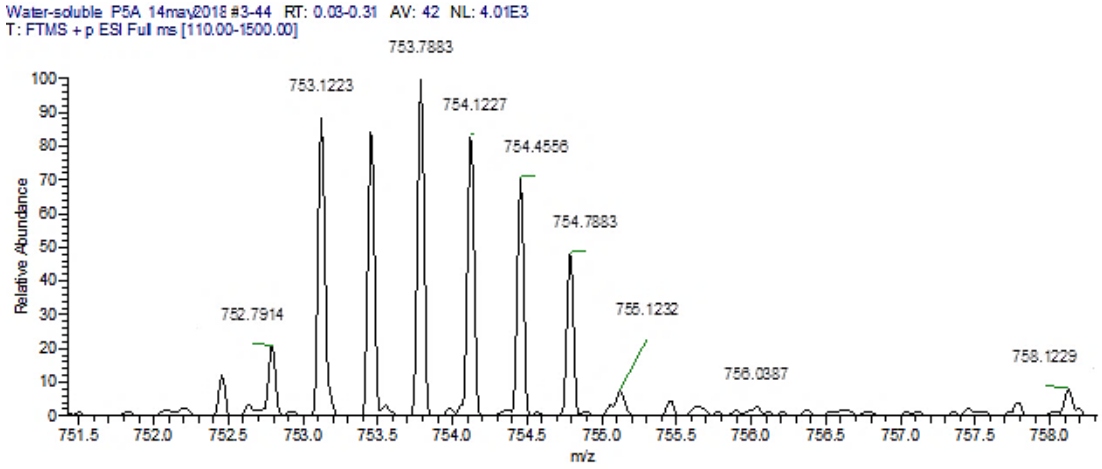

Figure 5.16: $[M - 3Br]^{3+}$ Calculated $C_{95}H_{121}O_{10}N_{20}Br_7$ 754.1270

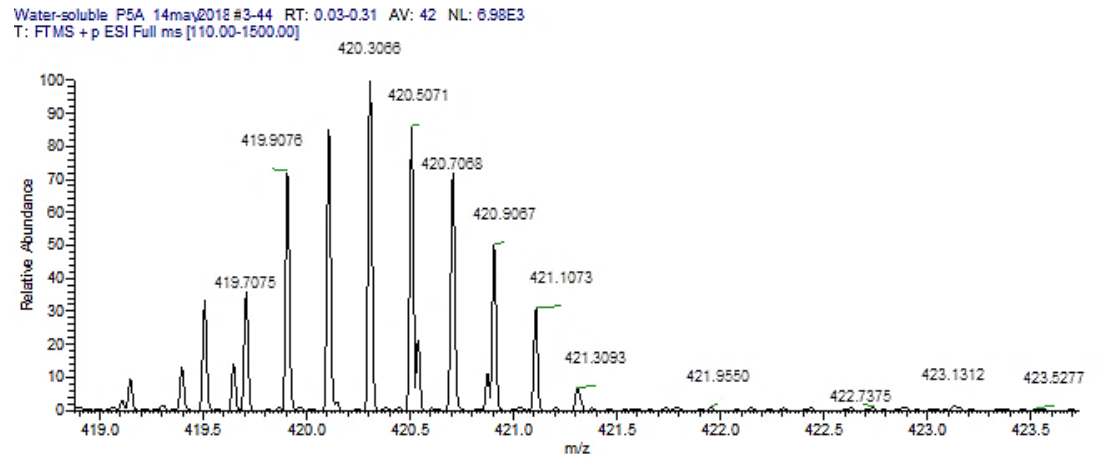

Figure 5.17: $[M - 5Br]^{5+}$ Calculated $C_{95}H_{121}O_{10}N_{20}Br_5$ 420.1090

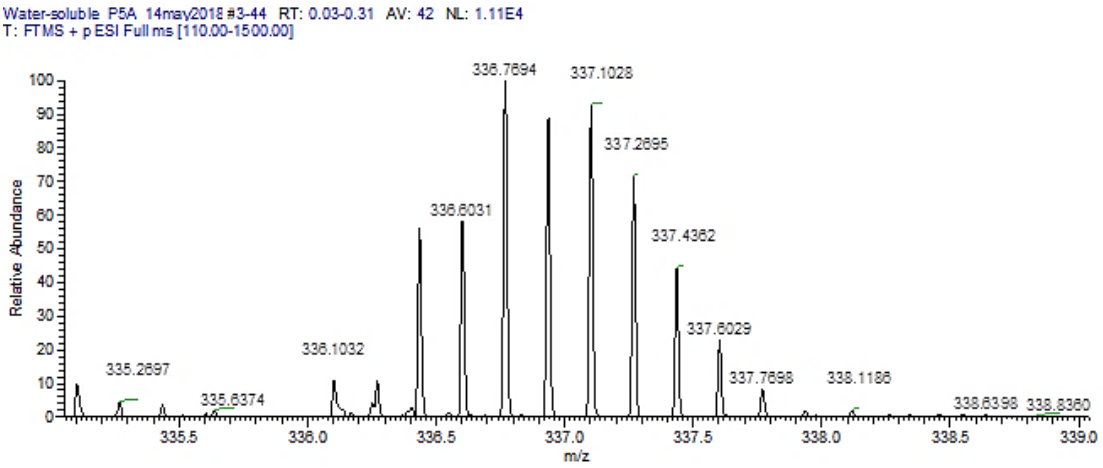

Figure 5.18: $[M - 6Br]^{6+}$ Calculated $C_{95}H_{121}O_{10}N_{20}Br_4$ 336.9378

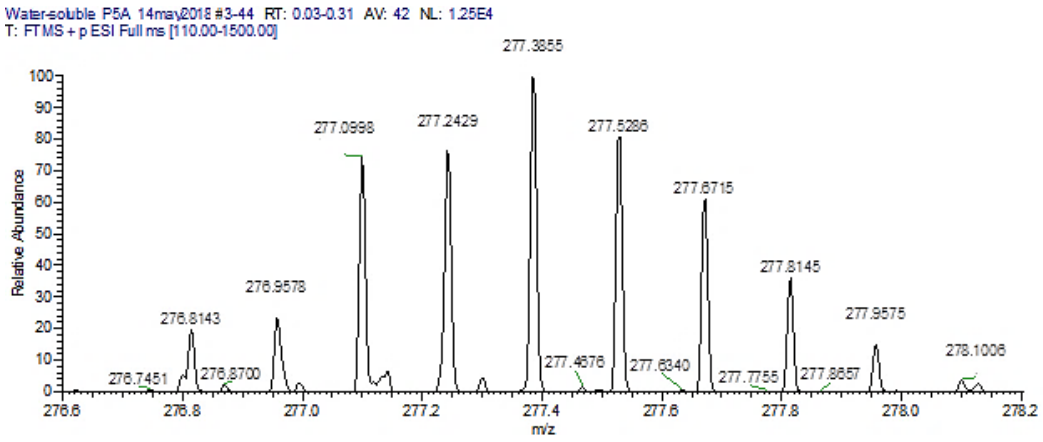

Figure 5.19: $[M - 7Br]^{7+}$ Calculated $C_{95}H_{121}O_{10}N_{20}Br_3$ 277.2442

Synthesis of proapargylated monomer

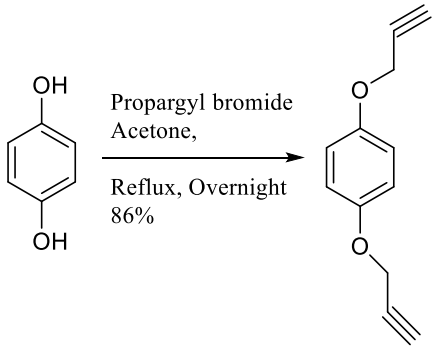

Hydroquinone and anhydrous potassium carbonate were added into a solution of acetonitrile in RBF. Then the reaction mixture was placed in an ice bath. Next, the propargyl bromide was added in dropwise. Then, the reaction solution was stirred 20 hours at 60 °C. Once the reaction was completed, the solvent was removed via rotary evaporation. Dichloromethane (100 ml) was added into the RBF, and this was transferred into a separatory funnel for further washes. Washing steps were conducted using 2.5 M NaOH (3 x 100 ml) followed with DI water (3 x 100 ml) and finally with brine (2 x 100 ml). Then the DCM layer was collected and dried over anhydrous sodium sulfate. The final mixture was subjected to dry loaded automated flash chromatography. ^{1}H NMR and ^{13}C NMR were performed using $CDCl_3$. ^{1}H NMR (400 MHz, DMSO-d6) δ 6.95 (s, 4H), 4.74 (d, J = 2.5 Hz, 4H), 3.53 (t, J = 2.4 Hz, 2H). ^{13}C NMR (101 MHz, DMSO-d6) δ 147.6, 111.3, 74.1, 70.6, 51.7.

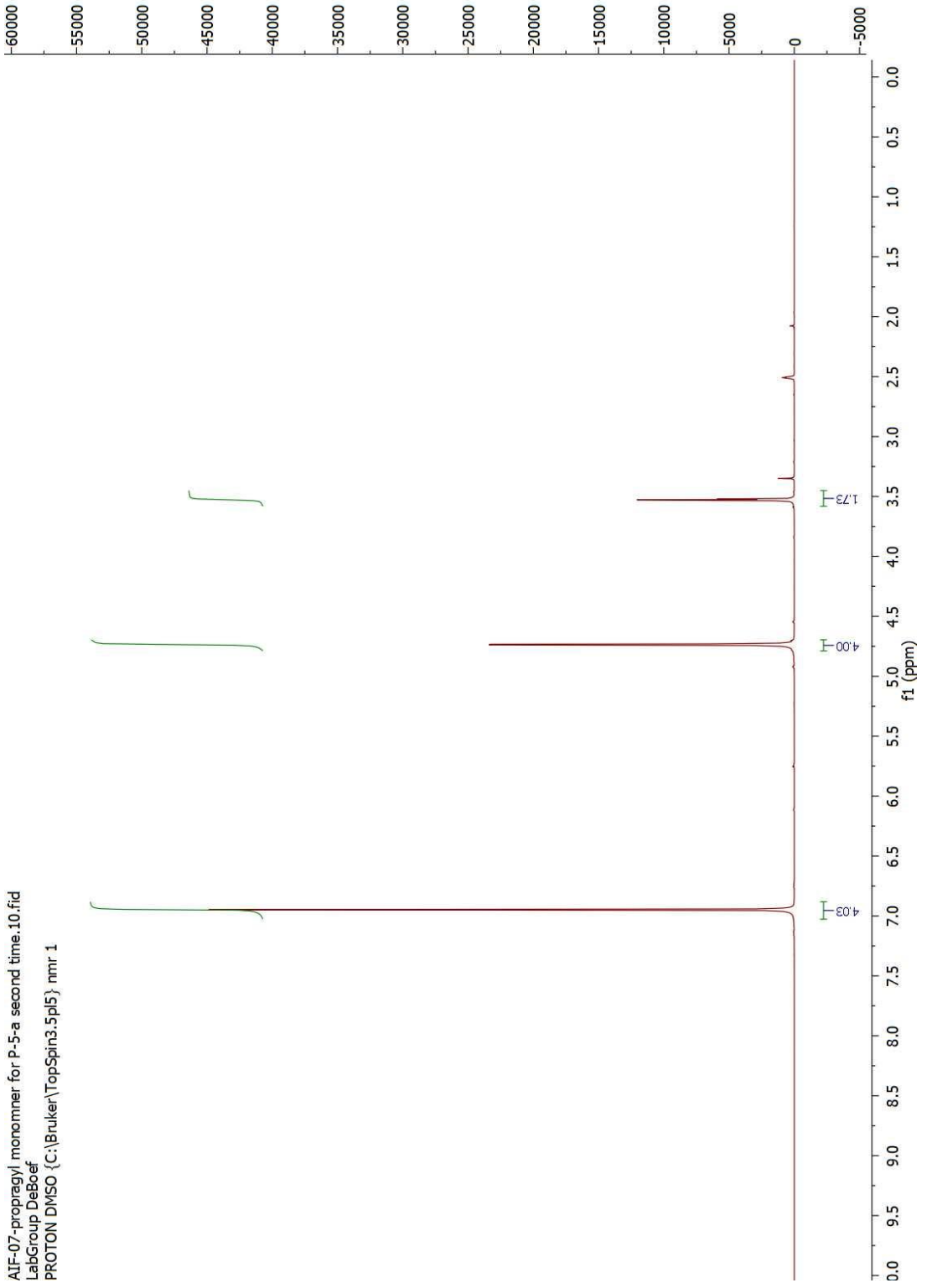

Figure 5.20: ^{1}H spectrum of proapargylated monomer

Synthesis of proapargylated P5A

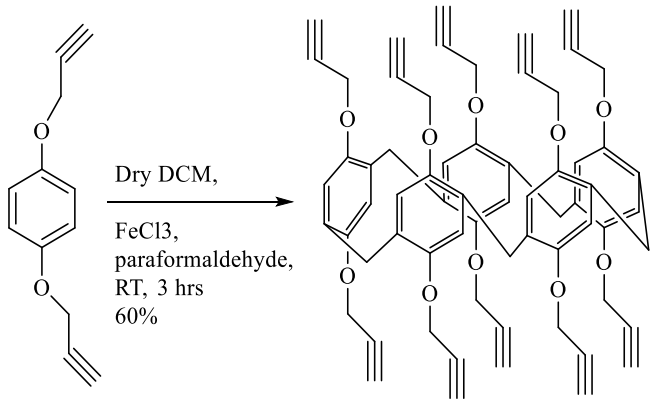

Proapargylated monomer (3.0 g) and paraformaldehyde (1.45 g) were added into an anhydrous solution of DCM. Then $FeCl_3$ was added. The complete reaction mixture was stirred for 3 hours at room temperature. Once the 3 hours was over, the reaction was quenched by adding in 200 ml of DI water. The organic layer was extracted and washed with 200 ml of brine solution. The collected organic layer was dried over anhydrous sodium sulfate and subjected to rotatory evaporation. Next, this was packed with silica and dry loaded into automated flash chromatography instrument. The final product was light brown.^{1}H NMR and ^{13}C NMR were performed using $CDCl_3$. ^{1}H NMR (400 MHz, Chloroform-d) δ 6.76 (s, 10H), 4.47 (d, J = 2.4 Hz, 21H), 3.74 (s, 10H), 2.21 (t, J = 2.4 Hz, 10H).

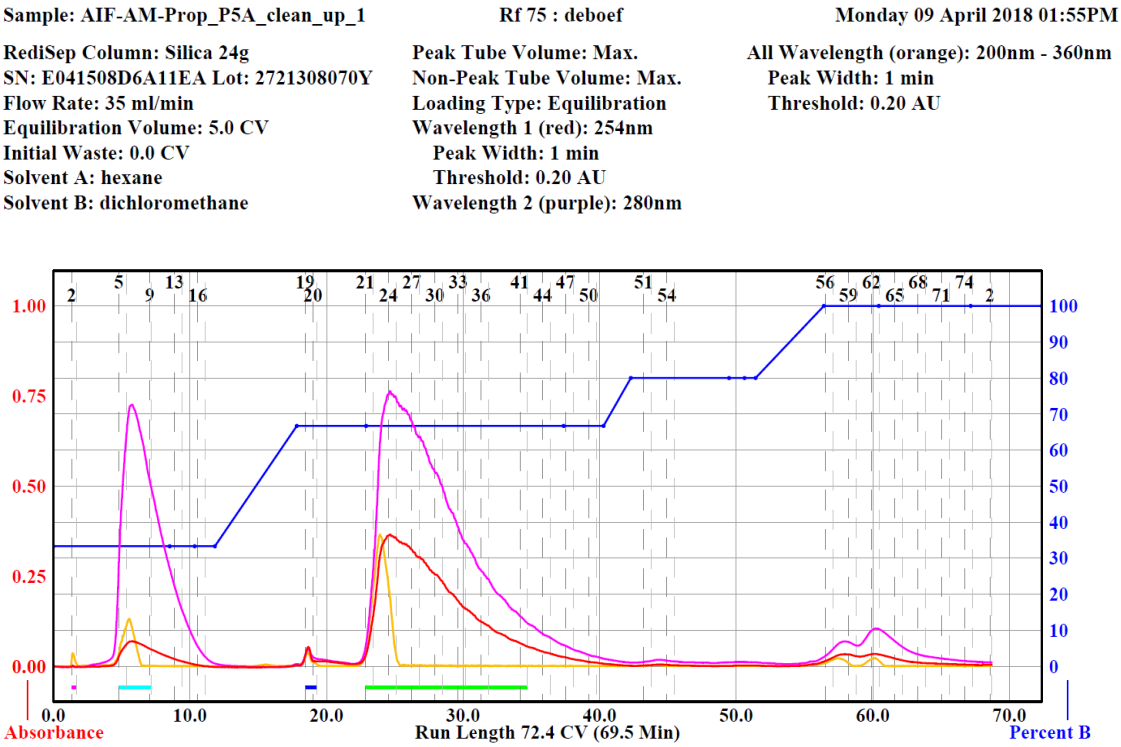

Figure 5.21: Flash chromatogram for the purification of Proapargylated P5A, Product was separated at 23 – 35 CV. First peak corresponds to the unreacted proapargylated monomer

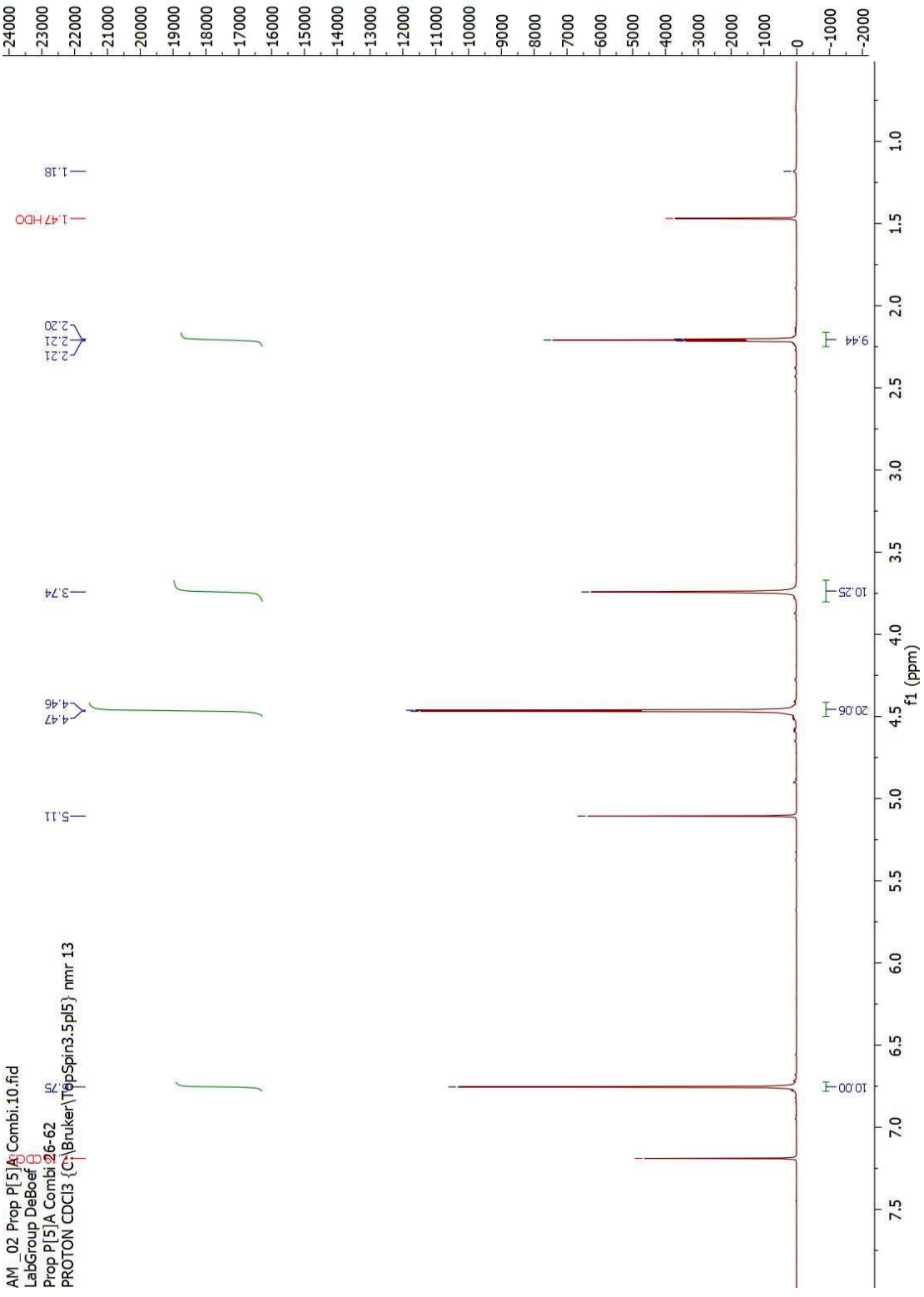

Figure 5.22: ^{1}H NMR of proapargylated P5A

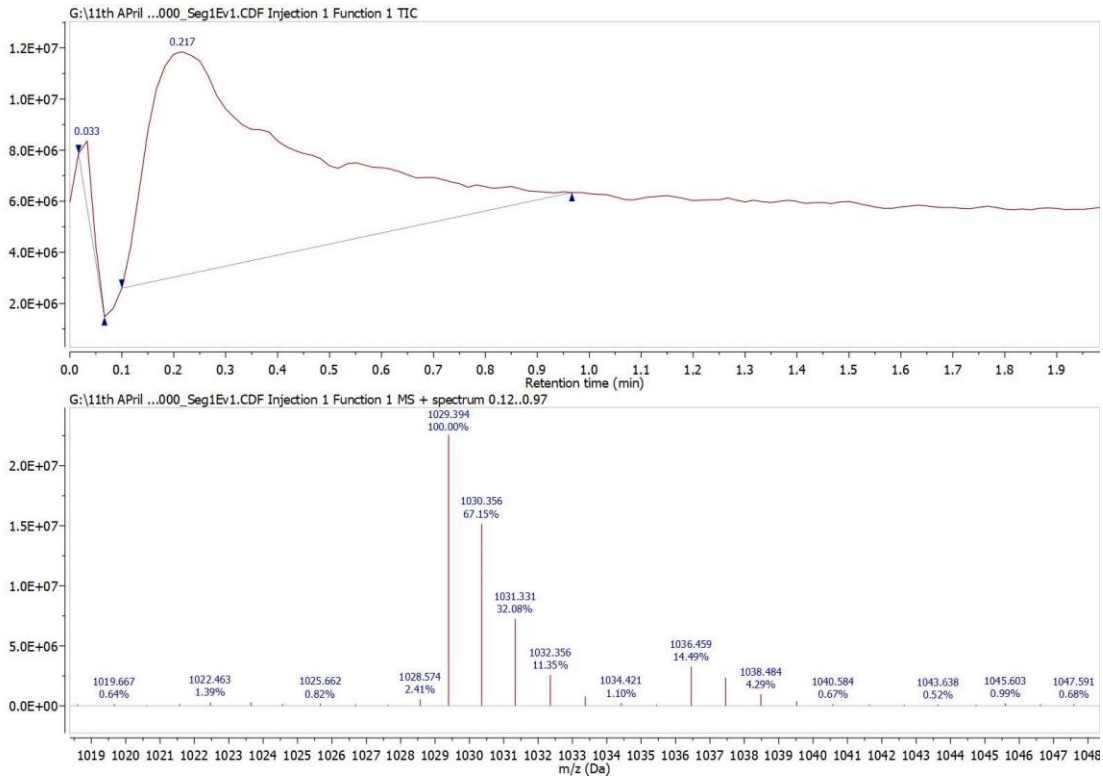

Figure 5.23: Mass spectrum of proapargylated P5A

Methods for Job's Plot Experiments

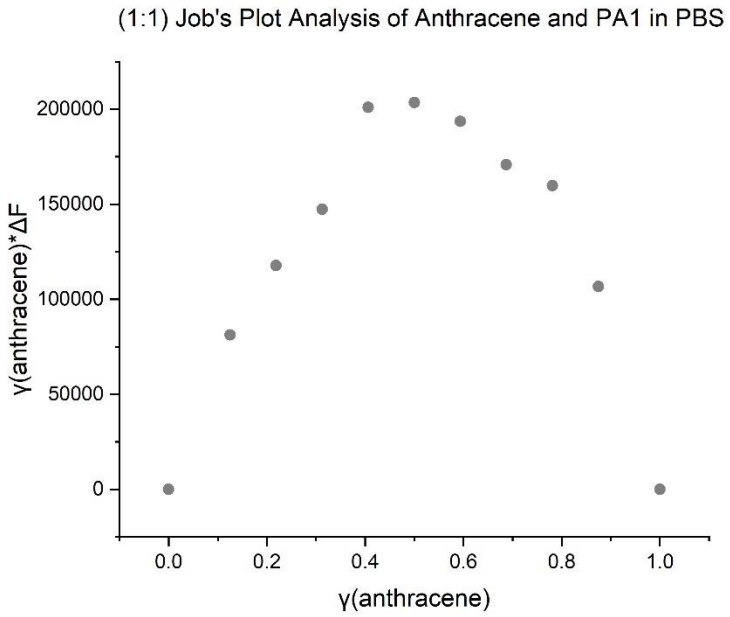

Figure S15 - Job's plot of anthracene and PA1 in PBS obtained by fluorescence spectroscopy indicating a 1:1 anthracene – PA2 binding mode (γ_{max} = 0.5). γ is mole fraction of guest and ΔF is the change in fluorescence integration.

γ(PA1)	γ(PA1)*ΔF
1	0
0.875	106699
0.78	159832
0.68	170877
0.59	193647
0.50	203499
0.41	200956
0.31	147395
0.22	117708
0.125	81313
0	0

Table 1 – Tabulated data of the Job's plot analysis of the host-guest binding of PA1 with anthracene in PBS. γ is mole fraction of guest and ΔF is the change in fluorescence integration.

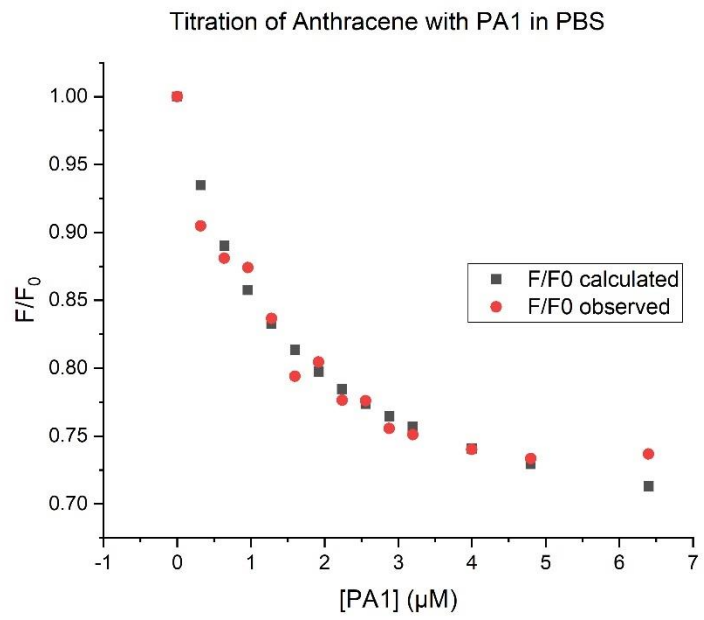

Figure S16 - Fluorescence titration of anthracene with PA1 in PBS fit to a 1:1 anthracene - PA2 stoichiometry. K_a = 7.18 (0.000076) x 10^5 M^{-1}; Sum(χ2) = 0.0014.

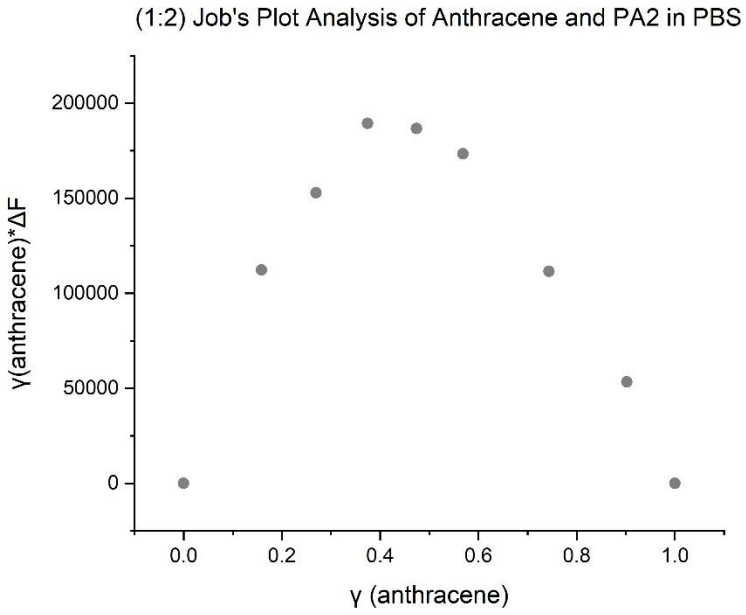

Figure S17 – Job's plot of anthracene and PA2 in PBS obtained by fluorescence spectroscopy indicating a 1:2 anthracene – PA2 binding mode (γ_{max} = 0.37). γ is mole fraction of guest and ΔF is the change in fluorescence integration. Moderately sharp peak indicates a relatively high association constant.

γ(PA2)	γ(PA2)*ΔF
1	0
0.90	53301
0.74	111496
0.57	173350
0.47	186621
0.37	189407
0.27	152836
0.16	112304
0	0

Table 2 – Tabulated data of the Job's plot analysis of the host-guest binding of PA2 with anthracene in PBS. γ is mole fraction of guest and ΔF is the change in fluorescence integration.

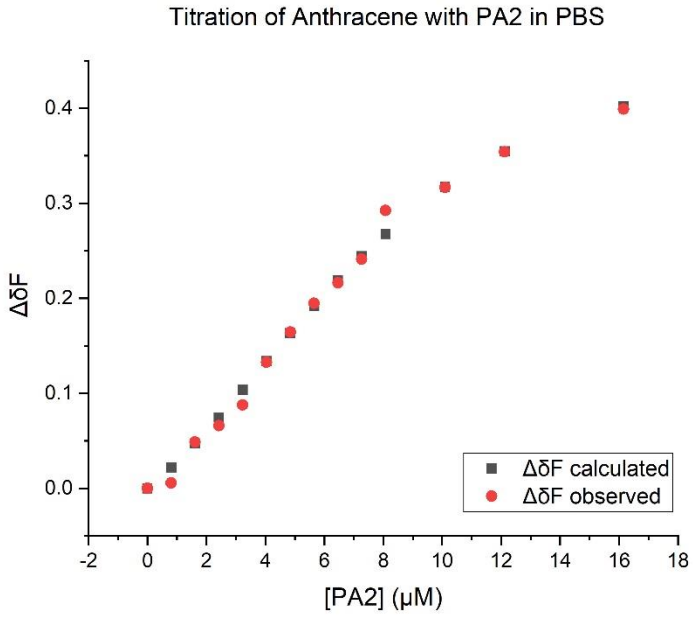

Figure S18– Fluorescence titration of anthracene with PA2 in PBS fit to a 1:2 anthracene - PA2 stoichiometry. K_{a1} = 7.34 (0.39) M^{-1}; K_{a2} = 1.13 (0.0097) x 10^9 M^{-1}; Sum(χ2) = 0.0012.

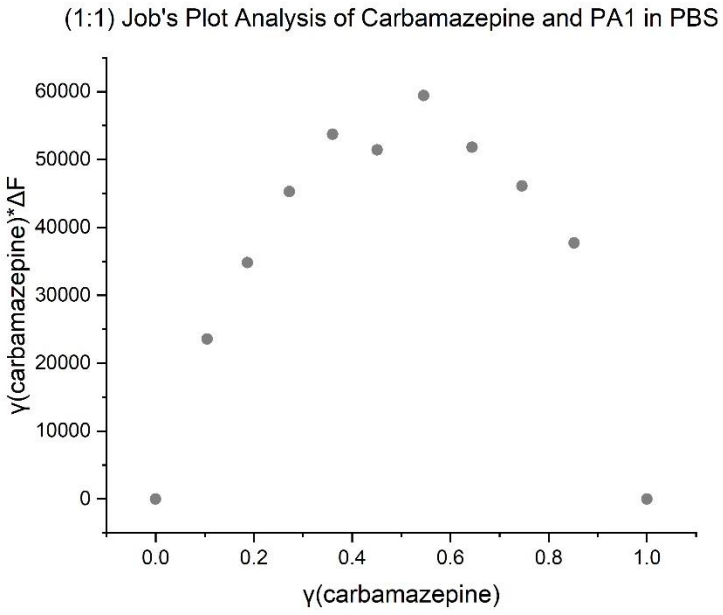

Figure S19 - Job's plot analysis of carbamazepine and PA1 in PBS obtained by fluorescence spectroscopy. Indicates a likely 1:1 PA1 – carbamazepine binding mode ($\gamma_{max} = 0.55$). γ is mole fraction of guest and ΔF is the change in fluorescence integration. Sharp profile indicated high association constant.

γ(carbamazepine)	**γ(carbamazepine)*ΔF**
1	0
0.85	37710
0.75	46092
0.64	51796
0.55	59415
0.45	51421
0.36	53709
0.27	45267
0.19	34796
0.11	23555
0	0

Table 3 – Tabulated data of the Job's plot analysis of the host-guest binding of PA1 with carbamazepine in PBS. γ is mole fraction of guest and ΔF is the change in fluorescence integration.

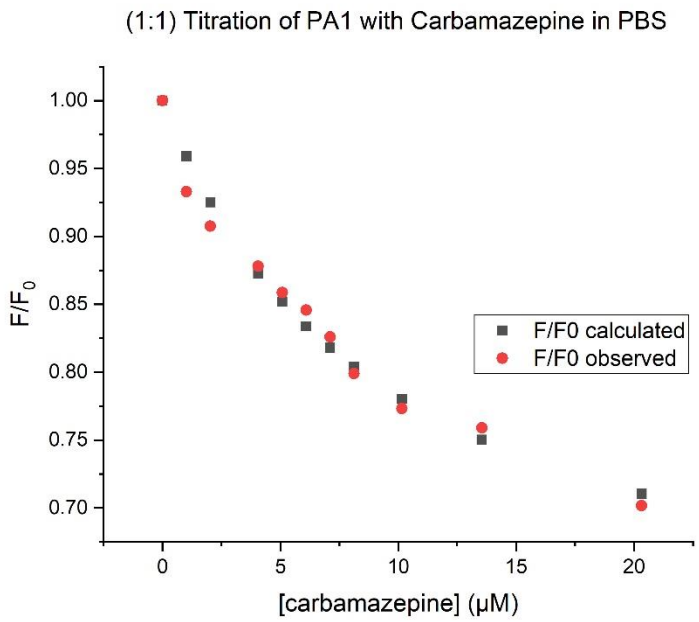

Figure S20 - Fluorescence titration of PA1 with carbamazepine in PBS fit to a 1:1 stoichiometry. K_a = 1.06(0.12) x 10^5 M^{-1}; Sum(χ2) = 0.0017.

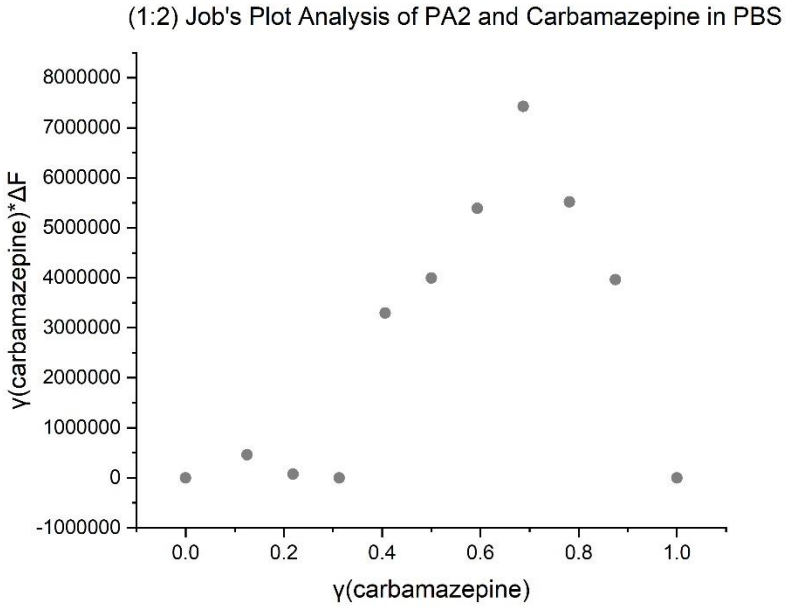

Figure S21 – Job's plot analysis of carbamazepine and PA2 in PBS obtained by fluorescence spectroscopy. Indicates a likely 1:2 PA2 – carbamazepine binding mode (γ_{max} = 0.68). γ is mole fraction of guest and ΔF is the change in fluorescence integration. Sharp profile indicated high association constant.

γ(carbamazepine)	γ(carbamazepine)*ΔF
1	0
0.875	3961737
0.78	5517031
0.68	7427062
0.59	5385965
0.5	3994950
0.41	3293915
0.31	726593
0.22	75621
0.125	461212
0	0

Table 4 – Tabulated data of the Job's plot analysis of the host-guest binding of PA2 with carbamazepine in PBS. γ is mole fraction of guest and ΔF is the change in fluorescence integration.

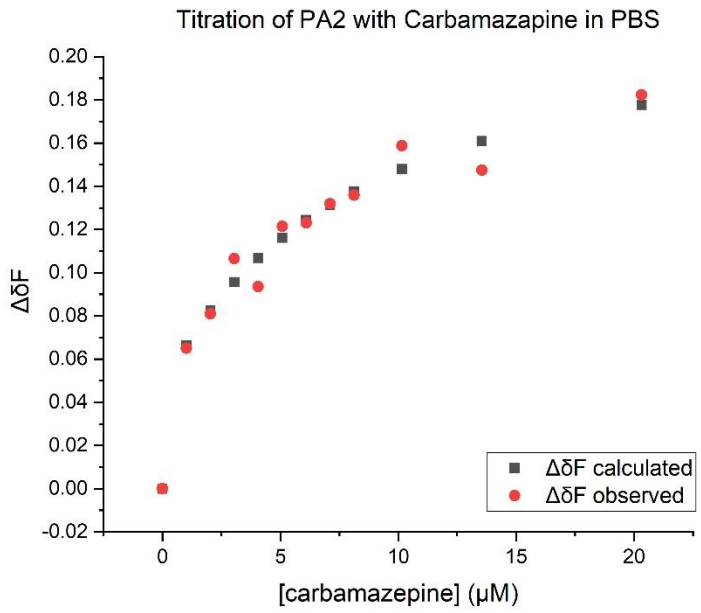

Figure S22 – Fluorescence titration of PA2 with carbamazepine in PBS fit to a 1:2 stoichiometry. K_{a1} = 2.43 (0.000000036) x 10^{12} M^{-1}; K_{a2} = 1.06 (0.12) x 10^{5} M^{-1}; Sum(χ2) = 0.00066.

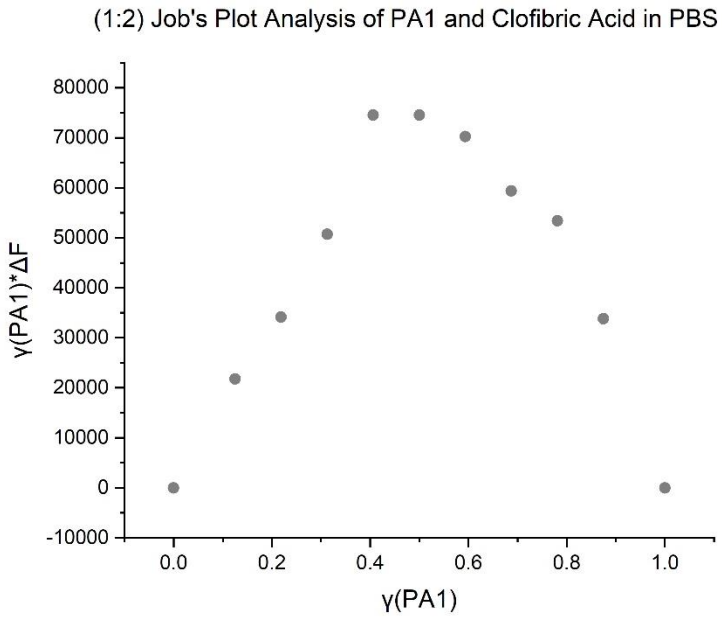

Figure S23 - Job's plot analysis of clofibric acid and PA1 in PBS obtained by fluorescence spectroscopy. Indicates a likely 1:2 PA1 – clofibric acid binding mode (γ_{max} = 0.41). γ is mole fraction of guest and ΔF is the change in fluorescence integration. Sharp profile indicated high association constant.

γ(PA1)	**γ(PA1)*ΔF**
1	0
0.875	33832
0.78	53374
0.68	59387
0.59	70250
0.5	74500
0.41	74550
0.31	50702
0.22	34148
0.125	21776
0	0

Table 5 – Tabulated data of the Job's plot analysis of the host-guest binding of PA1 with clofibric acid in PBS. γ is mole fraction of guest and ΔF is the change in fluorescence integration.

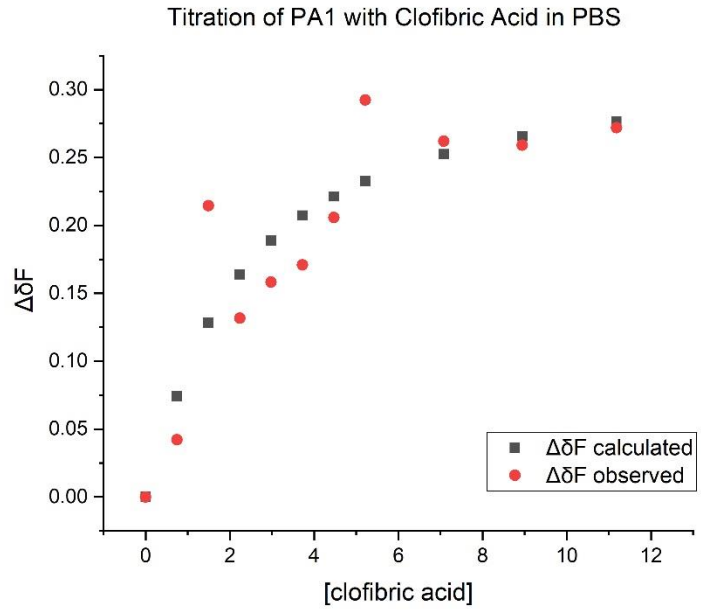

Figure S24 - Fluorescence titration of PA1 with clofibric acid in PBS fit to a 1:2 stoichiometry. K_{a1} = 6.34 (1.27) x 10^6 M^{-1}; K_{a2} = 4.77 (0.32) x 10^5 M^{-1}; Sum(χ2) = 0.016.

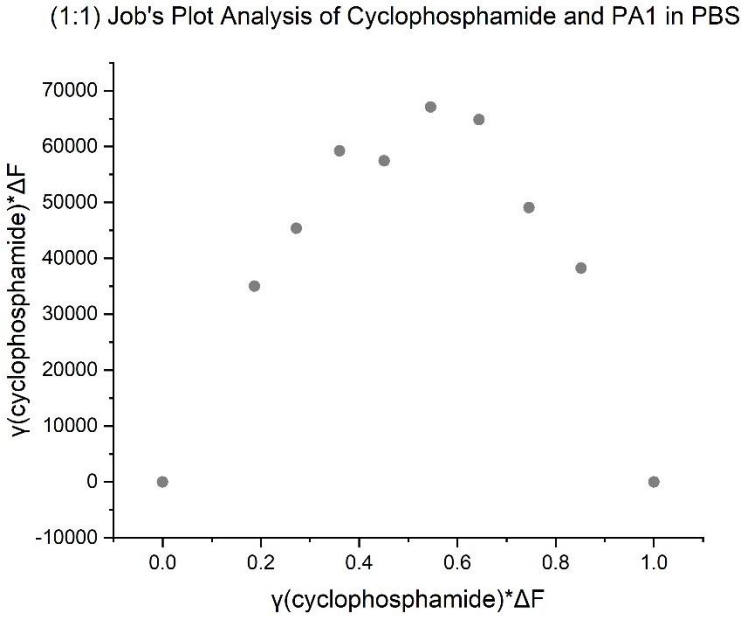

Figure S25 - Job's plot analysis of cyclophosphamide and PA1 in PBS obtained by fluorescence spectroscopy. Indicates a likely 1:1 stoichiometry (γ_{max} = 0.55). γ is mole fraction of guest and ΔF is the change in fluorescence integration.

γ(cyclophosphamide)	γ(cyclophosphamide)*ΔF
1	0
0.85	38243
0.75	49068
0.64	64809
0.55	67065
0.45	57459
0.36	59221
0.27	45382
0.19	35006
0	0

Table 6 – Tabulated data of the Job's plot analysis of the host-guest binding of PA1 with cyclophosphamide PBS. γ is mole fraction of guest and ΔF is the change in fluorescence integration.

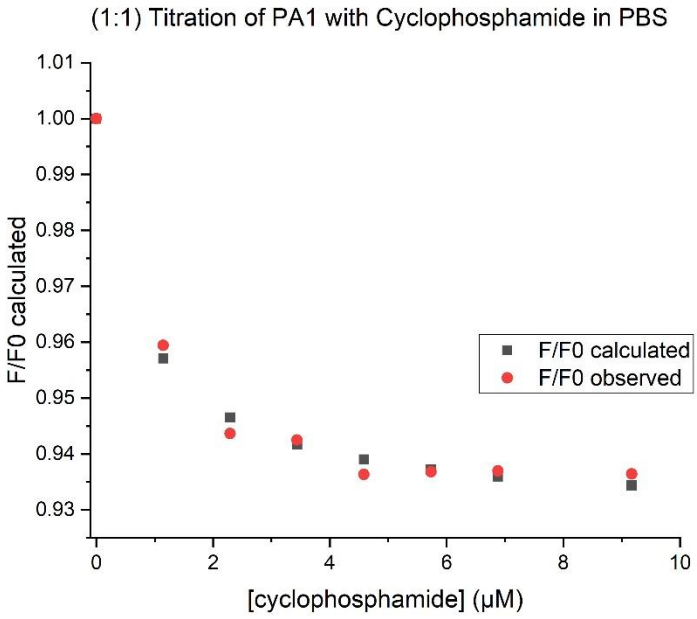

Figure S26 – Fluorescence titration of PA1 with cyclophosphamide in PBS fit to a 1:1 host-guest stoichiometry. K_a = 1.33 (0.19) x 10^6 M^{-1}; Sum(χ2) = 0.000040.

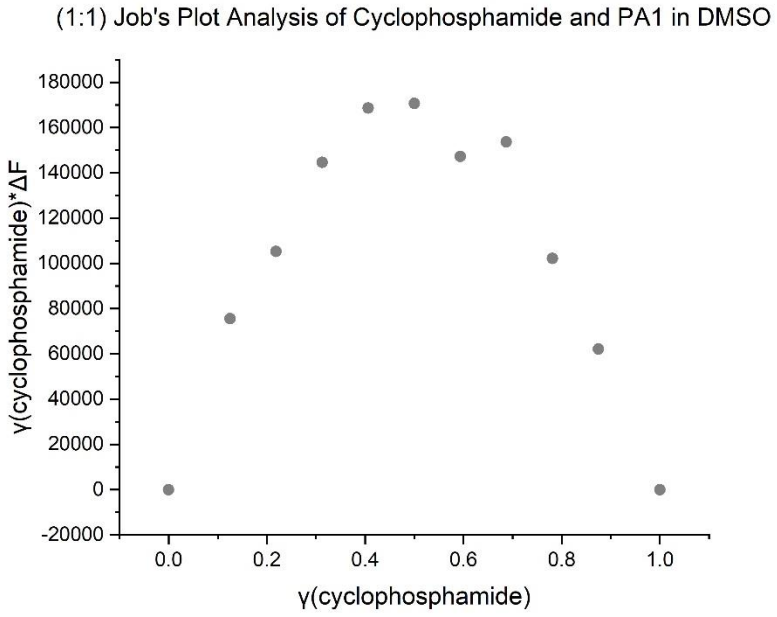

Figure S27 - Job's plot analysis of cyclophosphamide and PA1 in DMSO obtained by fluorescence spectroscopy. Indicates a likely 1:1 stoichiometry ($\gamma_{max} = 0.5$). γ is mole fraction of guest and ΔF is the change in fluorescence integration.

γ(cyclophosphamide)	γ(cyclophosphamide)*ΔF
1	0
0.875	62124
0.78	102147
0.68	153694
0.59	147182
0.5	170639
0.41	168673
0.31	144670
0.22	105210
0.125	75556
0	0

Table 7 – Tabulated data of the Job's plot analysis of the host-guest binding of PA1 with cyclophosphamide PBS. γ is mole fraction of guest and ΔF is the change in fluorescence integration.

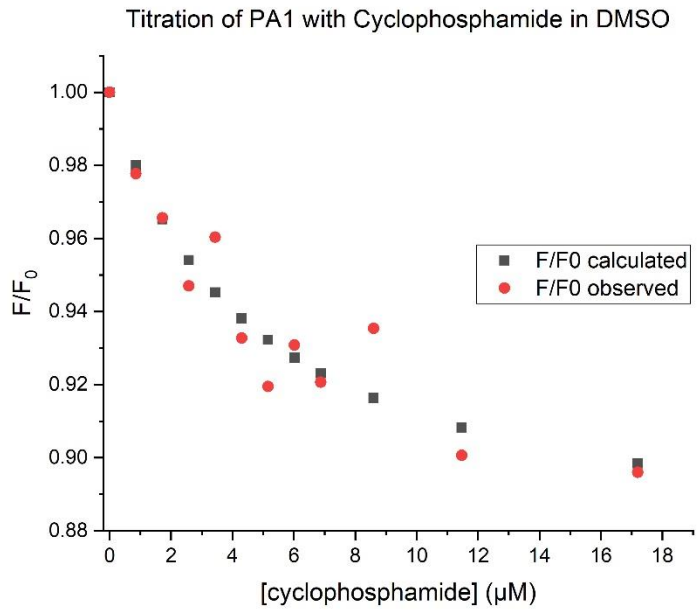

Figure S28 – Fluorescence titration of PA1 with cyclophosphamide monohydrate in DMSO fit to a 1:1 host-guest stoichiometry. K_a = 2.17 (0.35) x 10^5 M^{-1}; Sum(χ2) = 0.00113.

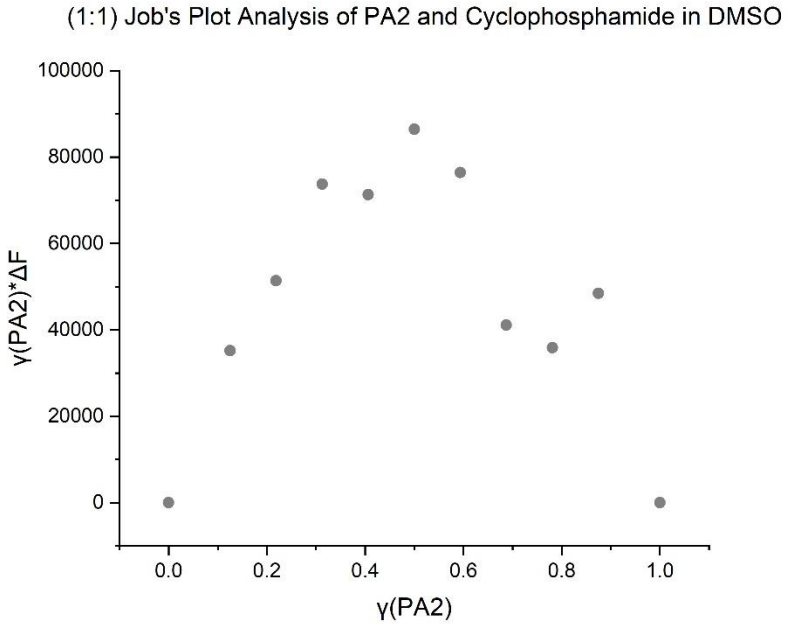

Figure S29 - Job's plot analysis of cyclophosphamide and PA2 in DMSO obtained by fluorescence spectroscopy. Indicates 1:1 host – guest stoichiometry (γ_{max} = 0.50). γ is mole fraction of guest and ΔF is the change in fluorescence integration.

γ(cyclophosphamide)	γ(cyclophosphamide)*ΔF
1	0
0.875	48486
0.78	35875
0.69	41085
0.59	76436
0.5	86439
0.41	71293
0.31	73743
0.22	51353
0.125	35179
0	0

Table 8 – Tabulated data of the Job's plot analysis of the host-guest binding of PA2 with cyclophosphamide in DMSO. γ is mole fraction of guest and ΔF is the change in fluorescence integration.

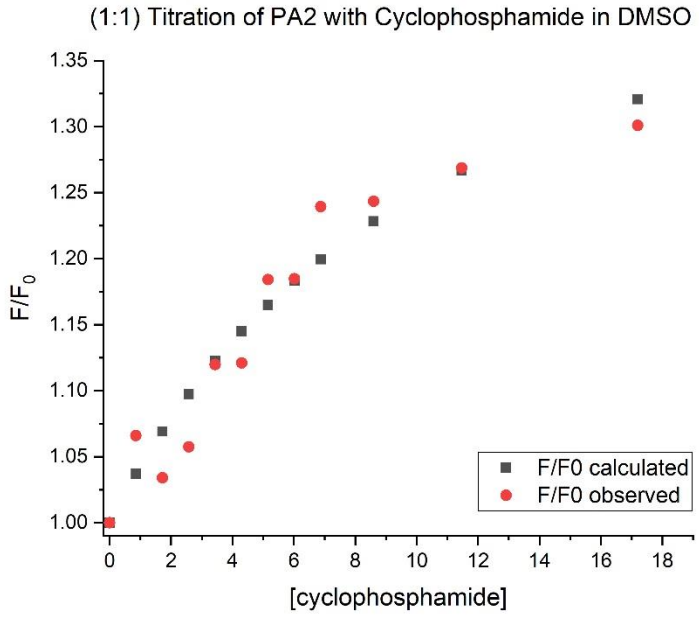

Figure S30 – Fluorescence titration of PA2 with cyclophosphamide in DMSO fit to a 1:1 host-guest stoichiometry. K_a = 9.44 (0.59) x 10^4 M^{-1}; Sum(χ2) = 0.0080.

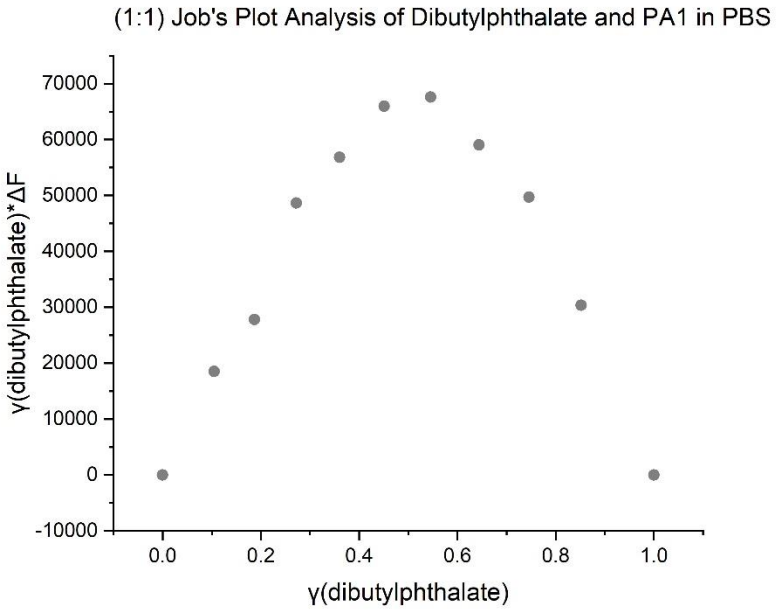

Figure S31 – Job's plot analysis of dibutylphthalate and PA1 in PBS obtained by fluorescence spectroscopy. Indicates a 1:1 host-guest stoichiometry (γ_{max} = 0.55). γ is mole fraction of guest and ΔF is the change in fluorescence integration.

γ(dibutylphthalate)	**γ(dibutylphthalate)*ΔF**
1	0
0.85	30345
0.745	49700
0.64	59034
0.545	67596
0.45	65952
0.36	56825
0.27	48619
0.19	27800
0.105	18541
0	0

Table 9 – Tabulated data of the Job's plot analysis of the host-guest binding of PA1 with dibutylphthalate in PBS. γ is mole fraction of guest and ΔF is the change in fluorescence integration.

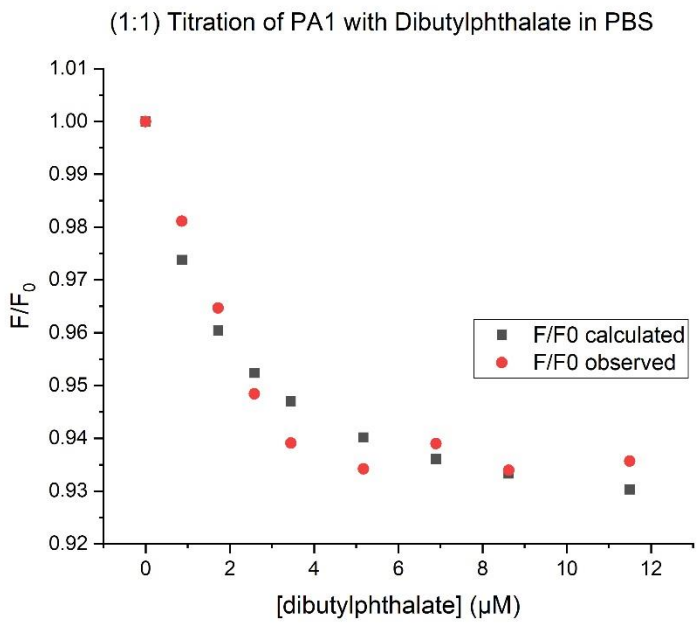

Figure S32 - Fluorescence titration of PA1 with dibutylphthalate in PBS fit to a 1:1 host-guest stoichiometry. K_a = 5.67 (0.95) x 10^5 M^{-1}; Sum(χ2) = 0.00028.

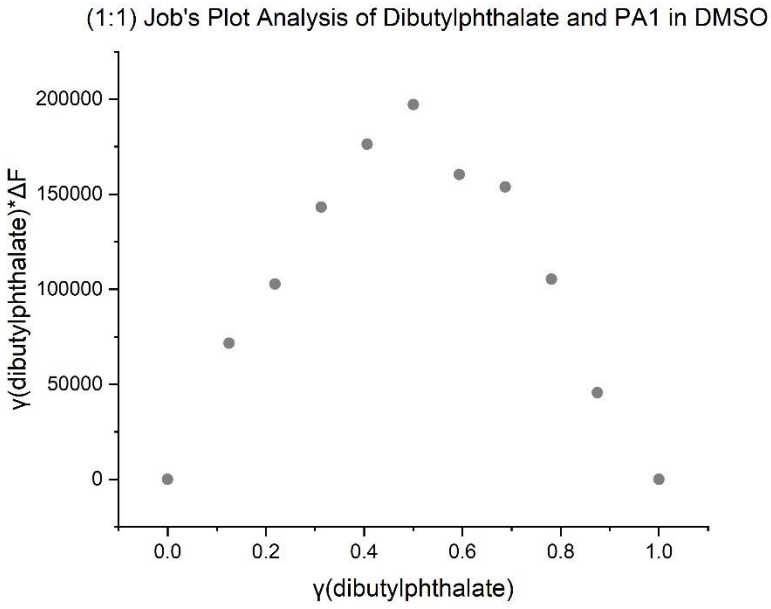

Figure S33 – Job's plot analysis of dibutylphthalate and PA1 in DMSO obtained by fluorescence spectroscopy. Indicates 1:1 host – guest stoichiometry (γ_{max} = 0.50). γ is mole fraction of guest and ΔF is the change in fluorescence integration. Sharp peak indicates a high association constant.

γ(dibutylphthalate)	γ(dibutylphthalate)*ΔF
1	0
0.875	45565
0.78	105280
0.69	153838
0.59	160319
0.5	197152
0.41	176401
0.31	143167
0.22	102695
0.125	71629
0	0

Table 10 – Tabulated data of the Job's plot analysis of the host-guest binding of PA1 with dibutylphthalate in DMSO. γ is mole fraction of guest and ΔF is the change in fluorescence integration.

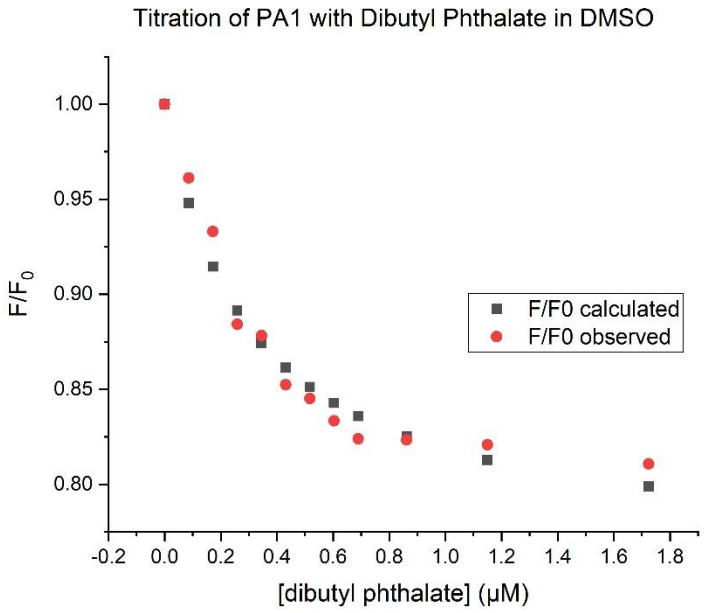

Figure S34 – Fluorescence titration of PA1 with dibutylphthalate in DMSO fit to a 1:1 host-guest stoichiometry. K_a = 3.32 (0.45) x 10^5 M^{-1}; Sum(χ2) = 0.00144..

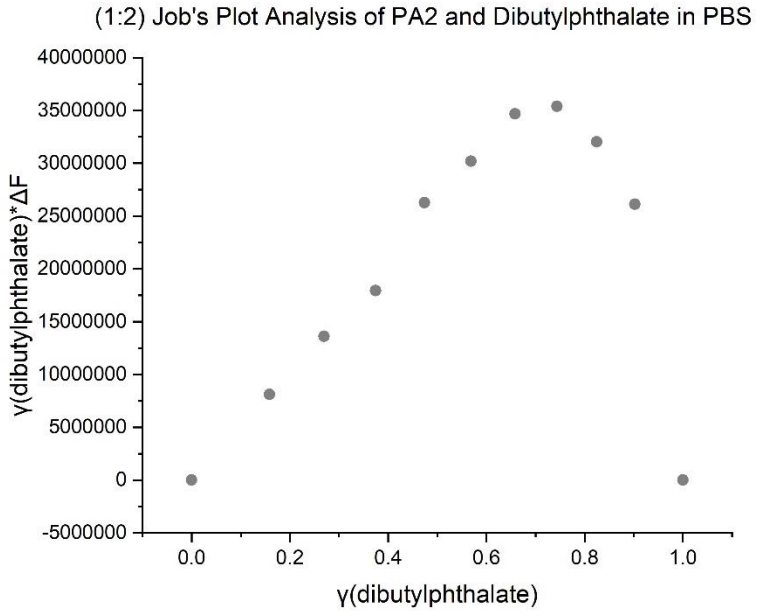

Figure S35 - Job's plot analysis of dibutylphalate and PA2 in PBS obtained by fluorescence spectroscopy. Indicates a likely 1:2 PA2 - dibutylphthalate binding (γ_{max} = 0.74). γ is mole fraction of guest and ΔF is the change in fluorescence integration.

γ(dibutylpthalate)	**γ(dibutylphthalate)*ΔF**
1	0
0.90	26135622
0.82	32020706
0.74	35383754
0.66	34671733
0.57	30192845
0.47	26285783
0.37	17952058
0.27	13621627
0.16	8121965
0	0

Table 11 – Tabulated data of the Job's plot analysis of the host-guest binding of PA2 with dibutylphthalate in PBS. γ is mole fraction of guest and ΔF is the change in fluorescence integration.

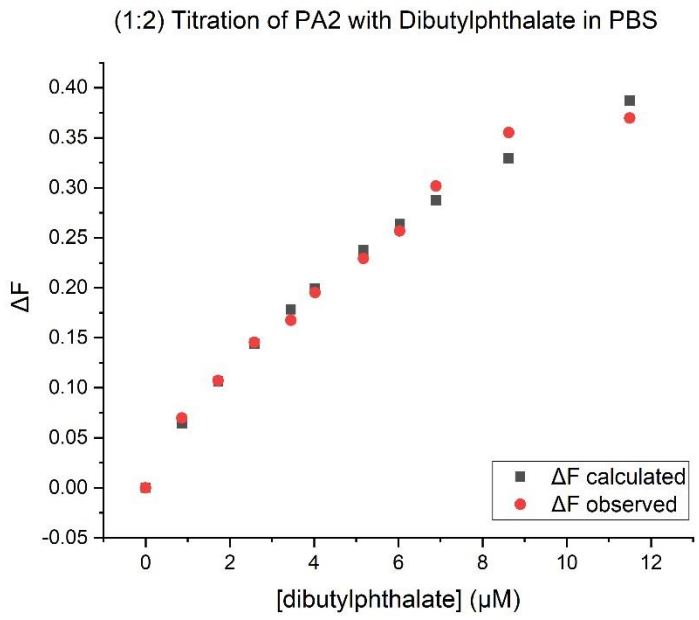

Figure S36 – Fluorescence titration of PA2 with dibutylphthalate in PBS fit to a 1:2 host-guest stoichiometry. K_{a1} = 6.05 (0.0011) x 10^{10} M^{-1}; K_{a2} = 7.14 (2.52) x 10^{4} M^{-1}; Sum(χ2) = 0.0016.

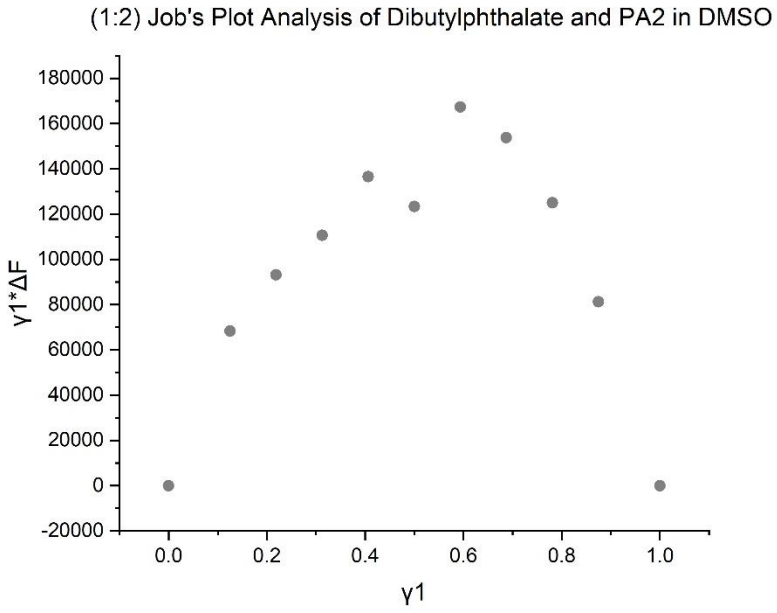

Figure S37 – Job's plot analysis of dibutylphalate and PA2 in DMSO obtained by fluorescence spectroscopy. Indicates a likely 1:2 PA2 - dibutylphthalate binding (γ_{max} = 0.59). γ is mole fraction of guest and ΔF is the change in fluorescence integration.

γ(dibutylpthalate)	γ(dibutylphthalate)*ΔF
1	0
0.875	81301
0.78	124959
0.69	153719
0.59	167295
0.5	123351
0.41	136497
0.31	110655
0.22	93099
0.125	68344
0	0

Table 12 – Tabulated data of the Job's plot analysis of the host-guest binding of PA2 with dibutylphthalate in DMSO. γ is mole fraction of guest and ΔF is the change in fluorescence integration.

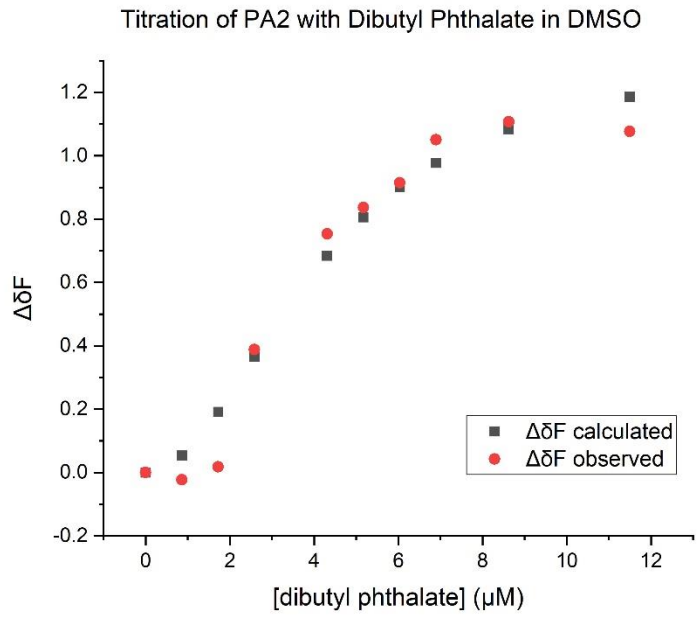

Figure S38 – Fluorescence titration of PA2 with dibutyl phthalate in DMSO fit to a 1:2 host-guest stoichiometry. K_{a1} = 6.73 (0.72) M^{-1}; K_{a2} = 9.10 (0.78) x 10^9 M^{-1}; Sum(χ2) = 0.066.

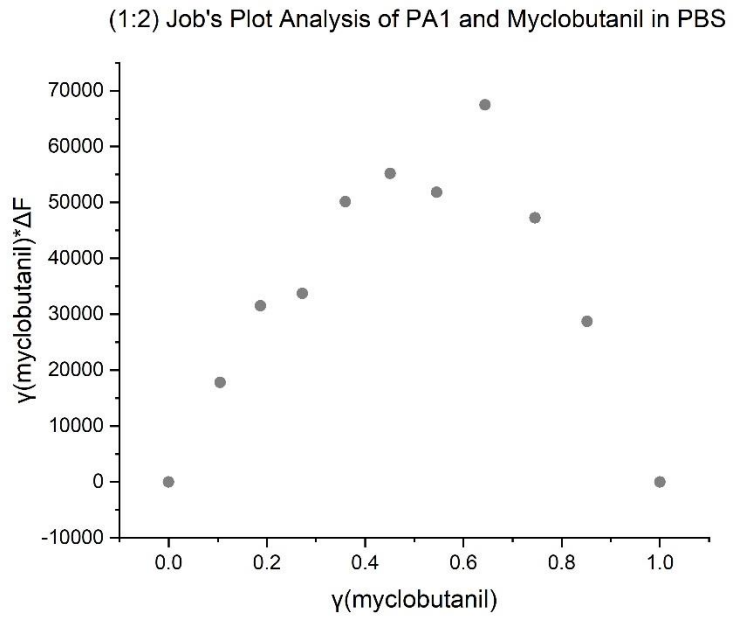

Figure S39 – Job's plot analysis of PA1 and myclobutanil in PBS obtained by fluorescence spectroscopy. Indicates a 1:2 PA1 – myclobutanil stoichiometry (γ_{max} = 0.64). γ is a mole fraction of guest and ΔF is the change in fluorescence integration.

γ(myclobutanil)	γ(myclobutanil)*ΔF
1	0
0.85	28700
0.745	47267
0.64	67438
0.545	51800
0.45	55205
0.36	50117
0.27	33720
0.19	31537
0.105	17782
0	0

Table 13 – Tabulated data of the Job's plot analysis of the host-guest binding of PA2 with dibutyl phthalate in DMSO. γ is a mole fraction of guest and ΔF is the change in fluorescence integration.

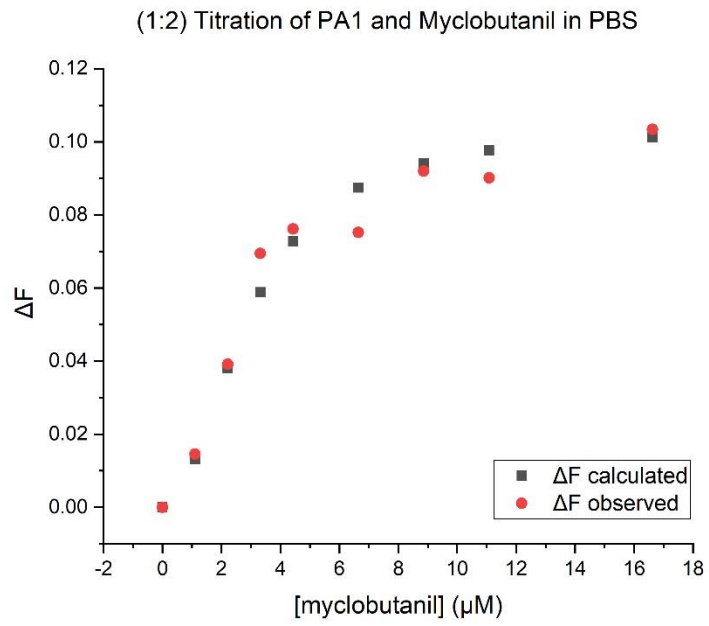

Figure S40 – Fluorescence titration of PA1 with myclobutanil in PBS fit to a 1:2 host-guest stoichiometry. K_{a1} = 5.10 (0.92) M^{-1}; K_{a2} = 2.62 (0.0044) x 10^{10} M^{-1}; Sum(χ2) = 0.00045.

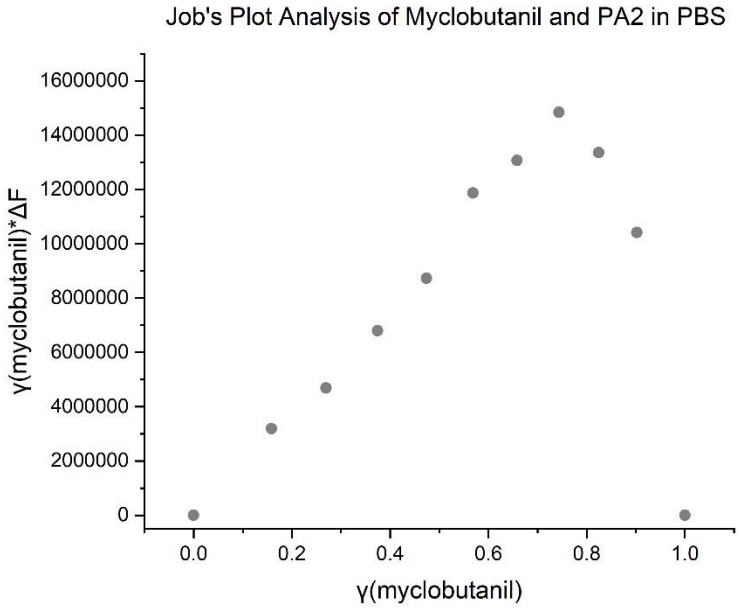

Figure S41 – Job's plot fluorescence analysis of myclobutanil and PA2 in PBS. Indicates no host-guest binding. γ is mole fraction of guest and ΔF is the change in fluorescence integration.

γ(myclobutanil)	γ(myclobutanil)*ΔF
1	0
0.90	10417838
0.82	13358125
0.74	14847663
0.66	13068972
0.57	11874350
0.47	8733928
0.37	6798844
0.27	4689125
0.16	3188900
0	0

Table 14 – Tabulated data of the Job's plot analysis of the host-guest binding of PA1 with **GUEST** in PBS. γ is mole fraction of guest and ΔF is the change in fluorescence integration.

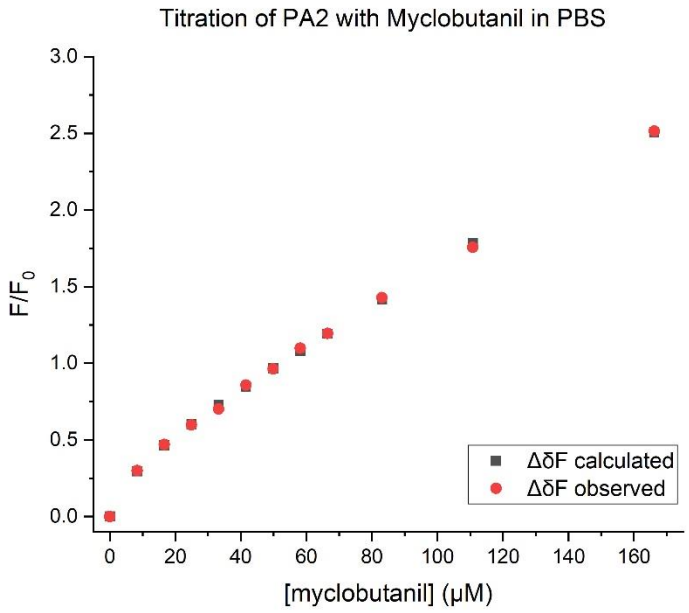

Figure S42 – Fluorescence titration of PA2 with myclobutanil in PBS. Indicates no host-guest binding.

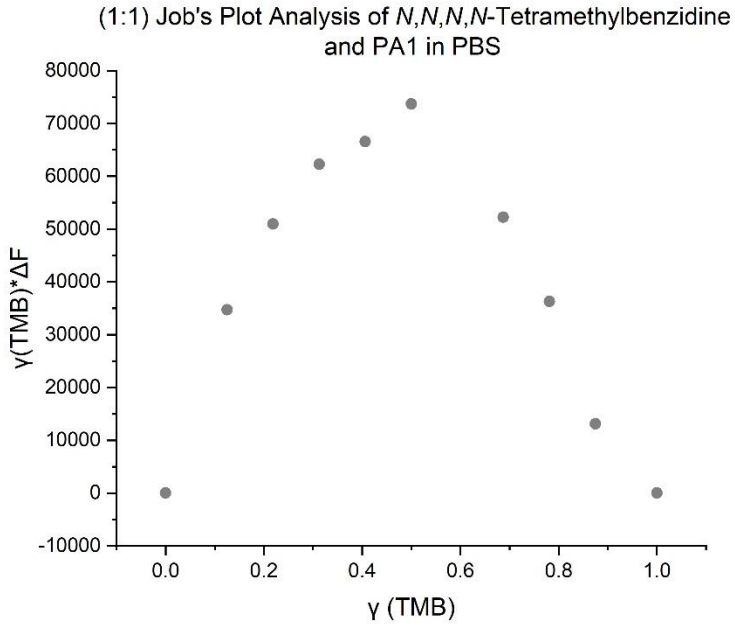

Figure S43– Job's plot titration analysis of N,N,N,N-tetremethylbenzidine and PA1 in PBS obtained by fluorescence spectroscopy. Indicates a 1:1 host-guest binding. γ is mole fraction of guest and ΔF is the change in fluorescence integration.

γ (TMB)	γ(TMB)*ΔF
1	0
0.875	13122.45
0.78	36299.1
0.68	52250.05
0.59	47104.49
0.5	73686.17
0.41	66586.39
0.31	62295.91
0.22	50968.7
0.125	34709.95
0	0

Table 15 – Tabulated data of the Job's plot analysis of the host-guest binding of PA1 with N,N,N,N-tetramethylbenzidine in PBS. γ is mole fraction of guest and ΔF is the change in fluorescence integration.

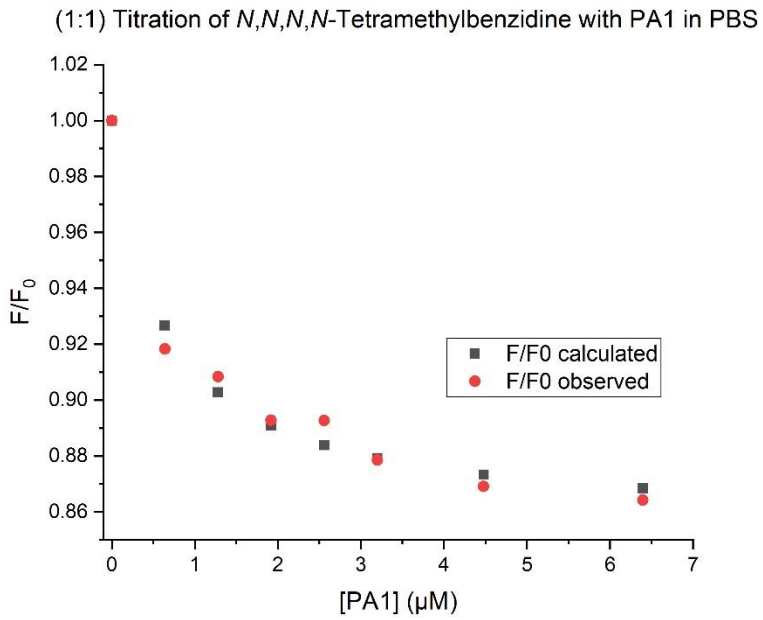

Figure S44 – Fluorescence titration of N,N,N,N-tetramethylbenzidine with PA1 in PBS fit to a 1:1 host-guest stoichiometry. K_a = 1.62 (0.12) x 10^6 M^{-1}; Sum(χ2) = 0.00023.

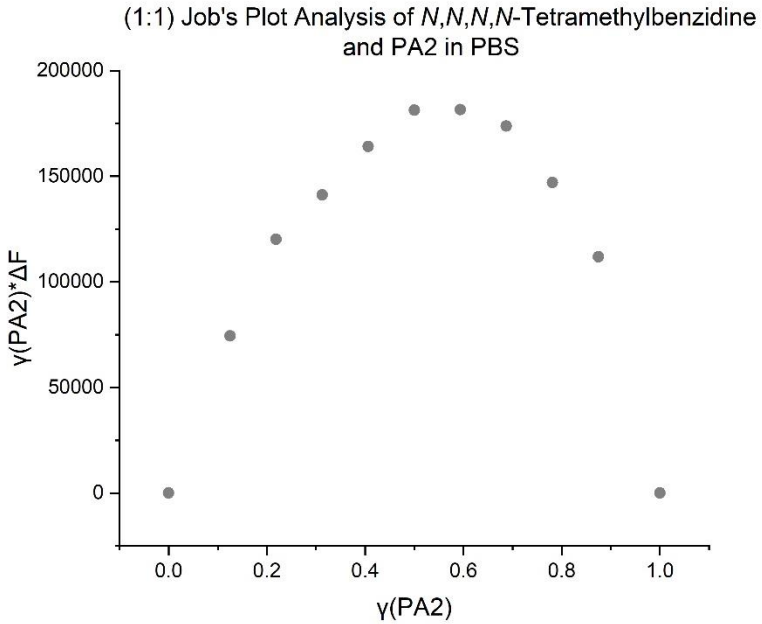

Figure S45 - Job's plot analysis of N,N,N,N-tetramethylbenzidine and PA2 in PBS obtained by fluorescence spectroscopy indicating a 1:1 host-guest stoichiometry. γ is mole fraction of guest and ΔF is the change in fluorescence integration.

γ (TMB)	γ(TMB)*ΔF
1	0
0.875	111850.2
0.78	147019.3
0.68	173735.7
0.59	181535.2
0.5	181265.3
0.41	164089.6
0.31	141234.2
0.22	120231.6
0.125	74424.13
0	0

Table 16 – Tabulated data of the Job's plot analysis of the host-guest binding of PA2 with N,N,N,N-tetramethylbenzidine in PBS. γ is mole fraction of guest and ΔF is the change in fluorescence integration.

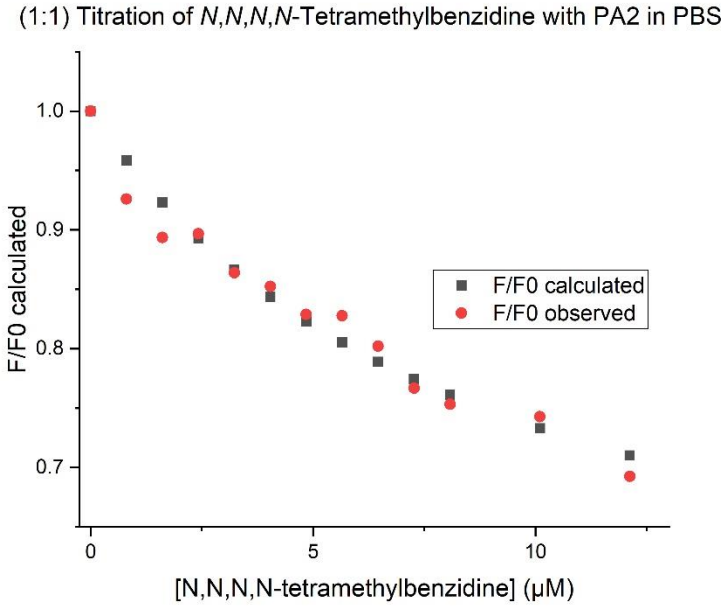

Figure S46 – Fluorescence titration of N,N,N,N-tetramethylbenzidine with PA2 in PBS fit to a 1:1 host-guest stoichiometry. K_a = 1.11 (0.19) x 10^5 M^{-1}; Sum(χ2) = 0.0034.

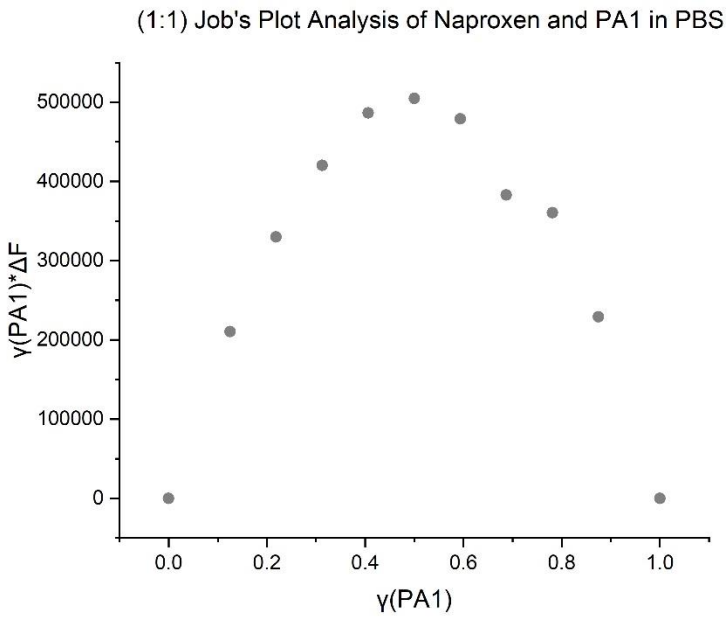

Figure S47 – Job's plot analysis of naproxen and PA1 in PBS obtained by fluorescence spectroscopy indicating a 1:1 host-guest stoichiometry. γ is mole fraction of guest and ΔF is the change in fluorescence integration.

γ (PA1)	γ(PA1)*ΔF
1	0
0.875	229185
0.78	360646
0.69	382989
0.59	479015
0.5	505076
0.41	486672
0.31	420425
0.22	330083
0.125	210426
0	0

Table 17– Tabulated data of the Job's plot analysis of the host-guest binding of PA1 with naproxen in PBS. γ is mole fraction of guest and ΔF is the change in fluorescence integration.

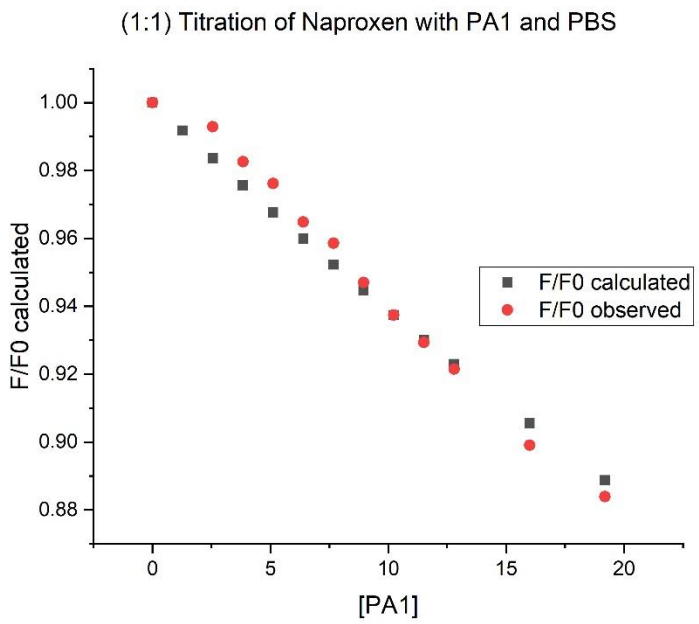

Figure S48 – Fluorescence titration of naproxen with PA1 in PBS fit to a 1:1 host-guest stoichiometry. K_a = 6.51 (0.011) x 10^3 M^{-1}; Sum(χ2) = 0.00051.

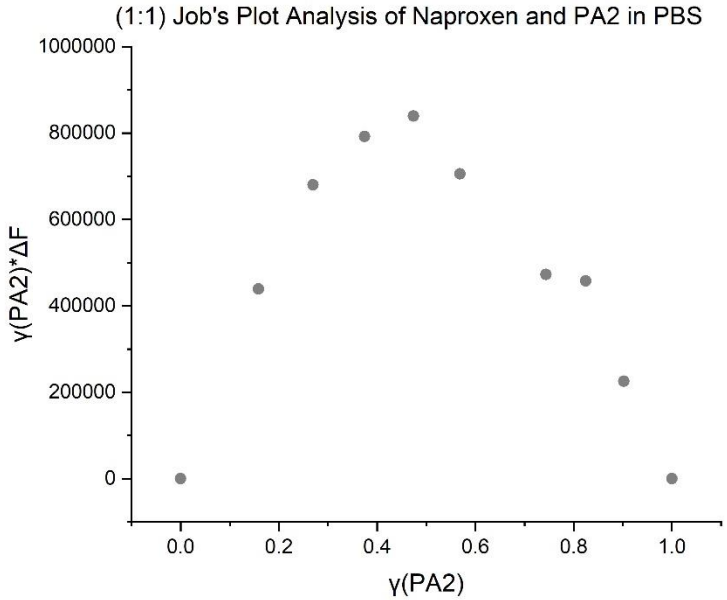

Figure S49 - Job's plot analysis of naproxen and PA2 in PBS obtained by fluorescence spectroscopy indicating a 1:1 host-guest stoichiometry (γ_{max} = 0.47). γ is mole fraction of guest and ΔF is the change in fluorescence integration.

γ (PA2)	γ(PA2)*ΔF
1	0
0.90	225597
0.82	457604
0.74	472464
0.66	795249
0.57	705349
0.47	839436
0.37	792306
0.27	679991
0.16	439301
0	0

Table 18 – Tabulated data of the Job's plot analysis of the host-guest binding of PA2 with naproxen in PBS. γ is mole fraction of guest and ΔF is the change in fluorescence integration.

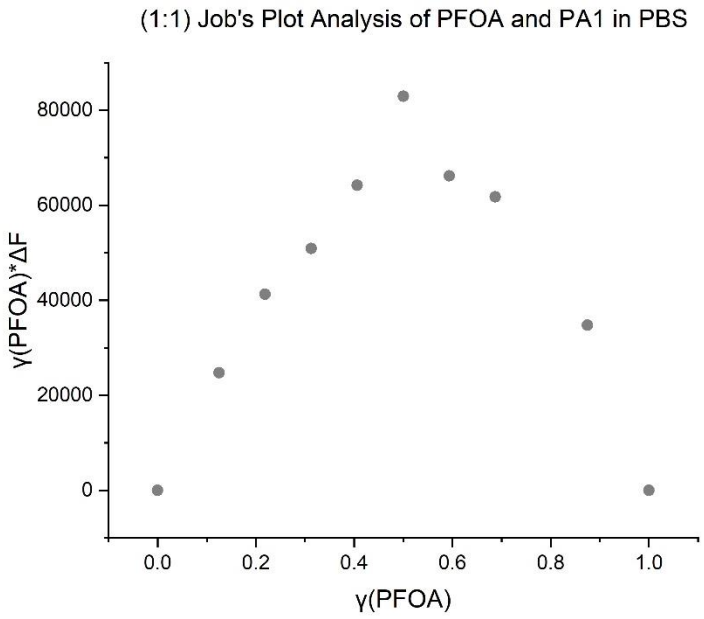

Figure S50 – Job's plot analysis of perfluorooctanoic acid and PA1 in PBS obtained by fluorescence spectroscopy indicating a 1:1 host-guest stoichiometry. γ is mole fraction of guest and ΔF is the change in fluorescence integration. Sharp peak indicates a high association constant.

γ (PA1)	γ(PA1)*ΔF
1	0
0.875	34780.01
0.78	67396.37
0.69	61746.16
0.59	66159.53
0.5	82911.04
0.41	64180.84
0.31	50905.04
0.22	41277.98
0.125	24741.22
0	0

Table 19 – Tabulated data of the Job's plot analysis of the host-guest binding of PA1 with naproxen in PBS. γ is mole fraction of guest and ΔF is the change in fluorescence integration.

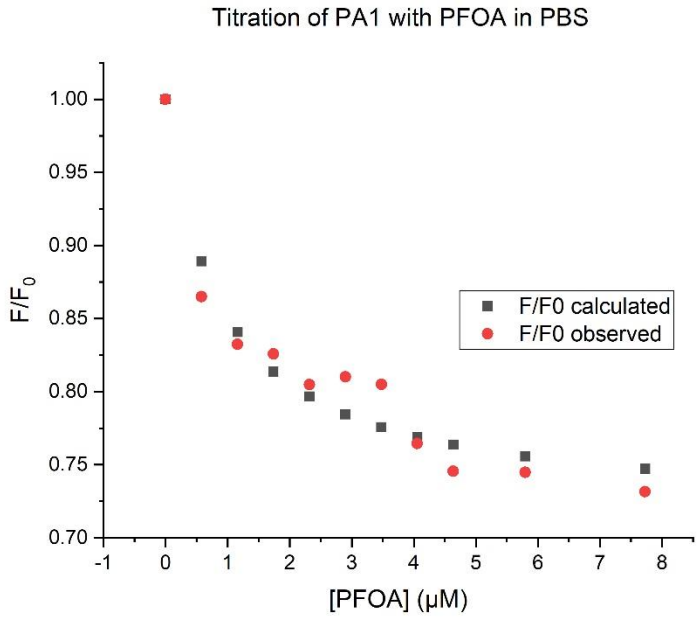

Figure S51 – Fluorescence titration of PA1 with PFOA in PBS fit to a 1:1 host-guest stoichiometry. K_a = 1.13 (0.13) x 10^6 M^{-1}; Sum(χ2) = 0.0039.

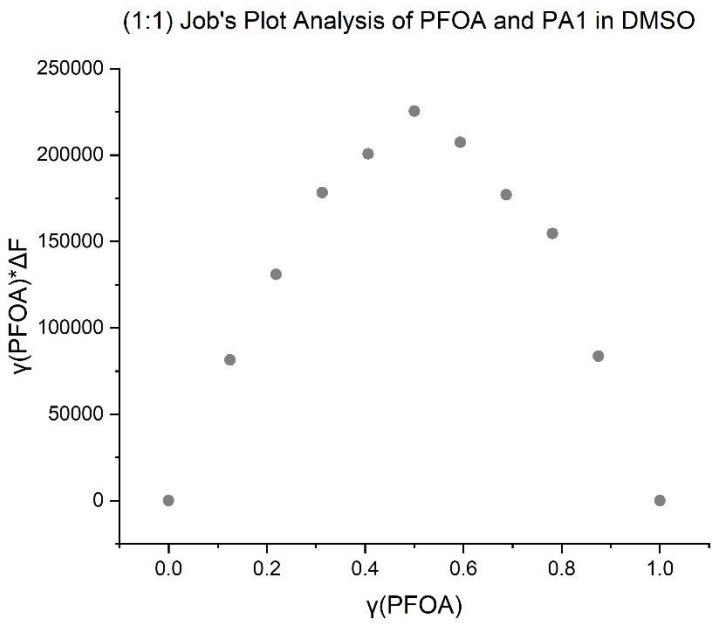

Figure S52 – Job's plot fluorescence analysis of PFOA and PA1 in DMSO. Indicates a 1:1 host-guest stoichiometry ($\gamma_{max} = 0.5$). γ is mole fraction of guest and ΔF is the change in fluorescence integration.

γ(PFOA)	γ(PFOA)*ΔF
1	0
0.875	83616.51
0.78	154572.9
0.69	177051.2
0.59	207423.2
0.5	225409
0.41	200726
0.31	178311.5
0.22	130961.6
0.125	81500.66
0	0

Table 20 – Tabulated data of the Job's plot analysis of the host-guest binding of PA1 with PFOA in DMSO. γ is mole fraction of guest and ΔF is the change in fluorescence integration.

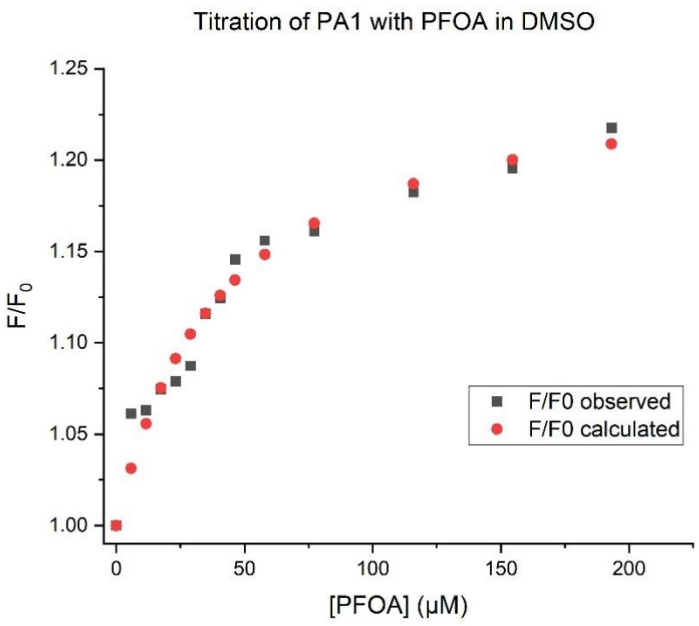

Figure S53 – Fluorescence titration of PA1 with PFOA in DMSO fit to a 1:1 host-guest stoichiometry. K_a = 2.44 (0.17) x 10^4 M^{-1}; Sum(χ2) = 0.0018.

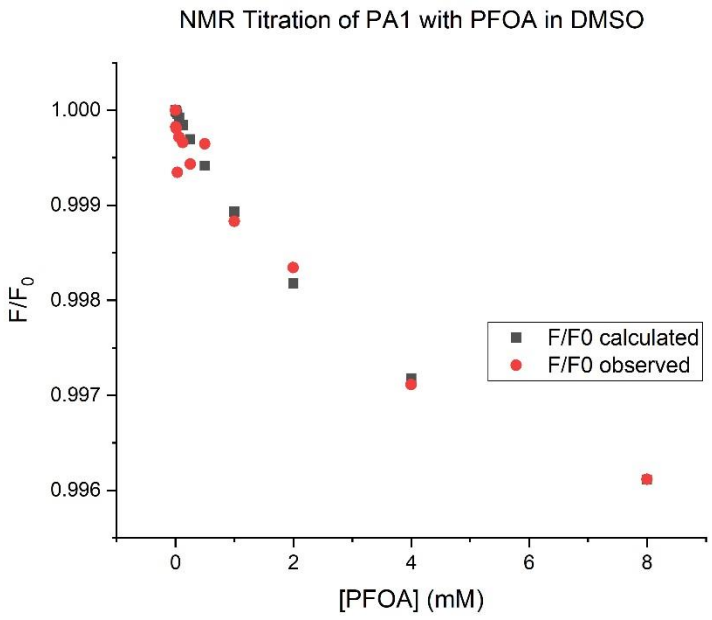

Figure S54 – NMR titration of PA1 with PFOA in DMSO fit to a 1:1 stoichiometry. K_a = 2.06 (0.0000060) x 10^2 M^{-1}; Sum(χ2) = 0.00000079.

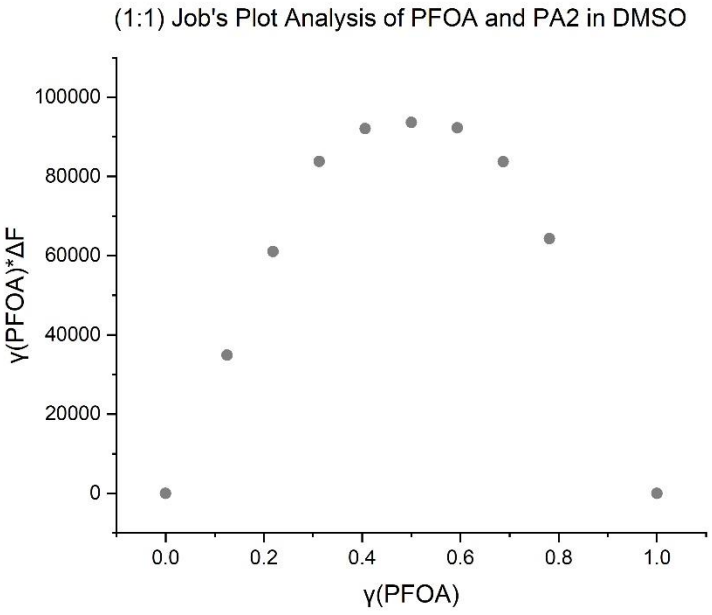

Figure S55 – Job's plot fluorescence analysis of PFOA and PA2 in DMSO. Indicates a 1:1 host-guest binding stoichiometry (γ_{max} = 0.5). γ is mole fraction of guest and ΔF is the change in fluorescence integration.

γ(PFOA)	γ(PFOA)*ΔF
1	0
0.78	64300
0.68	83733
0.59	92254
0.5	93618
0.41	92091
0.31	83826
0.22	61046
0.125	34855
0	0

Table 21 – Tabulated data of the Job's plot analysis of the host-guest binding of PA1 with PFOA in DMSO. γ is mole fraction of guest and ΔF is the change in fluorescence integration.

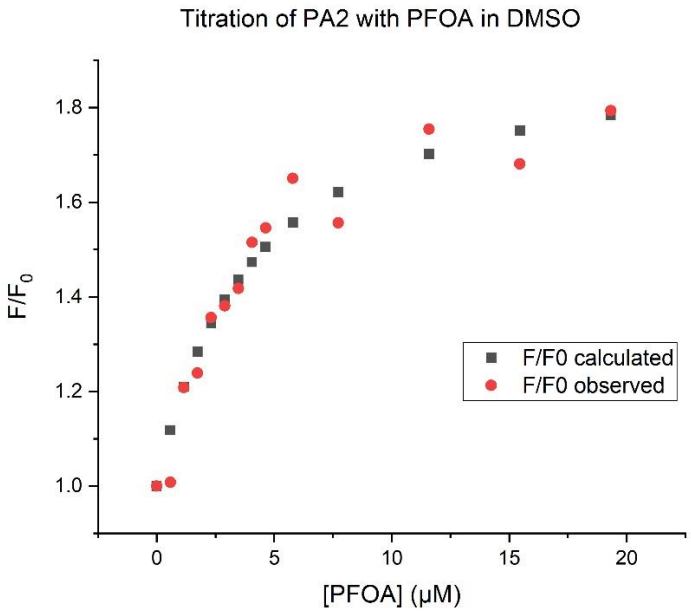

Figure S56- Fluorescence titration of PA2 with PFOA in DMSO fit to a 1:1 host-guest stoichiometry. K_a = 2.45 (0.21) x 10^5 M^{-1}; Sum(χ2) = 0.0477.

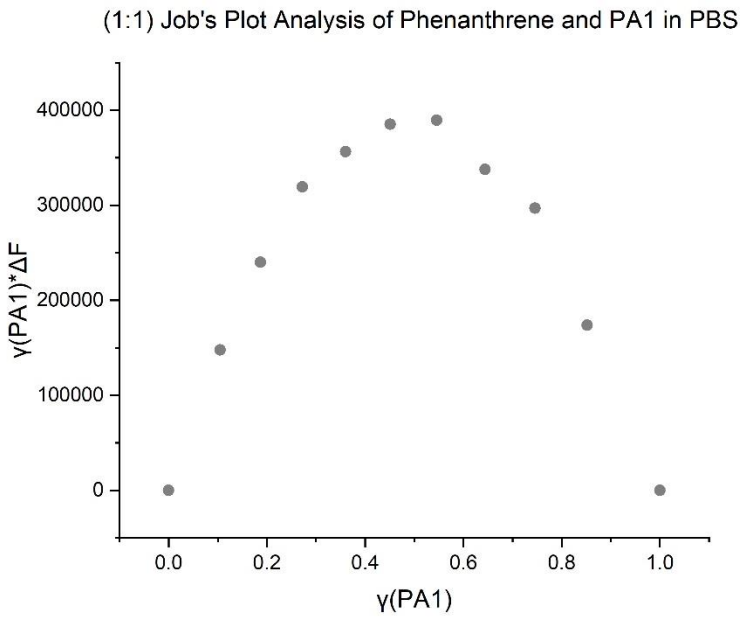

Figure S57 – Job's plot analysis of phenanthrene and PA1 in PBS, obtained by fluorescence spectroscopy, indicating 1:1 stoichiometry (γ_{max} = 0.54). γ is mole fraction of guest and ΔF is the change in fluorescence integration.

γ(PA1)	γ(PA1)*ΔF
1	0
0.85	173913
0.75	296923
0.64	337636
0.54	389594
0.45	385205
0.36	356463
0.27	319288
0.19	240142
0.11	147871
0	0

Table 22– Tabulated data of the Job's plot analysis of the host-guest binding of PA1 with phenanthrene in PBS. γ is mole fraction of guest and ΔF is the change in fluorescence integration.

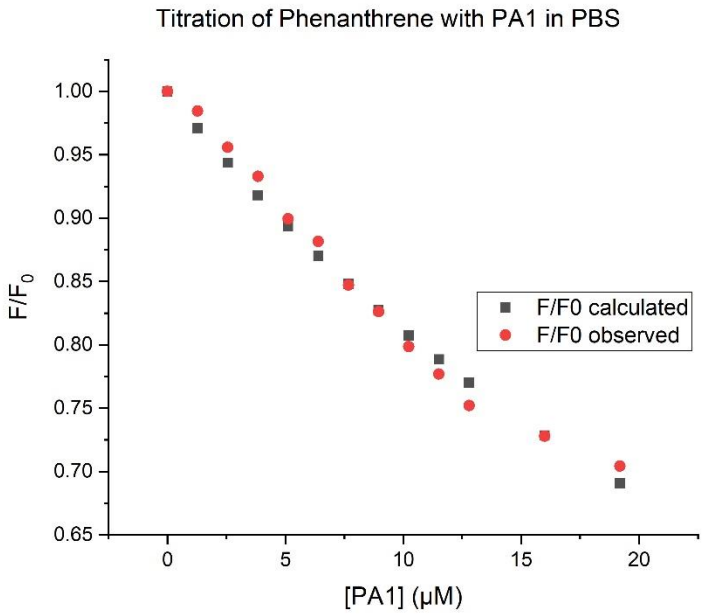

Figure S58 – Fluorescence titration of phenanthrene with PA1 in PBS fit to a 1:1 stoichiometry. K_a = 2.32 (0.020) x 10^4 M^{-1}; Sum(χ2) = 0.0016.

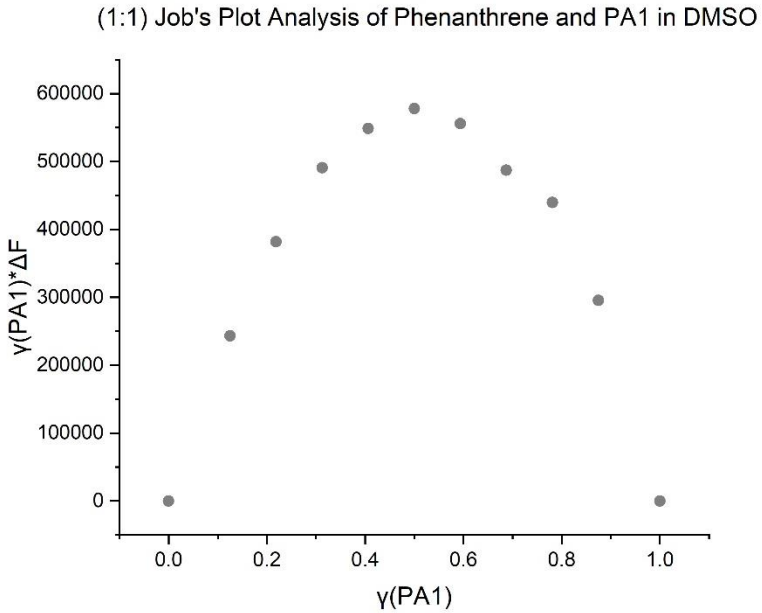

Figure S59 – Job's plot fluorescence analysis of phenanthrene and PA1 in DMSO. Indicates a 1:1 host-guest stoichiometry (γ_{max} = 0.5). γ is mole fraction of guest and ΔF is the change in fluorescence integration.

γ(PA1)	γ(PA1)*ΔF
1	0
0.875	295283
0.78	439788
0.69	487040
0.59	555976
0.5	578021
0.41	548629
0.31	490763
0.22	381913
0.125	243145
0	0

Table 23– Tabulated data of the Job's plot analysis of the host-guest binding of PA1 with phenanthrene in DMSO. γ is mole fraction of guest and ΔF is the change in fluorescence integration.

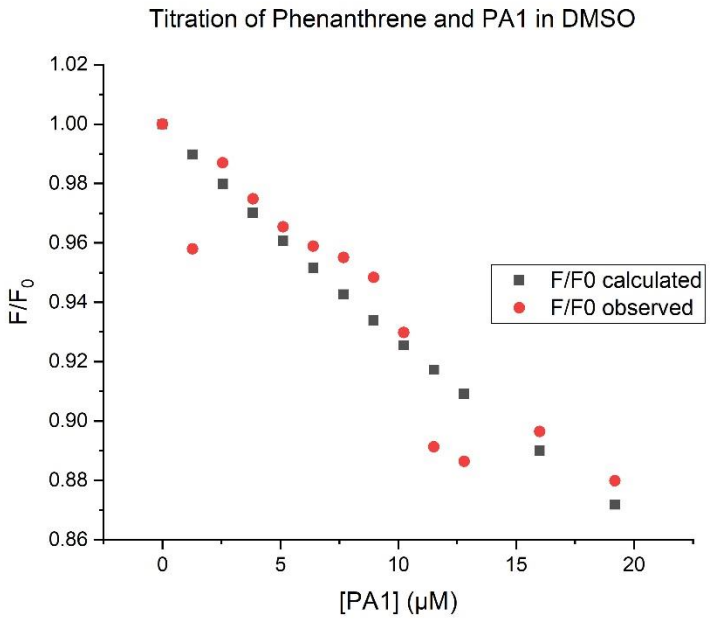

Figure S60 – Fluorescence titration of phenanthrene with PA1 in DMSO fit to a 1:1 stoichiometry. K_a = 8.1 (1.8) x 10^3 M^{-1}; Sum(χ2) = 0.0029.

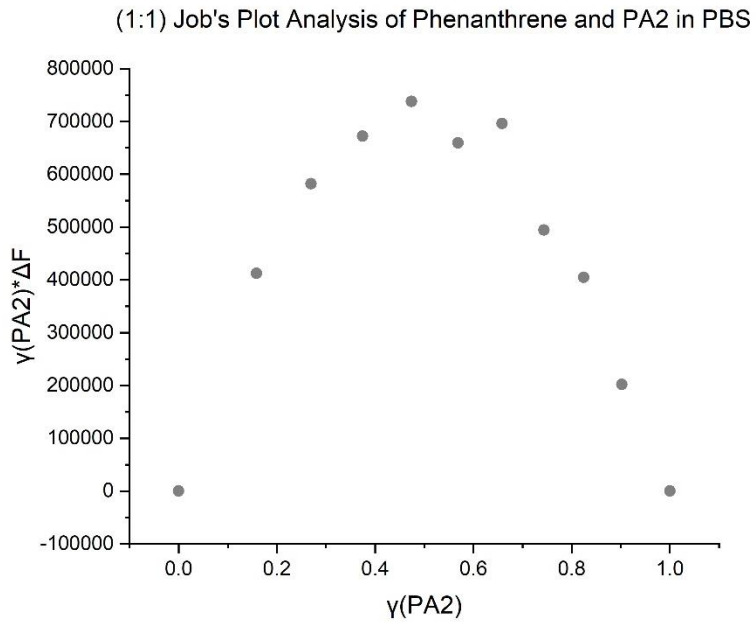

Figure S61 – Job's plot fluorescence analysis of phenanthrene and PA2 in PBS. Indicates a 1:1 stoichiometry (γ_{max} = 0.47). γ is mole fraction of guest and ΔF is the change in fluorescence integration.

γ(PA2)	γ(PA2)*ΔF
1	0
0.90	201867
0.82	404914
0.74	494296
0.66	696248
0.57	659321
0.47	738205
0.37	672004
0.27	581949
0.16	412505
0	0

Table 24 – Tabulated data of the Job's plot analysis of the host-guest binding of PA2 with phenanthrene in PBS. γ is mole fraction of guest and ΔF is the change in fluorescence integration.

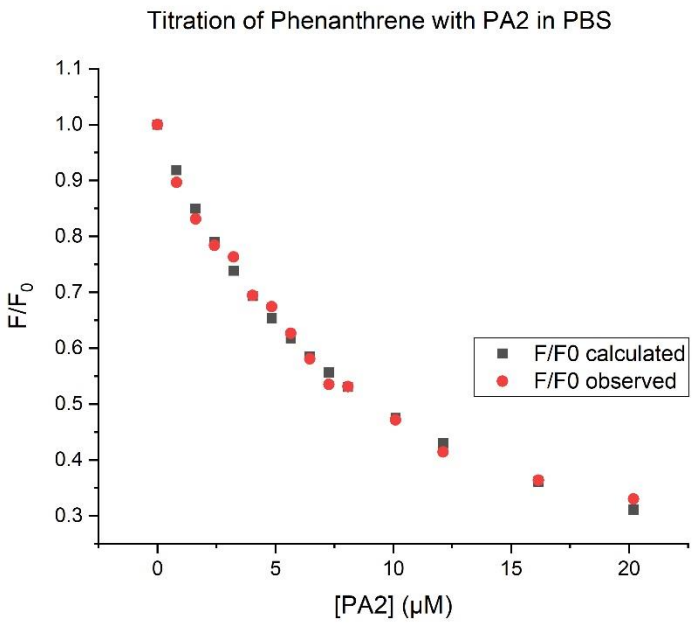

Figure S62 – Fluorescence titration of phenanthrene and PA2 in PBS fit to a 1:1 stoichiometry. K_a = 1.10 (0.011) x 10^5 M^{-1}; Sum(χ2) = 0.0032.

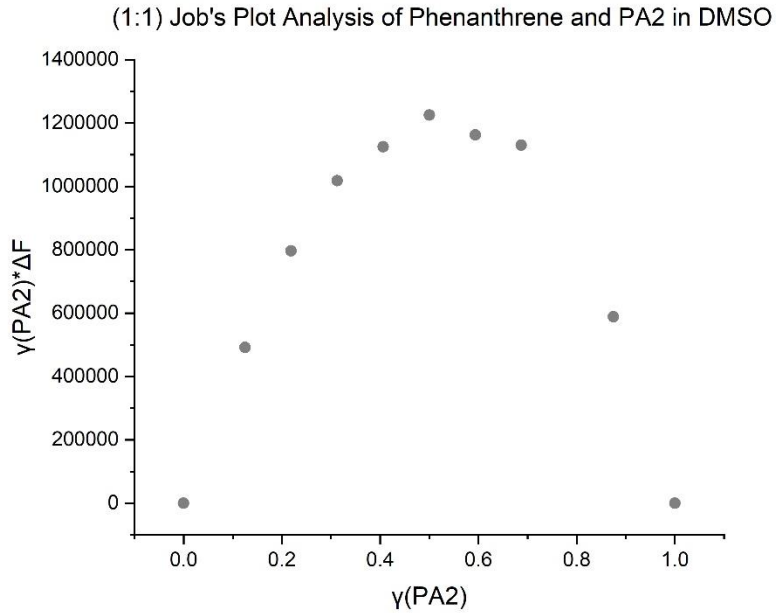

Figure S63 – Job's plot analysis of phenanthrene and PA2 in DMSO obtained by fluorescence spectroscopy. Indicates a 1:1 stoichiometry (γ_{max} = 0.5). γ is mole fraction of guest and ΔF is the change in fluorescence integration.

γ(PA2)	γ(PA2)*ΔF
1	0
0.875	588262
0.69	1130353
0.59	1162188
0.5	1225575
0.41	1125203
0.31	1017866
0.22	796796
0.125	491291
0	0

Table 25 – Tabulated data of the Job's plot analysis of the host-guest binding of PA2 with phenanthrene in DMSO. γ is mole fraction of guest and ΔF is the change in fluorescence integration.

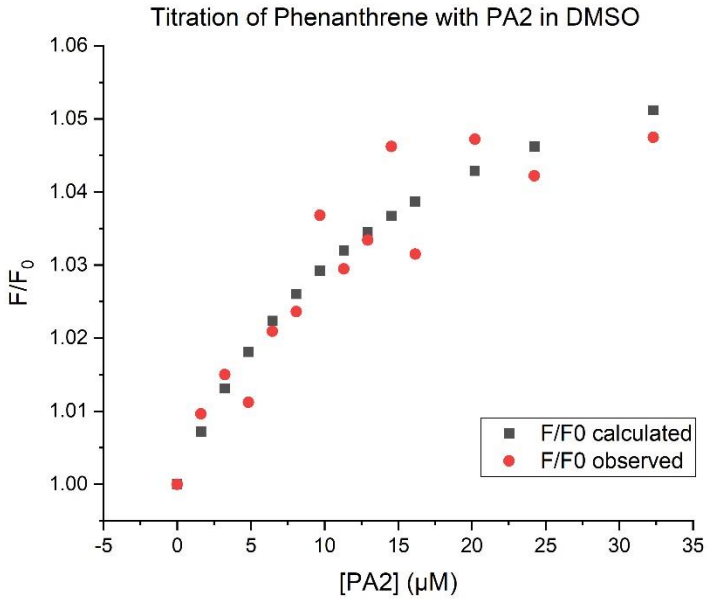

Figure S64 – Fluorescence titration of phenanthrene with PA2 in DMSO fit to a 1:1 stoichiometry. K_a = 5.04 (0.81) x 10^4 M^{-1}; Sum(χ2) = 0.00060.

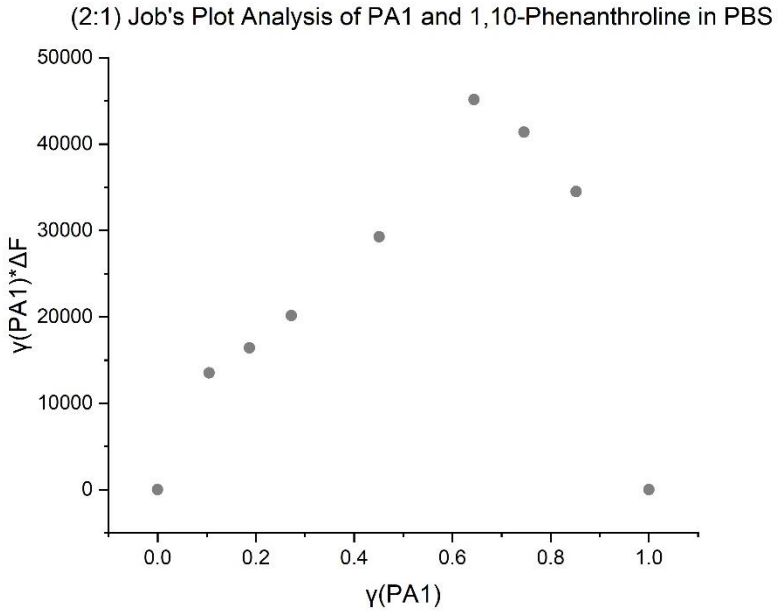

Figure S65 - Job's plot analysis of 1,10-phenanthroline and PA1 in PBS obtained by fluorescence spectroscopy. Indicates a 2:1 PA1 – 1,10-phenanthroline stoichiometry ($\gamma_{max} = 0.64$). γ is mole fraction of guest and ΔF is the change in fluorescence integration.

γ(PA1)	γ(PA1)*ΔF
1	0
0.85	34488.69
0.75	41389.97
0.64	45144.56
0.55	27294.92
0.45	29286.59
0.36	17361.3
0.27	20136.69
0.19	16426.48
0.11	13523.37
0	0

Table 26 – Tabulated data of the Job's plot analysis of the host-guest binding of PA1 with 1,10-phenanthroline in PBS. γ is mole fraction of guest and ΔF is the change in fluorescence integration.

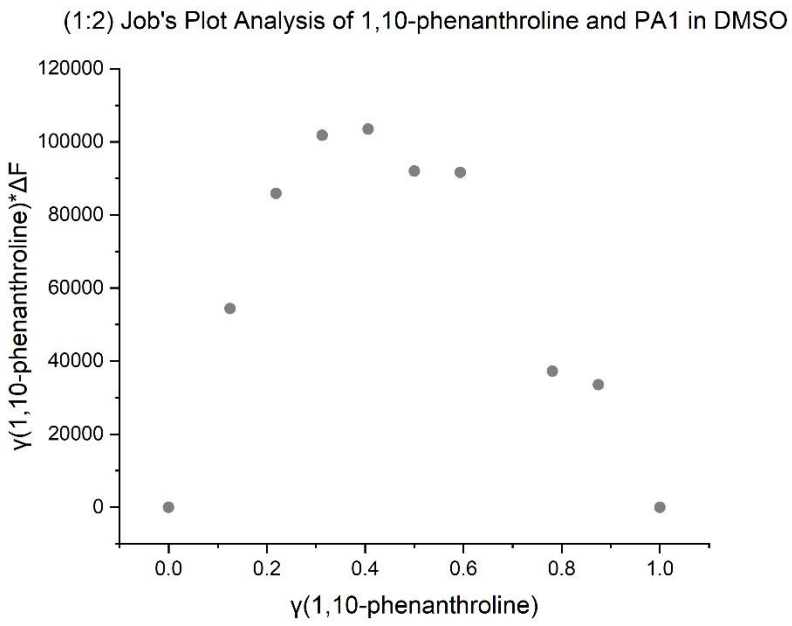

Figure S66 - Job's plot analysis of 1,10-phenanthroline and PA1 in DMSO obtained by fluorescence spectroscopy. Indicates a 1:2 1,10-phenanthroline - PA1 stoichiometry ($\gamma_{max} = 0.41$). γ is mole fraction of guest and ΔF is the change in fluorescence integration.

γ(1,10-phenanthroline)	**γ(1,10-phenanthroline)*ΔF**
1	0
0.875	33515.75
0.78	37238.53
0.59	91632.53
0.5	91982.69
0.41	103467.7
0.31	101743.1
0.22	85906.53
0.125	54374.94
0	0

Table S27 – Tabulated data of the Job's plot analysis of the host-guest binding of PA1 with 1,10-phenanthroline in DMSO. γ is mole fraction of guest and ΔF is the change in fluorescence integration.

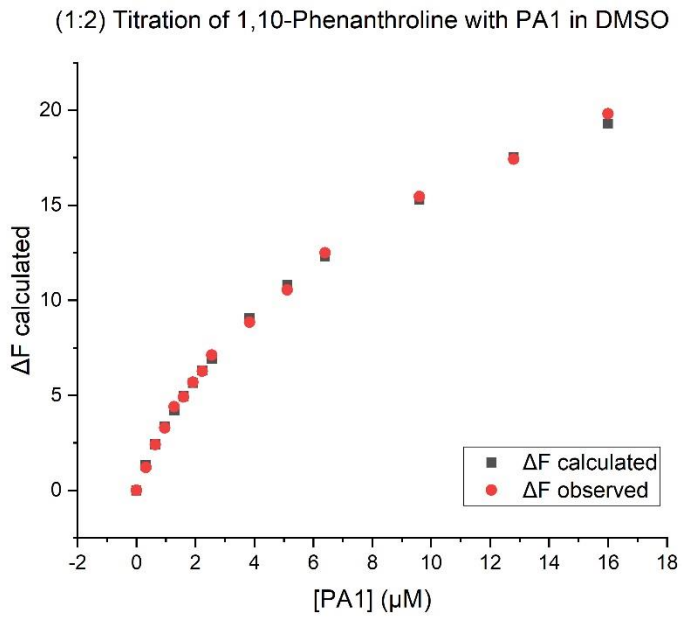

Figure S67 - Fluorescence titration of 1,10-phenanthroline with PA1 in DMSO fit to a 1:2 1,10-phenanthroline-PA1 stoichiometry. K_{a1} = 4.40 (0.027) x 10^5 M^{-1}; K_{a2} = 2.67 (0.24) x 10^4 M^{-1}; Sum(χ2) = 0.17.

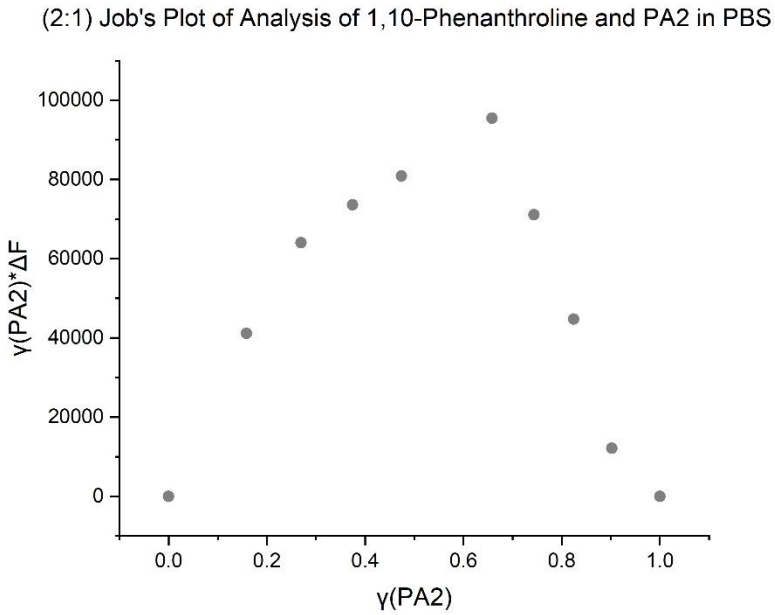

Figure S68- Job's plot analysis of 1,10-phenanthroline and PA2 in PBS obtained by fluorescence spectroscopy. Indicates a 1:2 1,10-phenanthroline - PA1 stoichiometry (γ_{max} = 0.66). γ is mole fraction of guest and ΔF is the change in fluorescence integration.

γ(1,10-phenanthroline)	γ(1,10-phenanthroline)*ΔF
1	0
0.90	12111
0.82	44767
0.74	71112
0.66	95513
0.47	80894
0.37	73608
0.27	64035
0.16	41137
0	0

Table 28 – Tabulated data of the Job's plot analysis of the host-guest binding of PA2 with 1,10-phenanthroline in PBS. γ is mole fraction of guest and ΔF is the change in fluorescence integration.

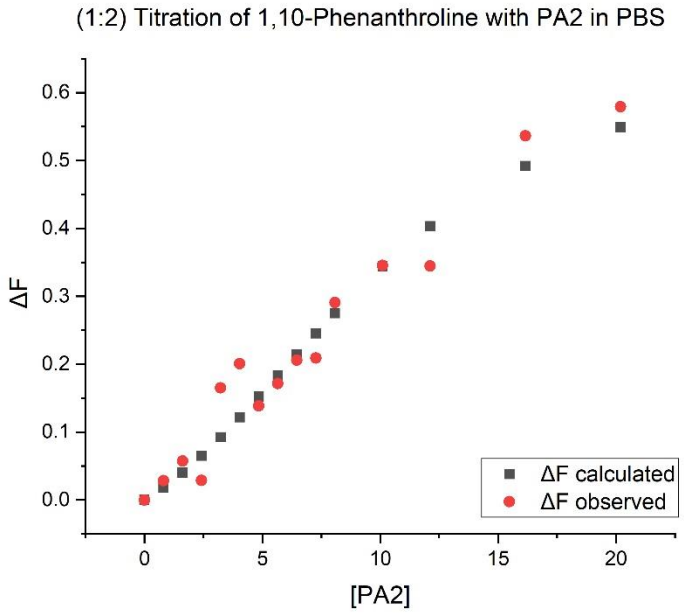

Figure S69 - Fluorescence titration of 1,10-phenanthroline with PA2 in PBS; fit to a 1:2 1,10-phenanthroline-PA2 stoichiometry. K_{a1} = 4.19 (0.46) M^{-1}; K_{a2} = 1.18 (0.052) x 10^9 M^{-1}; Sum(χ2) = 0.029.

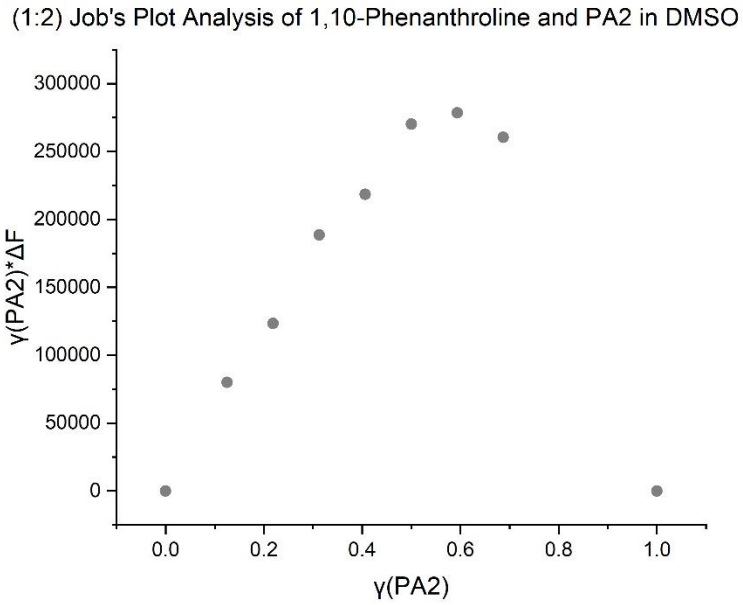

Figure S70 - Job's plot analysis of 1,10-phenanthroline and PA2 in DMSO obtained by fluorescence spectroscopy. Indicates a 1:2 1,10-phenanthroline - PA1 stoichiometry ($\gamma_{max} = 0.59$). γ is mole fraction of guest and ΔF is the change in fluorescence integration.

γ(PA2)	**γ(PA2)*ΔF**
1	0
0.6875	260452
0.59375	278432
0.5	270227
0.40625	218522
0.3125	188525
0.21875	123410
0.125	79874
0	0

Table S29 – Tabulated data of the Job's plot analysis of the host-guest binding of PA2 with 1,10-phenanthroline in DMSO. γ is mole fraction of guest and ΔF is the change in fluorescence integration.

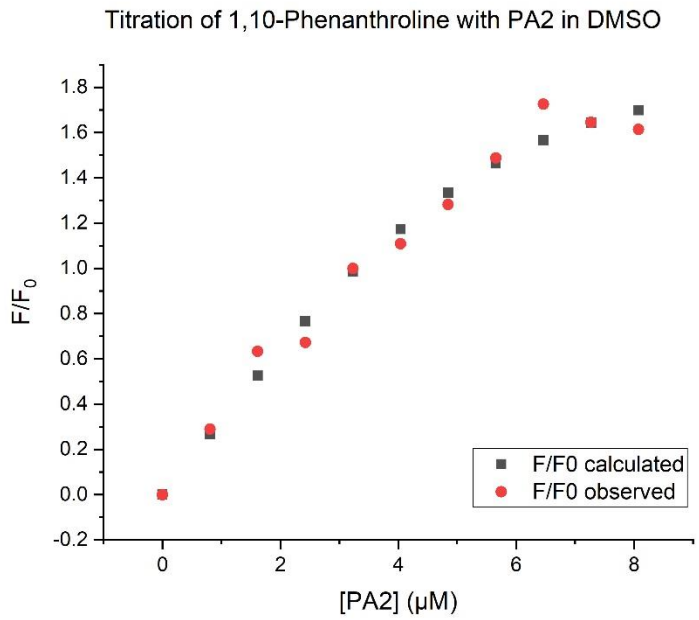

Figure S71 – Fluorescence titration of 1,10-phenanthroline with PA2 in DMSO fit to a 1:2 phenanthroline:PA2 stoichiometry. K_{a1} = 3.08 (0.041) x 10^2 M^{-1}; K_{a2} = 2.89 (0.12) x 10^7 M^{-1}; Sum(χ2) = 0.066.

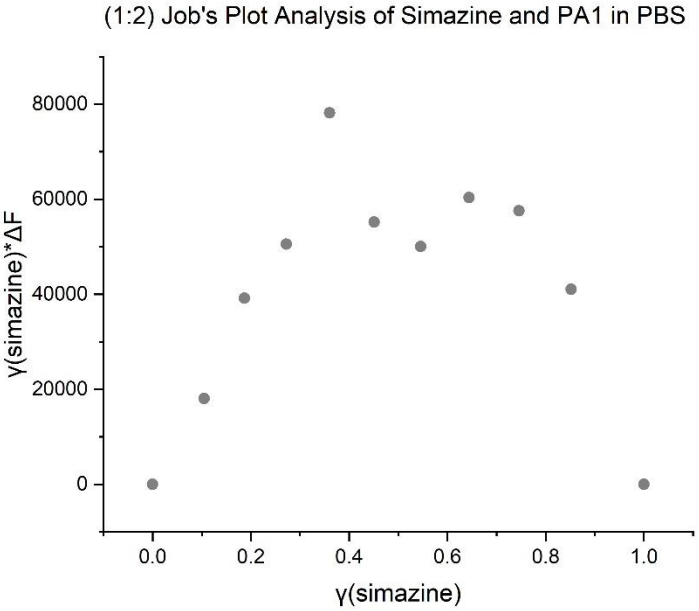

Figure S72– Job's plot fluorescence analysis of simazine and PA1 in PBS. Indicates a 2:1 PA1-simzaine stoichiometry (γ_{max} = 0.36). γ is mole fraction of guest and ΔF is the change in fluorescence integration.

γ	γ*ΔF
1	0
0.85	41046.37
0.75	57558.8
0.64	60336.2
0.55	50067.1
0.45	55206.53
0.36	78167.7
0.27	50534.78
0.19	39151.16
0.11	18074.73
0	0

Table S30 – Tabulated data of the Job's plot analysis of the host-guest binding of PA1 with simazine in PBS. γ is mole fraction of guest and ΔF is the change in fluorescence integration.

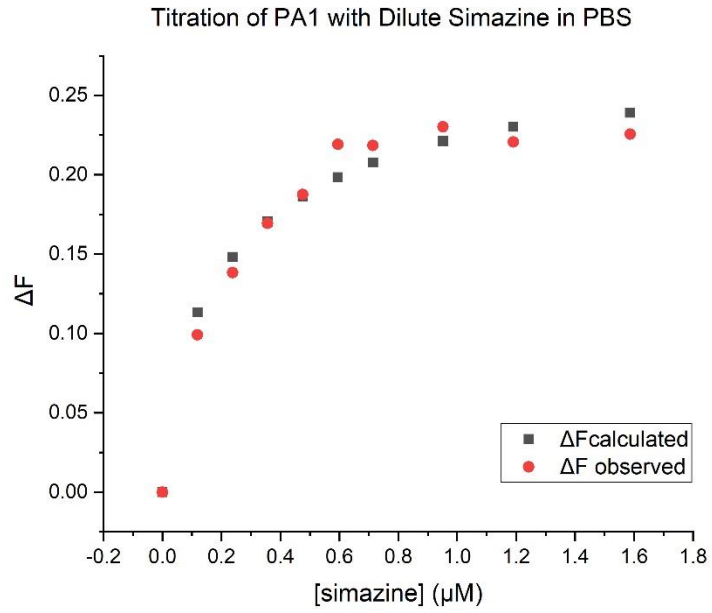

Figure S73 – Fluorescence titration of PA1 with dilute simazine in PBS fit to a 2:1 host-guest stoichiometry. K_{a1} = 1.37 (0.22) x 10^{10} M^{-1}; K_{a2} = 6.47 (1.42) x 10^{9} M^{-1}; Sum(χ2) = 0.00073.

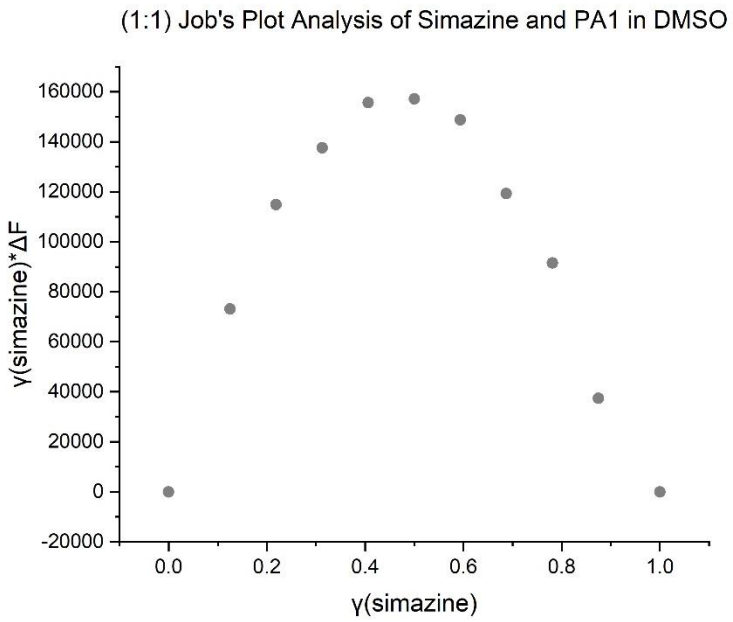

Figure S74– Job's plot analysis of simazine and PA1 in DMSO obtained by fluorescence spectroscopy indicating a 1:1 host-guest stoichiometry (γ_{max} = 0.5). γ is mole fraction of guest and ΔF is the change in fluorescence integration.

γ	γ*ΔF
1	0
0.875	37444
0.78	91458
0.69	119288
0.59	148709
0.5	157071
0.41	155605
0.31	137561
0.22	114808
0.125	73085
0	0

Table S31– Tabulated data of the Job's plot analysis of the host-guest binding of PA1 with simazine in DMSO. γ is mole fraction of guest and ΔF is the change in fluorescence integration.

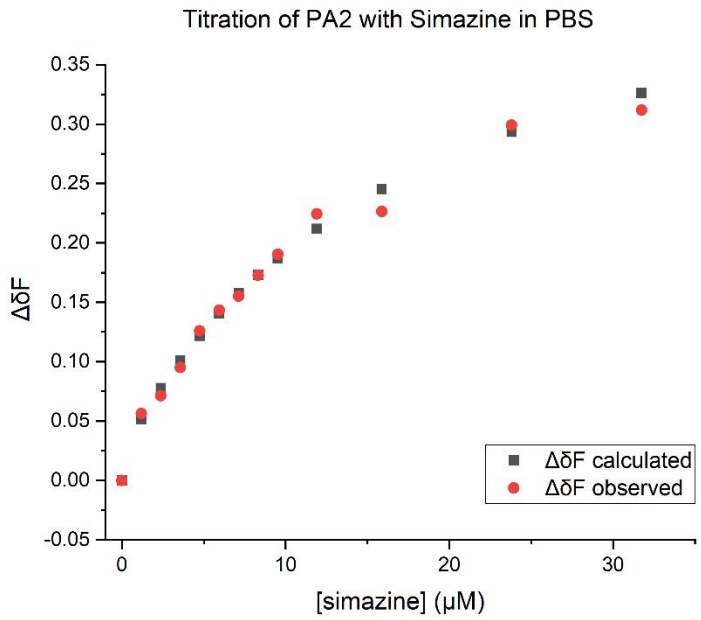

Figure S75 – Fluorescence titration of PA2 with simazine in PBS fit to a 1:2 host-guest stoichiometry. K_{a1} = 7.52 (0.000065) x 10^{11} M^{-1}; K_{a2} = 5.80 (0.42) x 10^{4} M^{-1}; Sum(χ2) = 0.00073.

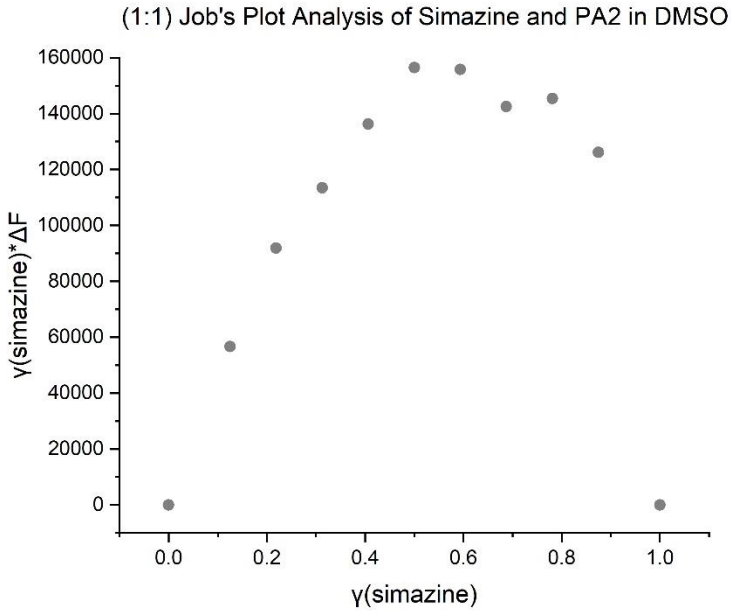

Figure S76 – Job's plot fluorescence analysis of simazine and PA2 in DMSO indicating a 1:1 host-guest stoichiometry (γ_{max} = 0.5). γ is mole fraction of guest and ΔF is the change in fluorescence integration.

γ	γ*ΔF
1	0
0.875	126139
0.78	145421
0.69	142554
0.59	155742
0.5	156445
0.41	136213
0.31	113450
0.22	91863
0.125	56677
0	0

Table S32 *– Tabulated data of the Job's plot analysis of the host-guest binding of PA2 with simazine in DMSO. γ is mole fraction of guest and ΔF is the change in fluorescence integration*

Molecular modeling and stabilization energies

Two major software packages were used to energy minimize structures, and for docking purposes, first one is Spartan16 and the second software is MOE 2018. Spartan was used to perform semi-empirical level calculations on the complexes, guests and host. These energies obtained after PM3 calculations were further used for obtaining stabilization energy for complex formation. MOE software was used to visualize these structures and to dock specific guests into the cavity of the WSP5A using docking tools. For docking receptor was chosen to be the WSp5a, and the ligand was chosen to be as the any of the toxicants. Docking parameters were as follows; no wall constraints were used to enhance free movement of both ligand and receptor. The docking placement method used was "Triangle Matcher," and the docking score was done using "London dG" and "GBVI/WSA dG." Docking refinement was performed using the "induced fit" method. Out of 100 possible confirmations the best 5 were chosen and, and out of the best 5 highest docking score placement was used for obtaining ligand interaction diagrams.

Toxicants	Toxicant / kJ mol^{-1}	WS P5A / kJ mol^{-1}	WSP5A and Toxicant / kJ mol^{-1}	Stabilization energy / kJ mol^{-1}	Docking score / kcal mol^{-1}
Anthracene	242.6439	11053.948	11210.6926	-85.8993	-8.8798
Phenanthrene	213.8413	11053.948	11235.4887	-32.3006	-8.6756
1,10-Phenanthroline mono hydrate	770.1826	11053.948	11276.176	-547.9546	-5.4557
Cyclophosphamide mono hydrate	329.438	11053.948	10563.1687	-820.2173	-10.5119
Myclobutanil	344.917	11053.948	11295.111	-103.754	-8.5231
N,*N*,*N*,*N*-Tetramethylbenzidine	144.785	11053.948	11131.1368	-67.5962	-9.8271
Naproxen	476.927	11053.948	10577.8805	-952.9945	-11.4858
PFOA	-2422.938	11053.948	7699.1544	-931.8556	-11.8114
Dibutylpthalate	-758.6346	11053.948	10247.378	-47.9354	-9.7201
Carbamazepine	106.135	11053.948	11098.568	-61.515	-8.2642
Clofibric acid	-486.3014	11053.948	10487.153	-80.4936	-9.9923
Simazine	300.1766	11053.948	11037.9903	-316.1343	-10.7143

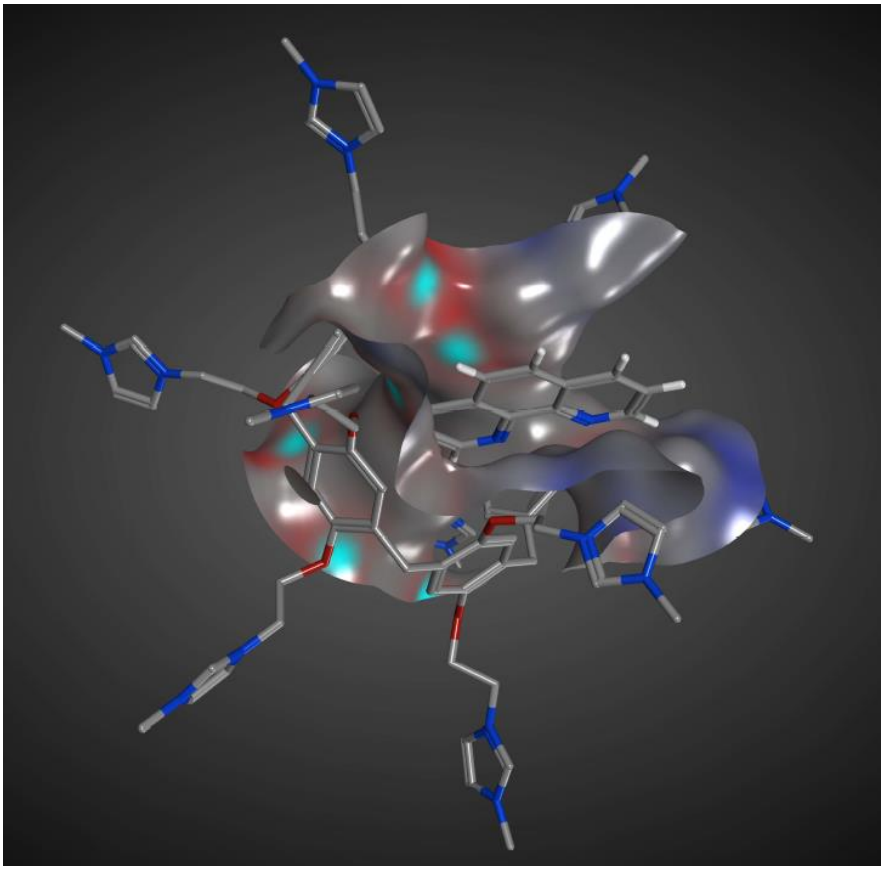

Figure S77. Docking of 1,10-phenonthraline in WSP5A

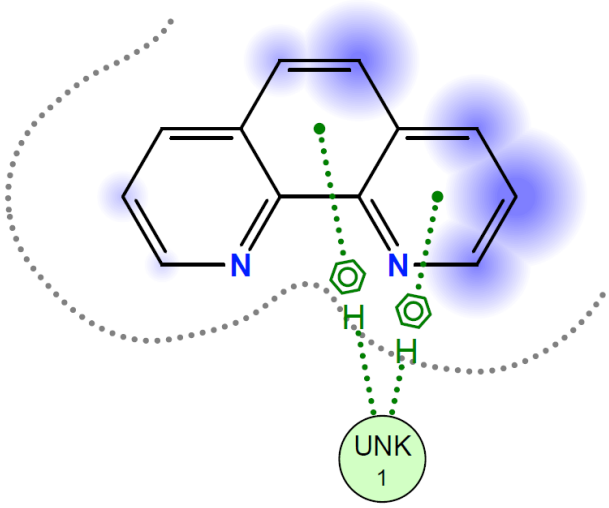

Figure S78. Ligand interaction of 1,10-phenanthroline in WSP5A

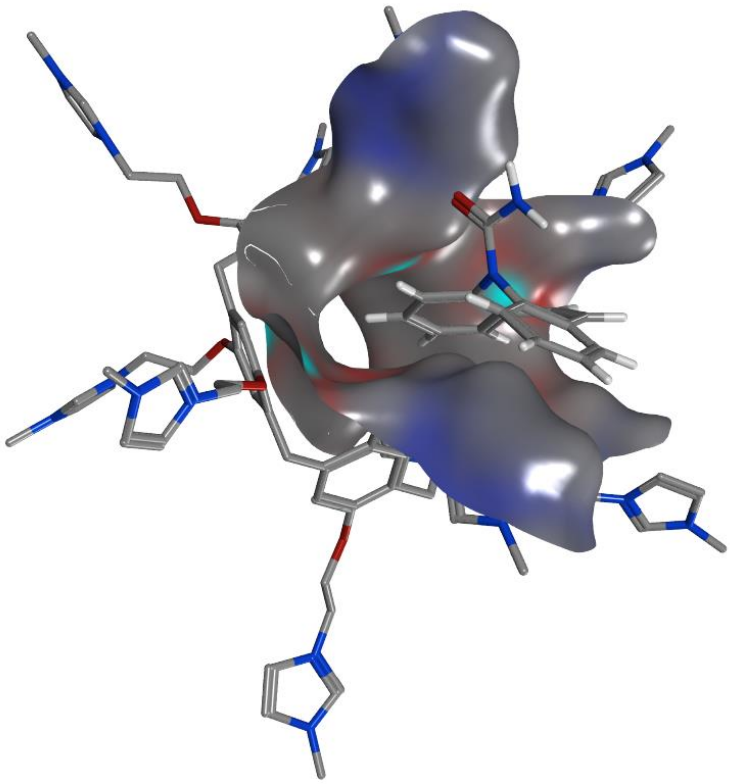

Figure S79. Docking of Carbamazepine in WSP5A

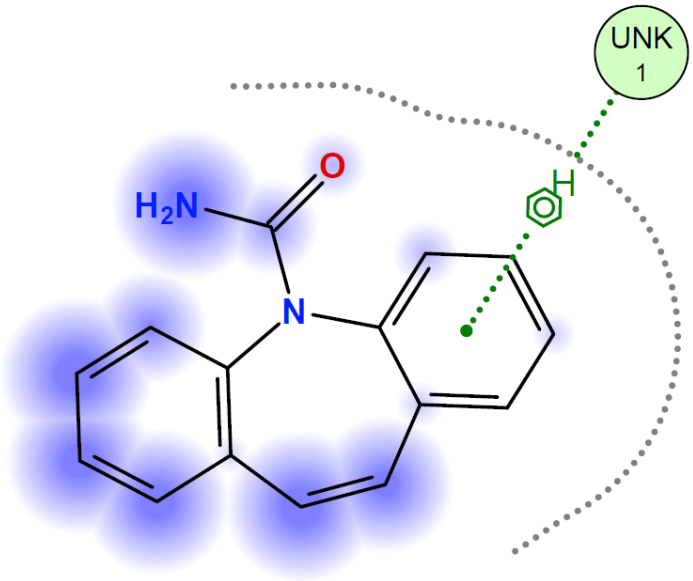

Figure 80. Ligand interaction of Carbamazepine in WSP5A

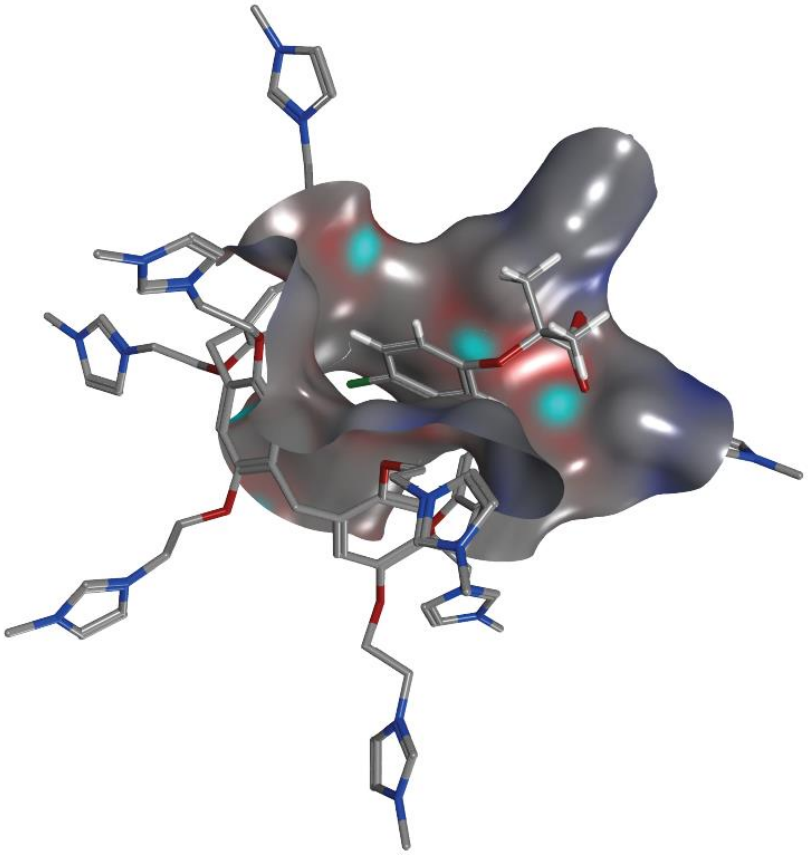

Figure S81. Docking of Clofibric acid in WSP5A

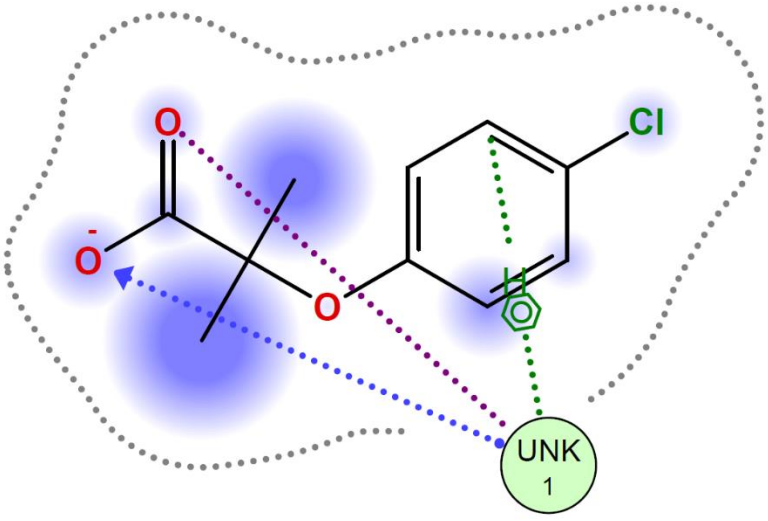

Figure S82. Ligand interaction of Clofibric acid in WSP5A

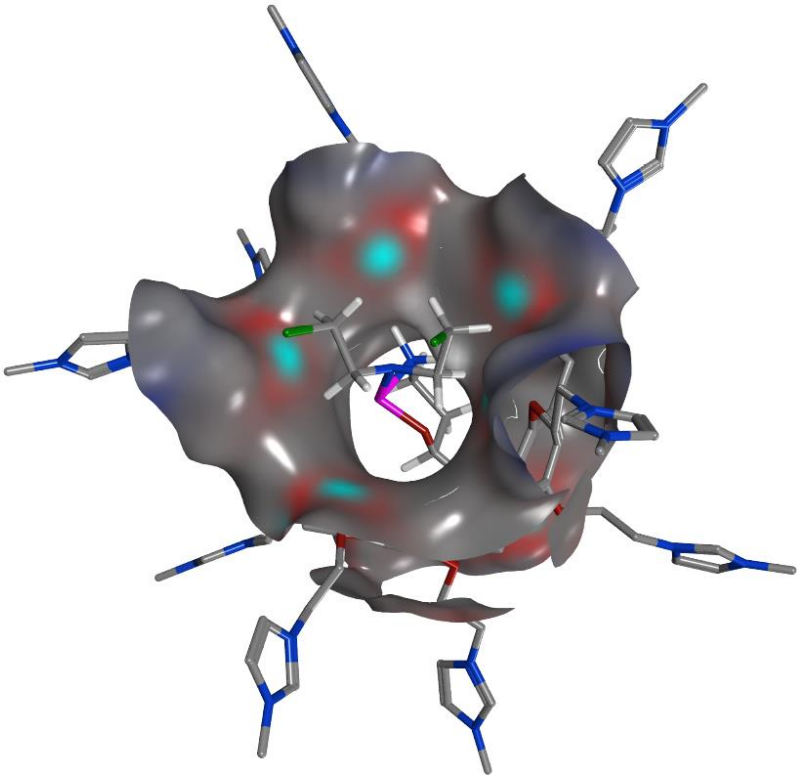

Figure S83. Docking of Cyclophosphamide acid in WSP5A

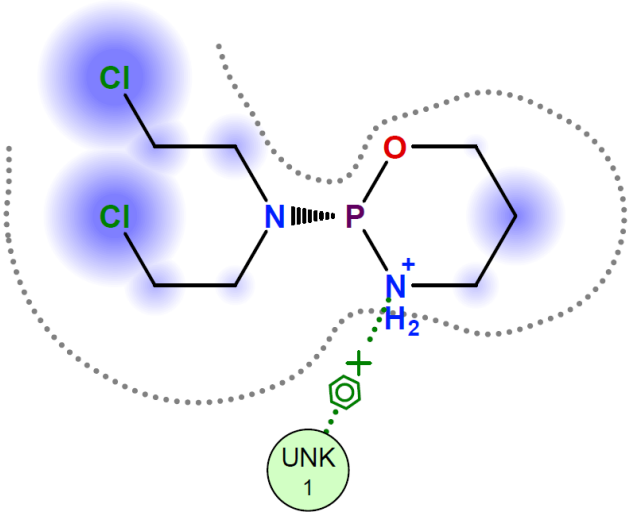

Figure S84. Ligand interaction of Cyclophosphamide acid in WSP5A

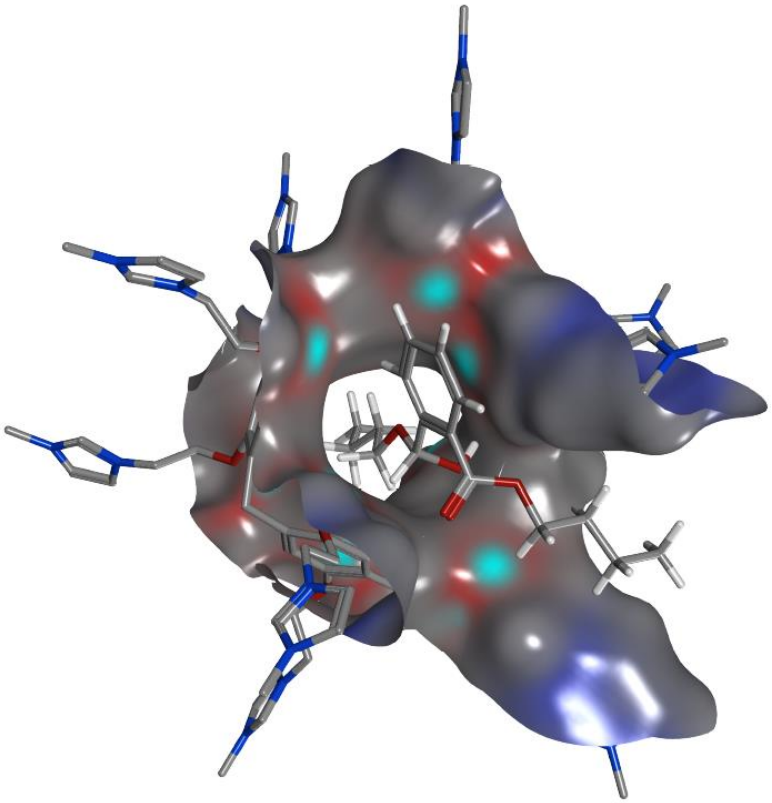

Figure 85. Docking of Dibutyl phthalate acid in WSP5A

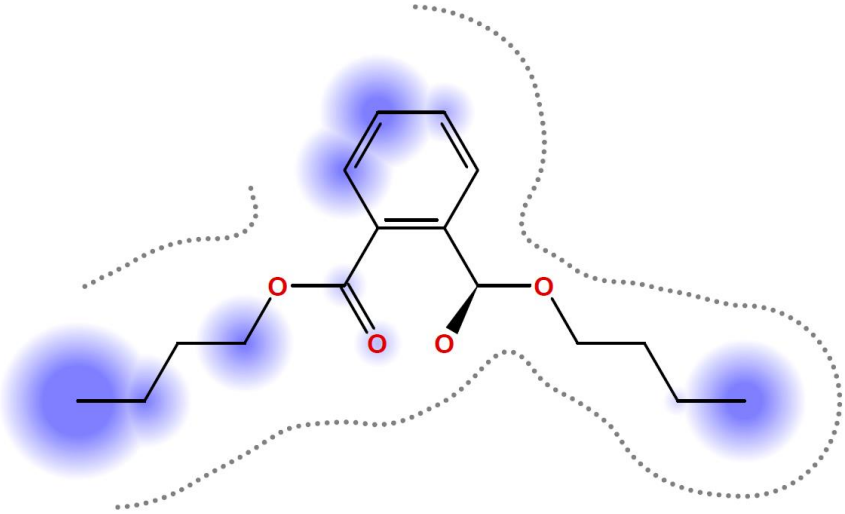

Figure S86. Ligand interaction of Dibutyl phthalate acid in WSP5A

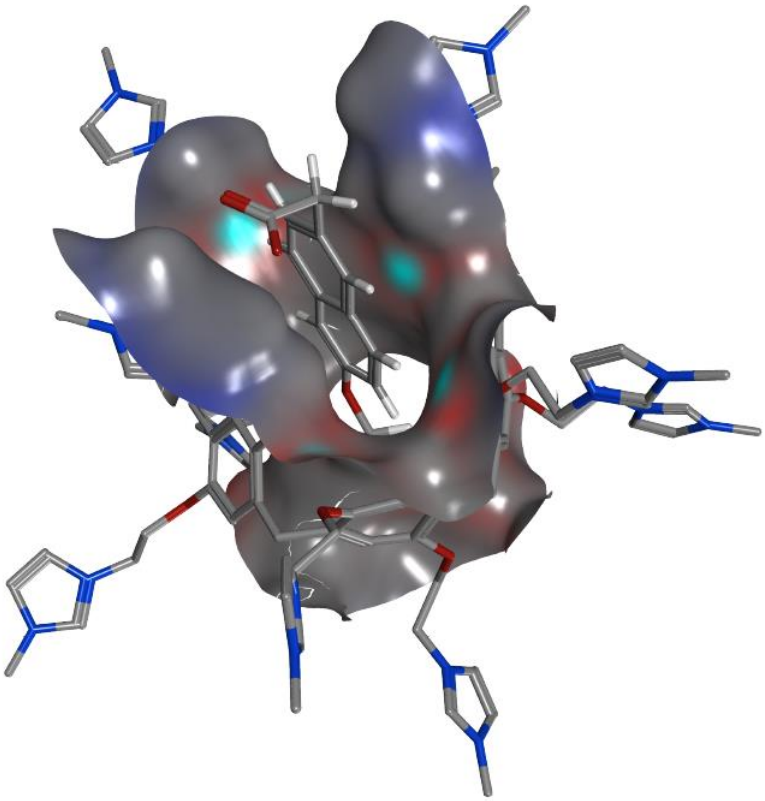

Figure S87. Docking of Naproxen in WSP5A

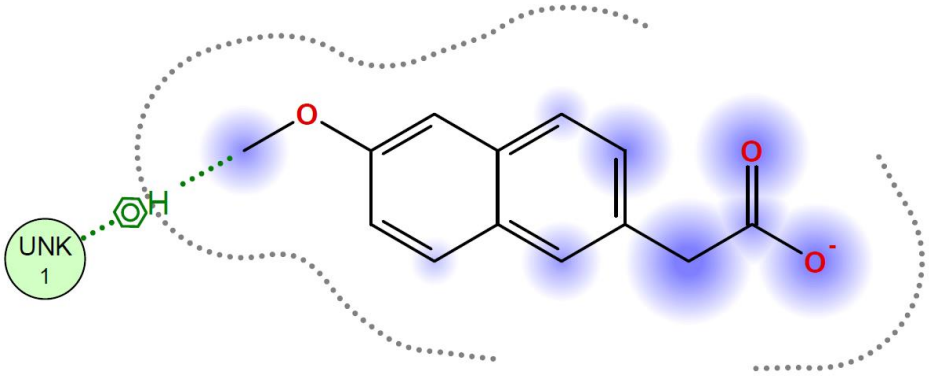

Figure S88. Ligand interaction of Naproxen in WSP5A

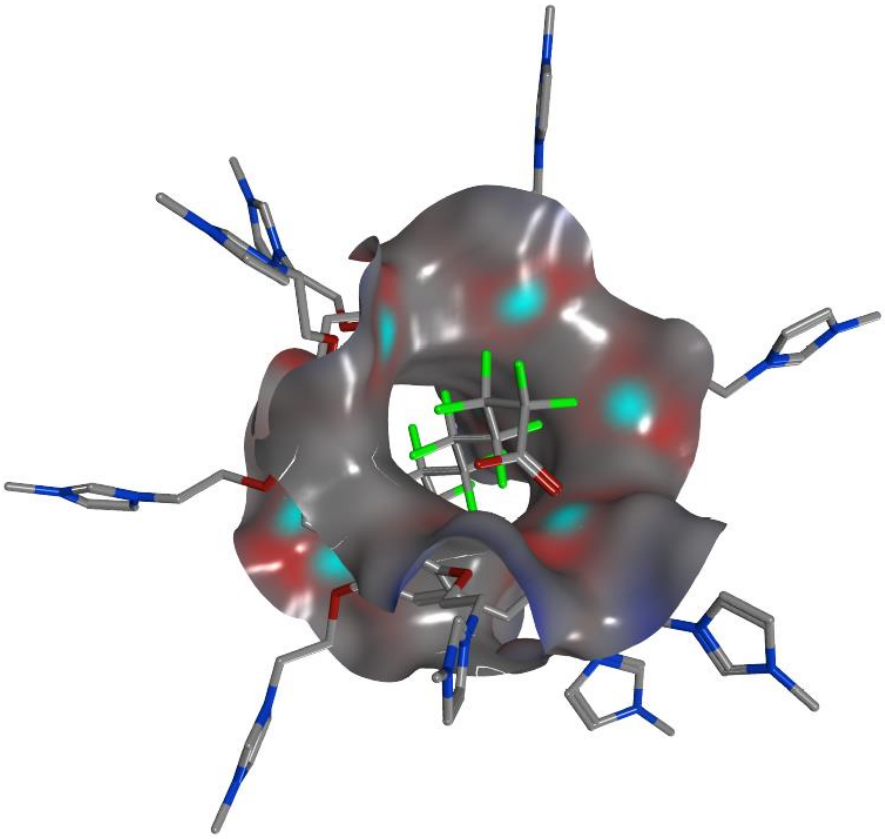

Figure S89. Docking of PFOA in WSP5A

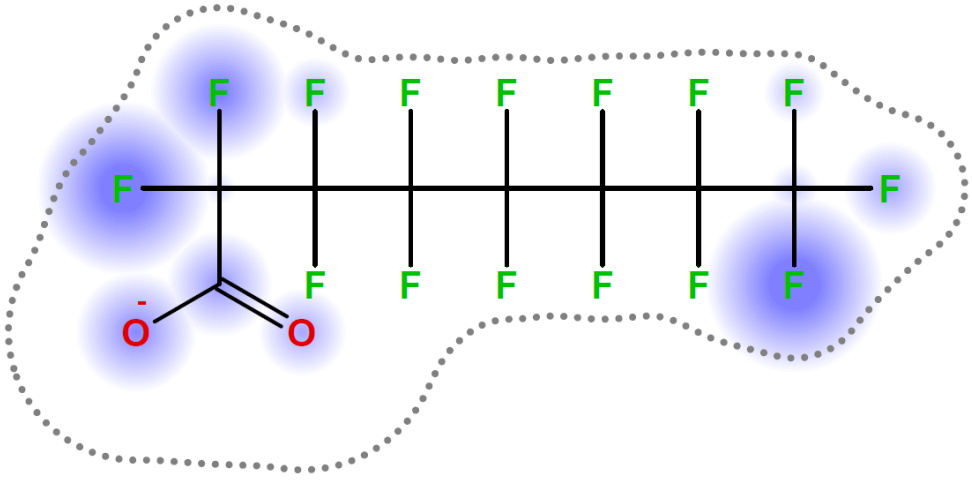

Figure S90. Ligand interaction of PFOA in WSP5A

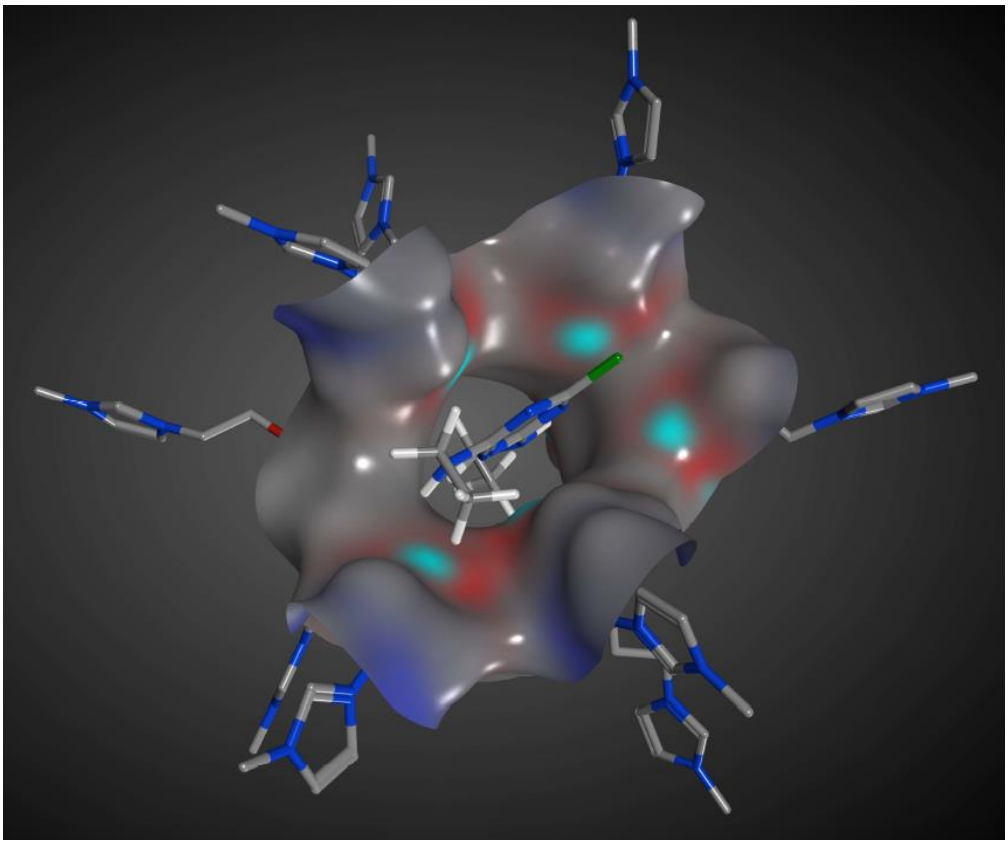

Figure S91. Docking of Simazine in WSP5A

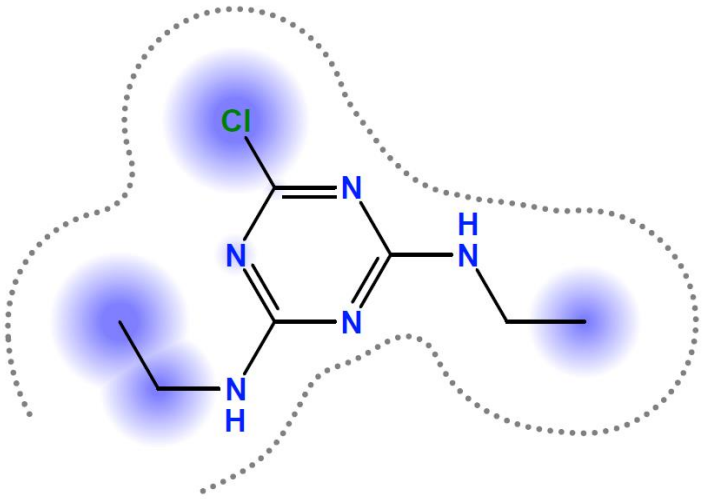

Figure S92. Ligand interaction of Simazine in WSP5A

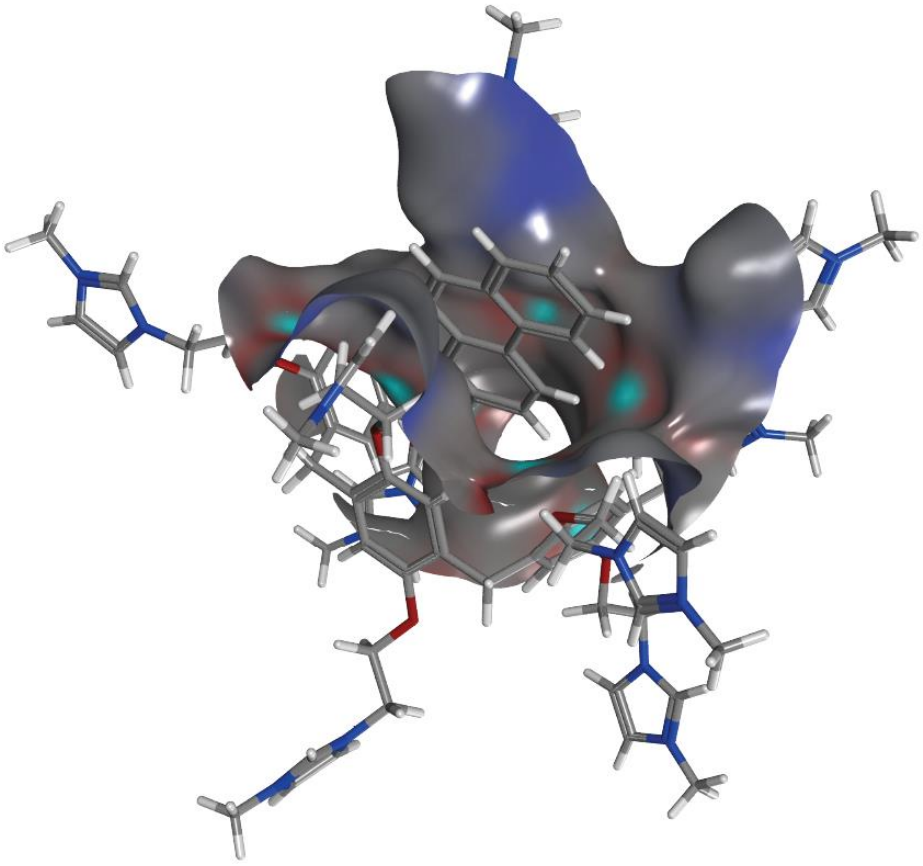

Figure S93. Docking of Phenancene in WSP5A

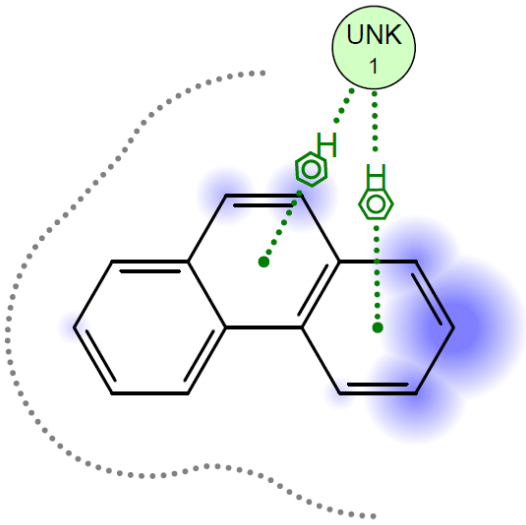

Figure S94. Ligand interaction of Phenancene in WSP5A

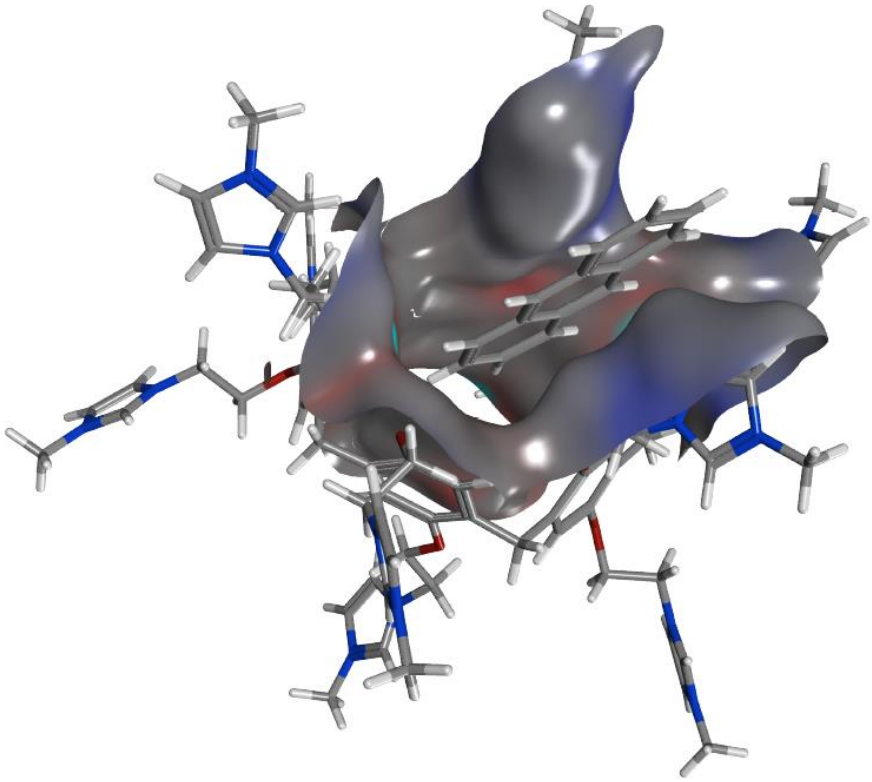

Figure S95. Docking of Anthracene in WSP5A

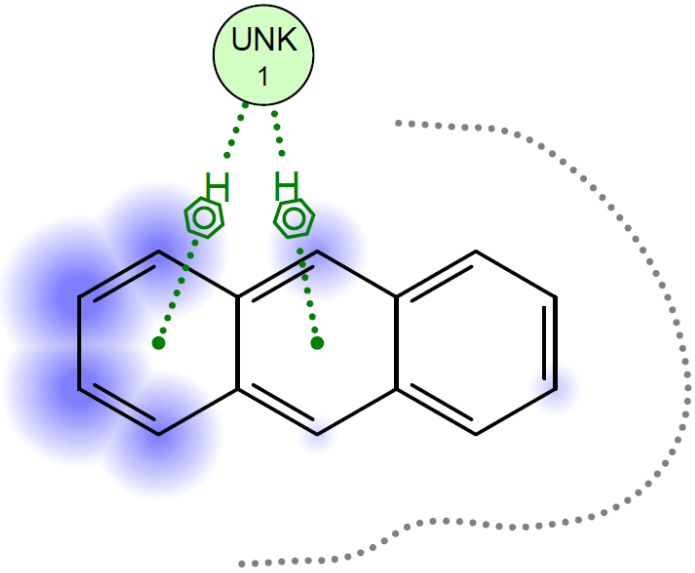

Figure S96. Ligand interaction of Anthracene in WSP5A

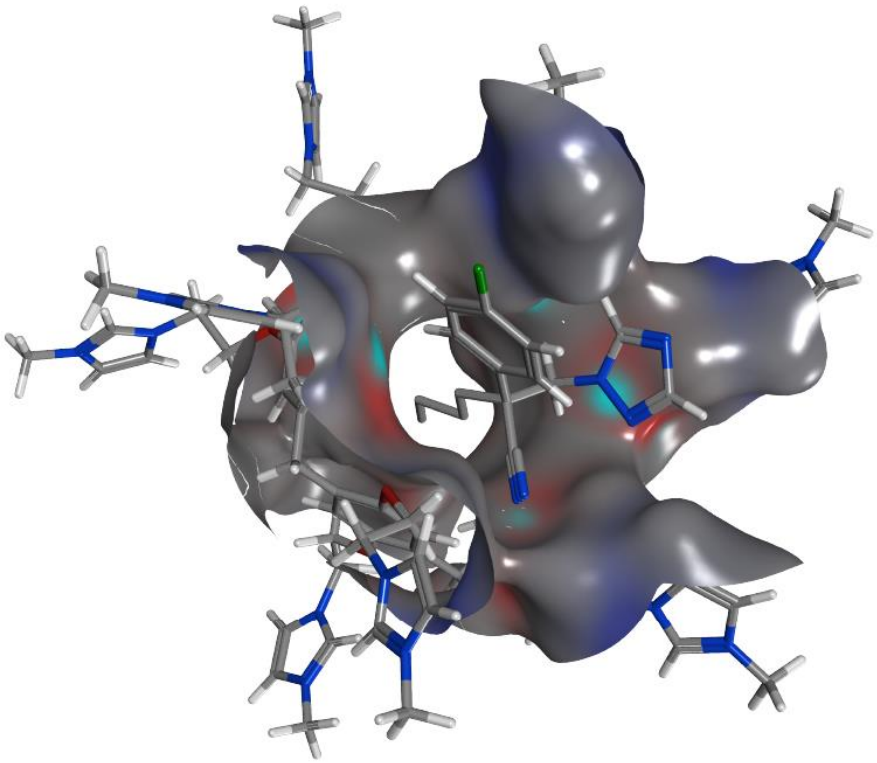

Figure S97. Docking of Myclobutanil in WSP5A

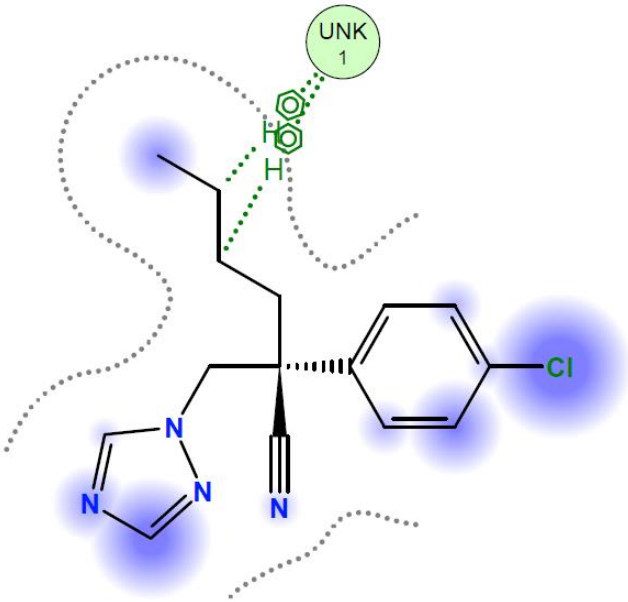

Figure S98. Ligand interaction of Myclobutanil in WSP5A

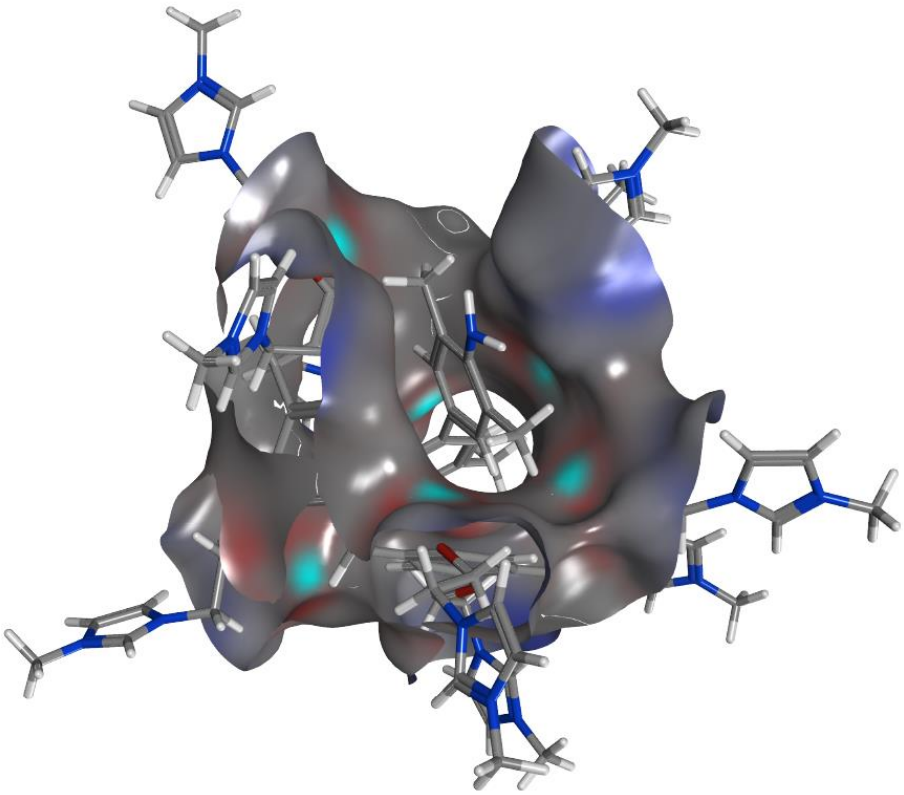

Figure S99. Docking of tetramethylbenzidine in WSP5A

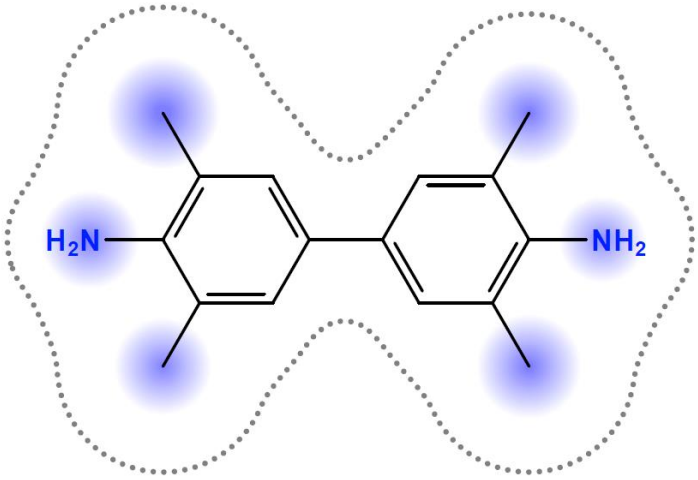

Figure S100. Ligand interaction of tetramethylbenzidine in WSP5A

NMR experiments

Equimolar concentrations (10mM) of WSP5A and Toxicants were prepared in DMSO-d_6; the reason for using DMSO was used because some of the toxicants are not soluble in water. Then these solutions were mixed in a 1:1 ratio in an NMR tube. These were then ultrasonicated for 5 minutes to enhance complexation. They were allowed out to equilibrate for another 10 minutes. Once equilibration was completed all NMR was performed in 400 MHz Bruker NMR spectrometer with 16 scans.

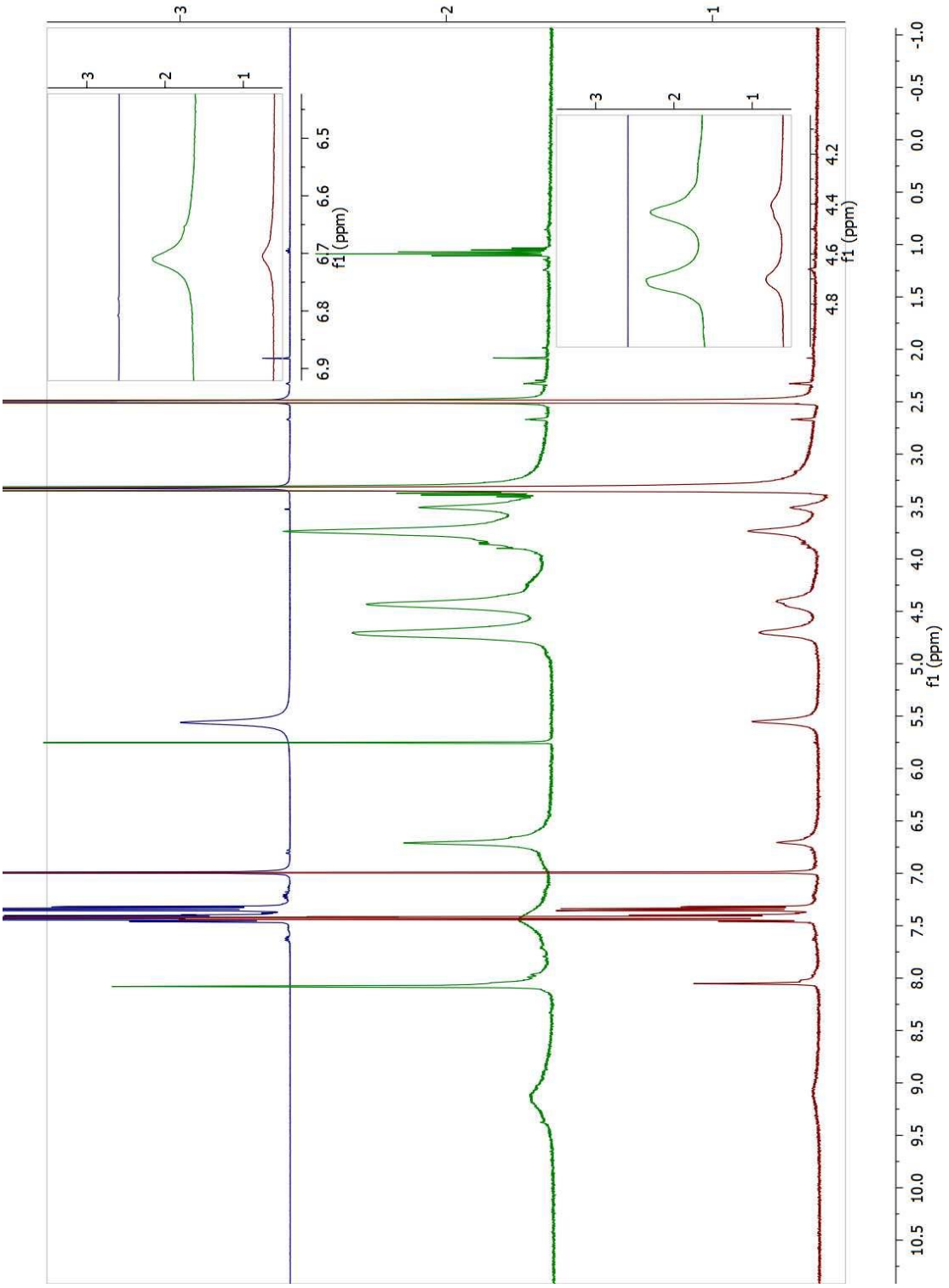

Figure S101. ^{1}H- NMR stacked spectra of Carbamazepine, WSP5A and complex

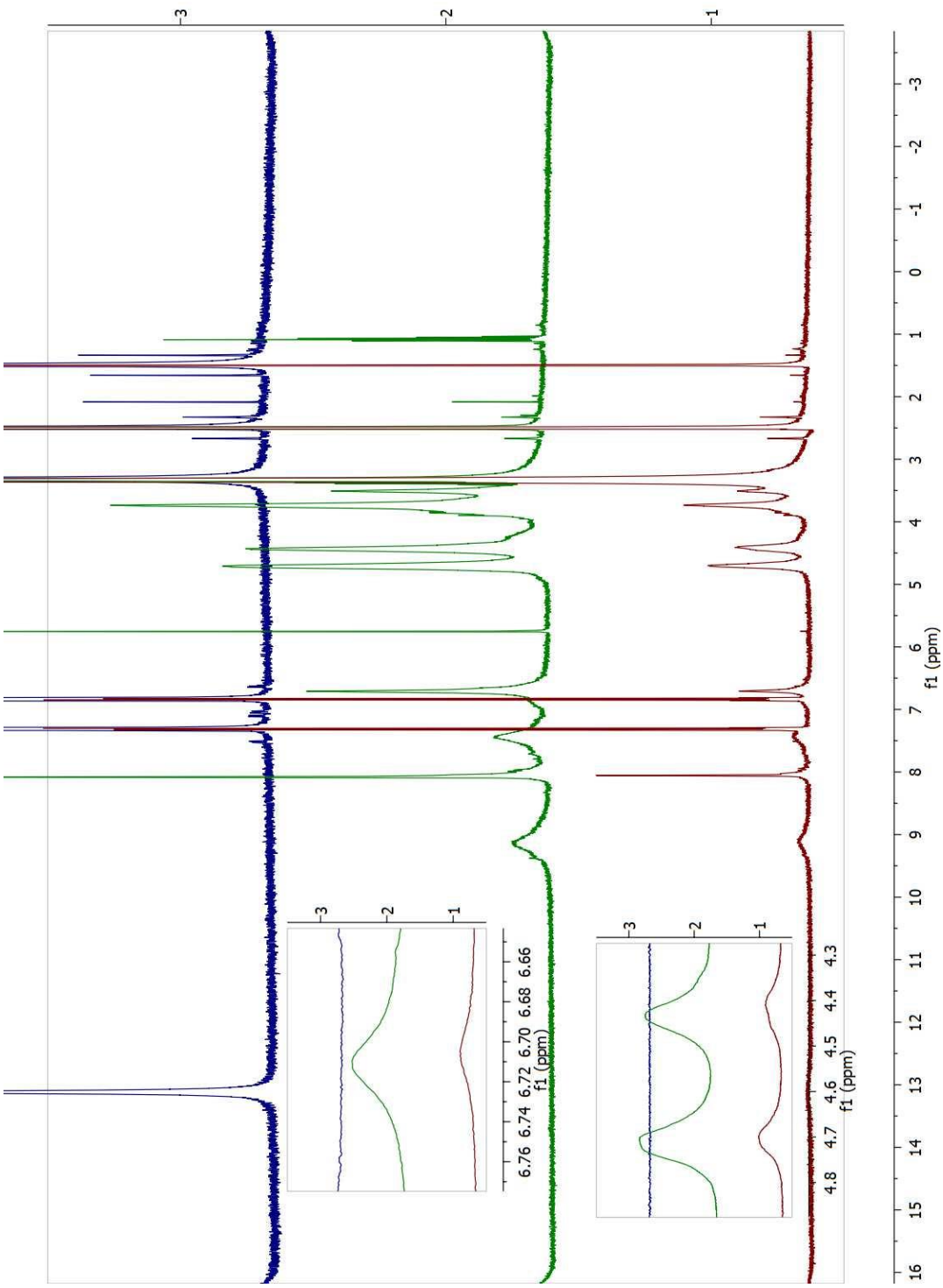

Figure S102. ^{1}H- NMR stacked spectra of Clofibric acid, WSP5A and complex

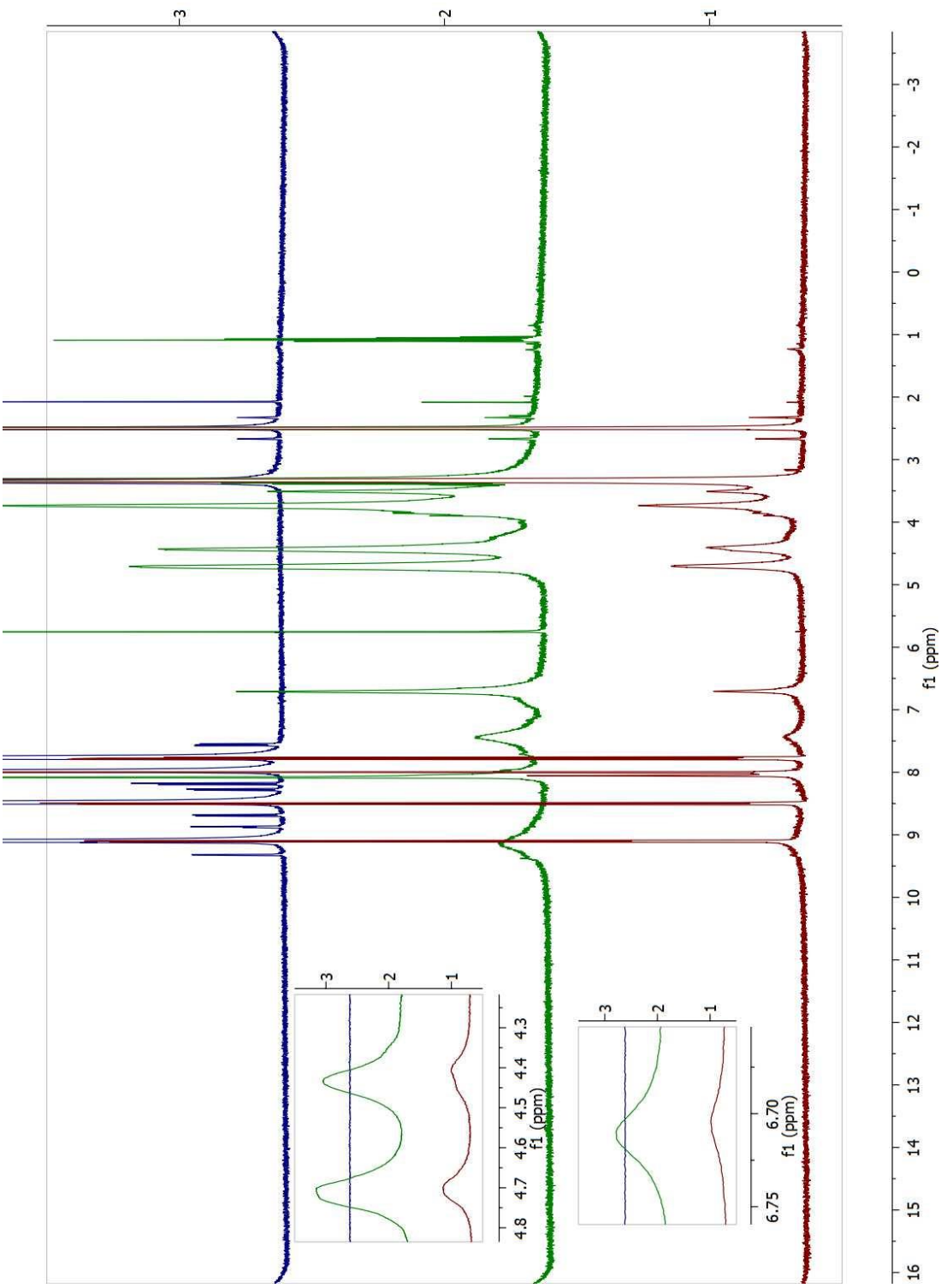

Figure S103. ^{1}H- NMR stacked spectra of 1,10-phenonthraline, WSP5A and complex

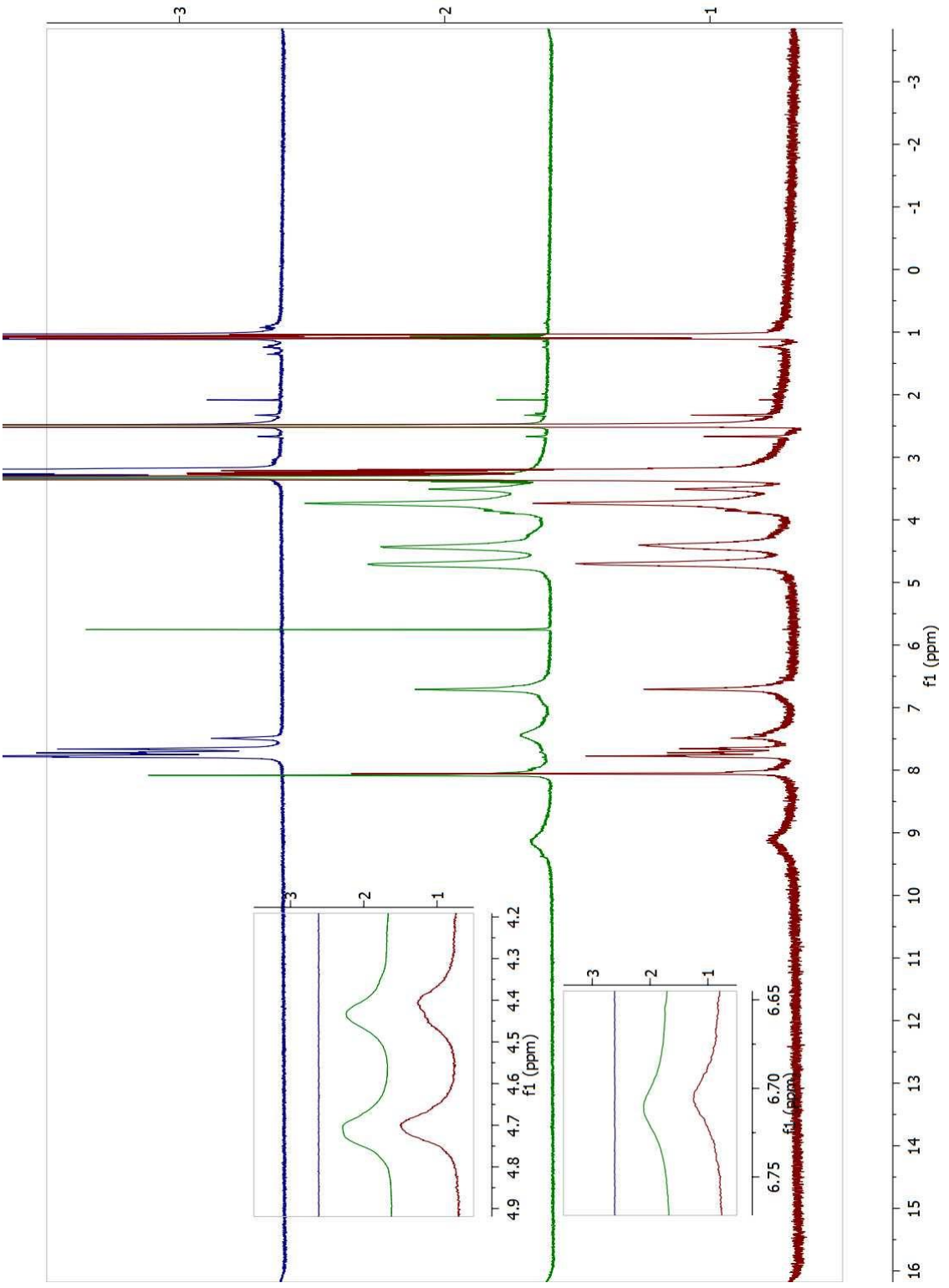

Figure S103. ^{1}H- NMR stacked spectra of Simazine, WSP5A and complex

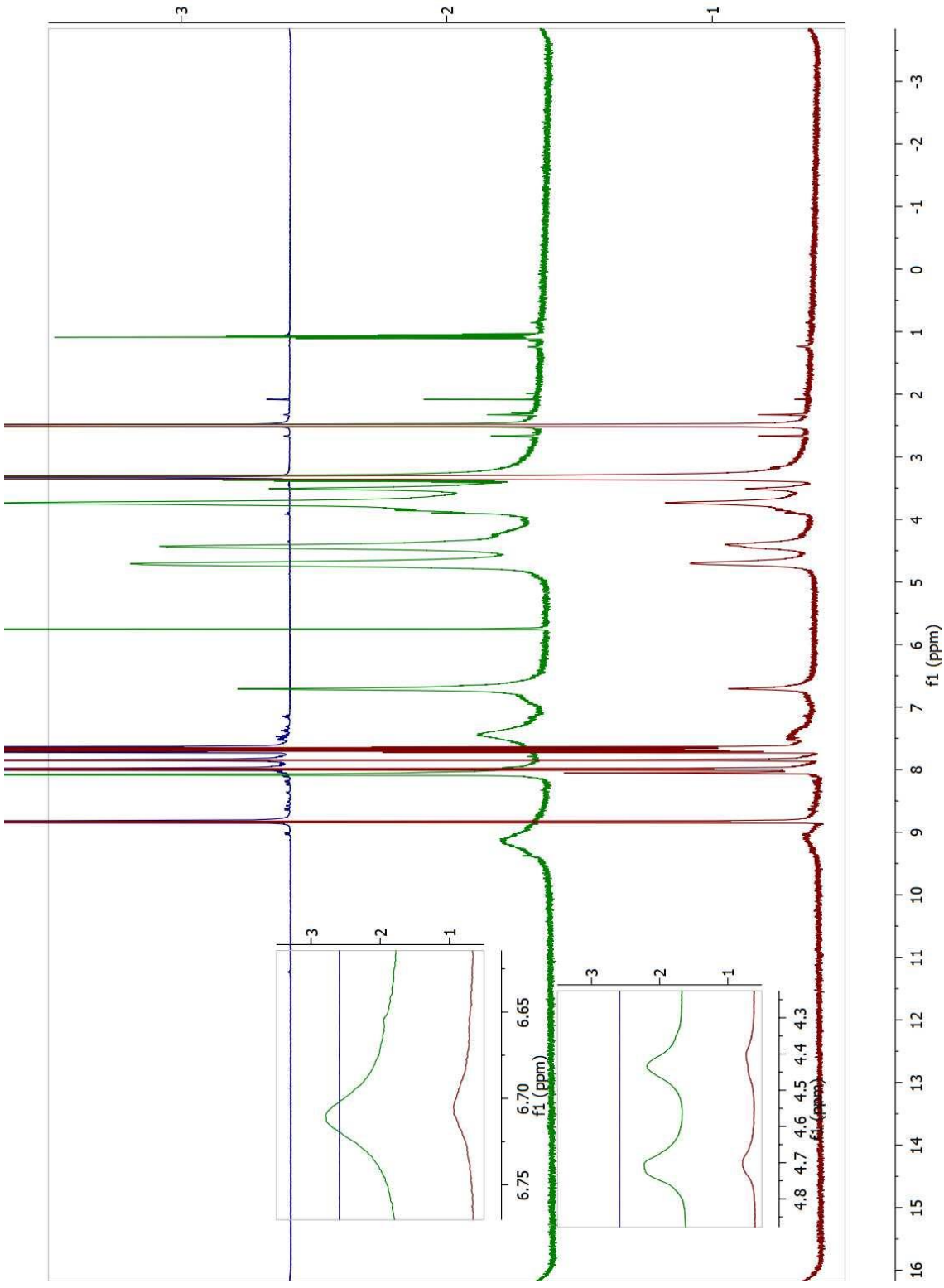

Figure S104. [1]H- NMR stacked spectra of Phenanthrene, WSP5A and complex

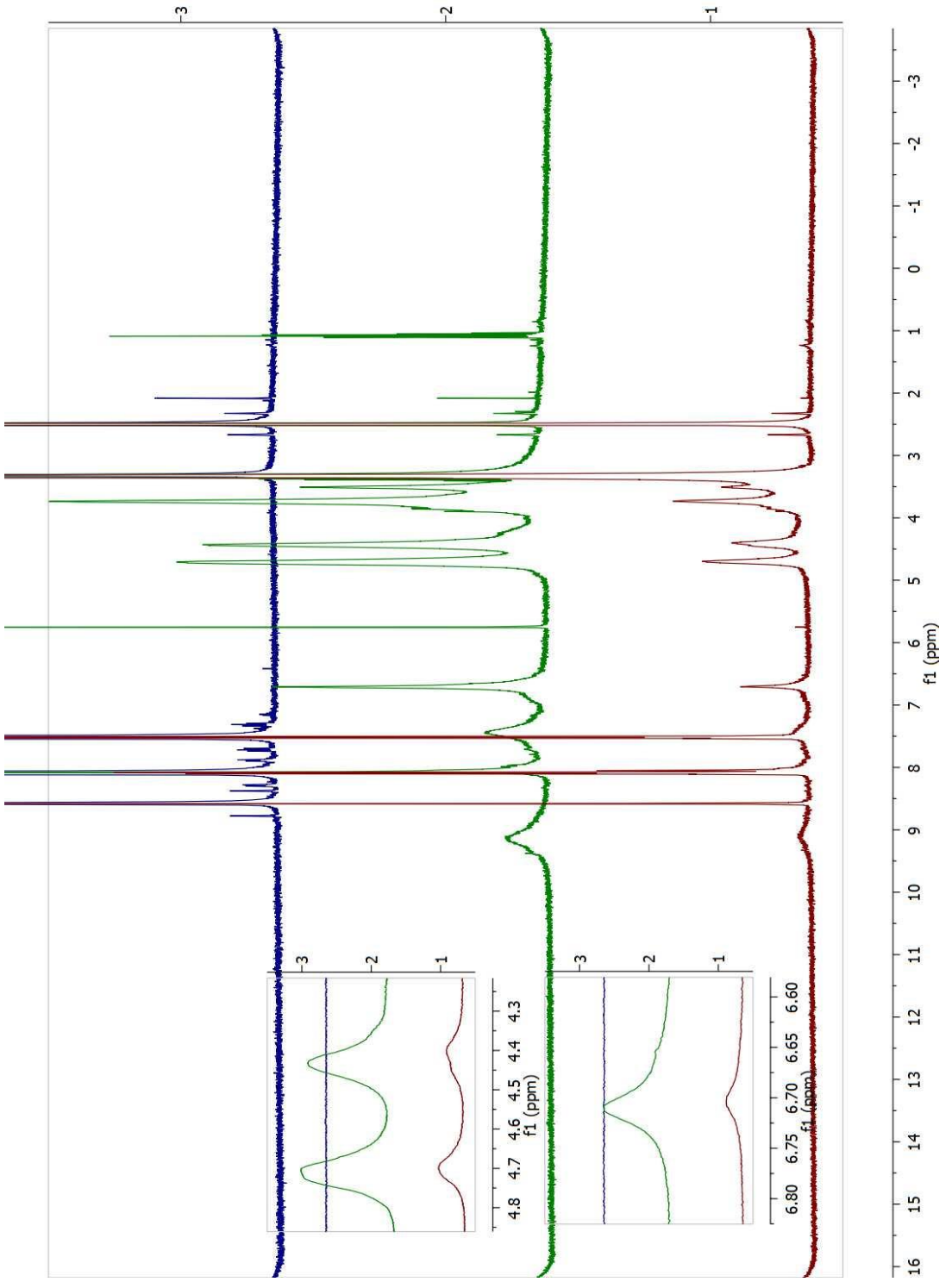

Figure S105. ^{1}H- NMR stacked spectra of Anthracene, WSP5A and complex

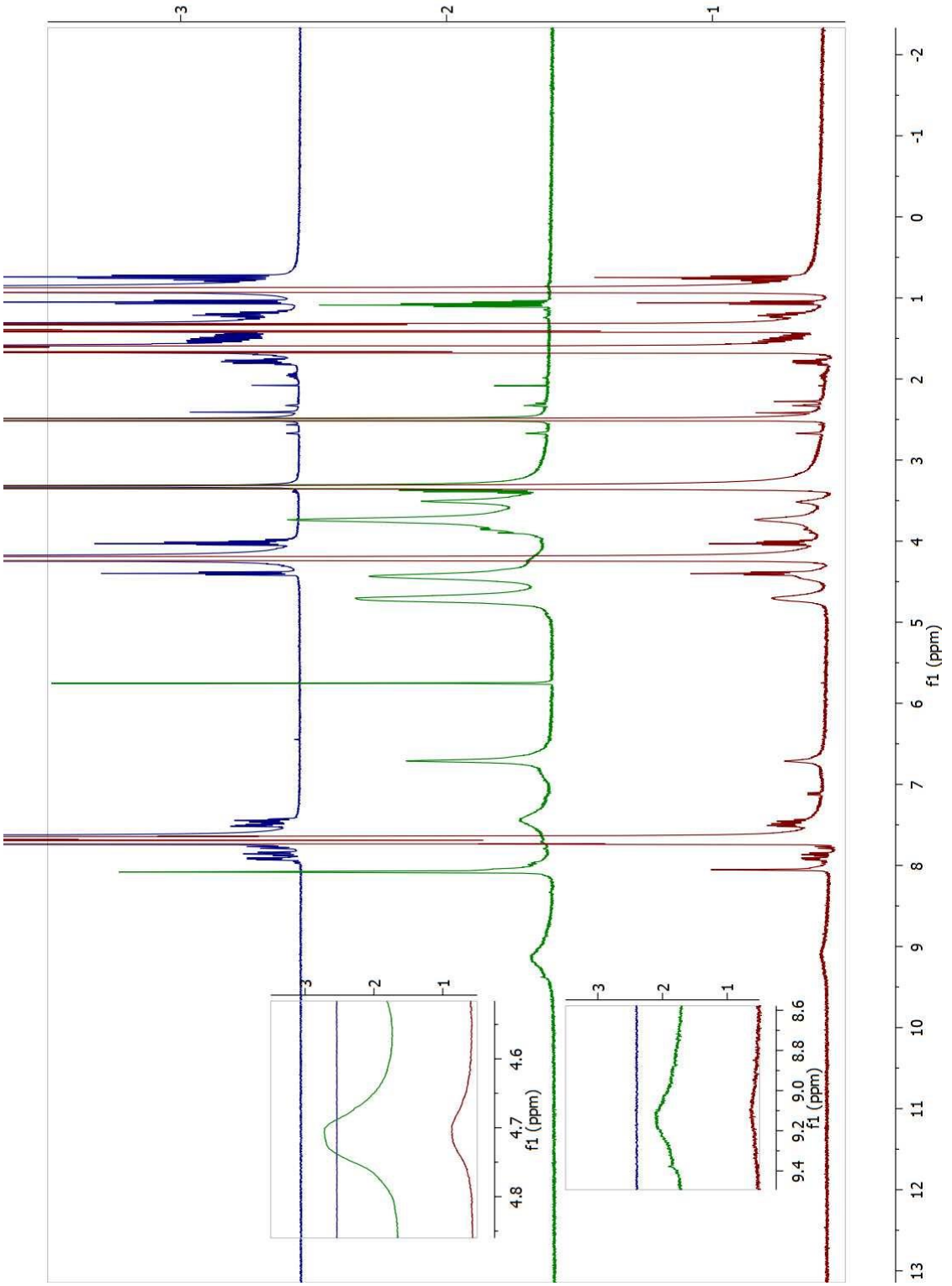

Figure S106. ^{1}H- NMR stacked spectra of dibutyl phthalate, WSP5A and complex

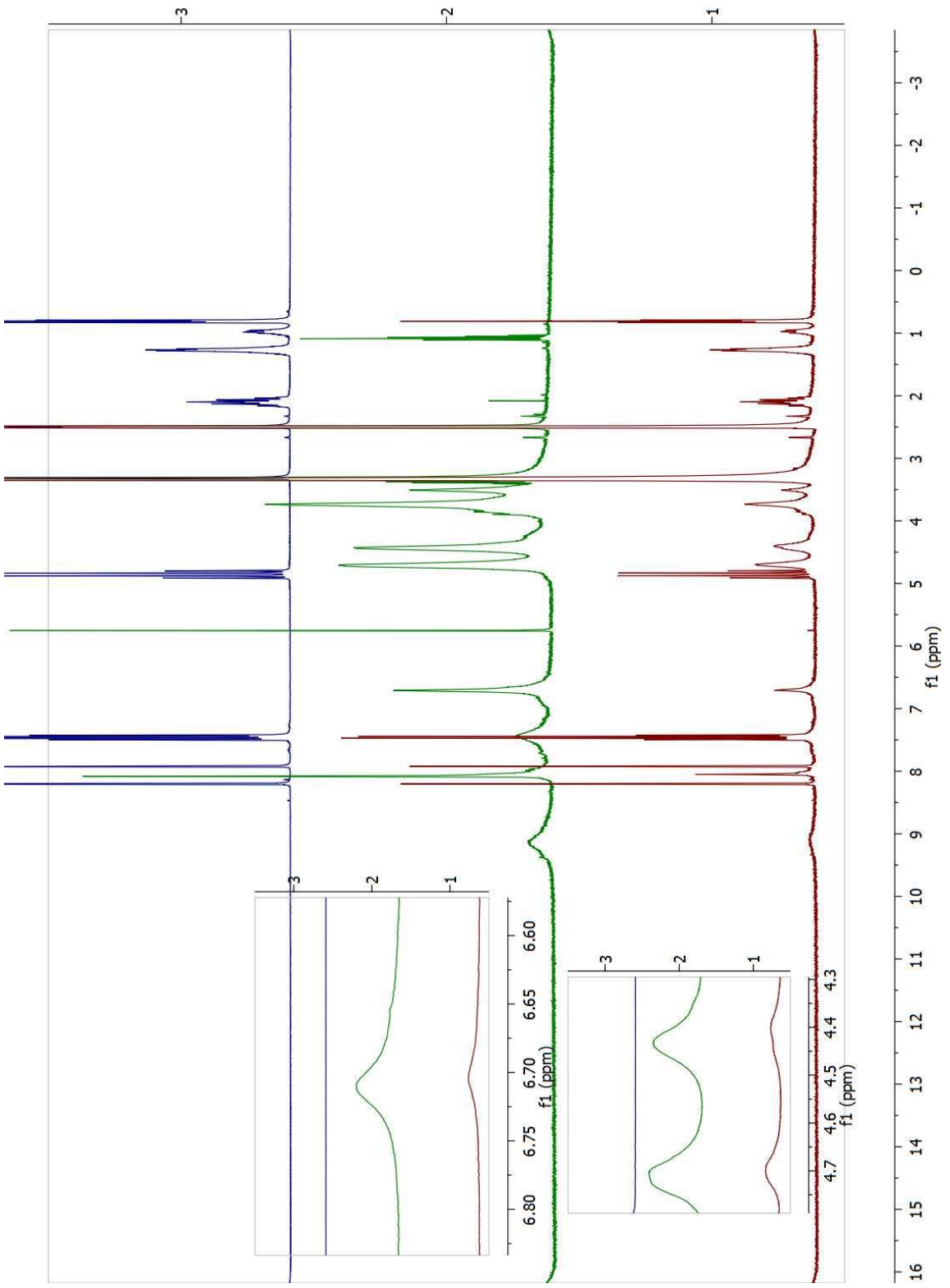

Figure S106. ^{1}H- NMR stacked spectra of myclobutanil, WSP5A and complex

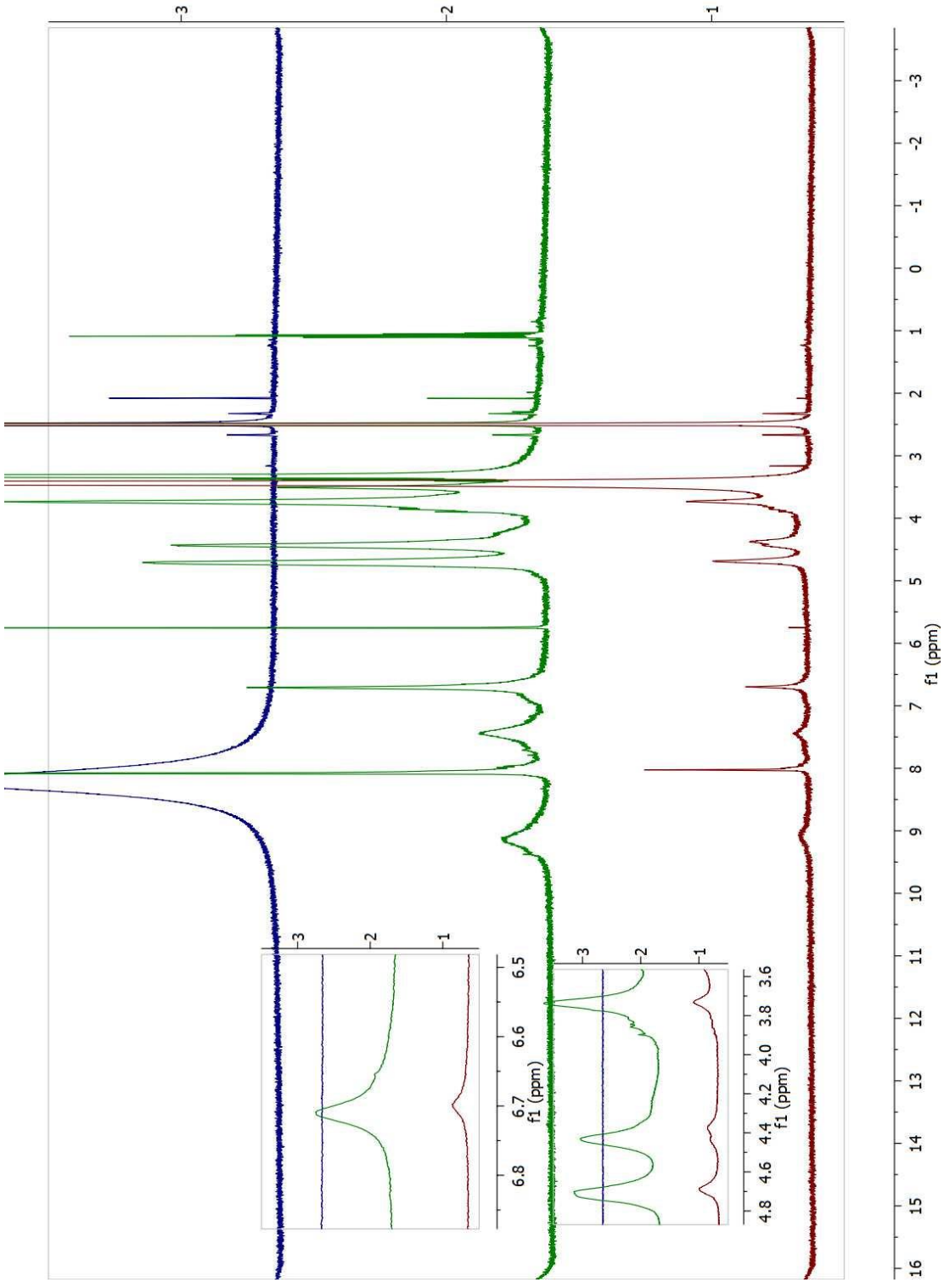

Figure S107. ^{1}H- NMR stacked spectra of PFOA, WSP5A and complex

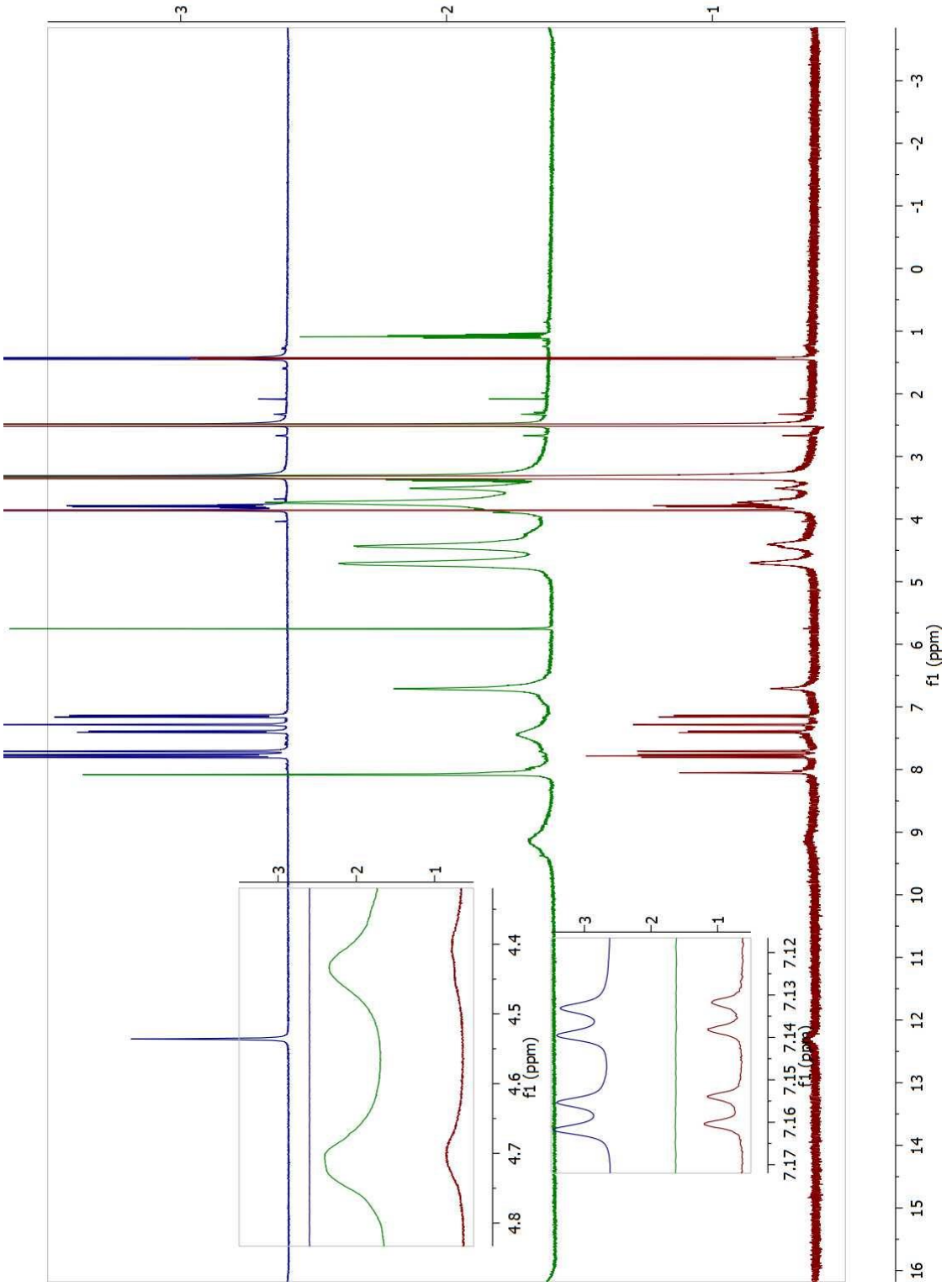

Figure S107. ^{1}H- NMR stacked spectra of Naproxen, WSP5A and complex

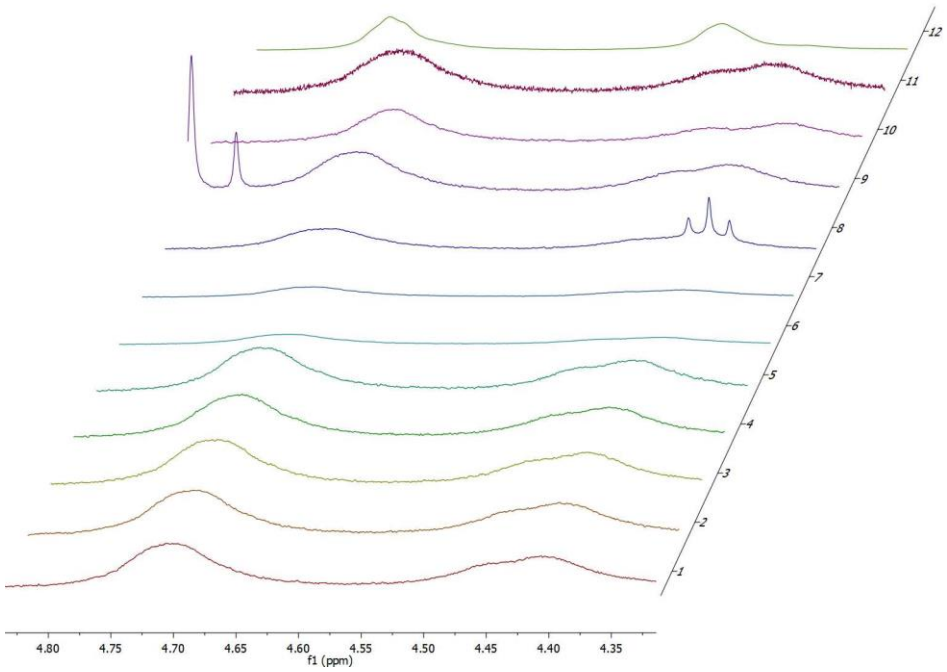

Figure **S108**. Stacked ^{1}H NMR of all toxicants in WSp5A with respect to reference WSp5A at 4.60 ppm

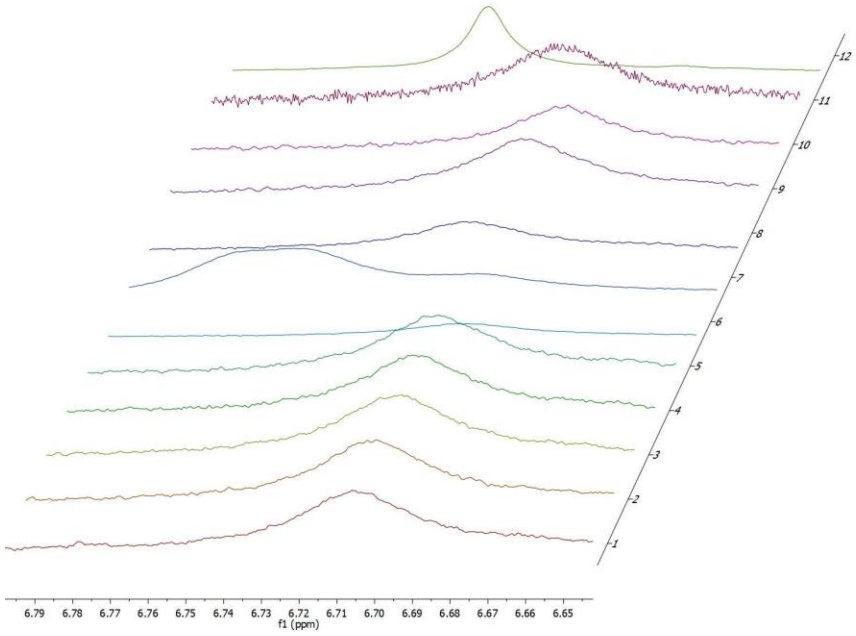

Figure **S109**. Stacked ^{1}H NMR of all toxicants in WSp5A with respect to reference WSp5A at 6.72 ppm

6 CHAPTER 6

Will be published in *ACS Biomacromolecules*

Double-stranded DNA-Water soluble P5A based self-aggregate composite material for removal of PFOA from an aqueous environment

Ashvin I Fernando, Paul Cesana, Adriana Mendieta, Jason R Dwyer and Brenton DeBoef

Department of Chemistry, University of Rhode Island, 140 Flagg Road, Kingston, Rhode Island 02881, United States

Abstract

We prepared water-insoluble self-assembled composite materials by stoichiometric mixing of water-soluble decamethylimidazolium pillar[5]arene (WSP5A) with dsDNA obtained from salmon milt. The WSP5A has the ability to encapsulate organic molecules into its intramolecular cavity; subsequent addition of dsDNA then forms the insoluble network material. By employing this strategy, the WSP5A-dsDNA composite material was used for the sequestration and removal of the environmental pollutant, perfluorooctanoic acid (PFOA), from aqueous media.

Introduction

Double-stranded DNS (dsDNA) is a very stable structure and has unique structural properties.[1] The dsDNA contains a backbone that is consists of phosphate groups which can act as a negative charge barrier. In this study, we used dsDNA that is cheap and readily available from salmon testes. It was reported in the *Hokkaido Bureau of Economy Journal* that more than 10,000 tons/year of milt from salmon trout and others have been removed as industrialized wastes from fishery industries in Hokkaido, Japan[2] The cost of using milt is low, which enables us to use milt as a cost-effective material in this study and to be expanded into practical applications. Also, milt is an environmentally friendly biomaterial that has no hazardous effects on the environment after use.

The high anionic charge present salmon milt, due to the phosphate backbone in the DNA has been previously used for capturing rare earth elements.[2] This dsDNA is stable and can be used for several months when its stored at 4 °C. In general applications, salmon testes DNA is used as a substrate for deoxyribonuclease assays and other molecular biological techniques.

Pillar[5]arenes (P5A) were first discovered by Ogoshi and his group;[3] these five-membered supramolecular structures are formed via a Lewis acid-mediated Friedls-Crafts reaction between formaldehyde and hydroquinone derivatives. In the recent past, this structure has been widely used in multiple applications, such as rotaxane synthesis, drug delivery, imaging applications, etc. P5As are highly versatile and can be functionalized in various ways. P5A is also used for host-guest studies because the hydrophobic cavity can bind small molecules tightly.

Perfluoroalkylated substances (PFAS) are both environmentally persistent[4] and lack straightforward detectable methods, which means that the development of methods for their removal from contaminated environments is particularly urgent.[5] Currently utilized methods for PFAS removal include the use of covalent organic frameworks to remove PFAS,[6] cyclodextrin

polymers for micropollutant (including PFAS) removal,[7] chemical oxidation procedures to generate highly polar, water-soluble PFAS byproducts,[8] and the use of carbon adsorbents to remove PFAS from contaminated water,[9] Practical drawbacks to these methods include the fact that oxidation procedures that generate water-soluble waste products still result in contamination of the water supply, and the use of carbon-based absorbents is often non-selective.

The use of a soluble supramolecular based material for PFAS sequestration and removal has not been reported to date, even though such macrocycles could provide maximum flexibility by binding PFAS while in solution and could be designed to be removed from solution with ease.

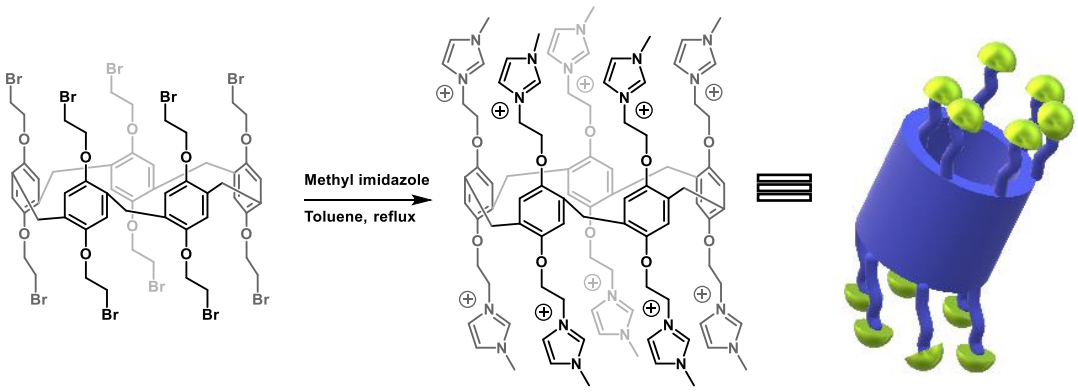

Figure 6.1: Synthesis of dmWSP5A (left), cartoon representation of the dmWSP5A (right)

This project focused on using the dsDNA as an anchor to hold a host structure. The host structure of choice was water soluble methyl imidazolium pillar-5-arene. The methyl dmWSP5A has been used for toxicant removal in our previous studies. The concept we wanted to show in this study is the use of simple electrostatic interactions in aqueous media to form a self-assembled structure that will capture small molecules from water and clump together. This complexed material with the harmful toxicant can then be removed from solution by physical means.

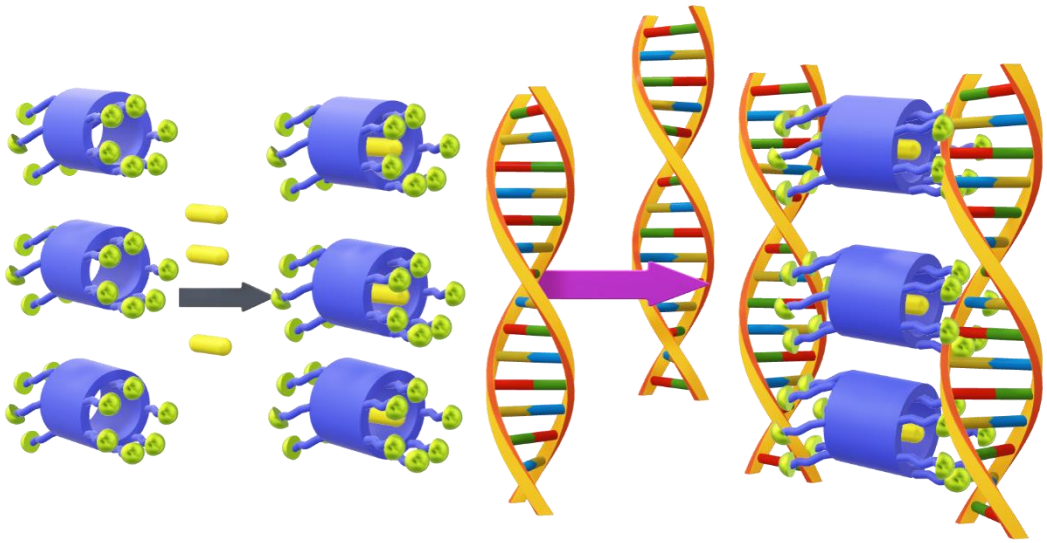

Scheme 6-1: Schematic representation of the self-assembled dsDNA-dmWSP5A composite material for encapsulation of PFOA

Experimental section

Materials. Double-stranded DNA (sodium salt from salmon milt, molecular weight approx. 5×10^6). Carbon tetrabromide, PFOA, boron trifluoride etherate, and *N*-methylimidazole were purchased from Fisher Scientific. Paraformaldehyde was purchased from Baker Chemicals. All solvents and chemicals were purchased from Sigma-Aldrich or Fisher Scientific. Decabromopillararene, **1**, was synthesized according to literature procedure.[16]

Synthesis of decamethylimidazolium pillar[5]arene, A mixture of **1** (1.68 g, 1.00 mmol) and *N*-methylimidazole (1.64 g, 20.0 mmol) in toluene (25 mL) was stirred in a 40 mL pressure tube at 120 ºC for 24 hours.[16] (The use of a pressure tube was essential for the success of the reaction in our hands.) After cooling, the solvent was removed by rotatory evaporation. The collected residue was recrystallized from ethanol/diethyl ether (1:2) to give a white solid (2.1 g, 87%). NMR and mass spectra are shown in the attached supplementary information.

Preparation of dsDNA-dmWSP5A Composite Material, When an aqueous solution of double-stranded DNA sodium salt (dsDNA) combined with an aqueous solution of WSP5A, a white, gelatanous precipitate formed. The composite material can be formed using a stoichiometric 1:1 ratio of dmWSP5A: dsDNA. This fact is interesting in that similar composite materials require a much greater ratio of dsDNA to the host.

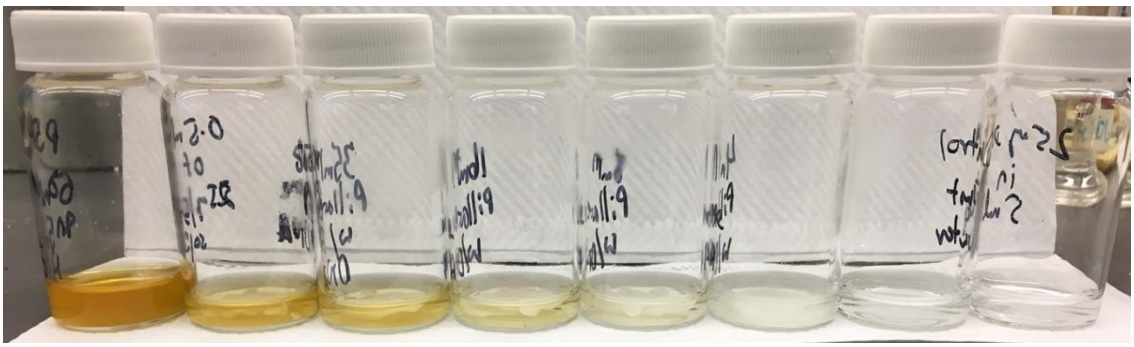

Figure 6.2: Stochiometric assay of dsDNA with dmWSP5A. From R to L decreasing WSP5A concentration while the dsDNA concentration was held constant

Accumulation of harmful PFOA This is done by first adding 40 mM WSP5A solution to a solution of 20 mM PFOA. The WSP5A rapidly encapsulated the PFOA as it reached equilibrium. Next, dsDNA was added to the PFOA/WSP5A mixture, the complex was formed instantly, and it could subsequently be removed from the vial. The resulting supernatant solution was tested for PFOA using ^{19}F NMR. The precipitate was allowed to sit in fresh water to test whether PFOA would leach from the sold. After 6 months, no leaching was observed.

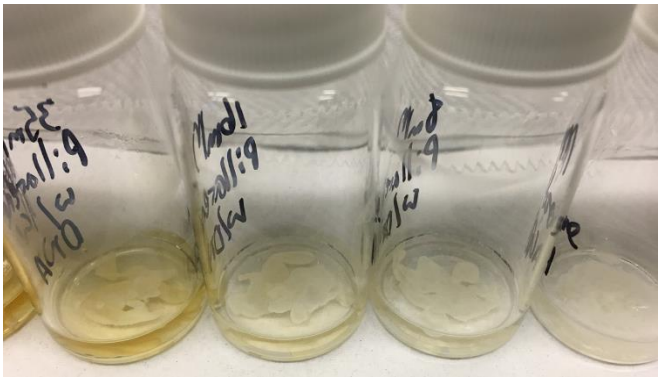

Figure 6.3: Zoomed image of self-assembled composite material in aqueous media (gelatinous)

Results and Discussion

The formation of the dsDNA-WSP5A material was obtained by simple mixing of the aqueous dsDNA (100 μL, 20 mg/mL) and WSP5A (10-100 μL, 200 mg/mL) solutions. We conducted a concentration variation assay, to find the most optimum concentrations for the formation of the composite material. Hence, we discovered that at very low concentrations (below 0.1 mM) of WSP5A such formation is weak, but after 1:1 or slightly higher concentrations/stoichiometries more composite material were observed as seen in Figure 6-2 and 6-3. At very high concentrations of WSP5A (500 mM), we did not see any composite material formation; we assume that this is due to the lack of enough dsDNA to accommodate the excess WSP5A. The visual observation cue for this experiment is the formation of white gel-like material from solution. This gel looks like a "Lava lamp" and is a very distinct way of identifying product formation. This gelatinous material is insoluble in water and common organic solvents such as dichloromethane, ether, methanol, DMSO or NMP. This gel can be then be stored in ultra-pure water for more than six months without any degradation of the structure (Figure 4). All the composite material was made at pH 7, and the material was stable at pH 7. The figure shows the changes in composite material formation going from lower stoichiometric ratios to higher ratios (0 to 1.8 equivalents of WSP5A).

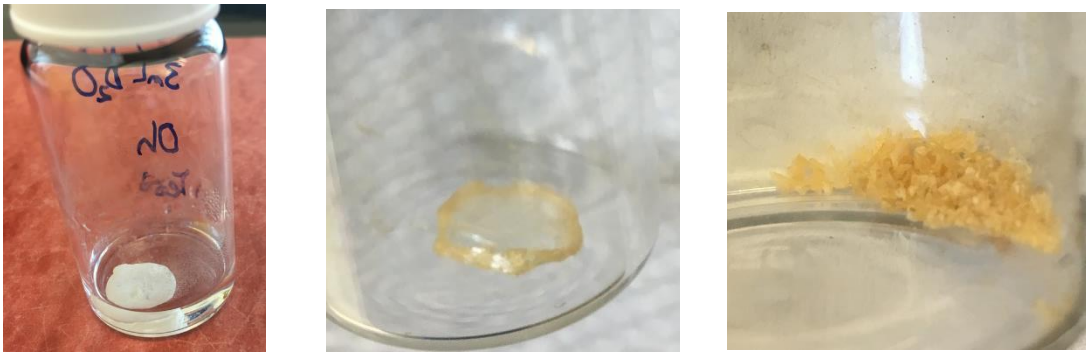

Figure 6.4: L to R, Stable self-assembled composite material in ultra-pure water after six months, Composite material after drying under vacuum and crushed dried composite material

Another interesting phenomenon was the dependence of the rate of addition of dsDNA solution into the WSP5A solution; the cloudy white material takes on different forms. If dsDNA is added slowly or dropwise, individual strands or drops of the composite material can be formed in the solution. If dsDNA is added quickly, the composite material forms a long string. Our general hypothesis is that electrostatic interactions between the negatively charged phosphate backbone[11] of the dsDNA and the ten positive charges from the methylimidazolium groups on the P5A form the composite material.

Furthermore, the composite material can be removed from the aqueous solution after being formed using only tweezers, making it very easy to manipulate and use. This material can also be dried to produce a long rigid string of material that is still brittle enough to be broken. Its brittleness allows one to obtain a powder of the composite material.

Characterization of dsDNA-dmWSP5A composite material. Though the composite material's ability to precipitate from solution and its insolubility are significant assets to our work, it also provides drawbacks in terms of structure determination. The pseudorandom nature of the dsDNA sequence makes crystallography unsuitable. However, we were able to obtain IR spectroscopy measurements and thermogravimetric analysis (TGA). As shown in Figure 6-5, WSP5A (green)

has a broad IR signal at 3000 cm^{-1} which indicates C-H stretching vibrations for WSP5A and the broadening significantly shows the vibration of these flexible imidazole containing arms. When these imidazoles form a strong interaction with the negatively charged backbone of the double-stranded DNA the flexibility is converted into a more rigid structure; hence the 3000 cm^{-1} broad signal is no longer seen. Another significant change is shown in the phosphate vibrations; The 1238 cm^{-1} peak has moved from left to right going from free DNA to self-assembled complex, which represents the interaction of DNA with WSP5A. This data aligns with a similar study performed by Hasimato.[12]

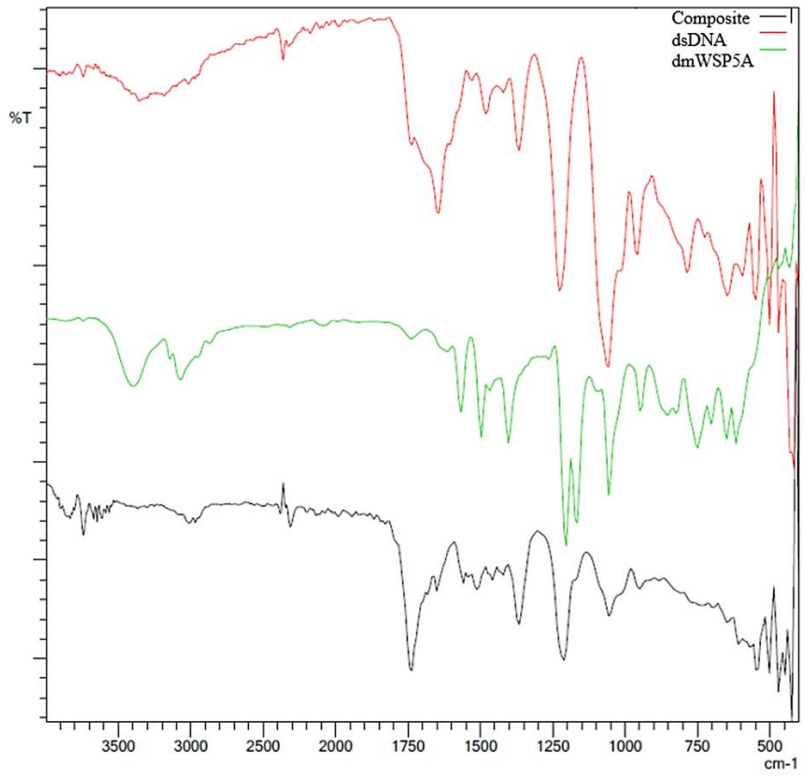

Figure 6.5: IR analysis of the starting materials and the dried composite material

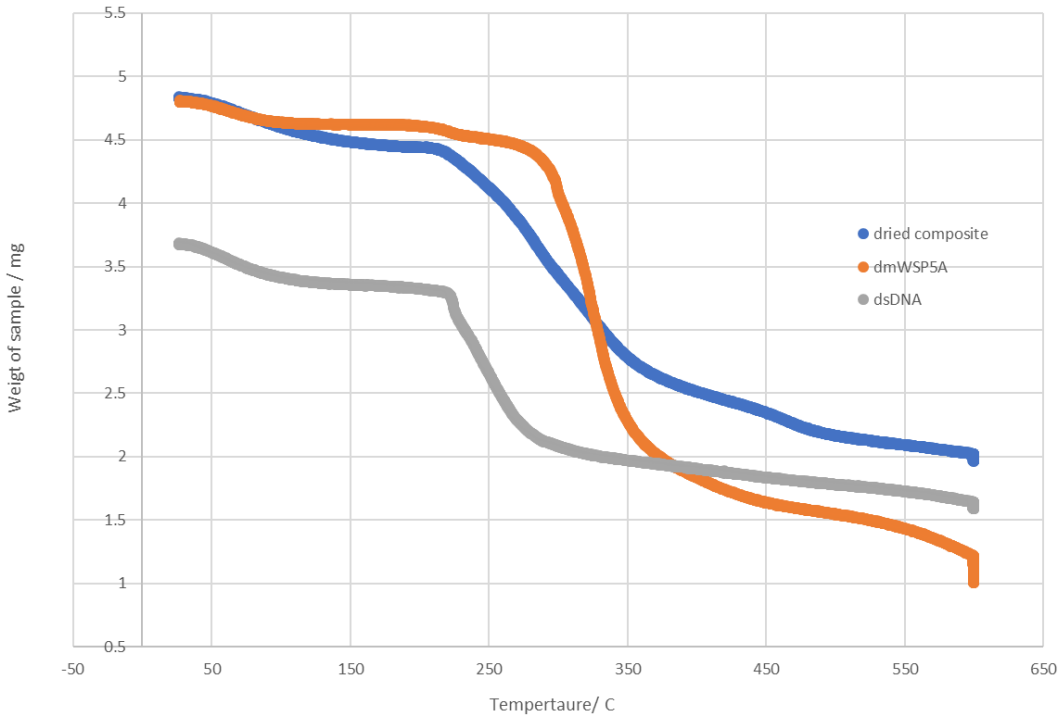

Figure 6.6: Thermogravimetric analysis (TGA) of dsDNA, dmWSP5A and dried composite

As observed in the TGA study, WSP5A and dsDNA show a sharp decrease in weight, showing that the starting materials are pure and un-complexed with other material. The curve for the dried composite clearly shows that the decomposition rate has been significantly lowered. This data indicates that dsDNA and WSP5A have formed a composite material, presumably via strong electrostatic interactions because it requires more time and heat to break these interactions, as compared to the starting materials.

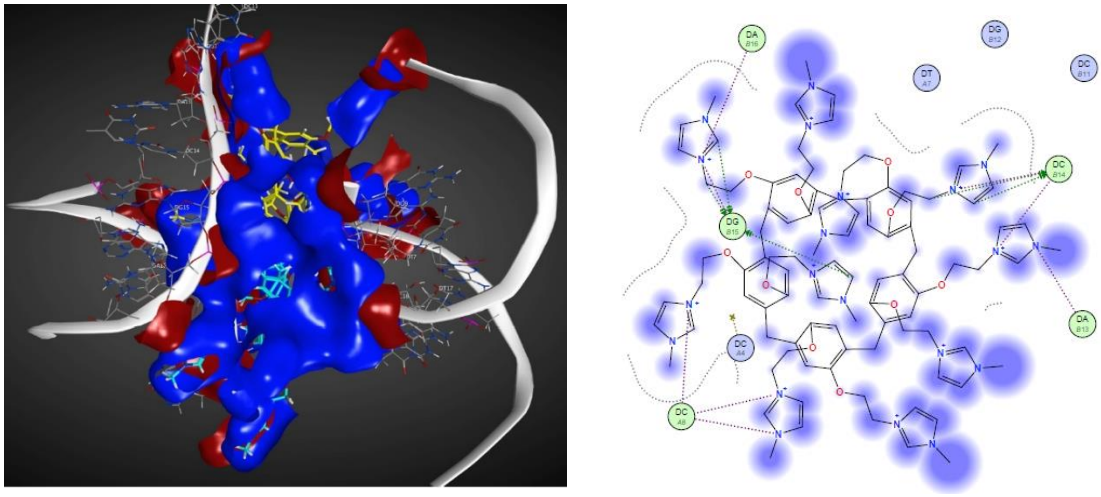

Figure 6.7: L to R, Protein patch map, the blue is positively charged WSP5A, and red regions are for negatively charged phosphate backbone, Ligand interaction diagram of WSP5A to dsDNA

Figure 6-7 shows that electrostatic interactions play a significant role in bringing the dsDNA and the WSP5A together to form a complex. Electrostatic potential maps support our prediction by highlighting the positive and negative areas coming together. Also, the ligand interaction diagram shows the critical role the positively charged imidazolium ions are playing in order to form the complex. Therefore, this rationale can be used to explain the self-aggregated structures.

Accumulation and efficient removal of PFOA from solution and leaching investigations. Potential Applications of the Material; DNA is a well-known intercalator for planar molecules[13], and pillar[n]arenes are known for their ability to encapsulate a guest molecule within their central hydrophobic cavity[14]. Therefore, combining these two materials into one composite material allows for the combination of their properties to encapsulate small molecules. A natural conclusion from these observations is to experiment with encapsulating a socially-relevant small molecule.

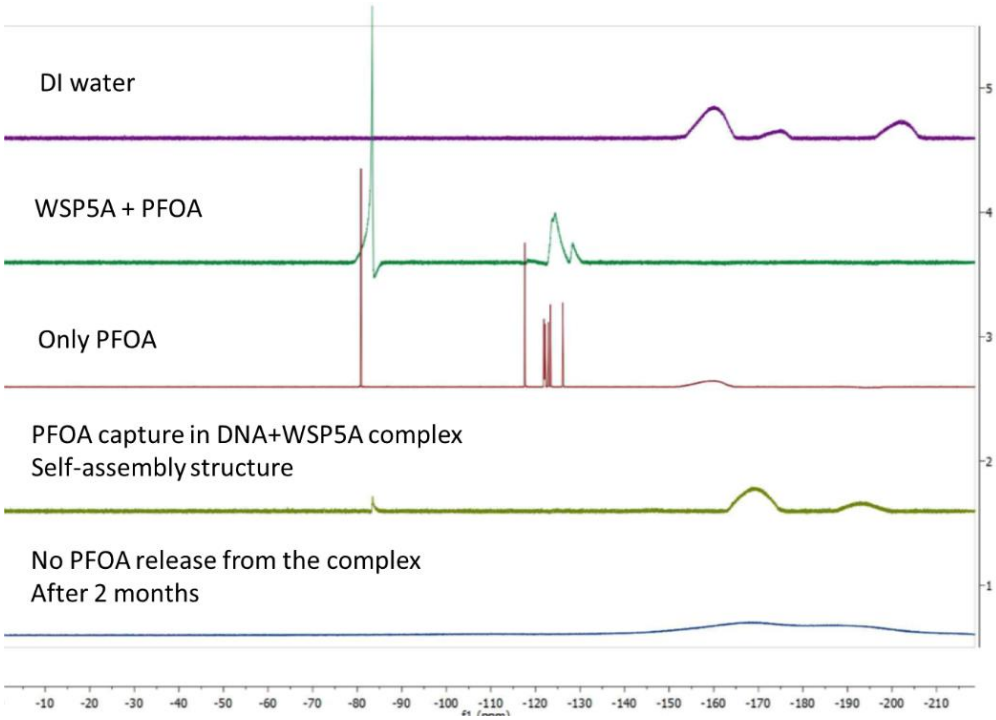

Figure 6.8: 19F NMR of PFOA capture through the self-assembled composite material

Perfluorinated compounds have recently been newsworthy because they are harmful byproducts of industry suspected to be carcinogens[15]. Perfluorooctanoic acid (PFOA) is the guest we chose to encapsulate within the complex. We first investigated the PFOA binding towards the dmWSP5A by conducting UV-Vis absorbance studies, which revealed that PFOA binds to the cavity of the dmWSP5A with an association constant of $1.13 \pm 0.1 \times 10^6$ M^{-1}. Also, the binding was a 1:1 complexation. This was further proven by conducting docking studies followed by molecular dynamics computations (Figure 6-8). The experiment was started by first adding 40 mM P5A solution to a solution of 20 mM PFOA, and the P5A is allowed to encapsulate the PFOA as it reaches equilibrium. Next, dsDNA is added to the PFOA/P5A mixture, the complex is formed, and it can be removed from the vial. The resulting supernatant solution was tested for PFOA using 19F NMR, and no PFOA fluorine peaks were observed in the spectra even after 15,000 scans. We presume the composite material is capturing all the PFOA within its structure. This Experiment

worked even with a stoichiometrically small amount of composite material as compared to PFOA. Our experiments ranged from 0.2 equivalents complex to 1.8 equivalents and showed (according to ^{19}F NMR) that there was no fluorine within the supernatant solution. We also tested the idea that this composite material could be useful as an environmentally sustainable encapsulation device. By using a 1:1 ratio of PFOA to the composite material, we tested the supernatant solution of complexes in fresh water over time in order to determine whether PFOA leached out of the composite material. These tests also gave positive results, signaling that no PFOA was found to leach from the material throughout over 6 months. In addition, Figure 6-9 clearly shows that there is binding of PFOA inside the cavity of the WSP5A, due to when it binds the ^{19}F NMR is showing broadening of peaks compared to non-complexed.

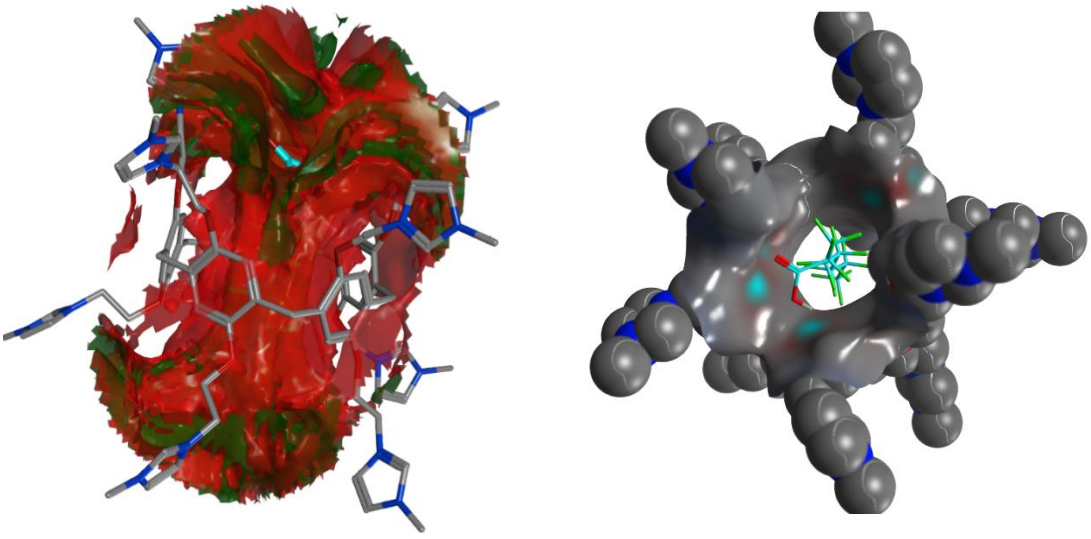

Figure 6.9: L to R, hydrophobic pocket present in dmWSP5A, Docked PFOA inside the dmWSP5A

We performed a sub-stoichiometric NMR titration of WSP5A (20 mM) and dsDNA (20 mM) in a 1:1 ratio to a PFOA (20 mM) solution, with an external standard (1-Fluoro-2,4,6-trimethyl-pyridinium tetrafluoroborate) in order to quantify the efficiency of the removal. The result of the titration clearly shows the encapsulation of the PFOA in WSP5A, and once the dsDNA was added,

the broad peak shrunk in size, signaling that the encapsulated PFOA was complexed inside the self-aggregated dsDNA complex. Also, we can observe that a sharp PFOA peak is seen. This peak corresponds to the un-complexed PFOA that is present in the solution. Due to the presence of the internal standard, we were able to integrate the area for the PFOA bound, and with that, we can conclude that 90% complexed PFOA was removed via the self-aggregation process with the use of dsDNA. Furthermore, the final concentration of PFOA in the supernatant solution was found out to be 2 mM. Hence, we can assume that with two more cycles of purification that can be taken out of the water.

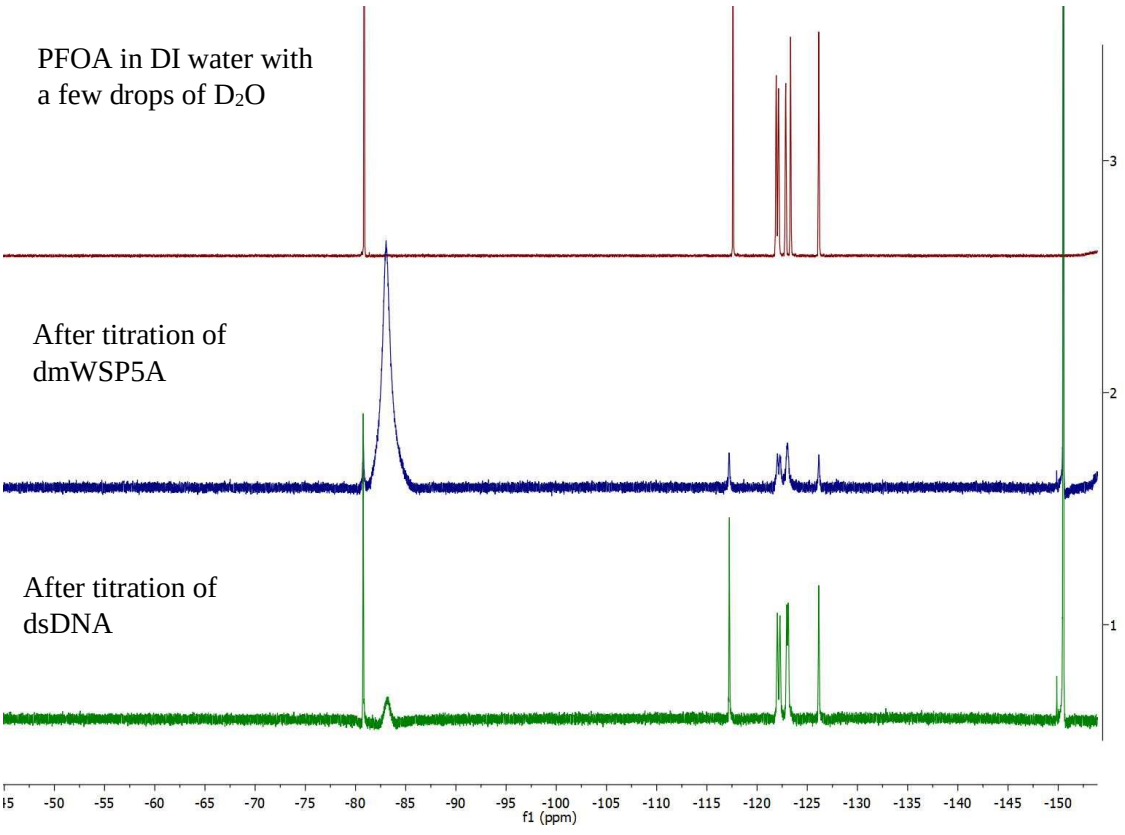

Figure 6.10: ^{19}F NMR of PFOA capture through the self-assembled composite material

Conclusion

The dmWSP5A-dsDNA composite system was used as a successful method to encapsulate and removal of PFOA with 90% removal from an aqueous environment.

6.1 REFERENCES

(1) Ghosh, I.; Stains, C. I.; Ooi, T.; Segal, D. J. Direct Detection of Double-Stranded DNA : Molecular Methods and Applications for DNA Diagnostics {. **2006**. https://doi.org/10.1039/b611169f.

(2) Takahashi, Y.; Kondo, K.; Miyaji, A.; Watanabe, Y. Recovery and Separation of Rare Earth Elements Using Salmon Milt. **2014**, No. Iii, 1–15. https://doi.org/10.1371/journal.pone.0114858.

(3) Ogoshi, T.; Yamagishi, T.; Nakamoto, Y. Pillar-Shaped Macrocyclic Hosts Pillar [n] Arenes : New Key Players for Supramolecular Chemistry. **2016**. https://doi.org/10.1021/acs.chemrev.5b00765.

(4) Cheremisinoff, N. P. Perfluorinated Chemicals (PFCS). **2016**. https://doi.org/10.1002/9781119363828.

(5) Post, G. B.; Cohn, P. D.; Cooper, K. R. Perfluorooctanoic Acid (PFOA), an Emerging Drinking Water Contaminant: A Critical Review of Recent Literature. *Environ. Res.* **2012**, *116*, 93–117. https://doi.org/10.1016/j.envres.2012.03.007.

(6) Ji, W.; Xiao, L.; Ling, Y.; Ching, C.; Matsumoto, M.; Bisbey, R. P.; Helbling, D. E.; Dichtel, W. R. Removal of GenX and Perfluorinated Alkyl Substances from Water by Amine-Functionalized Covalent Organic Frameworks. *J. Am. Chem. Soc.* **2018**, *140* (40), 12677–12681. https://doi.org/10.1021/jacs.8b06958.

(7) Xiao, L.; Ling, Y.; Alsbaiee, A.; Li, C.; Helbling, D. E.; Dichtel, W. R. β-Cyclodextrin Polymer Network Sequesters Perfluorooctanoic Acid at Environmentally Relevant Concentrations. *J. Am. Chem. Soc.* **2017**, *139* (23), 7689–7692. https://doi.org/10.1021/jacs.7b02381.

(8) Dombrowski, P. M.; Kakarla, P.; Caldicott, W.; Chin, Y.; Sadeghi, V.; Bogdan, D.; Barajas-Rodriguez, F.; Chiang, S. Y. D. Technology Review and Evaluation of Different Chemical Oxidation Conditions on Treatability of PFAS. *Remediation* **2018**, *28* (2), 135–150. https://doi.org/10.1002/rem.21555.

(9) Zhi, Y.; Liu, J. Adsorption of Perfluoroalkyl Acids by Carbonaceous Adsorbents: Effect of Carbon Surface Chemistry. *Environ. Pollut.* **2015**, *202*, 168–176. https://doi.org/10.1016/j.envpol.2015.03.019.

(10) Post, G. B.; Gleason, J. A.; Cooper, K. R. Key Scientific Issues in Developing Drinking Water Guidelines for Perfluoroalkyl Acids: Contaminants of Emerging Concern. *PLoS Biol.* **2017**, *15* (12), 1–12. https://doi.org/10.1371/journal.pbio.2002855.

(11) Sayantani Basu, Settimio Pacelli, A. P. BioIntel Research Laboratory, Department of Chemical and Petroleum Engineering, School of Engineering, University of Kansas, Lawrence, KS, USA. 4.

(12) Yamada, M.; Hashimoto, K. DNA - Cyclodextrin Composite Material for Environmental. **2008**, *9* (12).

(13) Wuite, G. J. L. Force-Dependent Binding Kinetics. *Nat. Commun.* **2015**, *6*, 1–12. https://doi.org/10.1038/ncomms8304.

(14) Hua, B.; Zhou, J.; Yu, G. Hydrophobic Interactions in the Pillar [5] Arene-Based Host-Guest Complexation and Their Application in the Inhibition of Acetylcholine Hydrolysis. *Tetrahedron Lett.* **2015**, *56* (8), 986–989. https://doi.org/10.1016/j.tetlet.2015.01.064.

(15) Barry, V.; Winquist, A.; Steenland, K. Perfluorooctanoic Acid (PFOA) Exposures and Incident Cancers among Adults Living Near a Chemical Plant. **2013**, *121* (11), 1313–1318.

(16) Yao, Y.; Xue, M.; Chi, X.; Ma, Y.; He, J.; Abliz, Z.; Huang, F. *Chemical Communications* **2012**, *48*(52), 6505.

6.2 SUPPORTING INFORMATION

Double-stranded DNA-Water soluble P5A based self-aggregate composite material for removal of PFOA from an aqueous environment

Reagents

Substrates, including CBr_4, dry acetonitrile, dry 1,2-dichloroethane, boron trifluoride ethane, triphenyl phosphine, methylimidazole were purchased from Sigma-Aldrich, Fisher Scientific, and TCI chemicals. All reagents were stored under an inert atmosphere before use. Unless otherwise noted, all reactions were performed under N_2.

Instrumentation

NMR spectra were obtained using Bruker Avance 300 MHz and 400 MHz spectrometers. Low-resolution mass spectrometry was performed using a Shimadzu LRMS-2020. High-resolution mass spectrometry was performed using a Thermo Scientific LTQ Orbitrap XL™ instrument. UV-Vis spectroscopy, Fluorescence spectroscopy

The synthesis of the dmWSP5A is the same as mentioned in chapter 3 and chapter 5 supporting information.

Stoichiometry Experiment

40 mM stock solutions of Pillar[5]arene and DNA from salmon milt were first prepared. The P5A stock solution consisted of dissolving 1.000 g P5A into 10 mL of ultrapure water. The DNA stock solution was determined using the molecular weight per base pair, so 208 mg of DNA was dissolved in 10 mL ultrapure water to obtain a 40 mM/b.p. stock solution. The experiment consisted of forming ten complexes separately and then allowing them to rest in fresh water for a set period of time. 1 mL of DNA solution was added into each of the 10 vials. The ratio of P5A to DNA was varied from 0 to 1.8 eq. See the chart below for equivalents and volumes of solutions added.

Equivalents dmWSP5A to dsDNA	Mol. DNA	Mol. P5A	Volume (mL) of dmWSP5A
0	4×10^{-5}	0	0
0.2		8×10^{-6}	0.2
0.4		1.6×10^{-5}	0.4
0.6		2.4×10^{-5}	0.6
0.8		3.2×10^{-5}	0.8
1.0		4.0×10^{-5}	1.0
1.2		4.8×10^{-5}	1.2
1.4		5.6×10^{-5}	1.4
1.6		6.4×10^{-5}	1.6
1.8		7.2×10^{-5}	1.8

First, the DNA solution was added to the vials. Then, the corresponding amount of DNA was added in order to aggregate the complex spontaneously. These solutions were allowed to rest overnight. The amount of complex formed was studied and examined in order to determine the optimal ratio of DNA to P5A needed for complexation.

Leaching Experiment

40 mM stock solutions of Pillar[5]arene and DNA from salmon milt were first prepared. The P5A stock solution consisted of dissolving 1.000 g P5A into 10 mL of ultrapure water. The DNA stock solution was determined using the molecular weight per base pair, so 208 mg of DNA was dissolved in 10 mL ultrapure water to obtain a 40 mM/b.p. stock solution. PFOA solutions were prepared at the maximum solubility of PFOA (20 mM) by dissolving 165.6 mg PFOA in 20 mL ultrapure water. The leaching experiment consisted of forming ten complexes separately and then allowing them to rest in fresh water for a set period. 2.0 mL PFOA was placed into each of the 10 vials. Then, the ratio of complex to PFOA was varied from 0 to 1.8 eq. See the chart below for equivalents and volumes of solutions added.

Equivalents Complex to PFOA	Mol. PFOA	Mol. Complex (equivalent amounts of dmWSP5A and dsDNA)	Volume (mL) of dmWSP5A and dsDNA solutions added to PFOA
0	4×10^{-5}	0	0/0
0.2		8×10^{-6}	0.2/0.2
0.4		1.6×10^{-5}	0.4/0.4
0.6		2.4×10^{-5}	0.6/0.6
0.8		3.2×10^{-5}	0.8/0.8
1.0		4.0×10^{-5}	1.0/1.0
1.2		4.8×10^{-5}	1.2/1.2
1.4		5.6×10^{-5}	1.4/1.4
1.6		6.4×10^{-5}	1.6/1.6
1.8		7.2×10^{-5}	1.8/1.8

First, the P5A solution was added to the PFOA solutions in order for the PFOA to be encapsulated by the P5A. This mixture was allowed to rest for 10 min. Then, the corresponding amount of DNA was added in order to spontaneously aggregate the complex. These solutions were allowed to rest overnight, and then the excess liquid was analyzed using NMR spectroscopy. The 1:1 equivalent PFOA to the complex was placed in 3 mL fresh D2O and was analyzed using NMR spectroscopy

to determine PFOA leaching at 0 h, 1 h, 1 d, 4 d, 7d, and 14 d. No PFOA leaching was found to occur.

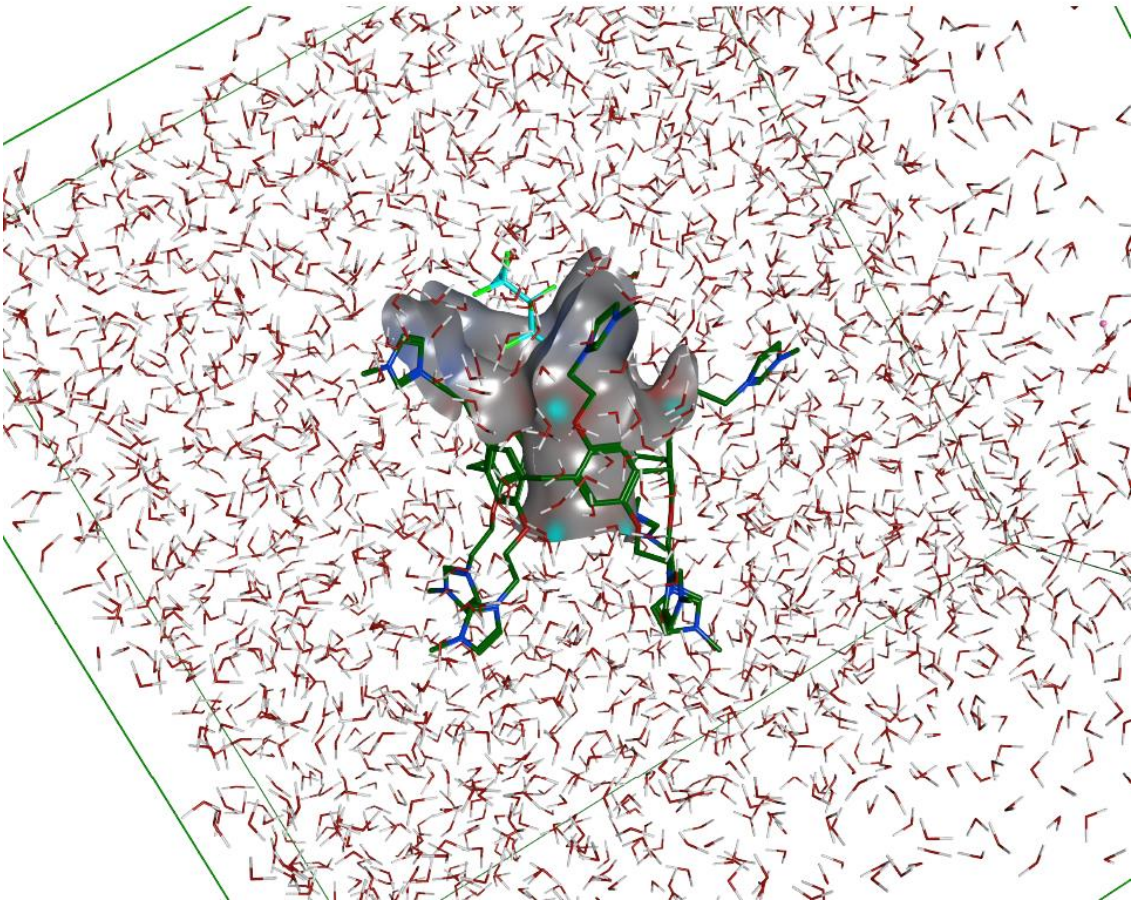

Figure 6.11: PFOA bound inside the cavity of the dmWSP5A after multiple iterations using molecular dynamics with *AMBER 19* force field

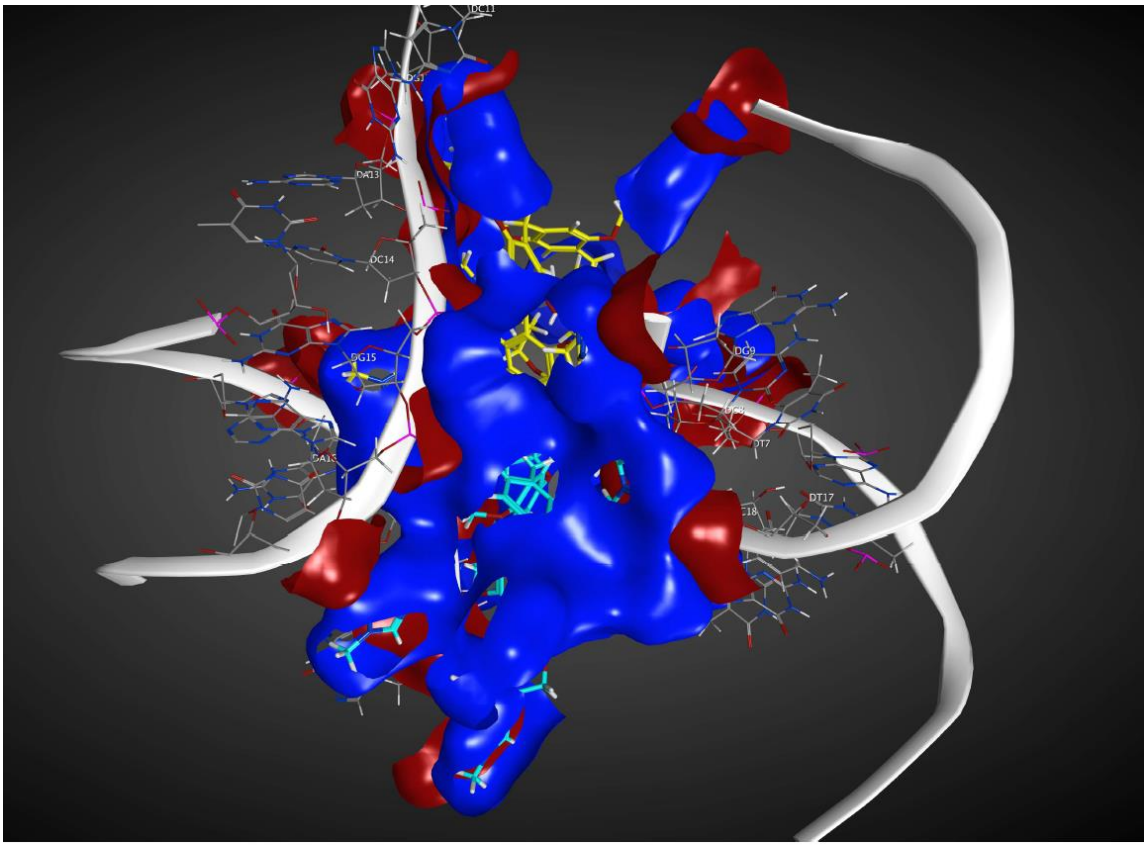

Figure 6.12: Protein patches representation of the dsDNA and WSP5A

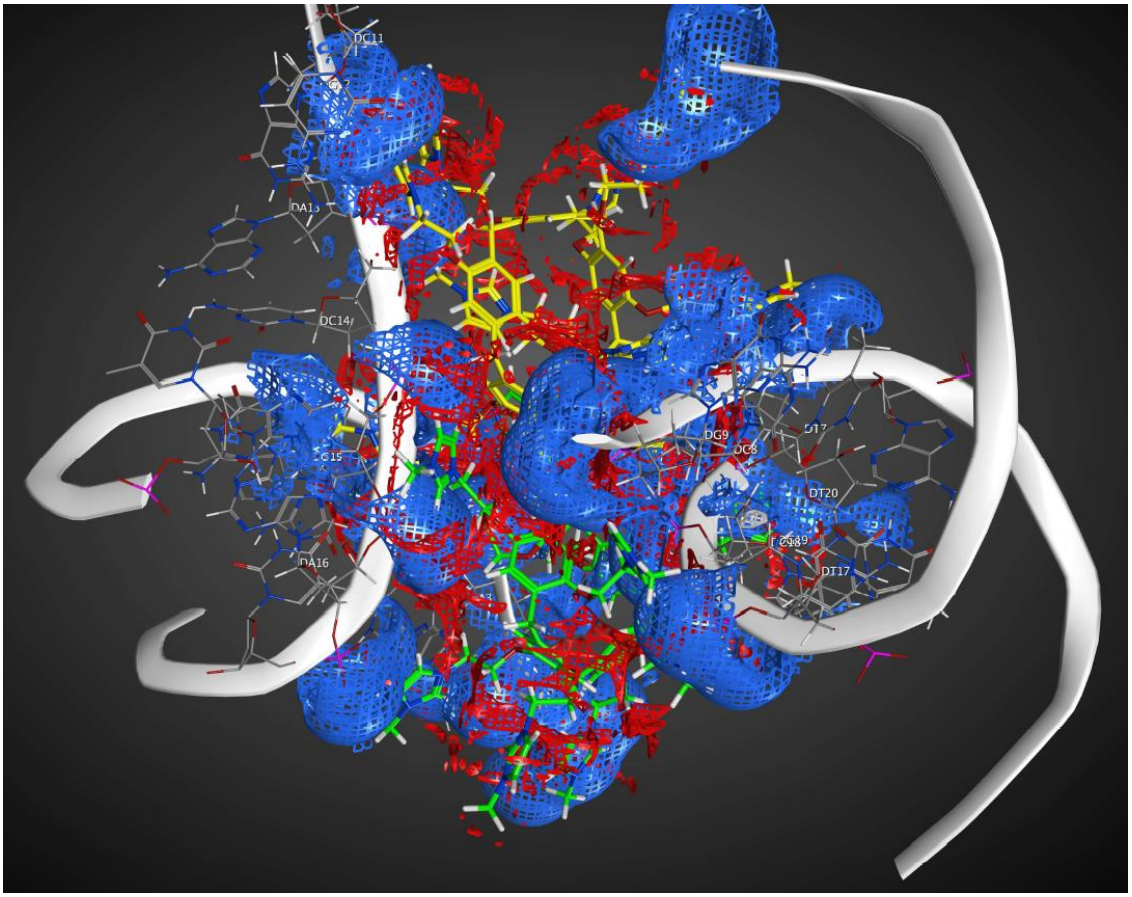

Figure 6.13: Electrostatic potential map representation of dsDNA and WSP5A

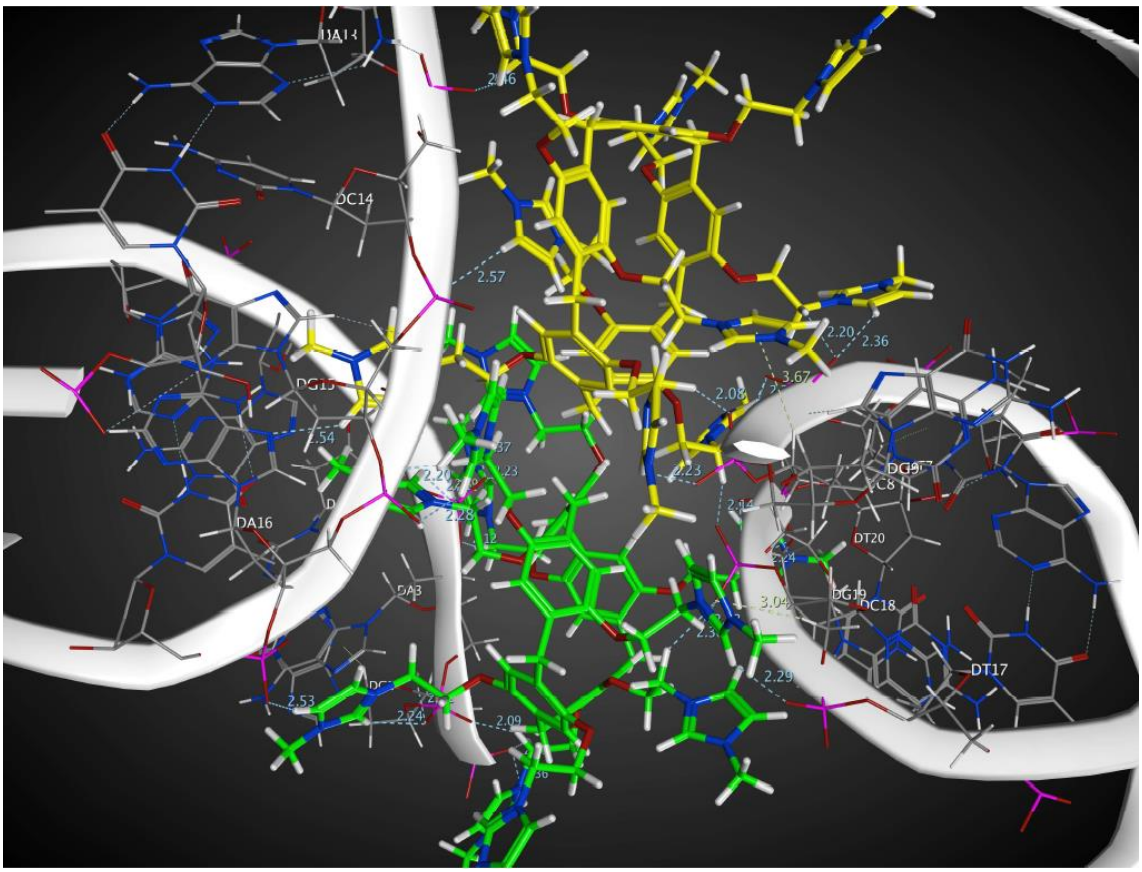

Figure 6.14: H-bonding interactions between the WSP5A and dsDNA

7 CHAPTER 7

Will be submitted to *Nature Antibiotics*

Inhibition of chloramphenicol-resistant bacteria by rationally-designed semi-synthetic chloramphenicol derivatives

Samantha A. Donahue[1], Ashvin Fernando[2], Gerwald Jogl[3], Paul Cesana[2], Breton DeBoef[2], and Steven T. Gregory[1]

[1]Department of Cell and Molecular Biology, University of Rhode Island Kingston, RI 02881

[2]Department of Chemistry, University of Rhode Island Kingston, RI 02881

[3]Department of Molecular Biology, Cell Biology, and Biochemistry, Brown University Providence, RI 02881

ABSTRACT

Chloramphenicol is an inhibitor of peptide bond formation by the ribosome and acts by binding to the peptidyl transferase active site of the 50S ribosomal subunit. Resistance to chloramphenicol can arise from mutations in the 23S rRNA of the ribosome or, more commonly, by inactivation of the antibiotic by chloramphenicol acetyltransferase (CAT). Using crystal structures of ribosome-chloramphenicol and CAT-chloramphenicol complexes as guides, we have synthesized derivatives of chloramphenicol rationally modified to impair binding to CAT while still allowing binding to ribosomes. While less potent than native chloramphenicol, several derivatives inhibit the growth of *Bacillus subtilis* expressing type III CAT expressed from the resistance determinant pC194. We predict that crystal structures of ribosomes bound to modified chloramphenicol will allow more precise predictions for the second generation of semi-synthetic derivatives.

INTRODUCTION

Chloramphenicol (CAM) is a bacteriostatic protein synthesis inhibitor effective against both Gram-positive and Gram-negative bacteria[1]. It acts as a competitive inhibitor of peptide bond formation by binding to the peptidyltransferase active site of the 50S ribosomal subunit, and base substitutions in 23S rRNA residues that comprise the drug binding site confer resistance. Early crystal structures of chloramphenicol bound to the 50S subunits[2] of the bacterium *Deinococcus radiodurans* and the archaeon Haloarcula marismortui[3] led to conflicting interpretations of the correct binding mode of chloramphenicol. While the H. marismortui structure was at a higher resolution, the *D. radiodurans* structure was more consistent with known chloramphenicol-resistant mutations[4]. Further, the fact that chloramphenicol does not normally inhibit Archaeal protein synthesis added to the confusion. This issue was ultimately resolved by crystal structures of chloramphenicol bound to 70S ribosomes from the bacteria *Escherichia coli*[5] and *Thermus thermophilus*.

Current literature cites various ways CAM has been functionalized, ranging from the attachment of amino acids, sugar moieties and bulky groups such as adamantly groups, heterocycles, spermine, palmitate, and etc[6]. Chloramphenicol Acetyltransferase (CAT, EC 2.3.1.28) mono- and di-acetylates chloramphenicol using acetyl-coenzyme A (Ac-CoA) as the acyl donor, producing coenzyme A (CoA-SH) and acetyl-chloramphenicol (Ac-CHL) and di-acetylated chloramphenicol (Ac2-CHL) as reaction products. Acetylation presumably sterically hinders interaction with the binding site on the ribosome. The crystal structure of type III CAT in complex with chloramphenicol has been solved to 1.75 Å resolution. (Leslie, 1990).

The primary goal of this project was to functionalize CAM in a simple synthetic manner, binding studies through in-silico methods and obtain ribosomal based results to continue on further studies.

MATERIALS AND METHODS

Synthesis of chloramphenicol derivatives. Chloramphenicol (56-75-7) was purchased from Sigma Chemical. **Assay for antibiotic sensitivity**, *Bacillus subtilis 168* and *B. subtilis 168* carrying plasmid pC194 were obtained from the Bacillus Genetic Stock Center (The Ohio State University) and grown in LB medium and plated on Tryptose Blood Agar Base (TBAB). Approximately 108 cells from a saturated overnight culture were plated onto TBAB. A disc (Whatmann)

Assay for chloramphenicol acetyltransferase activity, CAT enzyme activity was measured using a spectrophotometric assay according to the manufacturer's instructions (Sigma). This assay is based on the transfer of the acetyl group of acetyl-CoA to chloramphenicol, and the subsequent reaction of CoA-SH with 5,5'-dithio-bis (2-nitrobenzoic acid; DTNB). Acetyl-CoA, (cat no.), DTNB (cat no. D8130) and CAT (cat no. C8413) were purchased from Sigma.

RESULTS & DISCUSSION

Rational design of chloramphenicol derivatives. We took advantage of high-resolution co-crystal structures of ribosome-chloramphenicol (Dunkle et al. 2010; Bulkley et al., 2010) and CAT-chloramphenicol (Leslie et al. 1988; Leslie 1990) complexes in order to determine the direct contact sites between chloramphenicol and these two enzymes. Fortuitously, the interaction of chloramphenicol and the two enzymes involve distinct sets of contacts (Figure 1), allowing the prediction of sites of modification that would impair recognition by CAT while allowing binding to the ribosome.

As mentioned earlier literature has reported multiple ways to synthesize derivatives of CAM. Our group also investigated multiple synthetic procedures. Out of all the procedures, we discovered that obtaining CAM base which is the free amine form of the CAM can be obtained with sufficiently high yields. The method suggested the use of a 0.1 M NaOH solution in the dark overnight at room temperature. We were able to optimize the yields significantly by using 1.46 M NaOH solution.

Previous synthesis of CAM base required the use of recrystallization from water. The use of 1.46 M NaOH instead of the lower concentration helped us to achieve higher yield with approximately 100% conversion of CAM to CAM-base without the need for recrystallization. The CAM base was then subjected to multiple reactions such as peptide coupling, reaction with an acid chloride, etc. The most promising derivatives were obtained using isothiocyanates. The reaction between amine and iso-thiocyanates or iso-cyanates is known to proceed with high yields and with ease of synthesis. This was confirmed by in-silico methods. MOE, molecular operating environment computational package was used for this screening process. Out of multiple derivatives, we selected a couple of the isothiocyanate derivatives that shows high binding to the 70s ribosome pocket.

Furthermore, we docked these same derivatives to the pocket of chloramphenicol acetyltransferase (CAT), to see if the binding is decreased towards the enzyme. This rationale was used in computations, due to the commercially available CAM is known to be inactivated due to the binding of CAM to acetyltransferase enzyme, once bound it acetylates the CAM and its anti-biotic properties no longer exists. The thiourea derivatives that we synthesize are too large for the pocket of the CAM enzyme; hence it does not bind into the enzyme pocket. Binding to the ribosome was much higher and we concluded that the thiourea derivatives will still have anti-biotic properties even with the presence of CAT.

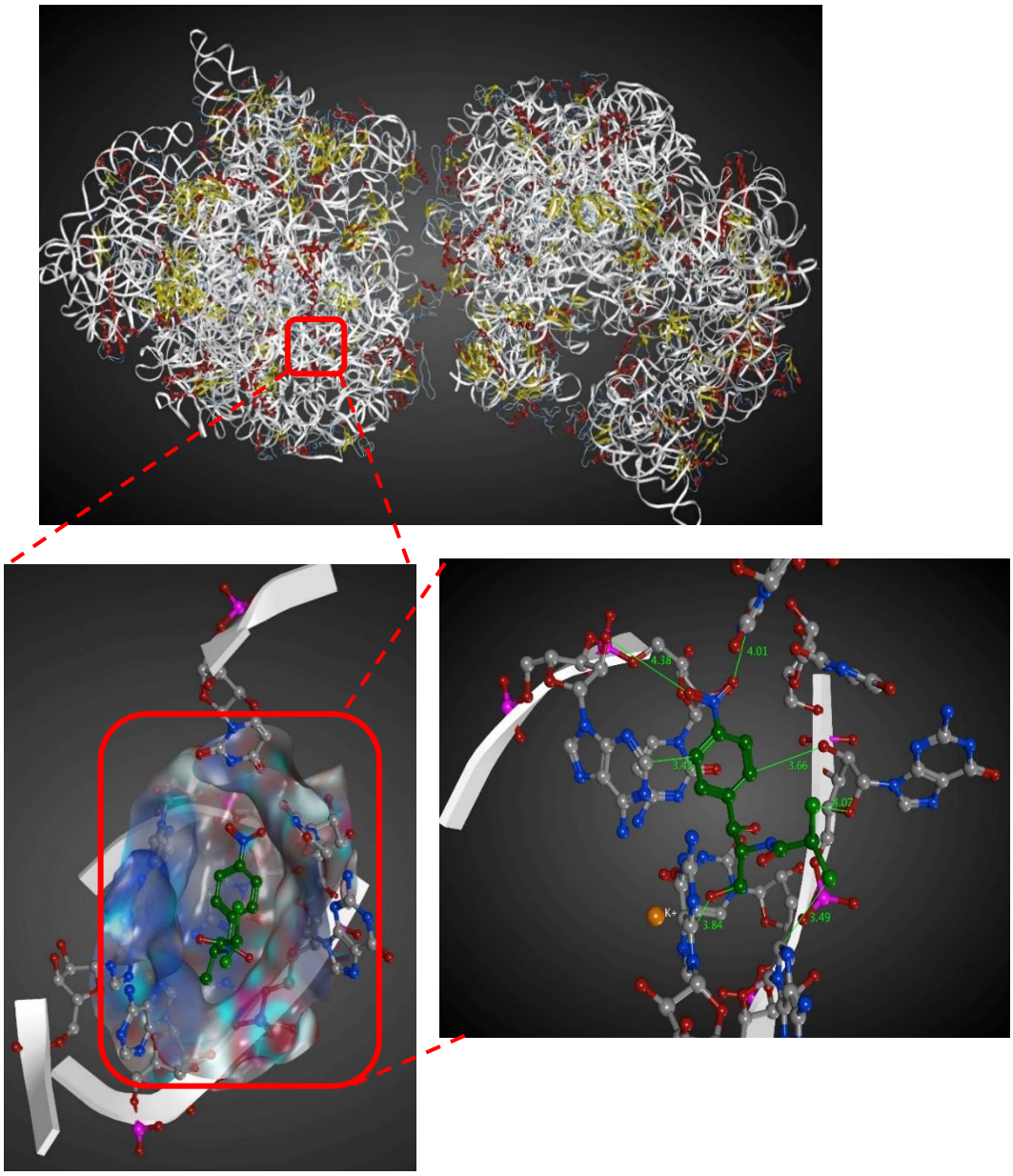

Figure 7.1: Topmost, Complete structure of Thermus thermophilus 70S ribosome in its native form, (Bottom left) Active pocket inside the ribosome docked with CAM, (Bottom right) Distances from CAM towards surrounding amino acids present inside the pocket

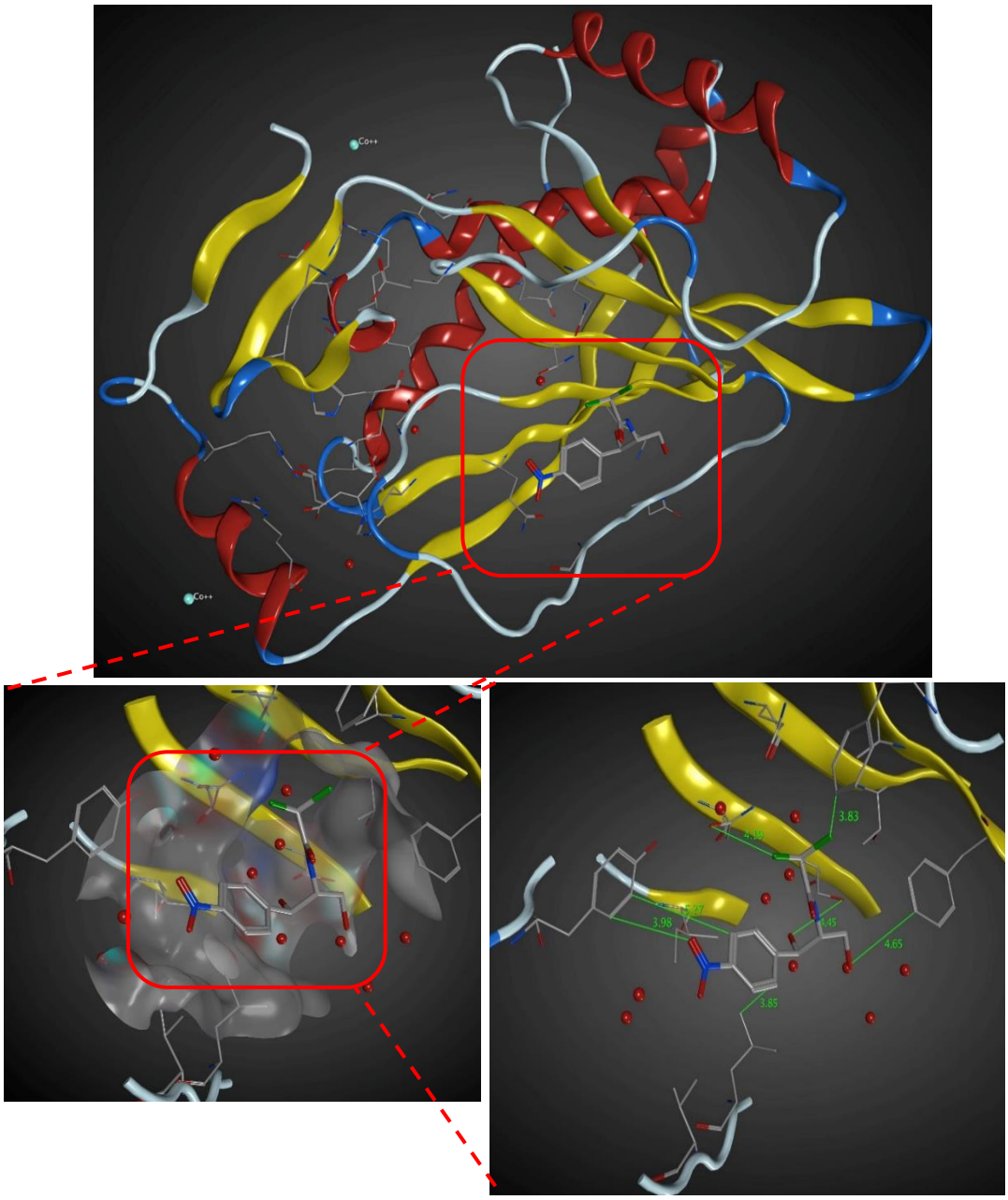

Figure 7.2: Topmost, Complete structure of Chloramphenicol acetyltransferase. (Bottom left) Active pocket inside the CAT enzyme docked with CAM (A more open pocket compared to the ribosome pocket), (Bottom right) Distances from CAM towards surrounding amino acids

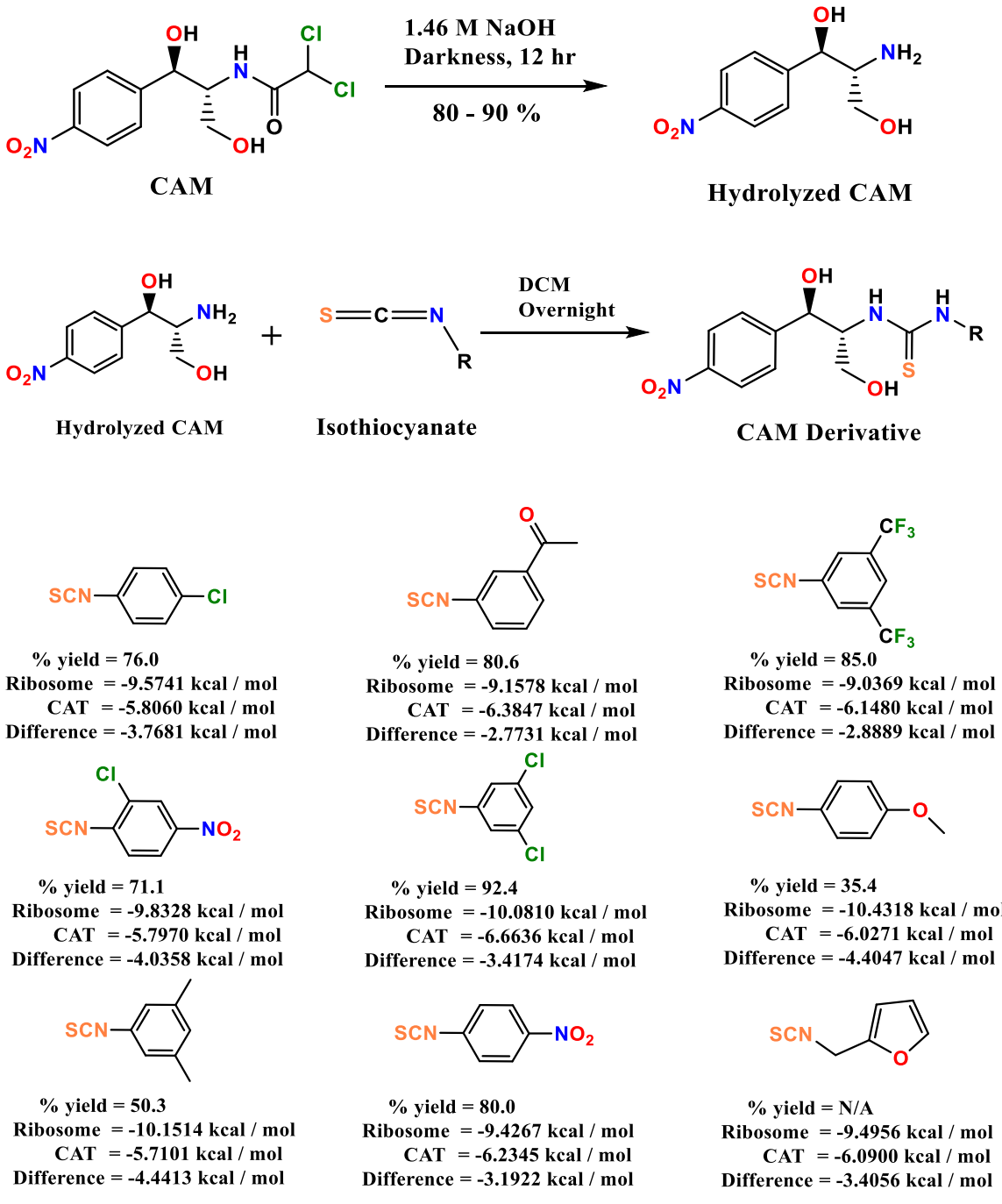

Figure 7.3: Synthetic scheme and substrate scope for the synthesis of derivatives of CAM using isothiocyanates

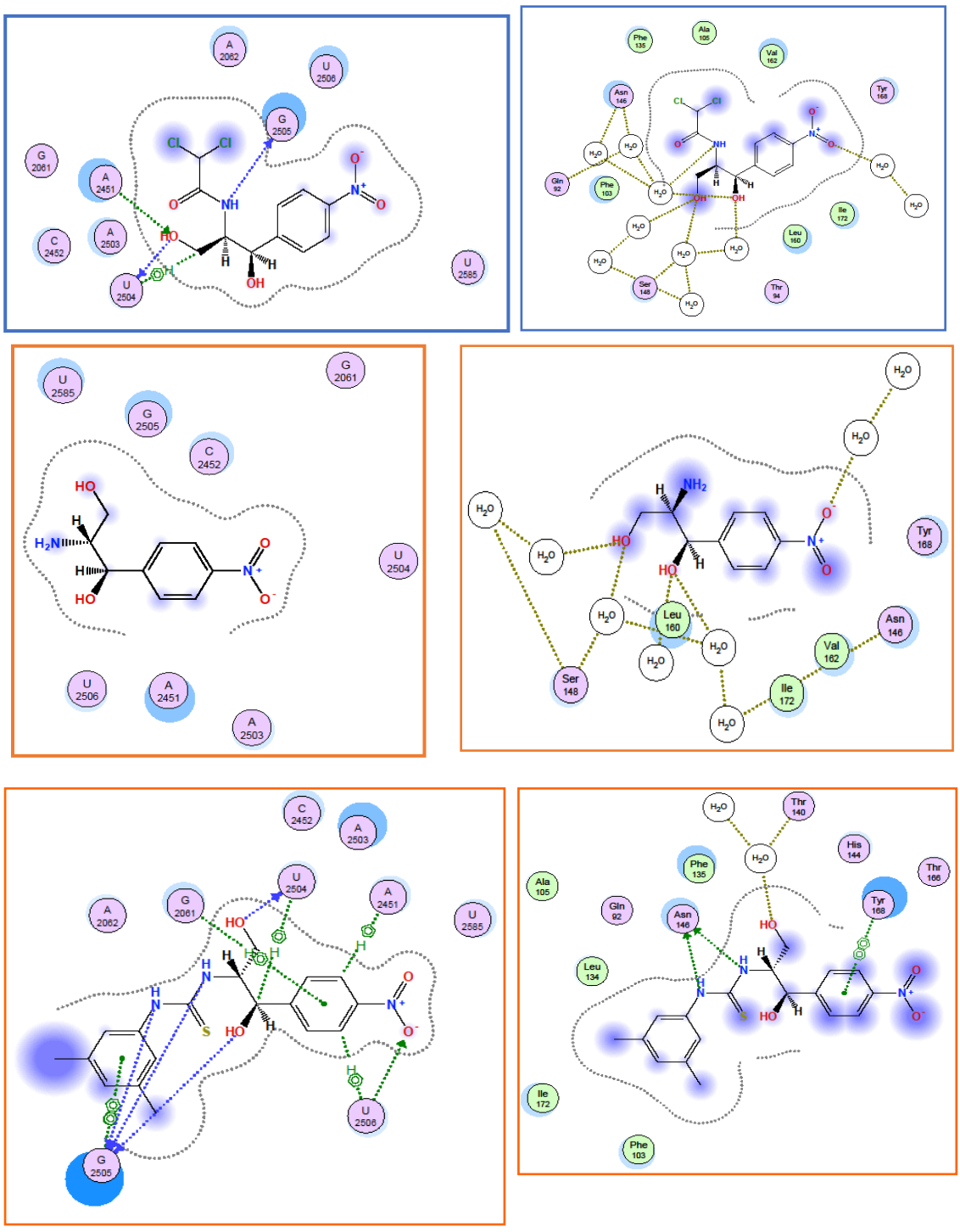

Figure 7.4: Ligand interaction diagrams for CAM, CAM base and CAM derivative compared with ribosome pocket binding (Left side images) and CAM acetyltransferase binding (right side images)

As seen in figure 4, compared to CAM and CAM base, the novel thiourea derivative shows more interactions with surrounding amino acids present inside the cavity of the ribosome pocket. This is due to the introduction of multiple interaction points in the novel derivative such as the thiourea moiety along with aromatics and other functional groups these help to form new interactions, which in return results in stronger binding to the ribosome pocket. We postulate that due to the tight ribosome binding with a high number of interactions, this results in lower or no binding towards the incoming CAM acetyltransferase enzyme. This is further clarified with ligand interaction diagrams that are related to the enzyme binding. Comparatively the CAM is bound in the tight pocket as seen from the pocket dimensions represented in dashed lines. Hence, in CAM derivative the binding is seen in a more open pocket, also there more blue spots which shows the ligand exposure to the outside of the cavity, which clearly shows that the derivative binding interactions are less.

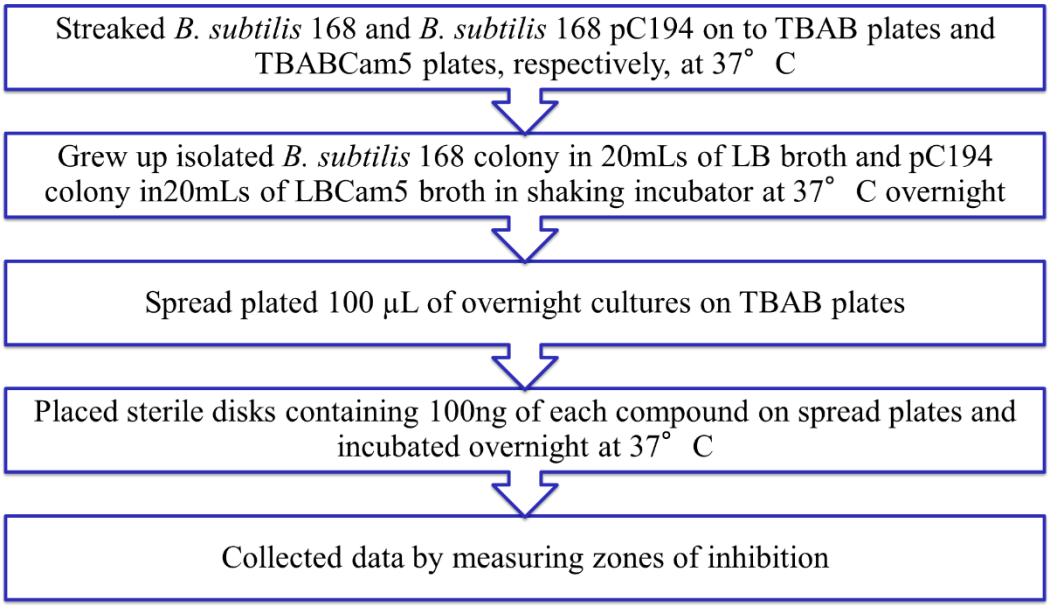

Figure 7.5: Flow chart diagram representation of the procedure implemented for the growth inhibition zone study in growth media described in methods

Growth inhibition of *B. subtilis* and *B. subtilis/pC194* expressing chloramphenicol acetyltransferase. We initially tested the inhibitory activity of chloramphenicol derivatives using the Gram-positive species *B. subtilis 168* due to its sensitivity to this drug, and because of the availability of this strain containing the Staphylococcus aureus chloramphenicol-resistance plasmid pC194 (Löfdahl et al. 1978). This plasmid expresses a type III CAT enzyme.

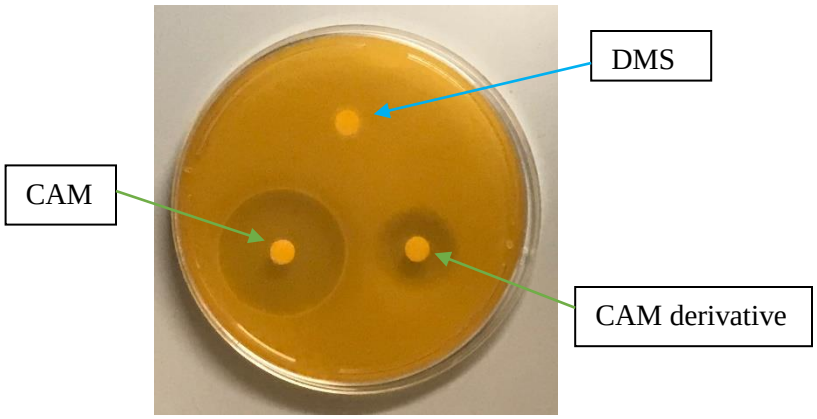

Figure 7.6: Representation of a disk assay and the control disk, the dark area is an indication of no growth zone of the bacteria or knows as an inhibition zone

Chloramphenicol derivatives are poor substrates for acetylation by CAT. CAT enzyme assays typically use thin-layer chromatography to detect mono- and di-acetylation of [14C]-chloramphenicol (Gorman et al. 1982). This assay is not practical for working with semi-synthetic chloramphenicol derivatives. Instead, we employed a colorimetric assay (see Materials and Methods) based on the detection of deacetylated coenzyme A reaction product by its subsequent reaction with DTNB via its free thiol group.

Effects of derivatives on the growth of Thermus thermophilus chloramphenicol-resistant mutants. While less common, resistance to chloramphenicol can be conferred by base substitutions in 23S rRNA in the peptidyltransferase active site. We have previously reported a number of such mutants of the thermophilic bacterium T. thermophilus (Gregory et al. 2005). These include the

base substitutions A2032G, G2061A, A2062G, G2447A, C2452U, A2453G, U2500C, A2503G, U2504G, U2504C, U2504A, and G2505A.

Protein synthesis inhibition of an E. coli extract. One possible explanation for growth inhibition by derivatives is the fortuitous generation of an alternative mode of action. The above experiment was to determine the inhibitory action of chloramphenicol derivatives against ribosomes specifically.

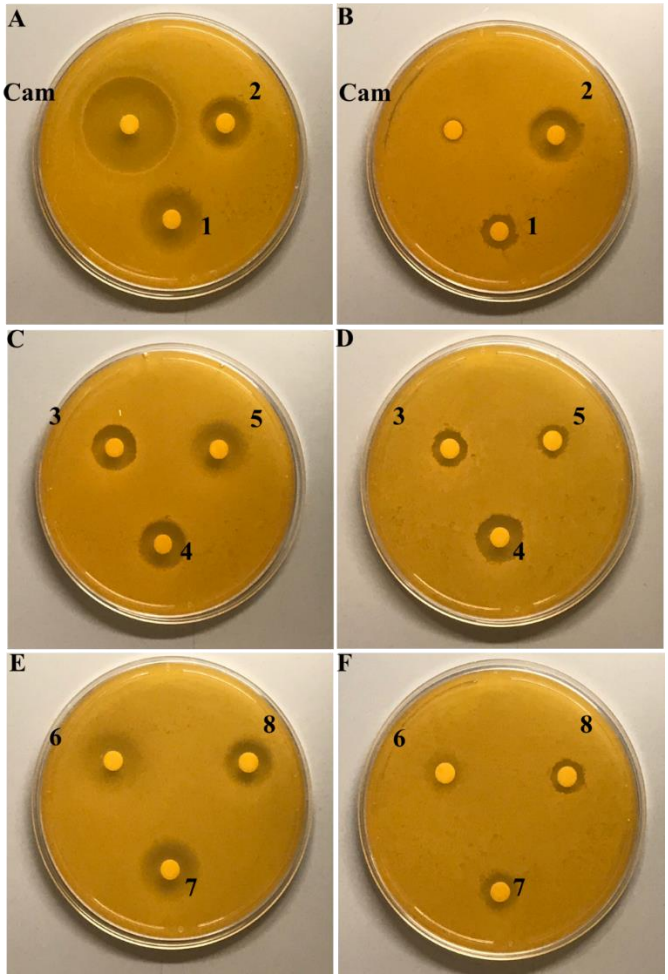

Figure 7.7: Left: B. subtilis 168 (Cam-sensitive); Right: B. subtilis with pC194 (Cam-resistant). All new derivatives inhibit Cam-resistant strain

The figure 7 shows the inhibition zones with and without the pC194 strain which results in the production of CAM acetyltransferase enzyme. This suggests that even with the presence of the enzyme all the derivatives show anti-bacterial activity. This data aligns with the data predicted from computational docking studies.

Compound	*B. Subtilis* 168	*B. Subtilis* 168 pC194
CAM	13mm	0.5mm
1	7mm	3mm
2	5mm	7mm
3	4mm	3mm
4	5mm	5mm
5	6mm	2mm
6	7mm	4mm
7	7mm	4mm
8	5mm	3mm

Table 7-1: Inhibition zones chart, all the above distances are measured from the end of the disk

In vitro protein synthesis was carried out using a kit supplied by NEB Labs (PURExpress® In Vitro Protein Synthesis Kit) which is a coupled transcription-translation system using E. coli ribosomes. The template DNA used was a plasmid containing a T7 polymerase promoter and a super folded GFP gene so raw fluorescence could be measured about protein synthesis. Using the BioSpectrometer from Eppendorf with the capability to measure fluorescence, an RFU520 value was taken every 15 minutes throughout 2 hours. CAM, CAM2, and CAM4 all show inhibition of protein synthesis in comparison to the “No Drug” control.

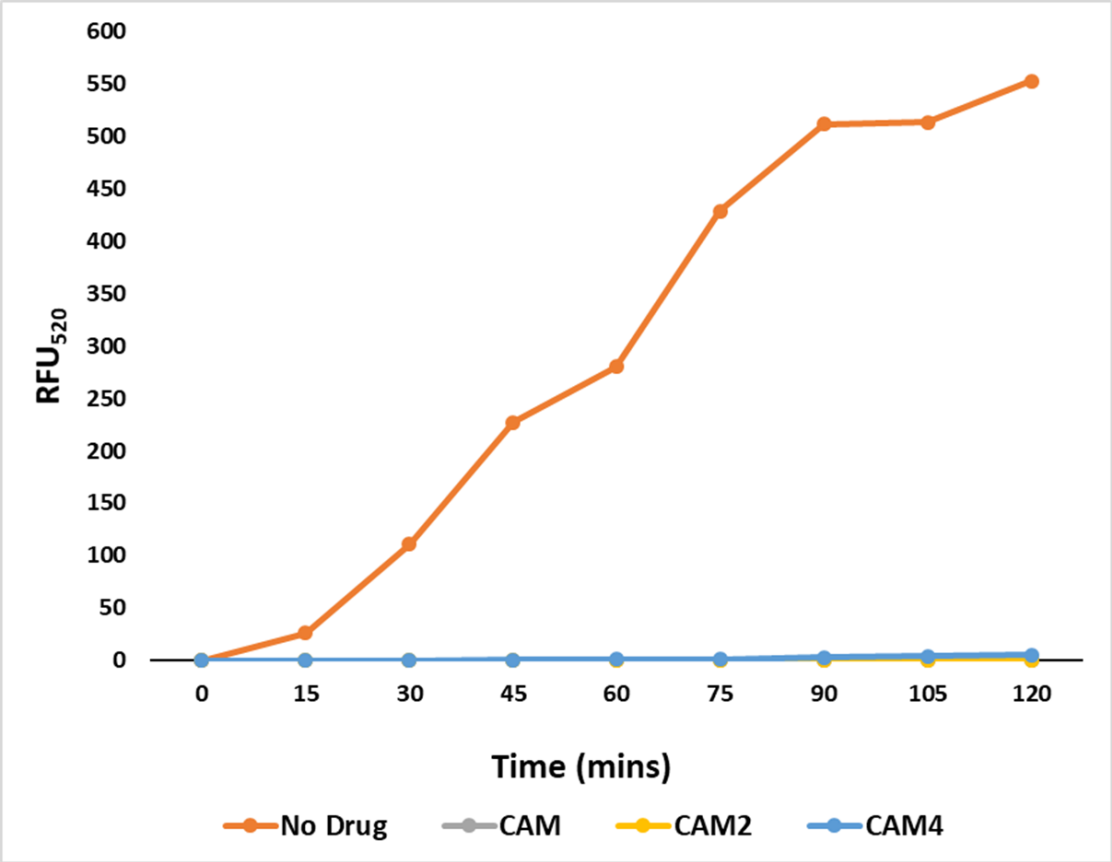

Figure 7.8: In vitro protein synthesis obtained via raw fluorescence units vs. time, excitation at 470 nm and emission is monitored at 520 nm

Conclusions

This study was able to show that eight novel derivatives of CAM has potential anti-bacterial effects and does not undergo acylation via the CAT enzyme while retaining their anti-biotic properties. Further studies will be conducted to investigate the toxicity of the CAM derivatives and possible drug formulations.

7.1 REFERENCES

(1) Company, A. C. Effect of Chloramphenicol in Cell-Free Preparations on Protein Synthesis of Escherichia CoZi *. **1962**, *237* (12).

(2) Bulkley, D.; Innis, C. A.; Blaha, G.; Steitz, T. A. Revisiting the Structures of Several Antibiotics Bound to the Bacterial Ribosome. **2010**, *107* (40). https://doi.org/10.1073/pnas.1008685107.

(3) Yang, Y.; Cui, H.; Zhou, P.; Liu, S. Haloarcula Amylolytica Sp . Nov ., an Extremely Halophilic Archaeon Isolated from Aibi Salt Lake In. **2019**, No. 2007, 103–106. https://doi.org/10.1099/ijs.0.64647-0.

(4) Gregory, S. T.; Carr, J. F.; Rodriguez-Correa, D.; Dahlberg, a. E. Mutational Analysis of 16S and 23S RRNA Genes of Thermus Thermophilus. *J. Bacteriol.* **2005**, *187* (14), 4804. https://doi.org/10.1128/JB.187.14.4804.

(5) Dunkle, J. A.; Xiong, L.; Mankin, A. S.; Cate, J. H. D. Structures of the Escherichia Coli Ribosome with Antibiotics Bound near the Peptidyl Transferase Center Explain Spectra of Drug Action. **2010**, *107* (40). https://doi.org/10.1073/pnas.1007988107.

(6) Dinos, G.; Athanassopoulos, C.; Missiri, D.; Giannopoulou, P.; Vlachogiannis, I.; Papadopoulos, G.; Papaioannou, D.; Kalpaxis, D. Chloramphenicol Derivatives as Antibacterial and Anticancer Agents: Historic Problems and Current Solutions. *Antibiotics* **2016**, *5* (2), 20. https://doi.org/10.3390/antibiotics5020020.

7.2 SUPPORTING INFORMATION

Inhibition of chloramphenicol-resistant bacteria by rationally-designed semi-synthetic chloramphenicol derivatives

Experimental section

Reagents

CAM, NaOH, Methanol, diethylether, all the isothiocyantes, dichloromethane were purchased from Sigma-Aldrich, Fisher Scientific, and TCI chemicals. All reagents were stored under an inert atmosphere before use. Unless otherwise noted, all reactions were performed under N_2.

Instrumentation

NMR spectra were obtained using Bruker Avance 300 MHz and 400 MHz spectrometers. Low resolution mass spectrometry was performed using a Shimadzu LRMS-2020. High resolution mass spectrometry was performed using a Thermo Scientific LTQ Orbitrap XL™ instrument.

Synthesis of CAM base

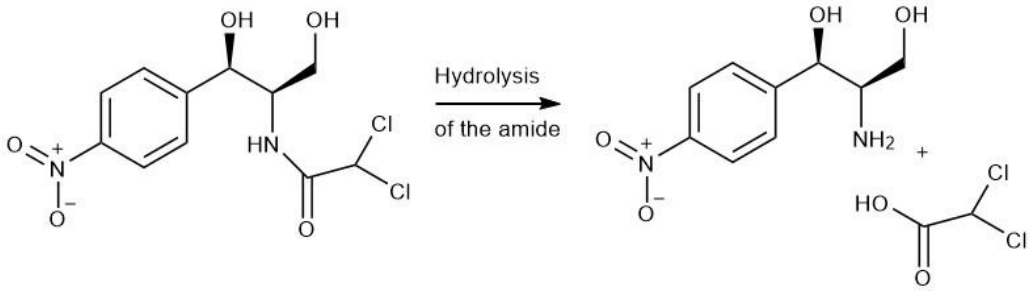

Chloramphenicol (3g) was charged with 1.46 N NaOH (200 ml) solution, then the RBF was left in dark, covered in aluminum foil at room temperature. The reaction time was 18 hours. Then extraction was performed as follows, 5 times with diethyl ether (200 ml each), and further extractions were performed using ethyl acetate (3 times 200 ml each). Both layers were dried over anhydrous sodium sulfate then followed with rotary evaporation. CAM base was obtained as an off-white product. This product was used without further purification for the next steps. ^{1}H NMR and ^{13}C NMR was performed using DMSO-d_6. ^{1}H NMR (400 MHz, DMSO-d_6) δ 8.21 – 8.14 (m, 2H), 7.63 – 7.56 (m, 2H), 5.58 – 5.40 (m, 1H), 4.68 (d, J = 4.3 Hz, 1H), 4.60 (t, J = 5.4 Hz, 1H), 3.18 (ddd, J = 10.3, 6.0, 4.1 Hz, 1H), 2.71 (td, J = 5.9, 4.3 Hz, 1H), 1.35 (s, 2H).

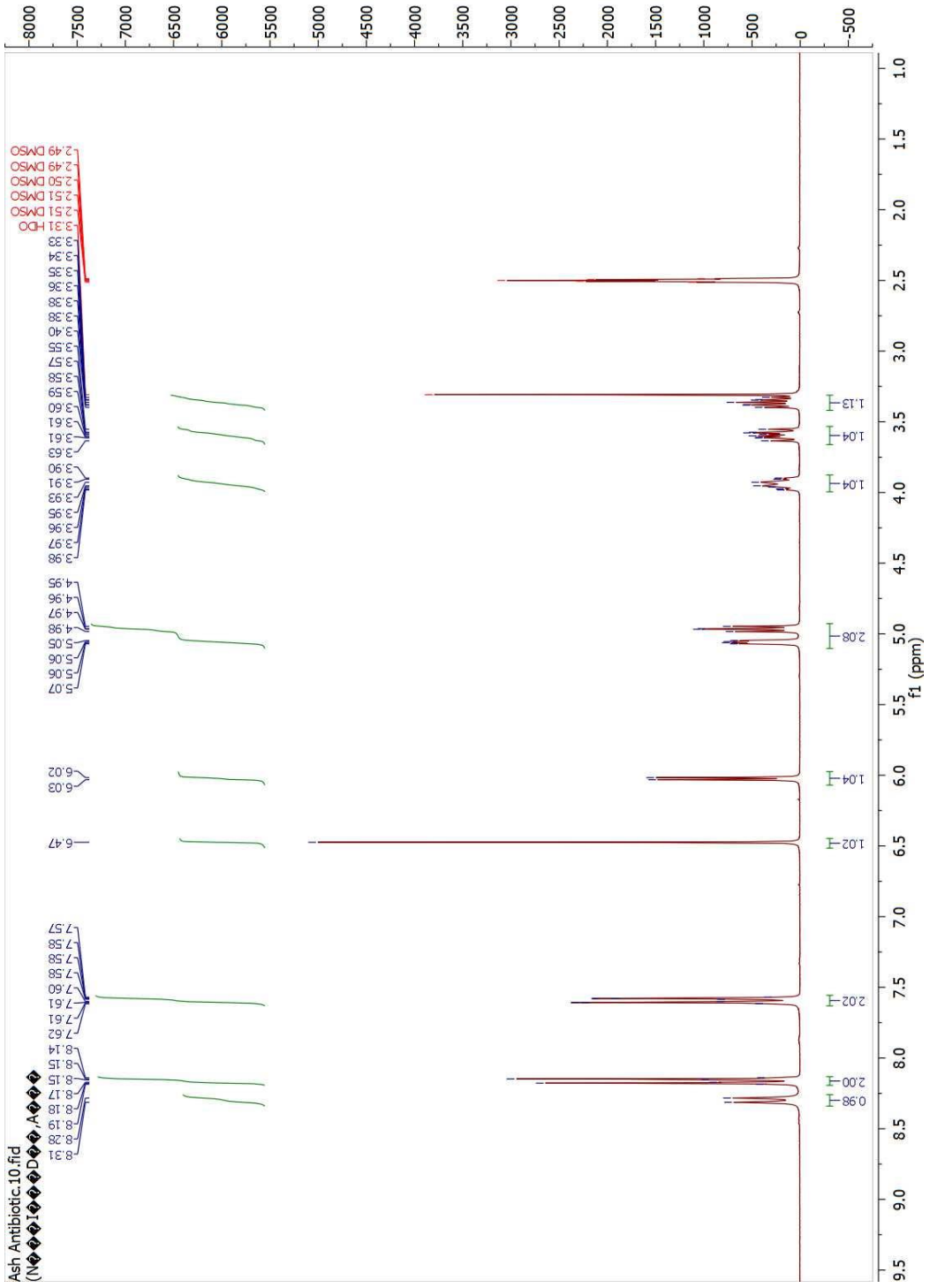

Figure 7.9: Chloramphenicol reference ^{1}H NMR before the hydrolysis

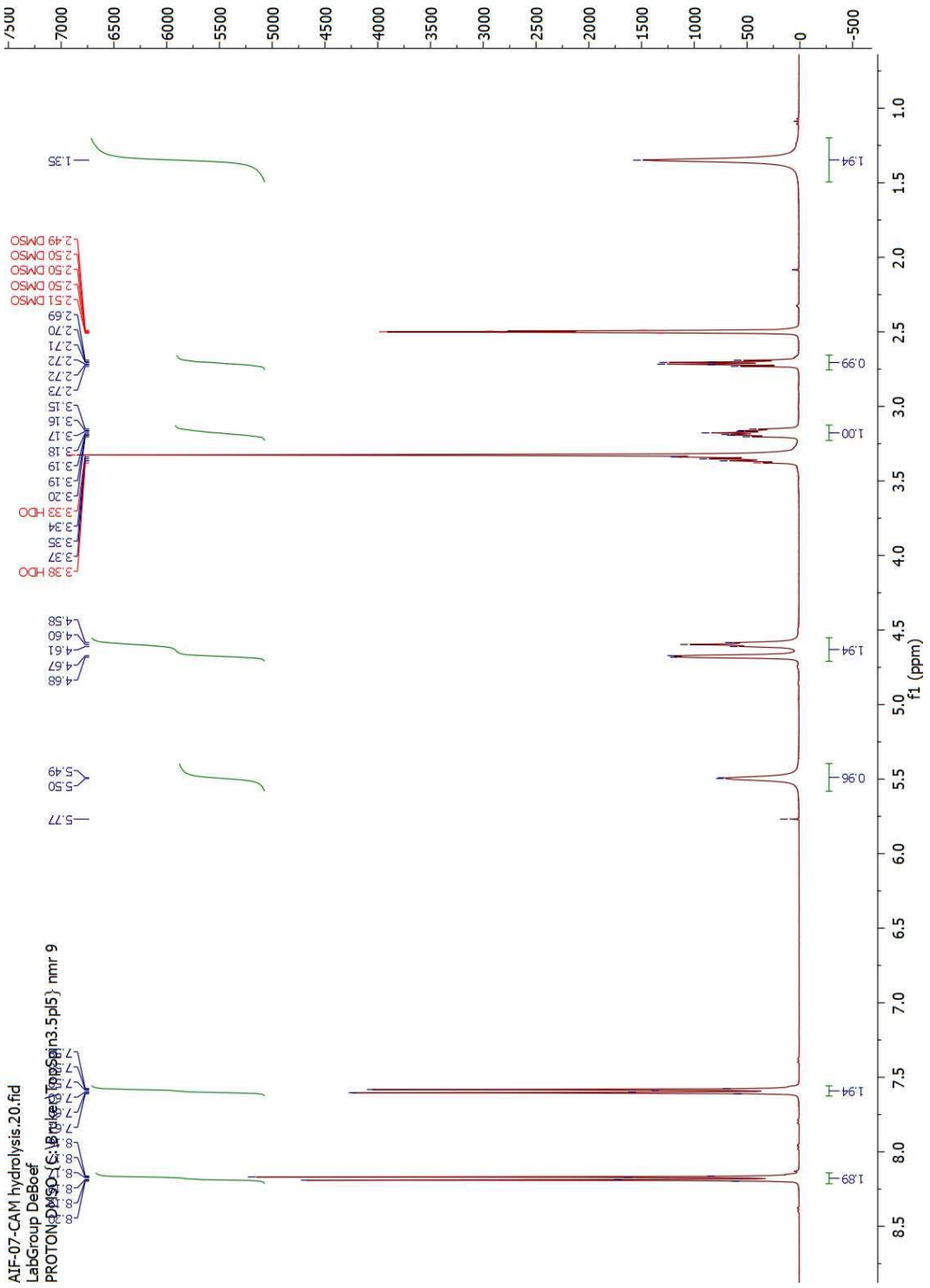

Figure 7.10: 1H NMR of CAM base (Hydrolysis of CAM

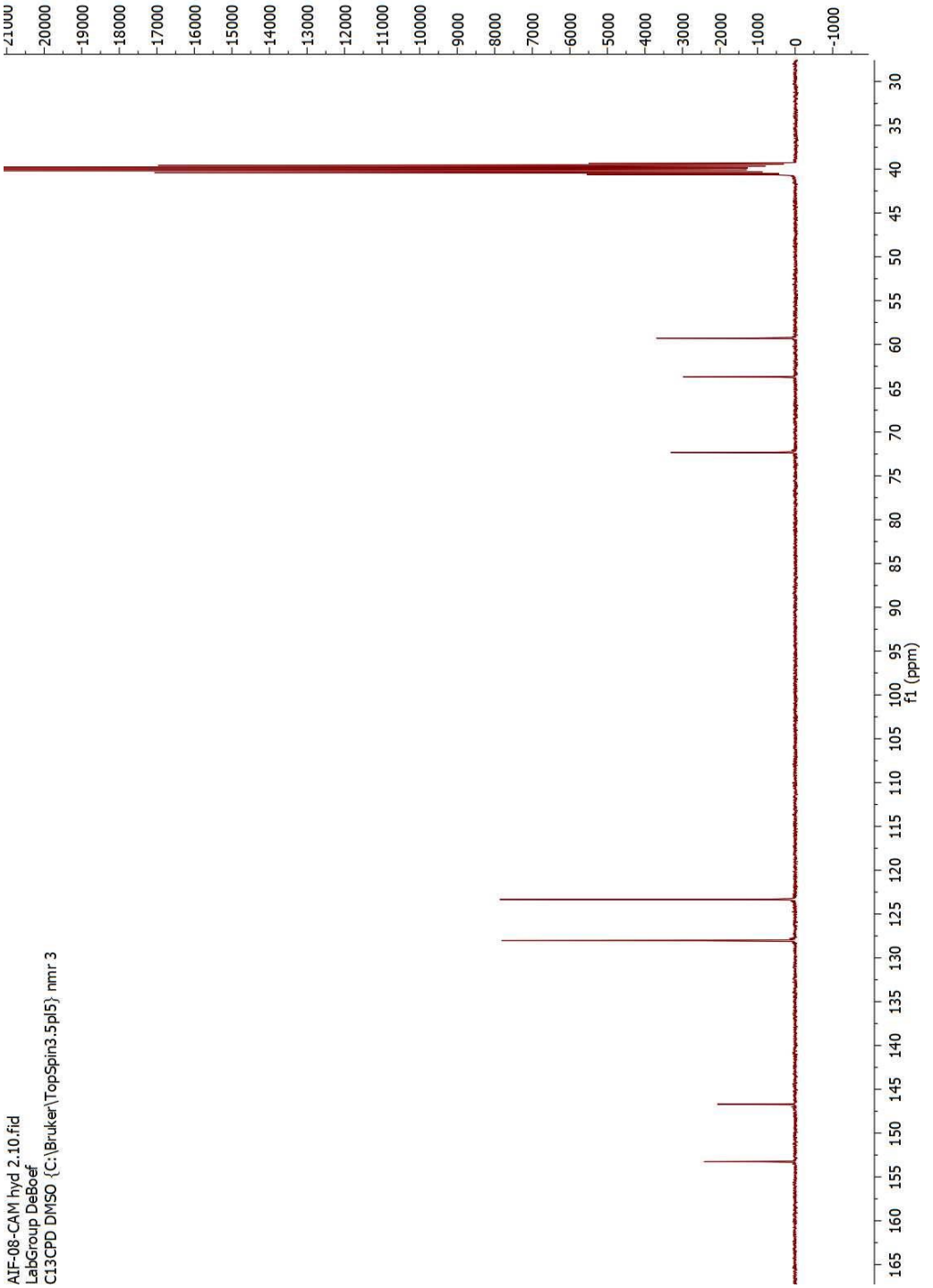

Figure 7.11: ^{13}C NMR of CAM base

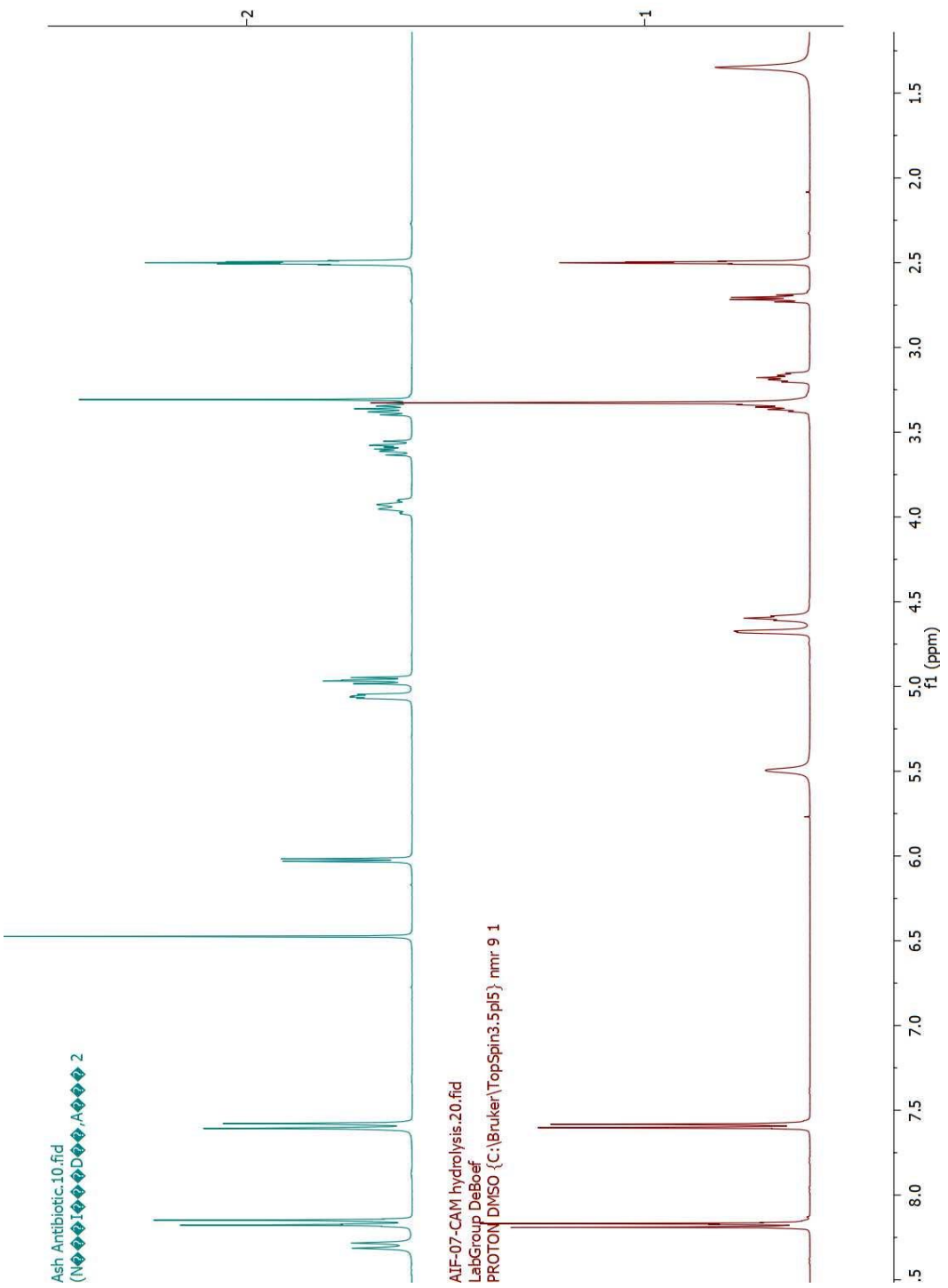

Figure 7.12: Stacked ^{1}H NMR of CAM and CAM base

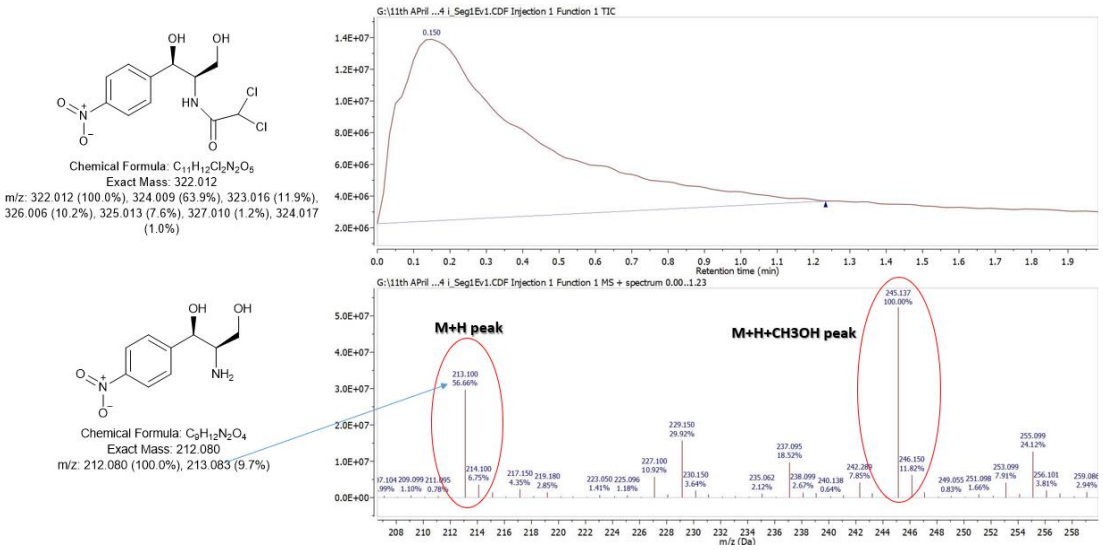

Figure 7.13: Mass spectrum of CAM base

Synthesis of 1-((1R,2R)-1,3-dihydroxy-1-(4-nitrophenyl)propan-2-yl)-3-(4nitrophenyl)thiourea

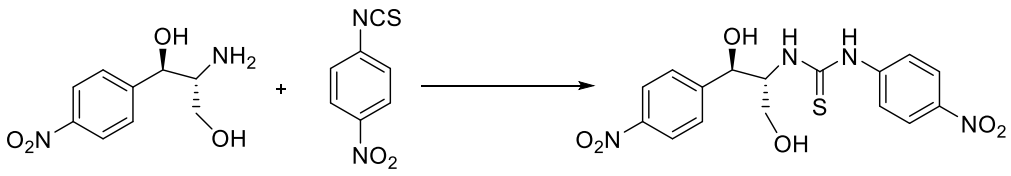

CAM base was added in with isothiocyanate moiety in 1 : 1.2 equivalents. Both were dissolved in anhydrous dichloromethane. The reaction solution was stirred for 12 hours at room temperature. Next, the reaction solution was subjected to rotatory evaporation. Then it was subjected to flash chromatography. ^{1}H NMR and ^{13}C NMR was performed using DMSO-d_6. ^{1}H NMR (400 MHz, DMSO-d6) δ 10.36 (s, 1H), 8.32 – 8.28 (m, 2H), 8.22 – 8.19 (m, 2H), 8.16 – 8.13 (m, 2H), 8.02 (d, J = 8.6 Hz, 1H), 7.92 – 7.87 (m, 2H), 7.68 (d, J = 2.3 Hz, 2H), 6.25 (d, J = 4.4 Hz, 1H), 5.25 – 5.16 (m, 1H), 5.11 (br, 1H), 4.60 (qt, J = 5.9, 2.1 Hz, 1H), 3.62 – 3.51 (m, 2H).

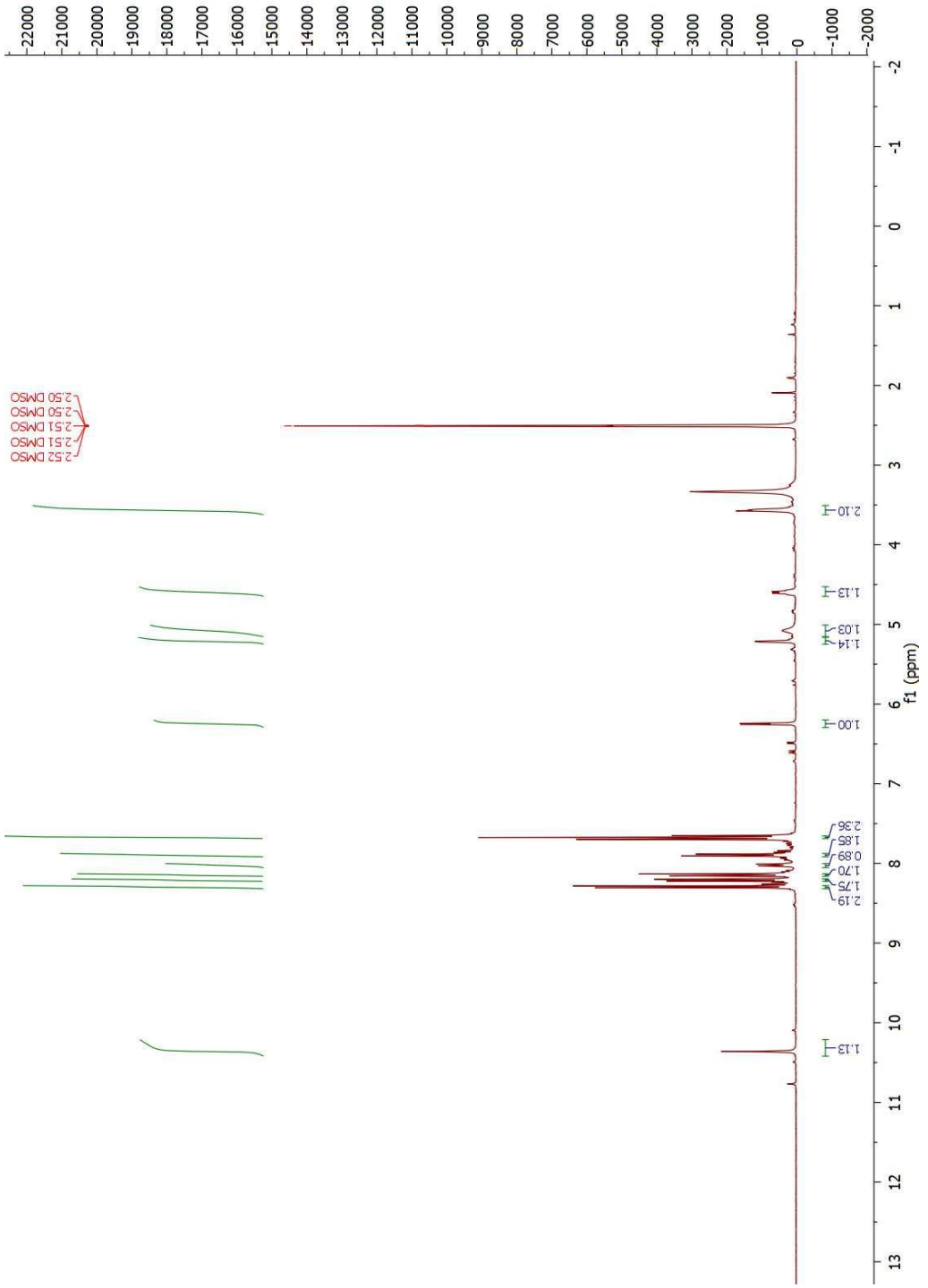

Figure 7.14: ^{1}H NMR of 1-((1R,2R)-1,3-dihydroxy-1-(4-nitrophenyl)propan-2-yl)-3-(4nitrophenyl)thiourea

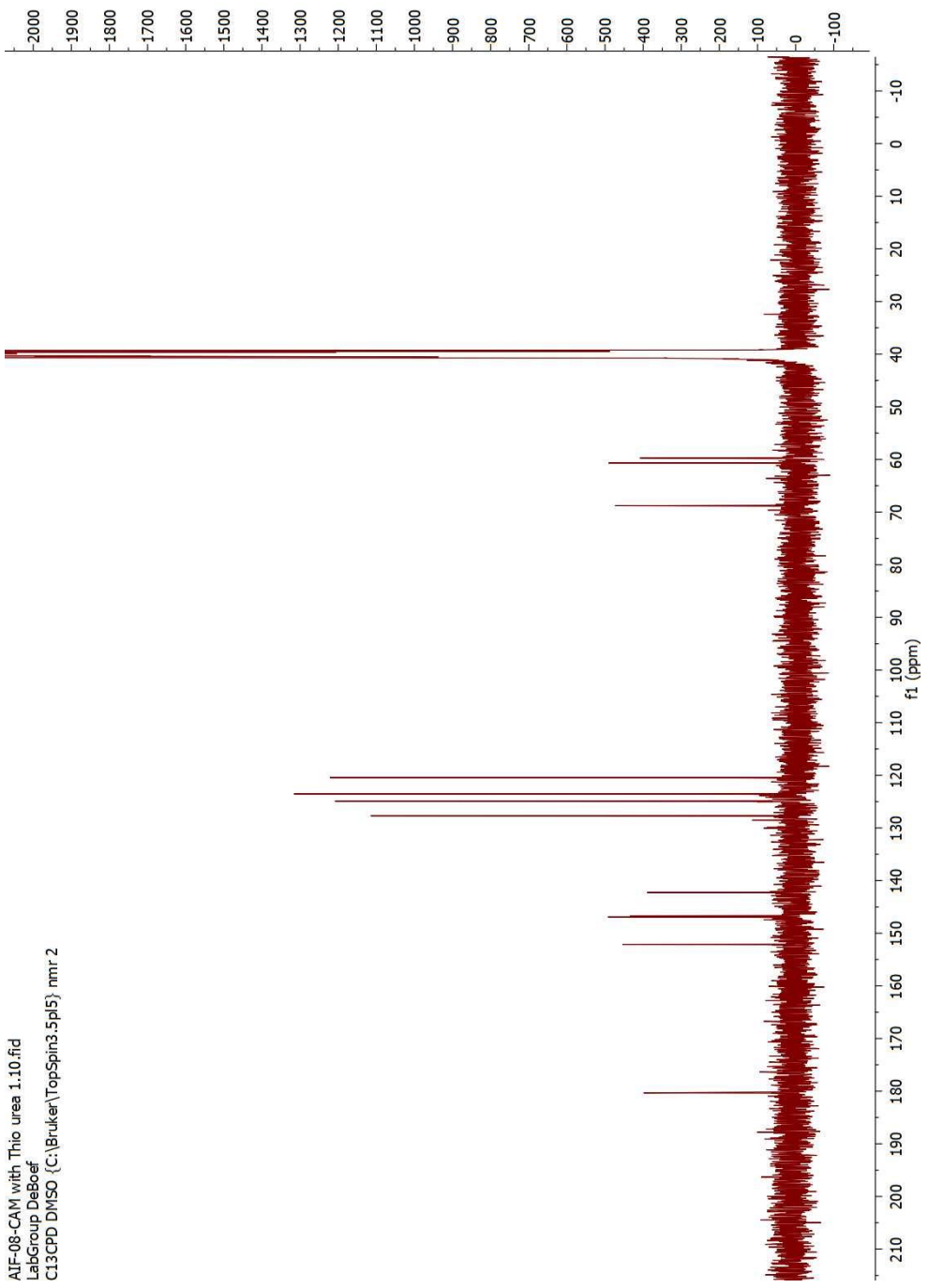

Figure 7.15: ^{13}C NMR of 1-((1R,2R)-1,3-dihydroxy-1-(4-nitrophenyl)propan-2-yl)-3-(4nitrophenyl)thiourea

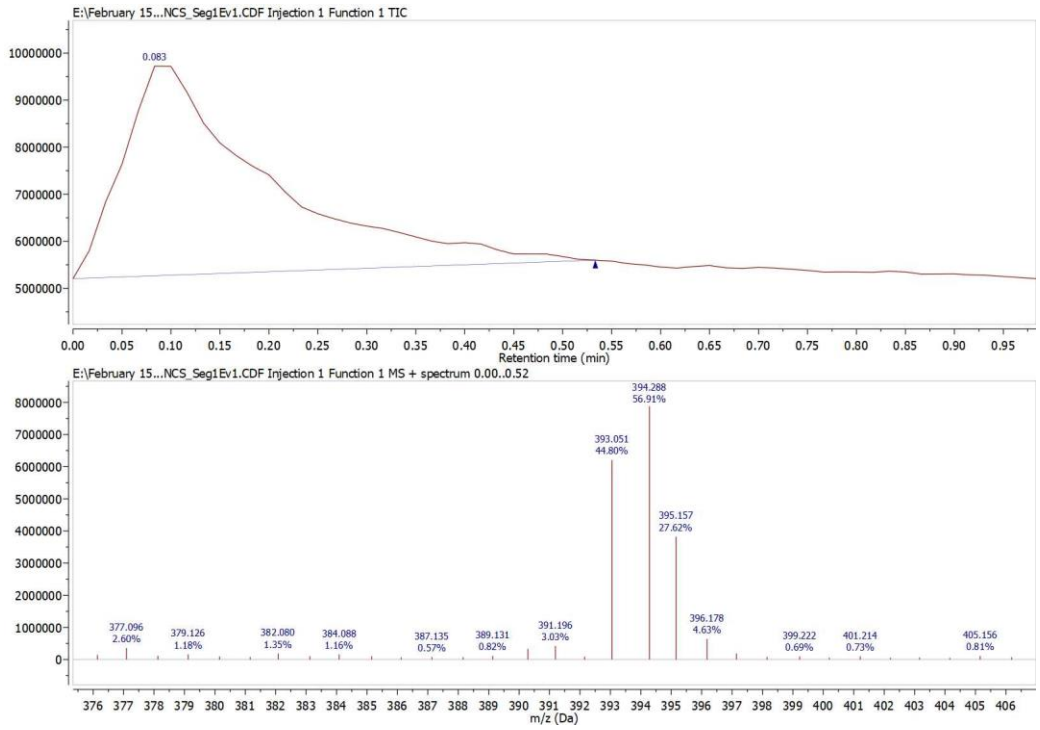

Figure 7.16: Mass spectrum of 1-((1R,2R)-1,3-dihydroxy-1-(4-nitrophenyl)propan-2-yl)-3-(4nitrophenyl)thiourea

Synthesis of 1-(4-chlorophenyl)-3-((1R,2R)-1,3-dihydroxy-1-(4-nitrophenyl)propan-2-yl)thiourea

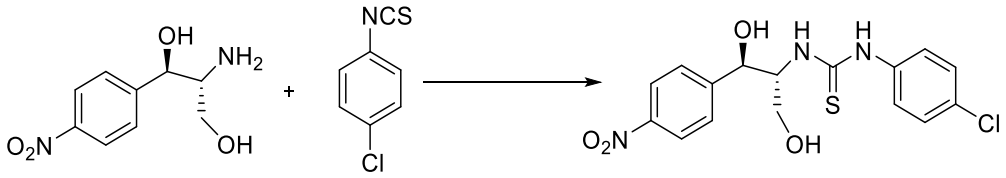

CAM base was added in with isothiocyanate moiety in 1 : 1.2 equivalents. Both were dissolved in anhydrous dichloromethane. The reaction solution was stirred for 12 hours at room temperature. Next, the reaction solution was subjected to rotatory evaporation. Then it was subjected to flash chromatography. ^{1}H NMR and ^{13}C NMR was performed using DMSO-d_6 as a solvent. 1H NMR (400 MHz, DMSO-d6) δ 10.01 (s, 5H), 8.25 – 8.18 (m, 11H), 7.83 (d, J = 8.6 Hz, 5H), 7.68 – 7.61 (m, 22H), 7.24 (t, J = 1.9 Hz, 5H), 6.22 (d, J = 4.4 Hz, 5H), 5.23 – 5.16 (m, 5H), 5.05 (dd, J = 6.1, 4.8 Hz, 6H), 4.57 (d, J = 7.6 Hz, 6H), 3.60 – 3.48 (m, 11H), 2.09 (s, 4H), 1.70 (s, 1H).

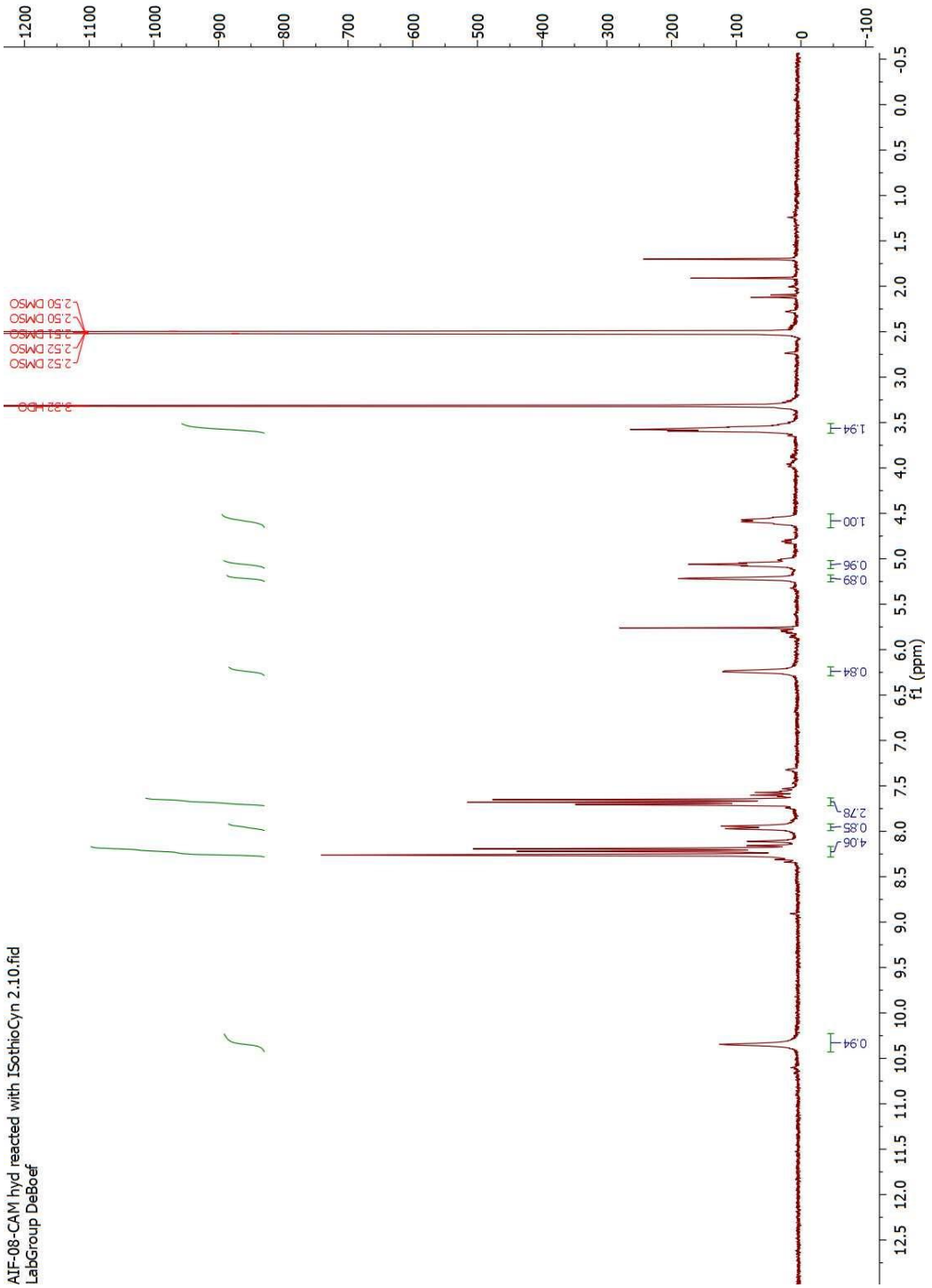

Figure 7.17: ^{1}H NMR of 1-(4-chlorophenyl)-3-((1R,2R)-1,3-dihydroxy-1-(4-nitrophenyl)propan-2-yl)thiourea

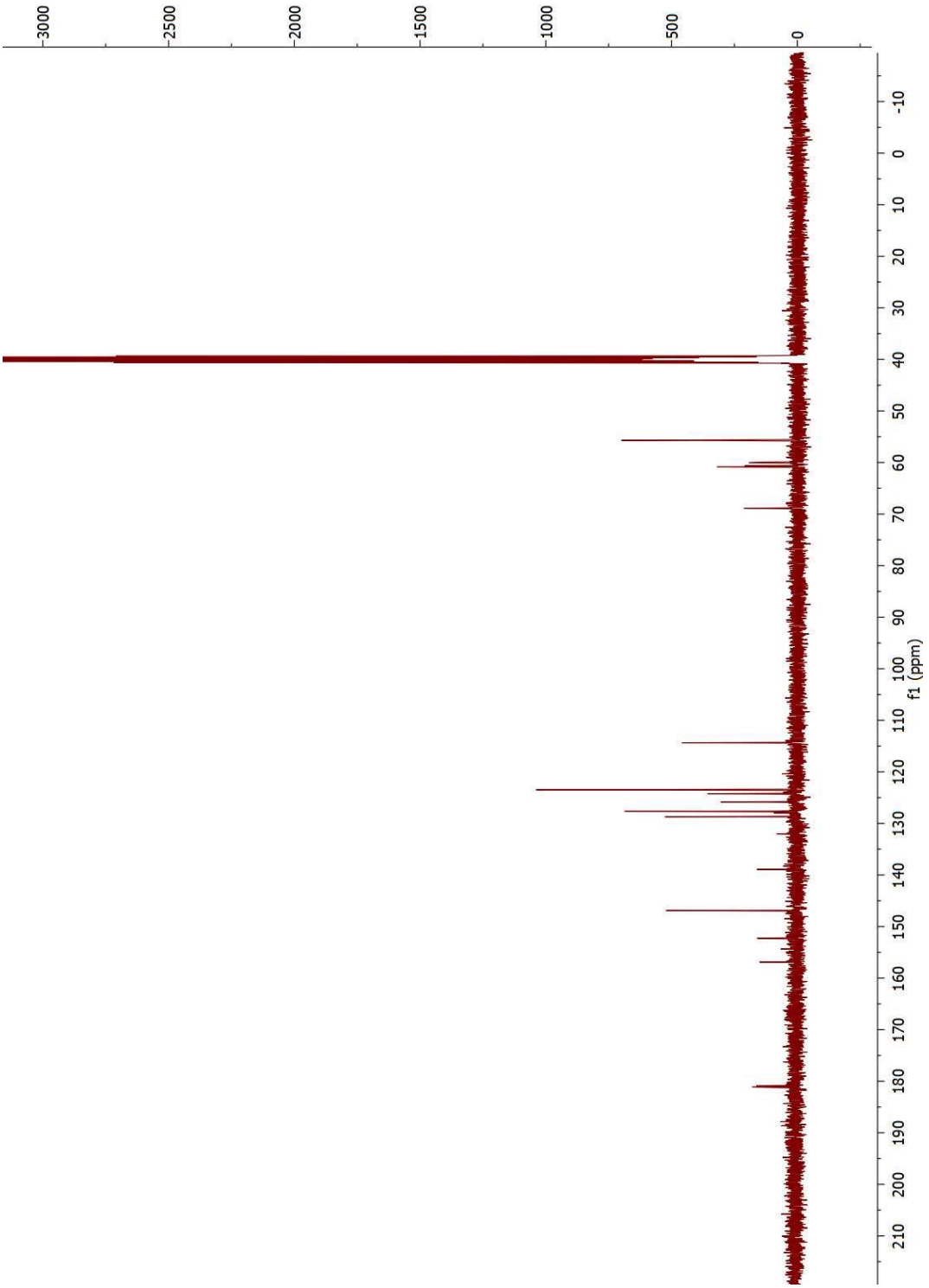

Figure 7.18: ^{13}C NMR of 1-(4-chlorophenyl)-3-((1R,2R)-1,3-dihydroxy-1-(4-nitrophenyl)propan-2-yl)thiourea

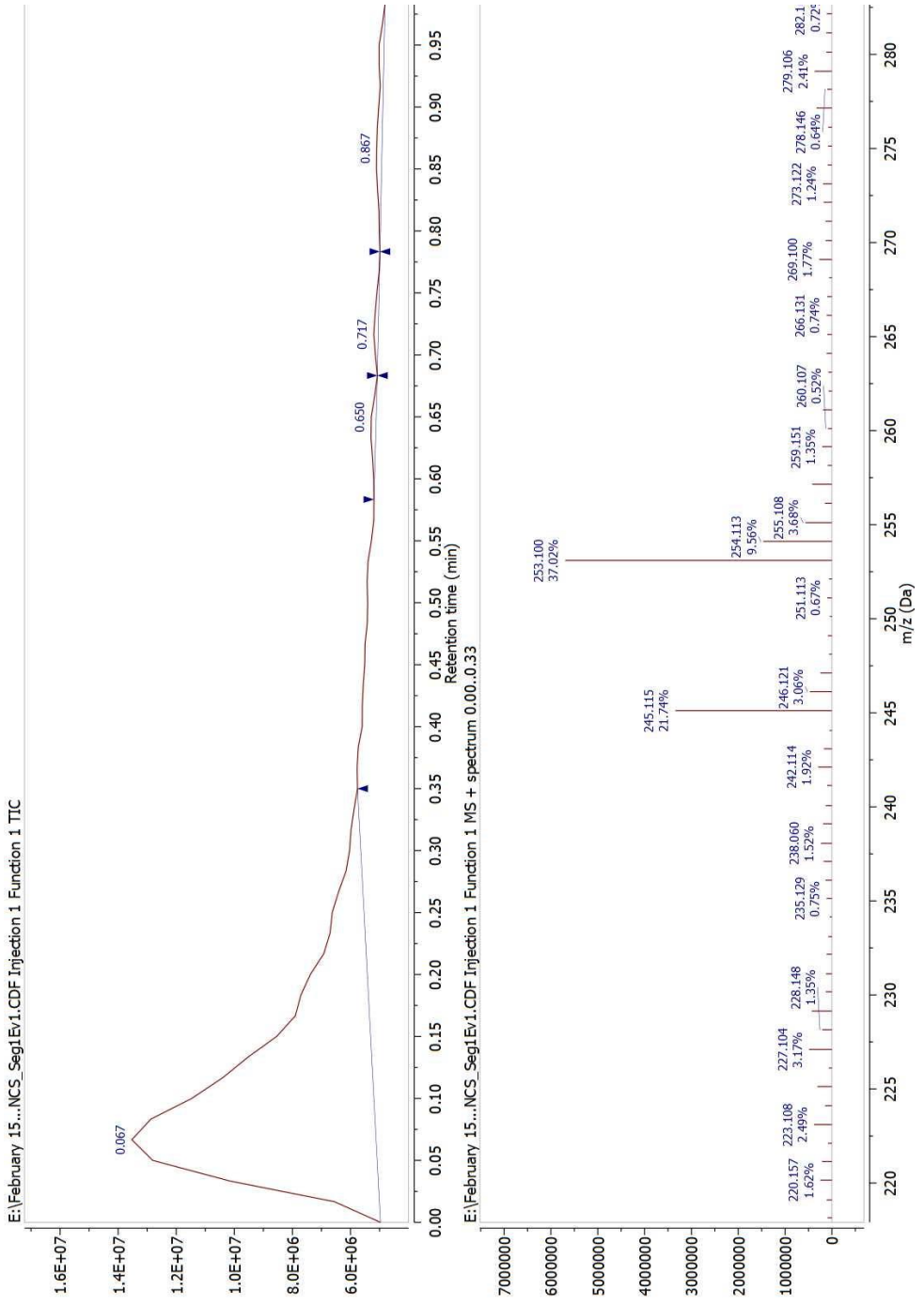

Figure 7.19: Mass spectrum of 1-(4-chlorophenyl)-3-((1R,2R)-1,3-dihydroxy-1-(4-nitrophenyl)propan-2-yl)thiourea

Synthesis of 1-(4-acetylphenyl)-3-((1R,2R)-1,3-dihydroxy-1-(4-nitrophenyl)propan-2-yl)thiourea

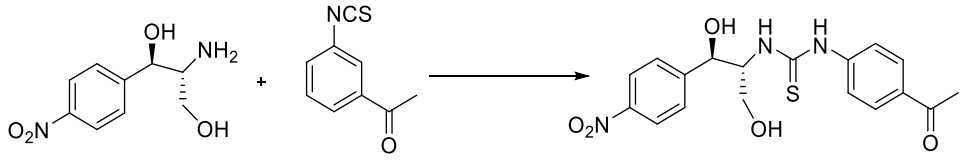

CAM base was added in with isothiocyanate moiety in 1 : 1.2 equivalents. Both were dissolved in anhydrous dichloromethane. The reaction solution was stirred for 12 hours at room temperature. Next, the reaction solution was subjected to rotatory evaporation. Then it was subjected to flash chromatography. ^{1}H NMR and ^{13}C NMR was performed using DMSO-d_6 as a solvent. 1H NMR (400 MHz, DMSO-d6) δ 9.94 (s, 1H), 8.24 – 8.19 (m, 2H), 8.07 (t, J = 1.9 Hz, 1H), 7.74 – 7.70 (m, 1H), 7.69 – 7.60 (m, 4H), 7.42 (t, J = 7.9 Hz, 1H), 6.22 – 6.11 (m, 1H), 5.20 (d, J = 3.5 Hz, 1H), 5.04 (s, 1H), 4.58 (t, J = 7.5 Hz, 1H), 3.63 – 3.26 (m, 4H).

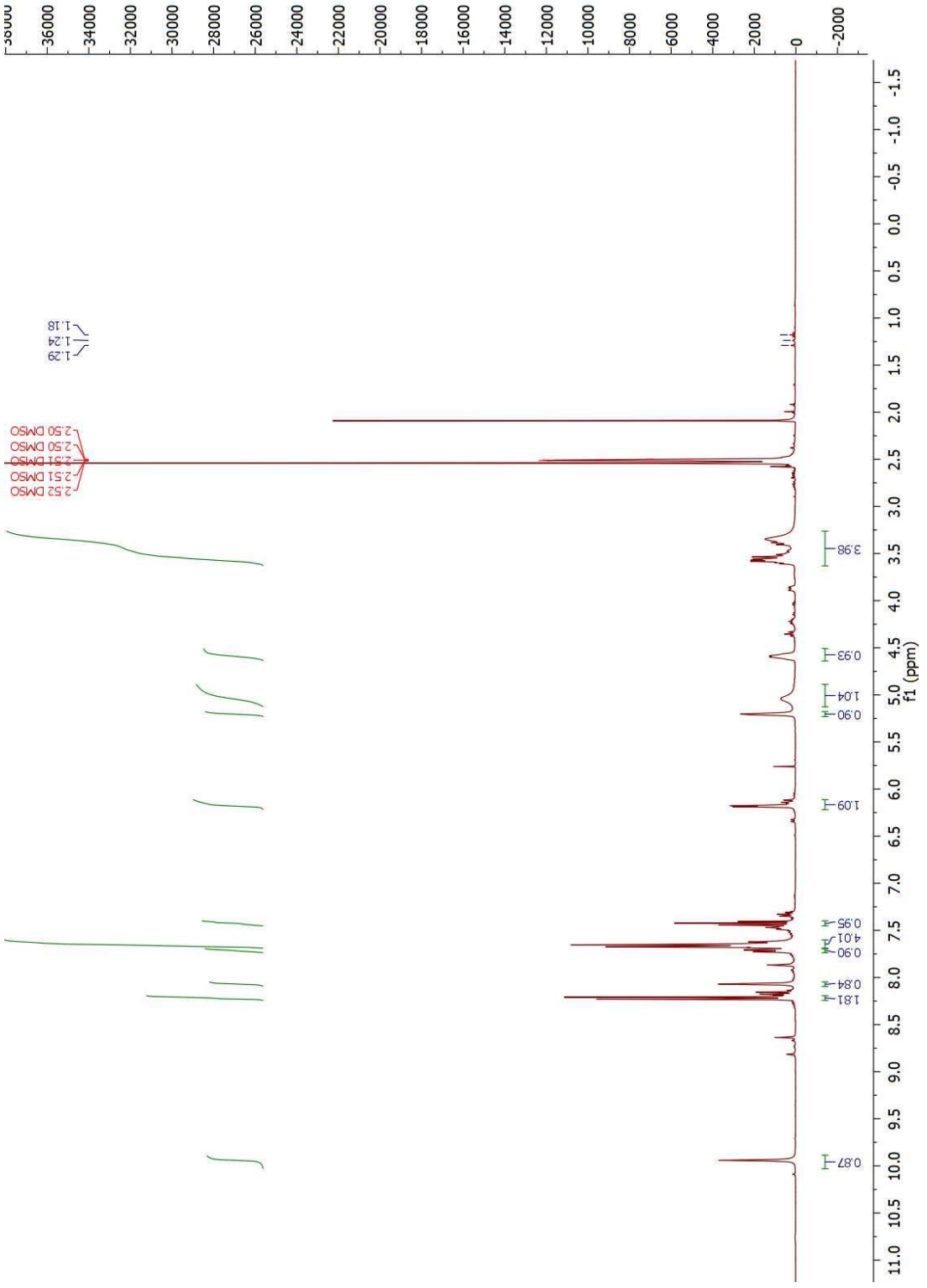

Figure 7.20: ^{1}H NMR of 1-(4-acetylphenyl)-3-((1R,2R)-1,3-dihydroxy-1-(4-nitrophenyl)propan-2-yl)thiourea

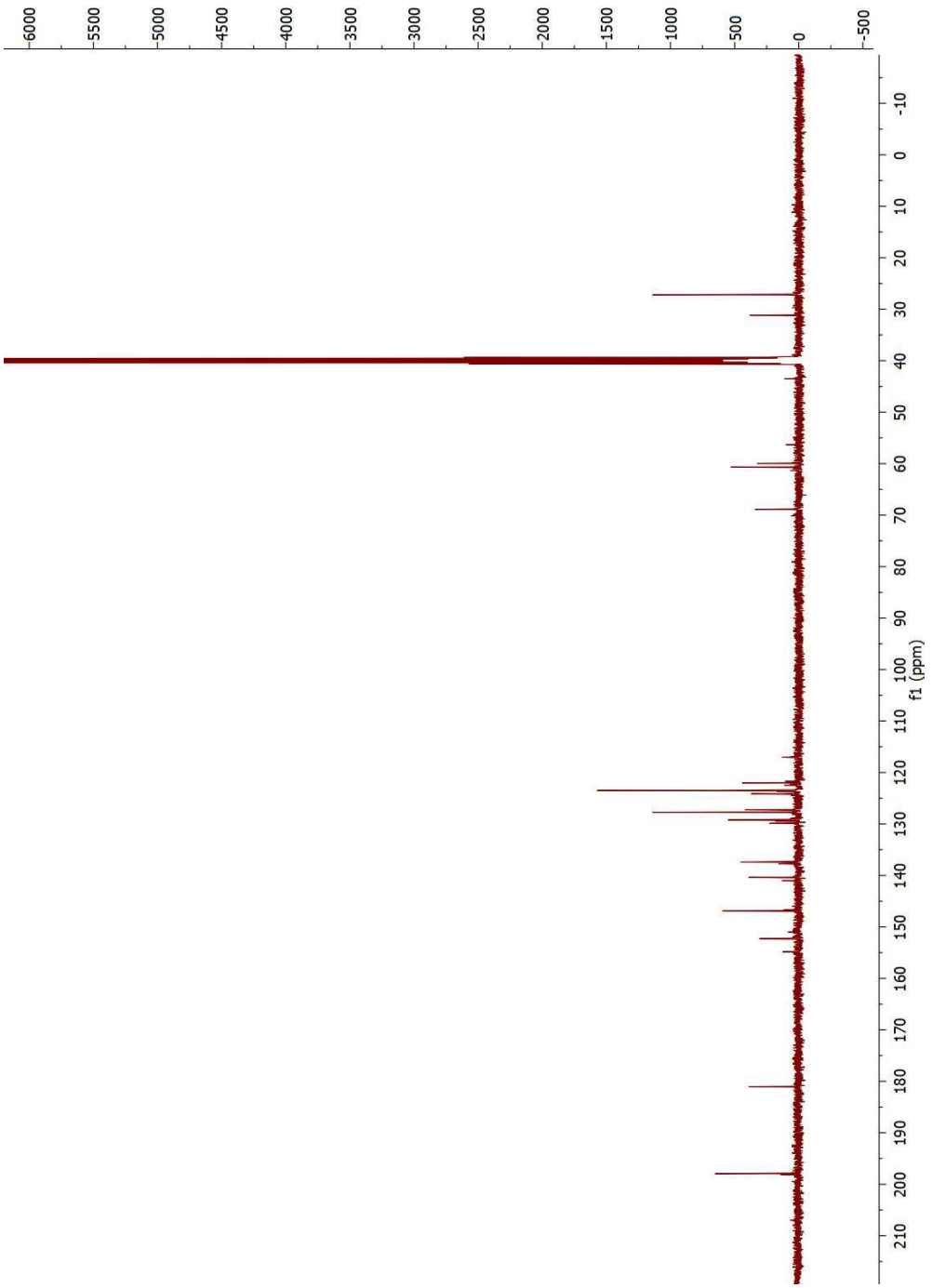

Figure 7.21: ^{13}C NMR of 1-(4-acetylphenyl)-3-((1R,2R)-1,3-dihydroxy-1-(4-nitrophenyl)propan-2-yl)thiourea

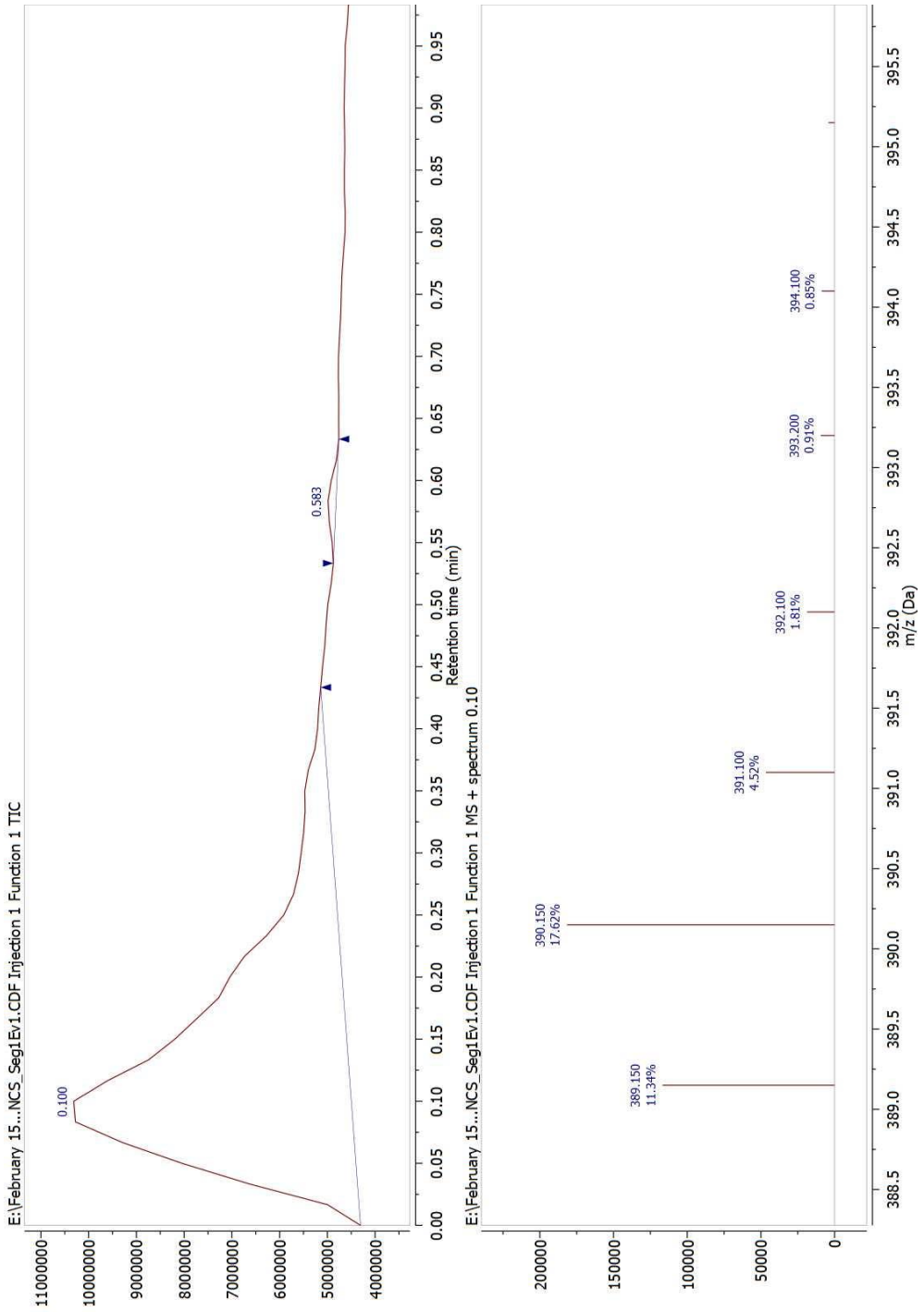

Figure 7.22: Mass spectrum of 1-(4-acetylphenyl)-3-((1R,2R)-1,3-dihydroxy-1-(4-nitrophenyl)propan-2-yl)thiourea

Synthesis of 1-(3,5-bis(trifluoromethyl)phenyl)-3-((1R,2R)-1,3-dihydroxy-1-(4-nitrophenyl)propan-2-yl)thiourea

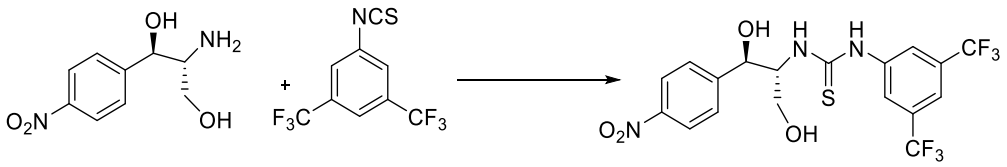

CAM base was added in with isothiocyanate moiety in 1 : 1.2 equivalents. Both were dissolved in anhydrous dichloromethane. The reaction solution was stirred for 12 hours at room temperature. Next, the reaction solution was subjected to rotatory evaporation. Then it was subjected to flash chromatography. ^{1}H NMR and ^{13}C NMR was performed using DMSO-d_6 as a solvent. ^{1}H NMR (400 MHz, DMSO-d_6) δ 10.34 (s, 1H), 8.30 – 8.17 (m, 4H), 7.95 (d, J = 8.6 Hz, 1H), 7.72 – 7.63 (m, 3H), 6.25 (d, J = 4.4 Hz, 1H), 5.22 (t, J = 2.9 Hz, 1H), 5.07 (s, 1H), 4.58 (dtd, J = 8.8, 6.4, 5.9, 2.8 Hz, 1H), 3.61 – 3.50 (m, 2H).

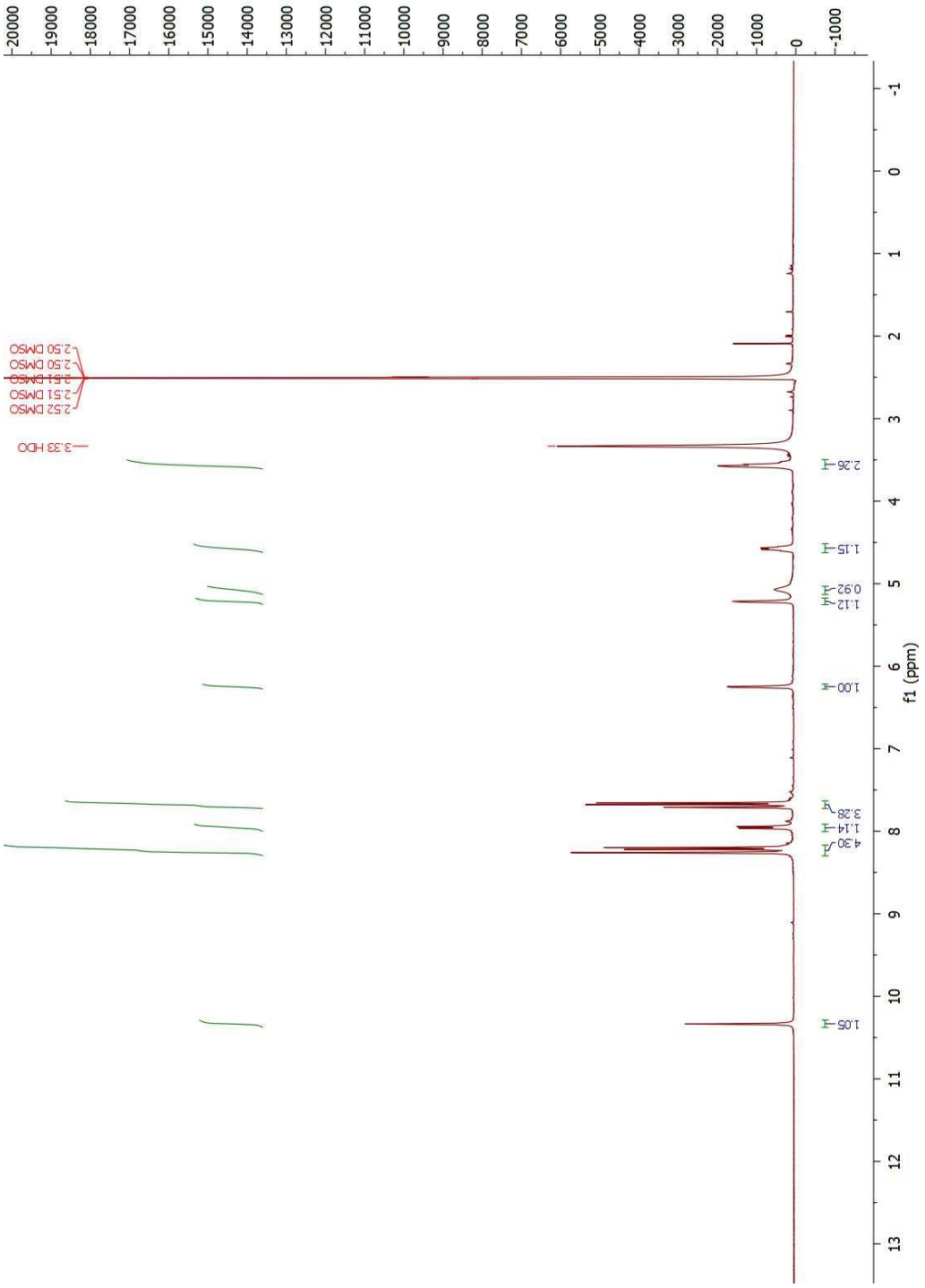

Figure 7.23: ^{1}H NMR of 1-(3,5-bis(trifluoromethyl)phenyl)-3-((1R,2R)-1,3-dihydroxy-1-(4-nitrophenyl)propan-2-yl)thiourea

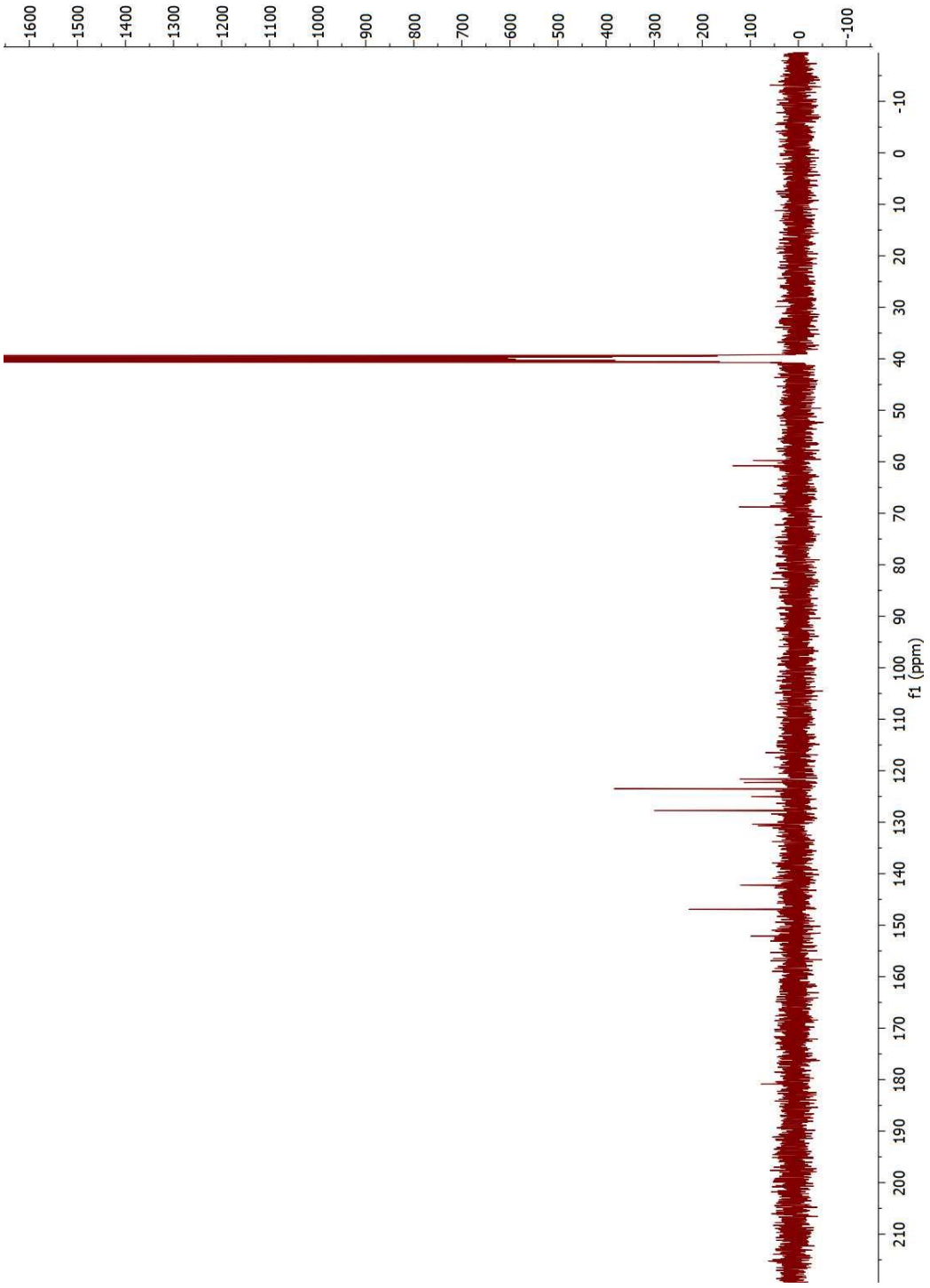

Figure 7.24: ^{13}C NMR of 1-(3,5-bis(trifluoromethyl)phenyl)-3-((1R,2R)-1,3-dihydroxy-1-(4-nitrophenyl)propan-2-yl)thiourea

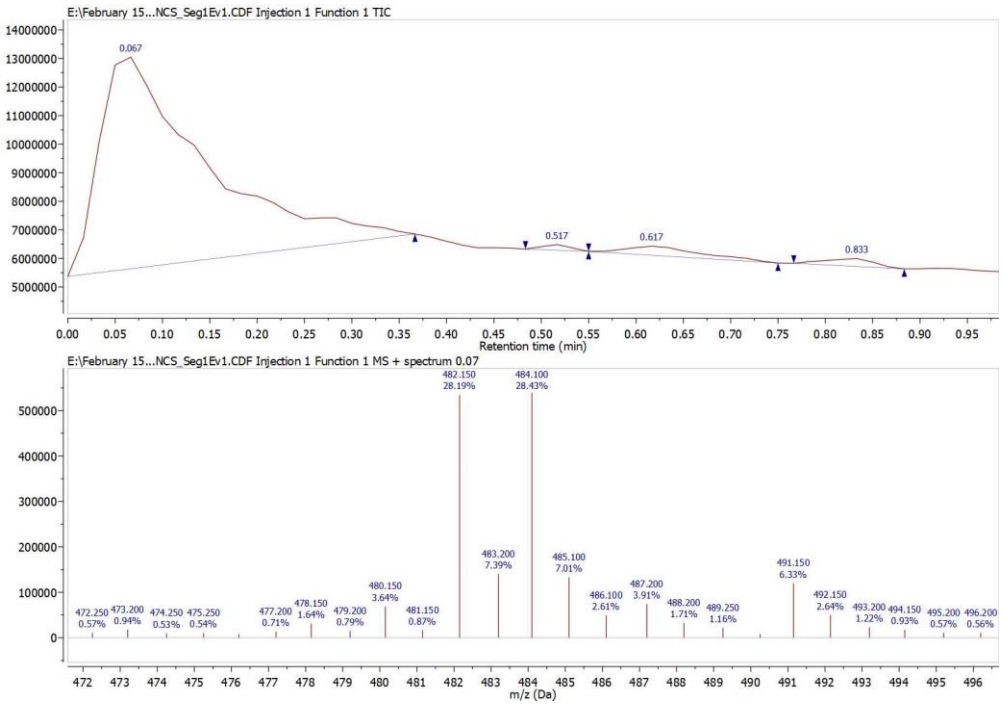

Figure 7.25: Mass spectrum of 1-(3,5-bis(trifluoromethyl)phenyl)-3-((1R,2R)-1,3-dihydroxy-1-(4-nitrophenyl)propan-2-yl)thiourea

Synthesis of 1-(2-chloro-4-nitrophenyl)-3-((1R,2R)-1,3-dihydroxy-1-(4-nitrophenyl)propan-2-yl)thiourea

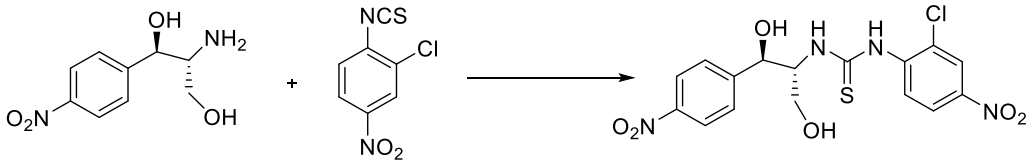

CAM base was added in with isothiocyanate moiety in 1 : 1.2 equivalents. Both were dissolved in anhydrous dichloromethane. The reaction solution was stirred for 12 hours at room temperature. Next, the reaction solution was subjected to rotatory evaporation. Then it was subjected to flash chromatography. ^{1}H NMR and ^{13}C NMR was performed using DMSO-d_6 as a solvent. ^{1}H NMR (400 MHz, DMSO-d6) δ 9.74 (s, 1H), 8.74 (d, J = 8.7 Hz, 1H), 8.35 – 8.30 (m, 2H), 8.23 – 8.18 (m, 2H), 8.10 (dd, J = 9.2, 2.7 Hz, 1H), 7.69 – 7.64 (m, 2H), 6.21 (d, J = 4.3 Hz, 1H), 5.22 (dd, J = 4.5, 2.1 Hz, 1H), 5.08 (dd, J = 6.2, 4.6 Hz, 1H), 4.62 (q, J = 7.3 Hz, 1H), 3.58 (dtd, J = 19.4, 10.0, 6.0 Hz, 2H).

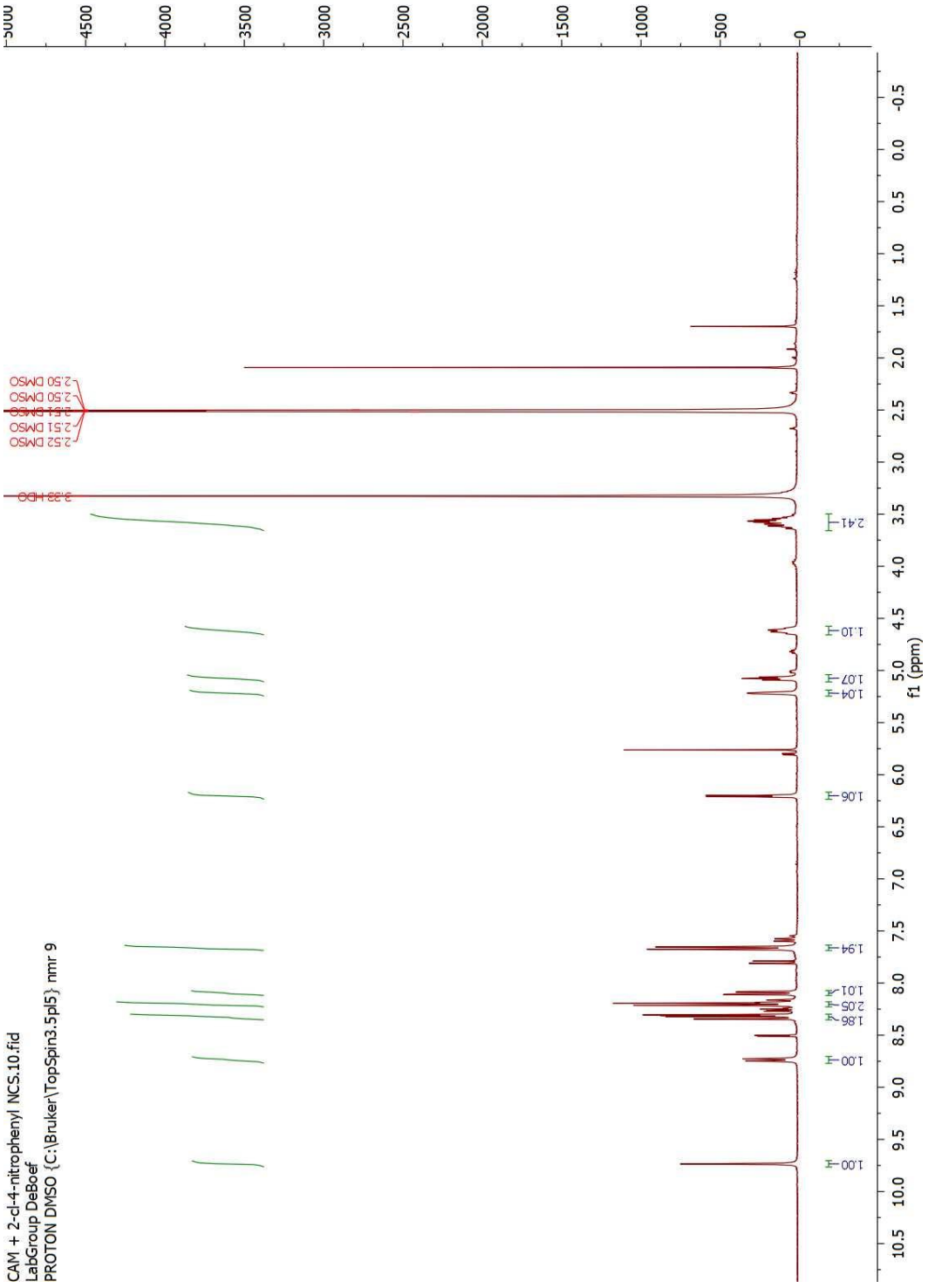

Figure 7.26: ^{1}H NMR of 1-(2-chloro-4-nitrophenyl)-3-((1R,2R)-1,3-dihydroxy-1-(4-nitrophenyl)propan-2-yl)thiourea

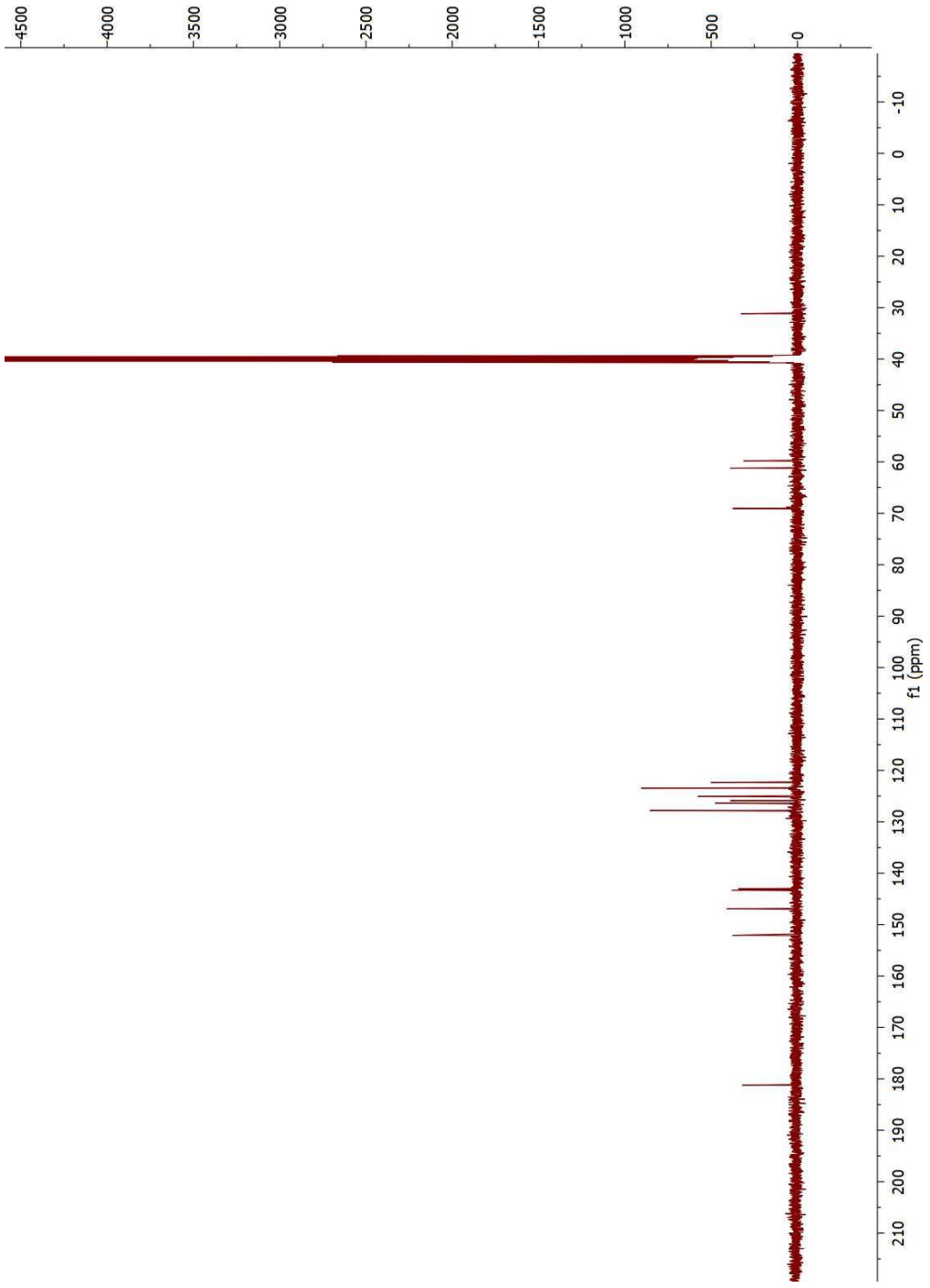

Figure 7.27: ^{13}C of 1-(2-chloro-4-nitrophenyl)-3-((1R,2R)-1,3-dihydroxy-1-(4-nitrophenyl)propan-2-yl)thiourea

Synthesis of 1-(3,5-dichlorophenyl)-3-((1R,2R)-1,3-dihydroxy-1-(4-nitrophenyl)propan-2-yl)thiourea

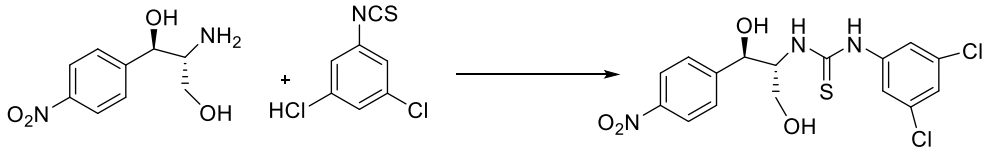

CAM base was added in with isothiocyanate moiety in 1 : 1.2 equivalents. Both were dissolved in anhydrous dichloromethane. The reaction solution was stirred for 12 hours at room temperature. Next, the reaction solution was subjected to rotatory evaporation. Then it was subjected to flash chromatography. ^{1}H NMR and ^{13}C NMR was performed using DMSO-d_6 as a solvent. ^{1}H NMR (400 MHz, DMSO-d6) δ 10.02 (s, 1H), 8.26 – 8.16 (m, 2H), 7.83 (d, J = 8.6 Hz, 1H), 7.69 – 7.60 (m, 4H), 7.24 (t, J = 1.9 Hz, 1H), 6.22 (d, J = 4.4 Hz, 1H), 5.20 (dd, J = 4.5, 2.0 Hz, 1H), 5.05 (t, J = 5.4 Hz, 1H), 4.63 – 4.51 (m, 1H), 3.54 (dt, J = 8.6, 4.1 Hz, 2H).

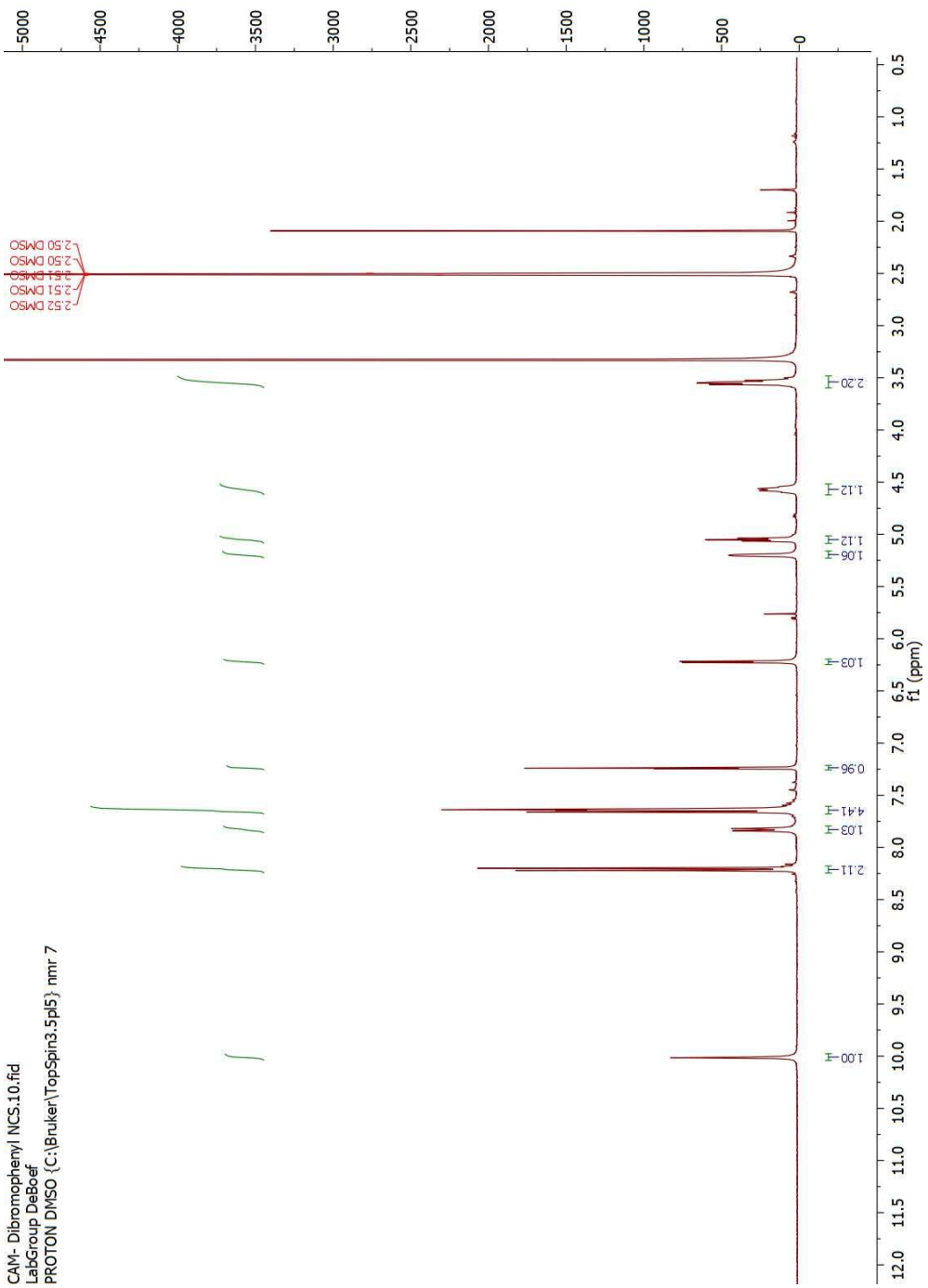

Figure 7.28: ^{1}H NMR of 1-(3,5-dichlorophenyl)-3-((1R,2R)-1,3-dihydroxy-1-(4-nitrophenyl)propan-2-yl)thiourea

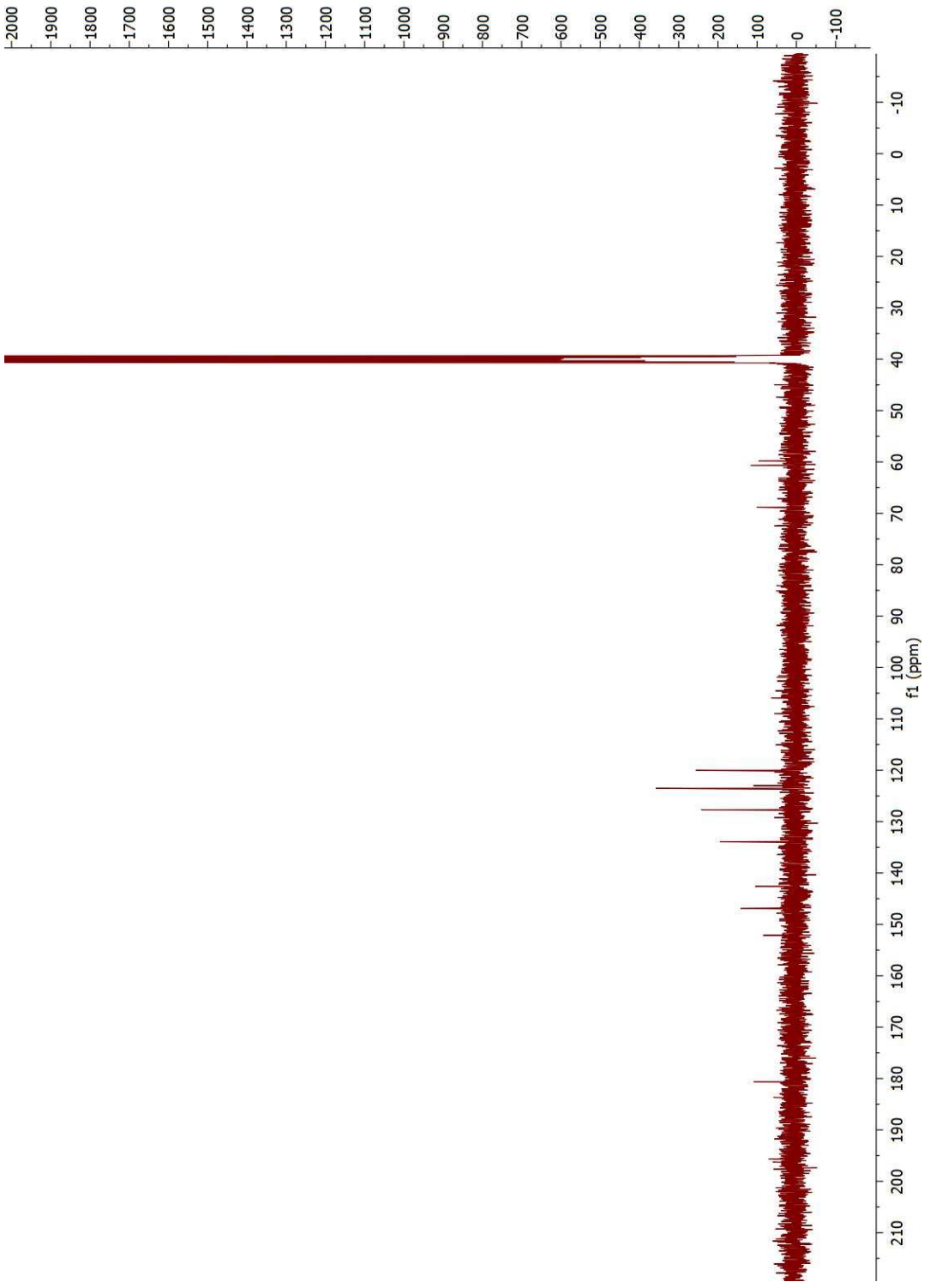

Figure 7.29: ^{13}C NMR of 1-(3,5-dichlorophenyl)-3-((1R,2R)-1,3-dihydroxy-1-(4-nitrophenyl)propan-2-yl)thiourea

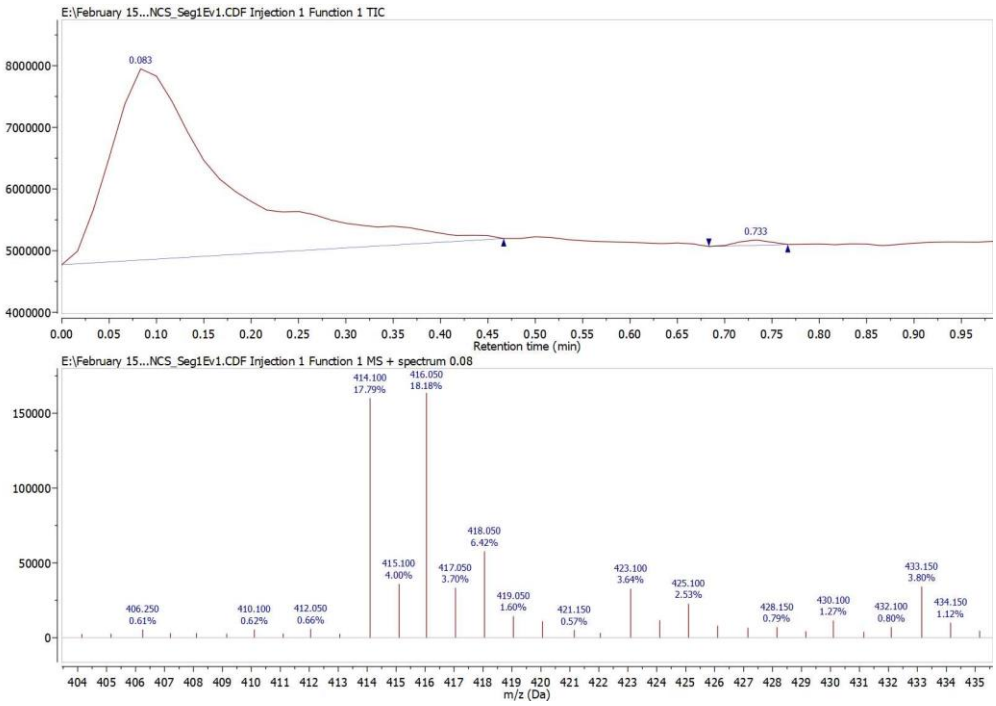

Figure 7.30: Mass spectrum of 1-(3,5-dichlorophenyl)-3-((1R,2R)-1,3-dihydroxy-1-(4-nitrophenyl)propan-2-yl)thiourea

Synthesis of 1-((1R,2R)-1,3-dihydroxy-1-(4-nitrophenyl)propan-2-yl)-3-(4-methoxyphenyl)thiourea

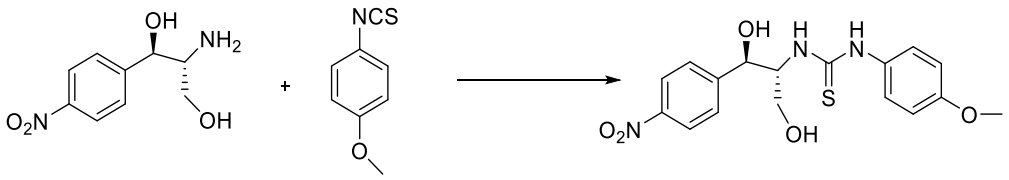

CAM base was added in with isothiocyanate moiety in 1 : 1.2 equivalents. Both were dissolved in anhydrous dichloromethane. The reaction solution was stirred for 12 hours at room temperature. Next, the reaction solution was subjected to rotatory evaporation. Then it was subjected to flash chromatography. ^{1}H NMR and ^{13}C NMR was performed using DMSO-d_6 as a solvent. ^{1}H NMR (400 MHz, DMSO-d6) δ 9.52 (s, 1H), 8.26 – 8.19 (m, 2H), 7.65 – 7.55 (m, 2H), 7.44 – 7.35 (m, 3H), 7.24 – 7.15 (m, 2H), 7.04 – 6.95 (m, 3H), 6.93 – 6.86 (m, 2H), 6.10 (d, J = 4.5 Hz, 1H), 5.16 (s, 1H), 5.00 (dd, J = 6.4, 4.4 Hz, 1H), 4.55 (s, 1H), 3.78 (s, 4H), 3.74 (s, 3H), 3.57 (dt, J = 9.5, 4.6 Hz, 1H), 3.48 (td, J = 9.4, 6.4 Hz, 1H).

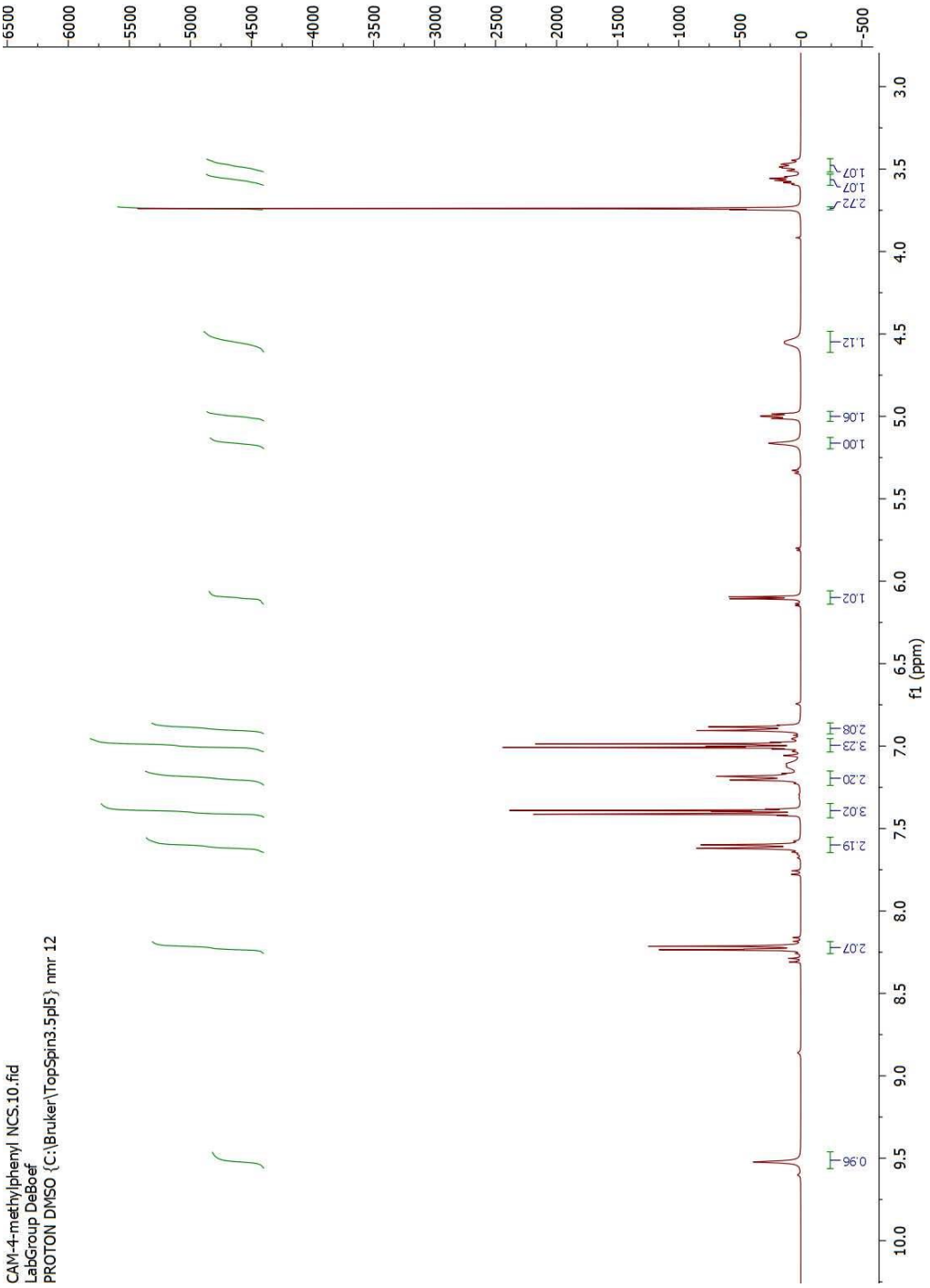

Figure 7.31: ^{1}H NMR of 1-((1R,2R)-1,3-dihydroxy-1-(4-nitrophenyl)propan-2-yl)-3-(4-methoxyphenyl)thiourea

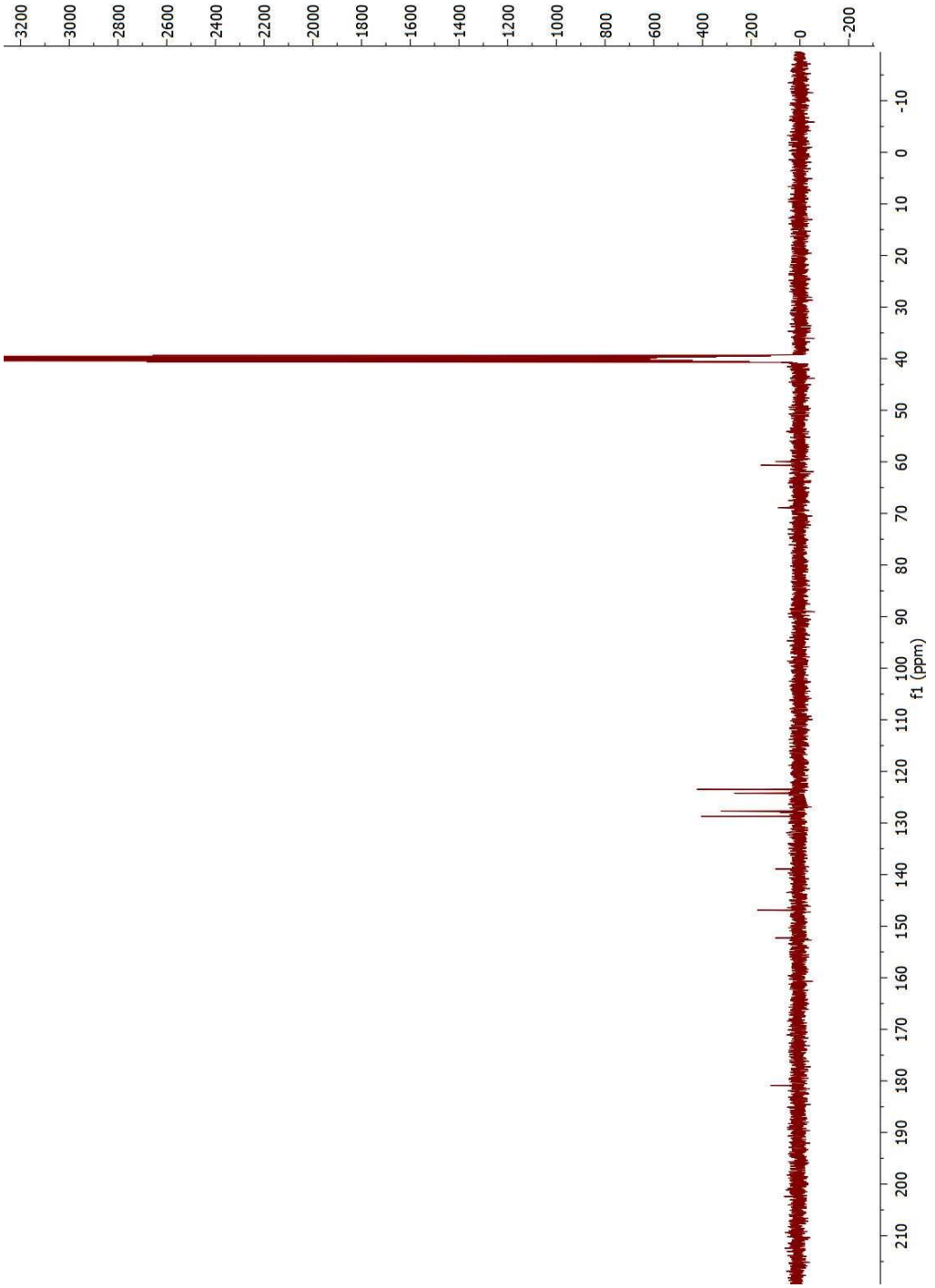

Figure 7.32: ^{13}C NMR of 1-((1R,2R)-1,3-dihydroxy-1-(4-nitrophenyl)propan-2-yl)-3-(4-methoxyphenyl)thiourea

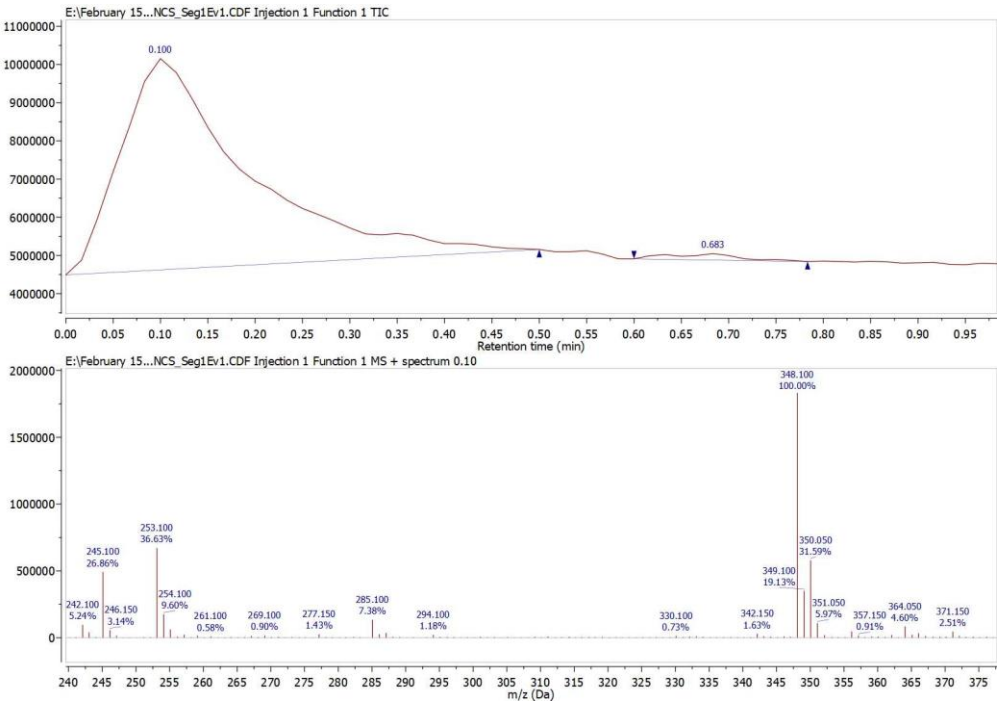

Figure 7.33: Mass spectrum of 1-((1R,2R)-1,3-dihydroxy-1-(4-nitrophenyl)propan-2-yl)-3-(4-methoxyphenyl)thiourea

Synthesis of 1-((1R,2R)-1,3-dihydroxy-1-(4-nitrophenyl)propan-2-yl)-3-(3,5-dimethylphenyl)thiourea

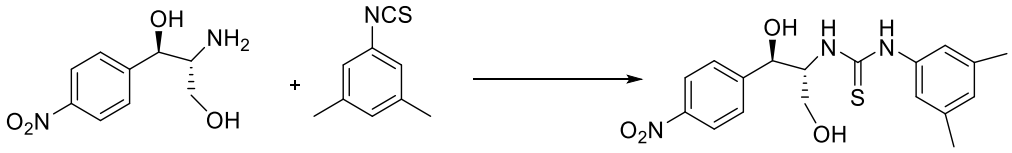

CAM base was added in with isothiocyanate moiety in 1 : 1.2 equivalents. Both were dissolved in anhydrous dichloromethane. The reaction solution was stirred for 12 hours at room temperature. Next, the reaction solution was subjected to rotatory evaporation. Then it was subjected to flash chromatography. ^{1}H NMR and ^{13}C NMR was performed using DMSO-d6 as a solvent. 1H NMR (400 MHz, DMSO-d6) δ 9.60 (s, 1H), 8.25 – 8.20 (m, 2H), 7.66 – 7.58 (m, 2H), 7.31 (d, J = 8.6 Hz, 1H), 7.04 (ddt, J = 10.5, 1.6, 0.8 Hz, 4H), 6.96 (s, 2H), 6.74 (dq, J = 1.7, 0.8 Hz, 1H), 6.14 (d, J = 4.5 Hz, 1H), 5.21 – 5.14 (m, 1H), 5.01 (dd, J = 6.4, 4.4 Hz, 1H), 4.58 (d, J = 6.9 Hz, 1H), 3.57 (dt, J = 9.6, 4.7 Hz, 1H), 3.49 (td, J = 9.5, 6.4 Hz, 1H), 2.25 – 2.20 (m, 6H).

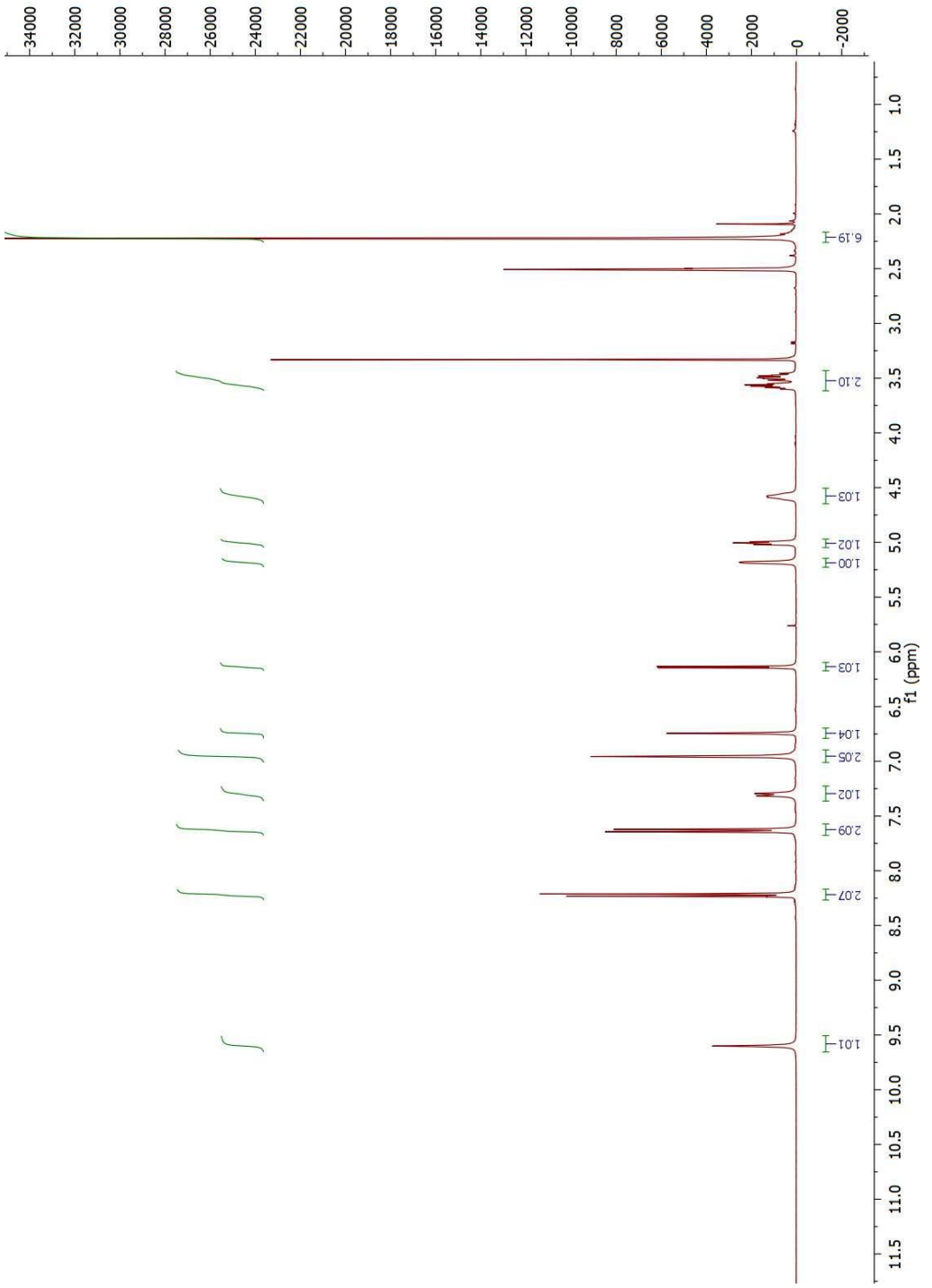

Figure 7.34: ^{1}H NMR of 1-((1R,2R)-1,3-dihydroxy-1-(4-nitrophenyl)propan-2-yl)-3-(3,5-dimethylphenyl)thiourea

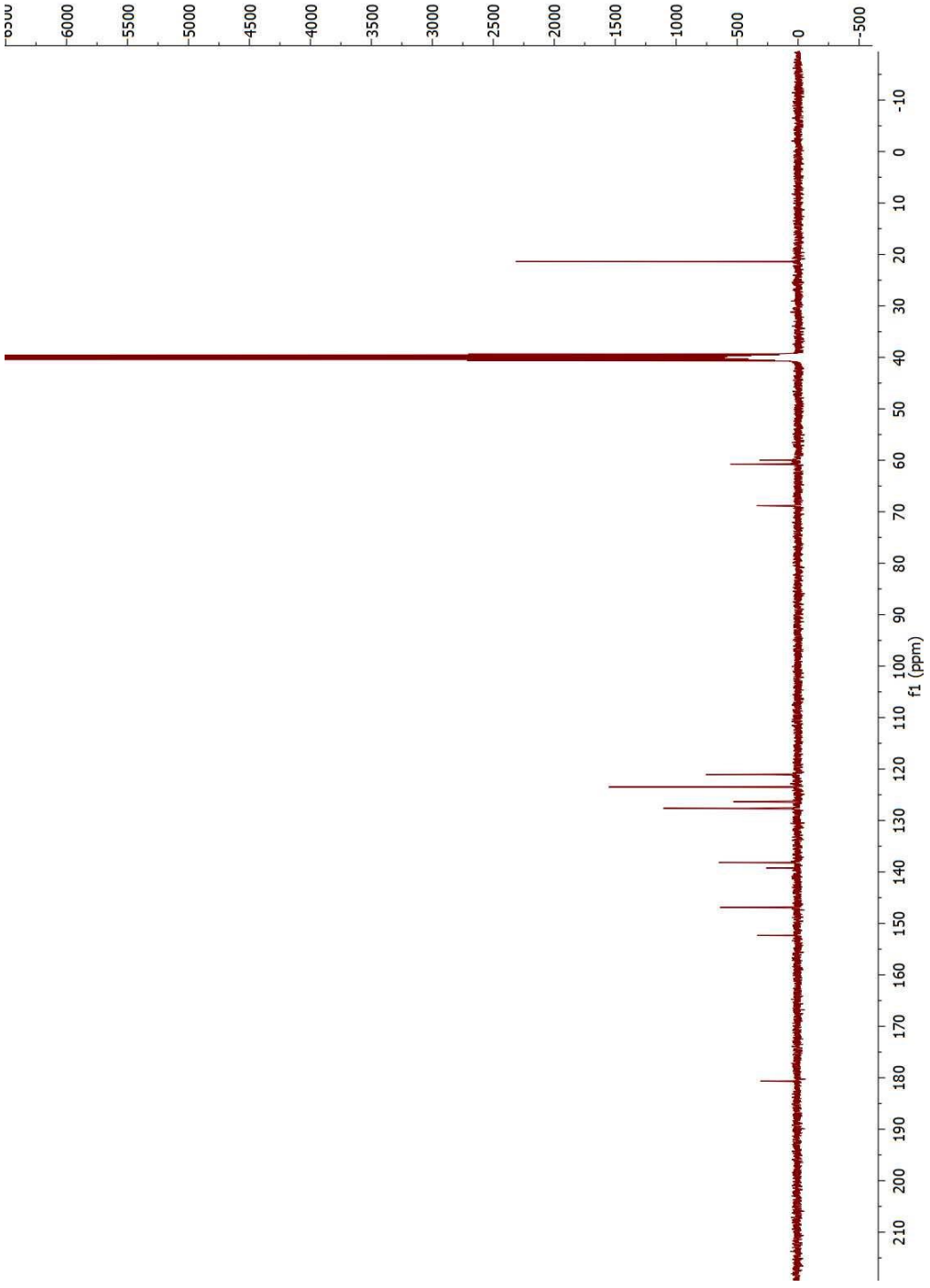

Figure 7.35: ^{13}CNMR of 1-((1R,2R)-1,3-dihydroxy-1-(4-nitrophenyl)propan-2-yl)-3-(3,5-dimethylphenyl)thiourea

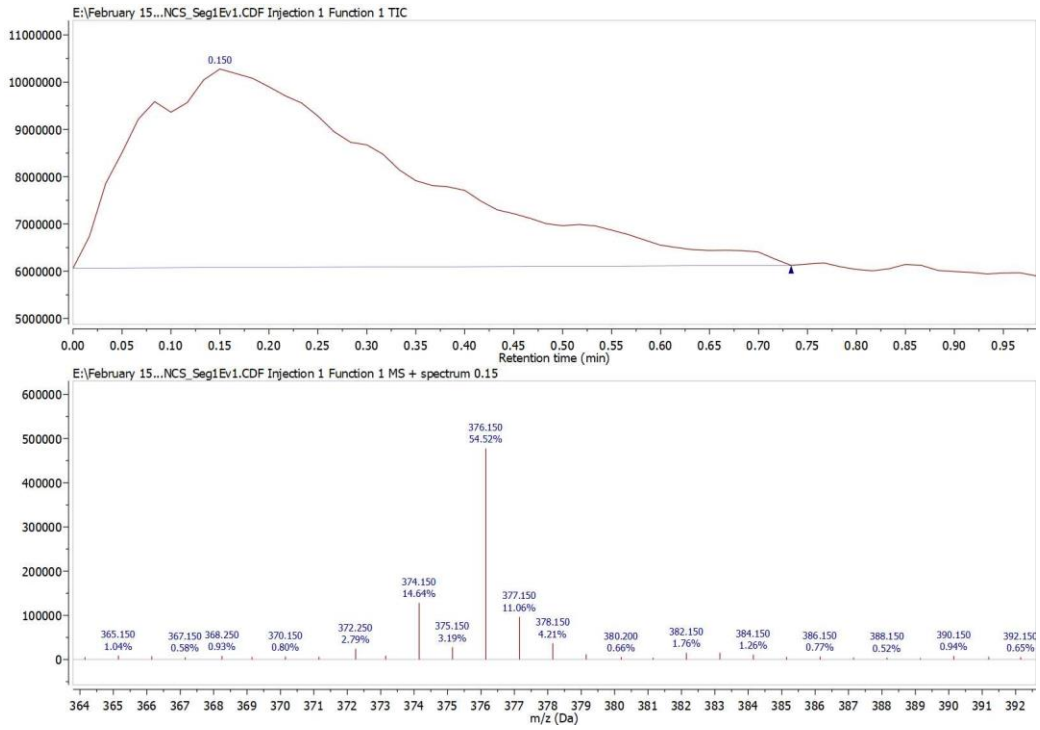

Figure 7.36: Mass spectrum for 1-((1R,2R)-1,3-dihydroxy-1-(4-nitrophenyl)propan-2-yl)-3-(3,5-dimethylphenyl)thiourea

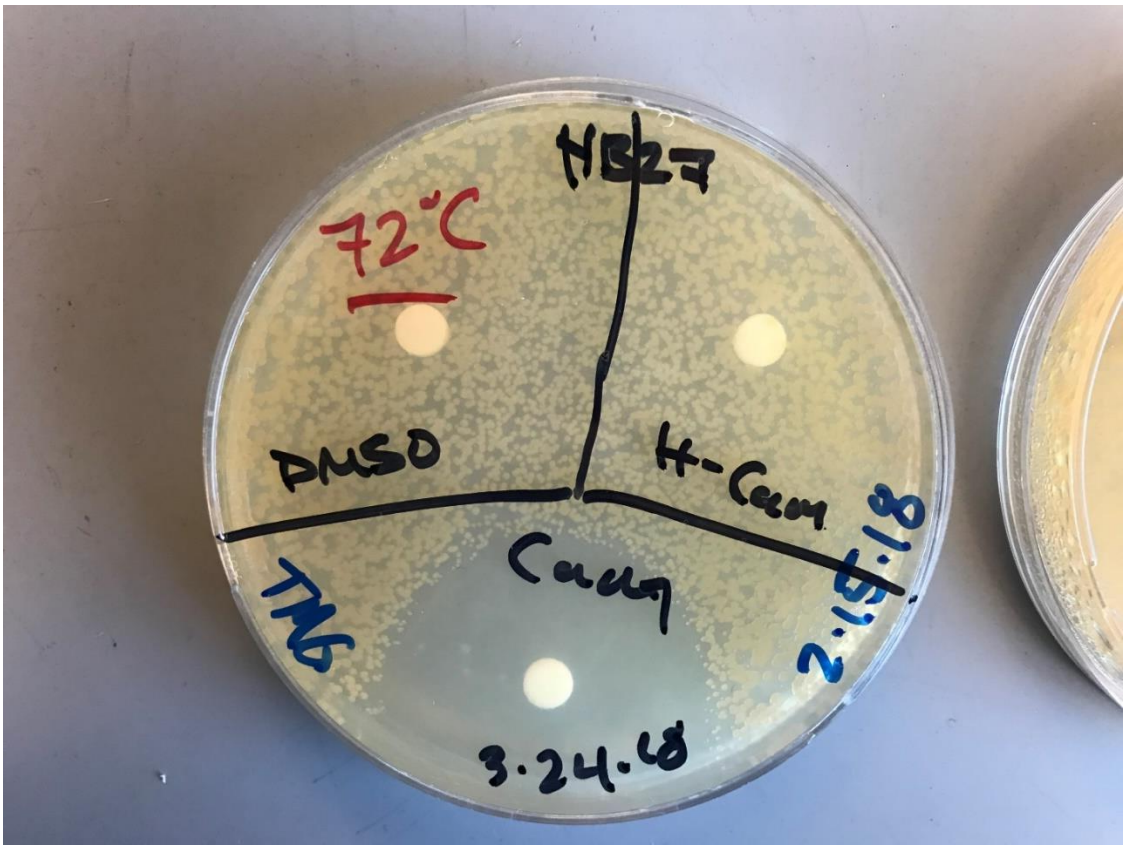

Figure 7.37: Disk assay for CAM base without any functionalization using Thermus thermophilus HB27

Molecular modelling and docking studies

The PDB structures that was used are 4V7W and 1PD5. Both structures had CAM docked in to them in their crystal form. Hence this was a starting point for our calculations. We kept the CAM at the same bound site and we changed the functional groups accordingly, then molecular dynamics was performed to investigate the most optimum flexible assignment. Once this was obtained the CAM derivative was then docked. The docking method used was triangle matcher, with London dG scoring system. 100 poses were allowed. Refinement was performed using rigid receptor method with a scoring function of GBVI/WSA dG. Next the best 5 poses were refined, and the top one with the highest docking score was used to find ligand interactions and surfaces.

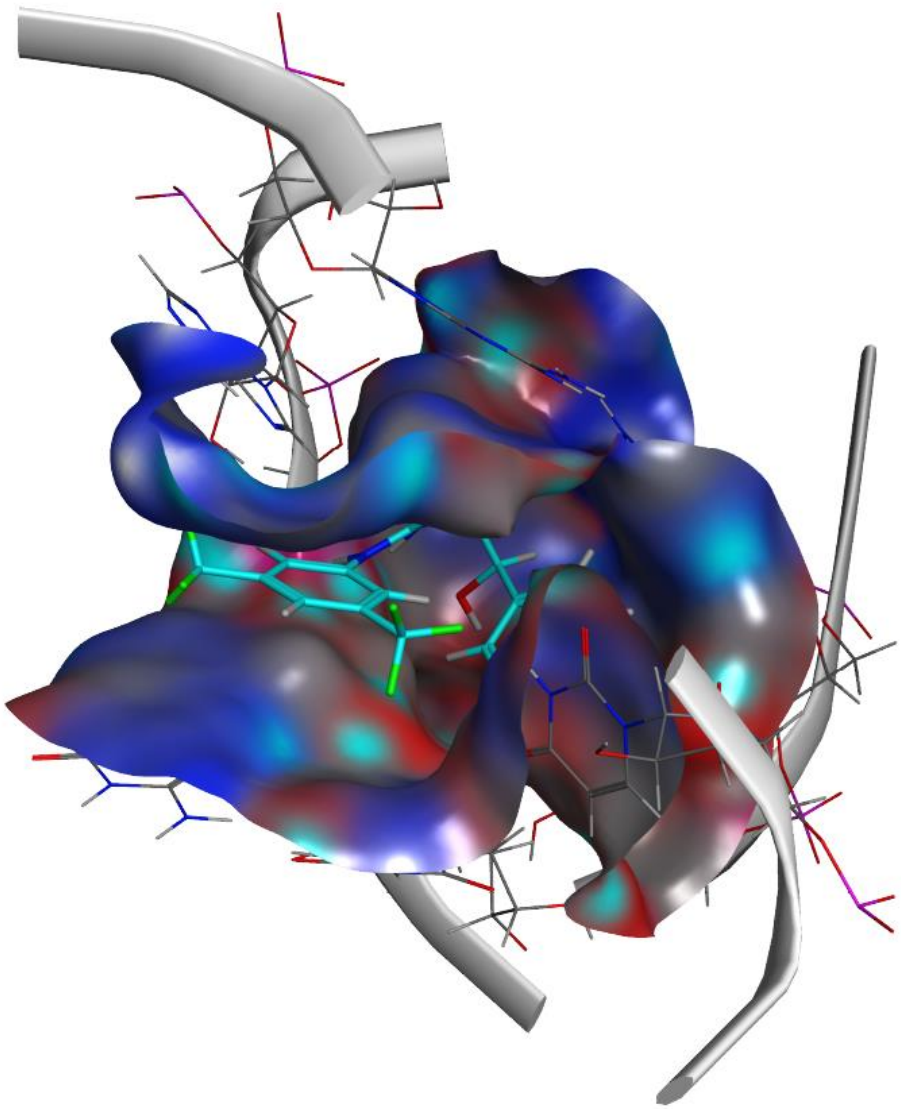

Figure 7.38: Binding of 1-(3,5-bis(trifluoromethyl)phenyl)-3-((1R,2R)-1,3-dihydroxy-1-(4-nitrophenyl)propan-2-yl)thiourea to the ribosome pocket, with the generated surface for the receptor

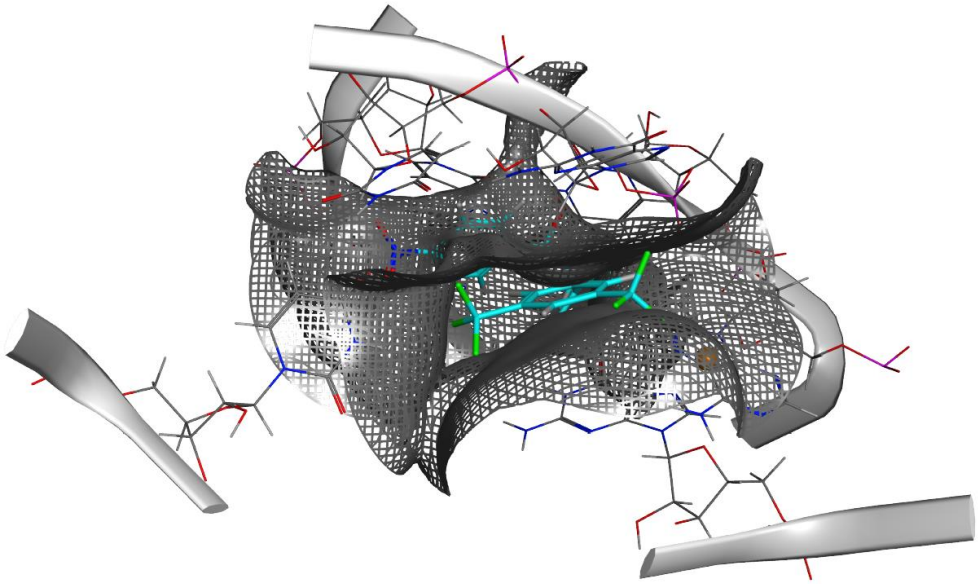

Figure 7.39: Van der Waals interactions of 1-(3,5-bis(trifluoromethyl)phenyl)-3-((1R,2R)-1,3-dihydroxy-1-(4-nitrophenyl)propan-2-yl)thiourea with the ribosome amino acids

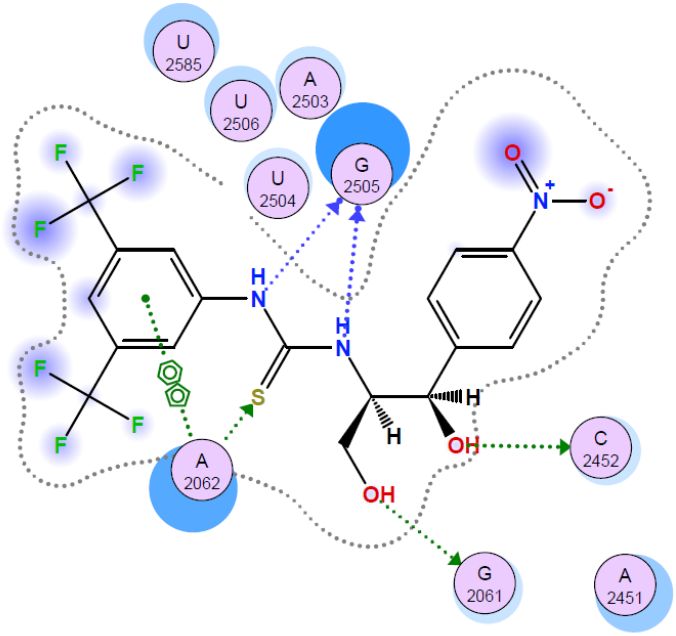

Figure 7.40: Ligand interaction diagram of 1-(3,5-bis(trifluoromethyl)phenyl)-3-((1R,2R)-1,3-dihydroxy-1-(4-nitrophenyl)propan-2-yl)thiourea to the ribosome

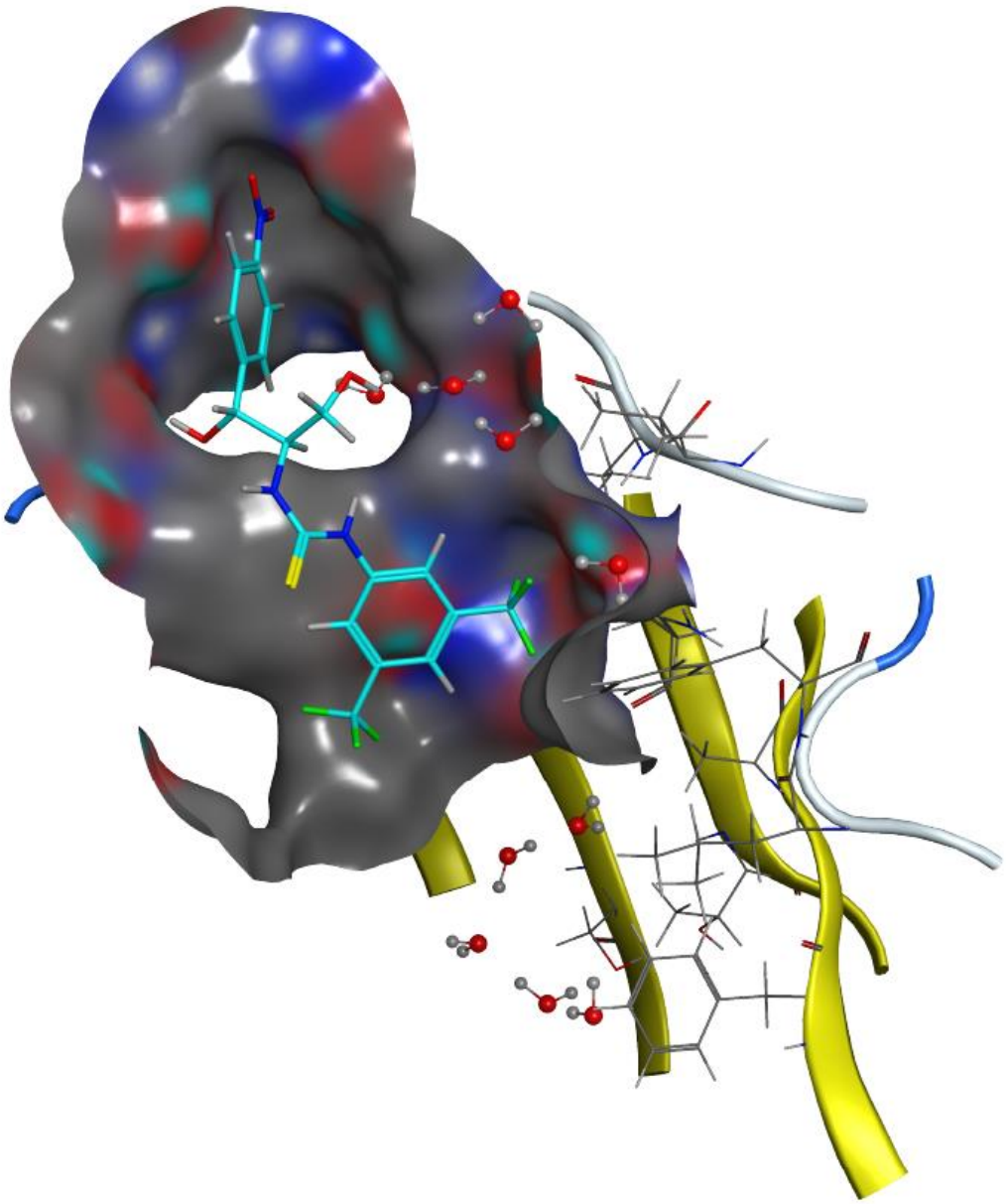

Figure 7.41: Binding of 1-(3,5-bis(trifluoromethyl)phenyl)-3-((1R,2R)-1,3-dihydroxy-1-(4-nitrophenyl)propan-2-yl)thiourea to the CAM acetyl transferase pocket, with the generated surface for the receptor

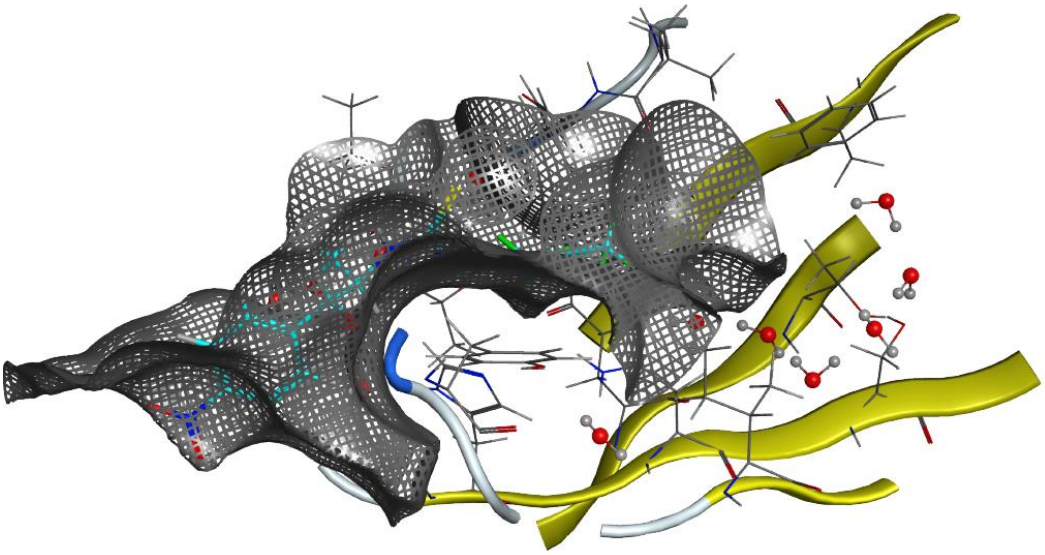

Figure 7.42: Van der Waals interactions of of 1-(3,5-bis(trifluoromethyl)phenyl)-3-((1R,2R)-1,3-dihydroxy-1-(4-nitrophenyl)propan-2-yl)thiourea with the CAM acetyl transferase amino acids

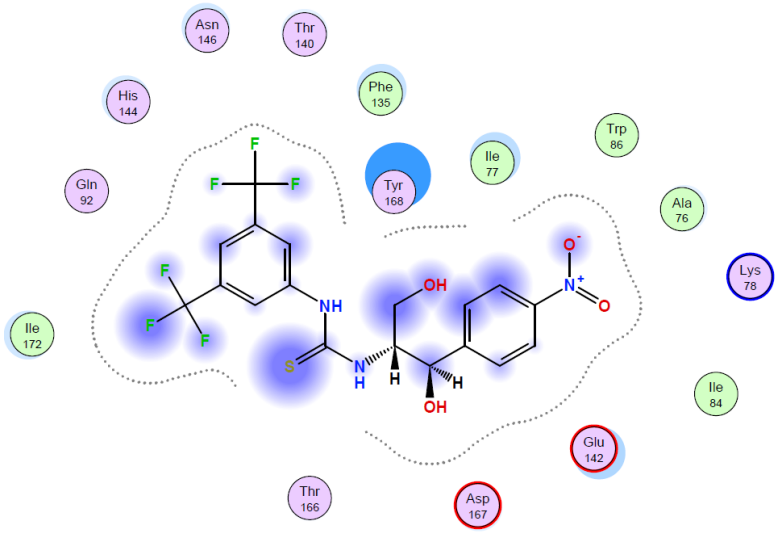

Figure 7.43: Ligand interaction diagram of 1-(3,5-bis(trifluoromethyl)phenyl)-3-((1R,2R)-1,3-dihydroxy-1-(4-nitrophenyl)propan-2-yl)thiourea for the CAM acetyl transferase enzyme

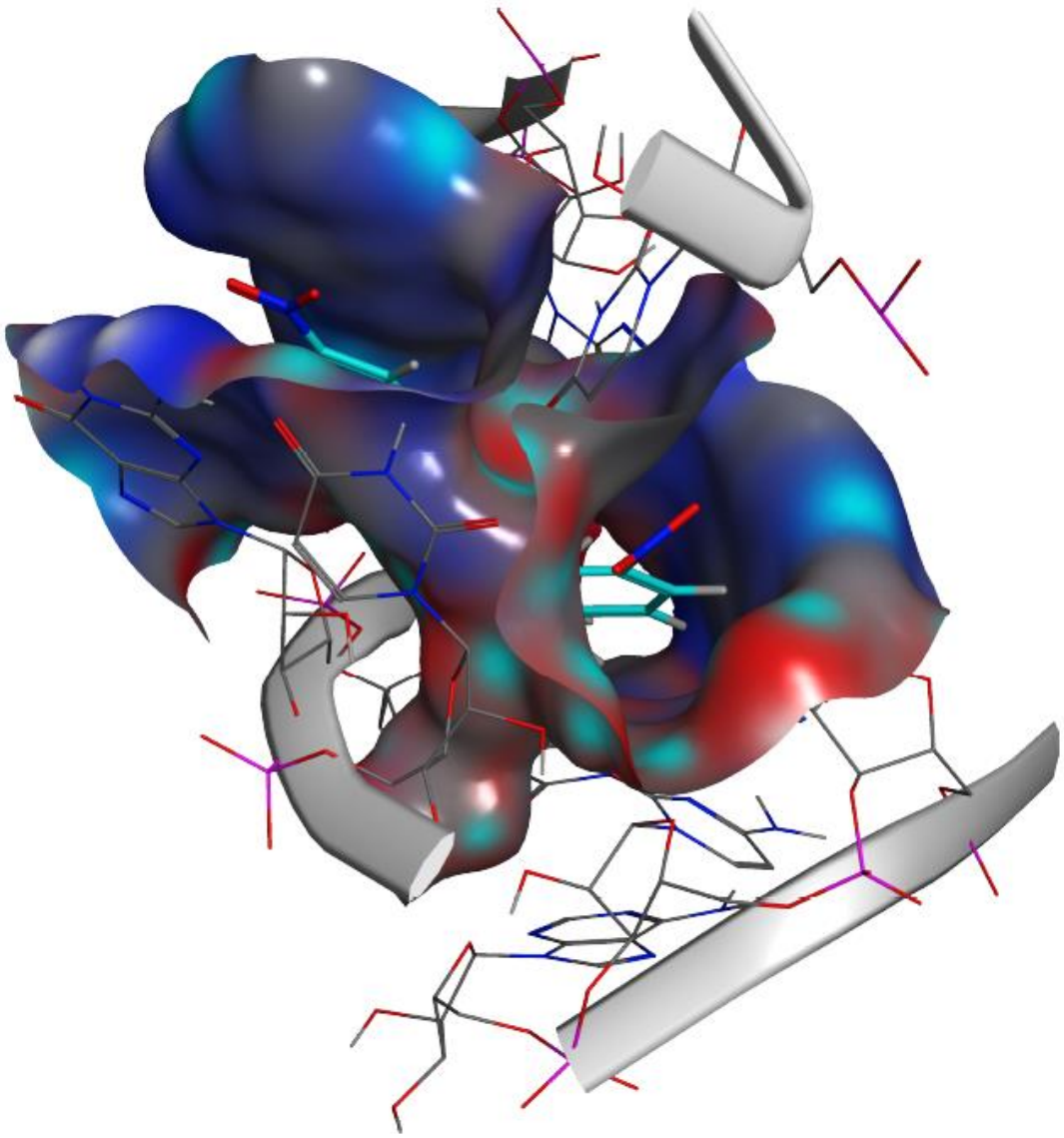

Figure 7.44: Binding of 1-((1R,2R)-1,3-dihydroxy-1-(4-nitrophenyl)propan-2-yl)-3-(4nitrophenyl)thiourea to the ribosome pocket, with the generated surface for the receptor

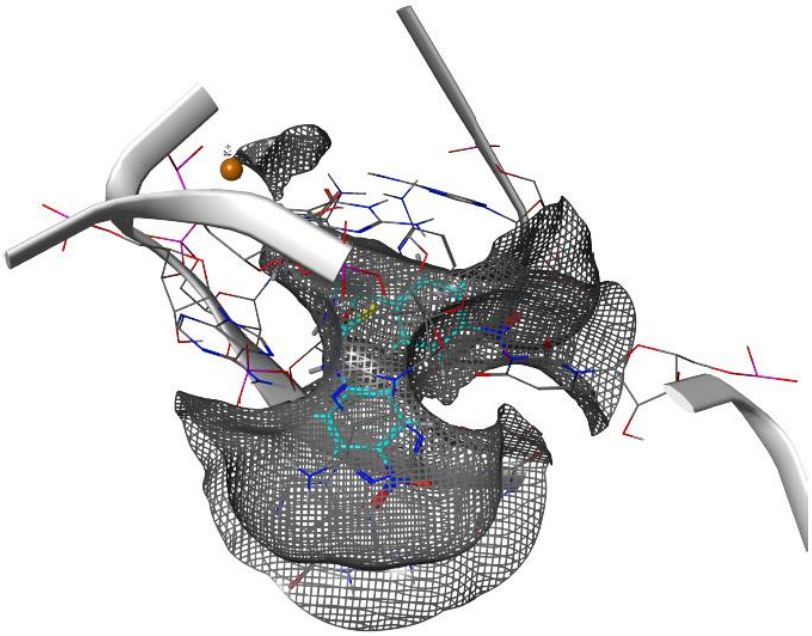

Figure 7.45: Van der Waals interactions of 1-((1R,2R)-1,3-dihydroxy-1-(4-nitrophenyl)propan-2-yl)-3-(4nitrophenyl)thiourea with the CAM acetyl transferase amino acids

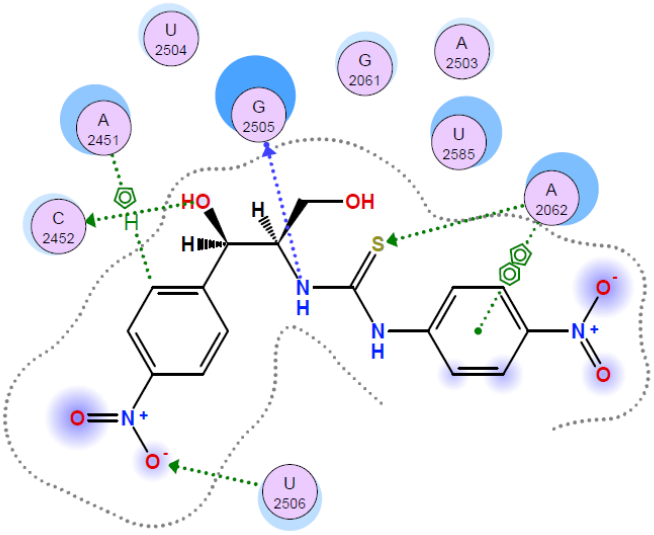

Figure 7.46: Ligand interaction diagram of 1-((1R,2R)-1,3-dihydroxy-1-(4-nitrophenyl)propan-2-yl)-3-(4nitrophenyl)thiourea for the CAM acetyl transferase enzyme

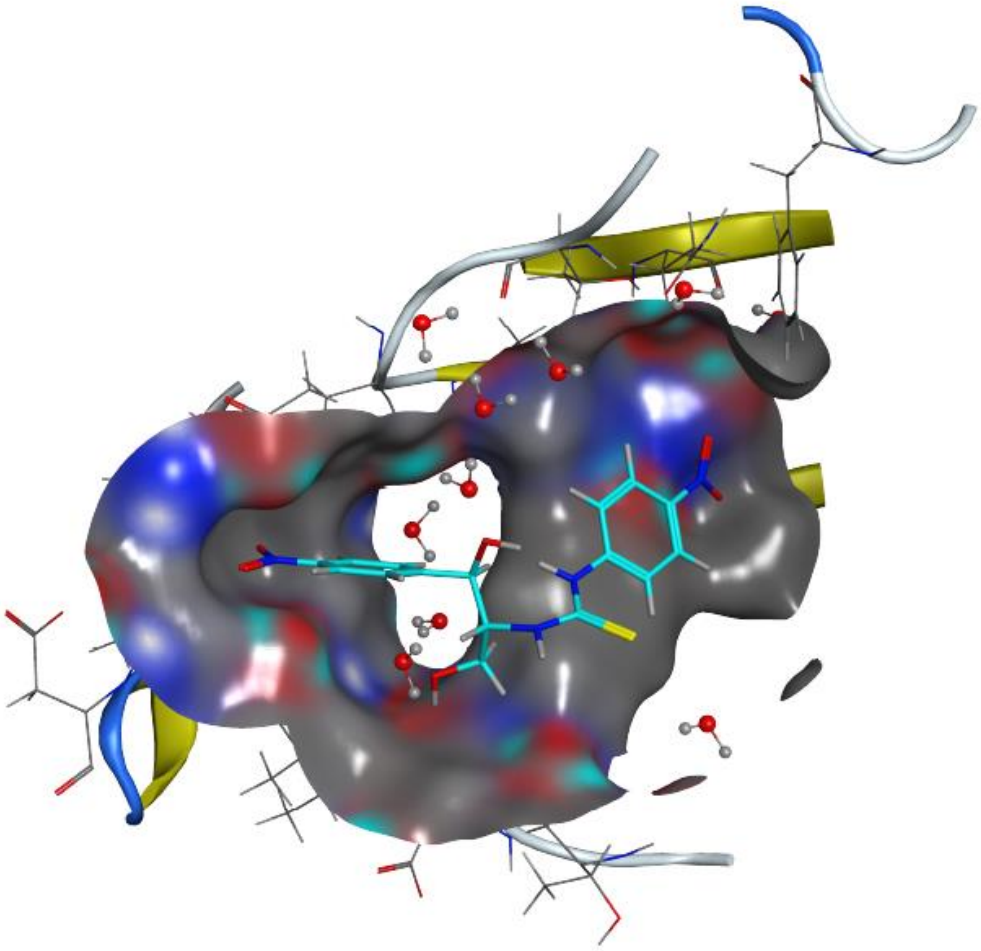

Figure 7.47: Binding of 1-((1R,2R)-1,3-dihydroxy-1-(4-nitrophenyl)propan-2-yl)-3-(4nitrophenyl)thiourea to the CAM acetyl transferase pocket, with the generated surface for the receptor

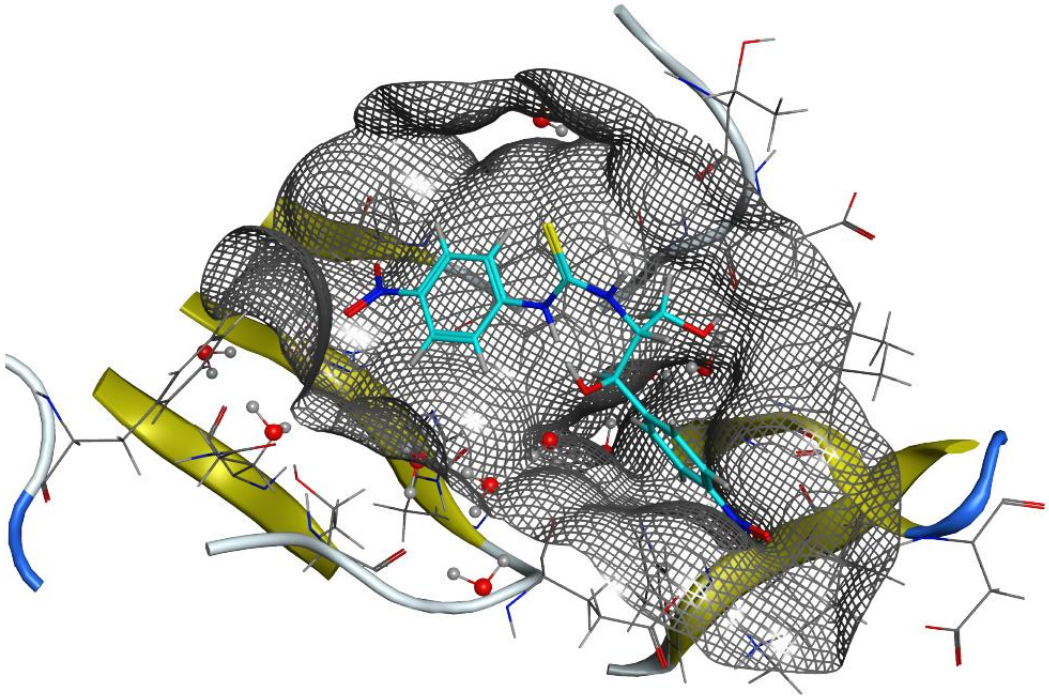

Figure 7.48: Van der Waals interactions of 1-((1R,2R)-1,3-dihydroxy-1-(4-nitrophenyl)propan-2-yl)-3-(4nitrophenyl)thiourea with the CAM acetyl transferase amino acids

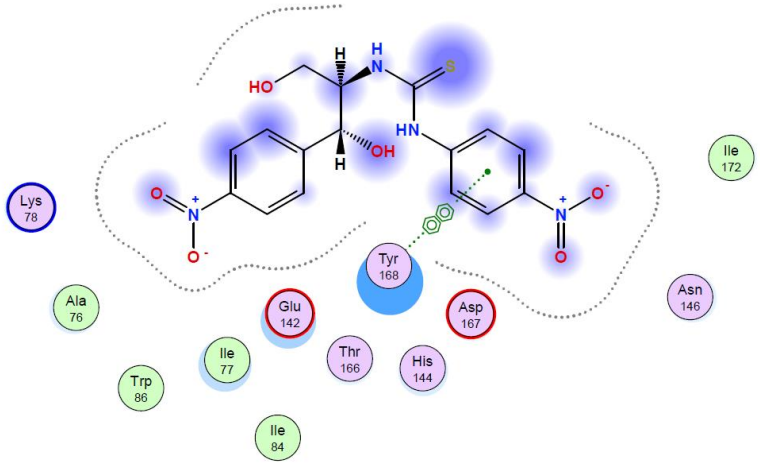

Figure 7.49: Ligand interaction diagram of 1-((1R,2R)-1,3-dihydroxy-1-(4-nitrophenyl)propan-2-yl)-3-(4nitrophenyl)thiourea for the CAM acetyl transferase enzyme

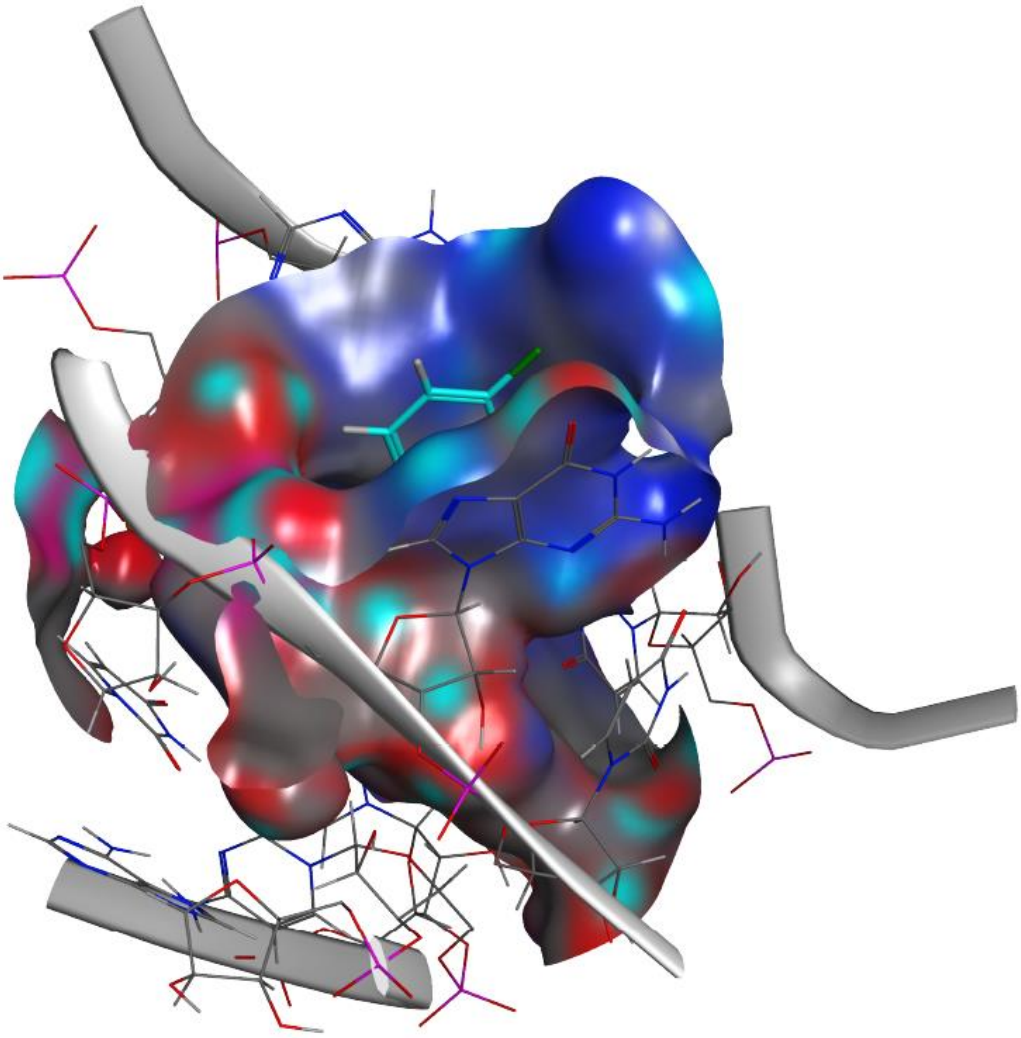

Figure 7.50: Binding of 1-(4-chlorophenyl)-3-((1R,2R)-1,3-dihydroxy-1-(4-nitrophenyl)propan-2-yl)thiourea to the ribosome pocket, with the generated surface for the receptor

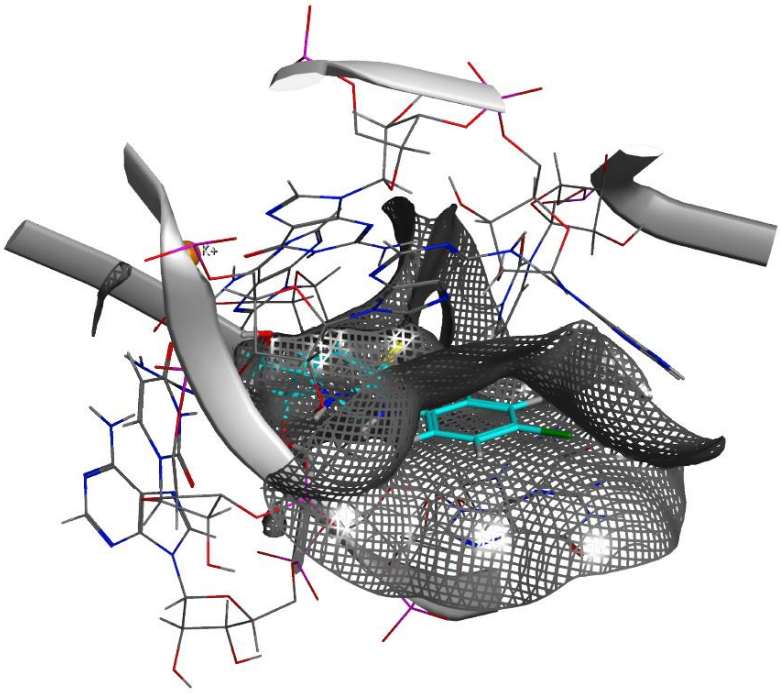

Figure 7.51: Van der Waals interactions of 1-(4-chlorophenyl)-3-((1R,2R)-1,3-dihydroxy-1-(4-nitrophenyl)propan-2-yl)thiourea with the ribosome amino acids

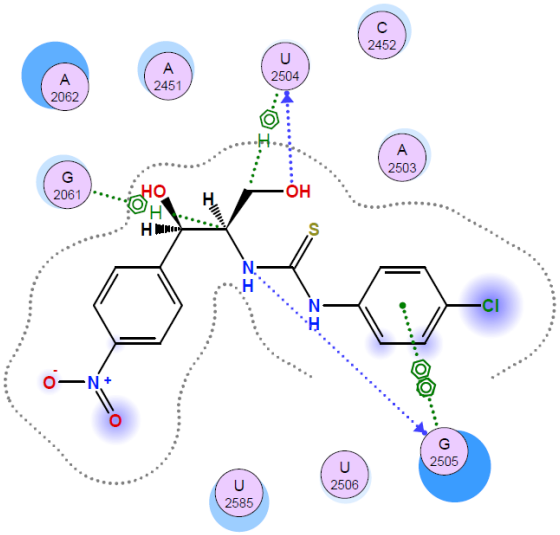

Figure 7.52: Ligand interaction diagram of 1-(4-chlorophenyl)-3-((1R,2R)-1,3-dihydroxy-1-(4-nitrophenyl)propan-2-yl)thiourea to the ribosome

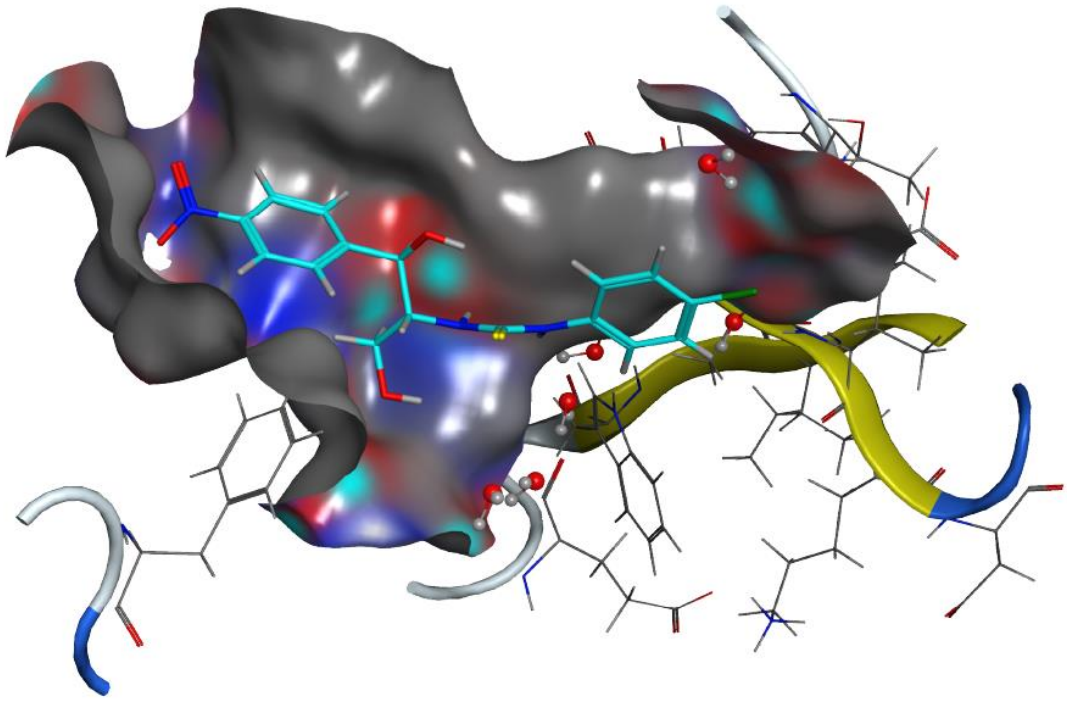

Figure 7.53: Binding of of 1-(4-chlorophenyl)-3-((1R,2R)-1,3-dihydroxy-1-(4-nitrophenyl)propan-2-yl)thiourea to the CAM acetyl transferase pocket, with the generated surface for the receptor

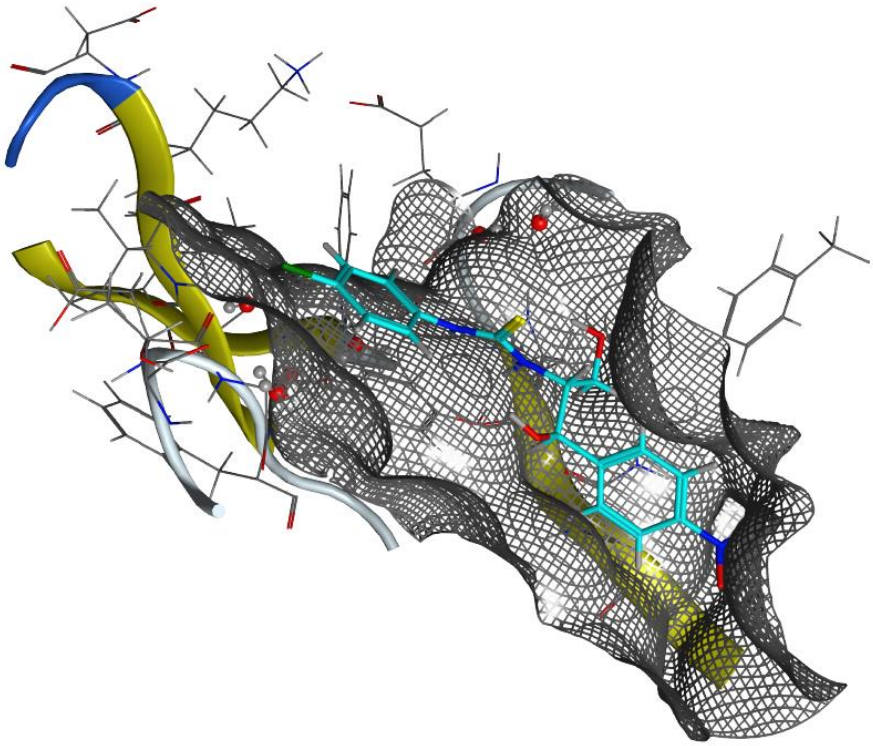

Figure 7.54: Van der Waals interactions of 1-(4-chlorophenyl)-3-((1R,2R)-1,3-dihydroxy-1-(4-nitrophenyl)propan-2-yl)thiourea with the CAM acetyl transferase amino acids

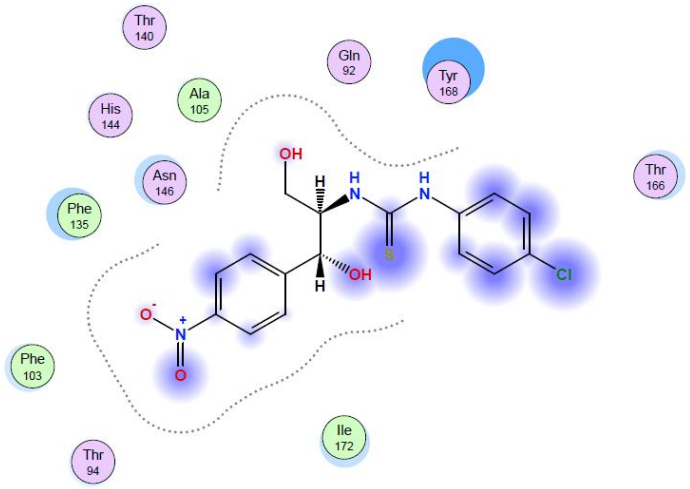

Figure 7.55: Ligand interaction diagram of 1-(4-chlorophenyl)-3-((1R,2R)-1,3-dihydroxy-1-(4-nitrophenyl)propan-2-yl)thiourea for the CAM acetyl transferase enzyme

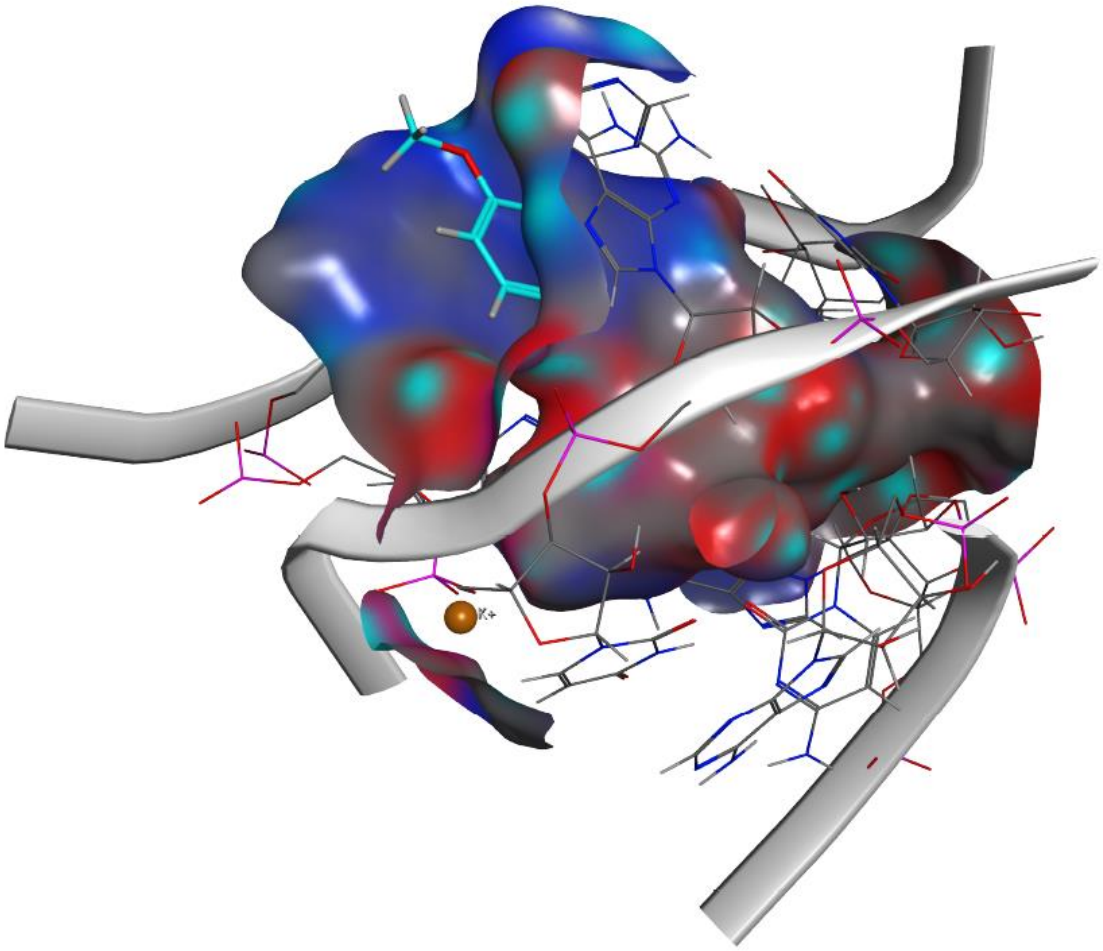

Figure 7.56: Binding of 1-((1R,2R)-1,3-dihydroxy-1-(4-nitrophenyl)propan-2-yl)-3-(4-methoxyphenyl)thiourea to the ribosome pocket, with the generated surface for the receptor

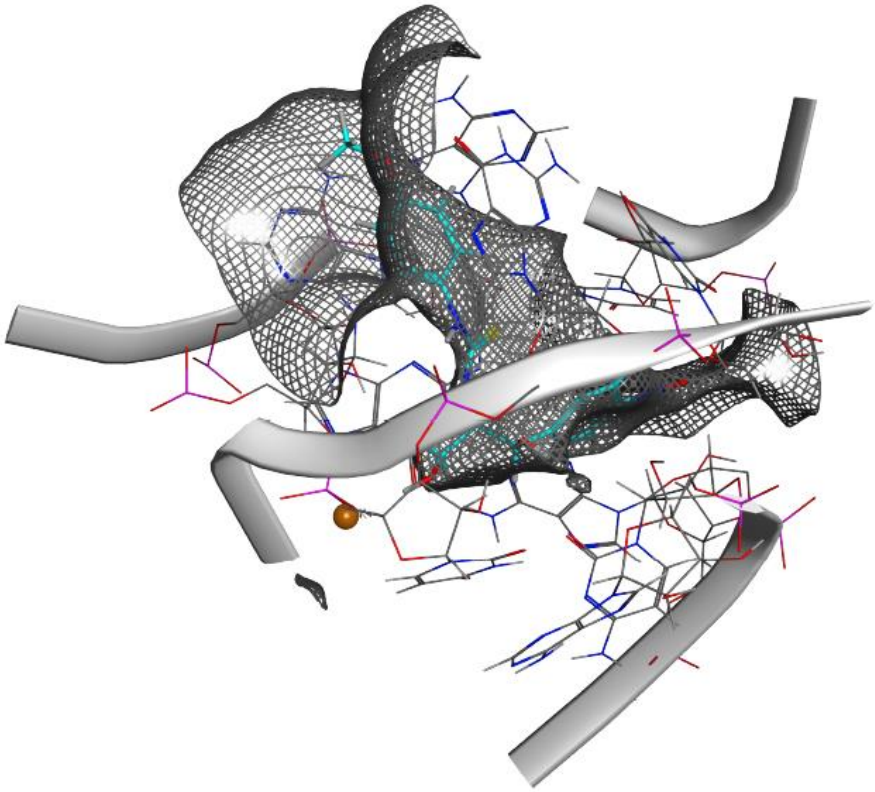

Figure 7.57: Van der Waals interactions of 1-((1R,2R)-1,3-dihydroxy-1-(4-nitrophenyl)propan-2-yl)-3-(4-methoxyphenyl)thiourea with the ribosome amino acids

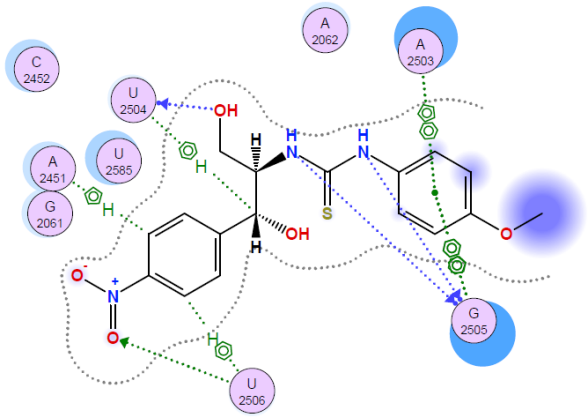

Figure 7.58: Ligand interaction diagram of 1-((1R,2R)-1,3-dihydroxy-1-(4-nitrophenyl)propan-2-yl)-3-(4-methoxyphenyl)thiourea to the ribosome

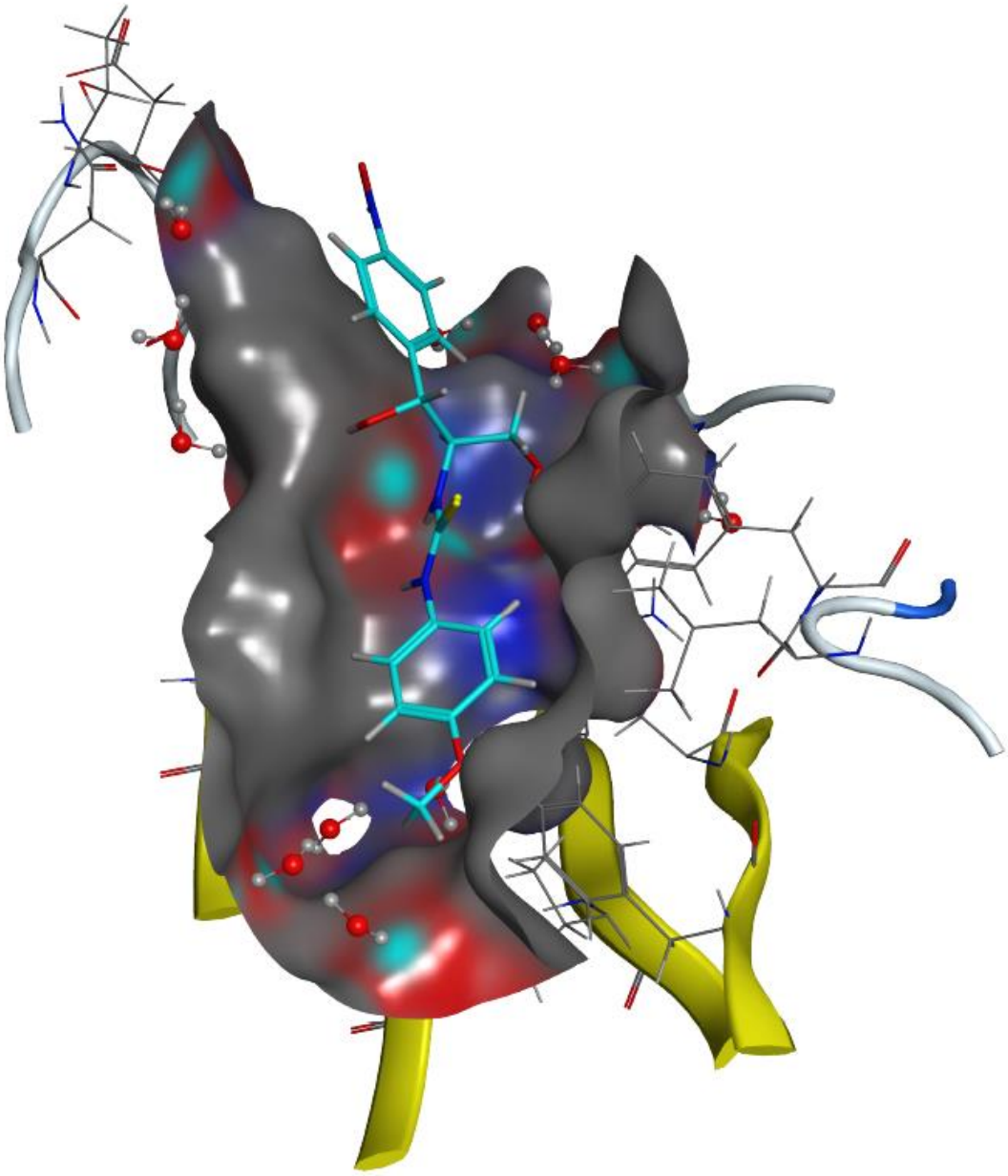

Figure 7.59: Binding of 1-((1R,2R)-1,3-dihydroxy-1-(4-nitrophenyl)propan-2-yl)-3-(4-methoxyphenyl)thiourea to the CAM acetyl transferase pocket, with the generated surface for the receptor

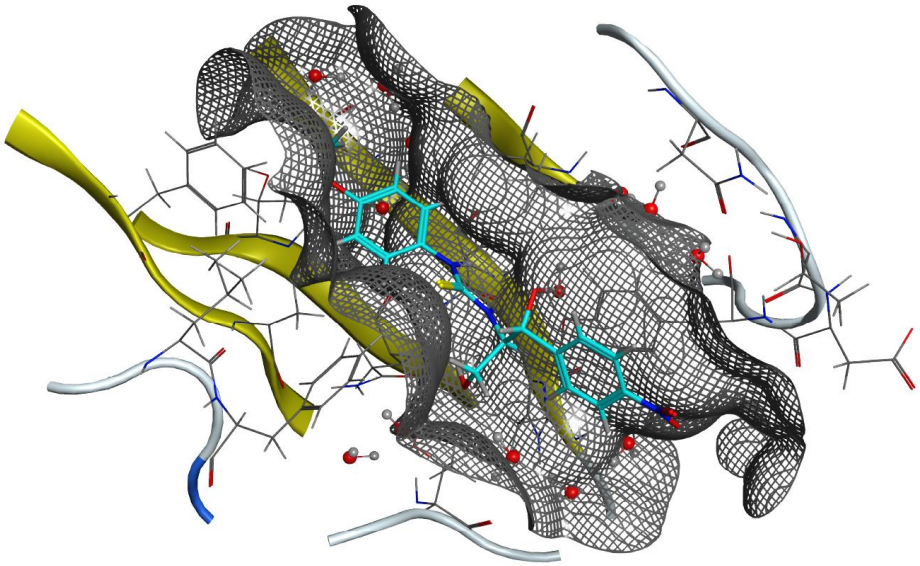

Figure 7.60: Van der Waals interactions of 1-((1R,2R)-1,3-dihydroxy-1-(4-nitrophenyl)propan-2-yl)-3-(4-methoxyphenyl)thiourea with the CAM acetyl transferase amino acids

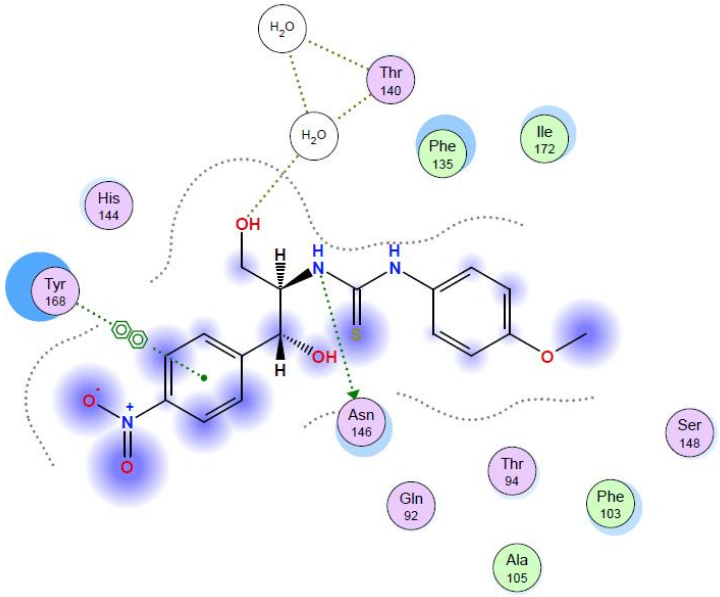

Figure 7.61: Ligand interaction diagram of 1-((1R,2R)-1,3-dihydroxy-1-(4-nitrophenyl)propan-2-yl)-3-(4-methoxyphenyl)thiourea for the CAM acetyl transferase enzyme

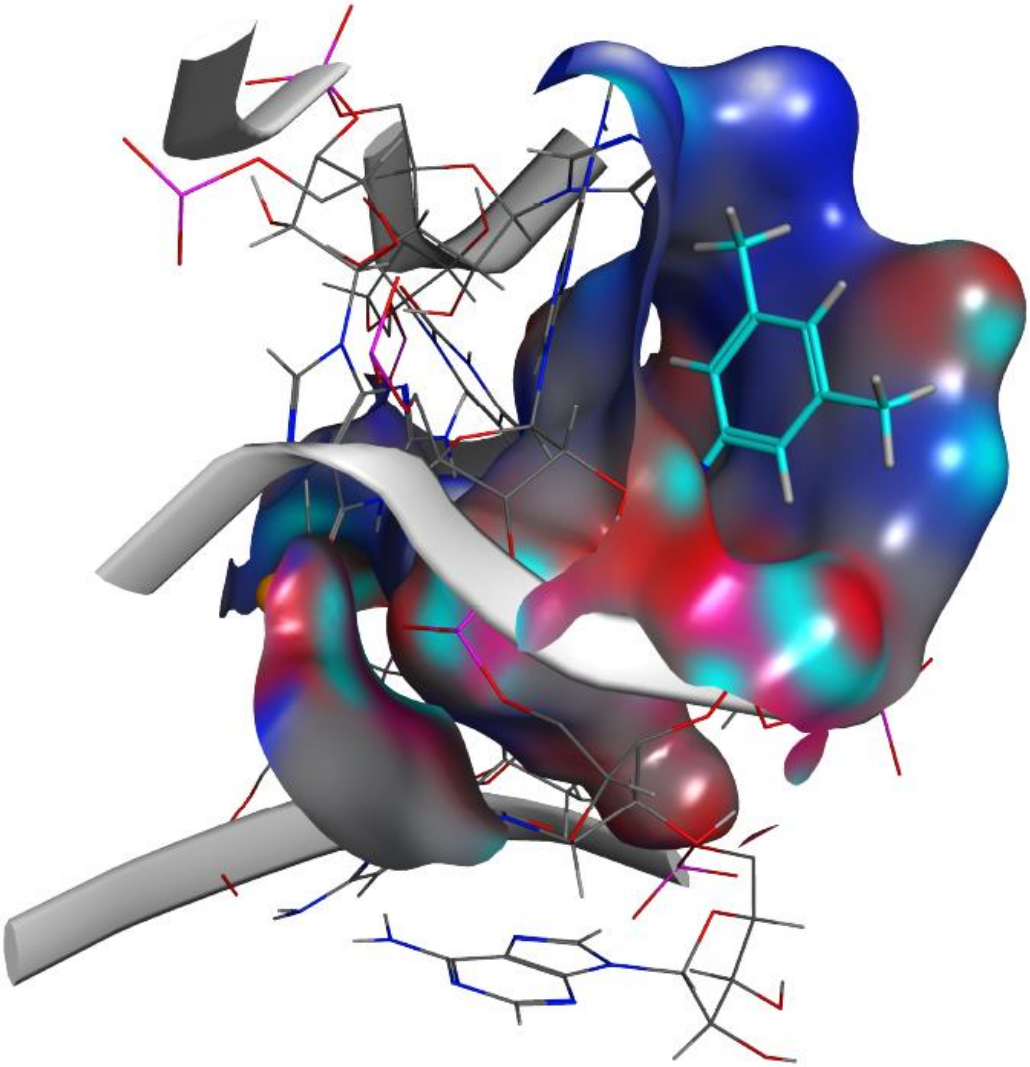

Figure 7.62: Binding of 1-((1R,2R)-1,3-dihydroxy-1-(4-nitrophenyl)propan-2-yl)-3-(3,5-dimethylphenyl)thiourea to the ribosome pocket, with the generated surface for the receptor

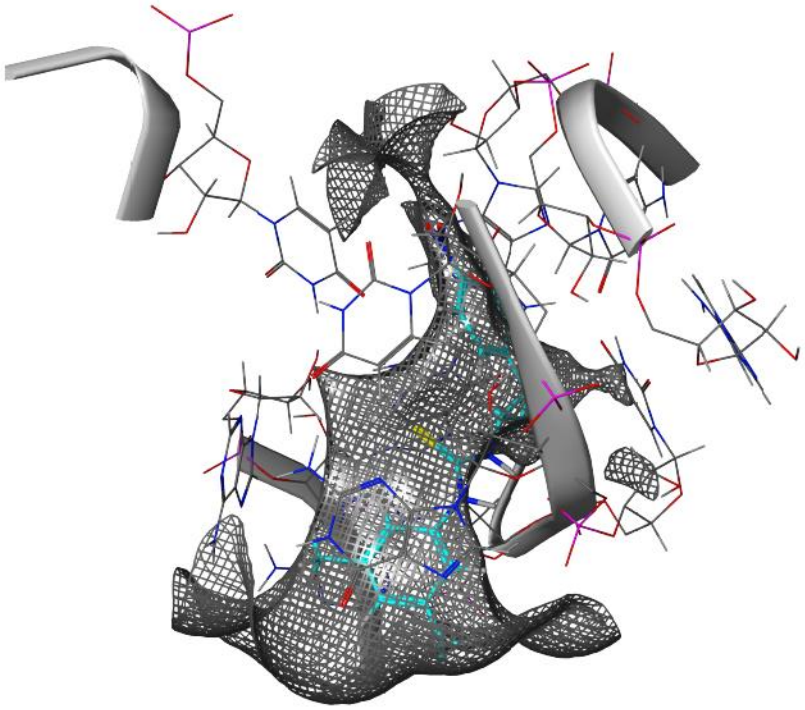

Figure 7.63: Van der Waals interactions of 1-((1R,2R)-1,3-dihydroxy-1-(4-nitrophenyl)propan-2-yl)-3-(3,5-dimethylphenyl)thiourea with the ribosome amino acids

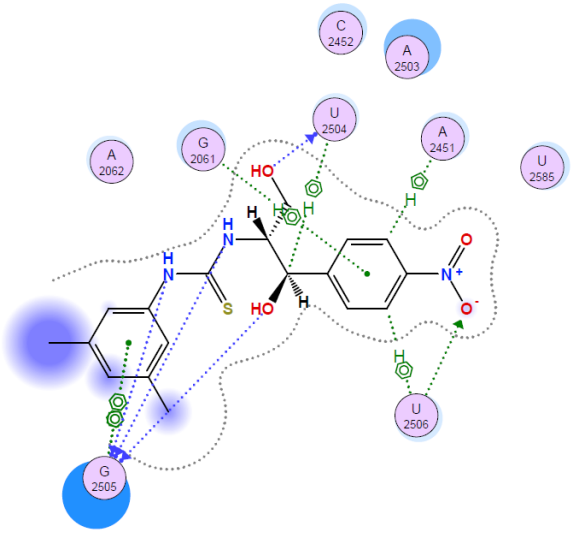

Figure 7.64: Ligand interaction diagram of 1-((1R,2R)-1,3-dihydroxy-1-(4-nitrophenyl)propan-2-yl)-3-(3,5-dimethylphenyl)thiourea to the ribosome

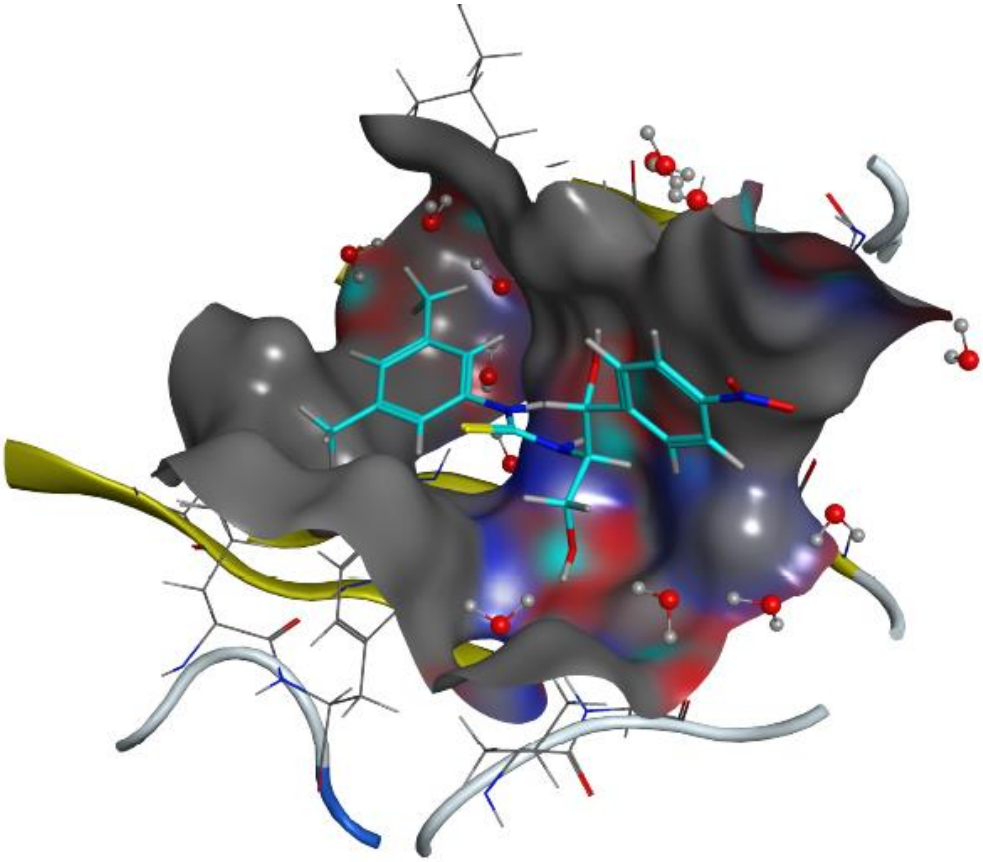

Figure 7.65: Binding of 1-((1R,2R)-1,3-dihydroxy-1-(4-nitrophenyl)propan-2-yl)-3-(3,5-dimethylphenyl)thiourea to the CAM acetyl transferase pocket, with the generated surface for the receptor

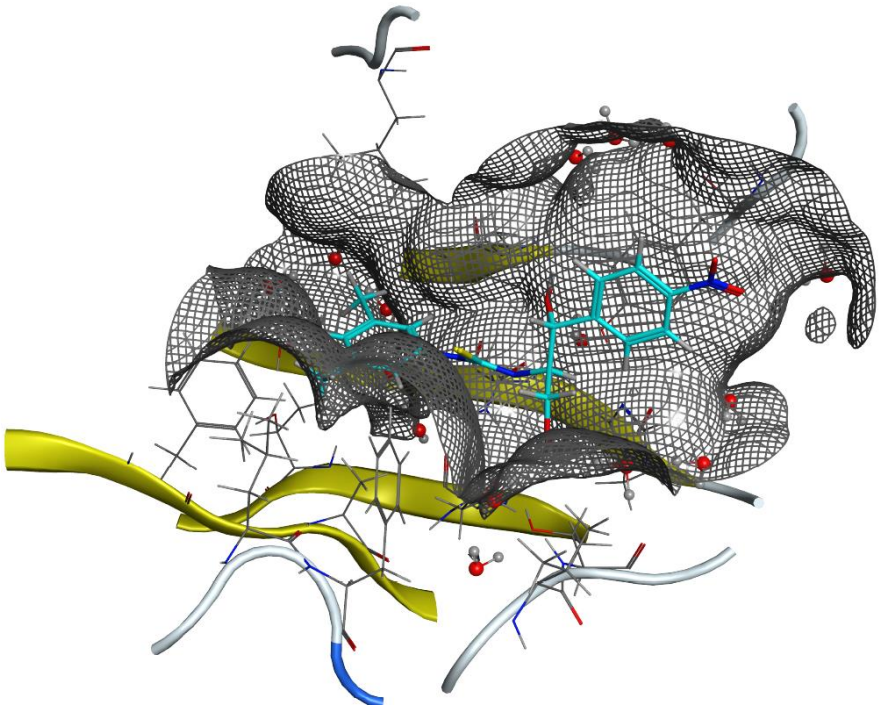

Figure 7.66: Van der Waals interactions of 1-((1R,2R)-1,3-dihydroxy-1-(4-nitrophenyl)propan-2-yl)-3-(3,5-dimethylphenyl)thiourea with the CAM acetyl transferase amino acids

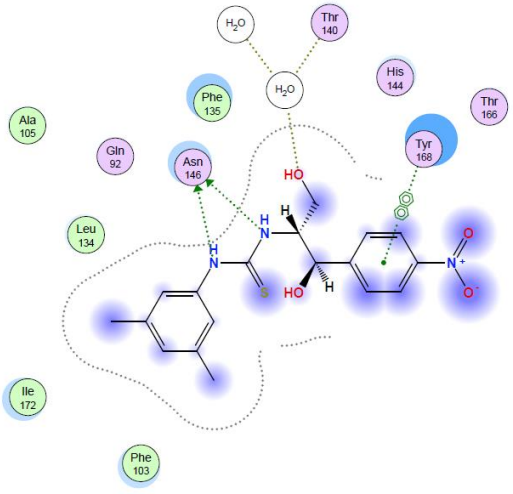

Figure 7.67: Ligand interaction diagram of 1-((1R,2R)-1,3-dihydroxy-1-(4-nitrophenyl)propan-2-yl)-3-(3,5-dimethylphenyl)thiourea for the CAM acetyl transferase enzyme

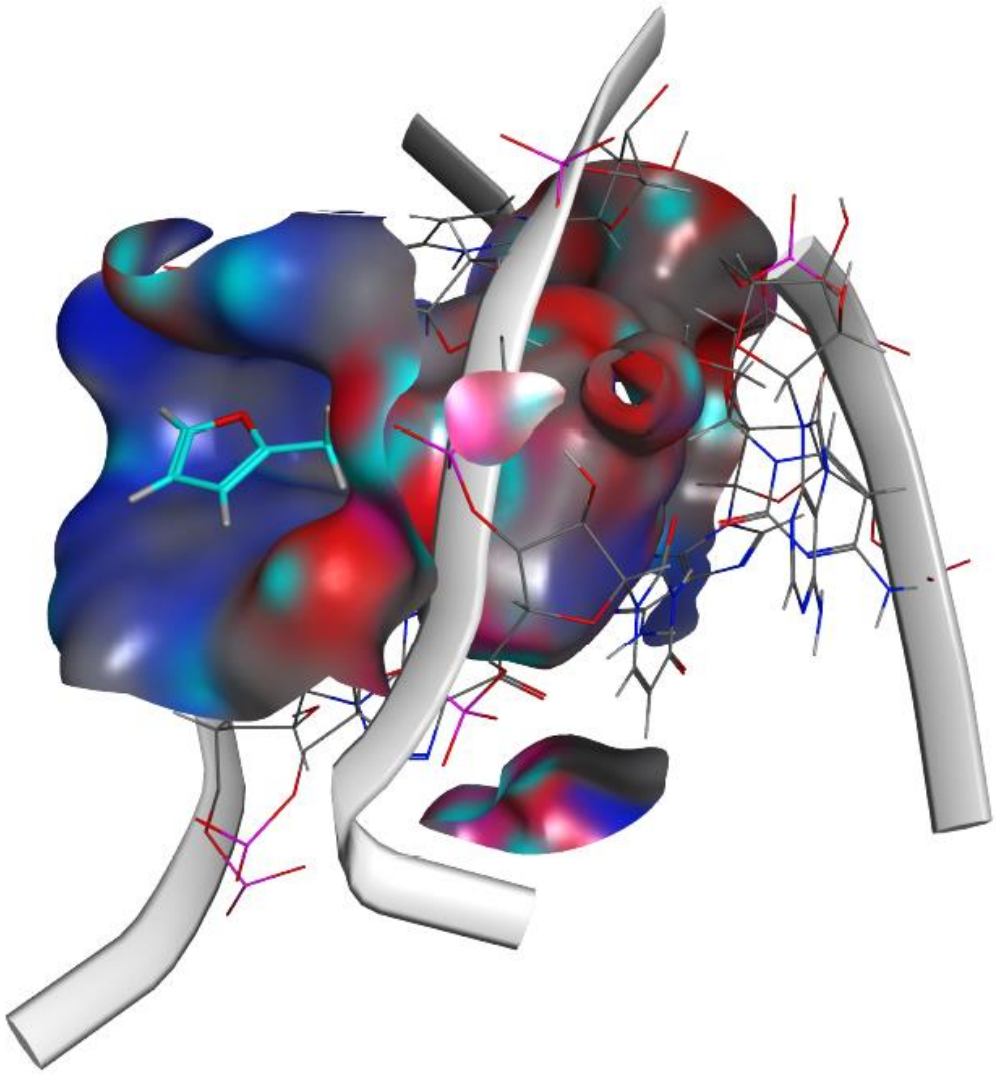

Figure 7.68: Binding of 1-(2,5-dihydrofuran-2-yl)-3-((1R,2R)-1,3-dihydroxy-1-(4-nitrophenyl)propan-2-yl)thiourea to the ribosome pocket, with the generated surface for the receptor

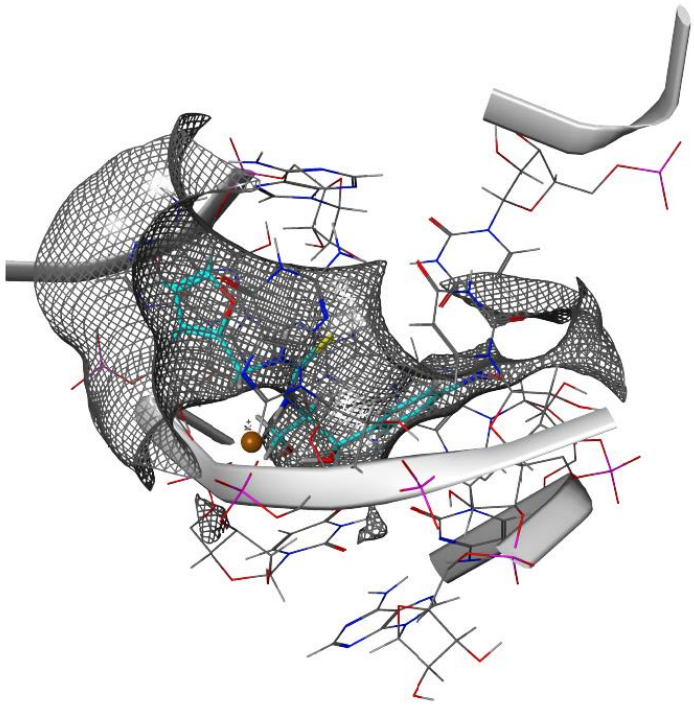

Figure 7.69: Van der Waals interactions of 1-(2,5-dihydrofuran-2-yl)-3-((1R,2R)-1,3-dihydroxy-1-(4-nitrophenyl)propan-2-yl)thiourea with the ribosome amino acids

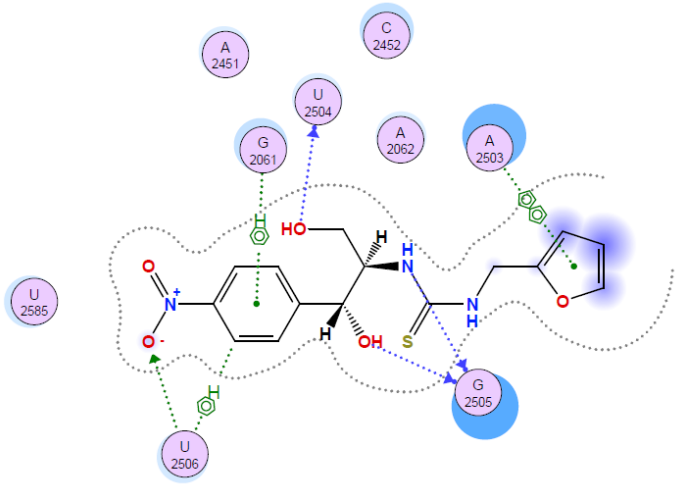

Figure 7.70: Ligand interaction diagram of 1-(2,5-dihydrofuran-2-yl)-3-((1R,2R)-1,3-dihydroxy-1-(4-nitrophenyl)propan-2-yl)thiourea to the ribosome

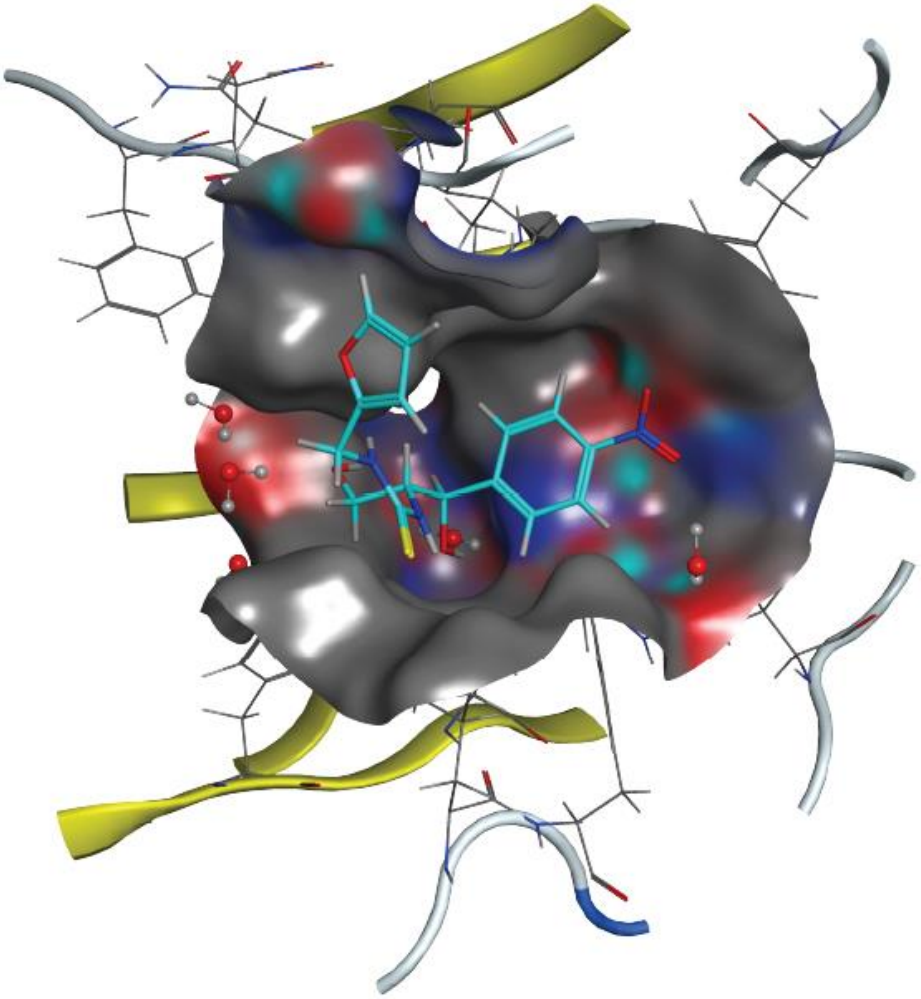

Figure 7.71: Binding of 1-(2,5-dihydrofuran-2-yl)-3-((1R,2R)-1,3-dihydroxy-1-(4-nitrophenyl)propan-2-yl)thiourea to the CAM acetyl transferase pocket, with the generated surface for the receptor

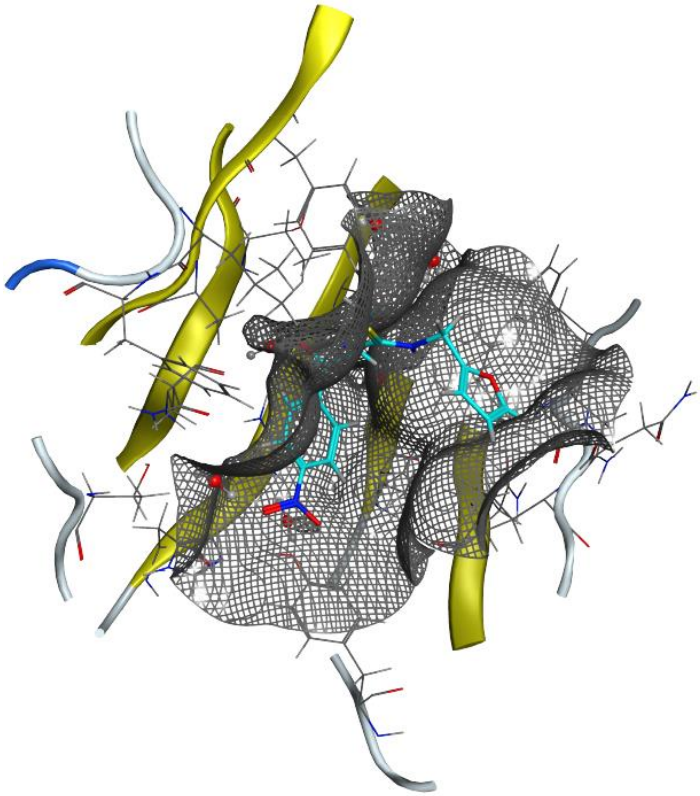

Figure 7.72: Van der Waals interactions of 1-(2,5-dihydrofuran-2-yl)-3-((1R,2R)-1,3-dihydroxy-1-(4-nitrophenyl)propan-2-yl)thiourea with the CAM acetyl transferase amino acids

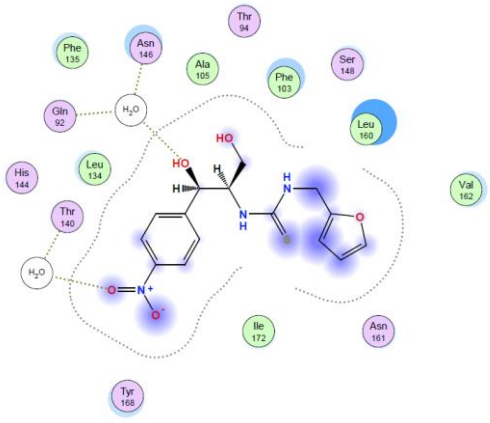

Figure 7.73: Ligand interaction diagram of 1-(2,5-dihydrofuran-2-yl)-3-((1R,2R)-1,3-dihydroxy-1-(4-nitrophenyl)propan-2-yl)thiourea for the CAM acetyl transferase enzyme

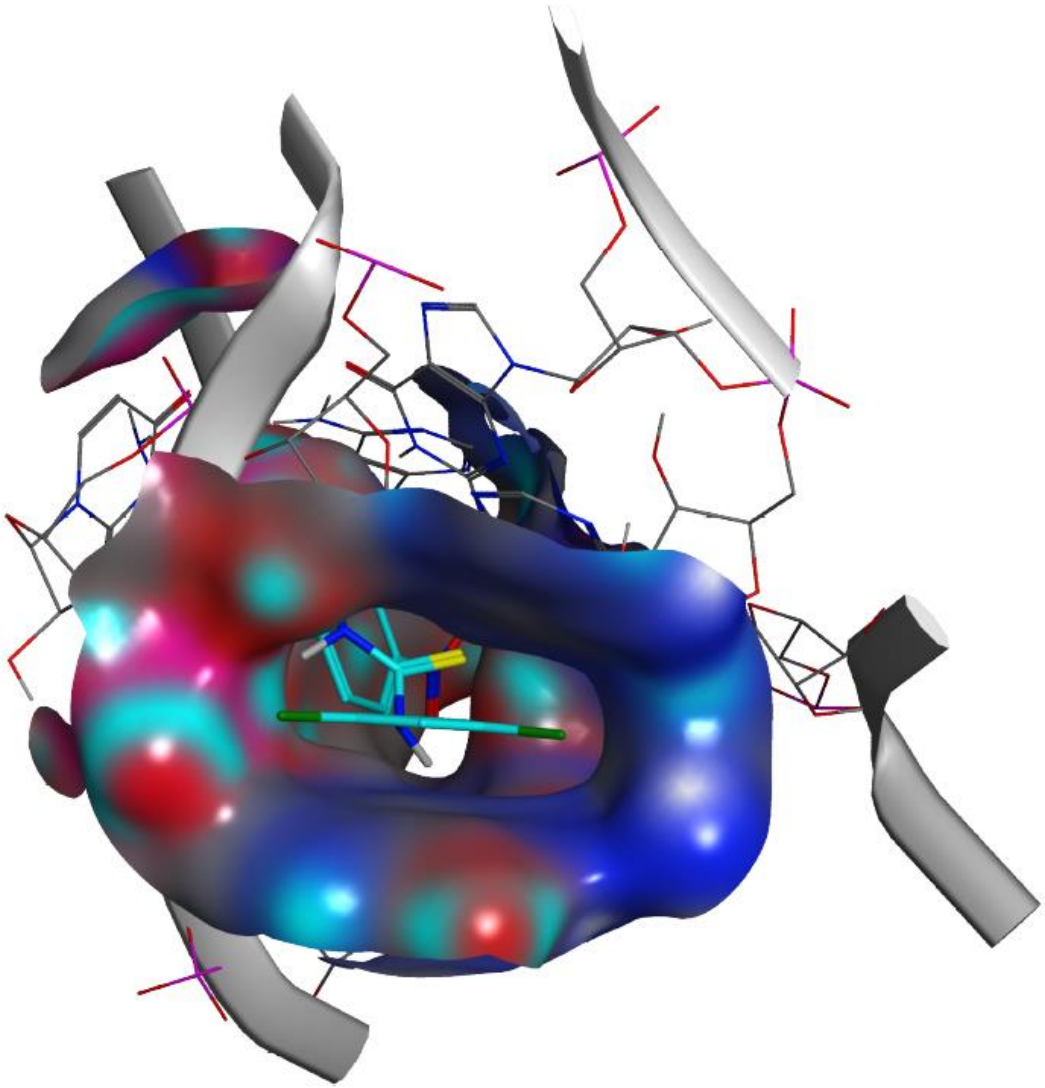

Figure 7.74: Binding of 1-(3,5-dichlorophenyl)-3-((1R,2R)-1,3-dihydroxy-1-(4-nitrophenyl)propan-2-yl)thiourea to the ribosome pocket, with the generated surface for the receptor

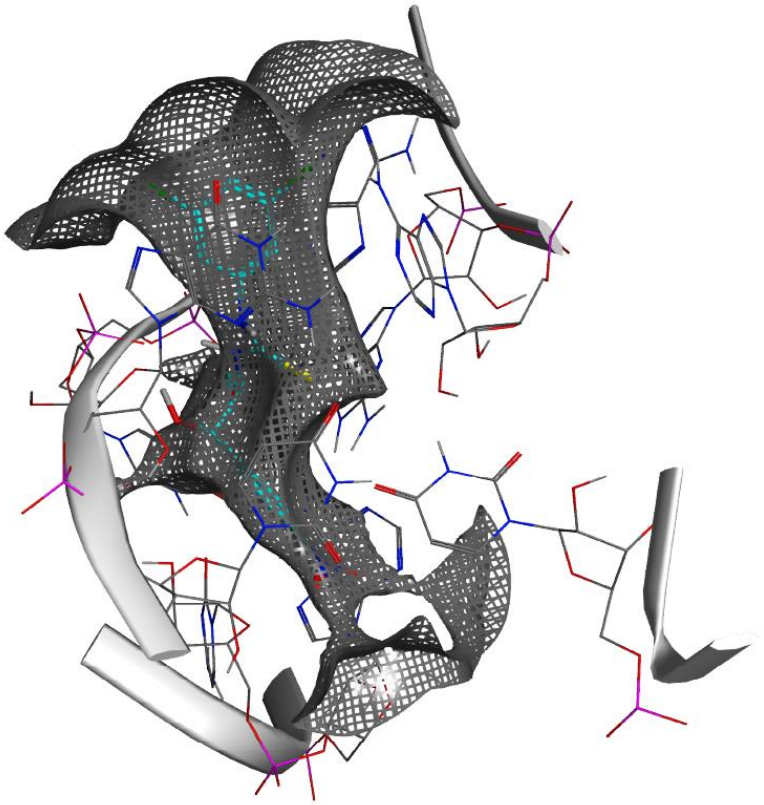

Figure 7.75: Van der Waals interactions of 1-(3,5-dichlorophenyl)-3-((1R,2R)-1,3-dihydroxy-1-(4-nitrophenyl)propan-2-yl)thiourea with the ribosome amino acids

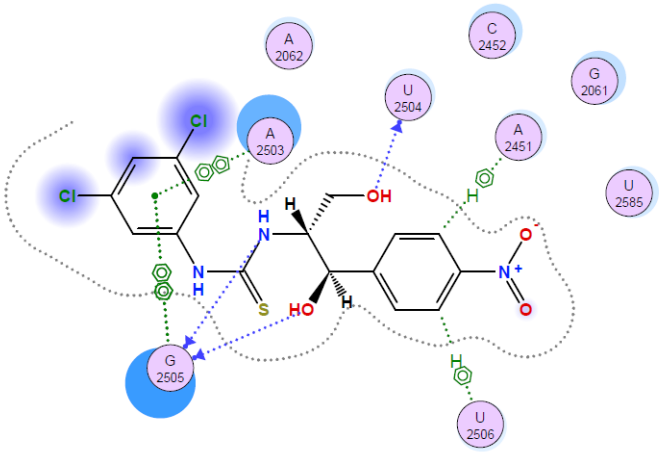

Figure 7.76: Ligand interaction diagram of 1-(3,5-dichlorophenyl)-3-((1R,2R)-1,3-dihydroxy-1-(4-nitrophenyl)propan-2-yl)thiourea to the ribosome

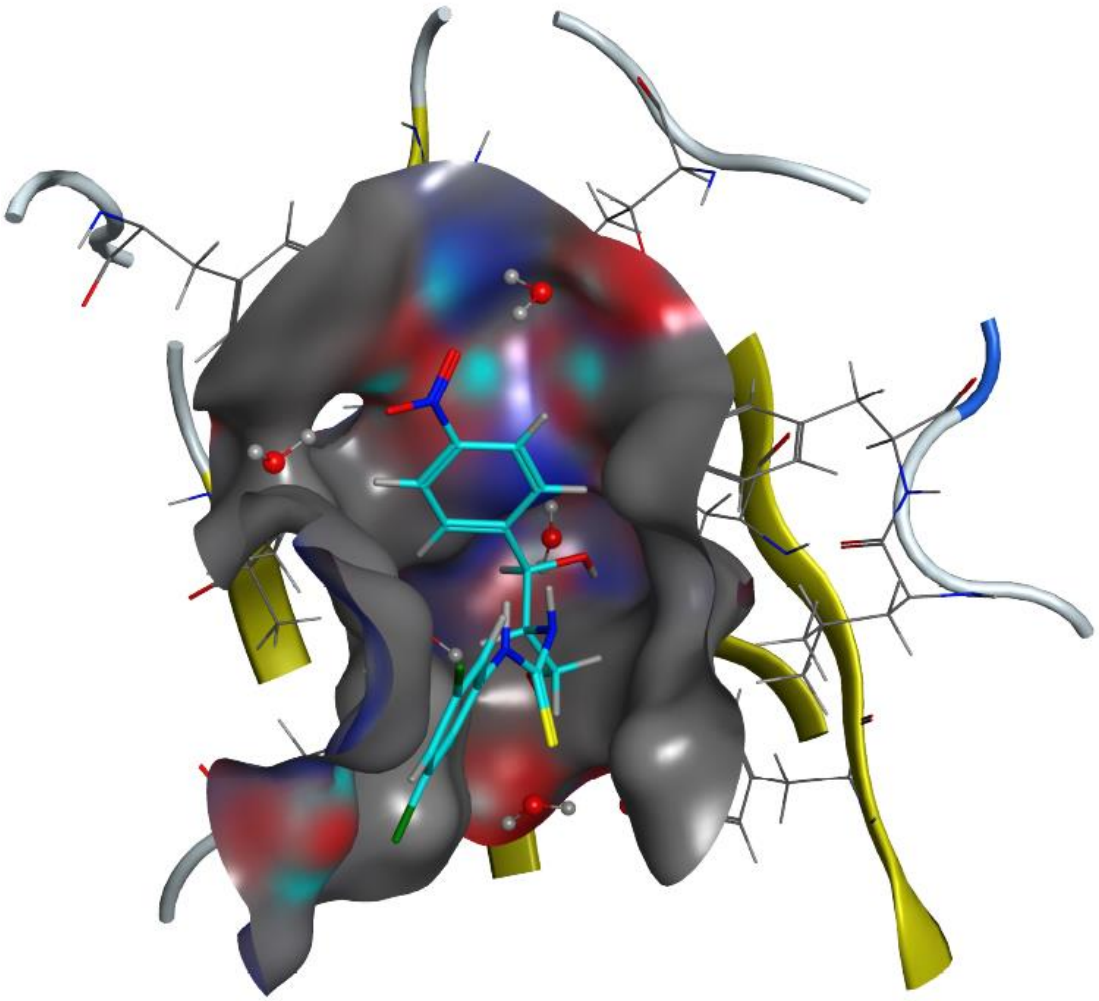

Figure 7.77: Binding of 1-(3,5-dichlorophenyl)-3-((1R,2R)-1,3-dihydroxy-1-(4-nitrophenyl)propan-2-yl)thiourea to the CAM acetyl transferase pocket, with the generated surface for the receptor

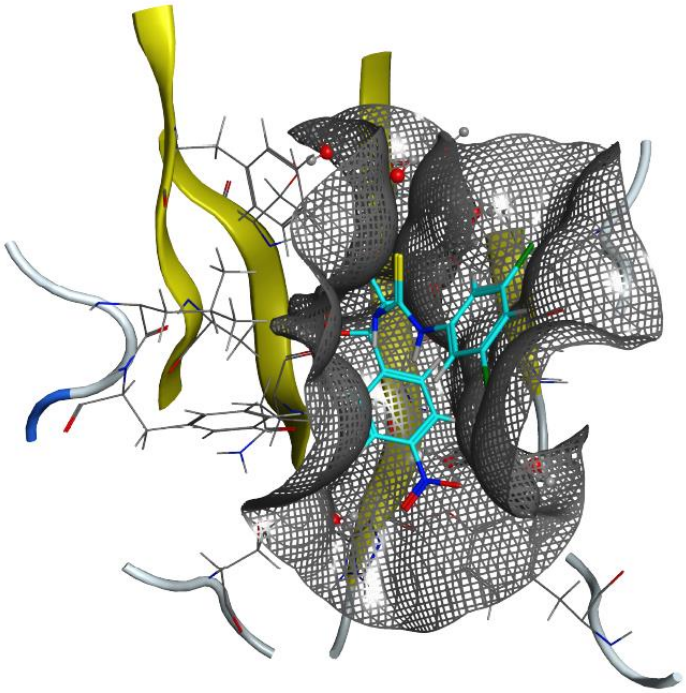

Figure 7.78: Van der Waals interactions of 1-(3,5-dichlorophenyl)-3-((1R,2R)-1,3-dihydroxy-1-(4-nitrophenyl)propan-2-yl)thiourea with the CAM acetyl transferase amino acids

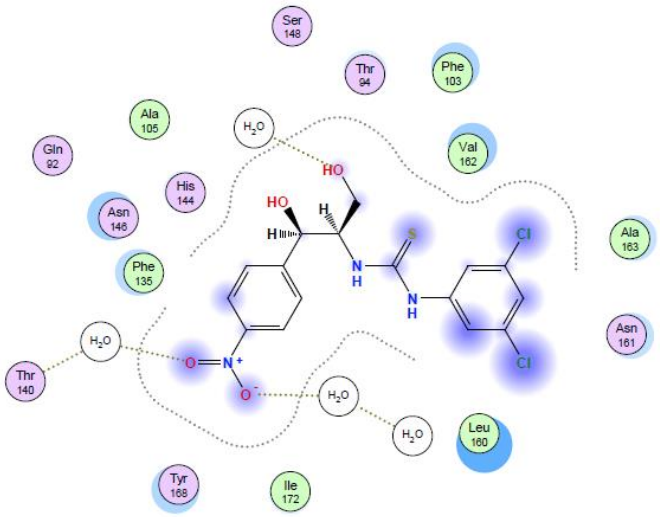

Figure 7.79: Ligand interaction diagram of 1-(3,5-dichlorophenyl)-3-((1R,2R)-1,3-dihydroxy-1-(4-nitrophenyl)propan-2-yl)thiourea for the CAM acetyl transferase enzyme

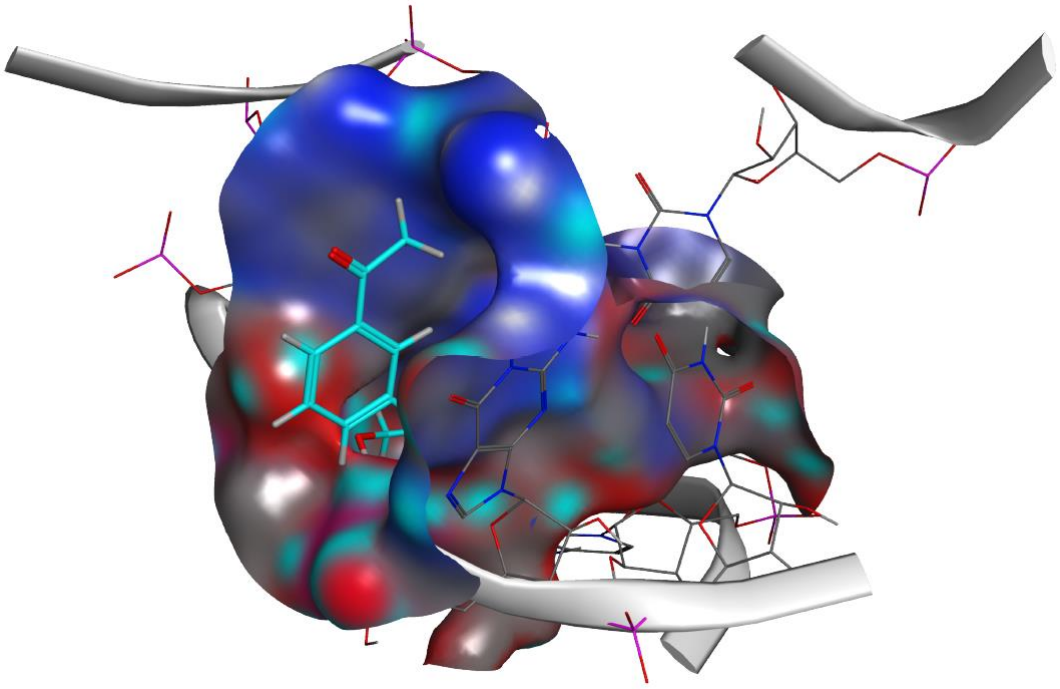

Figure 7.80: Binding of 1-(4-acetylphenyl)-3-((1R,2R)-1,3-dihydroxy-1-(4-nitrophenyl)propan-2-yl)thiourea to the ribosome pocket, with the generated surface for the receptor

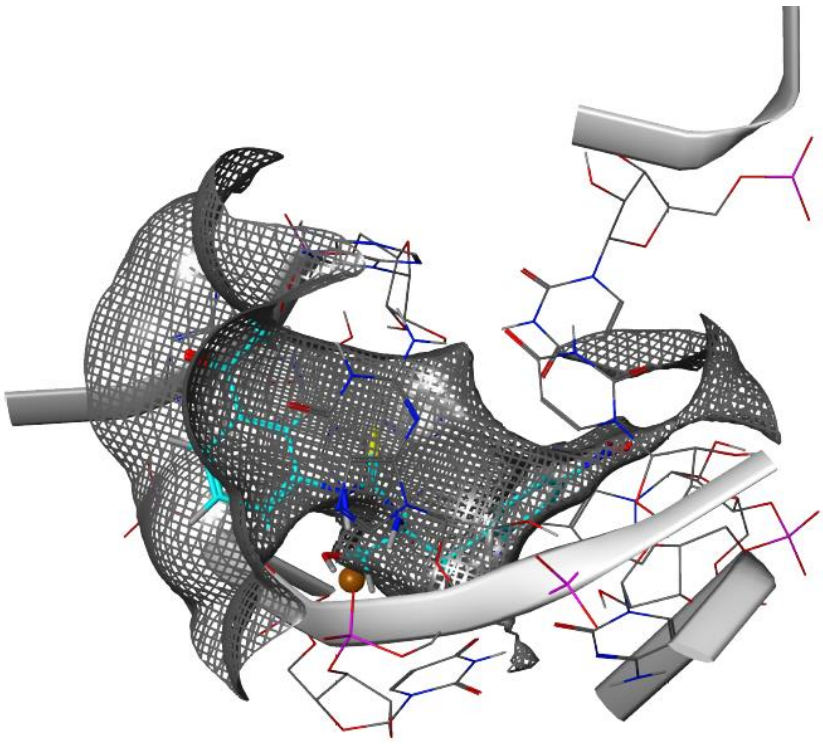

Figure 7.81: Van der Waals interactions of 1-(4-acetylphenyl)-3-((1R,2R)-1,3-dihydroxy-1-(4-nitrophenyl)propan-2-yl)thiourea with the ribosome amino acids

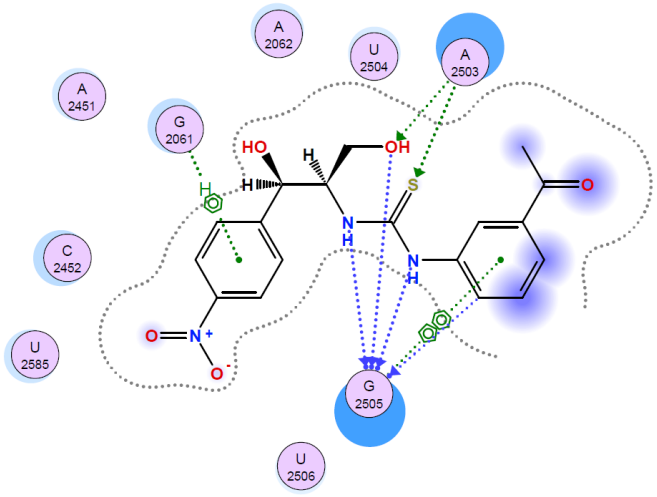

Figure 7.82: Van der Waals interactions of 1-(4-acetylphenyl)-3-((1R,2R)-1,3-dihydroxy-1-(4-nitrophenyl)propan-2-yl)thiourea with the ribosome amino acids

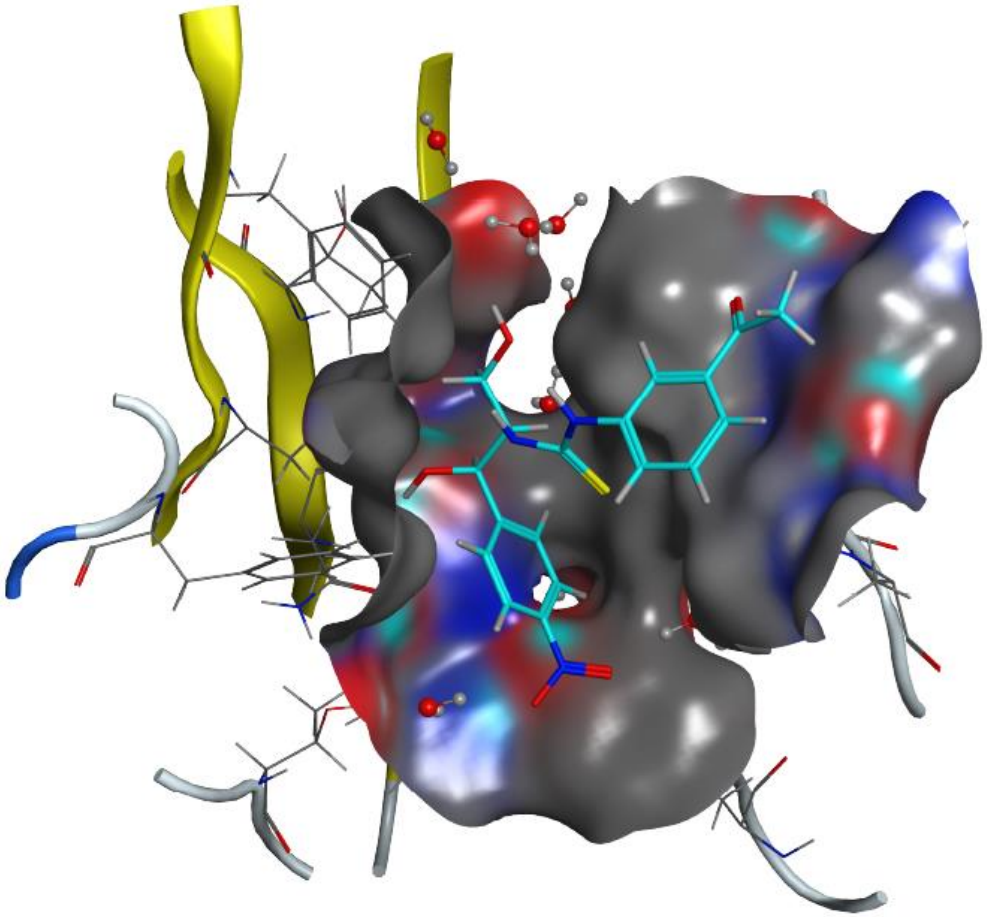

Figure 7.83: Binding of 1-(4-acetylphenyl)-3-((1R,2R)-1,3-dihydroxy-1-(4-nitrophenyl)propan-2-yl)thiourea to the CAM acetyl transferase pocket, with the generated surface for the receptor

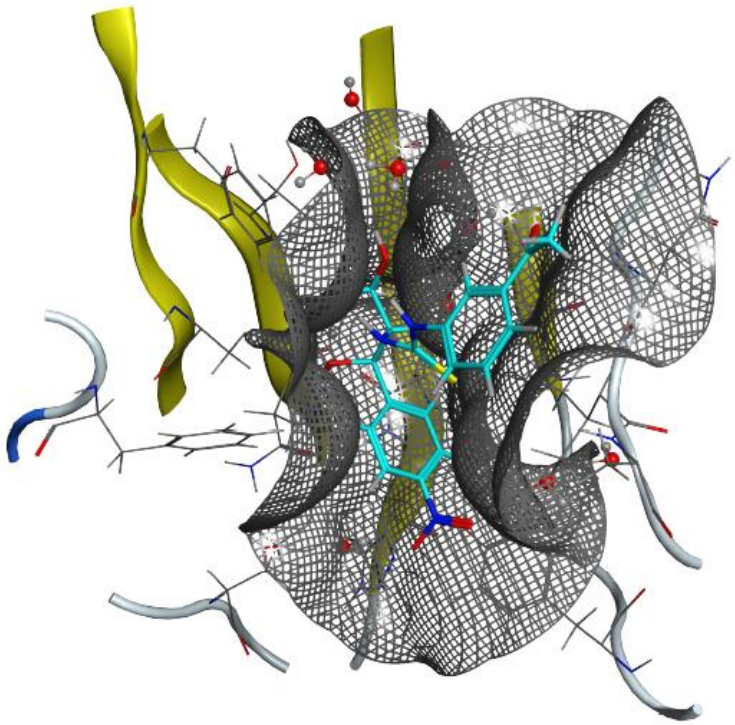

Figure 7.84: Binding of 1-(4-acetylphenyl)-3-((1R,2R)-1,3-dihydroxy-1-(4-nitrophenyl)propan-2-yl)thiourea to the CAM acetyl transferase pocket, with the generated surface for the receptor

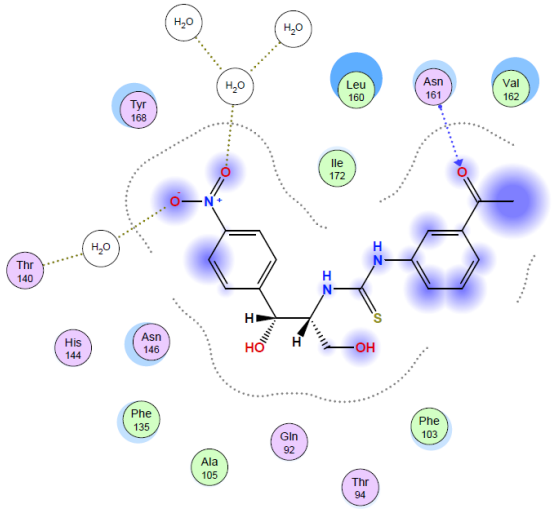

Figure 7.85: Ligand interaction diagram of 1-(4-acetylphenyl)-3-((1R,2R)-1,3-dihydroxy-1-(4-nitrophenyl)propan-2-yl)thiourea for the CAM acetyl transferase enzyme

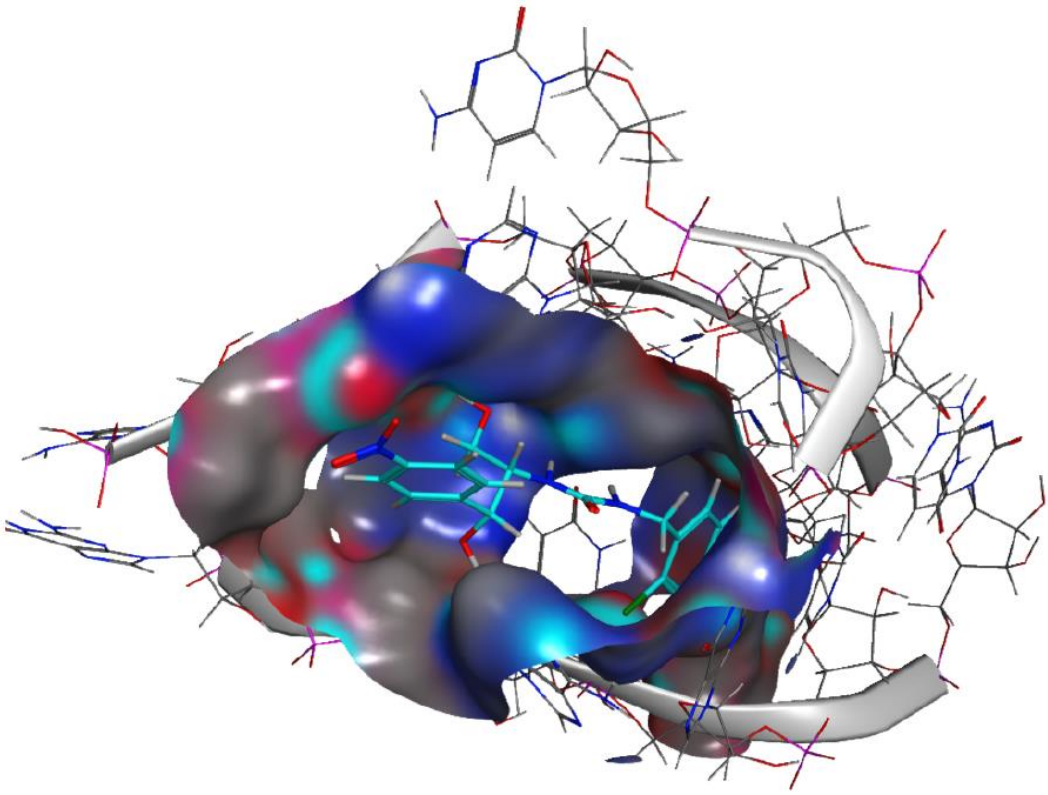

Figure 7.86: Binding of 1-(2-chloro-4-nitrophenyl)-3-((1R,2R)-1,3-dihydroxy-1-(4-nitrophenyl)propan-2-yl)thiourea to the ribosome pocket, with the generated surface for the receptor

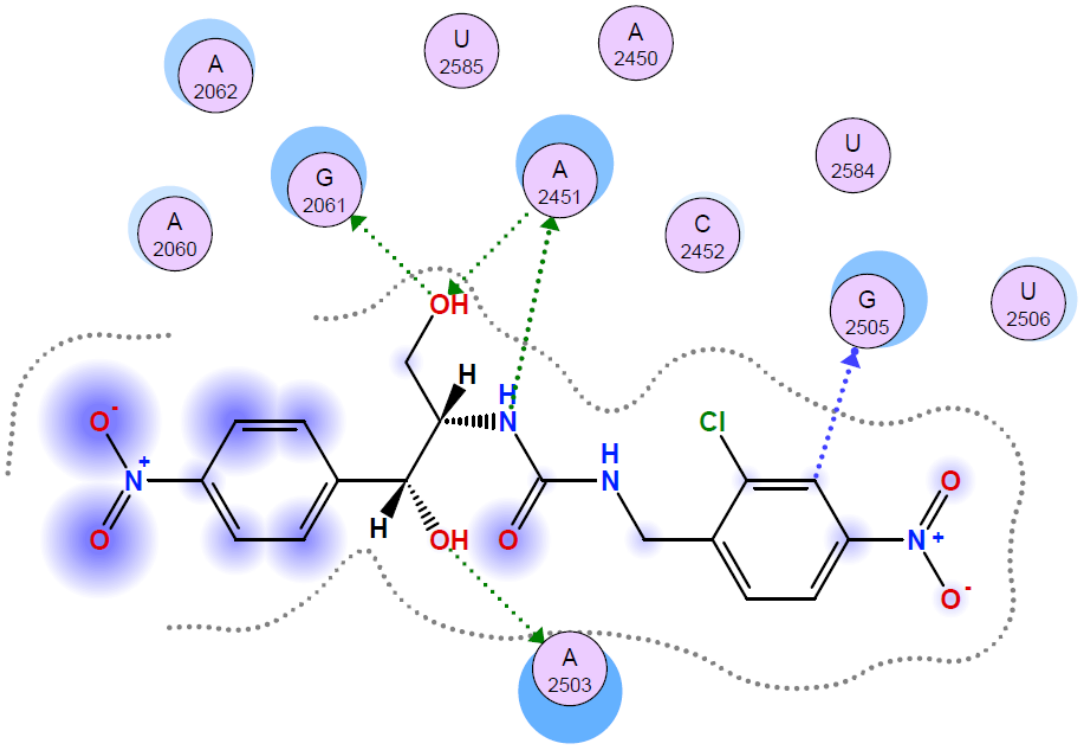

Figure 7.87: Ligand interaction diagram of 1-(2-chloro-4-nitrophenyl)-3-((1R,2R)-1,3-dihydroxy-1-(4-nitrophenyl)propan-2-yl)thiourea to the ribosome

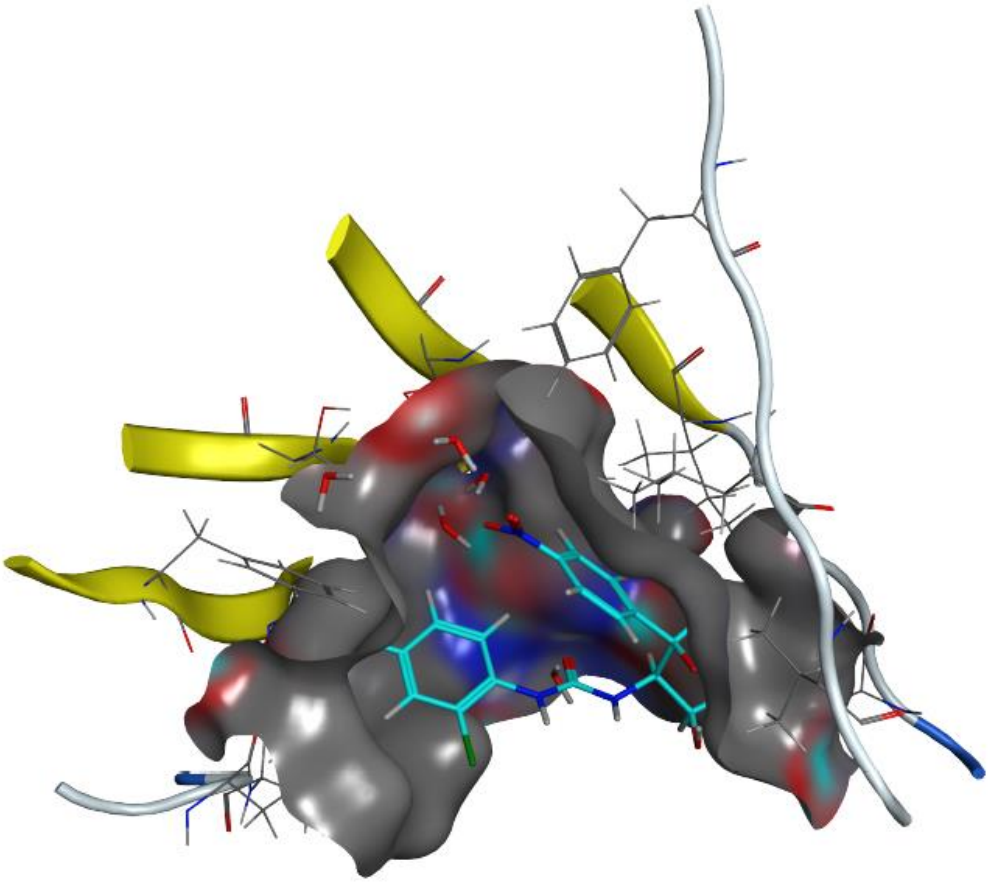

Figure 7.88: Binding of 1-(2-chloro-4-nitrophenyl)-3-((1R,2R)-1,3-dihydroxy-1-(4-nitrophenyl)propan-2-yl)thiourea to the CAM acetyl transferase pocket, with the generated surface for the receptor

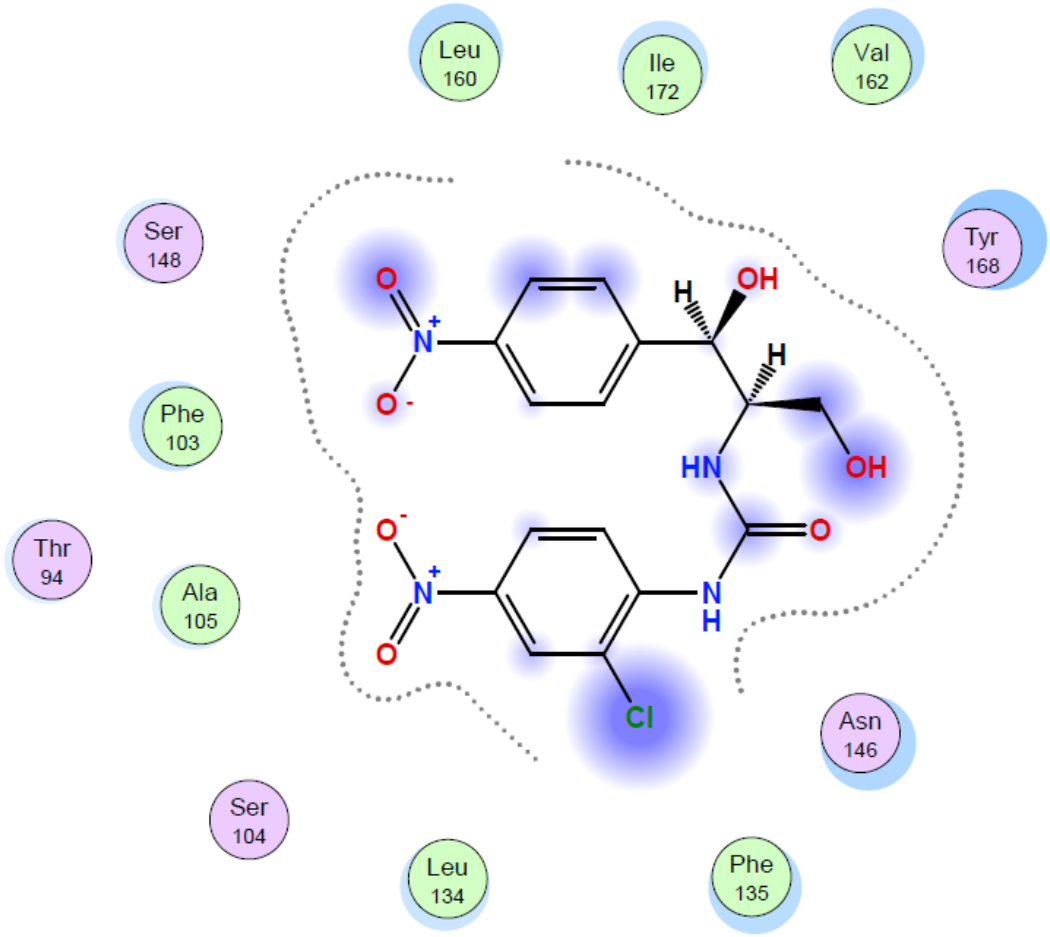

Figure 7.89: Ligand interaction diagram of 1-(2-chloro-4-nitrophenyl)-3-((1R,2R)-1,3-dihydroxy-1-(4-nitrophenyl)propan-2-yl)thiourea for the CAM acetyl transferase enzyme